

法人番号	231029
プロジェクト番号	S1201019

**平成24年度～平成28年度「私立大学戦略的研究基盤形成支援事業」  
研究成果報告書概要**

- 1 学校法人名 名城大学      2 大学名 名城大学
- 3 研究組織名 名城大学・窒化物半導体基盤技術研究センター
- 4 プロジェクト所在地 名古屋市天白区塩釜口1-501 名城大学天白キャンパス内
- 5 研究プロジェクト名 窒化物半導体・新領域エレクトロニクス
- 6 研究観点 研究拠点を形成する研究(5年)

## 7 研究代表者

研究代表者名	所属部局名	職名
赤崎 勇	理工学研究科	教授

プロジェクト参加研究者数 7 名

- 9 該当審査区分 理工・情報      生物・医歯      人文・社会

## 10 研究プロジェクトに参加する主な研究者

研究者名	所属・職名	プロジェクトでの研究課題	プロジェクトでの役割
赤崎 勇	名城大学・理工学研究科・教授	窒化物半導体の結晶成長技術の革新とそれによる革新的な窒化物半導体デバイスの実現	窒化物半導体ナノ構造/超ヘテロ構造の導入
上山 智	名城大学・理工学研究科・教授	半導体ナノ構造技術と光デバイスへの応用	ナノコラム結晶成長、ナノ構造の物性評価、高性能ナノ発光材料、デバイスの実現
竹内 哲也	名城大学・理工学研究科・准教授	窒化物半導体の結晶成長技術の革新とそれによる革新的な窒化物半導体デバイスの実現	Sb・B を窒化物半導体に添加する技術を開発し、革新的なデバイスを実現する
岩谷 素顕	名城大学・理工学研究科・准教授	窒化物半導体のデバイスプロセス技術の革新・貼り合わせ・基板剥離技術の確立・ドーピング技術の確立・電子線励起レーザ・太陽電池・ディテクターの実現	貼り合わせ・基盤剥離技術やプラズモンを活用する技術を開発する

法人番号	231029
プロジェクト番号	S1201019

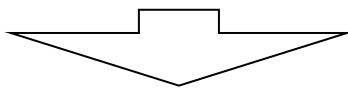
(共同研究機関等) 天野 浩	名古屋大学・工学研究科・教授	窒化物半導体の結晶成長技術の革新とそれによる革新的な窒化物半導体デバイスの実現	窒化物半導体ナノ構造/超ヘテロ構造による GaInN・AlGaIn の開拓
Christian Wetzel	レンセラー工科大学・教授	窒化物半導体の結晶成長技術の革新とそれによる革新的な窒化物半導体デバイスの実現	高 InN モル分率 GaInN によるデバイスの開拓
Haiyan Ou	デンマーク工科大学・准教授	窒化物半導体のデバイスプロセス技術の革新	金属プラズモンの応用

<研究者の変更状況(研究代表者を含む)>

旧

プロジェクトでの研究課題	所属・職名	研究者氏名	プロジェクトでの役割

(変更の時期:平成 26 年 4 月 1 日)



新

変更前の所属・職名	変更(就任)後の所属・職名	研究者氏名	プロジェクトでの役割
ソニー株式会社	名城大学・理工学研究科・教授	宮嶋 孝夫	窒化物半導体の物性の解明

法人番号	231029
プロジェクト番号	S1201019

## 11 研究の概要(※ 項目全体を10枚以内で作成)

## (1) 研究プロジェクトの目的・意義及び計画の概要

本研究拠点を形成する目的は、これまで窒化物半導体研究において世界的に高い成果を残してきた名城大学 窒化物半導体基盤技術研究センターを中核に、名古屋大学、デンマーク工科大学、およびレンセラー工科大学の研究グループなど世界中の研究機関の技術を結集することによって、新しい結晶成長技術・デバイスプロセス技術を確立する。具体的には、窒化物半導体トンネル接合、窒化物半導体ナノコラム結晶の作製技術、さらにはウェハ接合技術など窒化物半導体において新機能デバイスを実現する上で不可欠な基盤技術の確立をすることを目標に研究を進めた。さらにこれらの基盤技術を基に、最終的に革新的なデバイスの実現し、世界に情報を発信する研究拠点として整備することが本研究課題の目的・意義である。

## (2) 研究組織

学内:

本研究プロジェクトにこれまで参画した研究者は以下の 8 名(学内 5 名、学外 3 名)である

所属・職	研究者名	研究プロジェクトにおける研究課題	当該研究課題の成果が研究プロジェクトに果たす役割
理工学研究科・教授	赤崎 勇	研究総括	窒化物半導体・新領域エレクトロニクスの実現
理工学研究科・教授	上山 智	窒化物半導体ナノ構造の作製・表面プラズモン・高濃度 Si ドーピング	窒化物半導体・新領域エレクトロニクスの実現
理工学研究科・准教授	竹内 哲也	アンチモン・ボロン添加窒化物半導体の実現・AlInN 結晶成長・トンネル接合	窒化物半導体・新領域エレクトロニクスの実現
理工学研究科・准教授	岩谷 素顕	貼り合わせ・基板剥離技術の確立・ドーピング技術の確立・電子線励起レーザ・太陽電池・ディテクターの実現	窒化物半導体・新領域エレクトロニクスの実現
理工学研究科・教授	宮嶋 孝夫	窒化物半導体光物性の解析と評価	窒化物半導体の物理の解明(H26 年度より研究組織に追加)

## その他 (特記事項)

H24 から H26 年 3 月まで博士研究員として飯田大輔を雇用し、研究に参加させてきた。主に結晶成長全般およびプラズモンを用いた LED、基板剥離技術等を担当した。H26 年 4 月から東京理科大学・理学部応用物理学科・助教として栄転・着任し、H29.3 からサウジアラビア・

法人番号	231029
プロジェクト番号	S1201019

KAIST の Assistant Professor として着任予定である。

さらに、H27 から H29 年 3 月まで、博士研究員として小出典克を雇用し、研究に参画させてきた。

大学院生に関しては本研究グループで以下の通りである。

H24 博士課程学生 3 名 修士課程学生 39 名 (修了 19 名)

H25 博士課程学生 3 名(修了 1 名) 修士課程学生 39 名 (修了 18 名)

H26 博士課程学生 2 名 修士課程学生 35 名 (修了 20 名)

H27 博士課程学生 5 名 修士課程学生 38 名 (修了 17 名)

H28 博士課程学生 5 名(修了 2 名) 修士課程学生 36 名(修了 18 名)

H26 から 2 名の博士課程学生(松井健城・安田俊輝)、さらに H27 から 1 名を追加(小塚祐吾)を RA として雇用し、本戦略的基盤形成支援事業の取組に従事させている。上記の大学院生および博士研究員は招待講演 6 件、受賞 12 件などの成果をあげた。

また、研究支援のため秘書を 3 名雇用している(大学予算・科研費・奨学寄附金で執行)

#### 共同研究機関等の連携状況

所属・職	研究者名	研究プロジェクトにおける研究課題	当該研究課題の成果が研究プロジェクトに果たす役割
名古屋大学・教授	天野 浩	窒化物ナノワイヤ・量子ドット・原子層エピタキシーの成長・評価・デバイス応用、電子線励起レーザーや太陽電池、分極を用いた紫外 LED の開発等で連携	窒化物半導体・新領域エレクトロニクスの実現
デンマーク工科大学・准教授	Haiyan Ou	表面プラズモンの理論計算と作製、PD の飯田大輔を派遣、博士課程学生を 2 名(各 1~2 か月)受け入れ	窒化物半導体・新領域エレクトロニクスの実現
レンセラー工科大学・教授	Christian Wetzel	緑色領域の LED 作製、太陽電池の作製	窒化物半導体・新領域エレクトロニクスの実現

#### (3) 研究施設・設備等

(研究施設)◆クリーンルーム 150m<sup>2</sup>+155m<sup>2</sup>、デバイス・光学評価室 55m<sup>2</sup> 使用者: 4 名  
(研究装置)◆有機金属化合物気相成長装置(①、④、⑩、29に相当) 4 台(利用時間: 1 日 12 時間)◆フォトリソグラフィ装置(⑧、⑪)+電子ビーム露光装置(30)(利用時間: 1 日 12 時間)◆ICP エッチング 装置(⑤)(利用時間: 1 日 12 時間)◆エキシマレーザー(31)(利用時間: 1 日 12 時間)◆EB 蒸着装置(28)(利用時間: 1 日 12 時間) ◆スパッタリング装置(32)(利用時間: 1 日 12 時間)◆カソードルミネッセンス装置付き走査電子顕微鏡(2,15)(利用時間:

法人番号	231029
プロジェクト番号	S1201019

1日5時間)◆FIB・マイクロサンプリング機能付き透過電子顕微鏡(利用時間: 1日3時間)  
 (33)◆X線回折装置(34)(利用時間: 1日12時間)◆フォトルミネッセンス装置(利用時間:  
 1日3時間)◆レーザ顕微鏡装置(35)(利用時間: 1日3時間)◆半導体デバイス評価装置  
 (14、27、26)(利用時間: 1日3時間)◆結晶評価装置(3、12、17、21、25)(利用時間: 1日  
 12時間)◆デバイスシミュレータ(SiLENSe、TCAD等)(利用時間: 1日12時間)  
 および本予算で導入したウェハー接合装置(9)(H24)(利用時間: 1日12時間)、半導体原  
 料供給設備(22)(利用時間: 1日12時間)、昇華法装置(H25)(7)(利用時間: 1日6時間)

(4)研究成果の概要 ※下記、13及び14に対応する成果には下線及び\*を付すこと。

<現在までの進捗状況及び達成度>

本研究グループは、窒化物半導体材料を中核とし、これまでに世界で初めて同材料の高品質単結晶の実現、伝導性制御などを達成し、世界に先駆けて窒化物半導体による青色/紫色LEDをはじめ、世界最短波長半導体レーザ、高効率紫外LED、超高速トランジスタなど、フロンティアデバイスを実現してきた。本研究プロジェクトでは、これまで構築してきた研究基盤を基に結晶成長技術およびデバイスプロセス技術を革新し、最終的に革新的なデバイスの実現を目指すことを目指している。結晶成長・デバイスプロセスにおいて以下のような成果を残した。

1. 有機金属化合物気相成長法におけるその場観察X線回折測定法の確立を行い、それをGaNおよびGaInN/GaNヘテロ接合に適用する技術を確認(\*1に対応)
2. アンチモンを窒化物半導体に0.4%取り込むことに成功(\*2に対応)
3. AllnNの高速・高品質結晶成長技術の確立(\*3に対応)
4. デバイス適用可能な超低抵抗n型窒化物半導体( $5.9 \times 10^{-4} \Omega \text{cm}$ )の実現(\*4に対応)
5. 低抵抗窒化物半導体トンネル接合およびそれをデバイスに適用(\*5に対応)
6. バルクAlN基板上へのホモエピタキシャル成長技術の確立(\*6に対応)
7. 紫外/可視LEDにおける分極の理解(\*7に対応)
8. ITO電極を用いた基板貼り合わせ技術を確認(\*8に対応)
9. AlGaInPと窒化物半導体の直接接合技術を確認(\*9に対応)
10. GaN基板からのレーザ剥離技術を確認(\*10に対応)
11. ナノインプリントを用いたプラズモン適用技術を確認(\*11に対応)
12. AlGaInPと窒化物半導体をITOを用いたウェハ接合技術の確立
13. ナノコラム結晶・量子殻構造の作製技術の確立
14. 周期利得構造を目指した電子・正孔注入効率を制御する技術を確認

さらに、これらの結晶成長技術/デバイスプロセスを基に以下のような革新的なデバイスを実現した。

- ① 窒化物半導体・超高感度・可視光/紫外線ディテクターの実現(受光感度  $10^4 \text{A/W}$  以上)の実現(\*12に対応)
- ② 窒化物半導体において世界最高効率の変換効率を持つ太陽電池の実現(\*13に対応)
- ③ GaN/AlGaIn系においては世界初となる電子線励起のレーザの実現(\*14に対応)
- ④ 反射率99.9%以上のAllnN半導体多層膜反射鏡の実現(\*15に対応)
- ⑤ キャリア注入制御2波長で発光する窒化物半導体可視LEDの実現(\*16に対応)
- ⑥ 電流ドループが極めて少ない近紫外LEDの実現(\*17に対応)
- ⑦ トンネル接合を用いた電流狭窄・マイクロLEDの実現(\*18に対応)
- ⑧ 窒化物半導体トンネル接合を用いた多接合窒化物半導体太陽電池の実現(\*19に対応)
- ⑨ 光出力3mW(世界最高出力:H29.3時点)の窒化物半導体面発光レーザを実現
- ⑩ 窒化物半導体面発光レーザに於いて、DBR層に電流を流す縦伝導デバイスを実現
- ⑪ 周期利得構造を用いたデバイス構造において、窒化物半導体面発光レーザを実現

法人番号	231029
プロジェクト番号	S1201019

上記のように、この約 5 年間で予定していた研究内容に加え、新たなるデバイスを実現するなどの成果を残してきた。

#### <優れた成果が上がった点>

上記に記載した研究成果のうち特に優れた研究成果としては、①有機金属化合物気相成長法におけるその場観察 X 線回折測定法の確立を行い、それを GaN、GaInN/GaN ヘテロ接合、AlGaIn/GaN 接合、GaInN/GaN 超格子構造に適用する技術を確立②窒化物半導体・超高感度・可視光/紫外線ディテクターの実現、③GaN においては世界初となる電子線励起のレーザの実現④キャリア注入を制御することによって 2 波長で発光する LED の実現⑤低抵抗窒化物半導体トンネル接合の実現⑥窒化物半導体太陽電池において世界最高効率⑦分極ドーピングを紫外 LED に適用⑦世界最高出力の窒化物半導体系面発光レーザを実現があげられる。以下に本成果の概説をする。

① 有機金属化合物気相成長法におけるその場観察 X 線回折測定法の確立を行い、それを GaN および GaInN/GaN ヘテロ接合に適用する技術を確立

窒化物半導体デバイスのほとんどは有機金属化合物気相成長法で作製されている。その結晶成長技術を極限まで追求する上で、その場観察技術は極めて重要である。これまでに、光を用いた、膜厚・基板の反り・温度等をその場観察する技術が広く報告されており、実際にデバイス製造に用いられている。本研究ではさらに一歩進め、X 線を用いたその場観察技術を検討した。これまでの検討で、光では観測できなかった GaInN の緩和過程を正確にモニターすることが可能であることを報告するなど極めて優れた成果を残した。これらの成果は 5 件の招待講演、学生の受賞 1 件など対外的に高い評価を得ている。

② 窒化物半導体・超高感度・可視光/紫外線ディテクターの実現

窒化物半導体のバンドギャップエネルギーは紫外から可視全域、赤外領域にわたっており、発光素子だけでなく受光素子としての応用も期待されている。これまで、本グループをはじめとした世界中の研究機関から pin フォトダイオードや光導電セルなど様々なデバイスが報告されてきたが、受光感度が低いことなど実用化には程遠い物しか得られていなかった。本研究課題では、その問題点を解決するために、AlGaIn/GaN ヘテロ接合を用いた 2 次元電子ガスと pn 接合によって形成された空乏層を活用する構造を新たに開発し、それによって極めて高い受光感度が得られることを明らかにした。本デバイスの性能は、既存の窒化物半導体を用いた受光素子の性能を凌駕するだけでなく、Si を用いた pin フォトダイオードやアバランシェフォトダイオードの受光感度を 3~4 桁程度凌駕しており、受光素子としては最も受光感度が高い光電子増倍管と同程度の物を実現可能であることを明らかにした。また、受光波長は AlGaIn の組成や p 型層に GaInN を用いることによって制御可能であることも明らかにした。これらのデバイスは、紫外 LED の実用化にともないキーデバイスとして発展していくことが期待される。これらの成果は招待講演が 4 件、学生の受賞が 2 件に選出されるなど高い評価を得ている。

③窒化物半導体系においては世界初となる電子線励起のレーザの実現

窒化物半導体レーザは、これまでに青紫色・青色・緑色レーザが実用化されているが、物性的には紫外領域や可視全域、さらには赤外領域に互っている。このうち紫外領域は他の半導体材料では実現困難な領域であり、医療や工業用途向けに実現が強く期待されている。本研究グループでは、世界最短波長紫外レーザの実現(2007 年:当時)をするなど世界に先駆けた成果を多数残してきたが、さらなる短波長化は現状の技術の延長線では困難である。その最も大きな理由は、高い正孔濃度を持つ p 型 AlGaIn を実現することが困難であり、そのためレーザ発振に必要な電流注入ができないということである。その問題点を解決するためには他のキャリア注入の手法を確立することが重要であり、本グループでは電子線励起に注目した。電子線励起は電流注入の問題がなくなり、紫外レーザの実現が可能になると期待さ

法人番号	231029
プロジェクト番号	S1201019

れるが、これまで窒化物半導体材料において電子線励起によるレーザの報告はなかった。本グループでは、名古屋大学の天野教授さらにはスタンレー電気との共同研究を実施し、その問題点の解決を検討し、世界ではじめて電子線励起による窒化物半導体レーザの実現を確認した。今後は、同手法を紫外領域のデバイスに応用し、最終的には波長が制御可能な紫外線レーザの実現を目指す予定である。これらの結果は招待講演が 1 件など学術的に高い評価を得ている。

#### ④キャリア注入を制御することによって 2 波長で発光する LED の実現

一般に LED では一つの活性層を一つの pn 接合で挟み込むため、一つの波長でしか発光しない。本素子では、二つ以上の活性層を挟みこんで多波長で発光する LED の実現を目論んだ。この場合、各活性層への電子と正孔(キャリア)の均一な注入が必要である。本研究グループでは、キャリアの注入状態に着目し、その制御により 2 波長で発光することが可能であることを見出した。特に中間層と呼ぶ層を形成し、そこに適量の Mg を添加することによって、効率よく 2 つの波長で発光させることが可能になった。本成果は、学生が受賞(1 件)するなど高く評価され、今後低コスト白色光源や青色面発光レーザなどへの適用も期待できる。

#### ⑤低抵抗窒化物半導体トンネル接合の実現

窒化物半導体トンネル接合は多接合太陽電池や面発光レーザの基盤技術として重要であるが、これまでの報告ではトンネル接合部の抵抗が非常に高い( $\sim 50 \Omega$ )という問題点が存在した。本グループでは p 型 GaInN の適用、活性化処理の手法の確立などを行い、抵抗が 5  $\Omega$  程度という桁低いトンネル接合を実現した。また、この技術を電流狭窄構造や多接合太陽電池に適用し、世界で初めてのトンネル接合を用いた多接合太陽電池を実現するなどの成果を残した。これらの結果は招待講演が 3 件など学術的に高い評価を得ている。

#### ⑥ 窒化物半導体太陽電池において世界最高効率を実現

窒化物半導体太陽電池において、超格子構造・透明電極・集光器等を用いることによって窒化物半導体太陽電池において世界最高効率を実現した。これらの成果は招待講演 5 件など学会で高い評価を得ている。

#### <課題となった点>

上記のように、本研究課題では窒化物半導体の結晶成長をはじめとした基盤技術の確立を狙い、トンネル接合や分極ドーピング、貼りあわせ技術などこれまで窒化物半導体材料ではデバイス応用が進められていない多くの技術を確認した。その一方で、社会実装を考えると、これを 1 歩進めて革新的な光デバイスへの適用が不可欠であると考えられる。

#### <自己評価の実施結果と対応状況>

本プロジェクトでは、多数の外部発表や年 1 回のシンポジウムを主催し、外部の有識者からの評価・アドバイスをうけながら研究を推進した。

#### <外部(第三者)評価の実施結果と対応状況>

中間評価において学部の学識研究者による中間評価を実施し、それに基づいて適切な対応を行った。具体的には、研究拠点の創出に向けた取り組みを強化し、窒化物半導体研究に関する拠点形成を目指した。

#### <研究期間終了後の展望>

上述のように、本研究課題では、窒化物半導体の結晶成長やウェハーボンディング技術など新規の基盤技術を形成した。これらの基盤技術は新しい光デバイス創製に極めて有効であると考えられ、今後本グループでは新たなる光デバイスの創製に向け検討を進めていく予定である。

法人番号	231029
プロジェクト番号	S1201019

<研究成果の副次的効果>

本研究課題の研究代表者の赤崎勇および外部の共同研究者である天野浩は高効率青色LEDの発明による成果で2014年のノーベル物理学賞を受賞した。また、それをきっかけに、名古屋大学を中心にGaN研究コンソーシアムを形成し、本拠点も参画している。さらに、本研究を基に派生した技術を活用し、2016年度より名城大学光デバイス研究センターを開設し、本センターを中心に次世代の光デバイスの開発に取り掛かっている。さらに、本研究室の学生が以下のような受賞、招待講演に選ばれるなど研究拠点を中心に社会的に高い評価を得ている。

[学生の受賞]

1. 窒化物半導体研究会 発表奨励賞 (2012) : 石黒真未
2. 応用物理学会 講演奨励賞 (2012) : 石黒真未
3. 窒化物半導体研究会 研究奨励賞 (2013) : 飯田大輔
4. 窒化物半導体研究会 発表奨励賞 (2014) : 池山和希
5. 窒化物半導体研究会 発表奨励賞 (2014) : 小塚祐吾
6. 窒化物半導体研究会 発表奨励賞 (2014) : 松井健城
7. 窒化物半導体研究会 発表奨励賞 (2014) : 安田俊輝
8. 窒化物半導体研究会 発表奨励賞 (2013) : 山本泰司
9. ISGN Best Young Scientist Award (2015): A. Yoshikawa
10. ISGN Best Young Scientist Award (2015): K. Takeda
11. ISGN Best Young Scientist Award (2015): D. Komori
12. ISGN Best Young Scientist Award (2015): T. Furuta
13. ISGN Young Scientist Award (2015): K. Matsui
14. 応用物理学会 講演奨励賞 (2015) : 池山和希
15. LEDIA Best Student Award (2016): K. Matsui
16. 窒化物半導体結晶成長講演会 発表奨励賞 (2016) : 吉川陽
17. 窒化物半導体結晶成長講演会 発表奨励賞 (2016) : 牛田彩希
18. 応用物理学会 講演奨励賞 (2016) : 吉川陽

[学生の基調講演・招待講演リスト]

1. IWN (2012 札幌) : M. Ishiguro
2. 応用物理学会 (2012 東京) : 石黒真未
3. ACCGE (2013 アメリカ) : T. Yamamoto
4. ICMOVPE (2014 スイス) : T. Yamamoto
5. ISGN (2015 浜松) : K. Takeda
6. ECCG (2015 イタリア) : J. Ohsumi
7. 応用物理学会 (2016 新潟) 吉川陽
8. EMN meeting (2016 ハンガリー) K. Matsui
9. EMN meeting (2016 ハンガリー) A. Yoshikawa
10. 応用物理学会 (2016 東京) 池山和希
11. ISPlasma (2017、名古屋) 林 菜摘

12 キーワード(当該研究内容をよく表していると思われるものを8項目以内で記載してください。)

- |            |          |             |
|------------|----------|-------------|
| (1) 窒化物半導体 | (2) 結晶成長 | (3) その場観察技術 |
| (4) トンネル接合 | (5) LED  | (6) レーザ     |

法人番号	231029
プロジェクト番号	S1201019

(7) デテクター

(8) 太陽電池

## 13 研究発表の状況(研究論文等公表状況。印刷中も含む。)

上記、11(4)に記載した研究成果に対応するものには\*を付すこと。

## &lt;雑誌論文&gt;

論文名、著者名、掲載誌名、査読の有無、巻、最初と最後の頁、発表年(西暦)について記入してください(左記の各項目が網羅されていれば、項目の順序を入れ替えても可)。また、現在から発表年次順に遡り、通し番号を付してください。

1. "Laser lift-off of AlN/sapphire for UV light-emitting diodes" Hiroki Aoshima, Kenichiro Takeda, Kosuke Takehara, Shun Ito, Mikiko Mori, Motoaki Iwaya, Tetsuya Takeuchi, Satoshi Kamiyama, Isamu Akasaki, and Hiroshi Amano: *physica status solidi (c)* **Vol. 9** (2012) 753.
2. "Growth of GaN and AlGa<sub>N</sub> on (100) β-Ga<sub>2</sub>O<sub>3</sub> substrates" Shun Ito, Kenichiro Takeda, Kengo Nagata, Hiroki Aoshima, Kosuke Takehara, Motoaki Iwaya, Tetsuya Takeuchi, Satoshi Kamiyama, Isamu Akasaki and Hiroshi Amano: *physica status solidi (c)* **Vol. 9** (2012) 519.
3. "Small current collapse in AlGa<sub>N</sub>/GaN HFETs on a-plane GaN self-standing substrate" T. Sugiyama, Y. Honda, M. Yamaguchi, H. Amano, Y. Isobe, M. Iwaya, T. Takeuchi, S. Kamiyama, I. Akasaki, M. Imade, Y. Kitaoka and Y. Mori: *physica status solidi (c)* **Vol. 9** (2012) 875.
4. "Fabrication of AlInN/AlN/GaN/GaN heterostructure field-effect transistors" Kazuya Ikeda, Yasuhiro Isobe, Hiromichi Ikki, Tatsuyuki Sakakibara, Motoaki Iwaya, Tetsuya Takeuchi, Satoshi Kamiyama, Isamu Akasaki and Hiroshi Amano: *physica status solidi (c)* **Vol. 9** (2012) 942.
5. "Enhancement of two-dimensional electron gases in AlGa<sub>N</sub>-channel high-electron-mobility transistors with AlN barrier layers" Shin Hashimoto, Katsushi Akita, Yoshiyuki Yamamoto, Masaki Ueno, Takao Nakamura, Kenichiro Takeda, Motoaki Iwaya, Yoshio Honda, and Hiroshi Amano: *physica status solidi (a)* **Vol. 209** (2012) 501
6. \* "Properties of nitride-based photovoltaic cells under concentrated light illumination" Shota Yamamoto, Mikiko Mori, Yosuke Kuwahara, Takahiro Fujii, Tatsuo Nakao, Shinichiro Kondo, Motoaki Iwaya, Tetsuya Takeuchi, Satoshi Kamiyama, Isamu Akasaki and Hiroshi Amano: *physica status solidi (RRL)* - Rapid Research Letters, **Vol. 6** (2012) 145.(\*13 に対応)
7. "Epitaxial Indium Tin Oxide Film Deposited on Sapphire Substrate by Solid-Source Electron Cyclotron Resonance Plasma" Satoru Kaneko, Hironori Torii, Masayasu Soga, Kensuke Akiyama, Motoaki Iwaya, Mamoru Yoshimoto, and Takao Amazawa: *Japanese Journal of Applied Physics* **Vol. 51** (2012) 01AC02.
8. "Indium-Tin Oxide/Al Reflective Electrodes for Ultraviolet Light-Emitting Diodes" Kosuke Takehara, Kenichiro Takeda, Shun Ito, Hiroki Aoshima, Motoaki Iwaya, Tetsuya Takeuchi, Satoshi Kamiyama, Isamu Akasaki, and Hiroshi Amano: *Japanese Journal of Applied Physics* **Vol. 51** (2012) 042101.
9. "Crack-Free AlN/GaN Distributed Bragg Reflectors on AlN Templates" Kouta Yagi, Mitsuru Kaga, Kouji Yamashita, Kenichirou Takeda, Motoaki Iwaya, Tetsuya Takeuchi, Satoshi Kamiyama, Hiroshi Amano, and Isamu Akasaki: *Japanese Journal of Applied Physics* **51** (2012) 051001.
10. \* "Correlation between Device Performance and Defects in GaInN-Based Solar Cells" Mikiko Mori, Shinichiro Kondo, Shota Yamamoto, Tatsuro Nakao, Takahiro Fujii, Motoaki Iwaya, Tetsuya Takeuchi, Satoshi Kamiyama, Isamu Akasaki, and

法人番号	231029
プロジェクト番号	S1201019

- Hiroshi Amano: Applied Physics Express 5 (2012) 082301. (\*13 に対応)
11. "White light-emitting diode based on fluorescent SiC" Satoshi Kamiyama, Motoaki Iwaya, Tetsuya Takeuchi, Isamu Akasaki, Rositza Yakimova, and Mikael Syväjärvi: *Thin Solid Films* **522** (2012) 23-25.
  12. "MOVPE growth of nonpolar a-plane GaN with low oxygen contamination and specular surface on a freestanding GaN substrate" Yasuhiro Isobe, Hiromichi Ikki, Tatsuyuki Sakakibara, Motoaki Iwaya, Tetsuya Takeuchi, Satoshi Kamiyama, Isamu Akasaki, Takayuki Sugiyama, Hiroshi Amano, Mamoru Imade, Yusuke Mori: *Journal of Crystal Growth* Vol. 351 (2012) pp. 126-130.
  13. "Development of AlN/diamond heterojunction field effect transistors" Masataka Imura, Ryoma Hayakawa, Hirotaka Ohsato, Eiichiro Watanabe, Daiju Tsuya, Takahiro Nagata, Meiyong Liao, Yasuo Koide, Jun-ichi Yamamoto, Kazuhito Ban, Motoaki Iwaya, Hiroshi Amano: *Diamond and Related Materials* Vol. 24 (2012) pp. 206-209.
  14. \* "In situ X-ray diffraction monitoring during metalorganic vapor phase epitaxy growth of low-temperature-GaN buffer layer" Daisuke Iida, Mihoko Sowa, Yasunari Kondo, Daiki Tanaka, Motoaki Iwaya, Tetsuya Takeuchi, Satoshi Kamiyama, and Isamu Akasaki: *Journal of Crystal Growth* 361 (2012) 1. (\*1 に対応)
  15. \* "Nitride-based hetero-field-effect transistor-type photosensors with extremely high photosensitivity" Mami Ishiguro, Kazuya Ikeda, Masataka Mizuno, Motoaki Iwaya, Tetsuya Takeuchi, Satoshi Kamiyama, and Isamu Akasaki: *Physica Status Solidi RRL* **7** (2013) 215–217. (\*12 に対応)
  16. \* "Analysis of strain relaxation process in GaInN/GaN heterostructure by in situ X-ray diffraction monitoring during metalorganic vapor-phase epitaxial growth" Daisuke Iida, Yasunari Kondo, Mihoko Sowa, Toru Sugiyama, Motoaki Iwaya, Tetsuya Takeuchi, Satoshi Kamiyama, and Isamu Akasaki: *Physica Status Solidi RRL* **7** (2013) 211–214. (\*1 に対応)
  17. "Trench-Shaped Defects on AlGaInN Quantum Wells Grown under Different Growth Pressures" Tomoyuki Suzuki, Mitsuru Kaga, Kouichi Naniwae, Tsukasa Kitano, Keisuke Hirano, Tetsuya Takeuchi, Satoshi Kamiyama, Motoaki Iwaya, and Isamu Akasaki: *Japanese Journal of Applied Physics* **52** (2013) 08JB27.
  18. "Control of the Detection Wavelength in AlGaIn/GaN-Based Hetero-Field-Effect-Transistor Photosensors" Mami Ishiguro, Kazuya Ikeda, Masataka Mizuno, Motoaki Iwaya, Tetsuya Takeuchi, Satoshi Kamiyama, and Isamu Akasaki: *Japanese Journal of Applied Physics* **52** (2013) 08JF02.
  19. \* "Carrier Injections in Nitride-Based Light Emitting Diodes Including Two Active Regions with Mg-Doped Intermediate Layers" Kenjo Matsui, Koji Yamashita, Mitsuru Kaga, Takatoshi Morita, Tomoyuki Suzuki, Tetsuya Takeuchi, Satoshi Kamiyama, Motoaki Iwaya, and Isamu Akasaki: *Japanese Journal of Applied Physics* **52** (2013) 08JG02. (\*16 に対応)
  20. "Combination of Indium–Tin Oxide and SiO<sub>2</sub>/AlN Dielectric Multilayer Reflective Electrodes for Ultraviolet-Light-Emitting Diodes" Tsubasa Nakashima, Kenichiro Takeda, Hiroshi Shinzato, Motoaki Iwaya, Satoshi Kamiyama, Tetsuya Takeuchi, Isamu Akasaki, and Hiroshi Amano: *Japanese Journal of Applied Physics* **52** (2013) 08JG07.
  21. \* "Concentrating Properties of Nitride-Based Solar Cells Using Different Electrodes" Mikiko Mori, Shinichiro Kondo, Shota Yamamoto, Tatsuro Nakao, Motoaki Iwaya, Tetsuya Takeuchi, Satoshi Kamiyama, Isamu Akasaki, and Hiroshi Amano: *Japanese Journal of Applied Physics* **52** (2013) 08JH02. (\*13 に対応)
  22. \* "GaInN-Based Tunnel Junctions in n–p–n Light Emitting Diodes" Mitsuru Kaga,

法人番号	231029
プロジェクト番号	S1201019

- Takatoshi Morita, Yuka Kuwano, Kouji Yamashita, Kouta Yagi, Motoaki Iwaya, Tetsuya Takeuchi, Satoshi Kamiyama, and Isamu Akasaki: Japanese Journal of Applied Physics 52 (2013) 08JH07. (\*18 に対応)
23. \* “Investigations of Polarization-Induced Hole Accumulations and Vertical Hole Conductions in GaN/AlGaN Heterostructures” Toshiki Yasuda, Kouta Yagi, Tomoyuki Suzuki, Tsubasa Nakashima, Masahiro Watanabe, Tetsuya Takeuchi, Motoaki Iwaya, Satoshi Kamiyama, and Isamu Akasaki: Japanese Journal of Applied Physics 52 (2013) 08JJ05. (\*7 に対応)
  24. “Study on Efficiency Component Estimation of 405 nm Light Emitting Diodes from Electroluminescence and Photoluminescence Intensities” Kazuki Aoyama, Atsushi Suzuki, Tsukasa Kitano, Satoshi Kamiyama, Tetsuya Takeuchi, Motoaki Iwaya, and Isamu Akasaki: Japanese Journal of Applied Physics 52 (2013) 08JL16.
  25. “Dislocation density dependence of stimulated emission characteristics in AlGaIn/Al multiquantum wells” Yuko Matsubara, Tomoaki Yamada, Kenichiro Takeda, Motoaki Iwaya, Tetsuya Takeuchi, Satoshi Kamiyama, Isamu Akasaki and Hiroshi Amano: physica status solidi (c) Volume 10 (2013) pp. 1537–1540.
  26. \* “In situ X-ray diffraction monitoring of GaInN/GaN super lattice during organometallic vapor phase epitaxy growth” Journal of Crystal Growth 393 (2014) 108. (\*1 に対応)
  27. \* “Extremely Low-Resistivity and High-Carrier-Concentration Si-Doped Al<sub>0.05</sub>Ga<sub>0.95</sub>N Toru Sugiyama, Daisuke Iida, Toshiki Yasuda, Motoaki Iwaya, Tetsuya Takeuchi, Satoshi Kamiyama and Isamu Akasaki: Applied Physics Express Vol. 6 (2013) 121002. (\*4 に対応)
  28. \* “Homoepitaxial growth of AlN layers on freestanding AlN substrate by metalorganic vapor phase epitaxy” Tomohiro Morishita, Motoaki Iwaya, Tetsuya Takeuchi, Satoshi Kamiyama, Isamu Akasaki: Journal of Crystal Growth Volume 390 (2014) pp. 46-50. (\*6 に対応)
  29. \* “Multijunction GaInN-based solar cells using a tunnel junction” Hironori Kurokawa, Mitsuru Kaga, Tomomi Goda, Motoaki Iwaya, Tetsuya Takeuchi, Satoshi Kamiyama, Isamu Akasaki and Hiroshi Amano: Applied Physics Express Vol. 7 (2014) 034104. (\*20 に対応)
  30. \* “Control of growth mode in Mg-doped GaN/AlN heterostructure” Tomohiro Morishita, Kosuke Sato, Motoaki Iwaya, Tetsuya Takeuchi, Satoshi Kamiyama and Isamu Akasaki: Japanese Journal of Applied Physics Vol. 53 (2014) 030305. (\*6 に対応)
  31. \* “Control of crystallinity of GaN grown on sapphire substrate by metalorganic vapor phase epitaxy using in situ X-ray diffraction monitoring method” Journal of Crystal Growth 401 (2014) 367–371. (\*1 および \*13 に対応)
  32. “Laser lift-off technique for freestanding GaN substrate using an In droplet formed by thermal decomposition of GaInN and its application to light-emitting diodes” Daisuke Iida, Syunsuke Kawai, Nobuaki Ema, Takayoshi Tsuchiya, Motoaki Iwaya, Tetsuya Takeuchi, Satoshi Kamiyama, and Isamu Akasaki: Applied Physics Letters 105 (2014) 072101.
  33. 竹内哲也、岩谷素顕、上山 智、赤崎 勇、「窒化物半導体面発光レーザーの現状」、照明学会誌 第 100 巻第 5 号 (2016)

法人番号	231029
プロジェクト番号	S1201019

34. Matsui, K., Kozuka, Y., Ikeyama, K., Horikawa, K., Furuta, T., Akagi, T., ... & Akasaki, I. (2016). GaN-based vertical cavity surface emitting lasers with periodic gain structures. *Japanese Journal of Applied Physics*, 55(5S), 05FJ08.
35. Takeda, K., Iwaya, M., Takeuchi, T., Kamiyama, S., & Akasaki, I. (2016). Electrical properties of n-type AlGaN with high Si concentration. *Japanese Journal of Applied Physics*, 55(5S), 05FE02.
36. Komori, D., Takarabe, K., Takeuchi, T., Miyajima, T., Kamiyama, S., Iwaya, M., & Akasaki, I. (2016). GaNSb alloys grown with H<sub>2</sub> and N<sub>2</sub> carrier gases. *Japanese Journal of Applied Physics*, 55(5S), 05FD01.
37. Osumi, J., Ishihara, K., Yamamoto, T., Iwaya, M., Takeuchi, T., Kamiyama, S., & Akasaki, I. (2016). GaN barrier layer dependence of critical thickness in GaInN/GaN superlattice on GaN characterized by in situ X-ray diffraction. *Japanese Journal of Applied Physics*, 55(5S), 05FD11.
38. Furuta, T., Matsui, K., Horikawa, K., Ikeyama, K., Kozuka, Y., Yoshida, S., ... & Akasaki, I. (2016). Room-temperature CW operation of a nitride-based vertical-cavity surface-emitting laser using thick GaInN quantum wells. *Japanese Journal of Applied Physics*, 55(5S), 05FJ11.
39. Yamamoto, Y., Yoshikawa, A., Kusafuka, T., Okumura, T., Iwaya, M., Takeuchi, T., ... & Akasaki, I. (2016). Realization of high-performance hetero-field-effect-transistor-type ultraviolet photosensors using p-type GaN comprising three-dimensional island crystals. *Japanese Journal of Applied Physics*, 55(5S), 05FJ07.
40. Yoshikawa, A., Yamamoto, Y., Murase, T., Iwaya, M., Takeuchi, T., Kamiyama, S., & Akasaki, I. (2016). High-photosensitivity AlGaIn-based UV heterostructure-field-effect-transistor-type photosensors. *Japanese Journal of Applied Physics*, 55(5S), 05FJ04.
41. Mori, K., Takeda, K., Kusafuka, T., Iwaya, M., Takeuchi, T., Kamiyama, S., ... & Amano, H. (2016). Low-ohmic-contact-resistance V-based electrode for n-type AlGaIn with high AlN molar fraction. *Japanese Journal of Applied Physics*, 55(5S), 05FL03.
42. Yoshida, S., Ikeyama, K., Yasuda, T., Furuta, T., Takeuchi, T., Iwaya, M., ... & Akasaki, I. (2016). Electron and hole accumulations at GaN/AlInN/GaN interfaces and conductive n-type AlInN/GaN distributed Bragg reflectors. *Japanese Journal of Applied Physics*, 55(5S), 05FD10.
43. Takasuka, D., Akatsuka, Y., Ino, M., Koide, N., Takeuchi, T., Iwaya, M., ... & Akasaki, I. (2016). GaInN-based tunnel junctions with graded layers. *Applied Physics Express*, 9(8), 081005.
44. Ikeyama, K., Kozuka, Y., Matsui, K., Yoshida, S., Akagi, T., Akatsuka, Y., ... & Akasaki, I. (2016). Room-temperature continuous-wave operation of GaN-based vertical-cavity surface-emitting lasers with n-type conducting AlInN/GaN distributed Bragg reflectors. *Applied Physics Express*, 9(10), 102101.

法人番号	231029
プロジェクト番号	S1201019

1. “青い光に魅せられて 青色 LED 開発物語” 赤崎 勇、日本経済新聞出版社、233 ページ、(2013)
2. “ワイドギャップ半導体—あけぼのから最前線へ” 赤崎勇、松波 弘之、培風館 404 ページ(2013). (6.2 紫外線発光ダイオード応用(12 ページ)を岩谷素顕が担当
3. “ポストシリコン半導体 —ナノ成膜ダイナミクスと基板・界面効果—”(2.1 窒化物半導体の特徴とデバイス動向)、竹内哲也、エヌ・ティー・エス、11 ページ(2013).

<学会発表>

15. \*“窒化物半導体太陽電池の現状とその将来展望” 岩谷素顕、竹内哲也、上山智、赤崎勇、天野浩: 日本結晶成長学会ナノ構造・エピタキシャル成長分科会シンポジウム「高効率ナノエピタキシャル太陽電池の最先端」、東京大学、2012.4.26-27. **[特別講演]** (\*13 に対応)
16. “膜厚変化に伴う GaInN/GaN ヘテロ接合の微細構造観察” 松原大幸、飯田大輔、杉山 徹、近藤保成、曾和美保子、岩谷素顕、竹内哲也、上山智、赤崎勇: 第 4 回 窒化物半導体結晶成長講演会 (プレ IWN2012)、東京大学、2012.4.27-28.
17. \*“n 型 GaN 直下におけるトンネル接合および p 型 GaN 活性化の検討” 桑野侑香、山下浩司、加賀充、森田隆敏、竹内哲也、岩谷素顕、上山智、赤崎勇: 第 4 回 窒化物半導体結晶成長講演会 (プレ IWN2012)、東京大学、2012.4.27-28. (\*5 に対応)
18. “埋め込み型 GaN ナノコラム結晶の MOVPE 成長に関する検討” 梅田慎也、加藤嵩裕、北野司、近藤俊行、松原大幸、上山智、竹内哲也、岩谷素顕、赤崎勇: 第 4 回 窒化物半導体結晶成長講演会 (プレ IWN2012)、東京大学、2012.4.27-28.
19. “GaInN 量子井戸への Al 添加による AlGaInN 量子井戸の作製と評価” 鈴木智行、加賀充、北野司、難波江宏一、平野敬祐、竹内哲也、上山智、岩谷素、赤崎勇: 第 4 回 窒化物半導体結晶成長講演会 (プレ IWN2012)、東京大学、2012.4.27-28.
20. \*“X 線その場観察 MOVPE により評価した GaInN/GaN の臨界膜厚” 近藤保成、飯田大輔、杉山徹、曾和美保子、松原大幸、岩谷素顕、竹内哲也、上山智、赤崎勇: 第 4 回 窒化物半導体結晶成長講演会 (プレ IWN2012)、東京大学、2012.4.27-28. (\*1 に対応)
21. \*“中間層を用いた窒化物半導体二波長発光ダイオードにおけるキャリア注入の検討” 松井健城、山下浩司、加賀充、森田隆敏、鈴木智行、竹内哲也、上山智、岩谷素顕、赤崎勇: 第 4 回 窒化物半導体結晶成長講演会 (プレ IWN2012)、東京大学、2012.4.27-28. (\*16 に対応)
22. \*“III 族窒化物半導体を用いた低抵抗トンネル接合” 森田隆敏、加賀充、桑野侑香、山下浩司、松井健城、竹内哲也、上山智、岩谷素顕、赤崎勇: 第 4 回 窒化物半導体結晶成長講演会 (プレ IWN2012)、東京大学、2012.4.27-28. (\*5 に対応)
23. \*“p 型 GaInN を用いた高感度な FET 型光センサーに関する研究” 石黒真未、池田和弥、水野正隆、岩谷素顕、竹内哲也、上山智、赤崎勇: 第 4 回 窒化物半導体結晶成長講演会 (プレ IWN2012)、東京大学、2012.4.27-28. (\*12 に対応)
24. “非極性面上 III 族窒化物半導体電界効果トランジスタに関する研究” 水野正隆、池田和弥、石黒真未、松原大幸、岩谷素顕、竹内哲也、上山智、天野浩、赤崎勇: 第 4 回 窒化物半導体結晶成長講演会 (プレ IWN2012)、東京大学、2012.4.27-28.
25. \*“Optimizations of Nitride Semiconductor-Based Tunnel Junctions” Mitsuru Kaga, Kouji Yamashita, Takatoshi Morita, Yuka Kuwano, Kouta Yagi, Motoaki Iwaya, Tetsuya Takeuchi, Satoshi Kamiyama, and Isamu Akasaki: 16th International Conference on Metal Organic Vapor Phase Epitaxy (ICMOVPE-XVI), Pusan, Korea, 2012. 5.20-25. (\*5 に対応)
26. \* “In-Situ Real-Time X-Ray Diffraction Study during Ga<sub>1-x</sub>In<sub>x</sub>N/GaN

法人番号	231029
プロジェクト番号	S1201019

- Heterostructure Growth by MOVPE for Understanding Strain Relaxation Mechanism" Motoaki Iwaya, Daisuke Iida, Daiki Tanaka, Toru Sugiyama, Mihoko Sowa, Yasunari Kondo, Tetsuya Takeuchi, Satoshi Kamiyama, and Isamu Akasaki: 16th International Conference on Metal Organic Vapor Phase Epitaxy (ICMOVPE-XVI), Pusan, Korea, 2012. 5.20-25. (\*1 に対応)
27. "Microstructure of AlGa<sub>N</sub> on Low-Dislocation Density AlN Underlying Layer Grown by Epitaxial Lateral Overgrowth" Kimiyasu Ide, Junichi Yamamoto, Motoaki Iwaya, Satoshi Kamiyama, Tetsuya Takeuchi, Isamu Akasaki, and Hiroshi Amano: 16th International Conference on Metal Organic Vapor Phase Epitaxy (ICMOVPE-XVI), Pusan, Korea, 2012. 5.20-25.
28. "Investigation of AlN/GaN Multilayer Stacks for DBR Applications" Kouta Yagi, Mitsuru Kaga, Kouji Yamashita, Kenichirou Takeda, Motoaki Iwaya, Tetsuya Takeuchi, Satoshi Kamiyama, Hiroshi Amano, and Isamu Akasaki: 16th International Conference on Metal Organic Vapor Phase Epitaxy (ICMOVPE-XVI), Pusan, Korea, 2012. 5.20-25.
29. \* "基板・半導体層のナノ加工と半導体デバイスへの応用" 岩谷素顕: 日本機械学会 情報・知能・精密機器部門 分科会 第1回「窒化物半導体デバイスに関わる超精密加工プロセス研究会」発会記念 特別講演会、九州大学、2012年5月30日。【招待講演】 (\*1 に対応)
30. "窒化物半導体エピタキシャル成長の新展開" 天野浩、本田善央、山口雅史、今出完、森勇介、岩谷素顕: 応用物理学会 第 137 回結晶工学分科会研究会「窒化物半導体光デバイスの最前線-基板・エピ成長と評価技術-」京都テレサ、2012年6月15日。【特別講演】
31. \* "Observation of GaInN strain relaxation by in situ X-ray diffraction monitoring during metalorganic vapour phase epitaxy growth" M. Iwaya, D. Iida, T. Sugiyama, M. Sowa, Y. Kondo, H. Matsubara, T. Takeuchi, S. Kamiyama, and I. Akasaki: 4th International Symposium on Growth of III-Nitrides, St. Petersburg, Russia, 2012.7.16-7.19. (\*1 に対応)
32. \* "Composition dependence of critical thicknesses in GaInN/GaN characterized by in situ X-ray diffraction measurement", Y. Kondo, D. Iida, T. Sugiyama, M. Sowa, H. Matsubara, M. Iwaya, T. Takeuchi, S. Kamiyama, and I. Akasaki: 4th International Symposium on Growth of III-Nitrides, St. Petersburg, Russia, 2012.7.16-7.19. (\*1 に対応)
33. \* "Strain Relaxation Mechanism in GaInN/GaN Heterostructure Characterized by in situ X-ray Diffraction Monitoring During Metalorganic Vapor Phase Epitaxy Growth", Motoaki Iwaya, Yasunari Kondo, Hiroyuki Matsubara, Mihoko Sowa, Toru Sugiyama, Daisuke Iida, Tetsuya Takeuchi, Satoshi Kamiyama, and Isamu Akasaki: 39th International Symposium on Compound Semiconductors, University of California Santa Barbara, CA USA, August 27-30, 2012. (\*1 に対応)
34. "非極性 AlGa<sub>N</sub>/Ga<sub>N</sub> HFET の AlGa<sub>N</sub> バリアの AlN モル分率および Si 濃度依存性" 水野正隆, 磯部康裕, 池田和弥, 石黒真未, 岩谷素顕, 竹内哲也, 上山 智, 赤崎 勇, 天野 浩: 第 73 回応用物理学会講演会、愛媛大学・松山大学、2012年9月11日-14日。
35. \* "ピエゾ・自発分極電荷への正孔蓄積の検討" 安田俊輝, 矢木康太, 鈴木智行, 中嶋翼, 渡邊雅大, 竹内哲也, 上山 智, 岩谷素顕, 赤崎 勇: 第 73 回応用物理学会講演会、愛媛大学・松山大学、2012年9月11日-14日。(\*7 に対応)
36. \* "GaInN/GaN ヘテロ接合におけるミスフィット転位の観察" 松原大幸, 飯田大輔, 杉山徹, 近藤保成, 曾和美保子, 梅田慎也, 岩谷素顕, 竹内哲也, 上山 智, 赤崎 勇: 第 73 回応用物理学会講演会、愛媛大学・松山大学、2012年9月11日-14日。(\*1 に対応)

法人番号	231029
プロジェクト番号	S1201019

37. "AlGaIn/AIn における下地 AIn 転位密度依存性" 井手公康, 松原由布子, 岩谷素顕, 竹内哲也, 上山 智, 赤崎 勇, 天野 浩: 第 73 回応用物理学会講演会、愛媛大学・松山大学、2012 年 9 月 11 日-14 日.
38. "ITO と SiO<sub>2</sub>/AIn 誘電体多層膜を組み合わせた電極による 350nm 紫外 LED の高効率化" 中嶋 翼, 竹田健一郎, 新里紘史, 岩谷素顕, 上山 智, 竹内哲也, 赤崎 勇, 天野 浩: 第 73 回応用物理学会講演会、愛媛大学・松山大学、2012 年 9 月 11 日-14 日.
39. \*"窒化物半導体を用いた高感度な HFET 型光センサー" 石黒真未, 池田和弥, 水野正隆, 岩谷素顕, 竹内哲也, 上山 智, 赤崎 勇: 第 73 回応用物理学会講演会、愛媛大学・松山大学、2012 年 9 月 11 日-14 日. (\*12 に対応)
40. \*"窒化物半導体太陽電池の集光特性における電極構造の最適化" 森美貴子, 山本翔太, 近藤真一郎, 中尾達郎, 岩谷素顕, 竹内哲也, 上山 智, 赤崎 勇, 天野 浩: 第 73 回応用物理学会講演会、愛媛大学・松山大学、2012 年 9 月 11 日-14 日. (\*13 に対応)
41. \*"Mg ドープ中間層を用いた二波長発光ダイオードにおける電流注入依存性量の検討" 松井健城, 山下浩司, 加賀 充, 森田隆敏, 鈴木智行, 竹内哲也, 上山 智, 岩谷素顕, 赤崎 勇: 第 73 回応用物理学会講演会、愛媛大学・松山大学、2012 年 9 月 11 日-14 日. (\*16 に対応)
42. \*"III 族窒化物半導体トンネル接合を用いた n-p 接合 LED" 森田隆敏, 加賀 充, 桑野侑香, 松井健城, 竹内哲也, 上山 智, 岩谷素顕, 赤崎 勇: 第 73 回応用物理学会講演会、愛媛大学・松山大学、2012 年 9 月 11 日-14 日. (\*5 に対応)
43. "100 チャンネル 10 $\mu$ m 径マイクロ LED アレイの作製" 渡邊雅大, 山下浩司, 加賀 充, 鈴木智行, 森田隆敏, 竹内哲也, 上山 智, 岩谷素顕, 赤崎 勇: 第 73 回応用物理学会講演会、愛媛大学・松山大学、2012 年 9 月 11 日-14 日.
44. "EL と PL を組み合わせた LED 効率成分の導出方法の検討" 青山和樹, 鈴木敦志, 北野 司, 上山 智, 竹内哲也, 岩谷素顕, 赤崎 勇: 第 73 回応用物理学会講演会、愛媛大学・松山大学、2012 年 9 月 11 日-14 日.
45. \*"Realization of high efficiency nitride-based solar cells" Motoaki Iwaya, Mikiko Mori, Shinichiro Kondo, Shota Yamamoto, Tatsuro Nakao, Takahiro Fujii, Tetsuya Takeuchi, Satoshi Kamiyama, Isamu Akasaki, and Hiroshi Amano: The International Workshop on Nitride Semiconductors (IWN2012), Sapporo, Japan, 2012.10.14-19. **[Invited Talk]** (\*13 に対応)
46. \*"Optimization of crystalline quality of GaN using low temperature buffer layer by in situ X-ray diffraction monitoring" Daiki Tanaka, Daisuke Iida, Motoaki Iwaya, Tetsuya Takeuchi, Satoshi Kamiyama, and Isamu Akasaki: The International Workshop on Nitride Semiconductors (IWN2012), Sapporo, Japan, 2012.10.14-19. (\*1 に対応)
47. \*"AIN mole fraction dependence of polarization induced hole concentrations in GaN/AlGaIn heterostructures" Toshiki Yasuda, Kouta Yagi, Tomoyuki Suzuki, Tsubasa Nakashima, Masahiro Watanabe, Tetsuya Takeuchi, Satoshi Kamiyama, Motoaki Iwaya, and Isamu Akasaki: The International Workshop on Nitride Semiconductors (IWN2012), Sapporo, Japan, 2012.10.14-19. (\*7 に対応)
48. "Fabrication of AlInN/GaN MIS heterostructure field-effect transistors" Kazuya Ikeda, Yasuhiro Isobe, Hiromichi Ikki, Kimiyasu Ide, Motoaki Iwaya, Tetsuya Takeuchi, Satoshi Kamiyama, Isamu Akasaki, and Hiroshi Amano: The International Workshop on Nitride Semiconductors (IWN2012), Sapporo, Japan, 2012.10.14-19.
49. \* "High sensitivity extremely nitride-based heterofield-effect-transistor-type photosensors" Mami Ishiguro, Kazuya Ikeda, Masataka Mizuno, Motoaki Iwaya, Tetsuya Takeuchi, Satoshi Kamiyama, and Isamu Akasaki: The International

法人番号	231029
プロジェクト番号	S1201019

Workshop on Nitride Semiconductors (IWN2012), Sapporo, Japan, 2012.10.14-19.  
**[Invited Talk] (\*13 に対応)**

50. \* "Composition dependence of critical thicknesses in GaInN/GaN characterized by in situ X-ray diffraction measurement" Yasunari Kondo, Daisuke Iida, Toru Sugiyama, Hiroyuki Matsubara, Mihoko Sowa, Motoaki Iwaya, Tetsuya Takeuchi, Satoshi Kamiyama, and Isamu Akasaki: The International Workshop on Nitride Semiconductors (IWN2012), Sapporo, Japan, 2012.10.14-19. (\*1 に対応)
51. \* "Strain relaxation mechanism in GaInN/GaN heterostructure characterized by in situ XRD monitoring during growth and ex situ measurements" Hiroyuki Matsubara, Daisuke Iida, Toru Sugiyama, Yasunari Kondo, Mihoko Sowa, Shinya Umeda, Motoaki Iwaya, Tetsuya Takeuchi, Satoshi Kamiyama, and Isamu Akasaki: The International Workshop on Nitride Semiconductors (IWN2012), Sapporo, Japan, 2012.10.14-19. (\*1 に対応)
52. "Fabrication and characterization of AlGaInN quantum wells" Tomoyuki Suzuki, Mitsuru Kaga, Koichi Naniwae, Tsukasa Kitano, Kesuke Hirano, Tetsuya Takeuchi, Satoshi Kamiyama, Motoaki Iwaya, and Isamu Akasaki: The International Workshop on Nitride Semiconductors (IWN2012), Sapporo, Japan, 2012.10.14-19.
53. "Study on efficiency component estimation by electroluminescence and photoluminescence intensities" Kazuki Aoyama, Atsushi Suzuki, Tsukasa Kitano, Satoshi Kamiyama, Tetsuya Takeuchi, Motoaki Iwaya, and Isamu Akasaki: The International Workshop on Nitride Semiconductors (IWN2012), Sapporo, Japan, 2012.10.14-19.
54. "Nonpolar a-plane AlGaInN/GaN heterostructure field-effect transistor grown on freestanding GaN substrate" Masataka Mizuno, Yasuhiro Isobe, Kazuya Ikeda, Mami Isiguro, Motoaki Iwaya, Tetsuya Takeuchi, Satoshi Kamiyama, Isamu Akasaki, and Hiroshi Amano: The International Workshop on Nitride Semiconductors (IWN2012), Sapporo, Japan, 2012.10.14-19.
55. "Combination of ITO and SiO<sub>2</sub>/AlN dielectric multilayer reflective electrodes for UV light-emitting diodes" Tsubasa Nakashima, Kenichirou Takeda, Yuko Matsubara, Motoaki Iwaya, Tetsuya Takeuchi, Satoshi Kamiyama, Isamu Akasaki, and Hiroshi Amano: The International Workshop on Nitride Semiconductors (IWN2012), Sapporo, Japan, 2012.10.14-19.
56. \* "Carrier injections in nitride-based light emitting diodes including two active regions with Mg-doped intermediate layers" Kenjo Matsui, Koji Yamashita, Mitsuru Kaga, Takatoshi Morita, Tomoyuki Suzuki, Tetsuya Takeuchi, Satoshi Kamiyama, Motoaki Iwaya, and Isamu Akasaki: The International Workshop on Nitride Semiconductors (IWN2012), Sapporo, Japan, 2012.10.14-19. (\*1 に対応)
57. \* "Concentrating properties of nitride-based solar cells using different electrodes" Mikiko Mori, Shota Yamamoto, Shinichiro Kondo, Tatsuro Nakao, Motoaki Iwaya, Tetsuya Takeuchi, Satoshi Kamiyama, Isamu Akasaki, and Hiroshi Amano: The International Workshop on Nitride Semiconductors (IWN2012), Sapporo, Japan, 2012.10.14-19. (\*13 に対応)
58. \* "GaInN-based tunnel junctions in n-p-n light emitting diodes" Mitsuru Kaga, Takatoshi Morita, Yuka Kuwano, Kouji Yamashita, Kouta Yagi, Motoaki Iwaya, Tetsuya Takeuchi, Satoshi Kamiyama, and Isamu Akasaki: The International Workshop on Nitride Semiconductors (IWN2012), Sapporo, Japan, 2012.10.14-19. (\*5 に対応)
59. "Microstructure analysis of AlGaIn on AlN underlying layers with different threading dislocation densities" Kimiyasu Ide, Yuko Matsubara, Motoaki Iwaya, Tetsuya Takeuchi, Satoshi Kamiyama, Isamu Akasaki, and Hiroshi Amano: The International

法人番号	231029
プロジェクト番号	S1201019

- Workshop on Nitride Semiconductors (IWN2012), Sapporo, Japan, 2012.10.14-19.
60. "MOVPE growth of embedded GaN nanocolumn" Shinya Umeda, Takahiro Kato, Tsukasa Kitano, Toshiyuki Kondo, Hiroyuki Matsubara, Satoshi Kamiyama, Tetsuya Takeuchi, Motoaki Iwaya, and Isamu Akasaki: The International Workshop on Nitride Semiconductors (IWN2012), Sapporo, Japan, 2012.10.14-19.
61. \*"Lateral hydrogen diffusion at p-GaN layers in nitride-based LEDs with tunnel junctions" Yuka Kuwano, Mitsuru Kaga, Takatoshi Morita, Tetsuya Takeuchi, Motoaki Iwaya, Satoshi Kamiyama, and Isamu Akasaki: The International Workshop on Nitride Semiconductors (IWN2012), Sapporo, Japan, 2012.10.14-19. (\*5 に対応)
62. "Carrier profiling technique for DUV LEDs" Yuta Furusawa, Inazu Tetsuhiko, Shinya Fukahori, Cyril Pernot, Myonghee Kim, Takehiko Fujita, Yosuke Nagasawa, Akira Hirano, Masamichi Ippommatsu, Motoaki Iwaya, Tetsuya Takeuchi, Satoshi Kamiyama, Yoshio Honda, Masashi Yamaguchi, Hiroshi Amano, and Isamu Akasaki: The International Workshop on Nitride Semiconductors (IWN2012), Sapporo, Japan, 2012.10.14-19.
63. \*"窒化物半導体太陽電池の高効率化" 岩谷素顕、竹内哲也、上山智、赤崎勇、天野浩: 第 42 回結晶成長国内会議、九州大学、2012 年 11 月 9 日-11 日。【招待講演】(\*13 に対応)
64. "ドループ改善に向けた窒化物半導体 np 構造 LED の作製" 森田隆敏、加賀 充、桑野侑香、松井健城、竹内哲也、上山 智、岩谷素顕、赤崎勇: 電子情報通信学会 ED、CPM、LQE 合同研究会、大阪市立大学、2012 年 11 月 29 日-30 日。
65. "サファイア基板上へのモスアイ構造の形成方法の検討および LED への応用" 土屋貴義、梅田慎也、曾和美保子、近藤俊行、北野 司、森 みどり、鈴木敦志、難波江宏一、関根 均、岩谷素顕、竹内哲也、上山智、赤崎勇: 電子情報通信学会 ED、CPM、LQE 合同研究会、大阪市立大学、2012 年 11 月 29 日-30 日。
66. \*"n-GaN 表面層を有する構造内 p-GaN の Mg アクセプタ活性化" 桑野侑香、加賀充、森田隆敏、山下浩司、南川大智、竹内哲也、岩谷素顕、上山 智、赤崎勇: 電子情報通信学会 ED、CPM、LQE 合同研究会、大阪市立大学、2012 年 11 月 29 日-30 日。(\*5 に対応)
67. \*"Observation of group III nitride semiconductors by in situ X-ray diffraction monitoring during metalorganic vapor phase epitaxy growth" Motoaki Iwaya, Daisuke Iida, Mihoko Sowa, Yasunari Kondo, Daiki Tanaka, Tetsuya Takeuchi, Satoshi Kamiyama, and Isamu Akasaki: 2012 Collaborative Conference on Crystal Growth, Orland, FL, USA, 2012.12.11-14. 【Invited Talk】(\*1 に対応)
68. \*"High-sensitivity HFET type photosensors with a p-GaN gate" Mami Ishiguro, Kazuya Ikeda, Masataka Mizuno, Motoaki Iwaya, Tetsuya Takeuchi, Satoshi Kamiyama, Isamu Akasaki: SPIE Photonic west 2013, San Francisco, USA, 2013.2.2-8. (\*12 に対応)
69. "Influence of growth interruption on performance of nitride-based blue LED" Kazuki Aoyama, Atsushi Suzuki, Tsukasa Kitano, Naoki Sone, Satoshi Kamiyama, Tetsuya Takeuchi, Motoaki Iwaya, Isamu Akasaki: SPIE Photonic west 2013, San Francisco, USA, 2013.2.2-8.
70. "Introduction of the Moth-eye patterned sapphire substrate technology for cost effective high-performance LED" Koichi Naniwae, Midori Mori, Toshiyuki Kondo, Atsushi Suzuki, Tsukasa Kitano, Satoshi Kamiyama, Motoaki Iwaya, Tetsuya Takeuchi, Isamu Akasaki: SPIE Photonic west 2013, San Francisco, USA, 2013.2.2-8. 【Invited Talk】
71. "Fabrication of moth-eye patterned sapphire substrate (MPSS) and influence of

法人番号	231029
プロジェクト番号	S1201019

- height of corns on the performance of blue LEDs on MPSS" Takayoshi Tsuchiya, Shinya Umeda, Motoaki Iwaya, Tetsuya Takeuchi, Satoshi Kamiyama, Isamu Akasaki, Toshiyuki Kondo, Tsukasa Kitano, Midori Mori, Atsushi Suzuki, Fumiharu Teramae, Hitoshi Sekine: SPIE Photonic west 2013, San Francisco, USA, 2013.2.2-8.
72. "Performance of nitride-based light emitting diodes using an Indium-zinc-oxide transparent electrode with moth-eye structure" Shugo Mizutani, Satoshi Nakashima, Motoaki Iwaya, Tetsuya Takeuchi, Satoshi Kamiyama, Isamu Akasaki, Toshiyuki Kondo, Fumiharu Teramae, Atsushi Suzuki, Tsukasa Kitano, Midori Mori, Masahito Matsubara: SPIE Photonic west 2013, San Francisco, USA, 2013.2.2-8.
73. \*"GaNN トンネル接合素子の低抵抗化" 森田隆敏、加賀 充、桑野侑香、松井健城、渡邊雅大、竹内哲也、岩谷素顕、上山 智、赤崎 勇: 第 60 回応用物理学会春季学術講演会、神奈川工科大学、2013 年 3 月 26 日-30 日. (\*5 に対応)
74. \*"GaN 低温成長における Sb 添加の効果" 鈴木智行、笹島浩希、松原由布子、加賀 充、竹内哲也、上山 智、岩谷素顕、赤崎 勇: 第 60 回応用物理学会春季学術講演会、神奈川工科大学、2013 年 3 月 26 日-30 日. (\*2 に対応)
75. \*"LED 構造上 GaN トンネル接合の低抵抗化" 南川大智、加賀 充、岩谷素顕、竹内哲也、上山 智、赤崎 勇: 第 60 回応用物理学会春季学術講演会、神奈川工科大学、2013 年 3 月 26 日-30 日. (\*7 に対応)
76. \*"非対称 AlN/GaN 多層膜反射鏡の設計と作製" 萩原康大、矢木康太、安田俊輝、竹田健一郎、竹内哲也、岩谷素顕、上山 智、赤崎 勇: 第 60 回応用物理学会春季学術講演会、神奈川工科大学、2013 年 3 月 26 日-30 日. (\*15 に対応)
77. "ナノ ELO による m 面 GaInN 厚膜の検討" 小崎桂矢、近藤真一郎、土屋貴義、岩谷素顕、上山 智、竹内哲也、赤崎 勇: 第 60 回応用物理学会春季学術講演会、神奈川工科大学、2013 年 3 月 26 日-30 日.
78. \*"MOVPE 法による AlInN 高速成長の影響" 小塚祐吾、鈴木智行、森田隆敏、竹内哲也、上山 智、岩谷素顕、赤崎 勇: 第 60 回応用物理学会春季学術講演会、神奈川工科大学、2013 年 3 月 26 日-30 日. (\*3 に対応)
79. \*"MOVPE により作製した GaInN/GaN 超格子構造のその場観察 X 線回折法による評価" 山本泰司、飯田大輔、近藤保成、曾和美保子、岩谷素顕、竹内哲也、上山 智、赤崎 勇: 第 60 回応用物理学会春季学術講演会、神奈川工科大学、2013 年 3 月 26 日-30 日. (\*1 に対応)
80. \*"表面プラズモンカップリングを利用した GaInN/GaN 量子井戸の評価" 飯田大輔、Yuntian Chen, Yiyu Ou, Ahmed Fadil, Oleksii Kopylov、岩谷素顕、竹内哲也、上山 智、赤崎 勇、Haiyan Ou: 第 60 回応用物理学会春季学術講演会、神奈川工科大学、2013 年 3 月 26 日-30 日. (\*11 に対応)
81. \*"窒化物半導体 HFET 型光センサー構造の最適化" 石黒真未、池田和弥、水野正隆、岩谷素顕、上山 智、竹内哲也、赤崎 勇: 第 60 回応用物理学会春季学術講演会、神奈川工科大学、2013 年 3 月 26 日-30 日. [受賞記念講演] (\*12 に対応)
82. \*"GaNN 超格子構造最適化による窒化物半導体太陽電池の高性能化" 黒川泰視、近藤真一郎、山本翔太、森美貴子、岩谷素顕、竹内哲也、上山 智、赤崎 勇、天野浩: 第 60 回応用物理学会春季学術講演会、神奈川工科大学、2013 年 3 月 26 日-30 日. (\*13 に対応)
83. "350nm 紫外 LED の光取り出し効率の向上" 中嶋 翼、竹田健一郎、新里紘史、岩谷素顕、上山 智、竹内哲也、赤崎 勇、天野 浩: 第 60 回応用物理学会春季学術講演会、神奈川工科大学、2013 年 3 月 26 日-30 日.
84. "モスアイ加工サファイア基板による LED の光取り出し効率の改善" 土屋貴義、梅田慎

法人番号	231029
プロジェクト番号	S1201019

- 也、曾和美保子、河合俊介、近藤俊行、北野 司、森みどり、鈴木敦志、赤崎 勇、関根均、難波江宏一、岩谷素顕、竹内哲也、上山 智: 第 60 回応用物理学会春季学術講演会、神奈川工科大学、2013 年 3 月 26 日-30 日。
85. "電子ブロック層上活性層による電子オーバーフローの直接観測": 林 健人、松井健城、森田隆敏、鈴木智行、竹内哲也、上山 智、岩谷素顕、赤崎 勇: 第 60 回応用物理学会春季学術講演会、神奈川工科大学、2013 年 3 月 26 日-30 日。
86. "横方向 p 型活性化における雰囲気ガス依存性" 桑野侑香、加賀 充、森田隆敏、山下浩司、南川大智、竹内哲也、岩谷素顕、上山 智、赤崎 勇: 第 60 回応用物理学会春季学術講演会、神奈川工科大学、2013 年 3 月 26 日-30 日。
87. "窒化物半導体二波長発光ダイオードにおける発光強度比の安定性" 松井健城、山下浩司、加賀 充、森田隆敏、鈴木智行、竹内哲也、上山 智、岩谷素顕、赤崎 勇: 第 60 回応用物理学会春季学術講演会、神奈川工科大学、2013 年 3 月 26 日-30 日。
88. "Direct Evidence of Electron Overflow by Monitoring Emissions from Second Active Region in Nitride-Based Blue LEDs" K. Hayashi, K. Matsui, T. Morita, T. Suzuki, T. Takeuchi, S. Kamiyama, M. Iwaya, and I. Akasaki: Conference on LED and Its Industrial Application '13, Pacifico Yokohama, Yokohama, Japan, 2013.4.23-25.
89. \* "Nitride-Based p-Side Down LEDs on Tunnel Junction" T. Morita, M. Kaga, Y. Kuwano, K. Matsui, M. Watanabe, T. Takeuchi, S. Kamiyama, M. Iwaya, and I. Akasaki: Conference on LED and Its Industrial Application '13, Pacifico Yokohama, Yokohama, Japan, 2013.4.23-25. (\*5 に対応)
90. \* "Observation of GaInN/GaN Superlattice Structures by In Situ X-ray Diffraction Monitoring during Metalorganic Vapor-Phase Epitaxial Growth" T. Yamamoto, D. Iida, Y. Kondo, M. Sowa, S. Umeda, T. Kato, M. Iwaya, T. Takeuchi, S. Kamiyama, and I. Akasaki: Conference on LED and Its Industrial Application '13, Pacifico Yokohama, Yokohama, Japan, 2013.4.23-25. (\*1 および\*13 に対応)
91. "Threshold Power Density Reduction in AlGaIn/AlN Multiquantum Wells DUV (288 nm) Optical Pumped Laser" T. Yamada, Y. Matsubara, H. Shinzato, K. Takeda, M. Iwaya, T. Takeuchi, S. Kamiyama, I. Akasaki, and H. Amano: Conference on LED and Its Industrial Application '13, Pacifico Yokohama, Yokohama, Japan, 2013.4.23-25.
92. \* "Factors for obtaining a high open-circuit voltage in GaInN-based solar cells" Motoaki Iwaya, Shinichiro Kondo, Shota Yamamoto, Mikiko Mori, Yasushi Kurokawa, Tetsuya Takeuchi, Satoshi Kamiyama, Isamu Akasaki, Hiroshi Amano: Asia-Pacific Workshop on Widegap Semiconductors 2013, Tamsui, New Taipei City, Taiwan, May 12-15, 2013. (\*1 に対応)
93. \* "Bandgap dependence in nitride semiconductor-based tunnel junctions", D. Minamikawa, M. Kaga, Y. Kuwano, T. Morita, T. Takeuchi, S. Kamiyama, M. Iwaya, I. Akasaki: Asia-Pacific Workshop on Widegap Semiconductors 2013, Tamsui, New Taipei City, Taiwan, May 12-15, 2013. (\*5 に対応)
94. \* "High sensitivity group III nitride semiconductor based heterostructure field effect transistor type photosensors" Motoaki Iwaya, Mami Ishiguro, Masataka Mizuno, Kazuya Ikeda, Tetsuya Takeuchi, Satoshi Kamiyama, Isamu Akasaki: The Collaborative Conference on Crystal Growth (3CG), Cancun, Mexico, June 10-13, 2013. [invited Talk] (\*12 に対応)
95. \* "窒化物半導体における分極の影響と発光素子への応用" 竹内哲也、岩谷素顕、上山智、赤崎勇: 第 5 回 窒化物半導体結晶成長講演会、大阪大学、2013 年 6 月 21 日-22 日。[チュートリアル講演] (\*7 に対応)
96. "端面コーティングによる光励起 DUV レーザの閾値励起強度密度低減について" 山田

法人番号	231029
プロジェクト番号	S1201019

- 知明, 松原由布子, 新里紘史, 竹田健一郎, 岩谷素顕, 竹内哲也, 上山智, 赤崎勇, 天野浩: 第 5 回 窒化物半導体結晶成長講演会、大阪大学、2013 年 6 月 21 日-22 日.
97. “AlGaIn/AlN 多重量子井戸の誘導放出における転位密度依存性” 松原 由布子, 山田 知明, 中嶋 翼, 竹田 健一郎, 岩谷 素顕, 竹内 哲也, 上山 智, 赤崎 勇, 天野 浩: 第 5 回 窒化物半導体結晶成長講演会、大阪大学、2013 年 6 月 21 日-22 日.
98. \*“GaInN における InN 組成揺らぎの改善による窒化物太陽電池の高効率化” 黒川泰視, 近藤真一郎, 山本翔太, 森美貴子, 岩谷素顕, 竹内哲也, 上山智, 赤崎 勇, 天野浩: 第 5 回 窒化物半導体結晶成長講演会、大阪大学、2013 年 6 月 21 日-22 日. (\*13 に対応)
99. \*“その場観察 X 線回折法による GaInN/GaN 超格子構造の評価” 山本泰司, 飯田大輔, 近藤保成, 曾和美保子, 梅田慎也, 岩谷素顕, 竹内哲也, 上山智, 赤崎勇: 第 5 回 窒化物半導体結晶成長講演会、大阪大学、2013 年 6 月 21 日-22 日. (\*13 に対応)
100. \*“表面プラズモンカップリングを利用した緑色 LED の内部量子効率の向上” 飯田大輔, Yuntian Chen, Yiyu Ou, Ahmed Fadil, Oleksii Kopylov, 岩谷素顕、竹内哲也、上山智、赤崎勇、Haiyan Ou: 第 5 回 窒化物半導体結晶成長講演会、大阪大学、2013 年 6 月 21 日-22 日. (\*11 に対応)
101. \*“トンネル接合を有する青色マイクロ LED の電流電圧特性” 中島啓介, 渡邊雅大, 加賀 充, 鈴木智行, 南川大智, 竹内哲也, 上山 智, 岩谷素顕, 赤崎 勇: 第 5 回 窒化物半導体結晶成長講演会、大阪大学、2013 年 6 月 21 日-22 日. (\*5 に対応)
102. \*“新規 GaNSb 混晶の作製と GaSb モル分率成長温度依存性” 笹島浩希, 鈴木智行, 松原由布子, 竹内哲也, 上山智, 岩谷素顕, 赤崎勇: 第 5 回 窒化物半導体結晶成長講演会、大阪大学、2013 年 6 月 21 日-22 日. (\*2 に対応)
103. \*“In situ X-ray diffraction monitoring of OMVPE GaInN/GaN superlattice growth” Taiji Yamamoto, Daisuke Iida, Yasunari Kondo, Mihoko Sowa, Shinya Umeda, Motoaki Iwaya, Tetsuya Takeuchi, Satoshi Kamiyama, Isamu Akasaki: The 19th American Conference on Crystal Growth and Epitaxy, Keystone, Colorado, USA, July 21 - 26, 2013. (\*1 に対応)
104. \*“In situ X-ray diffraction monitoring of GaInN growth by metalorganic vapor phase epitaxy” Motoaki Iwaya, Taiji Yamamoto, Daisuke Iida, Yasunari Kondo, Mihoko Sowa, Shinya Umeda, Tetsuya Takeuchi, Satoshi Kamiyama, Isamu Akasaki: 17th International Conference on Crystal Growth and Epitaxy, Warsaw, Poland, August 11-16, 2013. (\*1 に対応)
105. \*“Extreme Low-Resistivity and High-Carrier-Concentration Si-Doped Al<sub>0.05</sub>Ga<sub>0.95</sub>N” Toru Sugiyama, Daisuke Iida, Motoaki Iwaya, Tetsuya Takeuchi, Satoshi Kamiyama, and Isamu Akasaki: 10th International Conference of Nitride Semiconductors, Washington DC, USA, August 25-30, 2013. (\*4 に対応)
106. \*“Realization of the High Conversion Efficiency Solar Cells using Nitride Semiconductors” Motoaki Iwaya, Yasushi Kurokawa, Yosuke Katsu, Taiji Yamamoto, Tetsuya Takeuchi, Satoshi Kamiyama, Isamu Akasaki, and Hiroshi Amano: 10th International Conference of Nitride Semiconductors, Washington DC, USA, August 25-30, 2013. **[Invited Talk]** (\*13, \*8, \*9, \*19 に対応)
107. \*“GaNSb Alloys Grown by Low Temperature Metalorganic Vapor Phase Epitaxy” Tornyuki Suzuki, Hiroki Sasajima, Yuuko Matsubara, Yugo Kozuka, Tetsuya Takeuchi, Satoshi Kamiyama, Motoaki Iwaya, and Isamu Akasaki: 10th International Conference of Nitride Semiconductors, Washington DC, USA, August 25-30, 2013. (\*1 に対応)
108. \*“Obtaining a High Open-Circuit Voltage in GaInN-Based Solar Cells” Hironori

法人番号	231029
プロジェクト番号	S1201019

- Kurokawa, Shinichiro Kondo, Mihoko Mori, Motoaki Iwaya, Tetsuya Takeuchi, Isamu Akasaki, and Hiroshi Amano: 10th International Conference of Nitride Semiconductors, Washington DC, USA, August 25-30, 2013. (\*13 に対応)
109. \*“Stable Balance of Emission Intensities from Two Active Regions in Nitride Semiconductor-Based Light Emitting Diodes” Kenjo Matsui, Koji Yamashita, Mitsuru Kaga, Takatoshi Morita, Yuka Kuwano, Tomoyuki Suzuki, Tetsuya Takeuchi, Satoshi Kamiyama, Motoaki Iwaya, and Isamu Akasaki: 10th International Conference of Nitride Semiconductors, Washington DC, USA, August 25-30, 2013. (\*16 に対応)
110. \* 10- $\mu$ m-Square Micro LED Array with Tunnel Junction” Masahiro Watanabe, Mitsuru Kaga, Koji Yamashita, Tomoyuki Suzuki, Daichi Minamikawa, Yuka Kuwano, Tetsuya Takeuchi, Satoshi Karniyarna, Motoaki Iwaya, and Isarnu Akasaki: 10th International Conference of Nitride Semiconductors, Washington DC, USA, August 25-30, 2013. (\*18 に対応)
111. “Advantages of the Moth-Eye Patterned Sapphire Substrate for the High Perfornance Nitride Based LEDs” Toshiyuki Kondo, Tsukasa Kitano, Atsushi Suzuki, Midori Mori, Koichi Naniwae, Motoaki Iwaya, Tetsuya Takeuchi, Satoshi Kamiyama, and Isamu Akasaki: 10th International Conference of Nitride Semiconductors, Washington DC, USA, August 25-30, 2013.
112. “Improvement of Light Extraction Efficiency in 350-nm Emission UV Light-Emitting Diodes” Tsubasa Nakashima, Kenitirou Takeda, Motoaki Iwaya, Tetsuya Takeuchi, Satoshi Kamiyama, Isamu Akasaki, and Hiroshi Amano: 10th International Conference of Nitride Semiconductors, Washington DC, USA, August 25-30, 2013.
113. \*“トンネル接合を活用した窒化物半導体多接合太陽電池の作製”黒川泰視, 合田智美, 加賀充, 岩谷素顕, 竹内哲也, 上山智, 赤崎勇, 天野浩: 第 74 回応用物理学会秋季学術講演会, 同志社大学, 2013 年 9 月 15 日-20 日. (\*13 および\*19 に対応)
114. \*“GaNSb 混晶 GaSb モル分率の Sb/N 比依存性” 笹島 浩希, 鈴木 智行, 松原由布子, 竹内 哲也, 上山 智, 岩谷 素顕, 赤崎 勇: 第 74 回応用物理学会秋季学術講演会, 同志社大学, 2013 年 9 月 15 日-20 日. (\*2 に対応)
115. \*“MOVPE 法による AlInN の高速成長” 小塚 祐吾, 安田 俊輝, 鈴木 智行, 竹内哲也, 上山 智, 岩谷 素顕, 赤崎 勇: 第 74 回応用物理学会秋季学術講演会, 同志社大学, 2013 年 9 月 15 日-20 日. (\*3 に対応)
116. \*“青色面発光レーザに向けた電流狭窄構造の検討” 中島 啓介, 渡邊 雅大, 加賀 充, 鈴木 智行, 南川 大智, 竹内 哲也, 上山 智, 岩谷 素顕, 赤崎 勇: 第 74 回応用物理学会秋季学術講演会, 同志社大学, 2013 年 9 月 15 日-20 日. (\*18 に対応)
117. \*“窒化物半導体を用いた HFET 型光センサーの暗電流検討” 石黒 真未, 池田和弥, 水野 正隆, 村瀬 卓弥, 岩谷 素顕, 上山 智, 赤崎 勇: 第 74 回応用物理学会秋季学術講演会, 同志社大学, 2013 年 9 月 15 日-20 日. (\*12 に対応)
118. “VSL 法を用いた AlGaIn/AlN 多重量子井戸の光学利得測定” 山田 知明, 松原 由布子, 竹田 健一郎, 岩谷 素顕, 竹内 哲也, 上山 智, 赤崎 勇, 天野 浩: 第 74 回応用物理学会秋季学術講演会, 同志社大学, 2013 年 9 月 15 日-20 日.
119. “AlGaIn/AlN 多重量子井戸の光学利得の転位密度依存性” 松原 由布子, 山田 知明, 竹田 健一郎, 岩谷 素顕, 竹内 哲也, 上山 智, 赤崎 勇, 天野 浩: 第 74 回応用物理学会秋季学術講演会, 同志社大学, 2013 年 9 月 15 日-20 日.
120. \*“In situ X-ray diffraction monitoring of GaInN/GaN superlattices growth by metalorganic vapor phase epitaxy” Taiji Yamamoto, Daisuke Iida, Yasunari Kondo, Mihoko Sowa, Shinya Umeda, Motoaki Iwaya, Tetsuya Takeuchi, Satoshi

法人番号	231029
プロジェクト番号	S1201019

- Kamiyama, and Isamu Akasaki: 2013 JSAP-MRS Joint Symposia, Doshisha Univ., Kyoto, Japan, September 18-19, 2013. (\*1 に対応)
121. \* "Enhanced internal quantum efficiency of green emission GaInN/GaN multiple quantum wells by surface plasmon coupling" Daisuke Iida, Yuntian Chen, Yiyu Ou, Ahmed Fadil, Oleksii Kopylov, Motoaki Iwaya, Tetsuya Takeuchi, Satoshi Kamiyama, Isamu Akasaki, and Haiyan Ou: 2013 JSAP-MRS Joint Symposia, Doshisha Univ., Kyoto, Japan, September 18-19, 2013. (\*11 に対応)
122. "Reduction of the threshold power density in AlGaIn/AlN multi-quantum wells DUV (288 nm) optical pumped lasers" Tomoaki Yamada, Yuko Matsubara, Hiroshi Shinzato, Kenichiro Takeda, Motoaki Iwaya, Tetsuya Takeuchi, Satoshi Kamiyama, Isamu Akasaki, and Hiroshi Amano: 2013 JSAP-MRS Joint Symposia, Doshisha Univ., Kyoto, Japan, September 18-19, 2013.
123. "Quantitative evaluation of electron overflow by monitoring emissions from second active region in nitride-based blue LEDs" Kento Hayashi, Kenjo Matsui, Takatoshi Morita, Tomoyuki Suzuki, Tetsuya Takeuchi, Satoshi Kamiyama, Motoaki Iwaya, and Isamu Akasaki: 2013 JSAP-MRS Joint Symposia, Doshisha Univ., Kyoto, Japan, September 18-19, 2013.
124. "10 um square micro LED and 100 channel array with tunnel junctions" Masahiro Watanabe, Mitsuru Kaga, Koji Yamashita, Tomoyuki Suzuki, Daichi Minamikawa, Yuka Kuwano, Tetsuya Takeuchi, Satoshi Kamiyama, Motoaki Iwaya, and Isamu Akasaki: 2013 JSAP-MRS Joint Symposia, Doshisha Univ., Kyoto, Japan, September 18-19, 2013.
125. "Asymmetric AlN/GaN-DBRs with high reflectivity" Koudai Hagiwara, Toshiki Yasuda, Kouta Yagi, Kenichiro Takeda, Motoaki Iwaya, Tetsuya Takeuchi, Satoshi Kamiyama, and Isamu Akasaki: 2013 JSAP-MRS Joint Symposia, Doshisha Univ., Kyoto, Japan, September 18-19, 2013.
126. "Moth-eye Patterned Sapphire Substrate technology for cost effective high performance LED" Toshiyuki Kondo, Tsukasa Kitano, Atsushi Suzuki, Midori Mori, Koichi Naniwae, Satoshi Kamiyama, Tetsuya Takeuchi, Motoaki Iwaya, and Isamu Akasaki: 2013 JSAP-MRS Joint Symposia, Doshisha Univ., Kyoto, Japan, September 18-19, 2013.
127. "MOVPE growth of embedded GaN nanocolumn" Shinya Umeda, Takahiro Kato, Tsukasa Kitano, Toshiyuki Kondo, Satoshi Kamiyama, Tetsuya Takeuchi, Motoaki Iwaya, and Isamu Akasaki: 2013 JSAP-MRS Joint Symposia, Doshisha Univ., Kyoto, Japan, September 18-19, 2013.
128. \* "Externally high sensitivity group III nitride semiconductor based heterostructure field effect transistor type photosensors" M. Ishiguro, M. Mizuno, M. Iwaya, T. Takeuchi, S. Kamiyama, I. Akasaki: 3rd International Conference on Materials and Applications for Sensors and Transducers, Prague, Czech Republic, September 13-17, 2013. (\*12 に対応)
129. \* "オーバーフロー抑制に向けた np 接合 GaInN-LED" 竹内哲也, 岩谷素顕, 上山智, 赤崎 勇: 日本学術振興会ワイドギャップ半導体光・電子デバイス第 162 委員会 第 86 回研究会, 名古屋, 2013 年 10 月 10 日. 【依頼講演】(\*7, \*17 に対応)
130. "Dislocation density dependence of stimulated emission characteristics in AlGaIn/AlN multi-quantum wells" Motoaki Iwaya, Yuko Matsubara, Tomoaki Yamada, Kenichiro Takeda, Tetsuya Takeuchi, Satoshi Kamiyama, Isamu Akasaki, and Hiroshi Amano: 8th International Workshop on Bulk Nitride Semiconductor, Kloster Seeon, Germany, September 30-October 5, 2013.
131. "近接昇華法による SiC 結晶のドーピング濃度均一化に関する検討" 畔柳有孝, 前田智彦, 赤澤絵理, 江間伸明, 寺前文晴, 藤元直樹, 難波江宏一 2, 上山智, 竹内哲

法人番号	231029
プロジェクト番号	S1201019

- 也, 岩谷素顕, 赤崎勇: 第 43 回結晶成長国内会議, 長野, 2013 年 11 月 6 日-8 日.
132. \*"新規 GaNSb 混晶の作製及び高 GaSb モル分率に向けた検討" 笹島浩希, 鈴木智行, 松原由布子, 竹内哲也, 上山智, 岩谷素顕, 赤崎勇: 第 43 回結晶成長国内会議, 長野, 2013 年 11 月 6 日-8 日. (\*2 に対応)
133. \*"AllnN の高速成長に関する研究" 小塚祐吾, 安田俊輝, 鈴木智行, 竹内哲也, 上山智, 岩谷素顕, 赤崎勇: 第 43 回結晶成長国内会議, 長野, 2013 年 11 月 6 日-8 日. (\*3 に対応)
134. "細線加工 m 面 GaN 基板上への GaInN 成長" 小崎桂矢, 近藤真一郎, 梅田慎也, 岩谷素顕, 竹内哲也, 上山智, 赤崎勇: 第五回薄膜太陽電池セミナープログラム, 名古屋大学, 2013 年 11 月 14 日-15 日.
135. \*"in-situ X 線を用いた GaInN/GaN 薄膜超格子構造の観察" 山本泰司, 飯田大輔, 近藤保成, 曾和美保子, 梅田慎也, 松原大幸, 岩谷素顕, 竹内哲也, 上山智, 赤崎勇: 第五回薄膜太陽電池セミナープログラム, 名古屋大学, 2013 年 11 月 14 日-15 日. (\*1 に対応)
136. \*"トンネル接合を用いた III 族窒化物半導体多接合型太陽電池" 合田智美, 黒川泰視, 森田隆敏, 岩谷素顕, 竹内哲也, 上山智, 赤崎勇, 天野浩: 応用物理学会 SC 東海地区学術講演会 2013, 名古屋大学, 2013 年 11 月 16 日. (\*19 に対応)
137. "モスアイ加工サファイア基板を用いた窒化物系 LED の性能向上検討" 曾和美保子, 北野司, 近藤俊行, 森みどり, 鈴木敦志, 難波江宏一, 上山智, 岩谷素顕, 竹内哲也, 赤崎勇: 応用物理学会 SC 東海地区学術講演会 2013, 名古屋大学, 2013 年 11 月 16 日.
138. \*"トンネル接合を用いた多接合窒化物半導体の検討" 黒川泰視, 合田智美, 加賀充, 岩谷素顕, 竹内哲也, 上山智, 赤崎勇, 天野浩: 電子情報通信学会 (ED, CPM, LQE 合同研究会), 大阪大学, 2013 年 11 月 28 日-29 日. (\*19 に対応)
139. "350nm 紫外 LED 光取り出し効率改善に関する研究" 中嶋翼, 竹田健一郎, 岩谷素顕, 上山智, 竹内哲也, 赤崎勇, 天野浩: 電子情報通信学会 (ED, CPM, LQE 合同研究会), 大阪大学, 2013 年 11 月 28 日-29 日.
140. \*"In situ X-ray diffraction monitoring of group III nitride growth by MOVPE" Motoaki Iwaya, Hironori Kurokawa, Yosuke Katsu, Taiji Yamamoto, Tetsuya Takeuchi, Satoshi Kamiyama, Isamu Akasaki: Workshop on Ultra-Precision Processing for III-Nitride, Santa Barbara, USA, October 16-18, 2013. **[Invited Talk]** (\*1 に対応)
141. \*"Homoepitaxial growth of AlN films on freestanding AlN (0001) substrates by metalorganic vapor phase epitaxy" Tomohiro Morishita, Motoaki Iwaya, Tetsuya Takeuchi, Satoshi Kamiyama, Isamu Akasaki: SPIE Photonics West 2014, San Francisco, USA, February 1-6, 2014. (\*6 に対応)
142. \*"Realization of the high conversion efficiency solar cells using high InN molar fraction GaInN active layer" Motoaki Iwaya, Hironori Kurokawa, Yosuke Katsu, Taiji Yamamoto, Tetsuya Takeuchi, Satoshi Kamiyama, Isamu Akasaki, Hiroshi Amano: SPIE Photonics West 2014, San Francisco, USA, February 1-6, 2014. **[Invited Talk]** (\*19 に対応)
143. "Improvement of photosensitivity in heterostructure-field-effect-transistor type photosensors with a p-GaInN gate" Mami Ishiguro, Kazuya Ikeda, Takuya Murase, Yuma Yamamoto, Tetsuya Takeuchi, Satoshi Kamiyama, Isamu Akasaki: ISPlasma, Meijo University, Japan, March 2-6, 2014.
144. "Nitride-based hetero-field-effect-transistor-type photosensors with extremely high photosensitivity and complete solar-blind" Takuya Murase, Mami Ishiguro,

法人番号	231029
プロジェクト番号	S1201019

- Yuma Yamamoto, Tetsuya Takeuchi, Satoshi Kamiyama, Isamu Akasaki: ISPlasma, Meijo University, Japan, March 2-6, 2014.
145. \*“Analysis of GaInN/GaN superlattices on GaN template during growth by in-situ X-ray diffraction” Taiji Yamamoto, Daisuke Iida, Yasunari Kondo, Mihoko Sowa, Shinya Umeda, Hiroyuki Matsubara, Motoaki Iwaya, Tetsuya Takeuchi, Satoshi Kamiyama, and Isamu Akasaki: ISPlasma, Meijo University, Japan, March 2-6, 2014. (\*1 に対応)
146. “Realization of m-plane GaInN thick films grown on submicron patterned groove-GaN substrate” Keiya Kozaki, Shinichiro Kondo, Shinya Umeda, Motoaki Iwaya, Satoshi Kamiyama, Tetsuya Takeuchi, and Isamu Akasaki: ISPlasma, Meijo University, Japan, March 2-6, 2014.
147. “High reflective and low resistive silver electrode on p-GaN” Shunsuke Kawai, Daisuke Iida, Motoaki Iwaya, Tetsuya Takeuchi, Satoshi Kamiyama, and Isamu Akasaki: ISPlasma, Meijo University, Japan, March 2-6, 2014.
148. \*“Current confinement by nitride-based buried tunnel junction” Y. Kuwano, M. Ino, T. Morita, D. Minamikawa, T. Takeuchi, S. Kamiyama, M. Iwaya, and I. Akasaki: ISPlasma, Meijo University, Japan, March 2-6, 2014. (\*18 に対応)
149. \*“Low resistive GaInN tunnel junctions with high InN mole fractions” D. Minamikawa, Y. Kuwano, S. Kawai, T. Morita, T. Takeuchi, S. Kamiyama, M. Iwaya, and I. Akasaki: ISPlasma, Meijo University, Japan, March 2-6, 2014. (\*5 に対応)
150. “Improvement of the light extraction efficiency in 350-nm-emission UV light-emitting diodes by novel distributed bragg reflector p-type electrode” T. Nakashima, K. Takeda, M. Iwaya, T. Takeuchi, S. Kamiyama, I. Akasaki, and H. Amano: ISPlasma, Meijo University, Japan, March 2-6, 2014.
151. “Technologies of nitride-based LEDs”, Satoshi Kamiyama, ISPlasma, Meijo University, Japan, March 2-6, 2014 **[Tutorial talk]**
152. \*“Observation of group III nitride semiconductors by in situ X-ray diffraction monitoring during MOVPE growth” Motoaki Iwaya, Taiji Yamamoto, Daisuke Iida, Mihoko Sowa, Yasunari Kondo, Tetsuya Takeuchi, Satoshi Kamiyama, and Isamu Akasaki: International Conference on Materials and Characterization Techniques, VIT University, Vellore, India, 10-12 March, 2014. **[Invited talk]** (\*1 に対応)
153. \*“表面プラズモンを利用した緑色 LED の高効率化に向けて” 飯田 大輔、岩谷 素顕、竹内 哲也、上山 智、赤崎 勇: 日本学術振興会ワイドギャップ半導体光・電子デバイス第 162 委員会 第 88 回研究会, 主婦会館, 2014 年 3 月 8 日 **[依頼講演]** (\*11 に対応)
154. “p 型 GaN 上の Ag 電極を用いた高反射電極の検討” 河合俊介, 飯田大輔, 岩谷素顕, 竹内哲也, 上山智, 赤崎勇: 第 61 回応用物理学会春季学術講演会、青山学院大学相模原キャンパス、2014 年 3 月 17 日-20 日.
155. “電子オーバーフロー直接観測を用いた青色 LED 電子ブロック層の検討” 林健人, 松井健城, 安田俊輝, 勝野翔太, 竹内哲也, 上山智, 岩谷素顕, 赤崎勇: 第 61 回応用物理学会春季学術講演会、青山学院大学相模原キャンパス、2014 年 3 月 17 日-20 日.
156. \*“分極制御による紫外発光素子のホール注入の検討” 安田俊輝, 林健人, 竹田健一郎, 中嶋翼, 竹内哲也, 岩谷素顕, 上山智, 赤崎勇, 天野浩: 第 61 回応用物理学会春季学術講演会、青山学院大学相模原キャンパス、2014 年 3 月 17 日-20 日. (\*6 に対応)
157. \*“Ⅲ族窒化物半導体トンネル接合上の高効率 LED” 森田隆敏, 井野匡貴, 桑野侑香, 渡邊雅大, 岩谷素顕, 竹内哲也, 上山智, 赤崎勇: 第 61 回応用物理学会春季学術講演会、青山学院大学相模原キャンパス、2014 年 3 月 17 日-20 日. (\*5 に対応)

法人番号	231029
プロジェクト番号	S1201019

158. \*“III 族窒化物半導体埋込みトンネル接合による電流狭窄構造” 桑野侑香, 堀川航佑, 森田隆敏, 井野匡貴, 竹内哲也, 上山智, 岩谷素顕, 赤崎勇: 第 61 回応用物理学会春季学術講演会、青山学院大学相模原キャンパス、2014 年 3 月 17 日-20 日. (\*18 に対応)
159. \*“GaInN/GaN ヘテロ接合における緩和過程の転位密度依存性” 石原耕史, 近藤保成, 松原大幸, 飯田大輔, 山本泰司, 曾和美保子, 岩谷素顕, 竹内哲也, 上山智, 赤崎勇: 第 61 回応用物理学会春季学術講演会、青山学院大学相模原キャンパス、2014 年 3 月 17 日-20 日. (\*1 に対応)
160. \*“窒化物半導体 HFET 型 UV 光センサーの火炎センサー応用” 山本雄磨, 村瀬卓弥, 石黒真未, 山田知明, 岩谷素顕, 竹内哲也, 上山智, 赤崎勇: 第 61 回応用物理学会春季学術講演会、青山学院大学相模原キャンパス、2014 年 3 月 17 日-20 日. (\*12 に対応)
161. “高温スパッタ法により堆積した AlN バッファ層に関する検討” 伊藤弘晃, 飯田大輔, 近藤保成, 曾和美保子, 岩谷素顕, 竹内哲也, 上山智, 赤崎勇: 第 61 回応用物理学会春季学術講演会、青山学院大学相模原キャンパス、2014 年 3 月 17 日-20 日.
162. \*“MOVPE 法を用いた高品質 AlInN の高速成長” 池山和希, 小塚祐吾, 安田俊輝, 竹内哲也, 上山智, 岩谷素顕, 赤崎勇: 第 61 回応用物理学会春季学術講演会、青山学院大学相模原キャンパス、2014 年 3 月 17 日-20 日. (\*3 に対応)
163. \*“高成長速度 AlInN による窒化物半導体多層膜反射鏡” 小塚祐吾, 池山和希, 安田俊輝, 竹内哲也, 上山智, 岩谷素顕, 赤崎勇: 第 61 回応用物理学会春季学術講演会、青山学院大学相模原キャンパス、2014 年 3 月 17 日-20 日. (\*3 および\*15 に対応)
164. \*“非極性 m 面 GaN 基板上に作製した GaInN 系太陽電池の特性” 小崎桂矢, 黒川泰視, 岩谷素顕, 上山智, 竹内哲也, 赤崎勇, 天野浩: 第 61 回応用物理学会春季学術講演会、青山学院大学相模原キャンパス、2014 年 3 月 17 日-20 日. (\*13 に対応)
165. “蛍光 SiC の窒化物系白色 LED への応用に向けた研究” 上山智, 岩谷素顕, 竹内哲也, 赤崎勇: 第 61 回応用物理学会春季学術講演会、青山学院大学相模原キャンパス、2014 年 3 月 17 日-20 日. [招待講演]
166. \*“高 InN モル分率 GaInN を用いたトンネル接合” 南川大智, 桑野侑香, 河合俊介, 森田隆敏, 岩谷素顕, 竹内哲也, 上山智, 赤崎勇: 第 61 回応用物理学会春季学術講演会、青山学院大学相模原キャンパス、2014 年 3 月 17 日-20 日. (\*5 に対応)
167. \*“その場観察 X 線回折法を用いた GaInN/GaN 超格子構造の最適化” 村瀬卓弥, 石黒真未, 山田知明, 岩谷素顕, 竹内哲也, 上山智, 赤崎勇: 第 61 回応用物理学会春季学術講演会、青山学院大学相模原キャンパス、2014 年 3 月 17 日-20 日. (\*1 に対応)
168. \*“高感度な窒化物半導体 HFET 型ソーラーブラインド紫外光センサー” 村瀬卓弥, 石黒真未, 山田知明, 岩谷素顕, 竹内哲也, 上山智, 赤崎勇: 第 61 回応用物理学会春季学術講演会、青山学院大学相模原キャンパス、2014 年 3 月 17 日-20 日. (\*13 に対応)
169. “窒化物系青色 LED における光取り出し効率改善のためのレーザ加工方法の検討” 花井駿, 鈴木敦志, 北野司, 梅田慎也, 加藤貴久, 上山智, 竹内哲也, 岩谷素顕, 赤崎勇: 第 61 回応用物理学会春季学術講演会、青山学院大学相模原キャンパス、2014 年 3 月 17 日-20 日.
170. \*“Investigation of Hole Injection in UV-LEDs Utilizing Polarization Effect” T. Yasuda, K. Hayashi, T. Nakashima, T. Takeuchi, S. Kamiyama, M. Iwaya, I. Akasaki, and H. Amano: Conference on LED and Its Industrial Application '14, Yokohama, Japan, 22-24 April, 2014. (\*7 に対応)
171. \*“Roles of Mg Doping in Nitride Semiconductor-Based Light Emitting Diodes

法人番号	231029
プロジェクト番号	S1201019

- with Two Active Regions” K. Matsui, T. Morita, T. Suzuki, T. Takeuchi, S. Kamiyama, M. Iwaya, and I. Akasaki: Conference on LED and Its Industrial Application '14, Yokohama, Japan, 22-24 April, 2014. (\*5 に対応)
172. \*“Nitride-Based Light Emitting Diodes with Buried Tunnel Junctions” M. Ino, Y. Kuwano, T. Morita, D. Minamikawa, T. Takeuchi, S. Kamiyama, M. Iwaya, and I. Akasaki: Conference on LED and Its Industrial Application '14, Yokohama, Japan, 22-24 April, 2014. (\*5 および\*17 に対応)
173. “Study of High-Reflective Ag-Based Electrode on p-Type GaN” S. Kawai, D. Iida, M. Iwaya, T. Takeuchi, S. Kamiyama, and I. Akasaki: Conference on LED and Its Industrial Application '14, Yokohama, Japan, 22-24 April, 2014.
174. “Fabrication of Nitride-Based Blue LED with Eliminating Light-Absorptive Laser Scribing Damages” S. Hanai, I. Nakatani, A. Suzuki, T. Kitano, D. Iida, T. Kato, M. Iwaya, T. Takeuchi, S. Kamiyama, and I. Akasaki: Conference on LED and Its Industrial Application '14, Yokohama, Japan, 22-24 April, 2014.
175. \*“An alternative hole injection: Nitride-based tunnel junctions” T. Takeuchi, D. Minamikawa, Y. Kuwano, M. Watanabe, M. Iwaya, S. Kamiyama, I. Akasaki: International Conference on Metamaterials and Nanophysics, Varadero, Cuba, 22 April to 1 May 2014. [Invited Talk] (\*5 に対応)
176. \*“Development of nitride-based photosensor” Motoaki Iwaya, Takuya Murase, Tetsuya Takeuchi, Satoshi Kamiyama, and Isamu Akasaki: International Conference on Metamaterials and Nanophysics, Varadero, Cuba, 22 April to 1 May 2014. [Invited Talk] (\*13 に対応)
177. \*“Solar blind and extremely high photosensitivity AlGaIn-based UV hetero-field-effect-transistor-type photosensors” Takuya Murase, Mami Ishiguro, Tomoaki Yamada, Motoaki Iwaya, Tetsuya Takeuchi, Satoshi Kamiyama, Isamu Akasaki: Compound Semiconductor Week 2014, Montpellier, France, May 11-15, 2014. (\*13 に対応)
178. \*“Fabrication of Multi-junction GaInN-Based solar cell” Hironori Kurokawa, Mitsuru Kaga, Tomomi Goda, Motoaki Iwaya, Tetsuya Takeuchi, Satoshi Kamiyama, Isamu Akasaki, Hiroshi Amano: Compound Semiconductor Week 2014, Montpellier, France, May 11-15, 2014. (\*19 に対応)
179. \*“Activation Energy of Extremely Low-Resistivity and High-Carrier-Concentration Si-Doped Al<sub>0.05</sub>Ga<sub>0.95</sub>N” Motoaki Iwaya, Daisuke Iida, Toru Sugiyama, Tetsuya Takeuchi, Satoshi Kamiyama, and Isamu Akasaki: 5th International Symposium on Growth of III-Nitrides, Atlanta, USA, May 18-22, 2014. (\*4 に対応)
180. “Dislocation Density Dependence of Modal Gain in AlGaIn/AlN Multiquantum Wells” Tomoaki Yamada, Kenichiro Takeda, Motoaki Iwaya, Tetsuya Takeuchi, Satoshi Kamiyama, Isamu Akasaki, and Hiroshi Amano: 5th International Symposium on Growth of III-Nitrides, Atlanta, USA, May 18-22, 2014.
181. “Development of GaN-based semiconductors of excellent quality and their p-n junction blue-light-emitting devices”, Isamu Akasaki, Japan-Sweden Science, Technology & Innovation Symposium 2014, Stockholm, Sweden, May 21, 2014. [Invited talk]
182. \*“GaInN/GaN ヘテロ接合における緩和過程の転位密度依存性” 石原耕史, 近藤保成, 松原大幸, 岩谷素顕, 上山 智, 竹内哲也, 赤崎 勇: 電子情報通信学会(ED・CPM・SDM 研究会), 名古屋大学、2014 年 5 月 28 日-29 日. (\*1 に対応)
183. \*“GaNSb の Sb 取り込みと表面形態に関する検討” 小森大資, 笹島浩希, 鈴木智行, 竹内哲也, 上山 智, 岩谷素顕, 赤崎 勇: 電子情報通信学会(ED・CPM・SDM 研

法人番号	231029
プロジェクト番号	S1201019

- 研究会), 名古屋大学、2014 年 5 月 28 日-29 日. (\*2 に対応)
184. \*“窒化物半導体 HFET 型紫外受光素子の火炎センサー応用”山本雄磨, 村瀬卓弥, 石黒真未, 山田知明, 岩谷素顕, 上山 智, 竹内哲也, 赤崎 勇: 電子情報通信学会(ED・CPM・SDM 研究会), 名古屋大学、2014 年 5 月 28 日-29 日. (\*13 に対応)
185. \*“窒化物半導体 LED におけるキャリア輸送への分極固定電荷の影響” 勝野翔太, 林 健人, 安田俊輝, 岩谷素顕, 竹内哲也, 上山 智, 赤崎 勇, 天野 浩: 電子情報通信学会(ED・CPM・SDM 研究会), 名古屋大学、2014 年 5 月 28 日-29 日. (\*7 に対応)
186. “窒化物系 LED 作製のレーザー加工による光取り出し効率向上の検討” 花井 駿, 鈴木敦志, 北野 司, 飯田大輔, 加藤貴久, 竹内哲也, 岩谷素顕, 上山 智, 赤崎 勇: 通信学会(ED・CPM・SDM 研究会), 名古屋大学、2014 年 5 月 28 日-29 日.
187. “モスアイ光取り出し構造を有する青色 LED”、上山 智: 光電相互変換第 125 委員会・産業用 LED 応用研究会合同研究会、名城大学(名城サテライト)、2014 年 7 月 11 日 [招待講演]
188. \*“Dislocation density dependence of the critical thickness in GaInN/GaN heterostructure” Taiji Yamamoto, Daisuke Iida, Yasunari Kondo, Mihoko Sowa, Hiroyuki Matsubara, Motoaki Iwaya, Tetsuya Takeuchi, Satoshi Kamiyama, and Isamu Akasaki: 17th International Conference on Metalorganic Vapor Phase Epitaxy, Lausanne, Switzerland, 13-18 July 2014. [Invited Talk] (\*1 に対応)
189. “AlGaN/AlN 多重量子井戸の光学利得の転位密度依存性” 山田知明, 岩谷素顕, 竹内哲也, 上山智, 赤崎勇, 天野浩: 第 6 回窒化物半導体結晶成長講演会, 名城大学, 2014 年 7 月 25-26 日.
190. \*“非極性 m 面 GaN 基板上 GaInN 系太陽電池の特性” 小崎桂矢, 黒川泰視, 山本泰司, 岩谷素顕, 竹内哲也, 上山智, 天野浩, 赤崎勇: 第 6 回窒化物半導体結晶成長講演会, 名城大学, 2014 年 7 月 25-26 日. (\*13 に対応)
191. \*“r 面サファイア基板上における a 面 GaN 成長に関する結晶性向上の検討” 加藤貴久, 水野尚之, 伊藤弘晃, 飯田大輔, 藤井高志, 福田承生, 上山 智, 竹内 哲也, 岩谷 素顕, 赤崎勇: 第 6 回窒化物半導体結晶成長講演会, 名城大学, 2014 年 7 月 25-26 日. (\*7 に対応)
192. \*“ナノインプリント技術による表面プラズモン緑色 LED の作製と評価” 飯田大輔, 河合俊介, 土屋貴義, 岩谷素顕, 竹内哲也, 上山智, 赤崎勇: 第 6 回窒化物半導体結晶成長講演会, 名城大学, 2014 年 7 月 25-26 日. (\*11 に対応)
193. “MOVPE 選択成長による GaN ナノコラム” 水野尚之, 上山智, 竹内哲也, 岩谷 素顕, 赤崎 勇: 第 6 回窒化物半導体結晶成長講演会, 名城大学, 2014 年 7 月 25-26 日.
194. “電子オーバーフロー直接観測を用いた青色 LED 電子ブロック層の検討” 林健人, 安田俊輝, 勝野翔太, 竹内哲也, 上山智, 岩谷素顕, 赤崎勇: 第 6 回窒化物半導体結晶成長講演会, 名城大学, 2014 年 7 月 25-26 日.
195. \*“高感度な窒化物半導体 AlGaN 系 HFET 型ソーラーブラインド紫外光センサー” 村瀬卓弥, 石黒真未, 山田知明, 山本雄磨, 岩谷素顕, 竹内哲也, 上山智, 赤崎勇: 第 6 回窒化物半導体結晶成長講演会, 名城大学, 2014 年 7 月 25-26 日. (\*13 に対応)
196. “p 型 GaN に対する Ag 電極上酸化保護層の検討” 河合俊介, 飯田大輔, 岩谷素顕, 竹内哲也, 上山智, 赤崎勇: 第 6 回窒化物半導体結晶成長講演会, 名城大学, 2014 年 7 月 25-26 日.
197. \*“窒化物半導体 AlGaN を用いた紫外受光素子の火炎センサー応用” 山本雄磨, 村瀬卓弥, 山田知明, 岩谷素顕, 竹内哲也, 上山智, 赤崎勇: 第 6 回窒化物半導体結晶成長講演会, 名城大学, 2014 年 7 月 25-26 日(\*13 に対応).

法人番号	231029
プロジェクト番号	S1201019

198. \*“窒化物半導体 LED における分極電荷の補償” 勝野翔太, 林健人, 安田俊輝, 岩谷素顕, 竹内哲也, 上山智, 天野浩, 赤崎勇: 第 6 回窒化物半導体結晶成長講演会, 名城大学, 2014 年 7 月 25-26 日. (\*7 に対応)
199. \*“二つの活性層を有する発光ダイオードにおける Mg の影響” 松井健城, 竹内哲也, 上山智, 岩谷素顕, 赤崎勇: 第 6 回窒化物半導体結晶成長講演会, 名城大学, 2014 年 7 月 25-26 日. (\*16 に対応)
200. \*“窒化物半導体 LED における正孔伝導に対する分極電荷の影響” 安田俊輝, 勝野翔太, 林健人, 竹内哲也, 岩谷素顕, 上山智, 赤崎勇, 天野浩: 第 6 回窒化物半導体結晶成長講演会, 名城大学, 2014 年 7 月 25-26 日. (\*7 に対応)
201. \*“III族窒化物半導体による埋め込みトンネル接合” 井野 匡貴, 南川 大智, 水野尚之, 竹内 哲也, 上山 智, 岩谷 素顕, 赤崎 勇: 第 6 回窒化物半導体結晶成長講演会, 名城大学, 2014 年 7 月 25-26 日. (\*5 に対応)
202. \*“GaInN 系トンネル接合を有する LED” 南川大智, 井野匡貴, 岩谷素顕, 竹内哲也, 上山智, 赤崎勇: 第 6 回窒化物半導体結晶成長講演会, 名城大学, 2014 年 7 月 25-26 日. (\*5 に対応)
203. “青色面発光レーザ共振器の内部損失の検討” 中島啓介, 渡邊雅大, 堀川航佑, 竹内哲也, 上山智, 岩谷素顕, 赤崎勇: 第 6 回窒化物半導体結晶成長講演会, 名城大学, 2014 年 7 月 25-26 日.
204. “窒化物半導体面発光レーザにおける電流狭窄構造の特性評価” 堀川航佑, 中島啓介, 小塚祐吾, 池山和希, 竹内哲也, 上山智, 岩谷素顕, 赤崎勇: 第 6 回窒化物半導体結晶成長講演会, 名城大学, 2014 年 7 月 25-26 日.
205. \*“その場観察 X 線回折法を用いた GaInN 系太陽電池構造の最適化” 山本泰司, 黒川泰視, 小崎桂矢, 岩谷素顕, 上山智, 竹内哲也, 赤崎勇: 第 6 回窒化物半導体結晶成長講演会, 名城大学, 2014 年 7 月 25-26 日. (\*1 に対応)
206. \*“高成長速度 AlInN 用いた多層膜反射鏡に関する研究” 小塚祐吾, 池山和希, 安田俊輝, 竹内哲也, 上山智, 岩谷素顕, 赤崎勇: 第 6 回窒化物半導体結晶成長講演会, 名城大学, 2014 年 7 月 25-26 日. (\*3 および\*15 に対応)
207. \*“GaInN/GaN ヘテロ接合における緩和過程の転位密度依存性” 石原耕史, 近藤保成, 松原大幸, 岩谷素顕, 上山智, 竹内哲也, 赤崎勇: 第 6 回窒化物半導体結晶成長講演会, 名城大学, 2014 年 7 月 25-26 日. (\*1 に対応)
208. \*“高品質 AlInN の高速成長の検討” 池山和希, 小塚祐吾, 安田俊輝, 竹内哲也, 上山智, 岩谷素顕, 赤崎勇: 第 6 回窒化物半導体結晶成長講演会, 名城大学, 2014 年 7 月 25-26 日. (\*3 に対応)
209. \*“MOCVD 法を用いた GaNSb の結晶成長” 小森大資, 笹島浩希, 鈴木智行, 竹内哲也, 岩谷素顕, 上山智, 赤崎勇: 第 6 回窒化物半導体結晶成長講演会, 名城大学, 2014 年 7 月 25-26 日. (\*2 に対応)
210. \*“MOCVD 法による Sb を添加した AlN および GaN の作製” 笹島 浩希, 小森 大資, 竹内 哲也, 岩谷 素顕, 上山 智, 赤崎 勇: 第 6 回窒化物半導体結晶成長講演会, 名城大学, 2014 年 7 月 25-26 日. (\*2 に対応)
211. “窒化物系 LED 技術最前線” 上山智: 第 6 回窒化物半導体結晶成長講演会, 名城大学, 2014 年 7 月 25-26 日. [チュートリアル講演]
212. \*“Lattice relaxation process in GaInN/GaN heterostructure system as function of dislocation density in underlying GaN layer” Motoaki Iwaya, Koji Ishihara, Taiji Yamamoto, Daisuke Iida, Yasunari Kondo, Hiroyuki Matsubara, Tetsuya Takeuchi, Satoshi Kamiyama, and Isamu Akasaki: The Workshop on Ultra-Precision Processing for Wide-Gap Semiconductors 2014, Bath, United Kingdom, August

法人番号	231029
プロジェクト番号	S1201019

20-22 2014. **[Invited talk]** (\*1 に対応)

213. \* “Nitride-based optoelectronic devices utilizing tunnel junctions” Tetsuya Takeuchi, Motoaki Iwaya, Satoshi Kamiyama, and Isamu Akasaki: Lester Eastman Conference on High Performance Devices 2014, Ithaca, USA August 5-7 2014. **[Invited Talk]** (\*5 および\*16 に対応)
214. \* “Demonstration of GaInN-based laser pumped by an electron beam” M. Iwaya, K. Kozaki, T. Yamada, T. Takeuchi, S. Kamiyama, I. Akasaki, Y. Honda, H. Amano, S. Iwayama, J. Matsuda, N. Matsubara, T. Matsumoto: International Workshop on Nitride semiconductor 2014, Wrocław, Poland August 24-29 2014. **[Invited Talk]** (\*14 に対応)
215. \* “Nitride-based tunnel junctions as an alternative hole injection” Tetsuya Takeuchi, Motoaki Iwaya, Satoshi Kamiyama, and Isamu Akasaki: International Workshop on Nitride semiconductor 2014, Wrocław, Poland August 24-29 2014. **[Invited Talk]** (\*5 および\*16 に対応)
216. \* “Laser lift-off technique of 380-nm light emitting diodes grown on GaN substrate” D. Iida, S. Kawai, T. Tsuchiya, N. Ema, M. Iwaya, T. Takeuchi, S. Kamiyama, and I. Akasaki: International Workshop on Nitride semiconductor 2014, Wrocław, Poland August 24-29 2014. (\*18 に対応)
217. \* “Fabrication of surface plasmon based green light emitting diodes by nanoimprint technique” D. Iida, S. Kawai, T. Tsuchiya, M. Iwaya, T. Takeuchi, S. Kamiyama, and I. Akasaki: International Workshop on Nitride semiconductor 2014, Wrocław, Poland August 24-29 2014. (\*11 に対応)
218. \* “Fabrication of nonpolar m-plane GaInN-based solar cell on freestanding m-plane GaN substrate” K. Kozaki, H. Kurokawa, M. Iwaya, T. Takeuchi, S. Kamiyama, and I. Akasaki: International Workshop on Nitride semiconductor 2014, Wrocław, Poland August 24-29 2014. (\*5 に対応)
219. “Lattice relaxation process in GaInN/GaN heterostructure system as function of dislocation density in underlying GaN layer” Motoaki Iwaya, Koji Ishihara, Taiji Yamamoto, Daisuke Iida, Yasunari Kondo, Hiroyuki Matsubara, Tetsuya Takeuchi, Satoshi Kamiyama, and Isamu Akasaki: Workshop on Ultra-Precision Processing for Wide Band Gap Semiconductors, Bath, UK, 20-22 August, 2014.
220. “Low Resistive and Low Absorptive Nitride-Based Tunnel Junctions” Daichi Minamikawa, Masataka Ino, Daiki Takasuka, Motoaki Iwaya, Tetsuya Takeuchi, Satoshi Kamiyama, and Isamu Akasaki: Material Research Society Fall Meeting, Boston, USA, Nov. 30-Dec. 5, 2014.
221. “Evaluation of Electron Overflow in Blue-LEDs with P-AlGa<sub>N</sub> Or P-GaN Electron Blocking Layer” Kento Hayashi, Toshiki Yasuda, Shota Katsuno, Tetsuya Takeuchi, Satoshi Kamiyama, Motoaki Iwaya, Isamu Akasaki: Material Research Society Fall Meeting, Boston, USA, Nov. 30-Dec. 5, 2014.
222. “Optimization of Carrier Distributions in Periodic Gain Structures towards Blue VCSELs” Kenjo Matsui, Kosuke Horikawa, Yugo Kozuka, Kazuki Ikeyama, Tetsuya Takeuchi, Satoshi Kamiyama, Motoaki Iwaya, Isamu Akasaki: Material Research Society Fall Meeting, Boston, USA, Nov. 30-Dec. 5, 2014.
223. “Study on the High Reflective Ag Ohmic Contact on High Carrier Concentration Si-Doped Al<sub>0.03</sub>Ga<sub>0.97</sub>N” Shunsuke Kawai, Daisuke Iida, Motoaki Iwaya, Tetsuya

法人番号	231029
プロジェクト番号	S1201019

- Takeuchi, Satoshi Kamiyama, Isamu Akasaki: Material Research Society Fall Meeting, Boston, USA, Nov. 30-Dec. 5, 2014.
224. "Analysis of GaInN/GaN Heterostructure Grown on GaN Underlying Layer with Different Dislocation Density" Koji Ishihara, Taiji Yamamoto, Daisuke Iida, Yasunari Kondo, Hiroyuki Matsubara, Motoaki Iwaya, Tetsuya Takeuchi, Satoshi Kamiyama, Isamu Akasaki: Material Research Society Fall Meeting, Boston, USA, Nov. 30-Dec. 5, 2014.
225. "Growths of AlInN Single Layers and Distributed Bragg Reflectors for VCSELs" Yugo Kozuka, Kazuki Ikeyama, Toshiki Yasuda, Tetsuya Takeuchi, Satoshi Kamiyama, Motoaki Iwaya, Isamu Akasaki: Material Research Society Fall Meeting, Boston, USA, Nov. 30-Dec. 5, 2014.
226. "Laser lift-off technique for freestanding GaN substrate using an In droplet formed by thermal decomposition of GaInN and its application to LED" Motoaki Iwaya, Daisuke Iida, Syunsuke Kawai, Nobuaki Ema, Takayoshi Tsuchiya, Tetsuya Takeuchi, Satoshi Kamiyama, and Isamu Akasaki: 10th International Symposium on Semiconductor Light Emitting Devices (ISSLED 2014) Kaohsiung, Taiwan, Dec. 14<sup>th</sup>-19<sup>th</sup>, 2014.
227. "In-situ x-ray diffraction analysis for MOVPE growth of nitride semiconductors" Motoaki Iwaya, Taiji Yamamoto, Koji Ishihara, Tetsuya Takeuchi, Satoshi Kamiyama, and Isamu Akasaki: SPIE Photonics West, San Francisco, USA, Feb. 7<sup>th</sup>-12<sup>th</sup>, 2015.
228. "Performance of nitride-based blue LED fabricated on sapphire substrate with nanostructured SiO<sub>2</sub>" Shun Hanai, Motoaki Iwaya, Tetsuya Takeuchi, Satoshi Kamiyama, Isamu Akasaki, and Tsukasa Kitano: SPIE Photonics West, San Francisco, USA, Feb. 7<sup>th</sup>-12<sup>th</sup>, 2015.
229. "Analysis of GaInN/GaN Superlattice on GaN by *in situ* X-Ray Diffraction Monitoring Attached with Metalorganic Vapor Phase Epitaxy Equipment" Motoaki Iwaya, Taiji Yamamoto, Daisuke Iida, Koji Ishihara, Tetsuya Takeuchi, Satoshi Kamiyama, Isamu Akasaki: Material Research Society Spring Meeting, San Francisco, USA, April 6-10, 2015.
230. "Electrical Properties of High Carrier Concentration n-Type AlGaIn" K. Takeda, K. Mori, T. Kusafuka, M. Iwaya, T. Takeuchi, S. Kamiyama, and I. Akasaki: The 3rd International Conference on Light-Emitting Devices and Their Industrial Applications (LEDIA '15), Pacifico Yokohama, Japan, Apr. 22<sup>nd</sup>-24<sup>th</sup>, 2015.
231. "Correlation between Crystal Qualities and Electrical Properties in Si-Doped Al<sub>0.6</sub>Ga<sub>0.4</sub>N" T. Yasuda, S. Katsuno, T. Takeuchi, M. Iwaya, S. Kamiyama, I. Akasaki, and H. Amano: The 3rd International Conference on Light-Emitting Devices and Their Industrial Applications (LEDIA '15), Pacifico Yokohama, Japan, Apr. 22<sup>nd</sup>-24<sup>th</sup>, 2015.
232. "AlN Epitaxial Growth on Sapphire with an Intermediate Layer" S. Katsuno, T. Yasuda, M. Iwaya, T. Takeuchi, S. Kamiyama, I. Akasaki, and H. Amano: The 3rd International Conference on Light-Emitting Devices and Their Industrial Applications (LEDIA '15), Pacifico Yokohama, Japan, Apr. 22<sup>nd</sup>-24<sup>th</sup>, 2015.

法人番号	231029
プロジェクト番号	S1201019

233. "AlN Growth on Sputtering AlN Template Substrate by Hydride Vapor Phase Epitaxy" D. Yasui, H. Miyake, K. Hiramatsu, M. Iwaya, I. Akasaki, and H. Amano: The 3rd International Conference on Light-Emitting Devices and Their Industrial Applications (LEDIA '15), Pacifico Yokohama, Japan, Apr. 22<sup>nd</sup>-24<sup>th</sup>, 2015.
234. "MOVPE Growth of AlNSb Alloys" K. Suzuki, D. Komori, H. Sasajima, K. Takarabe, T. Takeuchi, M. Iwaya, S. Kamiyama, and I. Akasaki: The 3rd International Conference on Light-Emitting Devices and Their Industrial Applications (LEDIA '15), Pacifico Yokohama, Japan, Apr. 22<sup>nd</sup>-24<sup>th</sup>, 2015.
235. "Carrier Gas Dependence on GaNSb MOVPE Growth" D. Komori, H. Sasajima, K. Takarabe, K. Suzuki, T. Takeuchi, S. Kamiyama, M. Iwaya, and I. Akasaki: The 3rd International Conference on Light-Emitting Devices and Their Industrial Applications (LEDIA '15), Pacifico Yokohama, Japan, Apr. 22<sup>nd</sup>-24<sup>th</sup>, 2015.
236. "Electrical Properties of GaNSb Grown at Low Temperatures" K. Takarabe, D. Komori, K. Suzuki, T. Takeuchi, M. Iwaya, S. Kamiyama, and I. Akasaki: The 3rd International Conference on Light-Emitting Devices and Their Industrial Applications (LEDIA '15), Pacifico Yokohama, Japan, Apr. 22<sup>nd</sup>-24<sup>th</sup>, 2015.
237. "Contact Characteristics of V-Based Electrode for High AlN Molar Fraction n-AlGaIn" K. Mori, K. Takeda, T. Kusafuka, M. Iwaya, T. Takeuchi, S. Kamiyama, I. Akasaki, and H. Amano: The 3rd International Conference on Light-Emitting Devices and Their Industrial Applications (LEDIA '15), Pacifico Yokohama, Japan, Apr. 22<sup>nd</sup>-24<sup>th</sup>, 2015.
238. "Nitride-Based Tunnel Junctions towards Deep UV-LEDs" D. Takasuka, D. Minamikawa, M. Ino, T. Takeuchi, M. Iwaya, S. Kamiyama, H. Amano, and I. Akasaki: The 3rd International Conference on Light-Emitting Devices and Their Industrial Applications (LEDIA '15), Pacifico Yokohama, Japan, Apr. 22<sup>nd</sup>-24<sup>th</sup>, 2015.
239. "Optimization of Periodic Gain Structures toward Blue VCSELs" K. Matsui, D. Komori, K. Horikawa, T. Takeuchi, S. Kamiyama, M. Iwaya, and I. Akasaki: The 3rd International Conference on Light-Emitting Devices and Their Industrial Applications (LEDIA '15), Pacifico Yokohama, Japan, Apr. 22<sup>nd</sup>-24<sup>th</sup>, 2015.
240. "Conductive n-Type AlInN/GaN Distributed Bragg Reflectors" K. Ikeyama, Y. Kozuka, T. Yasuda, T. Takeuchi, S. Kamiyama, M. Iwaya, and I. Akasaki: The 3rd International Conference on Light-Emitting Devices and Their Industrial Applications (LEDIA '15), Pacifico Yokohama, Japan, Apr. 22<sup>nd</sup>-24<sup>th</sup>, 2015.
241. "A Pulsed Operation of VCSELs on AlInN/GaN DBR Grown with High Growth Rate" Y. Kozuka, K. Ikeyama, T. Akagi, S. Iwayama, K. Nakata, T. Takeuchi, S. Kamiyama, M. Iwaya, I. Akasaki: The 3rd International Conference on Light-Emitting Devices and Their Industrial Applications (LEDIA '15), Pacifico Yokohama, Japan, Apr. 22<sup>nd</sup>-24<sup>th</sup>, 2015.
242. "Electrical properties of extremely low-resistivity and high-carrier-concentration Si-doped AlGaIn with low AlN molar fraction" Kunihiro Takeda, Kazuki Mori, Toshiki Kusafuka, Motoaki Iwaya, Tetsuya Takeuchi, Satoshi Kamiyama, and Isamu Akasaki: The 7th Asia-Pacific Workshop on Widegap Semiconductors (APWS 2015), Seoul, Korea, May 17-20, 2015.

法人番号	231029
プロジェクト番号	S1201019

243. "Growth of AlN layer on sputtered AlN template substrate by hydride vapor phase epitaxy" Shinya Tamaki, Daiki Yasui, Hideto Miyake, Kazumasa Hiramatsu, Motoaki Iwaya, Isamu Akasaki, and Hiroshi Amano: The 7th Asia-Pacific Workshop on Widegap Semiconductors (APWS 2015), Seoul, Korea, May 17-20, 2015.
244. "In situ X-ray diffraction analysis of GaInN/GaN heterostructure during MOVPE growth" Motoaki Iwaya, Taiji Kondo, Koji Ishihara, Junya Osumi, Tetsuya Takeuchi, Satoshi Kamiyama, and Isamu Akasaki: The 7th Asia-Pacific Workshop on Widegap Semiconductors (APWS 2015), Seoul, Korea, May 17-20, 2015.
245. "Extremely Low-resistivity and High-carrierconcentration Si-doped AlGaIn with Low AlN Molar Fraction for Improvement of Wall Plug Efficiency of Nitride-based LED" Motoaki Iwaya, Kunihiro Takeda, Daisuke Iida, Tetsuya Takeuchi, Satoshi Kamiyama, and Isamu Akasaki: The 11<sup>th</sup> Conference on Lasers and Electro-Optics Pacific Rim (CLEO-PR 2015), Busan, Korea, August 24-28, 2015.
246. "Extremely Low-resistivity and High-carrierconcentration Si-doped AlGaIn with Low AlN Molar Fraction for Improvement of Wall Plug Efficiency of Nitride-based LED" Motoaki Iwaya, Kunihiro Takeda, Daisuke Iida, Tetsuya Takeuchi, Satoshi Kamiyama, and Isamu Akasaki: The 11<sup>th</sup> International Conference on Nitride Semiconductor (ICNS-11), Beijiin, China, August 30-September 4, 2015.
247. "MOVPE法を用いたSi添加AlInN/GaNへテロ接合の電気的特性" 池山和希, 安田俊輝, 小塚祐吾, 堀川航佑, 竹内哲也, 上山智, 岩谷素顕, 赤崎勇: 第75回 応用物理学会秋季学術講演会, 北海道大学, 2014年9月17日-9月20日.
248. "Mg ドープAlGaInによるAlGaIn/GaN HFET型紫外フォトセンサーの高性能化" 山本雄磨, 村瀬卓弥, 草深敏匡, 岩谷素顕, 竹内哲也, 上山智, 赤崎勇: 第75回 応用物理学会秋季学術講演会, 北海道大学, 2014年9月17日-9月20日.
249. "SiCの陽極酸化プロセスにおける光照射に関する検討" 日高公崇香, 渡和樹, 岩谷素顕, 上山智, 赤崎勇: 第75回 応用物理学会秋季学術講演会, 北海道大学, 2014年9月17日-9月20日.
250. "GaInN/GaNへテロ接合における格子緩和の評価" 石原耕史, 近藤保成, 松原大幸, 岩谷素顕, 竹内哲也, 上山智, 赤崎勇: 第75回 応用物理学会秋季学術講演会, 北海道大学, 2014年9月17日-9月20日.
251. "高InNモル分率GaInNを用いたトンネル接合(2)" 南川大智, 井野匡貴, 高須賀大貴, 岩谷素顕, 竹内哲也, 上山智, 赤崎勇: 第75回 応用物理学会秋季学術講演会, 北海道大学, 2014年9月17日-9月20日.
252. "MOVPE選択成長によるGaInNナノコラムのマスクパターン依存性" 水野尚之, 加藤嵩裕, 上山智, 竹内哲也, 岩谷素顕, 赤崎勇: 第75回 応用物理学会秋季学術講演会, 北海道大学, 2014年9月17日-9月20日.
253. "高キャリア濃度Siドープn型Al<sub>0.03</sub>Ga<sub>0.97</sub>N上のAg電極を用いた高反射電極の検討" 河合俊介, 飯田大輔, 岩谷素顕, 竹内哲也, 上山智, 赤崎勇: 第75回 応用物理学会秋季学術講演会, 北海道大学, 2014年9月17日-9月20日.
254. "III族窒化物半導体トンネル接合を用いた電流狭窄構造の低抵抗化" 井野匡貴, 南川大智, 竹内哲也, 上山智, 岩谷素顕, 赤崎勇: 第75回 応用物理学会秋季学術講演会, 北海道大学, 2014年9月17日-9月20日.
255. "レーザーリフトオフ技術によるGaInN 基板を剥離した近紫外LED" 飯田大輔,

法人番号	231029
プロジェクト番号	S1201019

河合俊介, 土屋貴義, 江間伸明, 岩谷素顕, 竹内哲也, 上山智, 赤崎勇: 第75回 応用物理学会秋季学術講演会, 北海道大学, 2014年9月17日-9月20日.

256. “GaInN/GaN超格子を用いた窒化物太陽電池構造の検討” 山本泰司, 黒川泰視, 小崎桂矢, 岩谷素顕, 上山智, 竹内哲也, 赤崎勇: 第75回 応用物理学会秋季学術講演会, 北海道大学, 2014年9月17日-9月20日.
257. “r面サファイア基板上におけるa面GaN成長に関する検討” 加藤貴久, 水野尚之, 伊藤弘晃, 飯田大輔, 藤井高志, 福田承生, 上山智, 竹内哲也, 岩谷素顕, 赤崎勇: 第75回 応用物理学会秋季学術講演会, 北海道大学, 2014年9月17日-9月20日.
258. “AllnNエピタキシャル層の高速成長と多層膜反射鏡への応用” 池山和希, 竹内哲也, 岩谷素顕, 上山智, 赤崎勇: 第44回日本結晶成長学会国内会議, 学習院大学, 2014年11月6日-8日.
259. “スパッタ法AlNテンプレート基板を用いたAlNのHVPE成長” 安井 大貴, 三宅秀人, 平松 和政, 岩谷 素顕, 赤崎 勇, 天野 浩: 第62回応用物理学会春季学術講演会, 東海大学湘南キャンパス, 2015年3月11日-14日.
260. “高キャリア濃度n型AlGaInの電気的特性” 武田 邦宏, 森 一喜, 山田 知明, 岩谷 素顕, 竹内 哲也, 上山 智, 赤崎 勇: 第62回応用物理学会春季学術講演会, 東海大学湘南キャンパス, 2015年3月11日-14日.
261. “深紫外LEDに向けた窒化物半導体トンネル接合の検討” 高須賀 大貴, 南川大智, 井野 匡貴, 竹内 哲也, 岩谷 素顕, 上山 智, 天野 浩, 赤崎 勇: 第62回応用物理学会春季学術講演会, 東海大学湘南キャンパス, 2015年3月11日-14日.
262. “トンネル接合を用いたモノリシック型白色LEDの検討” 加藤 貴久, 飯田 大輔, 河合 俊介, 上山 智, 竹内 哲也, 岩谷 素顕, 赤崎 勇: 第62回応用物理学会春季学術講演会, 東海大学湘南キャンパス, 2015年3月11日-14日.
263. “GaN上に作製したGaInN単膜およびGaInN/GaN超格子のX線その場観察測定” 大角 純也, 石原 耕史, 山本 泰司, 岩谷 素顕, 竹内 哲也, 上山 智, 赤崎 勇: 第62回応用物理学会春季学術講演会, 東海大学湘南キャンパス, 2015年3月11日-14日.
264. “表面プラズモン共鳴のナノ構造と屈折率の依存性の検討” 丹羽 一将, 加藤貴久, 河合 俊介, 飯田 大輔, 上山 智, 竹内 哲也, 岩谷 素顕, 赤崎 勇: 第62回応用物理学会春季学術講演会, 東海大学湘南キャンパス, 2015年3月11日-14日.
265. “高Al組成のn-AlGaInにおけるV系電極のコンタクト特性” 森 一喜, 武田 邦宏, 草深 敏匡, 岩谷 素顕, 上山 智, 竹内 哲也, 赤崎 勇, 天野 浩: 第62回応用物理学会春季学術講演会, 東海大学湘南キャンパス, 2015年3月11日-14日.
266. “高性能近紫外LEDの作製に関する検討” 弦間 彩花, 河合 俊介, 岩谷 素顕, 竹内 哲也, 上山 智, 赤崎 勇: 第62回応用物理学会春季学術講演会, 東海大学湘南キャンパス, 2015年3月11日-14日.
267. “SiO<sub>2</sub>ナノ周期構造を有する基板上に作製した窒化物系青色LEDの発光特性” 花井 駿, 北野 司, 岩谷 素顕, 竹内 哲也, 上山 智, 赤崎 勇: 第62回応用物理学会春季学術講演会, 東海大学湘南キャンパス, 2015年3月11日-14日.
268. “ナノ構造導入によるLEDの性能向上に関する研究” 上山 智, 岩谷 素顕, 竹内 哲也, 赤崎 勇: 第62回応用物理学会春季学術講演会, 東海大学湘南キャンパス, 2015年3月11日-14日.

法人番号	231029
プロジェクト番号	S1201019

269. “高成長速度AllnN/GaN多層膜反射鏡を用いた面発光レーザのパルス発振” 小塚 祐吾、池山 和希、赤木 孝信、岩山 章、中田 圭祐、竹内 哲也、上山 智、岩谷 素顕、赤崎 勇: 第62回応用物理学会春季学術講演会、東海大学湘南キャンパス、2015年3月11日-14日.
270. “青色面発光レーザに向けたGalnN 活性層に関する研究” 古田貴土, 松井健城, 堀川航佑, 小塚祐吾, 池山和樹, 岩山 章, 赤木孝信, 竹内哲也, 上山 智, 岩谷素顕, 赤崎 勇: 第7回窒化物半導体結晶成長講演会、東北大学 片平キャンパス、2015年5月7-8日.
271. “AllnN 膜およびAllnN/GaN 多層膜反射鏡の電気的特性” 吉田翔太朗, 池山和希, 竹内哲也, 上山 智, 岩谷素顕, 赤崎 勇: 第7回窒化物半導体結晶成長講演会、東北大学 片平キャンパス、2015年5月7-8日.
272. “その場観察X線回折法を用いた GaN 上のGalnN 単膜およびGalnN/GaN 超格子の評価” 大角純也, 石原耕史, 山本泰司, 岩谷素顕, 竹内哲也, 上山 智, 赤崎 勇: 第7回窒化物半導体結晶成長講演会、東北大学 片平キャンパス、2015年5月7-8日.
273. “超高キャリア密度n型AlGaIn の結晶成長と電気伝導特性” 岩谷素顕, 武田邦宏, 飯田大輔, 杉山 徹, 竹内哲也, 上山 智, 赤崎 勇: 第7回窒化物半導体結晶成長講演会、東北大学 片平キャンパス、2015年5月7-8日.
274. “窒化物半導体面発光レーザの現状と照明応用に向けた将来展望” 平成 27 年度 (第 48 回) 照明学会全国大会 固体光源分科会シンポジウム 2015 年 8 月 27 日.
275. T. Takeuchi, M. Iwaya, S. Kamiyama, and I. Akasaki, "GaN-based tunnel junctions for novel optoelectronic devices", EMN Meeting on Photovoltaics, 2016, Hong Kong.
276. T. Takeuchi, M. Iwaya, S. Kamiyama, and I. Akasaki, "Current status of GaN-based vertical-cavity surface-emitting lasers (VCSELs)", 4th International Workshop on LEDs and Solar Applications, 2016, Nagoya.
277. T. Yasuda, S. Yoshida, T. Takeuchi, M. Iwaya, S. Kamiyama, I. Akasaki, and H. Amano, Polarization Induced Hole Accumulations in Nitride Semiconductor Heterostructures, LEDIA'16, Yokohama, Japan, (2016)
278. K. Matsui, K. Ikeyama, T. Furuta, Y. Kozuka, T. Akagi, T. Takeuchi, S. Kamiyama, M. Iwaya, and I. Akasaki, GaN-based VCSELs using Periodic Gain Structures, LEDIA'16, Yokohama, Japan, (2016)
279. N. Kuwabara, T. Yasuda, S. Katsuno, N. Koide, T. Takeuchi, M. Iwaya, S. Kamiyama, and I. Akasaki, ITO/Ga<sub>2</sub>O<sub>3</sub> Multilayer Electrodes Towards Deep UV-LEDs, LEDIA'16, Yokohama, Japan, (2016)
280. S. Ushida, A. Yoshikawa, M. Iwaya, T. Takeuchi, S. Kamiyama, and I. Akasaki, Temperature Dependence of the Nitride-based HFET Structure Photosensors, LEDIA'16, Yokohama, Japan, (2016)
281. K. Suzuki, K. Takarabe, D. Komori, D. Takasuka, N. Koide, T. Takeuchi, M. Iwaya, S. Kamiyama, and I. Akasaki, Low-Temperature Grown p-Side Structure with GaInN Tunnel Junction and n-GaN<sub>Sb</sub>, LEDIA'16, Yokohama, Japan, (2016)
282. T. Senga, N. Nagata, M. Iwaya, T. Takeuchi, S. Kamiyama, I. Akasaki, Si

法人番号	231029
プロジェクト番号	S1201019

- concentration dependence of laser oscillation characteristics in AlGaIn multiple quantum well active layer, ICCGE-18, Nagoya, Japan (2016).
283. J. Osumi, R. Kanayama, M. Iwaya, T. Takeuchi, S. Kamiyama, I. Akasaki, Observation of AlGaIn/GaN heterostructure by in situ XRD attached metalorganic vapor phase epitaxial equipment, ICCGE-18, Nagoya, Japan (2016).
284. Y. Akatsuka, D. Takasuka, M. Ino, T. Akagi, T. Takeuchi, M. Iwaya, S. Kamiyama, I. Akasaki, Low resistive GaInN tunnel junctions with high Si concentrations, ICCGE-18, Nagoya, Japan (2016).
285. Kenjo Matsui, Takashi Furuta, Natsumi Hayashi, Yugo Kozuka, Takanobu Akagi, Tetsuya Takeuchi, Satoshi Kamiyama, Motoaki Iwaya and Isamu Akasaki, 3-mW RT-CW GaN-Based VCSELs and Their Temperature Dependence, IWN2016, Florida, USA (2016).
286. Daiki Jinno, Shun Otsuki, Teruyuki Niimi, Hisayoshi Daicho, Motoaki Iwaya, Tetsuya Takeuchi, Satoshi Kamiyama and Isamu Akasaki, High Temperature Annealing of Sputtered AlN Buffer Layer on r-Plane Sapphire Substrate and its Effect on Crystalline Quality of a-Plane GaN, IWN2016, Florida, USA (2016).
287. Bo Monemar, Plamen P. Paskov, K. Takeda, Motoaki Iwaya, Tetsuya Takeuchi, Satoshi Kamiyama and Isamu Akasaki, Low Temperature Photoluminescence in Highly Si-Doped Al<sub>x</sub>Ga<sub>1-x</sub>N with  $x < 0.09$ , IWN2016, Florida, USA (2016).
288. Yuki Kurisaki, Satoshi Kamiyama, Tetsuya Takeuchi, Motoaki Iwaya and Isamu Akasaki, Theoretical Investigation of Nitride Nanowire-Based Quantum Shell Lasers, IWN2016, Florida, USA (2016).
289. Ryoma Seiki, Daisuke Komori, Kazuki Ikeyama, Toshiaki Ina, Takeyoshi Onuma, Takao Miyajima, Tetsuya Takeuchi, Satoshi Kamiyama, Motoaki Iwaya and Isamu Akasaki, Local Structural Analysis around In Atoms in Al<sub>0.82</sub>In<sub>0.18</sub>N alloy by Using X-Ray Absorption Fine-Structure Measurements, IWN2016, Florida, USA (2016).
290. Ryouzuke Kanayama, Junya Osumi, Motoaki Iwaya, Tetsuya Takeuchi, Satoshi Kamiyama and Isamu Akasaki, Characterization of AlGaIn/GaN Heterostructure by In Situ X-Ray Diffraction Attached Metal Organic Vapor Phase Epitaxy, IWN2016, Florida, USA (2016).
291. Takao Miyajima, Daisuke Komori, Toshiaki Ina, Ryoma Seiki, Kiyofumi Nitta, Tetsuya Takeuchi, Tomoya Uruga, Satoshi Kamiyama, Motoaki Iwaya and Isamu Akasaki, Determination of the Site of Sb Occupation in MOCVD-Grown GaN<sub>1-x</sub>Sb<sub>x</sub> Using X-Ray Absorption Fine-Structure Measurements, IWN2016, Florida, USA (2016).
292. Yasuto Akatsuka, Daiki Takasuka, Takanobu Akagi, Tetsuya Takeuchi, Motoaki Iwaya, Satoshi Kamiyama and Isamu Akasaki, Buried Tunnel Junctions Using Low Resistive GaInN Tunnel Junctions with High Si Concentrations, IWN2016, Florida, USA (2016).
293. Akira Yoshikawa, Saki Ushida, Motoaki Iwaya, Tetsuya Takeuchi, Satoshi Kamiyama and Isamu Akasaki, Physical Property of the High Photosensitive Field Effect Transistor Type UV Photosensors with AlGaIn/AlGaIn Hetero Structure,

法人番号	231029
プロジェクト番号	S1201019

- IWN2016, Florida, USA (2016).
294. Saki Ushida, Akira Yoshikawa, Motoaki Iwaya, Satoshi Kamiyama, Tetsuya Takeuchi and Isamu Akasaki, Temperature Dependence in AlGa<sub>N</sub>-Based Heterostructure Field-Effect Transistor Type UV Photosensors, IWN2016, Florida, USA (2016).
295. Akira Yoshikawa, Saki Ushida, Motoaki Iwaya, Tetsuya Takeuchi, Satoshi Kamiyama and Isamu Akasaki, Physical Property of the High Photosensitive Field Effect Transistor Type UV Photosensors with AlGa<sub>N</sub>/AlGa<sub>N</sub> Hetero Structure, IWN2016, Florida, USA (2016).
296. Junichiro Ogimoto, Yugo Kozuka, Takanobu Akagi, Natsumi Hayashi, Tetsuya Takeuchi, Satoshi Kamiyama, Motoaki Iwaya and Isamu Akasaki, Design and Fabrication of Modulation-Doped GaN-Based Vertical Cavities for Blue Surface-Emitting Lasers, IWN2016, Florida, USA (2016).
297. Toshiki Yasuda, Tetsuya Takeuchi, Motoaki Iwaya, Satoshi Kamiyama, Isamu Akasaki, Hole Accumulations to Polarization Charges in Relaxed AlGa<sub>N</sub> Heterostructures with High AlN Mole Fractions, IWN2016, Florida, USA (2016).
298. Noriaki Nagata<sup>1</sup>, Takashi Senga, Motoaki Iwaya, Tetsuya Takeuchi, Satoshi Kamiyama and Isamu Akasaki, Low Resistivity Ohmic Contact V-Based Electrode Contributed by Using Thin SiN<sub>x</sub> Intermediate Layer for High AlN Molar Fraction n-Type AlGa<sub>N</sub>, IWN2016, Florida, USA (2016).
299. 新實 輝行、神野 大樹、岩谷 素顕、竹内 哲也、上山 智、赤崎 勇、r 面サブ  
ァイア基板上 a 面 GaInN 量子井戸構造に関する検討、第 63 回応用物理学会春季学  
術講演会シンポジウム、東京、2015.
300. 栗崎 湧気、上山 智、竹内 哲也、岩谷 素顕、赤崎 勇、Ⅲ族窒化物ナノワイ  
ヤを用いた端面発光レーザの理論的検討、第 63 回応用物理学会春季学術講演会シ  
ンポジウム、東京、2015.
301. 千賀 崇史、永田 訓章、岩谷 素顕、竹内 哲也、上山 智、赤崎 勇、AlGa<sub>N</sub> 多  
重量子井戸構造のレーザ発振特性の Si 濃度依存性、第 63 回応用物理学会春季学術  
講演会シンポジウム、東京、2015.
302. 高西 徹、大角 純也、岩谷 素顕、上山 智、竹内 哲也、赤崎 勇、半極性(10-11)  
面自立 GaN 基板上 GaInN の成長機構の解析、第 63 回応用物理学会春季学術講演  
会シンポジウム、東京、2015.
303. 岩瀬 航平、Lim Stanley、澁谷 弘樹、岩谷 素顕、竹内 哲也、上山 智、赤崎 勇、  
Core-Shell 型 MQW における発光波長の成長条件依存性、第 63 回応用物理学会春  
季学術講演会シンポジウム、東京、2015.
304. 袴田 淳哉、草深 敏匡、千賀 崇史、岩谷 素顕、竹内 哲也、上山 智、三宅 秀  
人、赤崎 勇、アニール処理 AlN 下地層上 AlGa<sub>N</sub>/AlN-MQW の光学特性、第 63 回  
応用物理学会春季学術講演会シンポジウム、東京、2015.
305. 大角 純也、金山 亮介、高西 徹、岩谷 素顕、竹内 哲也、上山 智、赤崎 勇、  
その場観察技術を用いた MOVPE 法で作製する AlGa<sub>N</sub>/Ga<sub>N</sub> ヘテロ構造の観察、第  
63 回応用物理学会春季学術講演会シンポジウム、東京、2015.
306. 牛田 彩希、吉川 陽、山本 雄磨、奥村 俊紀、岩谷 素顕、上山 智、竹内 哲  
也、赤崎 勇、窒化物半導体 HFET 型光センサの温度特性、第 63 回応用物理学会春

法人番号	231029
プロジェクト番号	S1201019

季学術講演会シンポジウム、東京、2015.

307. 永田 訓章、森 一喜、武田 邦宏、草深 敏匡、岩谷 素顕、竹内 哲也、上山 智、赤崎 勇、Si<sub>3</sub>N<sub>4</sub> による高 AlN モル分率 n-AlGa<sub>N</sub> 用 V 系電極の低接触比抵抗化、第 63 回応用物理学会春季学術講演会シンポジウム、東京、2015.
308. 池山 和希、小塚 祐吾、吉田 翔太郎、松井 健城、赤木 孝信、岩山 章、竹内 哲也、上山 智、岩谷 素顕、赤崎 勇、n 型 AlInN/GaN DBR を有する微小共振器 LED、第 63 回応用物理学会春季学術講演会シンポジウム、東京、2015.
309. 鈴木 健太、財部 覚、小森 大資、高須賀 大貴、小出 典克、竹内 哲也、岩谷 素顕、上山 智、赤崎 勇、GaInN トンネル接合と n 型 GaNSb による低温 p 側構造の作製、第 63 回応用物理学会春季学術講演会シンポジウム、東京、2015.
310. 桑原 奈津子、安田 俊輝、勝野 翔太、小出 典克、竹内 哲也、岩谷 素顕、上山 智、赤崎 勇、深紫外 LED のための ITO/Ga<sub>2</sub>O<sub>3</sub> 多層膜透明電極の検討、第 63 回応用物理学会春季学術講演会シンポジウム、東京、2015.
311. K. Matsui, T. Furuta, Y. Kozuka, T. Akagi, T. Takeuchi, S. Kamiyama, M. Iwaya and I. Akasaki, GaN-based VCSEL using a periodic gain structure consisting of two GaInN 5QWs, 35th Electronic Materials Symposium, Biwako, Japan (2016).
312. T. Yasuda, S. Katsuno, N. Kuwabara, T. Takeuchi, M. Iwaya, S. Kamiyama, I. Akasaki, Improvement of p-type electrical property by polarization-doping in graded-AlGa<sub>N</sub> layer, 35th Electronic Materials Symposium, Biwako, Japan (2016).
313. 袴田 淳哉、岩谷 素顕、上山 智、竹内 哲也、三宅 秀人、赤崎 勇、高温アニール処理のスパッタ AlN 層における効果、第 8 回 窒化物半導体結晶成長講演会、京都 (2016)
314. 鈴木 健太、財部 覚、高須賀 大貴、小出 典克、竹内 哲也、岩谷 素顕、上山 智、赤崎 勇、GaInN トンネル接合と n 型 GaNSb による低温 p 側構造の作製、第 8 回 窒化物半導体結晶成長講演会、京都 (2016)
315. 吉川 陽、岩谷 素顕、竹内 哲也、上山 智、赤崎 勇、Nano-size concavo-convex (NCC) サファイア基板を用いた高品質 AlN 膜成長、第 8 回 窒化物半導体結晶成長講演会、京都 (2016)
316. 牛田 彩希、吉川 陽、岩谷 素顕、上山 智、竹内 哲也、赤崎 勇、窒化物半導体 HFET 型光センサの動作に関する温度依存性、第 8 回 窒化物半導体結晶成長講演会、京都 (2016)
317. 鈴木 健太、財部 覚、高須賀 大貴、小出 典克、竹内 哲也、岩谷 素顕、上山 智、赤崎 勇、GaInN トンネル接合と n 型 GaNSb による低温 p 側構造の作製、第 8 回 窒化物半導体結晶成長講演会、京都 (2016)
318. 上山 智、竹内 哲也、岩谷 素顕、赤崎 勇、窒化物系ナノワイヤーおよび量子殻構造の作製と、光デバイス応用、第 76 回応用物理学会秋季学術講演会シンポジウム、名古屋、2015
319. 牛田 彩希、吉川 陽、岩谷 素顕、竹内 哲也、上山 智、赤崎 勇、AlGa<sub>N</sub> 系 HFET 型光センサの SiN<sub>x</sub> パッシベーション効果、第 76 回応用物理学会秋季学術講演会シンポジウム、名古屋、2015
320. 安田 俊輝、竹内 哲也、岩谷 素顕、上山 智、赤崎 勇、天野 浩、分極電荷による高ホール濃度を有する p 型 AlGa<sub>N</sub> の作製、第 76 回応用物理学会秋季学術講演会シンポジウム、名古屋、2015

法人番号	231029
プロジェクト番号	S1201019

321. 澁谷 弘樹、上山 智、岩谷 素顕、竹内 哲也、赤崎 勇、低温下におけるⅢ族窒化物ナノワイヤの埋め込み成長に関する研究、第 76 回応用物理学会秋季学術講演会シンポジウム、名古屋、2015
322. 金山 亮介、大角 純也、岩谷 素顕、竹内 哲也、上山 智、赤崎 勇、X 線その場観察 MOVPE による AlGaIn/GaN ヘテロ構造評価、第 76 回応用物理学会秋季学術講演会シンポジウム、名古屋、2015
323. 清木 良麻、小森 大資、池山 和希、伊奈 稔哲、小沼 猛儀、宮嶋 孝夫、竹内 哲也、上山 智、岩谷 素顕、赤崎 勇、X 線吸収微細構造測定による Al<sub>0.82</sub>In<sub>0.18</sub>N の局所構造解析、第 76 回応用物理学会秋季学術講演会シンポジウム、名古屋、2015
324. 林 貴文、永田 訓章、千賀 崇史、金山 亮介、岩山 章、岩谷 素顕、竹内 哲也、上山 智、赤崎 勇、電子線励起法による GaInN/GaN-MQW レーザ、第 76 回応用物理学会秋季学術講演会シンポジウム、名古屋、2015
325. 宮嶋 孝夫、小森 大資、清木 良麻、伊奈 稔哲、新田 清文、鈴木 健太、竹内 哲也、宇留賀 朋哉、上山 智、岩谷 素顕、赤崎 勇、XAFS 法を用いた GaN<sub>1-x</sub>Sb<sub>x</sub> 混晶半導体中の Sb 占有位置評価、第 76 回応用物理学会秋季学術講演会シンポジウム、名古屋、2015

#### <研究成果の公開状況>(上記以外)

シンポジウム・学会等の実施状況、インターネットでの公開状況等

- 第 6 回窒化物半導体結晶成長講演会(日本結晶成長学会ナノエピ分科会と共同主催)

開催日:平成 26 年 7 月 25 日~26 日 実施場所 名城大学 天白キャンパス

講演者:基調・特別・チュートリアル・招待講演 8 名、一般講演 63 名

掲載 HP: <http://www.jacg.jp/jacg/japanese/nanoepi/2014.7.25-26/index.html>

- 2013 Meijo International Symposium on Nitride Semiconductors(主催)

開催日:平成 25 年 11 月 29 日 実施場所 名城大学 天白キャンパス内

HP 掲載: <http://nitride.meijo-u.ac.jp/iwaya/MSN/index-2013.html>

講演者: 記念講演 2 名、招待講演 2 名(海外)

備考:本シンポジウムに長年貢献頂いた Bo Monemar 教授および Bernard Gil 教授に名城大学名誉博士号を授与した。

(参照: <http://www.meijo-u.ac.jp/research/news/detail.html?id=8J94Jm>)

- 第 13 回赤崎記念研究センターシンポジウム(協賛)

開催日:平成 25 年 11 月 29 日 実施場所 名古屋大学ベンチャー・ビジネス・ラボラトリー 3 階 ベンチャーホール

講演者:一般講演 3 名、招待講演 6 名

- 2012 Meijo International Symposium on Nitride Semiconductors(主催)

開催日:平成 25 年 2 月 28 日、実施場所 名城大学 天白キャンパス内

講演者: 招待講演 5 件

HP 掲載: <http://nitride.meijo-u.ac.jp/iwaya/MSN/index-2012.html>

- 第 12 回赤崎記念研究センターシンポジウム(協賛)

開催日:平成 25 年 2 月 27 日 実施場所 名古屋大学東山キャンパス野依記念学術交流館

法人番号	231029
プロジェクト番号	S1201019

講演者: 一般講演 6 件、招待講演 6 件

- 2015 Meijo International Symposium on Nitride Semiconductors

開催日: 平成 27 年 11 月 21 日(土)、実施場所 名城大学天白キャンパス内

講演者: 一般講演 1 件、招待講演 3 件

- 第 15 回赤崎記念研究センターシンポジウム(協賛)

開催日: 平成 27 年 11 月 20 日(金)、実施場所 名古屋大学

講演者: 一般講演 8 件、招待講演 3 件

- The 4th International Workshop on LEDs and Solar Applications

開催日: 平成 28 年 3 月 30 日(水)-31 日(木)、実施場所 名城大学天白キャンパス内

講演者: 一般講演 3 件、招待講演 7 件

#### 14 その他の研究成果等

本研究拠点の整備にともない、多くの学生が大学院・修士課程および博士課程に進学し、博士課程修了学生 4 名(飯田・森下・安田・松井)および 80 名以上の大学院修士課程修了者を輩出した。これらの研究者は、国内はもとより海外(4 月よりサウジアラビアの KAIST で研究活動を実施予定)で活躍しており、この分野の発展に大きく貢献している。

法人番号	231029
プロジェクト番号	S1201019

## 15 「選定時」及び「中間評価時」に付された留意事項及び対応

## &lt;「選定時」に付された留意事項&gt;

基盤形成の観点から研究成果に留意してほしい

## &lt;「選定時」に付された留意事項への対応&gt;

本プロジェクトでは、名城大学の窒化物半導体に関する研究者を中心に、結晶成長・デバイスプロセスの革新が可能な体制を構築し、それによって革新的なデバイスを実現できる基盤を形成することを目的に研究を進めてきた。特に对外発表を重視し、多数の学会や論文発表が形成できることに留意して研究を進めてきた。

また、グローバル化に向けて多くの海外研究者と若手研究者の交流を進めてきており、4名の博士課程・修士課程学生の輩出など拠点を形成する上で重要な点に留意して研究を進めてきた。さらに本プロジェクト終了後にも多くの国家プロジェクトを継続的に実施する予定であり、研究基盤形成という観点から十分に多くの成果を残したと考えられる。

## &lt;「中間評価時」に付された留意事項&gt;

特になし

## &lt;「中間評価時」に付された留意事項への対応&gt;

特になし

## Properties of the main Mg-related acceptors in GaN from optical and structural studies

B. Monemar, P. P. Paskov, G. Pozina, C. Hemmingsson, J. P. Bergman, S. Khromov, V. N. Izyumskaya, V. Avrutin, X. Li, H. Morkoç, H. Amano, M. Iwaya, and I. Akasaki

Citation: *Journal of Applied Physics* **115**, 053507 (2014); doi: 10.1063/1.4862928

View online: <http://dx.doi.org/10.1063/1.4862928>

View Table of Contents: <http://aip.scitation.org/toc/jap/115/5>

Published by the [American Institute of Physics](#)

---

---



Small Conferences. BIG Ideas.

Applied Physics  
Reviews

SAVE THE DATE!  
**3D Bioprinting: Physical and Chemical Processes**  
May 2–3, 2017 • Winston Salem, NC, USA

The background of the banner features a blue-toned image of a human hand holding a glowing, branching structure that resembles a biological or chemical network, possibly representing bioprinting or nanotechnology.

## Properties of the main Mg-related acceptors in GaN from optical and structural studies

B. Monemar,<sup>1</sup> P. P. Paskov,<sup>1</sup> G. Pozina,<sup>1</sup> C. Hemmingsson,<sup>1</sup> J. P. Bergman,<sup>1</sup> S. Khromov,<sup>1</sup> V. N. Izyumskaya,<sup>2</sup> V. Avrutin,<sup>2</sup> X. Li,<sup>2</sup> H. Morkoç,<sup>2</sup> H. Amano,<sup>3</sup> M. Iwaya,<sup>4</sup> and I. Akasaki<sup>4</sup>

<sup>1</sup>*Department of Physics, Chemistry and Biology, Linköping University, S-581 83 Linköping, Sweden*

<sup>2</sup>*Department of Electrical and Computer Engineering and Physics Department, Virginia Commonwealth University, Richmond, Virginia 23284, USA*

<sup>3</sup>*Department of Electrical Engineering and Computer Science, Nagoya University, Chikusa-ku, Nagoya, 464-8603, Japan*

<sup>4</sup>*Department of Materials Science and Engineering, Meijo University, 1-501 Shiogamaguchi, Tempaku-ku, Nagoya 468-8502, Japan*

(Received 25 October 2013; accepted 9 January 2014; published online 3 February 2014)

The luminescent properties of Mg-doped GaN have recently received particular attention, e.g., in the light of new theoretical calculations, where the deep 2.9 eV luminescence band was suggested to be the main optical signature of the substitutional Mg<sub>Ga</sub> acceptor, thus, having a rather large binding energy and a strong phonon coupling in optical transitions. We present new experimental data on homoepitaxial Mg-doped layers, which together with the previous collection of data give an improved experimental picture of the various luminescence features in Mg-doped GaN. In *n*-type GaN with moderate Mg doping ( $<10^{18}$  cm<sup>-3</sup>), the 3.466 eV ABE1 acceptor bound exciton and the associated 3.27 eV donor-acceptor pair (DAP) band are the only strong photoluminescence (PL) signals at 2 K, and are identified as related to the substitutional Mg acceptor with a binding energy of  $0.225 \pm 0.005$  eV, and with a moderate phonon coupling strength. Interaction between basal plane stacking faults (BSFs) and Mg acceptors is suggested to give rise to a second deeper Mg acceptor species, with optical signatures ABE2 at 3.455 eV and a corresponding weak and broad DAP peak at about 3.15 eV. The 2.9 eV PL band has been ascribed to many different processes in the literature. It might be correlated with another deep level having a low concentration, only prominent at high Mg doping in material grown by the Metal Organic Chemical Vapor Deposition technique. The origin of the low temperature metastability of the Mg-related luminescence observed by many authors is here reinterpreted and explained as related to a separate non-radiative metastable deep level defect, i.e., not the Mg<sub>Ga</sub> acceptor. © 2014 AIP Publishing LLC. [<http://dx.doi.org/10.1063/1.4862928>]

### I. INTRODUCTION

Mg is so far the only acceptor dopant that can be used for *p*-doping in III-nitride based devices, such as light emitting diodes (LEDs) and laser diodes (LDs), for visible and ultraviolet (UV) wavelengths. Although much work has been done in an attempt to clarify the electronic and optical properties of Mg acceptors, there still remain open questions regarding the interpretation of experimental data on the properties of Mg-doped III-nitride materials. This holds true even for GaN, the most developed III-nitride compound in terms of crystal perfection and doping control. In this paper, we shall concentrate on the optical properties of Mg-doped GaN, specifically on luminescence with laser excitation (photoluminescence (PL)) and with electron excitation (cathodoluminescence (CL)). Such optical data give the most detailed information on the energy level structure of acceptors via their characteristic spectra, and also on the related recombination mechanisms of carriers and excitons.

The main PL (or CL) spectra related to acceptors in semiconductors are the acceptor bound exciton (ABE) and donor-acceptor pair (DAP) spectra, as reviewed for GaN in Ref. 1. These PL signatures for Mg-related acceptors were

established only in recent years,<sup>2-4</sup> with the ABE1 peak at 3.466 eV in unstrained GaN at 2 K and the corresponding DAP peaking at about 3.27 eV. The latter PL emission was studied in detail already four decades ago<sup>5,6</sup> and established as a DAP emission, but the connection with the Mg acceptor was not definitely known at the time. An unusual feature with Mg acceptors is that there are two ABEs present at high Mg doping, the additional one being a broader ABE2 peak at about 3.455 eV at 2 K.<sup>4</sup> Another puzzling observation is the instability of the Mg related spectra vs. UV excitation or electron excitation in the low temperature region for *p*-type materials, manifesting itself as the emission intensities going down with excitation time.<sup>4,7-9</sup> This effect is particularly strong before the Mg-activation anneal of the samples, and has raised questions whether the above-mentioned optical signatures are related to the substitutional Mg<sub>Ga</sub> acceptor or possibly to an unstable Mg-related complex.<sup>4</sup>

At lower photon energies additional spectra in Mg-doped GaN are noted. A broad peak at about 2.9 eV is commonly observed at high Mg doping concentrations in Metal-Organic Chemical Vapor Deposition (MOCVD) grown samples.<sup>10,11</sup> This has most often been assigned to the presence of Mg–nitrogen vacancy (Mg–V<sub>N</sub>) deep donor

complexes in the material.<sup>10</sup> In the deep red spectral region there is a broad band observed at about 1.8 eV, suggested as related to a deep Mg-related complex defect.<sup>12–14</sup>

In this paper, we will present additional PL and CL data obtained from MOCVD-grown GaN:Mg samples on low defect density bulk GaN substrates. These data allow a more definite identification of the above-mentioned characteristic ABE and DAP spectra for GaN:Mg. Furthermore, the reason for the apparent presence of two acceptor species will be discussed in terms of interaction between Mg acceptors and structural defects induced by the acceptor doping. For comparison, we also include new data from Mg-doped GaN samples grown by Halide Vapor Phase Epitaxy (HVPE).

## II. SAMPLES AND EXPERIMENTAL PROCEDURE

The MOCVD samples, used in this work, were grown on thick ( $>300\ \mu\text{m}$ ) bulk GaN templates. Some of these thick GaN substrates were grown with HVPE at Linköping University, and removed from the sapphire substrates with a laser lift-off technique, as reported previously.<sup>15</sup> Other bulk *c*-plane GaN substrates were supplied by Furukawa Co., Ltd., Japan. The *c*-plane Mg doped MOCVD samples were grown at Meijo University as well as at Bremen University, details of the growth procedure can be found in previous papers.<sup>4</sup> The *m*-plane GaN:Mg samples were grown at Virginia Commonwealth University, on *m*-plane bulk GaN substrates provided by Kyma, Inc.<sup>16</sup> Some HVPE grown thick (about  $11\ \mu\text{m}$ ) GaN:Mg layers on sapphire were provided by Oxford Instruments, the growth conditions are described in Ref. 17.

Thermal annealing at Meijo University and Linköping University was done at  $800\ ^\circ\text{C}$  for 10 min in  $\text{N}_2$  atmosphere. At Bremen University Rapid Thermal Annealing (RTA) was done during 1 min at  $800\ ^\circ\text{C}$ . Stationary PL spectra were measured with above band gap continuous wave UV excitation (laser photon energy of 4.65 eV) at temperatures from 2 K to 300 K, and detected by a UV enhanced liquid nitrogen cooled Charge Couple Device (CCD). PL transient measurements were done using femtosecond pulses from an amplified and frequency tripled Ti:sapphire laser (frequency 250 kHz and photon energy 4.65 eV), and detected with a UV sensitive Hamamatsu streak camera with a slow sweep unit. Cross-sectional Transmission Electron Microscope (TEM) analysis was done with a high resolution FEI Tecnai G2 200 keV Field Emission Gun (FEG) instrument. CL spectra were measured using a MonoCL4 system integrated with a LEO 1550 Gemini scanning electron microscope (SEM) and equipped with a liquid-He-cooled stage for low-temperature experiments. A fast CCD detection system or a Peltier cooled photo-multiplier tube (PMT) was used for spectral acquisition.

## III. EXPERIMENTAL RESULTS

### A. Photoluminescence spectra in the near bandgap region

The main features of Mg-related bound exciton (BE) spectra in GaN were discussed in Ref. 4. In Fig. 1(a), we

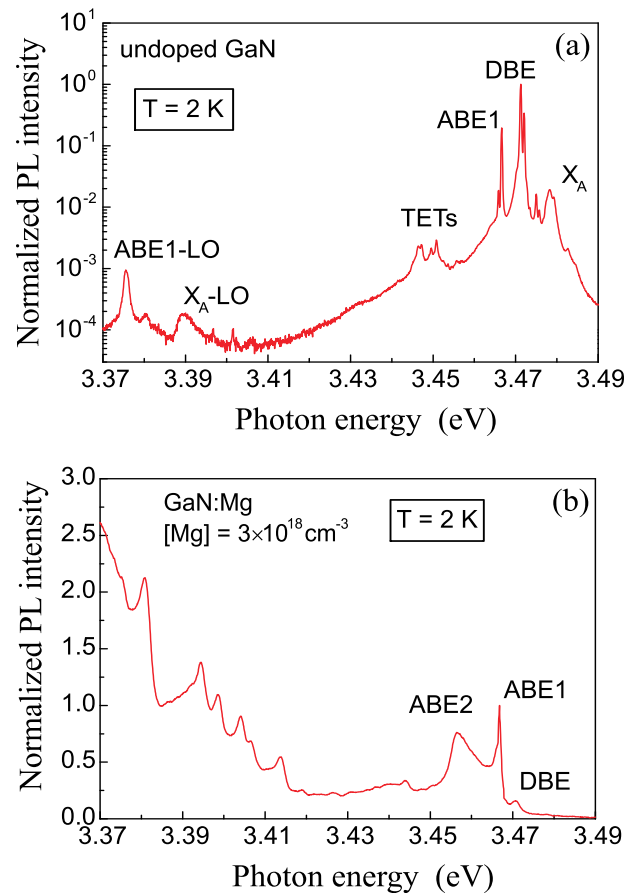


FIG. 1. Low-temperature near-bandgap spectra of nominally undoped (a) and Mg-doped ( $[\text{Mg}] = 3 \times 10^{18}\ \text{cm}^{-3}$ ) (b) homoepitaxial layers grown by MOCVD on *m*-plane bulk GaN substrates.

show new PL data that illustrate the difference in PL spectra at 2 K for nominally undoped GaN and highly Mg-doped GaN, in this case for *m*-plane samples. Separate Secondary Ion Mass Spectroscopy (SIMS) data on other samples indicate that for a nominally undoped GaN layer grown on a bulk GaN substrate the residual Mg concentration can be at most about  $1 \times 10^{17}\ \text{cm}^{-3}$  at the interface between the layer and the substrate, and decreases to low  $10^{16}\ \text{cm}^{-3}$  upon further growth. This Mg contamination can be ascribed to the well-known Mg memory effect in MOCVD growth,<sup>18</sup> and varies from sample to sample. The PL of the nominally undoped sample in Fig. 1(a) does indeed show the two silicon and oxygen related donor BEs (DBEs) at 3.472 eV and 3.471 eV, respectively, but also clearly the Mg-related ABE1 peak at 3.466 eV (in fact, consisting of two separate peaks, as may be expected for ABEs in GaN (Ref. 19)). We note that in this spectrum there is no trace of the second ABE2 peak previously reported for more highly doped GaN:Mg.<sup>4</sup> Likewise, there is no trace of other sharp line spectra related to Mg doping, previously reported in the region 3.35 eV to 3.42 eV.<sup>20</sup> In *n*-type samples with low Mg-doping, the metastable properties of the Mg-related luminescence are also absent. Another sample with a controlled Mg doping of  $[\text{Mg}] = 1 \times 10^{17}\ \text{cm}^{-3}$  shows very similar spectra as in Fig. 1(a).

In the *m*-plane sample doped with Mg to a concentration of  $3 \times 10^{18}\ \text{cm}^{-3}$  there is a broad ABE2 peak (Fig. 1(b)), in agreement with earlier data on *c*-plane samples.<sup>4</sup> This ABE2

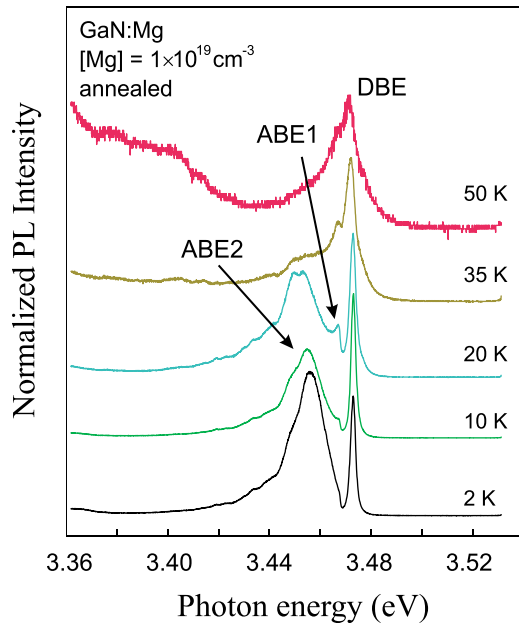


FIG. 2. PL spectra of *c*-plane MOCVD homoepitaxial GaN:Mg ( $[Mg] = 1 \times 10^{19} \text{ cm}^{-3}$ ) measured at different temperatures after annealing.

peak has a very similar polarization behavior as the ABE1 peak (dominantly  $E \perp c$ ), indicating that both are somehow related to a substitutional  $Mg_{Ga}$  acceptor. Moreover, there is also a series of rather strong peaks in the region 3.35–3.42 eV, in addition to the broadened phonon replicas related to free and bound excitons present in the same energy range. The origin of these lines is different basal plane stacking faults (BSFs), as discussed in Ref. 21.

Shown in Fig. 2 is the temperature dependence of PL for a *c*-plane MOCVD sample, with a Mg concentration of approximately  $1 \times 10^{19} \text{ cm}^{-3}$ . The sample is annealed, which in this case enhances the relative intensity of the ABE2 peak.<sup>4</sup> The spectral PL development with temperature is very much the same for the two peaks ABE1 and ABE2, and they both disappear at about 50 K, leaving behind only the DBE peak in the near bandgap region. Note that the narrower ABE1 peak is observed at the high energy flank of the broad ABE2 peak. These temperature dependent data are a support of the ABE nature of the broad ABE2 peak, which due to the spectral broadening cannot be established with standard spectroscopic means (e.g., via resolving the electronic substructure of the no-phonon line<sup>19</sup>). We note that the DBE PL features in GaN are stable up to much higher temperatures, e.g., 150 K in samples with low doping.<sup>22</sup>

In order to obtain a complete experimental picture, the spectra from an 11- $\mu\text{m}$ -thick HVPE grown GaN:Mg layer on sapphire was studied as well, as shown in Fig. 3. The Mg concentration was not exactly known in this sample, but the hole concentration was measured as  $2 \times 10^{18} \text{ cm}^{-3}$  at room temperature, which is consistent with an Mg concentration of about  $2 \times 10^{19} \text{ cm}^{-3}$ .<sup>17</sup> The spectra clearly show the two Mg related ABES with a similar appearance as in the MOCVD Mg-doped sample in Fig. 1(b). Previous work in literature also shows the presence of both the ABE1 and the ABE2 peak in Molecular Beam Epitaxy (MBE) grown GaN:Mg at high doping concentrations, although the identity

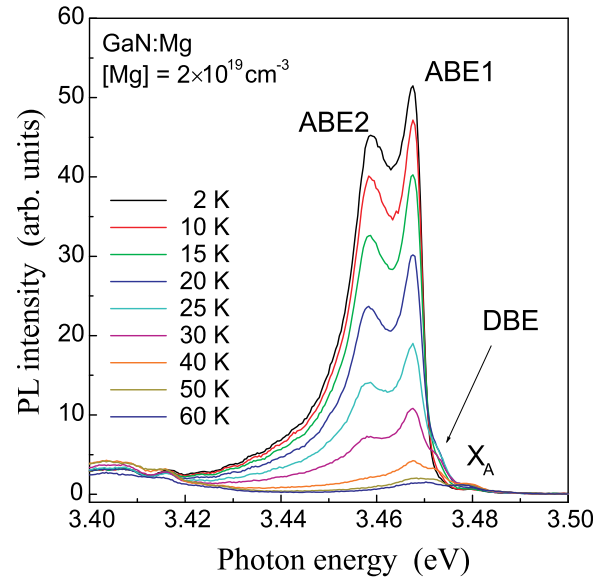


FIG. 3. Near-bandgap PL spectra of as-grown HVPE GaN:Mg layer ( $[Mg] = 2 \times 10^{19} \text{ cm}^{-3}$ ) at different temperatures.

of the peaks was incorrectly labeled.<sup>23</sup> Therefore, the presence of two Mg-related acceptor bound exciton near bandgap PL signatures in GaN appears to be universal.

## B. The DAP spectrum at 3.27 eV

A common feature in all acceptor related luminescence spectra in semiconductors is that the ABE spectra in the near bandgap region are accompanied by DAP spectra at lower energies, i.e., there is one DAP emission and one ABE peak for each particular acceptor species. For low Mg doping levels, the relation between the ABE1 peak at 3.466 eV and the 3.27 eV DAP peak (with accompanying LO phonon replicas at lower energies) has been established in the literature.<sup>2,3</sup> For Mg doping at concentrations  $[Mg] < 10^{18} \text{ cm}^{-3}$  these are the only acceptor related PL features in this energy range, and therefore have to be assigned to the substitutional Mg acceptor.

For higher Mg concentrations, the connection between the ABE2 peak and a weak broad background under the low energy part of the 3.27 eV peak has also been suggested.<sup>4</sup> In order to shed more light on this, we have carried out new time resolved PL measurements in the DAP region for an Mg-doped sample with  $[Mg] = 2 \times 10^{19} \text{ cm}^{-3}$ , see Fig. 4. From these data, it is obvious that at longer delay times (several  $\mu\text{s}$ ) a broad spectrum peaking at about 3.15 eV is dominant, which is then suggested to correspond to a broad DAP emission related to the A2 acceptor with a larger binding energy, consistent with the larger ABE2 binding energy (compared to ABE1) observed in the near bandgap spectra. A longer decay time for deeper DAP emissions is a general observation in semiconductors.<sup>1</sup> A discussion on the suggested interpretation of the corresponding deeper acceptors in terms of  $Mg_{Ga}$  acceptors interacting with structural defects is presented below.

## C. Deeper Mg-related spectra

At higher Mg doping levels, in the range of  $10^{20} \text{ cm}^{-3}$  for MOCVD samples, a strong broad PL band at about 2.9 eV is

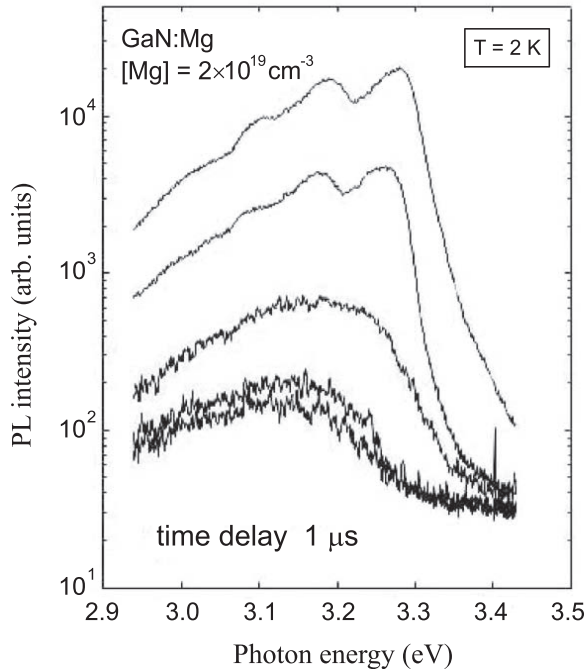


FIG. 4. Time-resolved PL spectra of *m*-plane MOCVD homoepitaxial GaN:Mg ( $[Mg] = 2 \times 10^{19} \text{ cm}^{-3}$ ) obtained with a time delay of  $1 \mu\text{s}$  between each curve. (The repetition rate of the femtosecond laser excitation was 250 kHz.)

noted and sometimes dominates the PL spectra.<sup>10–14</sup> We show such spectra in Fig. 5 for MOCVD grown samples, measured under different excitation conditions. In the sample with moderately high doping ( $1.5 \times 10^{19} \text{ cm}^{-3}$ ) clearly both the 3.27 eV and the 2.9 eV emission band are seen separately, while in the highly doped sample ( $1 \times 10^{20} \text{ cm}^{-3}$ ) only the 2.9 eV emission is present. This shows that these are two separate emissions, and that they are only moderately affected by potential fluctuations in the material.<sup>12,24</sup> The connection to Mg- $V_N$  complexes often suggested for the 2.9 eV emission (see, e.g., Ref. 10) also seems less probable, since such complexes are expected to have a low concentration after annealing.<sup>25–27</sup> The deep 2.9 eV emission seems to be strong only for highly doped MOCVD grown GaN:Mg, and not observable (or at least very weak) for the corresponding doping in MBE (Refs. 23 and 28) or HVPE grown materials (see, Fig. 6). This situation presumably reflects the very different growth conditions in these three growth techniques.

#### IV. DISCUSSION

##### A. Tentative model for the second deeper Mg related acceptor responsible for ABE2

Acceptor bound excitons at high doping level have previously been studied for other compound semiconductors like InP and ZnTe.<sup>29,30</sup> In these cases, a substantial broadening of the ABE peak (corresponding to ABE1 in our case) is observed; it broadens out towards lower energy and there is also some downshift in the mean peak position. The broadening on the low energy side is explained as an effect of the dispersion of the distances in the lattice for interacting acceptor pairs binding the excitons at high doping.<sup>29,30</sup> Our observations for the Mg acceptors in GaN with two distinct

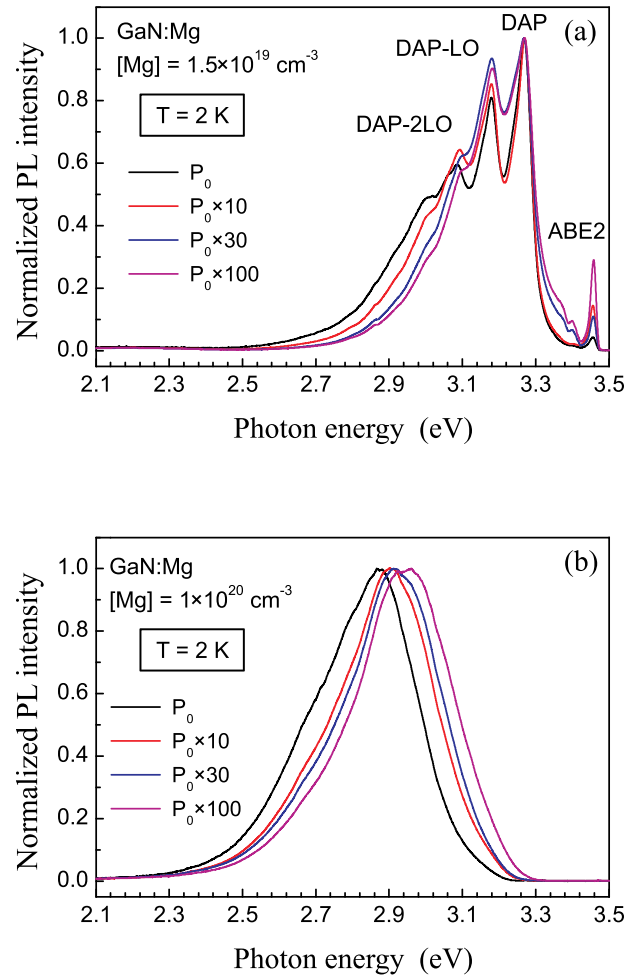


FIG. 5. Low-temperature spectra of *c*-plane MOCVD homoepitaxial GaN:Mg layers measured at different excitation powers: (a)  $[Mg] 1.5 \times 10^{19} \text{ cm}^{-3}$  and (b)  $[Mg] 1 \times 10^{20} \text{ cm}^{-3}$ .

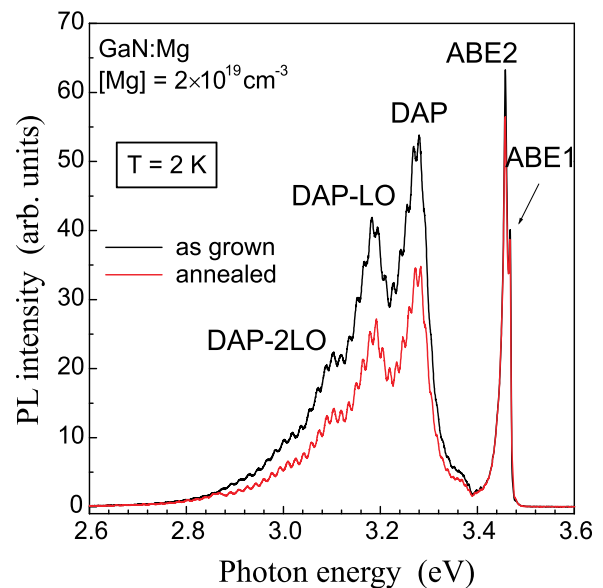


FIG. 6. Low-temperature bound-exciton and DAP spectra of as-grown and annealed HVPE GaN:Mg layer ( $[Mg] 2 \times 10^{19} \text{ cm}^{-3}$ ). (The modulation of the spectra is due to the interference effect.)

ABE peaks (ABE1 and ABE2) over the entire doping range, i.e., say  $1 \times 10^{18} \text{ cm}^{-3}$  to  $2 \times 10^{19} \text{ cm}^{-3}$ , are clearly different from the above traditional description of ABEs at interacting acceptors in the III-V and II-VI compounds. There is no appreciable shift of the main ABE1 acceptor peak with increased Mg doping, and the second ABE2 peak is well separated from ABE1 over this range of concentrations. So we conclude that the two ABE peaks correspond to two different acceptor species caused by the Mg doping. At an Mg concentration above about  $2 \times 10^{19} \text{ cm}^{-3}$ , the ABEs interact strongly so that a Mott-like transition occurs and excitons (ABEs) are no longer bound to the acceptors, thus the near bandgap ABE spectra disappear.

The unusual situation that two different acceptor levels are created by one acceptor dopant in the case of Mg-doped GaN has prompted new structural investigations of GaN:Mg.<sup>31,32</sup> The observation that the second acceptor responsible for the ABE2 signature is only observed in highly doped GaN:Mg suggests the possibility of a correlation with structural defects, that have also been observed in the GaN:Mg samples studied here.<sup>32</sup> These structural defects appear only significantly for  $[\text{Mg}] > 10^{18} \text{ cm}^{-3}$ , and are dominantly BSFs in the case of homoepitaxial material.<sup>31,32</sup> Some of these SF defects are very small in the *c*-plane samples (a couple of nm in size), and those could also be pyramid features, as reported for GaN:Mg grown on sapphire.<sup>33</sup> These defects are presumably induced during growth by the introduction of Mg atoms in the lattice.<sup>32</sup>

The observed properties of the A2 acceptor discussed here may be understood in a similar way as for the BSF-related PL in *n*-type GaN.<sup>34</sup> In that case, it was argued that the localization of electrons (and subsequently excitons) to BSFs in *n*-GaN is mainly induced by donor potentials in the vicinity of the BSF.<sup>34</sup> In the case of acceptor doping the acceptor potential is much more localized, within  $< 1 \text{ nm}$ , meaning that the acceptor hole may not easily delocalize to the BSF plane, but will distort the local potential at the BSF, thus assisting the BSF hole (and exciton) localization, so that the BSF luminescence is observed.<sup>32</sup> The acceptor will, in turn, be perturbed by the nearby BSF potential mainly governed by the spontaneous polarization field,<sup>21</sup> positioned on the average a few nm away in *p*-GaN with an Mg doping of  $10^{19} \text{ cm}^{-3}$ . This perturbed potential should be sufficiently different from an unperturbed Mg acceptor to give rise to the A2 acceptor and its characteristic ABE2 spectrum.

We note that there is independent evidence for the stimulation of BSF luminescence by acceptor doping, as recently observed in a series of *n*-type *m*-plane homoepitaxial GaN samples.<sup>35</sup> Also in our *m*-plane Mg-doped samples there are strong BSF-related spectra in the range 3.3–3.42 eV, apparently stimulated by the Mg doping (Fig. 7). These BSF PL spectra are different from the ABE2 peak, again emphasizing that the A2 acceptor is likely to be associated to a specific site of the Mg acceptor in relation to the BSF plane, i.e., not randomly distributed acceptors. The microscopic geometry of the A2 acceptor center remains to be revealed by future studies.

The PL spectrum of the unperturbed A1 acceptor has the appearance expected for an isolated Mg acceptor.<sup>19</sup> The complex defect aggregate (Mg acceptor plus BSF), on the other

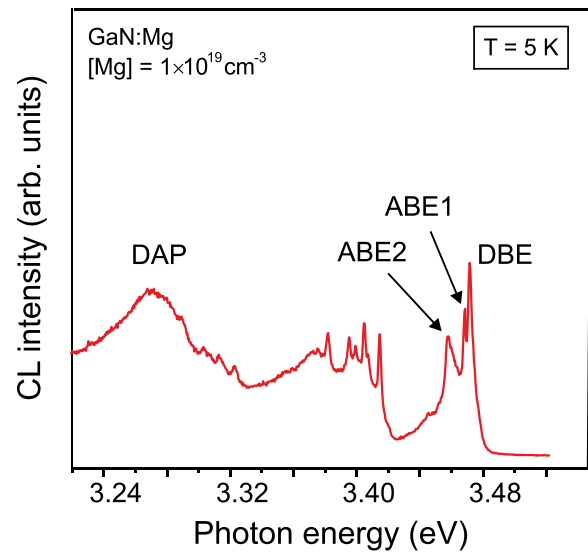


FIG. 7. Low temperature CL spectra of *m*-plane MOCVD homoepitaxial GaN:Mg ( $[\text{Mg}] = 1 \times 10^{19} \text{ cm}^{-3}$ ).

hand, is suggested to explain the additional binding energy (ABE2 is deeper than ABE1), and the broad lineshape of ABE2 (see, Figs. 1(b), 2, and 3). The peculiar lineshape observed for ABE2 may originate from a strong transfer process for excitons between different sites (from shallower BEs to deeper ones). Such excitonic transfer has been observed previously in other III-V and II-VI semiconductors and explained in terms of acoustic phonon assisted exciton tunneling.<sup>36,37</sup> Transient PL spectroscopy on a highly doped GaN:Mg sample clearly demonstrates decay processes dominated by such transfer, see Fig. 8. The range of acoustic phonons in GaN has been determined to cover phonon energies up to above 30 meV (Ref. 38) therefore the ABE2 peak at 3.455 eV is well within the range of a transfer process involving the ABE1 at 3.466 eV as the main original state. The intensity profile of ABE2 has a high energy portion, which is, continuously rising from ABE1 all the way down to the ABE2 peak. The position of ABE2 is rather well defined in all samples, and the acceptor binding energy (as well as the ABE2 binding energy) should be determined by the specific configuration of the defect center, i.e., the Mg acceptor–BSF combination.

The PL decay traces in Fig. 8(a) clearly show the fast initial decay of the shallower DBE and ABE1 signal, much faster than the radiative decay times observed in samples with lower doping.<sup>39</sup> In Fig. 8(b), a time resolved development of the ABE1–ABE2 pair of peaks is shown. These data show directly the spectral shift of the PL signal from the ABE1 position to ABE2, mostly during the first 100 ps. This is naturally explained as exciton transfer, as discussed above.

The broad ABE2 PL peak has a very specific dependence on excitation intensity, i.e., at low excitation levels the peak is just barely seen, while it increases superlinearly at high excitation levels (Fig. 9). This is again consistent with the exciton transfer processes. At low excitation levels there are few neutral acceptors and ABEs, and therefore the distance of an ABE site to another neutral acceptor is long. This means a low probability for transfer because the overlap matrix element is very small. With increasing excitation the

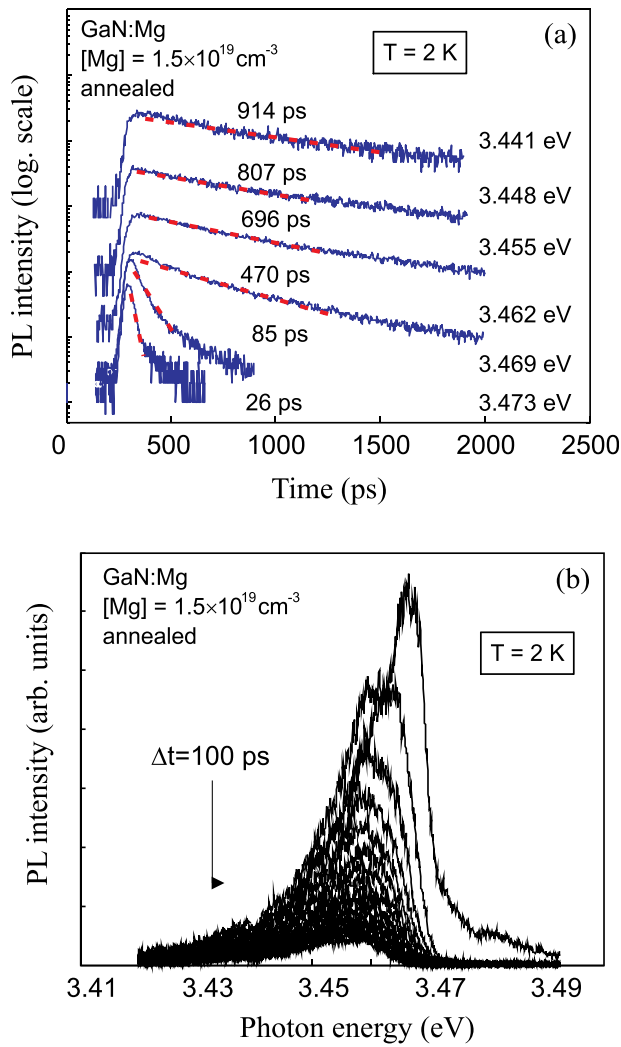


FIG. 8. (a) PL decay curves taken at different photon energies for *c*-plane MOCVD homoepitaxial GaN:Mg ( $[Mg] = 1.5 \times 10^{19} \text{ cm}^{-3}$ ) and (b) time-resolved PL spectra of the same sample.

occupation probability of both neutral acceptors and neutral ABEs (ABE1) increases, and as a result the distance between ABE1 sites and neutral A2 acceptors becomes favorable for transfer.

### B. The 3.27 eV DAP emission and blue PL band at 2.9 eV

While the relation of the 3.27 eV PL spectrum to the  $Mg_{Ga}$  acceptor seems to be well established experimentally, the identity of the blue PL band peaking at about 2.9 eV is confusing within the confines of the available data and their interpretation in the literature. As stated above, the early investigations focused on a DAP recombination model with a deep  $V_N$ -Mg donor complex together with a substitutional Mg acceptor.<sup>10</sup> This DAP model is only consistent with a high concentration of these donor complexes ( $>10^{19} \text{ cm}^{-3}$ ), while the investigations that followed estimated the actual concentration of these donors to be as low as  $10^{17} \text{ cm}^{-3}$  before annealing and much lower after anneal.<sup>25,26</sup> Further, the Optically Detected Magnetic Resonance (ODMR) investigations of GaN:Mg failed to show any evidence for deep donors.<sup>40</sup> Recently, another interpretation of this blue PL as

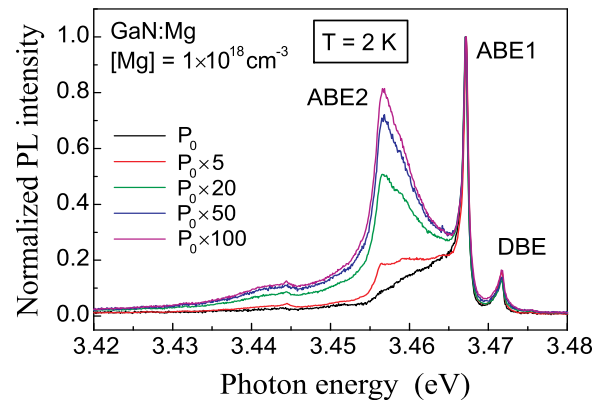


FIG. 9. Excitation intensity dependent PL spectra of *m*-plane MOCVD homoepitaxial GaN:Mg ( $[Mg] = 1 \times 10^{18} \text{ cm}^{-3}$ ).

a DAP involving shallow donors and the substitutional  $Mg_{Ga}$  acceptor was presented, based on theoretical calculations indicating that the Mg acceptor should be deeper than previously believed and have a strong phonon coupling.<sup>41</sup> This interpretation also means that the 3.27 eV DAP is not related to the  $Mg_{Ga}$  acceptor, but to an Mg-H complex. The blue PL is only strong in MOCVD grown GaN at high Mg doping, however, while the same material grown with MBE or HVPE does not show the blue PL peak, in spite of the fact that a similar number of  $Mg_{Ga}$  acceptors should be present. There are many early papers demonstrating the DAP nature of the 3.27 eV PL.<sup>5,6</sup> A most relevant recent paper on low Mg doped MBE samples demonstrate clearly both the DAP and the free-to-bound (FB) transition, at different temperatures, confirming the binding energy of the Mg acceptor as  $225 \pm 5 \text{ meV}$ .<sup>42</sup> An argument against the interpretation of the 3.27 eV emission as being related to a neutral Mg-H complex is that this complex (from theoretical results<sup>41</sup>) is only expected to be found in *p*-type samples with a high Mg doping, while in reality the 3.27 eV PL is also prominent in *n*-type GaN. It is, in fact, the only Mg-related PL emission in *n*-type GaN, and dominates the PL spectrum in all Mg-doped samples, except in very highly doped MOCVD samples where the 2.9 eV band is strong. This behavior is expected if the 3.27 eV DAP involves the  $Mg_{Ga}$  acceptor.

Returning to the deeper 2.9 eV band there is some evidence from ODMR data for a DAP recombination, since a shallow donor signal is observed for detection in this peak.<sup>43,44</sup> Thermal quenching of the emission is observed near room temperature with an activation energy of 0.3–0.4 eV.<sup>45</sup> This would be consistent with an acceptor level of similar binding energy, deeper than for the  $Mg_{Ga}$  acceptor. The oscillator strength for the deeper 2.9 eV transition is naturally weaker than that for the 3.27 eV PL line, explaining the frequently observed spectral upshift in this spectral range upon increasing excitation density.

The annealing studies in H plasma reported in Ref. 11 are interesting. It is shown that the 2.9 eV PL seems to be H-related, and the corresponding defect does not noticeably affect the hole concentration. The authors explain their data regarding a DAP process with an H-related deep donor (binding energy 0.37 eV) and the shallow Mg acceptor, similar to other work.<sup>45</sup> An alternative model would be a H-related

complex that gives rise to the 2.9 eV PL line, but has a concentration much lower than the [Mg] atomic concentration, and thus does not affect the hole concentration in *p*-GaN.

### C. Instabilities of acceptor related luminescence spectra

An important property that needs an explanation is the instability of the PL or CL spectra (ABE as well as 3.27 eV DAP spectra) during prolonged excitation with above bandgap UV light or energetic electrons.<sup>4,7-9</sup> This is particularly important for MOCVD material which usually contains an appreciable concentration of H. In our previous work, it was suggested that this property could be interpreted as evidence for instability of the acceptor responsible for the ABE1 and the 3.27 eV spectral features.<sup>4</sup> Since our later optical investigations discussed in this paper are only consistent with a model where the ABE1 and the 3.27 eV PL features are related to the substitutional Mg acceptor, we have tested alternative models to explain these instabilities. In Fig. 10, we show time sequential PL spectra of an *m*-plane Mg doped sample, obtained at time intervals of 10 s during continuous UV excitation. It is obvious that in this case, the dominant feature of this short term instability is a rapid degradation of the PL efficiency in the entire near bandgap region, evidence for a rapid nonradiative process induced by the UV excitation. Such a process is most naturally explained by the presence of a defect possessing instable properties, acting as a non-radiative shunt path for the near bandgap luminescence.

The involvement of another defect (i.e., not primarily the Mg acceptor) in the instability process is further indicated by time-resolved PL data of the DAP emission at 3.27 eV (see, Fig. 11). This figure shows that upon long term excitation there is a clear downshift in energy of the 3.27 eV DAP peak, evidence for a decrease of the hole occupation of the Mg acceptor.<sup>46,47</sup> This decrease means that the quasi Fermi level is raised in the bandgap during the long term excitation in this experiment, which is understood if another deeper (nonradiative) defect level is active in the recombination process, capturing photoexcited holes to a metastable state, which decreases the hole occupation in the Mg acceptor. This nonradiative defect is then directly

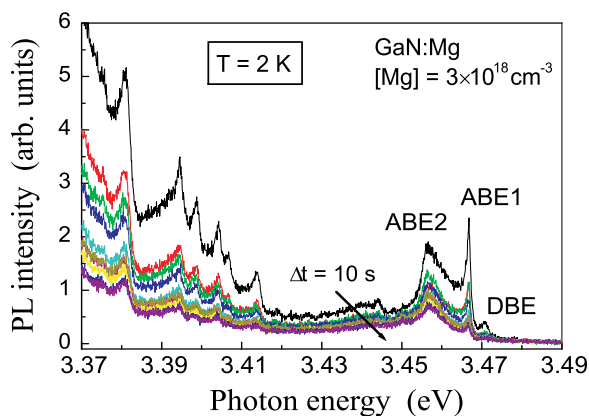


FIG. 10. Low-temperature spectra of *m*-plane MOCVD homoepitaxial GaN:Mg ( $[Mg] = 3 \times 10^{18} \text{ cm}^{-3}$ ) obtained at time intervals of 10 s during continuous UV excitation.

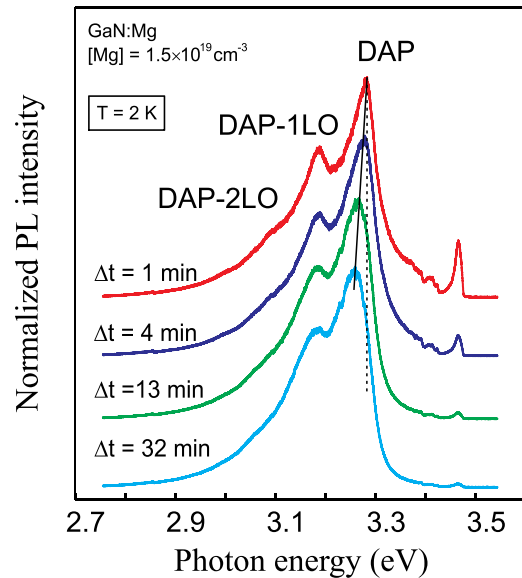


FIG. 11. Low-temperature spectra of *c*-plane MOCVD homoepitaxial GaN:Mg ( $[Mg] = 1.5 \times 10^{19} \text{ cm}^{-3}$ ) measured upon long term continuous UV excitation showing a clear red shift of the DAP emission.

responsible for the long term instability properties. To reveal specific properties of the defect responsible for the long term instability, more experiments to obtain Deep Level Transient Spectroscopy (DLTS) data are needed.

As mentioned above, this idea with an independent deep level defect responsible for the instability allows the interpretation of the strongest features in PL and CL data of Mg-doped GaN, the ABE1 peak and the 3.27 eV DAP, as connected to the regular substitutional Mg acceptor, a simpler model than the one discussed in Ref. 4. Unfortunately, electrical measurements to reveal properties of the metastable defect are very difficult in the low temperature range involved here, and very limited such data for Mg-doped *p*-GaN are found in the literature.<sup>48</sup> Metastable defects are also reported for *n*-GaN, suggested to be  $V_{Ga}$ -related.<sup>49,50</sup> Such defects related to  $V_{Ga}$  would be unlikely in *p*-GaN (Ref. 51) therefore, more work is needed to explore the identity of the metastable defect in Mg-doped GaN.

### V. CONCLUSIONS

We discuss new and previous optical data for the Mg acceptor in GaN, in an attempt to arrive at the simplest possible model that can explain all the data in aggregate. Intriguing properties discussed in previous work were the existence of two different acceptor signatures in low temperature PL spectra for bound excitons (ABE1 at 3.466 eV and ABE2 at 3.455 eV), and the corresponding DAP1 at 3.27 eV and the weaker DAP2 at about 3.15 eV. Since at low Mg doping (*n*-type samples) only ABE1 and DAP1 are observed, the above-mentioned spectra should be related to the substitutional Mg acceptors, i.e., no Mg-H related complexes as previously suggested in relation to the observed instabilities<sup>4</sup> are needed to explain these optical data. The second deeper set of broadened spectra ABE2 and DAP2 appear at higher doping ( $[Mg] > 10^{18} \text{ cm}^{-3}$ ), simultaneously, as structural defects (basal plane stacking faults) are introduced.<sup>32</sup> The

acceptors involved in the ABE2 and DAP2 peaks are therefore assigned to substitutional Mg acceptors perturbed by the induced structural defects (BSFs). This correlation was made possible in this work via the use of homoepitaxy on bulk GaN substrates, thus avoiding the more complex spectral behavior in samples grown on sapphire.<sup>52</sup> The unusual unstable behavior in the optical spectra at low temperatures for high Mg doping may then be explained by the presence of another nonradiative recombination path via a deeper defect level which is metastable in this low temperature range (<300 K), and affects the PL of the Mg-related spectra via the quasi-Fermi level under optical excitation. Since the deeper radiative PL emission at 2.9 eV only occurs at high doping levels in MOCVD samples (and is not regularly observed in similarly Mg-doped MBE and HVPE samples), it is implausible that this emission is related to the substitutional Mg acceptor, as recently suggested in theoretical work.<sup>41,53</sup> It may relate to a deeper acceptor of low concentration, introduced primarily in MOCVD growth.

## ACKNOWLEDGMENTS

We are grateful to S. Figge and D. Hommel at Bremen University for some of the homoepitaxial MOCVD samples used in this study and to A. Usikov at Oxford Instruments, Oxford, UK for a *p*-type Mg-doped HVPE sample. The Linköping group also acknowledges support from the K. A. Wallenberg Foundation for the financing of spectroscopic equipment and the Li-Li-IFM Linneaus project for partial support.

<sup>1</sup>H. Morkoc, *Handbook of Nitride Semiconductors and Devices* (Wiley, 2008).  
<sup>2</sup>L. Chen and B. J. Skromme, in *GaN and Related Alloys*, edited by C. Wetzel, E. T. Yu, J. S. Speck, A. Rizzi, and Y. Arakawa (Mater. Res. Soc. Symp. Proc., 2003), Vol. 743, p. L11.35.  
<sup>3</sup>B. Monemar, P. P. Paskov, J. P. Bergman, T. Paskova, S. Figge, J. Dennemarck, and D. Hommel, *Phys. Status Solidi B* **243**, 1604 (2006).  
<sup>4</sup>B. Monemar, P. P. Paskov, G. Pozina, C. Hemmingsson, J. P. Bergman, T. Kawashima, H. Amano, I. Akasaki, T. Paskova, S. Figge, D. Hommel, and A. Usui, *Phys. Rev. Lett.* **102**, 235501 (2009).  
<sup>5</sup>R. Dingle and M. Ilegems, *Solid State Commun.* **9**, 175 (1971).  
<sup>6</sup>O. Lagerstedt and B. Monemar, *J. Appl. Phys.* **45**, 2266 (1974).  
<sup>7</sup>F. Shahedipour and B. W. Wessels, *Appl. Phys. Lett.* **76**, 3011 (2000).  
<sup>8</sup>Y. Koide, D. E. Walker, Jr., B. D. White, L. J. Brillson, M. Murakami, S. Kamiyama, H. Amano, and I. Akasaki, *J. Appl. Phys.* **92**, 3657 (2002).  
<sup>9</sup>O. Gelhausen, M. R. Phillips, E. M. Goldys, T. Paskova, B. Monemar, M. Strassburg, and A. Hoffmann, *Phys. Rev. B* **69**, 125210 (2004).  
<sup>10</sup>U. Kaufmann, M. Kunzer, H. Obloh, M. Maier, Ch. Manz, A. Ramakrishnan, and B. Santic, *Phys. Rev. B* **59**, 5561 (1999).  
<sup>11</sup>Y. Kamiura, M. Kaneshiro, J. Tamura, T. Ishiyama, Y. Yamashita, T. Mitani, and T. Mukai, *Jpn. J. Appl. Phys., Part II* **44**, L926 (2005).  
<sup>12</sup>B. Han, J. M. Gregie, and B. W. Wessels, *Phys. Rev. B* **68**, 045205 (2003).  
<sup>13</sup>S. Zeng, G. N. Aliev, D. Wolverson, J. J. Davies, S. J. Bingham, D. A. Abdulmalik, P. G. Coleman, T. Wang, and P. J. Parbrook, *Appl. Phys. Lett.* **89**, 022107 (2006).  
<sup>14</sup>M. W. Bayerl, M. S. Brandt, O. Ambacher, M. Stutzmann, E. R. Glaser, R. L. Henry, A. E. Wickenden, D. D. Koleske, T. Suski, I. Grzegory, and S. Porowski, *Phys. Rev. B* **63**, 125203 (2001).  
<sup>15</sup>B. Monemar, H. Larsson, C. Hemmingsson, I. G. Ivanov, and D. Gogova, *J. Cryst. Growth* **281**, 17 (2005).  
<sup>16</sup>B. Monemar, P. P. Paskov, G. Pozina, C. Hemmingsson, P. Bergman, D. Lindgren, L. Samuelson, X. Ni, H. Morkoc, T. Paskova, Z. Bi, and J. Ohlsson, *Proc. SPIE* **7939**, 793907 (2011).  
<sup>17</sup>A. Usikov, O. Kovalenkov, V. Soukhoveev, V. Ivantsov, A. Syrkin, V. Dmitriev, A. Yu. Nikiforov, S. G. Sundaresan, S. J. Jeliakov, and A. V. Davydov, *Phys. Status Solidi C* **5**, 1829 (2008).

<sup>18</sup>H. Xing, D. S. Green, H. Yu, T. Mates, P. Kozodoy, S. Keller, S. P. DenBaars, and U. K. Mishra, *Jpn. J. Appl. Phys., Part I* **42**, 50 (2003).  
<sup>19</sup>B. Gil, P. Bigenwald, P. P. Paskov, and B. Monemar, *Phys. Rev. B* **81**, 085211 (2010).  
<sup>20</sup>R. Stepniewski, A. Wyszolek, M. Potemski, J. Lusakowski, K. Korona, K. Pakula, J. M. Baranowski, G. Martinez, P. Wyder, I. Grzegory, and S. Porowski, *Phys. Status Solidi B* **210**, 373 (1998).  
<sup>21</sup>J. Lähnemann, O. Brandt, U. Jahn, C. Pfuller, C. Roder, P. Dogan, F. Grosse, A. Belabbes, F. Bechstedt, A. Trampert, and L. Geelhaar, *Phys. Rev. B* **86**, 081302 (2012).  
<sup>22</sup>D. Kovalev, B. Averboukh, D. Volm, B. K. Meyer, H. Amano, and I. Akasaki, *Phys. Rev. B* **54**, 2518 (1996).  
<sup>23</sup>F. B. Naranjo, E. Calleja, Z. Bougrioua, A. Trampert, X. Kong, and K. H. Ploog, *J. Cryst. Growth* **270**, 542 (2004).  
<sup>24</sup>M. A. Reshchikov, J. Xie, L. He, X. Gu, Y. T. Moon, Y. Fu, and H. Morkoc, *Phys. Status Solidi C* **2**, 2761 (2005).  
<sup>25</sup>S. Hautakangas, J. Oila, M. Alatalo, K. Saarinen, L. Liskay, D. Seghier, and H. P. Gislason, *Phys. Rev. Lett.* **90**, 137402 (2003).  
<sup>26</sup>S. Hautakangas, K. Saarinen, L. Liskay, J. A. Freitas, Jr., and R. L. Henry, *Phys. Rev. B* **72**, 165303 (2005).  
<sup>27</sup>B. Monemar, P. P. Paskov, G. Pozina, C. Hemmingsson, J. P. Bergman, H. Amano, I. Akasaki, S. Figge, D. Hommel, T. Paskova, and A. Usui, *Phys. Status Solidi C* **7**, 1850 (2010).  
<sup>28</sup>E. R. Glaser, M. Murthy, J. A. Freitas, Jr., D. F. Storm, L. Zhou, and D. J. Smith, *Physica B* **401–402**, 327 (2007).  
<sup>29</sup>P. J. Dean and A. M. White, *Solid-State Electron.* **21**, 1351 (1978).  
<sup>30</sup>E. Molva and N. Magnea, *Phys. Status Solidi B* **102**, 475 (1980).  
<sup>31</sup>S. Khromov, B. Monemar, V. Avrutin, X. Li, H. Morkoc, L. Hultman, and G. Pozina, *Appl. Phys. Lett.* **100**, 172108 (2012).  
<sup>32</sup>S. Khromov, C. G. Hemmingsson, H. Amano, B. Monemar, L. Hultman, and G. Pozina, *Phys. Rev. B* **84**, 075324 (2011).  
<sup>33</sup>P. Vennégues, M. Benaissa, B. Beaumont, E. Feltin, P. De Mierry, S. Dalmaso, M. Leroux, and P. Gibart, *Appl. Phys. Lett.* **77**, 880 (2000).  
<sup>34</sup>P. Corfdir, P. Lefebvre, J. Ristic, J.-D. Ganière, and B. Deveaud-Plédran, *Phys. Rev. B* **80**, 153309 (2009).  
<sup>35</sup>S. Khromov *et al.*, private communication (2013).  
<sup>36</sup>E. Cohen and M. D. Sturge, *Phys. Rev. B* **25**, 3828 (1982).  
<sup>37</sup>M. Godlewski, W. M. Chen, and B. Monemar, *Phys. Rev. B* **37**, 2570 (1988).  
<sup>38</sup>T. Ruf, J. Serrano, M. Cardona, P. Pavone, M. Pabst, M. Krisch, M. D'Astuto, T. Suski, I. Grzegory, and M. Leszczynski, *Phys. Rev. Lett.* **86**, 906 (2001).  
<sup>39</sup>B. Monemar, P. P. Paskov, J. P. Bergman, G. Pozina, A. A. Toropov, T. V. Shubina, T. Malinauskas, and A. Usui, *Phys. Rev. B* **82**, 235202 (2010).  
<sup>40</sup>E. R. Glaser, J. A. Freitas, Jr., B. V. Shanabrook, D. D. Koleske, S. K. Lee, S. S. Park, and J. Y. Han, *Phys. Rev. B* **68**, 195201 (2003).  
<sup>41</sup>J. L. Lyons, A. Janotti, and C. G. Van de Walle, *Phys. Rev. Lett.* **108**, 156403 (2012).  
<sup>42</sup>M. A. Reshchikov, D. Huang, F. Yun, L. He, and H. Morkoc, *Appl. Phys. Lett.* **79**, 3779 (2001) (note, in particular, the data in Fig. 4 of that paper).  
<sup>43</sup>E. R. Glaser, W. E. Carlos, G. C. B. Braga, J. A. Freitas, Jr., W. J. Moore, G. V. Shanabrook, R. L. Henry, A. E. Wickenden, D. D. Koleske, H. Obloh, P. Kozodoy, S. P. DenBaars, and U. K. Mishra, *Phys. Rev. B* **65**, 085312 (2002).  
<sup>44</sup>G. N. Aliev, S. Zeng, J. J. Davies, D. Wolverson, and S. J. Bingham, *Phys. Rev. B* **71**, 195204 (2005).  
<sup>45</sup>M. A. Reshchikov, G. C. Yi, and B. W. Wessels, *Phys. Rev. B* **59**, 13176 (1999).  
<sup>46</sup>D. G. Thomas, J. J. Hopfield, and W. M. Augustyniak, *Phys. Rev.* **140**, 202 (1965).  
<sup>47</sup>B. Monemar, S. Khromov, G. Pozina, P. Paskov, P. Bergman, C. Hemmingsson, L. Hultman, H. Amano, V. Avrutin, X. Li, and H. Morkoc, *Jpn. J. Appl. Phys., Part I* **52**, 08JJ03 (2013).  
<sup>48</sup>C. Johansson, J. Y. Lin, H. X. Jiang, M. A. Khan, and C. J. Sun, *Appl. Phys. Lett.* **68**, 1808 (1996).  
<sup>49</sup>M. Toth, K. Fleischer, and M. R. Phillips, *Phys. Rev. B* **59**, 1575 (1999).  
<sup>50</sup>M. A. Reshchikov, F. Shahedipour, R. Y. Korotkov, and B. W. Wessels, *J. Appl. Phys.* **87**, 3351 (2000).  
<sup>51</sup>C. G. Van de Walle, *Phys. Rev. B* **56**, R10020 (1997).  
<sup>52</sup>G. Callsen, M. R. Wagner, T. Kure, J. S. Reparaz, M. Bugler, J. Brunmeier, C. Nenstiel, A. Hoffmann, M. Hoffmann, J. Tweedie, Z. Bryan, S. Aygun, R. Kirste, R. Collazo, and Z. Sitar, *Phys. Rev. B* **86**, 075207 (2012).  
<sup>53</sup>S. Lany and A. Zunger, *Appl. Phys. Lett.* **96**, 142114 (2010).

# Laser lift-off technique for freestanding GaN substrate using an In droplet formed by thermal decomposition of GaInN and its application to light-emitting diodes

Daisuke Iida<sup>1</sup>, Syunsuke Kawai, Nobuaki Ema, Takayoshi Tsuchiya, Motoaki Iwaya, Tetsuya Takeuchi, Satoshi Kamiyama, and Isamu Akasaki

Citation: *Appl. Phys. Lett.* **105**, 072101 (2014); doi: 10.1063/1.4893757

View online: <http://dx.doi.org/10.1063/1.4893757>

View Table of Contents: <http://aip.scitation.org/toc/apl/105/7>

Published by the American Institute of Physics

---

---



Small Conferences. BIG Ideas.

Applied Physics  
Reviews

**SAVE THE DATE!**  
**3D Bioprinting: Physical and Chemical Processes**  
May 2–3, 2017 • Winston Salem, NC, USA

The background of the banner features a stylized, glowing blue and red network of lines, resembling a biological or chemical structure, set against a dark blue background.

# Laser lift-off technique for freestanding GaN substrate using an In droplet formed by thermal decomposition of GaInN and its application to light-emitting diodes

Daisuke Iida,<sup>1,a)</sup> Syunsuke Kawai,<sup>1</sup> Nobuaki Ema,<sup>1</sup> Takayoshi Tsuchiya,<sup>1</sup> Motoaki Iwaya,<sup>1</sup> Tetsuya Takeuchi,<sup>1</sup> Satoshi Kamiyama,<sup>1</sup> and Isamu Akasaki<sup>1,2</sup>

<sup>1</sup>Faculty of Science and Technology, Meijo University, Nagoya 468-8502, Japan

<sup>2</sup>Akasaki Research Center, Nagoya University, Nagoya 464-8603, Japan

(Received 2 August 2014; accepted 8 August 2014; published online 18 August 2014)

We developed a laser lift-off technique for a freestanding GaN substrate using an In droplet formed by thermal decomposition of GaInN. A combination of an In droplet formed by thermal decomposition of GaInN during growth and a pulsed second-harmonic neodymium-doped yttrium aluminum garnet laser ( $\lambda = 532$  nm) realized the lift-off GaN substrate. After laser lift-off of the GaN substrate, it was used to achieve 380 nm ultraviolet light-emitting diodes with light output enhanced 1.7-fold. In this way, the light extraction can be improved by removing the GaN substrate. © 2014 AIP Publishing LLC. [<http://dx.doi.org/10.1063/1.4893757>]

Group-III-nitride-based light-emitting diode (LED) technology appears to be an excellent candidate for solid-state platforms. Currently, high-brightness GaInN-based visible LEDs have been commercialized.<sup>1–4</sup> In particular, the external quantum efficiency of blue LEDs has reached approximately 83%.<sup>5</sup> However, the ultraviolet (UV) LED still has a low external quantum efficiency because of a low internal quantum efficiency, low free hole carrier concentration in the p-layer, and high internal absorption by the metal electrodes and epilayer.<sup>6–10</sup> The UV LED is also a major focus in the research efforts of group-III-nitride-based LEDs.

High-efficiency UV-A LEDs are usually grown on sapphire substrates fabricated by a laser lift-off (LLO) technique and polishing/etching of the GaN epilayer after lift-off from the sapphire substrate.<sup>11</sup> It is well known that of UV-A LEDs are strongly dependent on the dislocation density of the underlying layer. With the adoption of a high-quality low-dislocation-density GaN substrate, the UV-A LEDs are expected to have improved internal quantum efficiency as a result of reduced nonradiative recombination.<sup>12,13</sup> It is significantly important to reduce the dislocation density of the underlying layer to realize high-performance devices. The light extraction efficiency can also be improved by using the surface texturing technique.<sup>14</sup> However, growing UV-A LEDs on GaN substrates is avoided because the GaN substrate has a degradation factor of light extraction owing to internal absorption loss due to the presence of impurities (e.g., oxygen and carbon) and their complexes.<sup>15,16</sup> For the realization of high-efficiency UV-A LEDs grown on GaN substrates, it is required to remove the GaN substrate. We look to expect a LLO, which is one technique of overcoming GaN absorption loss. According to several reports, the realization of LLO LEDs grown on sapphire substrates has almost been achieved.<sup>17–20</sup> A typical LLO technique enables us to separate the sapphire substrate from the interface with GaN using a high-energy pulsed UV laser (e.g., KrF pulsed excimer laser;  $\lambda = 248$  nm), because they have a huge

difference in absorption energy. Thus, the GaN layer nearby the interface with sapphire can strongly absorb the UV laser light, which induces a Ga droplet formed by the decomposition of GaN. However, it then leads to the degradation of the quality of the active layer owing to the absorption of the high-energy pulsed UV laser light. On the other hand, a GaN epilayer on the GaN substrate has almost the same absorption energy gap. Therefore, it is impossible to remove the GaN substrate from the UV-A LED structure by the typical LLO technique.

In this study, we developed a LLO technique for freestanding GaN substrate using adopting an In droplet layer formed by thermal decomposition of GaInN during growth. The In droplet layer is expected to absorb light at visible and infrared wavelengths by surface plasmon resonance.<sup>21</sup> Our LLO technique enabled the separation of the GaN substrate from the epilayer through the use of a pulsed second-harmonic neodymium-doped yttrium aluminum garnet (Nd:YAG) laser ( $\lambda = 532$  nm) as a result of the absorption of visible light in the In droplet layer. The LLO LED had improved electron-luminescence (EL) emission intensity owing to the reduced absorption loss of the GaN substrate. Specifically, our LLO technique is expected to be useful for the reuse of the GaN substrate and the utilization of some devices to realize low cost and high performance.

All the samples were grown by metalorganic vapor phase epitaxy in a face-down 2 in.  $\times$  3 wafer horizontal-flow reactor. We prepared a high-quality freestanding GaN substrate. The threading dislocation density of the GaN substrate was below  $10^6$  cm<sup>-2</sup>, as characterized by cathodoluminescence (CL) at room temperature. First, we investigated the crystalline quality of a 2- $\mu$ m-thick highly Si-doped n-Al<sub>0.03</sub>Ga<sub>0.97</sub>N layer grown on a GaN substrate with/without removing the layer of Ga<sub>0.85</sub>In<sub>0.15</sub>N/GaN superlattices (SLs). The samples with and without Ga<sub>0.85</sub>In<sub>0.15</sub>N/GaN SLs are assigned as samples (A) and (B) in Fig. 1, respectively. It is well known that GaInN is a very sensitive material with thermal stability.<sup>22</sup> After the growth of Ga<sub>0.85</sub>In<sub>0.15</sub>N/GaN SLs, they were transformed into In droplets by the thermal

<sup>a)</sup>E-mail: dft0tf16@meijo-u.ac.jp

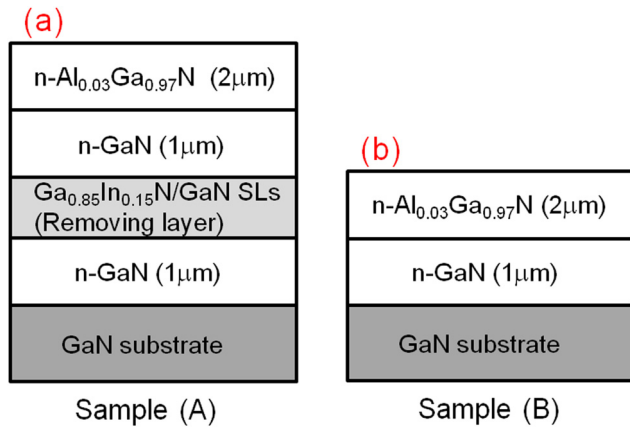


FIG. 1. Schematic view of n-Al<sub>0.03</sub>Ga<sub>0.97</sub>N layers (a) with and (b) without Ga<sub>0.85</sub>In<sub>0.15</sub>N/GaN SLs grown on GaN substrate. Ga<sub>0.85</sub>In<sub>0.15</sub>N/GaN SLs were transformed into In droplet layer by thermal decomposition of Ga<sub>0.85</sub>In<sub>0.15</sub>N during n-GaN and n-Al<sub>0.03</sub>Ga<sub>0.97</sub>N growth.

decomposition of GaInN during n-GaN and n-Al<sub>0.03</sub>Ga<sub>0.97</sub>N growth at 1040 °C. The characterization of an as-grown highly Si-doped n-Al<sub>0.03</sub>Ga<sub>0.97</sub>N layer with/without the In droplet layer grown on a GaN substrate by X-ray diffraction (XRD) (Regaku: Smart Lab), transmittance (Shimadzu: UV-2500PC), and CL (Hitachi: SU-70) revealed the crystal structure, optical property, and crystalline quality, respectively.

Second, we fabricated an UV-A LED with a GaInN multiple quantum well (MQW) active layer grown on a GaN substrate. Figure 2 shows the fabrication steps of LLO and control LEDs. The LLO LED consisted of 8 periods of Ga<sub>0.85</sub>In<sub>0.15</sub>N/GaN SLs in order to remove the GaN substrate, a 1-μm-thick Si-doped n-GaN layer, 2-μm-thick highly Si-doped n-Al<sub>0.03</sub>Ga<sub>0.97</sub>N layer, 10 periods of Ga<sub>0.97</sub>In<sub>0.03</sub>N(2 nm)/GaN(2 nm) SLs, 5 periods of Ga<sub>0.95</sub>In<sub>0.05</sub>N(6 nm)/GaN(12.5 nm) MQWs, a 20-nm-thick Mg-doped p-Al<sub>0.13</sub>Ga<sub>0.87</sub>N electron-blocking layer, and a 120-nm-thick Mg-doped p-GaN contact layer. Actually, the Ga<sub>0.85</sub>In<sub>0.15</sub>N/GaN SLs for the removing layer were almost completely transformed into In droplets by the thermal decomposition of GaInN with increasing temperature to 1040 °C during n-GaN and n-Al<sub>0.03</sub>Ga<sub>0.97</sub>N growth. After exposure of the

n-Al<sub>0.03</sub>Ga<sub>0.97</sub>N layer by inductively coupled plasma etching, a Ag(150 nm)/ITO(30 nm) contact was deposited on both n-Al<sub>0.03</sub>Ga<sub>0.97</sub>N and p-GaN layers. Bare LED chips of 500 × 600 μm<sup>2</sup> size were fabricated as flip-chip structures. After mounting bare LED chips on submounts with Au bumps, an epoxy resin was applied to fill the gap between the LED chip and the submount.<sup>20</sup> The LLO setup consists of a pulsed second-harmonic Nd:YAG laser (λ = 532 nm). The irradiation energy density was 125 mJ/cm<sup>2</sup>. After removing the GaN substrate, we etched the back surface to improve the light extraction efficiency, using hot potassium hydroxide (KOH) solution after LLO.<sup>12,20</sup> The control LED was composed of the 200-μm-thick GaN substrate without the Ga<sub>0.85</sub>In<sub>0.15</sub>N/GaN SLs for removing GaN substrate. Finally, light output power- and voltage-injection current (V-I, L-I) characteristics of each LED were measured using a luminescence characterization system (Otsuka Electronics: MCPD-9800).

The X-ray diffractions of samples (A) and (B) are shown in Fig. 3. We found that Ga<sub>0.85</sub>In<sub>0.15</sub>N/GaN SLs were almost destroyed by thermal decomposition during the growth of n-GaN and n-Al<sub>0.03</sub>Ga<sub>0.97</sub>N at 1040 °C. At the same time, it included the metal phase of In (i.e., In droplet) dissociated from GaInN. We confirmed the existence of the In droplet layer in sample (A) from the (101) diffraction. This result shows that the Ga<sub>0.85</sub>In<sub>0.15</sub>N/GaN SL removing layer was completely transformed to In droplets during growth.

We characterized the transmittances of samples (A) and (B), as shown in Fig. 4. Sample (A) exhibits absorption in a wide range from violet to infrared wavelengths. Regarding the X-ray diffraction results, it was found that light absorption was due to the In droplet layer. Insets of Fig. 4 show images of the as-grown samples. In particular, sample (A) had already turned black. It was found that the In droplet layer can absorb visible light by surface plasmon resonance. This causes selective absorption of visible or infrared pulse laser light by the In droplet layer, because neither the GaN substrate nor the LED structure can absorb visible and infrared light. In this way, we found that removing of the GaN substrate technique was possible using a visible or infrared pulse laser. Then, there is no worry about the degradation of

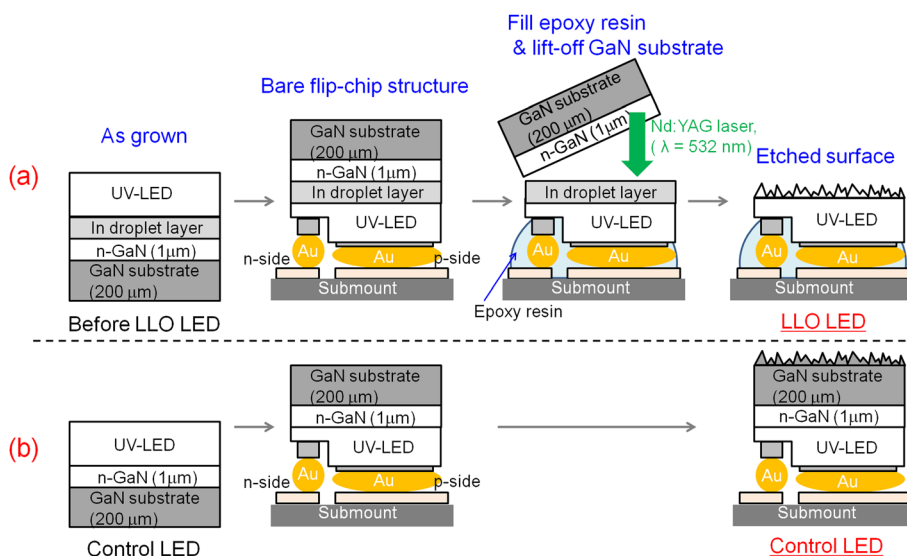


FIG. 2. Schematic view of fabrication steps of (a) LLO and (b) control LEDs.

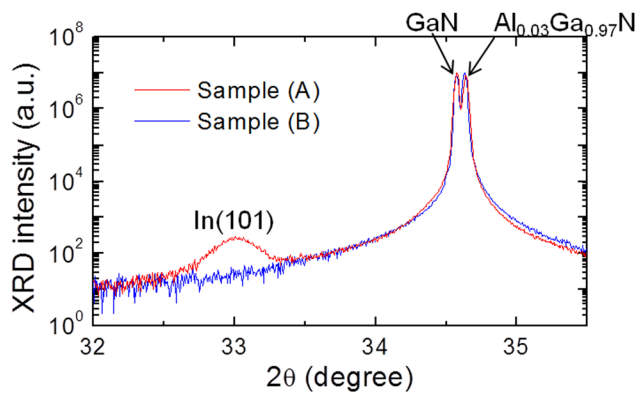


FIG. 3. XRD of samples (A) and (B) with and without removing layer, respectively. The diffracted X-ray at the (101) plane indicated the metal phase of In in sample (A) with the removing layer.

the quality of the MQW active layer owing to the absorption of high-energy laser light.

We observed threading dislocation densities of samples (A) and (B) by CL. From the CL results, threading dislocation densities of samples (A) and (B) were estimated to be  $5 \times 10^7$  and  $3 \times 10^6 \text{ cm}^{-2}$ , respectively. We found that sample (A) had an increased threading dislocation density. We consider that after the decomposition of  $\text{Ga}_{0.85}\text{In}_{0.15}\text{N}/\text{GaN}$  SLs during growth, the threading dislocations were induced via the generation of misfit dislocation in the interface between n-GaN and the In droplet layer. The LLO LEDs predict that the internal quantum efficiency will be degraded compared with that of the control LEDs. However, the dislocation density was sufficiently low compared with that of conventional GaN grown on a sapphire substrate, the typical value is  $2\text{--}5 \times 10^8 \text{ cm}^{-2}$ . The quality of sample (A) was sufficient for use in high-performance UV-A LEDs.

The EL spectra of LLO and control LEDs without and with the GaN substrate, respectively, are shown in Fig. 5. The LLO LED indicated strong EL emission compared with that of the control LED. The LLO LED showed enhanced light output power even though a decrease in internal

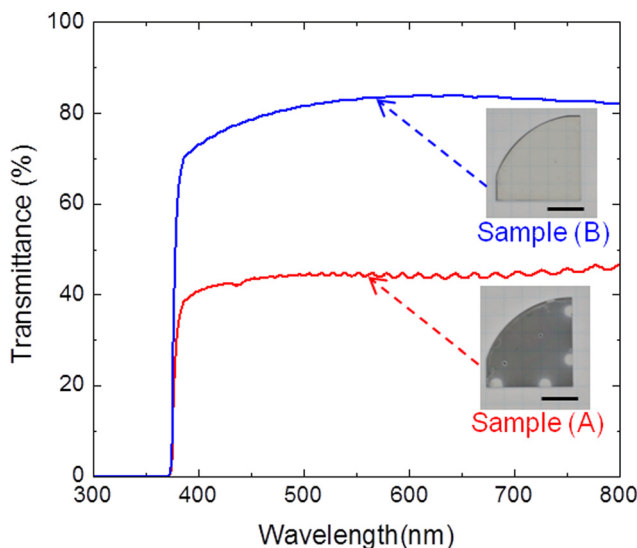


FIG. 4. Transmittance as a function of wavelength. Sample (A) absorbs light in the entire visible range. Insets show images of as-grown samples of different colors. Scale bars are 1 cm.

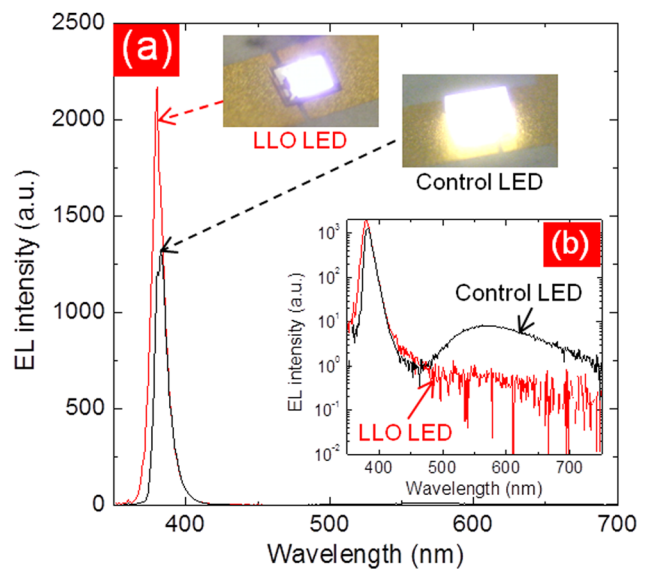


FIG. 5. (a) EL spectra of each LED at 50 mA. (b) Inset EL spectra are on the log scale. Insets shown are EL of LLO and control LEDs.

quantum efficiency due to the degradation of the crystalline quality of the underlying n-AlGaIn epilayer was predicted. We also found that the EL peak emission of LLO LED was shifted to a short wavelength from 383 to 380 nm. We consider that the EL intensity and wavelength were different because they were cut off at a shorter wavelength by the GaN substrate, which acted as an absorber. After LLO process, the yellow luminescence of the deep level recombination can be reduced.<sup>15,16</sup> The  $I$ - $I$  and  $V$ - $I$  characteristics of UV LEDs are shown in Fig. 6. The light output power of the LLO LED can be enhanced 1.7-fold at 50 mA compared with that of the control LED.  $V$ - $I$  characterizations were the same because the highly Si-doped n- $\text{Al}_{0.03}\text{Ga}_{0.97}\text{N}$  layer is an extremely low-resistance material.<sup>23</sup> These results confirm that we have realized the LLO of the GaN substrate. Our LLO technique can overcome the absorption loss due to the GaN substrate. It is very promising for improving the external quantum efficiency of UV-A LEDs.

We achieved the removing of the GaN substrate from the UV-A LED structure by a LLO technique.  $\text{Ga}_{0.85}\text{In}_{0.15}\text{N}/\text{GaN}$  SLs were transformed into an In droplet layer by the

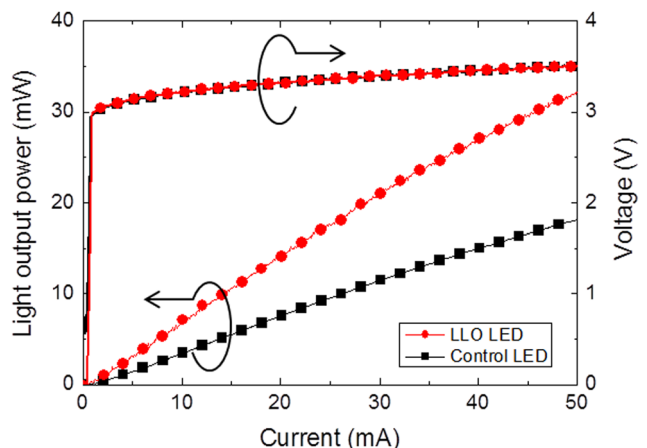


FIG. 6.  $I$ - $I$  and  $V$ - $I$  characteristics of LLO and control LEDs.

thermal decomposition of GaInN during growth. It was able to absorb light in the visible range, which enabled the use of the visible pulse laser. After the lift-off process, the UV-A LEDs show EL intensity enhanced by 1.7-fold. Therefore, it is very effective to improve light extraction by reducing the light absorption loss. Therefore, UV-A LEDs can also be grown on the GaN substrate by the LLO technique.

This work was supported by the Program for the Strategic Research Foundation at Private Universities, 2012–2016.

- <sup>1</sup>H. Amano, M. Kito, K. Hiramatsu, and I. Akasaki, *Jpn. J. Appl. Phys., Part 2* **28**, L2112 (1989).
- <sup>2</sup>S. Nakamura, M. Senoh, N. Iwasa, S. Nagahama, T. Yamada, and T. Mukai, *Jpn. J. Appl. Phys., Part 2* **34**, L1332 (1995).
- <sup>3</sup>S. Watanabe, N. Yamada, M. Nagashima, Y. Ueki, C. Sasaki, Y. Yamada, T. Taguchi, K. Tadatomo, H. Okagawa, and H. Kudo, *Appl. Phys. Lett.* **83**, 4906 (2003).
- <sup>4</sup>O. B. Shchekin, J. E. Epler, T. A. Trottier, T. Margalith, D. A. Steigerwald, M. O. Holcomb, P. S. Martin, and M. R. Krames, *Appl. Phys. Lett.* **89**, 071109 (2006).
- <sup>5</sup>Y. Narukawa, M. Ichikawa, D. Sanga, M. Sano, and T. Mukai, *J. Phys. D: Appl. Phys.* **43**, 354002 (2010).
- <sup>6</sup>J. Han, M. H. Crawford, R. J. Shul, J. J. Figiel, M. Banas, L. Zhang, Y. K. Song, H. Zhou, and A. V. Nurmikko, *Appl. Phys. Lett.* **73**, 1688 (1998).
- <sup>7</sup>T. Nishida, N. Kobayashi, and T. Ban, *Appl. Phys. Lett.* **82**, 1 (2003).
- <sup>8</sup>M. L. Nakarmi, K. H. Kim, M. Khizar, Z. Y. Fan, J. Y. Lin, and H. X. Jianga, *Appl. Phys. Lett.* **86**, 092108 (2005).
- <sup>9</sup>S.-R. Jeon, Z. Ren, G. Cui, J. Su, M. Gherasimova, J. Han, H.-K. Cho, and L. Zhou, *Appl. Phys. Lett.* **86**, 082107 (2005).
- <sup>10</sup>K. Takehara, K. Takeda, S. Ito, H. Aoshima, M. Iwaya, T. Takeuchi, S. Kamiyama, I. Akasaki, and H. Amano, *Jpn. J. Appl. Phys., Part 1* **51**, 042101 (2012).
- <sup>11</sup>D. Morita, M. Sano, M. Yamamoto, M. Nonaka, K. Yasutomo, K. Akaishi, S. Nagahama, and T. Mukai, *Phys. Status Solidi A* **200**(1), 114–117 (2003).
- <sup>12</sup>T. Nishida, H. Saito, and N. Kobayashi, *Appl. Phys. Lett.* **79**, 711 (2001).
- <sup>13</sup>A. Yasan, R. McClintock, K. Mayes, S. R. Darvish, H. Zhang, P. Kung, M. Razeghia, S. K. Lee, and J. Y. Han, *Appl. Phys. Lett.* **81**, 2151 (2002).
- <sup>14</sup>T. Fujii, Y. Gao, R. Sharma, E. L. Hu, S. P. DenBaars, and S. Nakamura, *Appl. Phys. Lett.* **84**, 855 (2004).
- <sup>15</sup>E. R. Glaser, T. A. Kennedy, H. C. Crookham, J. A. Freitas, Jr., M. Asif Khan, D. T. Olson, and J. N. Kuznia, *Appl. Phys. Lett.* **63**, 2673 (1993).
- <sup>16</sup>E. R. Glaser, T. A. Kennedy, K. Doverspike, L. B. Rowland, D. K. Gaskill, J. A. Freitas, Jr., M. Asif Khan, D. T. Olson, J. N. Kuznia, and D. K. Wickenden, *Phys. Rev. B* **51**, 13326 (1995).
- <sup>17</sup>W. S. Wong, T. Sands, N. W. Cheung, M. Kneissl, D. P. Bour, P. Mei, L. T. Romano, and N. M. Johnson, *Appl. Phys. Lett.* **72**, 599 (1998).
- <sup>18</sup>P. R. Tavernier and D. R. Clarke, *J. Appl. Phys.* **89**, 1527 (2001).
- <sup>19</sup>C.-F. Chu, C.-C. Yu, H.-C. Cheng, C.-F. Lin, and S.-C. Wang, *Jpn. J. Appl. Phys., Part 2* **42**, L147 (2003).
- <sup>20</sup>H. Aoshima, K. Takeda, K. Takehara, S. Ito, M. Mori, M. Iwaya, T. Takeuchi, S. Kamiyama, I. Akasaki, and H. Amano, *Phys. Status Solidi C* **9**(3–4), 753–756 (2012).
- <sup>21</sup>G. W. Ford and W. H. Weber, *Phys. Rep.* **113**, 195 (1984).
- <sup>22</sup>J. H. Rice, R. A. Oliver, J. W. Robinson, J. D. Smith, R. A. Taylor, G. A. D. Briggs, M. J. Kappers, C. J. Humphreys, and S. Yasin, *Physica E* **21**, 546 (2004).
- <sup>23</sup>T. Sugiyama, D. Iida, T. Yasuda, M. Iwaya, T. Takeuchi, S. Kamiyama, and I. Akasaki, *Appl. Phys. Express.* **6**, 121002 (2013).

## Internal quantum efficiency enhancement of GaInN/GaN quantum-well structures using Ag nanoparticles

Daisuke Iida, Ahmed Fadil<sup>1</sup>, Yuntian Chen<sup>1</sup>, Yiyu Ou, Oleksii Kopylov, Motoaki Iwaya, Tetsuya Takeuchi, Satoshi Kamiyama, Isamu Akasaki, and Haiyan Ou

Citation: *AIP Advances* **5**, 097169 (2015); doi: 10.1063/1.4931948

View online: <http://dx.doi.org/10.1063/1.4931948>

View Table of Contents: <http://aip.scitation.org/toc/adv/5/9>

Published by the [American Institute of Physics](#)

---

---

# HAVE YOU HEARD?

Employers hiring scientists and  
engineers trust

**PHYSICS TODAY | JOBS**

[www.physicstoday.org/jobs](http://www.physicstoday.org/jobs)



## Internal quantum efficiency enhancement of GaInN/GaN quantum-well structures using Ag nanoparticles

Daisuke Iida,<sup>1,2,3</sup> Ahmed Fadil,<sup>2,a</sup> Yuntian Chen,<sup>2,4,b</sup> Yiyu Ou,<sup>2</sup>  
Oleksii Kopylov,<sup>2</sup> Motoaki Iwaya,<sup>3</sup> Tetsuya Takeuchi,<sup>3</sup> Satoshi Kamiyama,<sup>3</sup>  
Isamu Akasaki,<sup>3,5</sup> and Haiyan Ou<sup>2</sup>

<sup>1</sup>Department of Applied Physics, Tokyo University of Science,  
Katsushika, 125-8585 Tokyo, Japan

<sup>2</sup>Department of Photonics Engineering, Technical University of Denmark,  
2800 Lyngby, Denmark

<sup>3</sup>Faculty of Science and Technology, Meijo University, 1-501 Shiogamaguchi Tempaku,  
468-8502 Nagoya, Japan

<sup>4</sup>School of Optical and Electronic Information, Huazhong University of Science  
and Technology, 430074 Wuhan, China

<sup>5</sup>Akasaka Research Center, Nagoya University, Furo-cho Chikusa, 464-8603 Nagoya, Japan

(Received 22 May 2015; accepted 16 September 2015; published online 24 September 2015)

We report internal quantum efficiency enhancement of thin p-GaN green quantum-well structure using self-assembled Ag nanoparticles. Temperature dependent photoluminescence measurements are conducted to determine the internal quantum efficiency. The impact of excitation power density on the enhancement factor is investigated. We obtain an internal quantum efficiency enhancement by a factor of 2.3 at 756 W/cm<sup>2</sup>, and a factor of 8.1 at 1 W/cm<sup>2</sup>. A Purcell enhancement up to a factor of 26 is estimated by fitting the experimental results to a theoretical model for the efficiency enhancement factor. © 2015 Author(s). All article content, except where otherwise noted, is licensed under a Creative Commons Attribution 3.0 Unported License. [<http://dx.doi.org/10.1063/1.4931948>]

### I. INTRODUCTION

An efficient high-brightness solid-state lighting solution is of central industrial and social relevance in terms of reducing energy consumption and environmental benefits. The GaInN-material based light-emitting diodes (LEDs) technology appears to be an excellent candidate in solid-state lighting platform. Improving the LEDs performance within the green gap is challenging, and is also a major focus in the research efforts of GaInN-based LEDs. The LEDs grown on c-plane sapphire substrate have a large piezoelectric field in the quantum well (QW) due to quantum confined Stark effect (QCSE).<sup>1,2</sup> The large piezoelectric field is one of the most critical factors limiting the internal quantum efficiency (IQE) in the green gap. In order to improve GaInN-based LEDs both enhancement of the IQE and development of an efficient light extraction techniques to ‘drag’ the photons out of the LED crystal are required.<sup>3,4</sup> It is well known that spontaneous emission, including the recombination rate and the emission profile, can be modified by the nearby photonic environments.<sup>5,6</sup> The key concept underlying plasmon enhanced light emission is the local density of optical states (LDOS), which accounts for the available number of modes per frequency at a certain position. Recent progress in nanophotonics and nanotechnology opens possibilities of engineering LDOS at nanometer scale and at highly advanced levels to achieve directional emission or enhanced light-matter interaction.<sup>7-14</sup> Such a nanophotonic approach has been applied to light emitting devices.<sup>15-22,24,25</sup> The rationale behind is that the transfer of energy from carriers in GaInN QW into localized optical plasmon supported by the metallic nanostructures will create an

<sup>a</sup>afad@fotonik.dtu.dk

<sup>b</sup>yuntian@hust.edu.cn

additional light emission channel called plasmonic channel. With a thin p-GaN layer plasmonic channel will dominate the spontaneous emission and significantly enhance the radiative recombination rate of light sources. As the rate of emitted photons is enhanced compared to the undesired non-radiative channels, which are unaffected by the plasmonic structures, we expect to overcome the challenge on IQE. Subsequently, the radiation captured by the plasmonic structure needs to be scattered into desired output angles by designed grating effects from periodic plasmonic structures or by exploiting random scattering from disordered plasmonic structures. Indeed, the IQE measurement of blue emission GaInN QWs indicates that significant plasmonic coupling can be achieved at approximately 6.8-folds when the distance of the active layer to the metals ( $D$ ) is very small, i.e.  $\sim 10$  nm.<sup>3</sup> The blue LEDs having a small  $D$  of 30 nm is reported to have enhanced optical output power by 38% using the nanoparticles embedded in p-GaN.<sup>17</sup> For a larger  $D$  of approximately 70 nm, the green emission output power based on the plasmonic coupling of the metals with active layer has been improved by approximately 90-220% with contribution from both IQE and light extraction efficiency.<sup>16</sup> It is also very interesting to note that the photoluminescence (PL) intensity of the green GaInN QW has been improved by a factor of 4.8 using periodic nanocylinders with a 5 nm spacing layer.<sup>20</sup> It has been shown that for very large  $D \sim 200$  nm, a 26% improvement of the optical output power due to enhanced light scattering can be achieved without benefits from plasmon enhanced IQE.<sup>19</sup> Despite the aforementioned evidences on improved PL or electroluminescence (EL) emission, to the best of our knowledge, there is no quantitative study of how original IQE affects the enhancement obtainable through LSP-coupling between metal and emitter.

In this paper, we experimentally demonstrated the IQE enhancement of plasmon-based LED epi-structures by depositing metallic nanoparticles on top of the GaN crystal using a low-cost solution. The IQE is estimated from low temperature PL measurements. We perform excitation power density dependent measurements, which show the IQE can be substantially enhanced with properly selected nanometallic structure. The paper is organized as follows: In section II, we outline the fabrication procedures of our LED structures and the metallic nanoparticles, and demonstrate the measurement setup. In section III, we present and discuss our experimental results of PL and IQE enhancement. Finally, section IV concludes the paper.

## II. METHODS

LED structures were grown by metalorganic vapor phase epitaxy (MOVPE) in a horizontal flow reactor. C-plane sapphire substrates were thermally cleaned in a  $H_2$  ambient at approximately 1050 °C. After that, approximately 20-nm-thick low temperature (LT)-GaN buffer layer was deposited at 535 °C.<sup>23</sup> After annealing process a 2- $\mu$ m-thick GaN layer was grown at 1050 °C on the annealed LT-GaN nucleation layer. The final LED structure consisted of a 2- $\mu$ m-thick n-GaN:Si layer, a 10 periods of GaInN:Si (3 nm) / GaN:Si (2 nm) superlattice layer, a 5 periods of GaN:Si (11.5 nm) / GaInN (2 nm) QWs active region covered with 5-nm-thick GaN capping layer, a 20-nm-thick p-GaN:Mg, and a 5-nm-thick  $p^+$ -GaN:Mg p-contact layer. The distance of last QW to LED surface was 30 nm. This LED structure had an optimized thin p-GaN layer for coupling of localized surface plasmon (LSP) to QWs, which is expected to enhance the light emission of QWs with LSP coupling. Self-assembled Ag NPs were fabricated by electron-beam evaporation and thermal annealing. Various-thickness Ag thin films were deposited on top of the LED surface. The samples were annealed at 200 °C for 30 min in  $N_2$  atmosphere. Ag thin film was transformed into random nanostructures during thermal annealing process.

The observations of Ag NPs on top of the LED surfaces were conducted by scanning electron microscope (SEM). Excitation power density dependent PL measurement was carried out to characterize the emission of GaInN/GaN QWs grown on c-plane sapphire substrate. The PL measurement setup consisted of a continuous wave GaInN-based diode laser and a spectrometer. The excitation laser operated at 405 nm and the output power density could be tuned from 1 to 756 W/cm<sup>2</sup>. PL measurement was carried out with excitation and collection via the backside of the polished sapphire substrate. The extinction spectrum of Ag NPs was extracted from a transmittance spectrum measurement. Transmittance was measured from the sapphire to the top surface p-GaN side, while

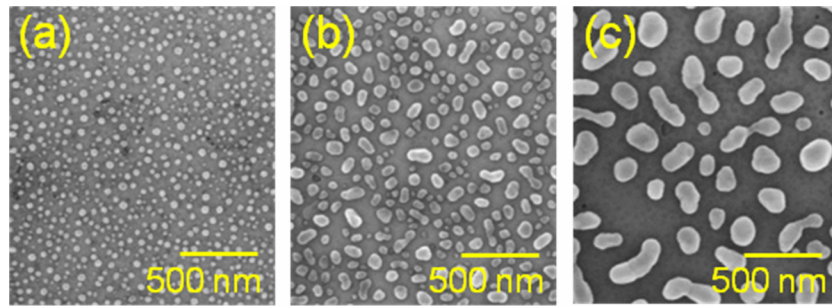


FIG. 1. SEM images of Ag NPs on LED surface after thermal annealing process. Ag deposition thicknesses are (a) 4 nm (sample A), (b) 9.5 nm (sample B) and (c) 17 nm (sample C), respectively.

reflectance was measured from the sapphire side. The light source used for the measurements was a white-light Xenon lamp.

### III. RESULTS AND DISCUSSIONS

#### A. Self-assembled Ag NPs

The Ag NPs were fabricated using a low-cost approach, i.e. by thermal annealing of Ag thin films on the surface of LED structure with designed thin p-GaN layers. Fig. 1 shows plan-view SEM images of Ag NPs with different Ag deposition thickness. Samples A, B and C are Ag films with a thickness of 4, 9.5 and 17 nm, respectively, which are transformed into random NPs after thermal annealing on top of the LED p-GaN surface. As the Ag film thickness increases, the size of Ag NPs becomes larger, while the density of Ag NPs decreases. Ag NPs had a tendency of becoming more irregular-shaped and with an increased size distribution as the thickness was increased.

Fig. 2 shows the extinction spectra of the three samples. PL emission spectrum of GaInN/GaN 5QWs LED without Ag NPs constituting a reference sample is also shown in Fig. 2. Considering the extinction spectra, each sample shows a characteristic peak. For sample A the extinction peak is located at 482 nm, and the peak position of sample B is 540 nm, while the main peak position of sample C is 672 nm. In the case of sample C a smaller peak is visible in the extinction spectrum at 410 nm. We attribute these peaks to the dipolar resonances in the NPs, hence for sample C a higher order mode is present at short wavelengths.<sup>20</sup> It is seen that the peaks red-shift with increasing average particle size, while the full width at half maximum (FWHM) increases. These self-assembled Ag NPs have different sizes and spacing, and this will in principle give rise to an inhomogeneous broadening of the LSP resonances from the distribution of the particle sizes.

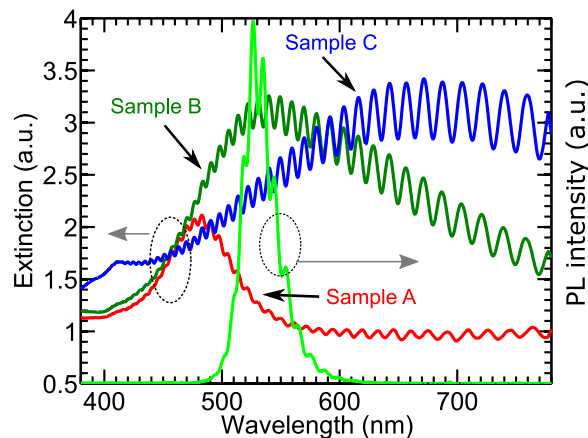


FIG. 2. Extinction spectra for samples A, B and C. Reference PL spectrum is shown for comparison.

Sample A has the most regular-shaped NPs with a small spread in size distribution, and is in effect showing a resonance peak with the smallest FWHM. Resonance peak of sample C seems to be located at around 700 nm, but has a large FWHM in contrast, the tail of which is covering the QWs emission spectrum. Sample B had a better spectral overlap with the QWs emission than the other Ag NPs structures. It is therefore expected that LSP coupling with QWs of sample B can be the most pronounced. The resonance peaks shift towards longer wavelengths as Ag NP size increases due to the red-shift of the dipolar resonance for larger diameter, as long as the dipole approximation is valid.<sup>9</sup>

## B. PL measurements

We investigated PL enhancement of GaInN/GaN QWs with various Ag NPs. For PL measurements the sample excitation and emission collection were done from the backside of the polished sapphire substrate, and the spectra measured at room temperature are shown in Fig. 3. It is seen that the PL emission of sample A has remained nearly unchanged compared to the bare LED emission, while PL enhancements are observed for sample B and C. Increasing the Ag thickness, hence also the average particle size, results in an increase in PL enhancement. The integrated PL enhancements of samples A-C relative the reference sample are 1.25, 2.59 and 6.02, respectively.

Other mechanisms could exist behind the PL enhancement in addition to LSP-QW coupling. One is an enhanced reflection from the top p-GaN surface of either the excitation laser signal, and/or the emission from the QWs, both of which would give an enhanced signal at the detector. The reflectance spectra (not shown) reveal that the Ag NPs formed on the p-GaN surface do not result in an increased reflection compared to the as-grown surface at the QWs emission wavelength. At the excitation wavelength the reflection is enhanced by 10 %, which results in an insignificant enhancement factor that is already taken into account in Fig. 3.<sup>20</sup> These factors are therefore excluded.

## C. Temperature dependent PL

We proceed to study the improvement of the IQE based on temperature dependent PL. We analyzed the IQE of the LEDs with various Ag NPs by measuring PL intensity versus temperature, as shown in Fig. 4. Under the assumption that non-radiative recombinations are inactivated at cryogenic temperatures, one can retrieve the IQE from the temperature dependence of integrated PL intensity  $I$ .<sup>26</sup> The IQE is defined by normalizing the integrated PL intensity to 1 at 20 K, i.e., assuming the IQE to be 100 %. Thus, the IQE at room temperature will be defined

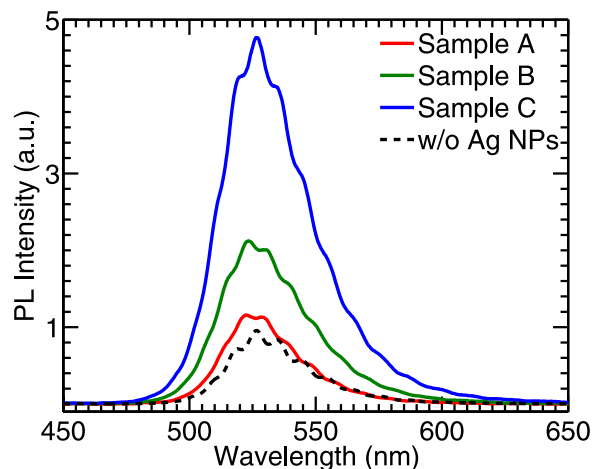


FIG. 3. Room temperature PL intensity of GaInN/GaN 5QWs with Ag NPs on top. Excitation power density is  $756 \text{ W/cm}^2$ , and emission peak is around 530 nm.

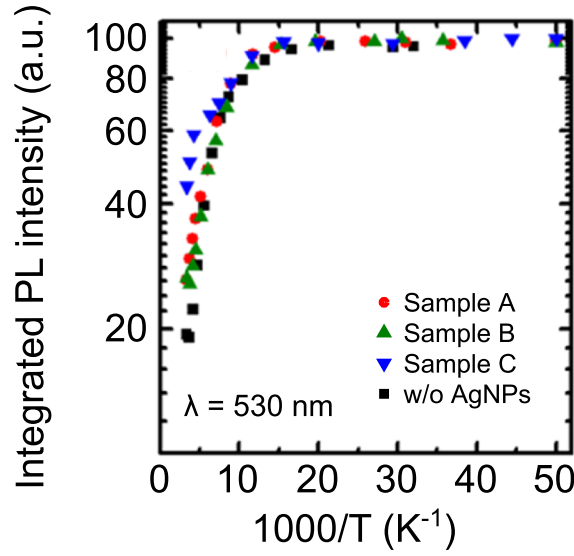


FIG. 4. Temperature dependence of integrated PL for estimating IQE. PL intensity has been normalized to 100 at the 20 K value.

as  $\text{IQE} = I_{295\text{K}}/I_{20\text{K}}$ . As the temperature increases, PL intensity degrades due to the activation of non-radiative recombination process. The IQE for the 530 nm emission was found to be 19.3 % for the reference sample. Regarding the Ag NP coated samples, the expression for the IQE will be modified due to LSP-coupling,  $\eta = (k_{\text{rad}} + k_{\text{SP}}\eta_{\text{LSP}})/(k_{\text{rad}} + k_{\text{nr}} + k_{\text{SP}})$ , where  $k_{\text{rad}}$ ,  $k_{\text{nr}}$  and  $k_{\text{SP}}$  are the radiative, non-radiative and LSP coupling rates, and  $\eta_{\text{LSP}}$  is the radiative coupling efficiency of the LSP mode. It has been demonstrated that  $k_{\text{SP}}$  and  $k_{\text{nr}}$  follow similar trends as a function of temperature, and it is therefore reasonable to estimate  $k_{\text{SP}} \sim 0$  at low temperatures and assume that IQE is approximately 100 % for the Ag NP coated samples.<sup>27</sup> We can then estimate the IQE of samples A-C the same way as the reference, and obtain 26.1 %, 26.4 % and 44.2 %, for samples A, B and C, respectively, with 756 W/cm<sup>2</sup> of excitation power density. Table I summarizes the IQE enhancement factors.

We note that the IQE of A is almost equal to that of B, and higher than the reference sample IQE, contrary to what was observed in the PL measurements of Fig. 3 where sample B had a considerably higher PL intensity. The integrated PL intensity is proportional to the external quantum efficiency, and as such it includes the effects of both IQE and light extraction efficiency (LEE). The observed difference between the integrated PL and IQE enhancement factor suggests a modified LEE for samples A-C. The IQE enhancement of sample A is higher than its integrated PL enhancement which indicates a degraded LEE. As for samples B and C is it seen that the integrated PL intensity has a higher enhancement than the IQE. Assuming the integrated PL intensity is proportional to the external quantum efficiency (EQE), the LEE enhancement can be estimated through the ratio between integrated PL enhancement and IQE enhancement. This follows since the integrated PL enhancement can be written as  $I_{\text{Ag}}/I_{\text{ref}} = \text{LEE}_{\text{Ag}}/\text{LEE}_{\text{ref}} \times \text{IQE}_{\text{Ag}}/\text{IQE}_{\text{ref}}$ . The LEE

TABLE I. Summary of enhancement parameters. Also given is the LSP radiative efficiency and Purcell factor obtained from power density variation and the relation between IQE enhancement and initial IQE.

Sample	Avg. size [nm]	Integrated PL enhancement <sup>a</sup>	Deduced LEE enhancement	High power IQE enhancement <sup>b</sup>	Low power IQE enhancement <sup>b</sup>	$\eta_{\text{LSP}}$	$F_P$
A	50	1.25	0.93	1.35	1.10	-	-
B	120	2.59	1.90	1.36	1.71	0.38	2.4
C	185	6.02	2.63	2.29	8.12	0.45	26.5

<sup>a</sup>At 295 K, and 756 W/cm<sup>2</sup> excitation power.

<sup>b</sup>High power: 756 W/cm<sup>2</sup>, Low power: 1 W/cm<sup>2</sup>.

ratios for samples A-C are listed in Table I, where sample B and C show an enhancement by a factor of 1.9 and 2.6, respectively, while A shows a reduced LEE based on these estimations.

The improved LEE due to Ag NPs is observed from sapphire-side emission, and is expected to be coming from the scattering of Ag NPs acting on the QW emission, i.e. the radiatively emitted light from the QWs that are not coupled to LSP modes. The emitted light from the QWs will see a modified interface when Ag NPs are included compared to a bare GaN-air interface, and this is expected to change the LEE.<sup>27</sup> In the following we will direct our attention to the IQE enhancement caused by the Ag NPs.

#### D. Excitation power density dependent IQE

We continue to study the excitation power density dependent IQE, which further supports the conclusion of improved IQE due to plasmonic coupling from temperature dependent PL measurement. In Fig. 5(a) we obtain the IQE at various excitation power densities for the emission point with 530 nm peak wavelength at 756 W/cm<sup>2</sup>. We first note the increasing IQE of the reference sample with increasing power densities. This effect is attributed to coulomb screening of the quantum-confined stark effect (QCSE) by the increasing carrier density.<sup>28</sup>

Fig. 5(b) shows the IQE enhancements with changing excitation power density. The trend for samples B and C is a decreasing enhancement with power density, while for sample A the opposite trend is observed, although weak. It is also noticed that the enhancements factors for sample A and B approach each other at high power density.

To understand the decrease in IQE enhancement, we need to keep in mind the increase in original (reference sample) IQE with increasing power density. The observed trend is that the lower the initial IQE is, the higher the enhancement factor is due to LSP coupling, and this is in agreement with the theoretical expectation of an inverse relation between IQE enhancement due to Ag NPs,  $K$ , and initial IQE without Ag NPs,  $\eta_i$ , which can be obtained as the ratio,<sup>29</sup>

$$K = \frac{(k_{rad} + k_{SP}\eta_{LSP}) / (k_{rad} + k_{SP} + k_{nrad})}{k_{rad} / (k_{rad} + k_{nrad})} = \frac{1 + F_p\eta_{LSP}}{1 + F_p\eta_i}, \quad (1)$$

where  $F_p = k_{SP}/k_{rad}$ , is the Purcell enhancement factor, and  $\eta_{LSP}$  is the radiative efficiency of the LSP-mode. This relation also implies that the requirement for IQE enhancement, i.e.  $K > 1$ , the LSP-mode radiative efficiency has been to be larger than the initial IQE,  $\eta_{LSP} > \eta_i$ . We plot the IQE enhancement factors of Fig. 5(b) as a function of the initial IQE in Fig. 6. The inverse relation is most clear for sample C, while sample B shows a similar but weak trend. For sample A, the opposite trend is observed. Using Eq. (1) we can roughly fit the data in Fig. 6 to obtain both the Purcell factor and the radiative efficiency of the Ag NPs. From these measurements, we estimate a Purcell enhancement factor of 26.5 and an LSP radiative efficiency of 45 % for the Ag NPs of sample C. The values obtained for sample B are 1.7 for the Purcell and 38 % for LSP radiative

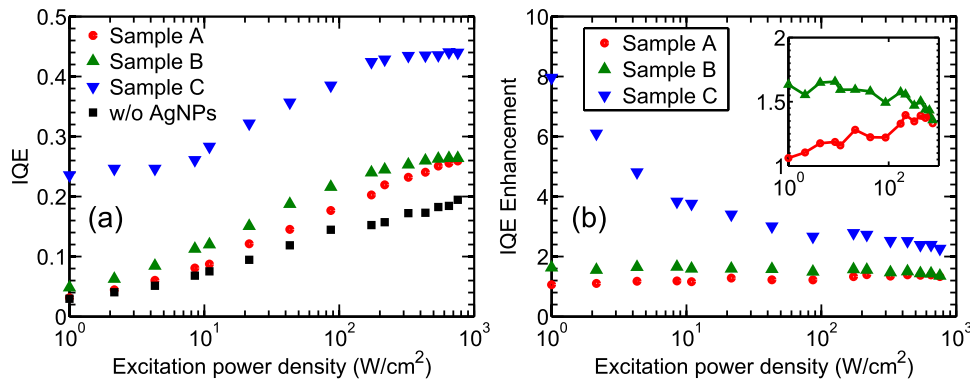


FIG. 5. (a) The estimated IQE and (b) IQE enhancement factor as a function of excitation power density at 295 K. Inset is the zoom in for sample A and B.

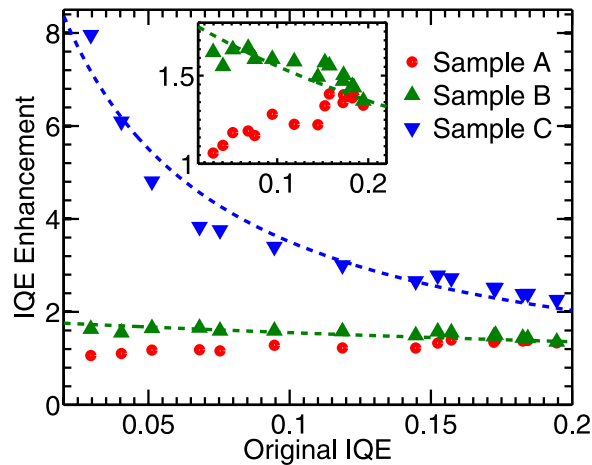


FIG. 6. IQE enhancement factor with initial IQE variation, calculated from the measurements of excitation power density variation. Dashed lines are fittings based on Eq. (1). Inset is the zoom-in at small IQE enhancement factor for sample A and B.

efficiency. The results are summarized in Table I. Due to the opposite trend observed for sample A, no parameters could be obtained. The difference in Purcell factors between sample B and C imply different LSP-QW coupling rates, where C has a higher coupling rate than B. Through numerical calculations we have previously investigated the decay rate enhancement in the plane of the QWs from Ag NPs, and have found that larger NPs exhibit larger enhancement factors for particle sizes up to about 200 nm in diameter.<sup>30</sup> The difference in average Ag NP size between sample B and C explains why the Purcell factor of C is larger than B.

As seen from the extinction spectra, the LSP resonance of sample A is blue-shifted relative to the emission peak, while those of B and C are red-shifted. When increasing the excitation power density, in addition to the increase in IQE, the GaInN/GaN QWs peak emission wavelength is blue-shifted due to the screening piezoelectric field by free-carriers.<sup>31,32</sup> For the reference sample the emission peak around 528 nm is red-shifted to 537 nm when the excitation power is decreased to 1 mW/cm<sup>2</sup>. Such a red-shift with decreasing excitation power is also present for samples A-C. For sample A this implies an emission peak shift towards the LSP resonance. As such, two competing mechanisms are present in the case of sample A when increasing the excitation power density; the first is the emission peak blue-shift, resulting in a better overlap with the LSP-mode resonance, and the second is an increase in original IQE from the increased carrier density, resulting in a reduced IQE enhancement factor from LSP-coupling. The increasing enhancement factor of sample A as seen from the inset of Fig. 6 when excitation power density is increased can therefore be expected to be the result of increasingly better spectral overlap between the QWs emission spectrum and the LSP-mode. The extinction spectra for sample B and C are relatively broad (FWHM larger than 200 nm), hence this effect would be insignificant for B and C. However, the extinction FWHM of sample A is around 50 nm, therefore an emission peak shift of about 10 nm is expected to have an effect on the LSP-QW coupling.

We also note that despite having the best spectral overlap between sample B resonance peak and the emission wavelength, sample B does not have the highest PL or IQE enhancement. This can be understood by considering the absorption and scattering properties of the Ag NPs. These effects were previously investigated and it was found that the scattering to absorption ratio is an important characteristic when determining whether Ag NPs can provide efficiency enhancement.<sup>30</sup> The absorption in the NP is the loss channel for the LSP mode, and reducing these losses relative to the scattering can ensure a higher LSP mode radiative efficiency. Despite the matching of the extinction or resonance peak of sample B with the emission wavelength, sample C is expected to have a higher scattering capacity at the emission wavelength due to its larger average Ag NP sizes relative to sample B.<sup>30,33</sup> This is because the scattering-to-absorption ratio of sample C is higher than B due to the larger Ag NPs. As such sample C is scattering dominated and sample A is absorption dominated, while sample B is in between these limits. As the emission is channeled

into the LSP mode, the scattering efficiency of the NP is crucial when energy is to be re-emitted into free-space radiation. This agrees with the parameters obtained by the fittings of Eq. (1), where sample B and C had LSP radiative efficiencies of 38 % and 45 %, respectively.

#### IV. CONCLUSIONS

We investigated the LSP-QW coupling and resulting IQE enhancement of GaInN/GaN QW LEDs with self-assembled Ag NPs. It was found that the strong PL enhancement was partly due to LSP-QW coupling, and partly due to LEE enhancement, and separating these effects we noted an IQE improvement due to LSP-QW coupling at 530 nm emission from 19.4% to 44.1% using large sized Ag NPs (sample C) at 756 W/cm<sup>2</sup>. It was also found that the IQE enhancement is strongly dependent on excitation power density, yielding highest enhancement factors at low free carrier densities. Where an IQE enhancement by a factor of 2.3 was observed at 756 W/cm<sup>2</sup>, an enhancement factor of 8.1 was observed at 1 W/cm<sup>2</sup>. Our results confirm the inverse relation between the aforementioned quantities, and implicate that it is imperative to take the excitation power density into account when conducting PL measurements to investigate the enhancement due to LSP-coupling. We therefore establish quantitative enhancement factors depending on original IQE, and further confirm the fact that the lower the IQE of a light emitting structure is, the higher the enhancement factor will be due to surface plasmonics from Ag NPs.

#### ACKNOWLEDGMENTS

This work was partially supported by a Strategic Young Researcher Overseas Visits Program for Accelerating Brain Circulation from Japan Society for the Promotion of Science, the Program for the Strategic Research Foundation at Private Universities, 2012–2016, supported by the Ministry of Education, Culture, Sports, Science and Technology, and the Scandinavia-Japan Sasakawa Foundation. Y. Chen acknowledges financial support from the Danish Research Council for Technology and Production Sciences (Grant No. 10093787), and the National Natural Science Foundation of China (Grant No. 61405067). A. Fadil and H. Ou acknowledge the support of Innovation Fund Denmark (Grant No. 0603-00494B).

- <sup>1</sup> T. Takeuchi *et al.*, “Quantum-Confined Stark Effect due to Piezoelectric Fields in GaInN Strained Quantum Wells,” *Jpn. J. Appl. Phys.* **382**, L382, DOI:10.1143/JJAP.36.L382 (1997).
- <sup>2</sup> C. Wetzel, T. Takeuchi, H. Amano, and I. Akasaki, “Quantized states in Ga<sub>1-x</sub>In<sub>x</sub>N/ GaN heterostructures and the model of polarized homogeneous quantum wells,” *Phys. Rev. B* **62**, R13302-R13305, DOI:10.1103/PhysRevB.62.R13302 (2000).
- <sup>3</sup> K. Okamoto *et al.*, “Surface-plasmon-enhanced light emitters based on InGaN quantum wells,” *Nat. Mater.* **3**, 601–5, DOI:10.1038/nmat1198 (2004).
- <sup>4</sup> Y. Narukawa, M. Ichikawa, D. Sanga, M. Sano, and T. Mukai, “White light emitting diodes with super-high luminous efficacy,” *J. Phys. D: Appl. Phys.* **43**, 354002, DOI:10.1088/0022-3727/43/35/354002 (2010).
- <sup>5</sup> E. M. Purcell, “Spontaneous emission probabilities at radio frequencies,” *Phys. Rev.* **69**, 681 (1946).
- <sup>6</sup> E. Yablonoitch, “Inhibited Spontaneous Emission in Solid-State Physics and Electronics,” *Phys. Rev. Lett.* **58**, 2059-2062 (1987).
- <sup>7</sup> S. Kühn, U. Hakanson, L. Rogobete, and V. Sandoghdar, “Enhancement of Single-Molecule Fluorescence Using a Gold Nanoparticle as an Optical Nanoantenna,” *Phys. Rev. Lett.* **97**, 017402 (2006).
- <sup>8</sup> D. E. Chang, A. S. Sørensen, P. R. Hemmer, and M. D. Lukin, “Quantum Optics with Surface Plasmons,” *Phys. Rev. Lett.* **97**, 053002, DOI:10.1103/PhysRevLett.97.053002 (2006).
- <sup>9</sup> H. Mertens, A. F. Koenderink, and A. Polman, “Plasmon-enhanced luminescence near noble-metal nanospheres: Comparison of exact theory and an improved Gersten and Nitzan model,” *Phys. Rev. B* **76**, 115123, DOI:10.1103/PhysRevB.76.115123 (2007).
- <sup>10</sup> A. V. Akimov *et al.*, “Generation of single optical plasmons in metallic nanowires coupled to quantum dots,” *Nature* **450**, 402-406, DOI:10.1038/nature06230 (2007).
- <sup>11</sup> T. Kosako, Y. Kadoya, and H. F. Hofmann, “Directional control of light by a nano-optical Yagi–Uda antenna,” *Nature Photonics* **4**, 312-315, DOI:10.1038/nphoton.2010.34 (2010).
- <sup>12</sup> Y. Chen, N. Gregersen, T. R. Nielsen, J. Mørk, and P. Lodahl, “Spontaneous decay of a single quantum dot coupled to a metallic slot waveguide in the presence of leaky plasmonic modes,” *Opt. Express* **18**, 12489-12498, DOI:10.1364/OE.18.012489 (2010).
- <sup>13</sup> Y. Chen, T. R. Nielsen, N. Gregersen, P. Lodahl, and J. Mørk, “Finite-element modeling of spontaneous emission of a quantum emitter at nanoscale proximity to plasmonic waveguide,” *Phys. Rev. B* **81**, 125431, DOI:10.1103/PhysRevB.81.125431 (2010).

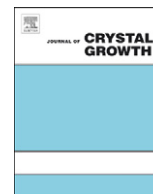
- <sup>14</sup> Y. Nishijima, L. Rosa, and S. Juodkakis, "Surface plasmon resonances in periodic and random patterns of gold nano-disks for broadband light harvesting," *Opt. Express* **20**, 11466-11477, DOI:10.1364/OE.20.011466 (2012).
- <sup>15</sup> J. Vučković, M. Lončar, and A. Scherer, "Surface plasmon enhanced light-emitting diode," *IEEE Journal of Quantum Electronics* **36**, 1131-1144, DOI:10.1109/3.880653 (2000).
- <sup>16</sup> D. M. Yeh, C. F. Huang, C. Y. Chen, Y. C. Lu, and C. C. Yang, "Localized surface plasmon-induced emission enhancement of a green light-emitting diode," *Nanotechnology* **19**, 345201, DOI:10.1088/0957-4484/19/34/345201 (2008).
- <sup>17</sup> C. Y. Cho *et al.*, "Surface plasmon-enhanced light-emitting diodes using silver nanoparticles embedded in p-GaN," *Nanotechnology* **21**, 205201, DOI:10.1088/0957-4484/21/20/205201 (2010).
- <sup>18</sup> C. C. Kao, Y. K. Su, C. L. Lin, and J. J. Chen, "Localized Surface Plasmon-Enhanced Nitride-Based Light-Emitting Diode With Ag Nanotriangle Array by Nanosphere Lithography," *IEEE Photonics Technology Letters* **22**, 984-986, DOI:10.1109/LPT.2010.2049013 (2010).
- <sup>19</sup> J. H. Sung *et al.*, "Enhancement of electroluminescence in GaN-based light-emitting diodes by metallic nanoparticles," *Appl. Phys. Lett.* **96**, 261105, DOI:10.1063/1.3457349 (2010).
- <sup>20</sup> J. Henson, J. DiMaria, E. Dimakis, T. D. Moustakas, and R. Paiella, "Plasmon-enhanced light emission based on lattice resonances of silver nanocylinder arrays," *Opt. Lett.* **37**, 79-81, DOI:10.1364/OL.37.000079 (2012).
- <sup>21</sup> G. Grzela *et al.*, "Nanowire antenna emission," *Nano Lett.* **12**, 5481-5486, DOI:10.1021/nl301907f (2012).
- <sup>22</sup> S. R. K. Rodriguez, S. Murai, M. A. Verschuuren, and J. Gómez Rivas, "Light-Emitting Waveguide-Plasmon Polaritons," *Phys. Rev. Lett.* **109**, 166803, DOI:10.1103/PhysRevLett.109.16680 (2012).
- <sup>23</sup> H. Amano, N. Sawaki, I. Akasaki, and Y. Toyoda, "Metalorganic vapor phase epitaxial growth of a high quality GaN film using an AlN buffer layer," *Appl. Phys. Lett.* **48**, 353, DOI:10.1063/1.96549 (1986).
- <sup>24</sup> J. Henson *et al.*, "Plasmon enhanced light emission from InGaN quantum wells via coupling to chemically synthesized silver nanoparticles," *Appl. Phys. Lett.* **95**, 151109, DOI:10.1063/1.3249579 (2009).
- <sup>25</sup> C.-W. Huang *et al.*, "Fabrication of surface metal nanoparticles and their induced surface plasmon coupling with subsurface InGaN/GaN quantum wells," *Nanotechnology* **22**, 475201, DOI:10.1088/0957-4484/22/47/475201 (2011).
- <sup>26</sup> S. Watanabe *et al.*, "Internal quantum efficiency of highly-efficient  $\text{In}_x\text{Ga}_{1-x}\text{N}$  based near ultraviolet light emitting diodes," *Appl. Phys. Lett.* **83**, 4906-4908, DOI:10.1063/1.1633672 (2003).
- <sup>27</sup> K. Okamoto *et al.*, "Surface plasmon enhanced spontaneous emission rate of InGaN/GaN quantum wells probed by time-resolved photoluminescence spectroscopy," *Appl. Phys. Lett.* **87**, 071102, DOI:10.1063/1.2010602 (2005).
- <sup>28</sup> Y. Lee *et al.*, "Study of the Excitation Power Dependent Internal Quantum Efficiency in InGaN / GaN LEDs Grown on Patterned Sapphire Substrate," *IEEE J. Sel. Top. Quantum Electron.* **15**, 1137-1143, DOI:10.1109/JSTQE.2009.2014967 (2009).
- <sup>29</sup> G. Sun, J. B. Khurgin, and R. Soref, "Plasmonic light-emission enhancement with isolated metal nanoparticles and their coupled arrays," *J. Opt. Soc. Am. B* **25**, 1748-1755, DOI:10.1364/JOSAB.25.001748 (2008).
- <sup>30</sup> A. Fadil *et al.*, "Surface plasmon coupling dynamics in InGaN/GaN quantum-well structures and radiative efficiency improvement," *Sci. Rep.* **4**, 1-7, DOI:10.1038/srep06392 (2014).
- <sup>31</sup> F. D. Sala, "Free-carrier screening of polarization fields in wurtzite GaN/InGaN laser structures," *Appl. Phys. Lett.* **74**, 2002-2004; DOI:10.1063/1.123727 (1999).
- <sup>32</sup> T. Kuroda and A. Tackeuchi, "Influence of free carrier screening on the luminescence energy shift and carrier lifetime of InGaN quantum wells," *J. Appl. Phys.* **92**, 3071-3074, DOI:10.1063/1.1502186 (2002).
- <sup>33</sup> S. Jiang *et al.*, "Resonant absorption and scattering suppression of localized surface plasmons in Ag particles on green LED," *Opt. Express* **21**, 12100-12110, DOI:10.1364/OE.21.012100 (2013).



ELSEVIER

Contents lists available at SciVerse ScienceDirect

## Journal of Crystal Growth

journal homepage: [www.elsevier.com/locate/jcrysgro](http://www.elsevier.com/locate/jcrysgro)

# MOVPE growth of nonpolar a-plane GaN with low oxygen contamination and specular surface on a freestanding GaN substrate

Yasuhiro Isobe<sup>a</sup>, Hiromichi Ikki<sup>a</sup>, Tatsuyuki Sakakibara<sup>a</sup>, Motoaki Iwaya<sup>a,\*</sup>, Tetsuya Takeuchi<sup>a</sup>, Satoshi Kamiyama<sup>a</sup>, Isamu Akasaki<sup>a,c</sup>, Takayuki Sugiyama<sup>b</sup>, Hiroshi Amano<sup>b,c</sup>, Mamoru Imade<sup>d</sup>, Yusuke Mori<sup>d</sup>

<sup>a</sup> Faculty of Science and Technology, Meijo University, Nagoya 468-8502, Japan

<sup>b</sup> Graduate School of Engineering, Nagoya University, Nagoya 464-8603, Japan

<sup>c</sup> Akasaki Research Center, Nagoya University, Nagoya 464-8603, Japan

<sup>d</sup> Graduate School of Engineering, Osaka University, Osaka 565-0871, Japan

## ARTICLE INFO

### Article history:

Received 22 December 2011

Received in revised form

19 April 2012

Accepted 20 April 2012

Communicated by C. Caneau

Available online 10 May 2012

### Keywords:

A1. Impurities

A3. Metalorganic vapor phase epitaxy

B2. Semiconducting gallium compounds

B3. High electron mobility transistors

## ABSTRACT

We investigated unintentionally doped nonpolar a- and m-plane GaN layers grown by metalorganic vapor phase epitaxy under several sets of conditions on freestanding a- and m-plane GaN substrates. Oxygen contamination in a-plane GaN is greatly reduced by increasing the V/III ratio during growth. As a result, a high-resistivity GaN buffer layer for an AlGaIn/GaN heterostructure field-effect transistor was realized.

© 2012 Elsevier B.V. All rights reserved.

## 1. Introduction

Nonpolar group III nitride semiconductors have attracted significant attention for use in optical and electronic device applications because of their lack of spontaneous and piezoelectric polarization fields [1]. Most III-nitride heterostructure field-effect transistor (HFET) devices are grown on c-plane [2–7] and have two possible operation modes; depression mode (D-mode) and enhancement mode (E-mode). D-mode HFETs are already practically applied in high-frequency circuits, whereas E-mode HFETs are expected to be used in future fail-safe circuits with low power dissipation.

In the case of HFET devices in the nonpolar GaN, the two-dimensional electron gas (2DEG) density in the channel layer can be controlled by intentional doping in the barrier layers [8]. Therefore, E-mode operation can be expected with a comparatively easy device fabrication process. However, there are several problems in the use of a nonpolar plane for HFET devices. First, heteroepitaxially grown nonpolar GaN films have a high density of dislocations and stacking faults [9,10]. This problem can be solved by performing growth on a

freestanding GaN substrate [11]. Second, nonpolar planes are chemically active. Therefore, contamination by oxygen is a serious problem [12]. Oxygen acts as a shallow donor in GaN [13], making the fabrication of HFETs with a high breakdown voltage difficult [14]. Fe-doping in polar and nonpolar HFETs has been used to compensate for the oxygen [15,16]. Although this is effective for reducing the leakage current, it tends to degrade the device performance through Fe segregation [17,18].

In this study, we investigated the residual oxygen contamination in nonpolar GaN by varying the growth temperature and V/III ratio during the growth of GaN by low-pressure metal organic vapor phase epitaxy (MOVPE). In particular, we characterized the surface morphology and oxygen contamination for each set of conditions.

## 2. Experimental details

All samples were grown by MOVPE. Trimethylgallium (TMGa), trimethylaluminum and ammonia (NH<sub>3</sub>) were used as the source gases. As the substrates, we used +c-, m- and a-plane freestanding GaN films grown by the Na-flux method [19]. The threading dislocation density and stacking fault density of these GaN substrates were determined to be less than  $5 \times 10^6 \text{ cm}^{-2}$  and less than  $2 \times 10^3 \text{ cm}^{-1}$ , respectively. These substrates were sliced with an

\* Corresponding author.

E-mail address: [iwaya@meijo-u.ac.jp](mailto:iwaya@meijo-u.ac.jp) (M. Iwaya).

offset angle of  $0 \pm 0.5^\circ$  and then subjected to chemical mechanical polishing. By using these freestanding GaN substrates, a GaN buffer with a specular surface morphology and good crystalline quality can be realized [20,21].

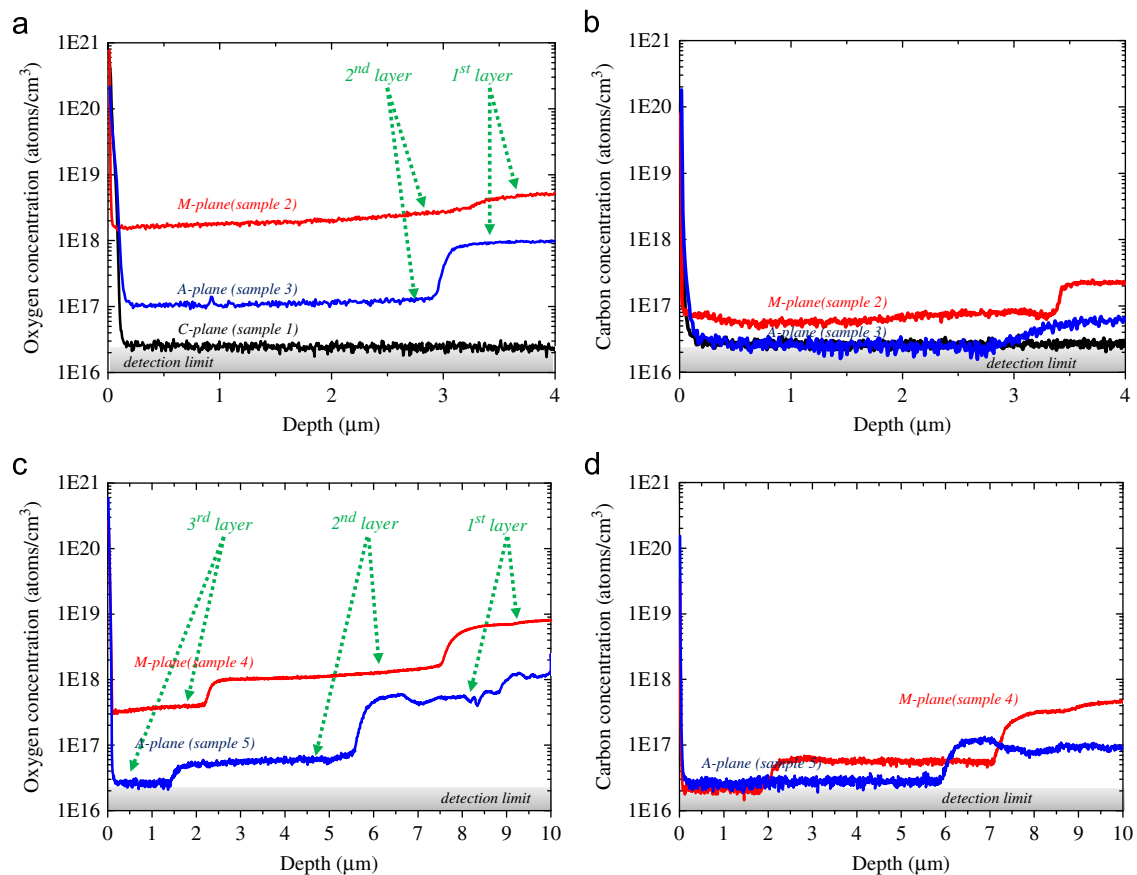
### 3. Results and discussion

Table 1 shows the growth conditions, the root mean square (RMS) surface roughness obtained by atomic force microscopy (AFM) and the oxygen concentration in the top GaN buffer obtained by secondary ion microprobe mass spectrometry (SIMS). Sample 1 was grown on a +c-plane GaN substrate. This sample was prepared as a reference for comparison. After 10 min thermal annealing at 1050 °C in NH<sub>3</sub> and hydrogen, an unintentionally doped GaN layer was grown. The growth conditions of GaN were as follows: V/III ratio: 1000, growth temperature: 1050 °C, reactor pressure: 200 hPa, TMGa flow rate: 150 μmol/min, NH<sub>3</sub> flow rate of 3 slpm. Samples 2 and 3 were grown on m- and a-plane Na-flux

GaN substrates, respectively. After 10 min thermal annealing at 1030 °C in NH<sub>3</sub> and hydrogen, an unintentionally doped GaN layer was grown. In the growth of a- and m-plane GaN, the surface morphology can be improved by performing growth under a low V/III ratio of as low as 200 and at a low growth temperature of 1030 °C [22,23]. The growth conditions for a- and m-plane GaN were as follows: V/III ratio: 250, growth temperature: 1030 °C, reactor pressure: 100 hPa. Next, an unintentionally doped GaN layer was grown at a V/III ratio of 1000, a growth temperature of 1030 °C and a reactor pressure of 100 hPa. Samples 4 and 5 were grown on m- and a-plane Na-flux GaN substrates, respectively. After 10 min thermal annealing at 1060 °C in NH<sub>3</sub> and hydrogen, an unintentionally doped GaN layer was grown. The growth temperature and pressure were fixed at 1060 °C and 100 hPa, respectively. The V/III ratio was increased from 250 to 1000 and then 2000. Note that the growth rate on each plane is different under the same growth conditions and that the total thickness is not exactly the same for all samples. For example, the growth rate of sample 1 (+c-plane) was approximately 3 μm/h. In a growth temperature of 1030 °C (sample 2 and

**Table 1**  
Growth conditions, surface roughness and oxygen concentration of epitaxial GaN.

	Plane	1st GaN layer		2nd GaN layer		3rd GaN layer		Surface roughness 5 × 5 μm <sup>2</sup> RMS (nm)	Epi-GaN of oxygen concentration (each top layer)
		Temperature (°C)	V/III ratio	Temperature (°C)	V/III ratio	Temperature (°C)	V/III ratio		
Sample 1	+c	1050	1000	–	–	–	–	0.29	Detection limit
Sample 2	m	1030	250	1030	1000	–	–	0.16	$2 \times 10^{18}$
Sample 3	a	1030	250	1030	1000	–	–	0.19	$1 \times 10^{17}$
Sample 4	m	1060	250	1060	1000	1060	2000	0.82	$3 \times 10^{17}$
Sample 5	a	1060	250	1060	1000	1060	2000	0.24	Detection limit



**Fig. 1.** Impurity profiles of epitaxial GaN layers measured by SIMS. (a, c) and (b, d) show the oxygen and carbon concentrations in samples 1–5, respectively.

3), although the growth rate was slightly higher for m-plane, it was almost same as c-plane. However, the growth rate of m-plane was approximately 15 to 30% higher than that of a-plane under high-temperature growth condition.

Fig. 1 shows the oxygen and carbon concentration profiles of each epitaxial GaN layer in samples 1–5. The detection limit of the oxygen and carbon concentrations in SIMS measurement is  $2 \times 10^{16} \text{ cm}^{-3}$ . According to Fig. 1(a) and (b), the oxygen and carbon concentrations in sample 1 (+c-plane) were below the detection limit. In contrast, samples 2 (m-plane) and 3 (a-plane) exhibit a relatively high oxygen density. The oxygen concentrations of samples 2 (m-plane) and 3 (a-plane) are  $2 \times 10^{18}$  and  $1 \times 10^{17} \text{ cm}^{-3}$ , respectively. Additionally, the carbon concentrations of samples 2 (m-plane) and 3 (a-plane) are  $7 \times 10^{17} \text{ cm}^{-3}$  and exceed the detection limit. Samples 1–3 are not significantly contaminated by carbon. The concentrations of silicon and hydrogen impurities are also below the detection limit at all samples.

To reduce the oxygen contamination, growth at a higher temperature is effective [12,24–26]. However, when m- and a-plane GaN were grown at a growth temperature of over  $1080^\circ\text{C}$ , the surface morphology deteriorated. Therefore, we fixed the growth temperature at  $1060^\circ\text{C}$  and changed the V/III ratio to control the oxygen concentration in samples 4 (m-plane) and 5 (a-plane). To decrease the oxygen concentration with increase in V/III ratio has already been reported [12], similarly, the SIMS profiles of these samples show that it was suppressed under these growth conditions. In particular, the top layer of sample 5 on a-plane GaN (V/III ratio: 2000) has an oxygen concentration below the detection limit. From these results, GaN is confirmed the difference in oxygen and carbon incorporation on a-, m- and c-plane GaN, differences in the incorporation of impurities with the crystal orientation have also been reported for other materials [27]. Similarly, we consider that the surface kinetics varies with the crystal orientation owing to the formation of dangling bonds.

Fig. 2 shows differential-interference-contrast microscopic (DIC) images and bird's-eye-view AFM images of each sample. Samples 1–3 exhibit specular surfaces in the DIC images. The AFM results also indicate atomically flat surfaces. The RMS surface roughness values of +c-, m- and a-plane GaN were 0.29, 0.16 and 0.19 nm, respectively. However, the surface morphologies of samples 4 and 5 were much rougher than those of samples 1–3. Such rough surfaces would cause difficulties in device fabrication processes.

Next, we grew a sample structure on a-plane GaN with the simultaneous aim of reducing the oxygen concentration and realizing a flat surface. The growth rate has been reported to affect the crystalline quality and surface morphology of c-plane GaN [28,29]. Fig. 3 shows a schematic view of the sample

structure. This sample structure was grown on a freestanding a-plane GaN substrate by a newly developed V/III ratio modulation process. After 10 min thermal annealing at  $1060^\circ\text{C}$  in  $\text{NH}_3$  and hydrogen, an unintentionally doped GaN layer was grown. The growth temperature and growth pressure were fixed at  $1060^\circ\text{C}$  and 100 hPa, respectively. In contrast, the V/III ratio was increased stepwise from 250 to 1000 and then 2000. The thicknesses of the films grown at each V/III ratio were set to 1, 1 and 2  $\mu\text{m}$ , respectively. The growth rate was 3  $\mu\text{m}/\text{h}$ . Then, a 1- $\mu\text{m}$ -thick GaN layer was grown at a low growth rate of approximately 1.0  $\mu\text{m}/\text{h}$  and a high V/III ratio of 3500, where the growth rate was controlled by adjusting the TMGa supply. A thick and highly resistive GaN buffer layer is indispensable even when using a GaN substrate owing to the n-type conductivity of the substrate and Si contamination at the interface between the GaN substrate and the first epilayer [30]. If the growth condition of the low-growth-rate layer only use, the time of the device fabrication is very long. It is very important to fabricate the device in a short time is important. So, we combined the growth conditions of conventional-growth-rate layer and the low-growth-rate layer. Subsequently, a 1-nm-thick unintentionally doped  $\text{Al}_{0.36}\text{Ga}_{0.64}\text{N}$  layer, a 3-nm-thick Si-doped  $\text{Al}_{0.36}\text{Ga}_{0.64}\text{N}$  layer and a 17-nm-thick unintentionally doped  $\text{Al}_{0.36}\text{Ga}_{0.64}\text{N}$  layer were grown,

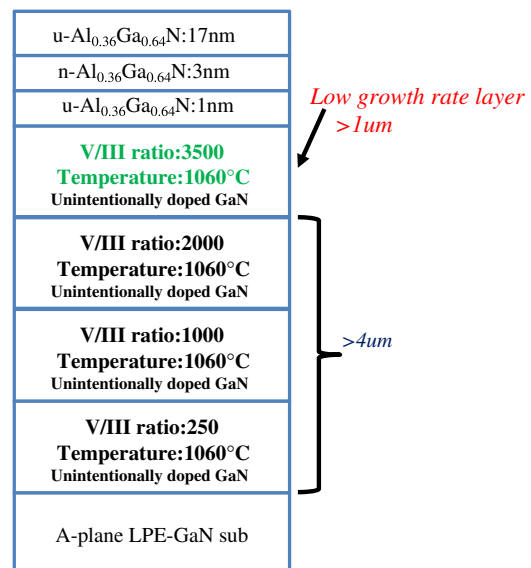


Fig. 3. Sample structure on freestanding a-plane GaN substrate obtained using newly developed V/III ratio modulation process.

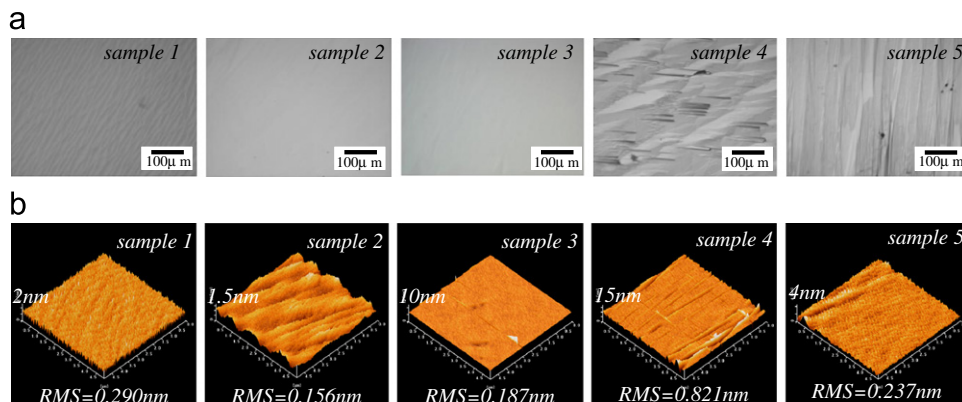
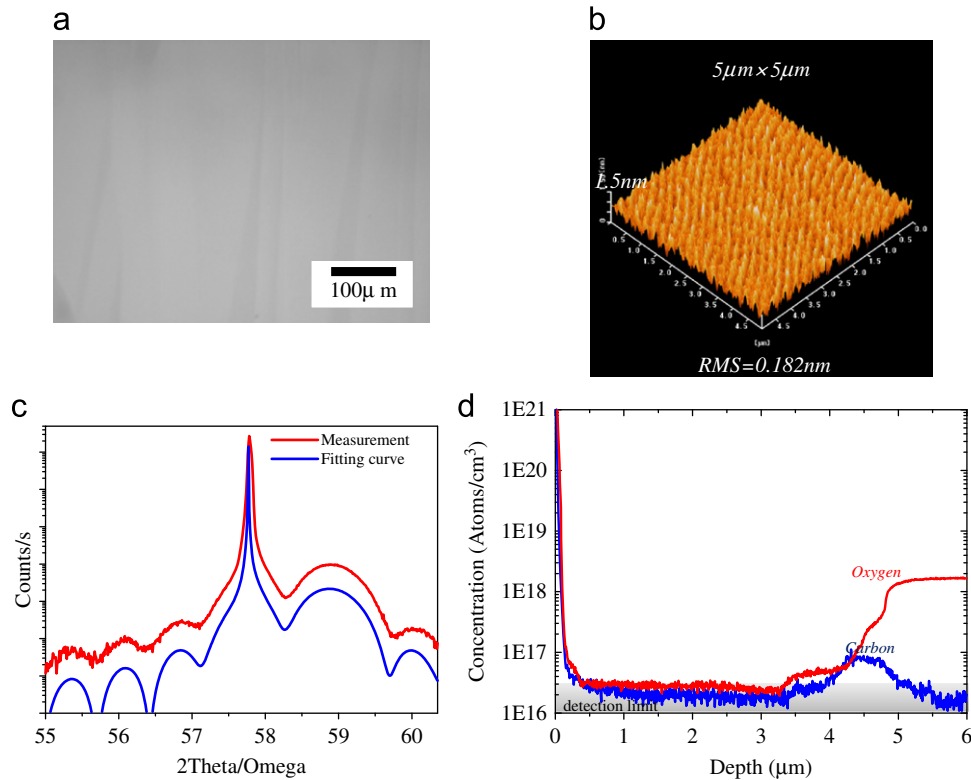
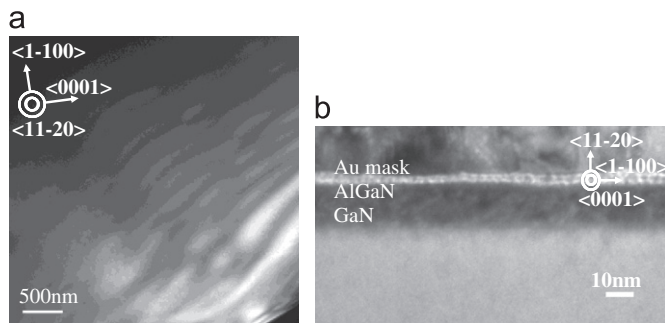


Fig. 2. Sample morphology of epitaxial GaN observed in (a) DIC images and (b) bird's-eye-view AFM images.



**Fig. 4.** a-Plane epitaxial AlGaIn/GaN structure in Fig. 3: (a) DIC microscopic image, (b) bird's-eye-view AFM image, (c) high-resolution XRD spectrum with  $2\theta/\omega$ -scan diffraction and (d) SIMS profile of oxygen and carbon concentrations.



**Fig. 5.** (a) Plan-view TEM and (b) cross-sectional TEM images of the structure in Fig. 3.

where the V/III ratio, growth temperature and growth pressure for each layer were 500, 1090 °C, and 100 hPa, respectively.

Fig. 4 shows the surface morphology of the sample shown in Fig. 3 obtained by high resolution X-ray diffraction (XRD) with a (11–20)  $2\theta/\omega$ -scan and SIMS profile of the oxygen and carbon concentrations of the sample. The RMS roughness of this sample was 0.18 nm over an area of  $5\ \mu\text{m} \times 5\ \mu\text{m}$ . A satellite peak was observed in the XRD  $2\theta/\omega$ -scan. As shown in Fig. 4(a) and (b), a macroscopically specular surface and an atomically flat surface were obtained by inserting the low-growth-rate layer. Furthermore, the oxygen concentration was under the detection limit.

Fig. 5 shows plan-view and cross-sectional TEM images of the sample shown in Fig. 3. The threading dislocation and stacking fault densities were determined to be less than  $5 \times 10^6\ \text{cm}^{-2}$  and less than  $2 \times 10^3\ \text{cm}^{-1}$ , respectively. Thus, the crystalline quality of epitaxial a-plane AlGaIn/GaN is similar to that of the Na-flux GaN substrate.

Using this growth method, a high-performance nonpolar a-plane GaN-based HFET can be realized on an unintentionally

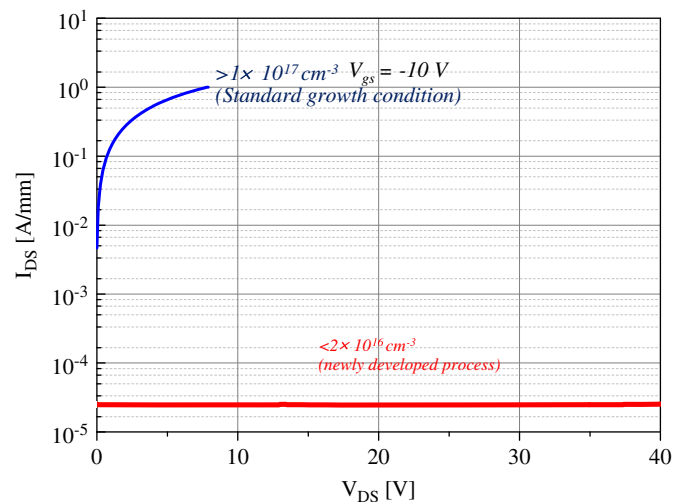


**Fig. 6.** Off-breakdown voltage of the structure in Fig. 3 at a gate bias is  $-10\ \text{V}$ . (For interpretation of the references to color in this figure, the reader is referred to the web version of this article.)

doped GaN buffer layer. Next, we measured the off-breakdown voltage of the structure in Fig. 3 at a gate bias of  $-10\ \text{V}$  to estimate the specific resistance. The result is shown in Fig. 6. Under the following device fabrication process conditions, mesa isolation was performed by removing approximately 300 nm of AlGaIn and GaN by reactive ion etching using  $\text{Cl}_2$  gas. The ohmic contact used for the drain/source, which was composed of Ti (30 nm)/Al (100 nm)/Ti (20 nm)/Au (150 nm), was annealed at  $850\ \text{°C}$  for 30 s in  $\text{N}_2$ . The gate electrode was composed of Ni (20 nm)/Au (80 nm). The gate length, width and spacing between the drain/source metals of the device were 2, 100 and  $8\ \mu\text{m}$ ,

respectively. The blue line in Fig. 6 is the leakage current of the sample with an oxygen concentration of over  $1 \times 10^{17} \text{ cm}^{-3}$ , which was grown under the standard growth conditions with the growth conditions of the GaN buffer layer in sample 3. The red line is the leakage current of the sample grown by the newly developed V/III ratio modulation process. These results show that we successfully achieved devices with a very low leakage current by using the new process. The resistivity of the newly fabricated a-plane GaN buffer layer is estimated to be higher than  $1 \times 10^3 \Omega \text{ cm}$ . Details of other device performances have been reported in a previous paper [8].

#### 4. Conclusion

Control of the V/III ratio and the growth temperature is effective for reducing oxygen contamination in an epitaxial GaN film as well as for realizing an atomically flat surface on an a-plane GaN substrate grown by the Na-flux method. We were able to fabricate a high-quality nonpolar a-plane AlGaIn/GaN wafer with a high-resistivity GaN buffer layer and a smooth surface. The results of this study can be applied to the growth of high-resistivity GaN buffer layers in nonpolar a-plane HFETs.

#### Acknowledgments

This study was supported by New Energy and Industrial Technology Development Organization.

#### References

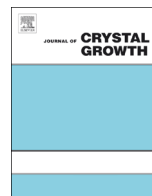
- [1] T. Takeuchi, C. Wetzel, S. Yamaguchi, H. Sakai, H. Amano, I. Akasaki, Y. Kaneko, S. Nakagawa, Y. Yamaoka, N. Yamada, *Applied Physics Letters* 73 (1998) 1691.
- [2] Y.-F. Wu, B.P. Keller, S. Keller, D. Kapolnek, P. Kozodoy, S.P. DenBaars, U.K. Mishra, *Applied Physics Letters* 69 (1996) 1438.
- [3] A. Endoh, Y. Yamashita, K. Ikeda, M. Higashiwaki, K. Hikosaka, T. Matsui, S. Hiyamizu, T. Mimura, *Japanese Journal of Applied Physics* 43 (2004) 2255.
- [4] H. Sun, A.R. Alt, H. Benedickter, C.R. Bolognesi, E. Feltin, J.-F. Carlin, M. Gonschorek, N. Grandjean, *Applied Physics Express* 3 (2010) 094101.
- [5] M.A. Khan, Q. Chen, C.J. Sun, J.W. Yang, M. Blasingame, M.S. Shur, H. Park, *Applied Physics Letters* 68 (1996) 514.
- [6] W.B. Lanford, T. Tanaka, Y. Otoki, I. Adesida, *Electronics Letters* 41 (2005) 449.
- [7] N. Tsuyukuchi, K. Nagamatsu, Y. Hirose, M. Iwaya, S. Kamiyama, H. Amano, I. Akasaki, *Japanese Journal of Applied Physics* 45 (2006) L319.
- [8] Y. Isobe, H. Ikki, T. Sakakibara, M. Iwaya, T. Takeuchi, S. Kamiyama, I. Akasaki, T. Sugiyama, H. Amano, M. Imade, Y. Kitaoka, Y. Mori, *Applied Physics Express* 4 (2011) 064102.
- [9] Z.H. Wu, A.M. Fischer, F.A. Ponce, B. Bastek, J. Christen, T. Wernicke, M. Weyers, M. Kneissl, *Applied Physics Letters* 92 (2008) 171904.
- [10] Y.S. Cho, Q. Sun, I.-H. Lee, T.-S. Ko, C.D. Yerino, J. Han, B.H. Kong, H.K. Cho, S. Wang, *Applied Physics Letters* 93 (2008) 111904.
- [11] D. Hanser, L. Liu, E.A. Preble, K. Udwardy, T. Paskova, K.R. Evans, *Journal of Crystal Growth* 310 (2008) 3953.
- [12] S.C. Cruz, S. Keller, T.E. Mates, U.K. Mishra, S.P. DenBaars, *Journal of Crystal Growth* 311 (2009) 3817.
- [13] A.J. Ptak, L.J. Holbert, L. Ting, C.H. Swartz, M. Moldovan, N.C. Giles, T.H. Myers, *Applied Physics Letters* 79 (2001) 2740.
- [14] Y. Cao, T. Zimmermann, H. Xing, D. Jena, *Applied Physics Letters* 96 (2010) 042102.
- [15] T. Aggerstam, M. Sjödin, S. Lourduoss, *Physica Status Solidi C: Current Topics in Solid State Physics* 3 (2006) 2373.
- [16] T. Fujiwara, S. Keller, M. Higashiwaki, J.S. Speck, S.P. DenBaars, U.K. Mishra, *Applied Physics Express* 2 (2009) 061003.
- [17] S. Heikman, S. Keller, T. Mates, S.P. DenBaars, U.K. Mishra, *Journal of Crystal Growth* 248 (2003) 513.
- [18] Y. Oshimura, K. Takeda, T. Sugiyama, M. Iwaya, S. Kamiyama, H. Amano, I. Akasaki, A. Bandoh, T. Udagawa, *Physica Status Solidi C: Current Topics in Solid State Physics* 7 (2010) 1974.
- [19] T. Iwahashi, Y. Kitaoka, F. Kawamura, M. Yoshimura, Y. Mori, T. Sasaki, R. Armitage, H. Hirayama, *Japanese Journal of Applied Physics* 46 (2007) 227.
- [20] Y. Isobe, D. Iida, T. Sakakibara, M. Iwaya, T. Takeuchi, S. Kamiyama, I. Akasaki, H. Amano, M. Imade, Y. Kitaoka, Y. Mori, *Physica Status Solidi A: Applications and Materials Science* 208 (2011) 1191.
- [21] Y. Isobe, D. Iida, T. Sakakibara, M. Iwaya, T. Takeuchi, S. Kamiyama, I. Akasaki, H. Amano, M. Imade, Y. Kitaoka, Y. Mori, *Physica Status Solidi C: Current Topics in Solid State Physics* 8 (2011) 2095.
- [22] Q. Sun, C.D. Yerino, Y. Zhang, Y.S. Cho, S.-Y. Kwon, B.H. Kong, H.K. Cho, I.-H. Lee, J. Han, *Journal of Crystal Growth* 311 (2009) 3824.
- [23] D. Iida, M. Iwaya, S. Kamiyama, H. Amano, I. Akasaki, *Journal of Crystal Growth* 311 (2009) 2887.
- [24] G. Parish, S. Keller, S. DenBaars, U. Mishra, *Journal of Electronic Materials* 29 (2000) 15.
- [25] D.D. Koleske, A. Wickenden, R. Henry, M. Twigg, *Journal of Crystal Growth* 242 (2002) 55.
- [26] N.A. Fichtenbaum, T.E. Mates, S. Keller, S.P. DenBaars, U.K. Mishra, *Journal of Crystal Growth* 310 (2008) 1124.
- [27] M. Kondo, C. Anayama, N. Okada, H. Sekiguchi, K. Domen, T. Tanahashi, *Journal of Applied Physics* 76 (1994) 914.
- [28] K. Matsumoto, H. Tokunaga, A. Ubukata, K. Ikenaga, Y. Fukuda, T. Tabuchi, Y. Kitamura, S. Koseki, A. Yamaguchi, K. Uematsu, *Journal of Crystal Growth* 310 (2008) 3950.
- [29] I. Kazutada, J. Yamamoto, A. Yamaguchi, Y. Yano, Y. Fukuda, T. Yabuchi, Y. Ban, K. Uchiyama, *Taiyo Nippon Sanso Technical Report* 28 (2009) 11. (in Japanese).
- [30] Y. Oshimura, T. Sugiyama, K. Takeda, M. Iwaya, T. Takeuchi, S. Kamiyama, I. Akasaki, H. Amano, *Physica Status Solidi A: Applications and Materials Science* 208 (2011) 1607.



ELSEVIER

Contents lists available at ScienceDirect

## Journal of Crystal Growth

journal homepage: [www.elsevier.com/locate/jcrysgr](http://www.elsevier.com/locate/jcrysgr)

# Control of crystallinity of GaN grown on sapphire substrate by metalorganic vapor phase epitaxy using *in situ* X-ray diffraction monitoring method



Motoaki Iwaya<sup>a,\*</sup>, Taiji Yamamoto<sup>a</sup>, Daiki Tanaka<sup>a</sup>, Daisuke Iida<sup>a</sup>, Satoshi Kamiyama<sup>a</sup>, Tetsuya Takeuchi<sup>a</sup>, Isamu Akasaki<sup>a,b</sup>

<sup>a</sup> Faculty of Science and Technology, Meijo University, Nagoya 468-8502, Japan

<sup>b</sup> Akasaki Research Center, Nagoya University, Nagoya 464-8603, Japan

## ARTICLE INFO

Available online 2 December 2013

## Keywords:

A1. Characterization  
A1. X-ray diffraction  
A3. Metalorganic vapor phase epitaxy  
B1. Nitrides

## ABSTRACT

In this study, we investigated the application of a novel *in situ* X-ray diffraction (XRD) monitoring method to control GaN crystal growth using a low-temperature (LT)-deposited buffer layer. We found that this method is useful in controlling the annealing of the LT-buffer layer, which strongly depends on the crystallinity of GaN. Accordingly, if we employ *in situ* XRD grown on GaN using LT-buffer layer on sapphire substrate, the optimization of the annealing conditions will become easier because it would be possible to determine by only one growth procedure. Therefore, we expect that this method will serve as a new and helpful optimization tool for crystal growth.

© 2013 Elsevier B.V. All rights reserved.

## 1. Introduction

Nowadays, high-brightness blue, green, and white light-emitting diodes (LEDs) [1] and high-power violet and blue laser diodes [2,3] based on group-III nitride semiconductors have been commercialized as a result of several breakthroughs such as the growth of high-crystallinity GaN on sapphire using a low-temperature (LT)-deposited buffer layer [4] and realization of conductivity control of nitrides [5–7]. Optoelectronics in the visible-short wavelength region has been established via the use of nitrides. These devices are typically fabricated by metalorganic vapor phase epitaxy (MOVPE) [8].

In device manufacturing, a key process is an *in situ* monitoring method for MOVPE. Such a method can be used to obtain information about some parameters during growth, such as the wafer bow, crystalline quality, and lattice constant. This information provides feedback about the growth condition and can be used to determine the growth mechanism. Therefore, *in situ* monitoring is expected to serve as a key technology to improve the device performance.

To obtain this information during growth, *in situ* monitoring methods based on different sources such as light, electron beams, and X-rays can be used. Among these sources, an electron beam is not suitable for MOVPE because it requires high vacuum. Thus, visible and infrared light are typically used [9–13]. Thus far, many studies have focused on *in situ* measurement methods using visible and infrared

light. Such methods can be used to measure the surface morphology, layer thickness, wafer curvature, and surface temperature. For example, because the reflectance intensity oscillates with an increase in the film thickness, this interference effect allows us to determine the growth rate [14]. Because the reflectance intensity also significantly affects the surface morphology, it is effective for controlling the coalescence of crystal nuclei during initial growth in the case of GaN growth via an LT-buffer layer on a sapphire substrate [15]. It is also possible to determine the critical film thickness from curvature measurement, such as an AlGaIn/GaN heterostructure [16,17]. Moreover, *in situ* monitoring devices for MOVPE are commercially available, and these systems have already been used to develop devices such as LEDs.

However, visible and infrared light cannot be used for nanoscale monitoring. Therefore, methods based on them cannot be used to measure the lattice constant, relaxation, and composition and crystalline quality of films. For example, when GaN films were grown on sapphire substrate using an LT-buffer layer, their crystallinity was found to be strongly dependent on the annealing condition of the LT-buffer layer [18]. However, *in situ* monitoring using visible and infrared light is not suitable for controlling the annealing condition of the LT-buffer layer.

In principle, *in situ* monitoring using X-rays is a candidate in this regard. The resolution of X-rays differs significantly from that of light, and therefore, *in situ* monitoring based on the former can be used to measure the lattice constant, thin-film nanostructure, and crystalline quality. Several studies have already focused on *in situ* monitoring using X-rays for MOVPE growth [19–24].

\* Corresponding author.

E-mail address: [iwaya@meijo-u.ac.jp](mailto:iwaya@meijo-u.ac.jp) (M. Iwaya).

However, most of these analyzed the crystal growth mechanism. Studies have hardly focused on feedback about the crystal growth, such as crystallinity, via *in situ* monitoring using X-rays.

In this study, we investigated the application of a novel *in situ* X-ray diffraction (XRD) monitoring method to control GaN crystal growth using an LT-buffer layer. As a result, we found that this method is useful for controlling the annealing of the LT-buffer layer, which strongly depends on the crystallinity of GaN.

## 2. Experimental procedure

GaN films were grown on (0 0 0 1) sapphire substrates using MOVPE apparatus with a horizontal water-cooled quartz reactor. Trimethyl-gallium (TMGa) and ammonia (NH<sub>3</sub>) were used as Ga and N source materials, respectively. Hydrogen (H<sub>2</sub>) and nitrogen (N<sub>2</sub>) were used as carrier gases. Table 1 and Fig. 1 show the GaN growth conditions for MOVPE and the timing chart of the growth process, respectively. After thermal cleaning of the sapphire substrates in H<sub>2</sub> gas at 1020 °C for 10 min, a ~20-nm-thick GaN LT-buffer layer was deposited at 520 °C for 3 min. The LT-buffer layer on sapphire was heated up to 1125 °C for 6 min, and its temperature was maintained with appropriate annealing time. After annealing, a 3- $\mu$ m-thick GaN film was grown at 1125 °C for 80 min.

We evaluated the LT-buffer layer and GaN epitaxial layer with symmetric (0 0 0 2) Bragg diffraction using an *in situ* XRD system. We equipped the MOVPE system with an *in situ* XRD monitoring device. A beryllium window was installed in the MOVPE to serve as a

viewport for passing X-rays. An *in situ* X-ray was focused on the sample surface using a Johansson curved crystal mirror. By this approach, the incidence angle of the X-ray can be changed without moving the X-ray source. Moreover, the diffracted X-ray was detected by a one-dimensional charge-coupled device [25,26]. By this method, the scattered X-ray can be detected without moving the substrate and detector. By using this configuration, this system realized the equivalent of a (0 0 0 2)  $2\theta/\omega$  scan without requiring the use of an analyzer crystal in 1 s during wafer rotation. Furthermore, the  $2\theta$  value was calibrated by the XRD peak from the sapphire substrate. In this system, the tilt component and distribution of the lattice constant *c* can be simultaneously characterized from the full width at half maximum (FWHM) [23,24]. Although the resolution limit decreases slightly, this *in situ* XRD system is excellent for measuring the equivalent of a (0 0 0 2)  $2\theta/\omega$  scan for a very short time and without moving the substrate, X-ray source, and detector. In this study, we measured the *in situ* XRD spectrum at a frequency of once per period. Further, FWHMs of the *in situ* XRD spectrum were analyzed by using a Gaussian fitting method. The growth temperature was measured by *in situ* optical monitoring. We also observed the crystallinity of GaN by a typical *ex situ* XRD measurement.

## 3. Result and discussions

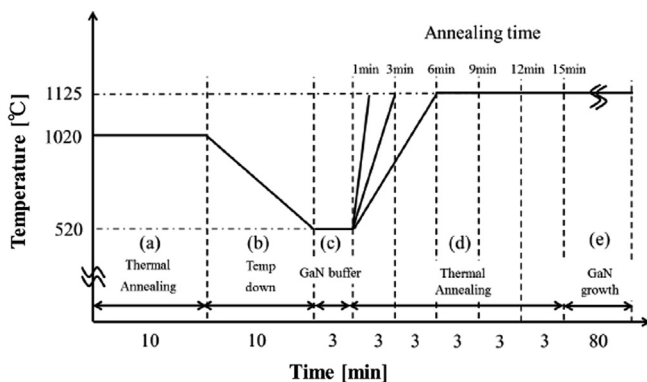
Fig. 2 shows the typical *in situ* XRD spectra with symmetric (0 0 0 2) diffraction of the LT-GaN buffer layers with different annealing times (as deposited (0), 1, 3, 6, 9, 12, and 15 min). In this study, we defined an annealing time of 0 min (as deposition of buffer layer) as the time at which buffer layer deposition is completed. These figures showed that the X-ray spectra of the deposited buffer layer included a clear peak attributable to the GaN crystal. This suggests the crystallization of hexagonal single crystals in the LT-GaN buffer layers before annealing. According to previous reports, these broadened *in situ* XRD spectra also suggest that the crystalline structure of the LT-GaN buffer layers is composed of a random amorphous-like phase, a cubic phase, or a mixed cubic-hexagonal phase [14,15,18,23,27–30]. Furthermore, the *in situ* XRD spectrum of the annealed LT-GaN buffer layer indicated that thermal annealing of the LT-GaN buffer layer immediately after its growth serves to induce the crystallization of hexagonal single crystals. Then, the intensity of the *in situ* XRD spectrum was strongest when the annealing time was 6 min, after which it began decreasing. In other words, the hexagonal single crystals were evaporated by thermal annealing for an annealing time exceeding 6 min. At this time, the crystal structure was almost completely transformed into hexagonal single-crystal islands. Although these results have been reported previously [18], this *in situ* XRD method can be used to determine the optimization of the growth condition through only one growth.

Fig. 3 and Table 2 summarize the peak intensity and FWHM of the *in situ* XRD spectrum from LT-GaN buffer layers during thermal annealing as a function of the annealing time. The figure shows that the X-ray intensity increases up to an annealing time of 6 min, after which it decreases. In contrast, the FWHM narrows with an increase in annealing time up to 9 min. The FWHM was the minimum at an annealing time of ~9 min, and it saturated. The FWHM then widened with a further increase in annealing time.

To consider the annealing effect of the LT-GaN buffer layer, we were evaluated to prepared LT-GaN buffer layer samples with annealing time of 3, 6, and 12 min. Fig. 4 shows the scanning electron microscopic (SEM) images of each sample. From these figure, we confirmed a marked difference in the surface morphology by annealing. Fig. 5 shows the schematic view of the changes due to annealing of the LT-GaN buffer layer by

**Table 1**  
Growth conditions in this study.

Process	Reactor pressure [hPa]	Gas
(a) Thermal cleaning	933	H <sub>2</sub>
(b) Temperature down	933	H <sub>2</sub>
(c) GaN buffer layer	933	TMGa H <sub>2</sub> NH <sub>3</sub>
(d) Thermal annealing	933–500	H <sub>2</sub> NH <sub>3</sub>
(e) GaN growth	500	TMGa H <sub>2</sub> NH <sub>3</sub>



**Fig. 1.** Timing chart of GaN growth process in this study. (a) Thermal cleaning in H<sub>2</sub> flow at 1020 °C for 10 min. (b) Temperature down at 520 °C for 10 min. (c) LT-GaN was deposited at 520 °C. (d) LT-GaN was annealed [Annealing time 1 (3, 6) min: Substrate was heated up to 1125 °C for 1 (3, 6) min. Annealing time 9 (12, 15) min: Substrate was heated up to 1125 °C for 6 min. Then, the temperature was maintained for 3 (6, 9) min. Therefore, the annealing time 9 (12, 15) is given by the ramp time (6 min) plus the holding time (3 (6, 9) min)]. (e) 3- $\mu$ m-thick GaN was grown at 1125 °C.

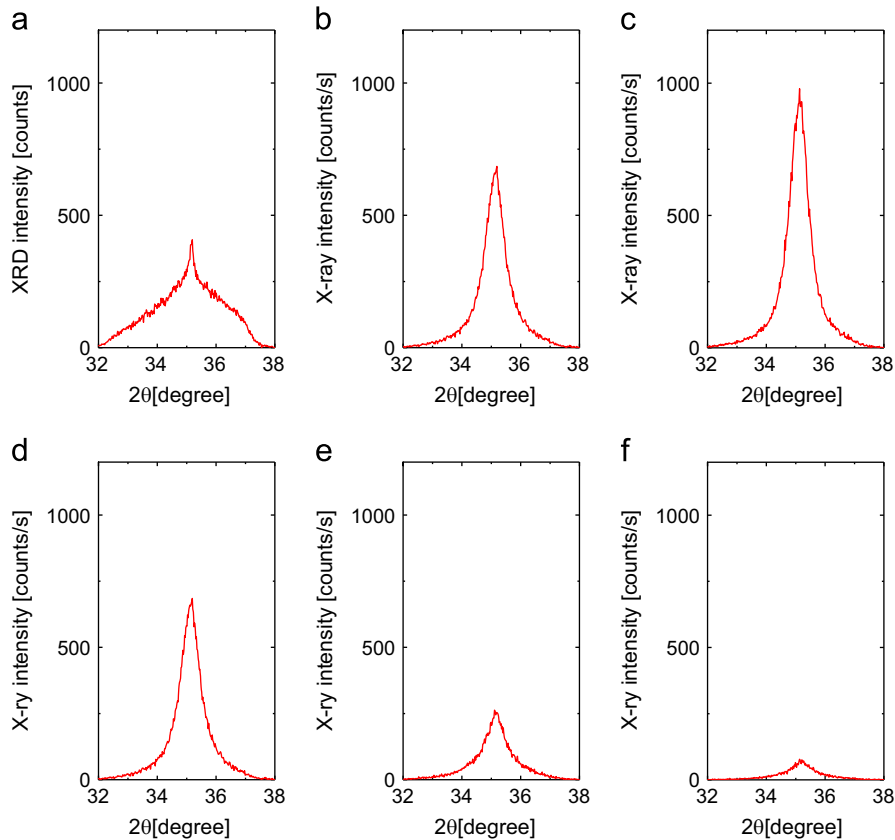


**Fig. 2.** X-ray spectra from LT-GaN buffer layer with various annealing times by using *in situ* XRD monitoring method. (a) 0 min, (b) 3 min, (c) 6 min, (d) 9 min, (e) 12 min and (f) 15 min.

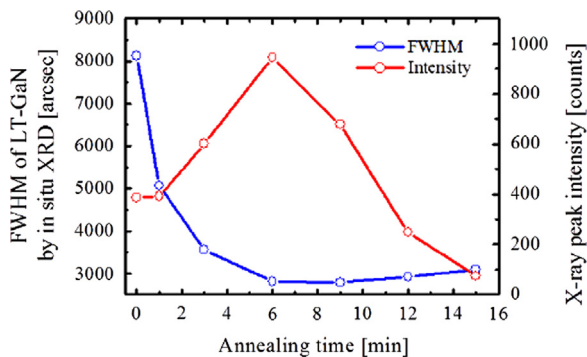


**Fig. 3.** Annealing time dependence of X-ray intensity and FWHM (002) from *in situ* XRD monitoring method.

**Table 2**  
Results of *in situ* and *ex situ* XRD.

Annealing time [min]	<i>In situ</i> XRD intensity [counts]	LT-GaN FWHM [arcs]	FWHM [arcs]	
			Tilt [0 0 2]	Twist [1 0 2]
3	602	3560	506	823
6	945	2800	285	314
9	678	2800	256	310
12	249	2990	280	325
15	74	3080	266	368

*in situ* XRD and SEM results. We considered etching and crystallization in LT-GaN buffer layer is in progress simultaneously in the initial time of annealing. And crystallization ends at a certain

period of time, while only etching continues. Accordingly, optimal annealing time of LT-GaN buffer layer should be present in order to obtain a high-quality GaN epitaxial layer.

Next, we discuss the correlation between the crystallinity of the GaN epitaxial layer and the *in situ* XRD measurement results. We investigated the crystalline quality of 3- $\mu\text{m}$ -thick GaN layers formed on LT-GaN buffer layers with various annealing times. In this investigation, the samples were prepared separately. Furthermore, for annealing times of 1 and 3 min, GaN films were grown after the temperature was increased to 1125 °C for 1 min after the end of annealing. Therefore, we thought that some error may exist for annealing times of 1 and 3 min. Fig. 6 shows the annealing time dependence of the FWHM of *ex situ* X-ray rocking curves (XRCs) from the (0 0 0 2) diffraction, which is a distribution of the tilt component, and the (1 -1 0 2) diffraction, which is a distribution of the twist component, of 3- $\mu\text{m}$ -thick GaN films. Although slight tilt component is also included from the (1 -1 0 2) diffraction, twist component is dominant in this measurement method [31,32]. Table 2 summarizes the FWHM of *ex situ* XRCs from the (0 0 0 2) and (1 -1 0 2) diffractions as a function of annealing time. The figure and table show that the tilt and twist distributions of GaN films are strongly dependent on the annealing time of the LT-GaN buffer layer. The FWHMs of the *ex situ* XRC from GaN narrowed with an increase in the annealing time up to 9 min. The FWHM was the minimum at an annealing time of  $\sim 9$  min, and it saturated. Then, the FWHM widened with a further increase in the annealing time. In other words, we found that the crystallinity of GaN is the best when it was grown on the narrowest FWHM of the annealed LT-buffer layer. By using the same technique, we could well reproduce the annealing time of the LT-buffer layer. Therefore, we found that this *in situ* XRD monitoring method is useful for controlling the annealing of the LT-buffer layer. Accordingly, if

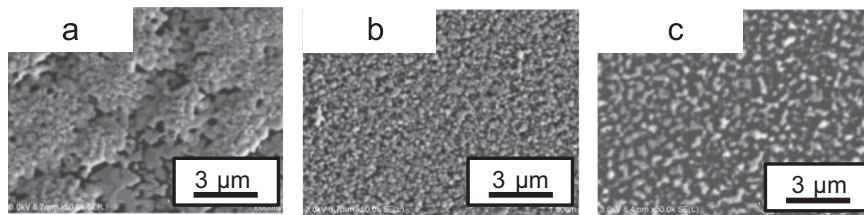


Fig. 4. Plan view SEM images of LT-buffer layer with annealing times of (a) 3 min, (b) 6 min, and (c) 12 min.

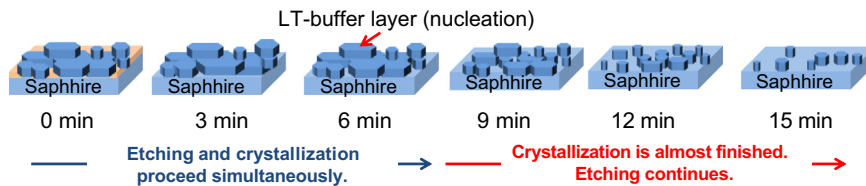


Fig. 5. Schematic view of the changes due to annealing of the LT-GaN buffer layer from experimental results.

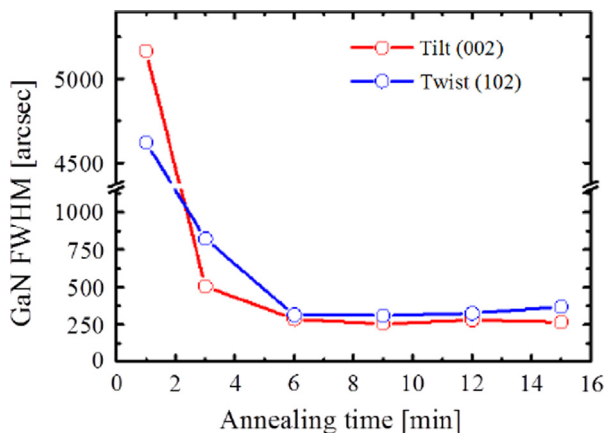


Fig. 6. Annealing time dependence of FWHM of tilt (002) and twist (1–102) distributions from 3- $\mu$ m-thick GaN films on LT-buffer layers with different annealing times.

we apply the *in situ* XRD monitoring system under various growth conditions, the optimization of growth conditions will be easier, because it would be possible to determine the optimized growth condition through only one growth. The *in situ* XRD monitoring system proposed herein enabled us to estimate the optimized annealing condition during growth. This implies that this system is extremely effective for the optimization of crystal growth.

#### 4. Conclusion

We examined the application of a novel *in situ* XRD monitoring method to control GaN crystal growth using an LT-buffer layer. The FWHM determined from the *in situ* XRD monitoring method could be used to accurately observe the changes in the LT-buffer layer with annealing. Accordingly, if we employ *in situ* XRD grown on GaN using LT-buffer layer on sapphire substrate, the optimization of the annealing conditions will become easier because it would be possible to determine by only one growth procedure. We found that this *in situ* XRD monitoring method is useful for controlling the annealing of the LT-buffer layer.

#### Acknowledgment

This study was supported by the Ministry of Education, Culture, Sports, Science and Technology of Japan through the Supported Program for the Strategic Research Foundation at Private Universities, 2012–2016.

#### References

- [1] I. Akasaki, H. Amano, *Jpn. J. Appl. Phys.* 45 (2006) 9001.
- [2] I. Akasaki, *J. Cryst. Growth* 300 (2007) 2.
- [3] S. Nagahama, T. Yanamoto, M. Sano, T. Mukai, *Appl. Phys. Lett.* 79 (2001) 1948.
- [4] H. Amano, N. Sawaki, I. Akasaki, Y. Toyoda, *Appl. Phys. Lett.* 48 (1986) 353.
- [5] H. Amano, M. Kitoh, K. Hiramatsu, I. Akasaki, *J. Electrochem. Soc.* 137 (1990) 1639.
- [6] H. Amano, M. Kitoh, K. Hiramatsu, I. Akasaki, *Jpn. J. Appl. Phys.* 28 (1989) L2112.
- [7] H. Amano, I. Akasaki, *Material Research Society Extended Abstract EA 21* (1990) 165.
- [8] I. Akasaki, in: *Proceeding of Material Research Society Symposium* 639 (2001) G8-1.1.
- [9] S.L. Wright, T.N. Jackson, R.F. Marks, *J. Vac. Sci. Technol.*, B 8 (1990) 288.
- [10] A.J. SpringThorpe, A. Majeed, *J. Vac. Sci. Technol.*, B 8 (1990) 266.
- [11] S. Figge, T. Bottcher, S. Einfeldt, D. Hommel, *J. Cryst. Growth* 221 (2000) 262.
- [12] T.-B. Ng, J. Han, R.M. Biefeld, M.V. Weckwerth, *J. Electron. Mater.* 27 (1998) 190.
- [13] P. Venngues, B. Beamont, S. Haffouz, M. Vaillie, P. Gibart, *J. Cryst. Growth* 187 (1998) 167.
- [14] S. Nakamura, *Jpn. J. Appl. Phys.* 30 (1991) 1620.
- [15] K. Hiramatsu, S. Itoh, H. Amano, I. Akasaki, N. Kuwano, T. Shiraishi, K. Oki, *J. Cryst. Growth* 115 (1991) 628.
- [16] M. Iwaya, S. Terao, N. Hayashi, T. Kashima, H. Amano, I. Akasaki, *Appl. Surf. Sci.* 159–160 (2000) 405.
- [17] S. Terao, M. Iwaya, T. Sano, T. Nakamura, S. Kamiyama, H. Amano, I. Akasaki, *J. Cryst. Growth* 237–239 (2002) 947.
- [18] T. Ito, M. Sumiya, Y. Takano, K. Ohtsuka, S. Fuke, *Jpn. J. Appl. Phys.* 38 (1999) 649.
- [19] A. Kharchenko, K. Lischka, K. Schmidegg, H. Sitter, J. Bethke, J. Woitok, *Rev. Sci. Instrum.* 76 (2005) 033101.
- [20] C. Simbrunner, K. Schmidegg, A. Bonanni, A. Kharchenko, J. Bethke, J. Woitok, K. Lischka, H. Sitter, *Phys. Status Solidi A* 203 (2006) 1704.
- [21] T. Sasaki, H. Suzuki, A. Sai, J.-H. Lee, M. Takahashi, S. Fujikawa, K. Arafune, I. Kamiya, Y. Ohshita, M. Yamaguchi, *Appl. Phys. Express* 2 (2009) 085501.
- [22] M. Tabuchi, Y. Takeda, *J. Cryst. Growth* 298 (2007) 12.
- [23] D. Iida, M. Sowa, Y. Kondo, D. Tanaka, M. Iwaya, T. Takeuchi, S. Kamiyama, I. Akasaki, *J. Cryst. Growth* 361 (2012) 1.
- [24] D. Iida, Y. Kondo, M. Sowa, T. Sugiyama, M. Iwaya, T. Takeuchi, S. Kamiyama, I. Akasaki, *Phys. Status Solidi RRL* 7 (2013) 211.
- [25] A. Kharchenko, K. Lischka, K. Schmidegg, H. Sitter, J. Bethke, J. Woitok, *Rev. Sci. Instrum.* 76 (2005) 033101.
- [26] C. Simbrunner, K. Schmidegg, A. Bonanni, A. Kharchenko, J. Bethke, J. Woitok, K. Lischka, H. Sitter, *Phys. Status Solidi A* 203 (2006) 1704.
- [27] X.H. Wu, D. Kapolnek, E.J. Tarsa, B. Heying, S. Keller, B.P. Keller, U.K. Mishra, S.P. DenBaars, J.S. Speck, *Appl. Phys. Lett.* 68 (1996) 1371.

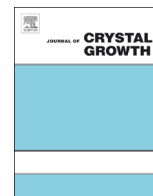
- [28] Y.-M.L. Vaillant, R. Bisaro, J. Olivier, O. Durand, J.-Y. Duboz, S. Ruffenach-Clur, O. Briot, B. Gil, R.-L. Aulombard, *J. Cryst. Growth* 189/190 (1998) 282.
- [29] T. Hashimoto, M. Yuri, M. Ishida, Y. Terakoshi, O. Imafuji, T. Sugino, K. Itoh, *Jpn. J. Appl. Phys.* 38 (1999) 6605.
- [30] K. Hoshino, N. Yanagita, M. Araki, K. Tadatomo, *J. Cryst. Growth* 298 (2007) 232.
- [31] P. Fini, X. Wu, E.J. Trasa, Y. Golan, V. Srikant, S. Keller, S.P. Denbaars, J.S. Speck, *Jpn. J. Appl. Phys.* 37 (1998) 4460.
- [32] J. Bai, T. Wanga, P.J. Parbrook, K.B. Lee, A.G. Cullis, *J. Cryst. Growth* 280 (2005) 290.



ELSEVIER

Contents lists available at ScienceDirect

## Journal of Crystal Growth

journal homepage: [www.elsevier.com/locate/jcrysgr](http://www.elsevier.com/locate/jcrysgr)

# *In situ* X-ray diffraction monitoring of GaInN/GaN superlattice during organometallic vapor phase epitaxy growth



Taiji Yamamoto<sup>a,\*</sup>, Daisuke Iida<sup>a</sup>, Yasunari Kondo<sup>a</sup>, Mihoko Sowa<sup>a</sup>, Shinya Umeda<sup>a</sup>,  
Motoaki Iwaya<sup>a</sup>, Tetsuya Takeuchi<sup>a</sup>, Satoshi Kamiyama<sup>a</sup>, Isamu Akasaki<sup>a,b</sup>

<sup>a</sup> Faculty of Science and Technology, Meijo University, Nagoya 468-8502, Japan

<sup>b</sup> Akasaki Research Center, Nagoya University, Nagoya 464-8603, Japan

## ARTICLE INFO

Available online 1 December 2013

## Keywords:

A1. X-ray diffraction

A3. Organometallic vapor phase epitaxy

B1. Nitrides

B3. Heterojunction semiconductor devices

## ABSTRACT

We observed the growth of the Ga<sub>0.80</sub>In<sub>0.20</sub>N (2 nm)/GaN (3 nm) superlattice (SL) structure by *in situ* X-ray diffraction (XRD) monitoring. The satellite peaks from the –1st to the +1st order can be obtained from these *in situ* XRD spectrums. From the full width at half maximums (FWHMs) of the 0th and –1st satellite peaks as a function of the SL periods, we observed a clear trend in each FWHM. It was found that by analyzing this trend along with fluorescence microscopic and transmission electron microscopic analysis, an analysis of the In segregation and misfit dislocation are possible. Accordingly, if we employ *in situ* XRD under various growth conditions, the optimization of the growth conditions will become easier because it would be possible to determine the number of periods at which In segregation and misfit dislocation increases by only one growth procedure.

© 2014 Published by Elsevier B.V.

## 1. Introduction

Because the bandgap of GaInN ternary alloys has a broad range from 0.65 eV to 3.43 eV [1,2], these alloys are suitable for solar cell applications. By using a combination of GaInN alloys, one can theoretically design a multijunction solar cell with a bandgap spanning the infrared to ultraviolet regions of the solar spectrum [3–5]. This makes it possible to achieve high-efficiency multijunction solar cells. Thus far, by improving the crystallinity of GaInN, improving the electrode structure, and using the concentration of sunlight, the conversion efficiency of GaInN-based solar cells has been improved by up to 4% [6]. We have reported that the superlattice (SL) structure is useful for improving the crystallinity of the GaInN active layer [7–12]. However, there are numerous practical problems that must first be solved. Although an increase in the SL periods and InN molar fraction is required for realizing high-performance GaInN-based solar cells, the crystallinity of GaInN SL will deteriorate rapidly by introduction of misfit dislocations [3], introduction of growth pits [13,14], and increase of In segregation [13–17] in GaInN, if the layer exceed the critical thickness. In particular, In segregation (composition fluctuation) will rapidly degrade the device performance such as GaInN-based blue and green laser diode and solar cells [16,17]. Also, In segregation can be measured from the dot emission density

determined by fluorescence microscopy. We found that the solar cell characteristics degrade rapidly when this dot emission density exceeds  $\sim 10^6 \text{ cm}^{-2}$  [17]. Therefore, it is very important to determine the optimal growth conditions under which the dot emission density is less than  $10^6 \text{ cm}^{-2}$ . In addition to the dot density, the device characteristics are also degraded by the presence of misfit dislocations. Therefore, numerous experiments will be required to explore the optimal growth conditions unless *in situ* observations are employed.

*In situ* monitoring in organometallic vapor phase epitaxy (OMVPE) is a key process in device manufacturing. This approach can provide information about the growth condition and help clarify its mechanism. Therefore, *in situ* monitoring is expected to serve as a key technique for improving the device performance. Thus far, *in situ* observation methods using visible/infrared light have been used to improve the device performances [18–21]. *In situ* monitoring can be used to measure the surface morphology, layer thickness, wafer curvature, and surface temperature. However, it is impossible to perform nanoscale measurements using visible/infrared light, because its wavelength exceeds several hundred nanometers. Therefore, we cannot measure with this technique the crystalline quality and structure of thin film layer such as SLs structures. In contrast, because the resolution of X-ray and visible/infrared light is significantly different, *in situ* monitoring using X-rays can be used to measure the SL structure. Several studies have reported on *in situ* observations using X-rays in OMVPE growth [22–27]. However, most of these have focused on the analysis of the crystal growth mechanism.

\* Corresponding author. Tel.: +81 528321151.

E-mail address: [133434039@ccalumni.meijo-u.ac.jp](mailto:133434039@ccalumni.meijo-u.ac.jp) (T. Yamamoto).

In this study, we have applied *in situ* X-ray diffraction (XRD) measurement to optimize the GaInN SL structure via the suppression of In segregation and the generation of misfit dislocations.

## 2. Experimental procedure

The samples were grown on *c*-plane sapphire substrates using OMVPE apparatus with a horizontal face down 2" × 3" reactor (TNMC: GRC-203). Trimethyl-gallium (TMGa), trimethyl-indium (TMI), and ammonia (NH<sub>3</sub>) were used as Ga, In, and N source materials, respectively. Hydrogen (H<sub>2</sub>) and nitrogen (N<sub>2</sub>) were used as the carrier gases. Revolution speed of the substrate susceptor was 5 rpm in constant. After the growth of a 3-μm-thick GaN template at 1050 °C on *c*-plane sapphire covered with a low-temperature GaN buffer layer [28,29] using H<sub>2</sub> carrier gas at 933 hPa, it was cooled to 750 °C and the carrier gas was changed to N<sub>2</sub>. Then, 75-period Ga<sub>0.80</sub>In<sub>0.20</sub>N (2 nm)/GaN (3 nm) SL was grown on the GaN template. The growth time of Ga<sub>0.80</sub>In<sub>0.20</sub>N and GaN are 42 s and 81 s, respectively. During growth of the Ga<sub>0.80</sub>In<sub>0.20</sub>N layer, the flow rates of the TMG of 65 μmol/min, TMI of 65 μmol/min, NH<sub>3</sub> of 800 mmol/min, V/III ratio of 8500, and N<sub>2</sub> of 16 l/min were used. The threading dislocation density of the GaN template was ~3 × 10<sup>8</sup> cm<sup>-2</sup>. We evaluated the GaInN films with symmetric (0002) Bragg diffraction using an *in situ* XRD system [26]. Fig. 1 shows the schematic view of the experimental setup. We attached *in situ* XRD observation equipment to the OMVPE apparatus. The X-ray monitoring system used in this study was

supplied by Rigaku Corporation. The OMVPE apparatus was equipped with a beryllium window that served as a viewport for passing X-rays. An *in situ* X-ray was focused on the sample surface using a Johansson curved crystal mirror. By using this method, the incidence angle of the X-rays can be changed without moving the X-ray source. Moreover, the diffracted X-ray was detected by a one-dimensional charge-coupled device. By using this method, the scattered X-ray can be detected without moving the substrate and detector. By using this configuration, this system realized the

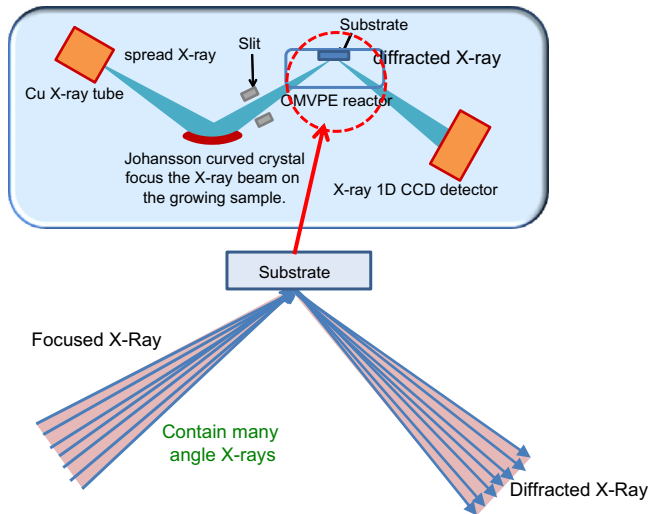


Fig. 1. Schematic view of the experimental setup.

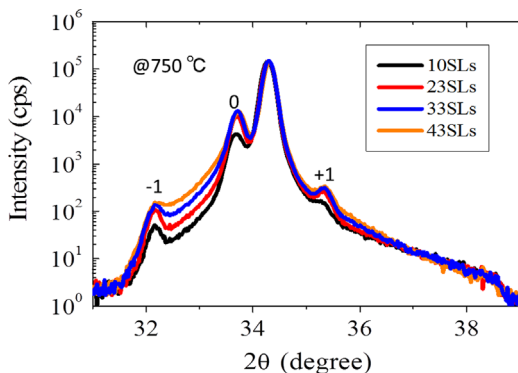


Fig. 2. In situ XRD spectrum of 75-period Ga<sub>0.80</sub>In<sub>0.20</sub>N (2 nm)/GaN (3 nm) SL during growth of 10, 23, 33, and 43 periods.

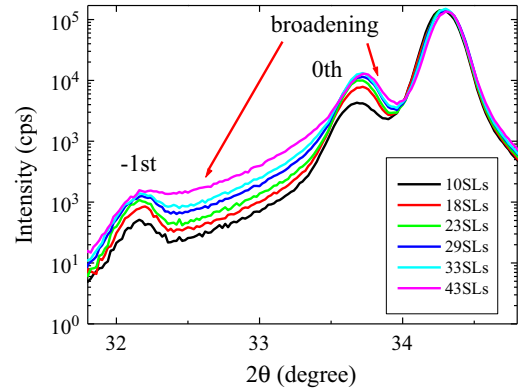


Fig. 3. Enlarged view of Fig. 1 at 0 and -1satellite peak region.

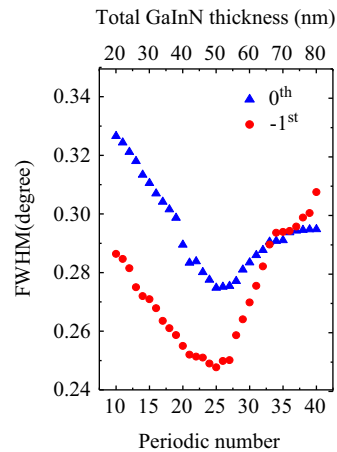


Fig. 4. FWHM of the 0th and -1st satellite peaks as a function of the SL periods.

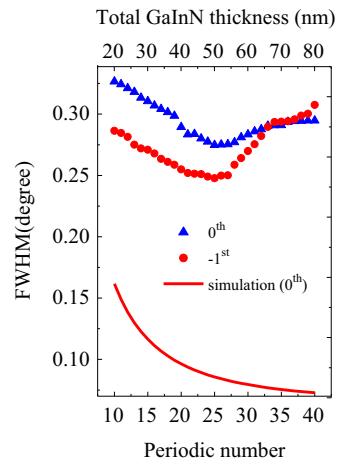


Fig. 5. This figure was inserted the results of the simulation in Fig. 4.

equivalent of a (0002)  $2\theta/\omega$  scan without requiring the use of an analyzer crystal in 1 s during the rotation of the wafers. Furthermore, the  $2\theta$  value was calibrated based on the GaN peak. Although the resolution limit decreases slightly, this *in situ* XRD system is able to perform the equivalent of a (0002)  $2\theta/\omega$  scan at a resolution of 1arcsec. In this setup, the full half width maximum

(FWHM) is both controlled by the dispersion in the lattice constant  $c$  and the mosaicity of the crystal [26,27]. Due to the diffraction geometry, we measure here the mosaicity tilt. In this study we acquired *in situ* XRD data at the frequency of one diffractogram per SL period. Further, FWHMs of the *in situ* XRD spectrum were analyzed by using a Gaussian fitting method.

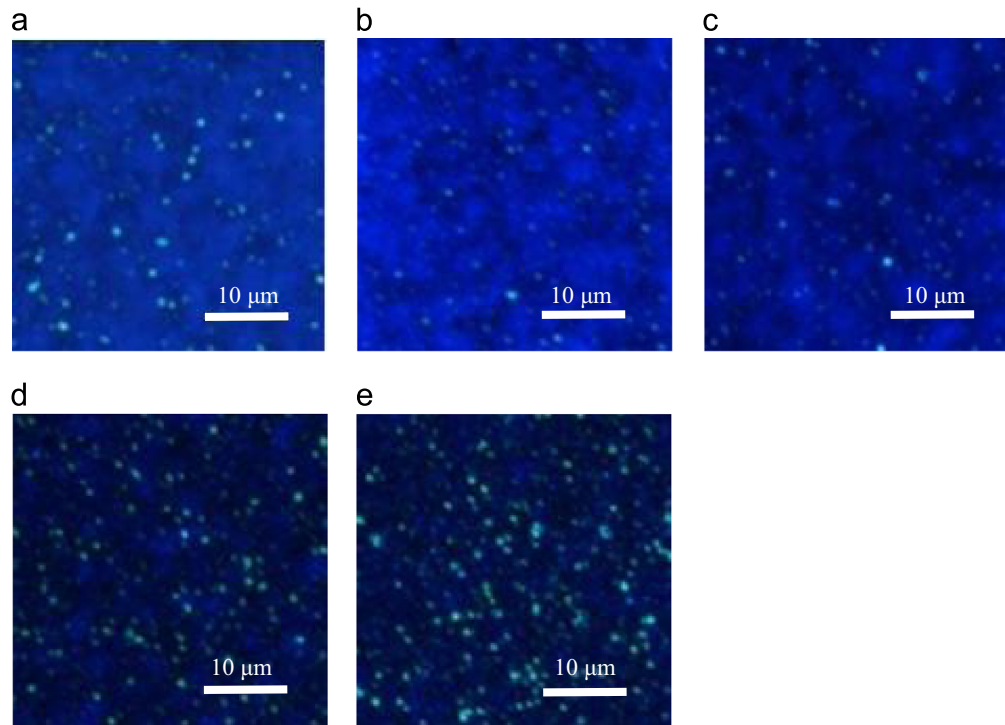


Fig. 6. Fluorescence microscopic images of (a) 10, (b) 20, (c) 25, (d) 30, and (e) 40-period GaInN SL samples.

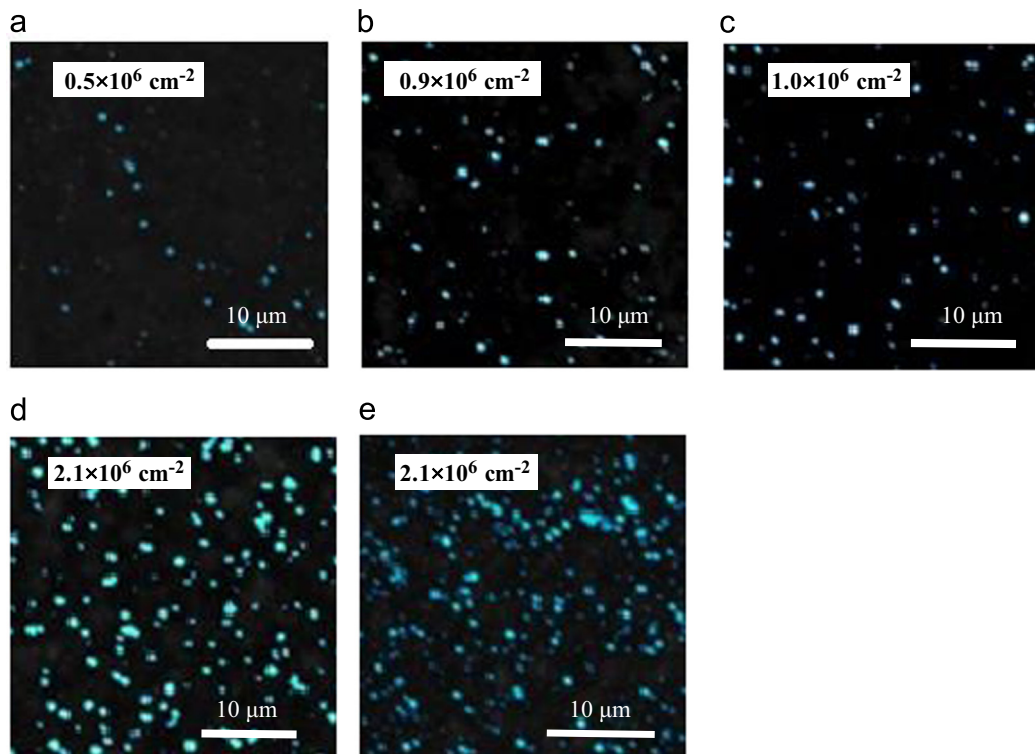


Fig. 7. Images corresponding to those shown in Fig. 5 (a)–(e) with blue light removed by using image processing. We have also shown the cyan dot emission density in each figure. (a) 10 periods, (b) 20 periods, (c) 25 periods, (d) 30 periods and (e) 40 periods. (For interpretation of the references to color in this figure legend, the reader is referred to the web version of this article.)

We also fabricated additional five  $\text{Ga}_{0.80}\text{In}_{0.20}\text{N}$  (2 nm)/GaN (3 nm) SL samples with 10, 20, 25, 30, and 40 periods for *ex situ* characterization. We evaluated the In segregation in each sample through fluorescence microscope (Nikon LV100D, Excitation light: Halogen lamp (50 W), excitation power density:  $\sim$ several  $\text{kW}/\text{cm}^2$ ) observations. And we used transmission electron microscopy (TEM) (HITACHI H-9000A) to observe misfit dislocations. The accelerating voltage of our TEM is 300 kV. In this condition, plan-view TEM images were observed.

### 3. Results and discussion

Fig. 2 shows the *in situ* XRD spectrum obtained from 75-period  $\text{Ga}_{0.80}\text{In}_{0.20}\text{N}$  (2 nm)/GaN (3 nm) SL during the growth of 10, 23, 33, and 43 periods. Also, Fig. 3 shows an enlarged view of Fig. 2 at 0 and  $-1$  satellite peak region. We confirmed clear satellite peaks from the  $-1$ st to the  $+1$ st order. Even though the measurement time was 1 s, the satellite peaks from the SL were observed and separated. Therefore, reasonably high resolution and short measurement time was achieved by this *in situ* XRD system. In addition, the FWHMs of the satellite peaks showed a certain trend. Up to a certain period, the FWHM of the satellite peaks in the *in situ* XRD spectrum reduced. Because the FWHM of XRD generally decreases with increasing film thickness, this is a reasonable result in theory [30]. In contrast, FWHM increased after a certain period. To exactly analyze this trend, we analyzed the FWHMs of the satellite peak of each period. Fig. 4 summarizes the FWHM of the 0th and  $-1$ st satellite peaks as a function of the SL periods. Moreover, Fig. 5 was inserted the results of the

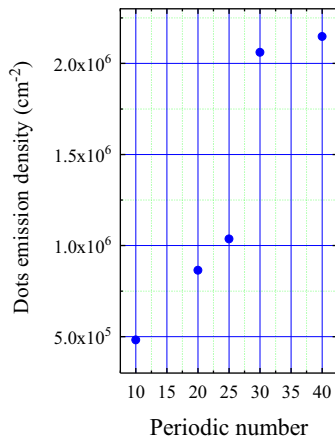


Fig. 8. Dot emission density as a function of the SL periods.

simulation (FWHM of 0th satellite peak) in Fig. 4. In this simulation, we have used the XRD simulator (Rigaku: GlobalFit). There is a difference between simulation and experimental results. We thought this difference is the effect of crystallinity of the underlying GaN layer and disorder of the GaInN/GaN superlattice. In particular, it is considered that the influence of crystallinity is greater because this *in situ* XRD does not use an analyzer crystal. However, the trend of the experimental results and the simulation is the almost same up to a certain period. We observed a clear trend in each FWHM. Up to 25 periods, the FWHMs from satellite peaks of XRD decreased continuously with an increase in the period. This trend is the same as the simulation result. However, we confirmed that the FWHM did not show this tendency and increased after  $\sim$ 25 periods. Therefore, we considered that a crystallographic change may have occurred. Next, we analyzed the additional SL samples having different periods. Through various analyses, we concluded that the FWHM increases with the In segregation. Fig. 6 show fluorescence microscopic images of 10-, 20-, 25-, 30-, and 40-period GaInN SL structures. These figures show significant differences. To clarify these differences, we applied image processing techniques to these fluorescence microscopic images. Fig. 7 show the images corresponding to those shown in Fig. 6 with the main blue emission from the SL removed by image processing. These figures showed cyan emission attributable to In segregation. The evolution of the dot emission density is summarized Fig. 8. It can be seen that the cyan dot density strongly increases after 30 SL periods. This particular SL thickness correlates with the onset of the FWHM increase observed by XRD during the *in situ* XRD measurement (Fig. 4). The main blue emission from the SL follows an opposite variation with a strong decrease for SL thicknesses over 30 periods. This effect is attributed to the generation of misfit dislocations, as observed later by TEM (Fig. 9). Fig. 10 show *ex situ* XRD reciprocal space maps of the asymmetric reflection (20–24) of sample with 25, 30 and 40 SL periods. The SL relaxation is not directly apparent with this *ex-situ* technique. In addition, we performed TEM analysis in order to analyze in detailed microstructure. Fig. 9 show plan-view TEM images at 25 and 30 period SL samples. Note that we could observe to the interface of GaN and GaInN, because the thickness of the TEM sample is approximately 150 nm. In 25 SLs sample, threading dislocations from the underlying GaN can be confirmed, but there was little misfit dislocations at GaInN/GaN interface. In contrast, in 30 SLs sample, many misfit dislocations at GaInN/GaN interface were confirmed. These experimental results could be explained as follows. Fig. 11 show the diagram of the growth model based on the obtained results. Up to 25 periods, few dot emissions attributable to In segregation are observed. In addition, misfit dislocations are not increased. Thus, the FWHM

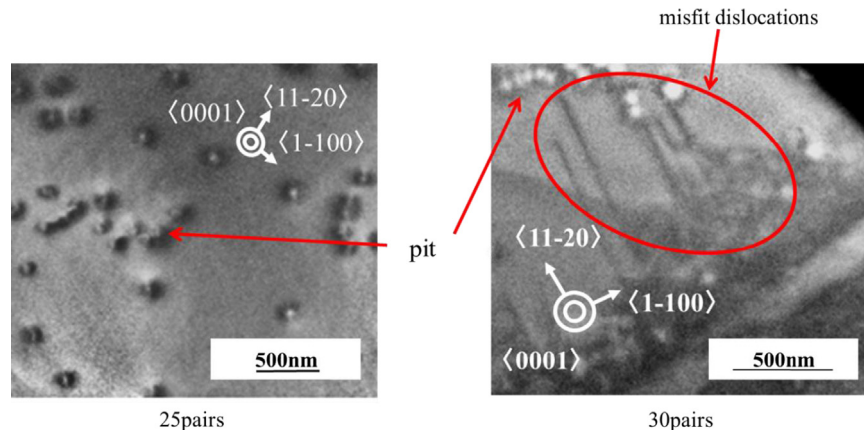


Fig. 9. Plan view TEM images of 25 and 30 period SL samples.

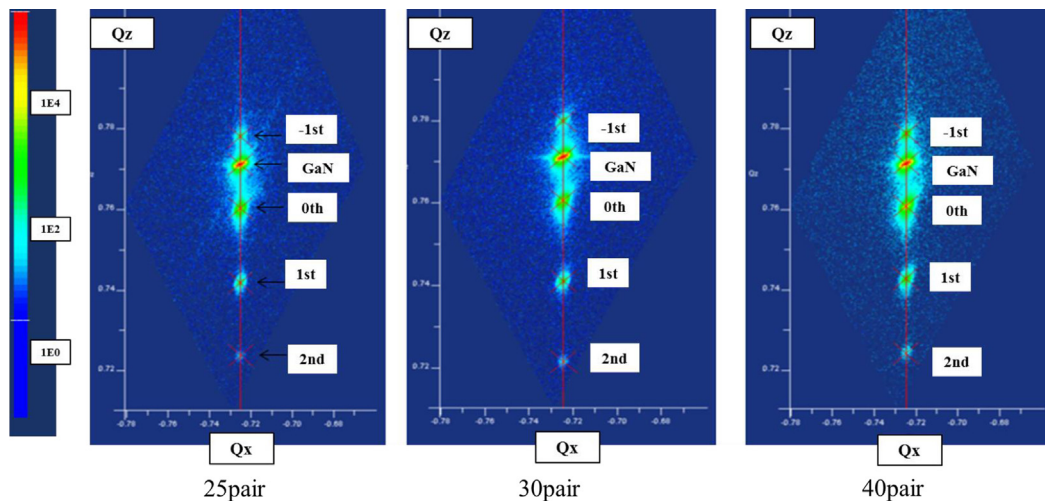


Fig. 10. XRD reciprocal space mapping images from 25, 30 and 40 period SL samples.

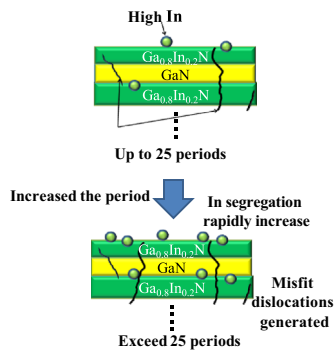


Fig. 11. Growth model diagram based on the obtained results.

from satellite peaks reduces in accordance with the increase in period, whereas In segregation and misfit dislocations rapidly increases after 25 periods. Because the periodicity of the SL is disturbed, the FWHM of the satellite peak increases. Accordingly, if we employ *in situ* XRD under various growth conditions, the optimization of the growth conditions will become easier because it would be possible to determine the number of periods at which In segregation and misfit dislocation increases by only one growth procedure. In addition, this result confirmed the improvement in the device performance. The device performance is reported in detail elsewhere [31].

#### 4. Summary

We observed the growth of the  $\text{Ga}_{0.80}\text{In}_{0.20}\text{N}$  (2 nm)/GaN (3 nm) SL by *in situ* XRD monitoring. The satellite peaks from the  $-1\text{st}$  to the  $+1\text{st}$  order can be obtained from these *in situ* XRD spectra. From the FWHMs of the 0th and  $-1\text{st}$  satellite peaks as a function of the SL periods, we observed a clear trend in each FWHM. Up to 25 periods, the FWHMs from the satellite peaks decreased with an increase in the period. We can theoretically describe this result. However, we confirmed that the FWHM did not continue to show this tendency and that it increased after  $\sim 25$  periods. This has been attributed to In segregation and misfit dislocations based on fluorescent microscopic and TEM analysis. Accordingly, if we employ *in situ* XRD under various growth conditions, the optimization of the growth conditions will become easier because it would be possible to determine the number of periods at which In segregation and misfit dislocations increase by

only one growth procedure. The *in situ* XRD monitoring system proposed herein enabled us to estimate the In segregation and misfit dislocations of the GaInN/GaN SL structure during growth. This implies that this *in situ* XRD observation is extremely effective for the optimization of the device performance.

#### Acknowledgments

This study was supported by the Ministry of Education, Culture, Sports, Science and Technology of Japan through the Supported Program for the Strategic Research Foundation at Private Universities, 2012–2016.

#### References

- [1] V.Y. Davydov, A.A. Klochikhin, R.P. Seisyan, V.V. Emtsev, S.V. Ivanov, F. Bechstedt, J. Furthmuller, H. Harima, A.V. Mudryi, J. Aderhold, O. Semichinova, J. Graul, Phys. Status Solidi B 229 (2002) R1.
- [2] B. Monemar, Phys. Rev. B10 (1974) 676.
- [3] R. Liu, J. Mei, S. Srinivasan, F.A. Ponce, H. Omiya, Y. Narukawa, T. Mukai, Appl. Phys. Lett. 89 (2006) 201911.
- [4] J. Wu, W. Walukiewicz, K.M. Yu, J.W. Ager III, E.E. Haller, H. Lu, W.J. Schaff, Y. Saito, Y. Nanishi, Appl. Phys. Lett. 80 (2002) 3967.
- [5] H. Hamzaoui, A.S. Bouazzi, B. Rezig, Sol. Energy Mater. Sol. Cells 87 (2005) 595.
- [6] M. Mori, S. Kondo, S. Yamamoto, T. Nakao, M. Iwaya, T. Takeuchi, S. Kamiyama, I. Akasaki, H. Amano, Jpn. J. Appl. Phys. 52 (2013) 08JH02.
- [7] Y. Kuwahara, Y. Fujiyama, M. Iwaya, S. Kamiyama, H. Amano, I. Akasaki, Phys. Status Solidi C 7 (2010) 1807.
- [8] T. Sugiyama, Y. Kuwahara, Y. Isobe, T. Fujii, K. Nonaka, M. Iwaya, T. Takeuchi, S. Kamiyama, I. Akasaki, H. Amano, Appl. Phys. Express 4 (2011) 015701.
- [9] Y. Kuwahara, T. Fujii, T. Sugiyama, D. Iida, Y. Isobe, Y. Fujiyama, Y. Morita, M. Iwaya, T. Takeuchi, S. Kamiyama, I. Akasaki, H. Amano, Appl. Phys. Express 4 (2011) 021001.
- [10] Y. Kuwahara, T. Fujii, Y. Fujiyama, T. Sugiyama, M. Iwaya, T. Takeuchi, S. Kamiyama, I. Akasaki, H. Amano, Appl. Phys. Express 3 (2010) 111001.
- [11] M. Mori, S. Kondo, S. Yamamoto, T. Nakao, T. Fujii, M. Iwaya, T. Takeuchi, S. Kamiyama, I. Akasaki, H. Amano, Appl. Phys. Express 5 (2012) 082301.
- [12] S. Yamamoto, M. Mori, Y. Kuwahara, T. Fujii, T. Nakao, S. Kondo, M. Iwaya, T. Takeuchi, S. Kamiyama, I. Akasaki, H. Amano, Phys. Status Solidi Rapid Res. Lett. 6 (2012) 145.
- [13] Y. Kawaguchi, M. Shimizu, K. Hiramatsu, N. Sawaki, Mater. Res. Soc. Symp. Proc. 449 (1997) 89.
- [14] K. Hiramatsu, Y. Kawaguchi, M. Shimizu, N. Sawaki, T. Zheleva, R.F. Davis, H. Tsuda, W. Taki, N. Kuwano, K. Oki, MRS Internet J. Nitride Semicond. Res. 2 (1997) 6. (article).
- [15] K.S. Ramaiah, Y.K. Su, S.J. Chang, C.H. Chen, F.S. Juang, H.P. Liu, I.G. Chen, Appl. Phys. Lett. 85 (2004) 401.
- [16] S. Nagahama, T. Yanamoto, M. Sano, T. Mukai, Jpn. J. Appl. Phys. 40 (2001) 3075.
- [17] H. Kurokawa, S. Kondo, S. Yamamoto, M. Mori, M. Iwaya, T. Takeuchi, S. Kamiyama, I. Akasaki, H. Amano, Phys. Status Solidi A (2013). (Submitted for publication).

- [18] J. Han, T.-B. Ng, R.M. Biefeld, M.H. Crawford, D.M. Follstaedt, *Appl. Phys. Lett.* 71 (1997) 3114.
- [19] J. Han, K.E. Waldrip, S.R. Lee, J.J. Figiel, S.J. Hearne, G.A. Petersen, S.M. Myers, *Appl. Phys. Lett.* 78 (2001) 67.
- [20] S.J. Hearne, J. Han, S.R. Lee, J.A. Floro, D.M. Follstaedt, E. Chason, I.S.T. Tsong, *Appl. Phys. Lett.* 76 (2000) 1534.
- [21] H. Amano, M. Iwaya, T. Kashima, M. Katsuragawa, I. Akasaki, J. Han, S. Hearne, J.A. Floro, E. Chason, *Jpn. J. Appl. Phys.* 37 (1998) L1540.
- [22] A. Kharchenko, K. Lischka, K. Schmidegg, H. Sitter, J. Bethke, J. Voitok, *Rev. Sci. Instrum.* 76 (2005) 033101.
- [23] C. Simbrunner, K. Schmidegg, A. Bonanni, A. Kharchenko, J. Bethke, J. Voitok, K. Lischka, H. Sitter, *Phys. Status Solidi A* 203 (2006) 1704.
- [24] T. Sasaki, H. Suzuki, A. Sai, J.-H. Lee, M. Takahasi, S. Fujikawa, K. Arafune, I. Kamiya, Y. Ohshita, M. Yamaguchi, *Appl. Phys. Express* 2 (2009) 085501.
- [25] M. Tabuchi, Y. Takeda, *J. Cryst. Growth* 298 (2007) 12.
- [26] D. Iida, M. Sowa, Y. Kondo, D. Tanaka, M. Iwaya, T. Takeuchi, S. Kamiyama, I. Akasaki, *J. Cryst. Growth* 361 (2012) 1.
- [27] D. Iida, Y. Kondo, M. Sowa, T. Sugiyama, M. Iwaya, T. Takeuchi, S. Kamiyama, I. Akasaki, *Phys. Status Solidi Rapid Res. Lett.* 7 (2013) 211.
- [28] H. Amano, N. Sawaki, I. Akasaki, Y. Toyoda, *Appl. Phys. Lett.* 48 (1986) 353.
- [29] S. Nakamura, *Jpn. J. Appl. Phys.* 30 (1991) L1705.
- [30] A. Segmuller, A.E. Blakeslee, *J. Appl. Cryst.* 6 (1973) 19.
- [31] T. Yamamoto, H. Kurokawa, D. Iida, Y. Kondo, M. Sowa, S. Umeda, M. Iwaya, T. Takeuchi, S. Kamiyama, I. Akasaki, *Jpn. J. Appl. Phys.* (2013). (Submitted for publication).

# Laser lift-off of AlN/sapphire for UV light-emitting diodes

Hiroki Aoshima<sup>\*1</sup>, Kenichiro Takeda<sup>1</sup>, Kosuke Takehara<sup>1</sup>, Shun Ito<sup>1</sup>, Mikiko Mori<sup>1</sup>, Motoaki Iwaya<sup>1</sup>, Tetsuya Takeuchi<sup>1</sup>, Satoshi Kamiyama<sup>1</sup>, Isamu Akasaki<sup>1,3</sup>, and Hiroshi Amano<sup>2,3</sup>

<sup>1</sup> Faculty of Science and Technology, Meijo University, Nagoya 468-8502, Japan

<sup>2</sup> Department of Electrical Engineering and Computer Science, Nagoya University, Nagoya 464-8603, Japan

<sup>3</sup> Akasaki Research Center, Nagoya University, Nagoya 464-8603, Japan

Received 1 August 2011, revised 12 October 2011, accepted 31 October 2011

Published online 14 February 2012

**Keywords** UV LED, laser lift-off

\* Corresponding author: e-mail 103434001@c alumni.meijo-u.ac.jp

We report on laser lift-off (LLO) of AlN/sapphire for UV light-emitting diodes (LEDs). Underfill between chip and submount is a key factor for the successful LLO of AlN/sapphire. We fabricated thin-film-flip-chip UV LEDs with a peak wavelength of 343 nm using the LLO.

Moreover surface texturing was carried out on the exfoliated AlN surface. The light output power from the UV LED after the LLO and the surface texture at exfoliated surface is 1.7 times higher than that before the LLO at 20 mA.

© 2012 WILEY-VCH Verlag GmbH & Co. KGaA, Weinheim

## 1 Introduction

UV light-emitting diodes (LEDs) are promising for various applications, such as bioagent detection, water and air purification, and dermatology [1]. Group III-nitride-based UV LEDs have been reported by several groups [2–6]. Although the internal quantum efficiencies (IQEs) of DUV/UV LEDs are higher than 70% by improving the crystalline quality of AlGaN [7], the external quantum efficiency (EQE) is still low. This is one of the most serious problems preventing the realization of high-efficiency devices. Therefore, technology for the improvement of the light extraction efficiency (LEE) is very important for high-efficiency DUV/UV-LEDs.

At present, there are many reports on improving the LEE in nitride-based LED by the laser lift-off (LLO) method [8], many of which are GaN/sapphire LLO, and the LLO of AlN/sapphire was few [9,10]. Moreover, details of the LLO conditions such as wavelength, irradiation condition, and implementation method have not been reported yet. In addition, LLO of AlN is considered to be more difficult than that of GaN, because the melting point of AlN is much higher and precipitated aluminum by LLO of AlN is difficult to remove.

In this study, we investigated LLO of AlN/sapphire in detail. We established the substrate separation of AlN/sapphire just by laser irradiation as a simple process. We also fabricated thin-film-flip-chip UV LEDs with a

peak wavelength of 343 nm by LLO. Moreover surface texturing was carried out at the exfoliated surface.

## 2 Experiments

UV LEDs were fabricated on a double side polished sapphire (0001) substrate by metal organic vapor phase epitaxy. First, we grew 2- $\mu\text{m}$ -thick AlN on a sapphire substrate at 1400 °C, then, a 2.5- $\mu\text{m}$ -thick Al<sub>0.25</sub>GaN<sub>0.75</sub> film was grown at 1100 °C. Next, the wafer was removed from the reactor, and grooves along the (1 $\bar{1}$ 00) direction were formed by conventional photolithography and reactive ion etching. The width, spacing, and depth of the grooves were 5, 5, and 1  $\mu\text{m}$ , respectively. Then, a thick Al<sub>0.25</sub>Ga<sub>0.75</sub>N layer was regrown for 4 h on the grooved underlying layer. The growth temperature and pressure during Al<sub>0.25</sub>Ga<sub>0.75</sub>N growth were 1100 °C and 6.6 $\times 10^4$  Pa, respectively. During the growth of the AlGa<sub>0.25</sub>N layer, the flow rates of TMGa, TMAI and ammonia were 0.030, 0.013, and 61 mmol/min, respectively. UV-LEDs were fabricated on this high-crystalline-quality AlGa<sub>0.25</sub>N underlying layer. Figure 1 shows a schematic of the device structure in this study. The thickness of the Si-doped n-Al<sub>0.25</sub>Ga<sub>0.75</sub>N layer was 4  $\mu\text{m}$ . Then, an unintentionally doped GaN (3 nm)/Al<sub>0.15</sub>Ga<sub>0.85</sub>N:Si (8 nm) three quantum well (QW) active layer, a p-Al<sub>0.5</sub>Ga<sub>0.5</sub>N (20 nm) blocking layer, a p-Al<sub>0.25</sub>Ga<sub>0.75</sub>N (50 nm) cladding layer, and a p-GaN (50 nm) contact layer were successively stacked. The size of the

LED was  $500 \times 500 \mu\text{m}^2$  with a p-contact area of  $500 \times 140 \mu\text{m}^2$ . After exposing the n-Al<sub>0.2</sub>Ga<sub>0.8</sub>N contact layer to Cl<sub>2</sub> RIE, a Ti/Al/Ti/Au (30/100/20/150 nm) contact was deposited on the exposed n-Al<sub>0.25</sub>Ga<sub>0.75</sub>N contact layer. The n-electrode annealing conditions were 800 °C in nitrogen ambient for 30 s. A Ni/Au (10/40 nm) contact pad was deposited on the p-GaN contact layer. The p-electrode annealing conditions were 550 °C in O<sub>2</sub> ambient for 1 min. The emission peak wavelength of the UV LED was 343 nm.

After dividing the above wafer into chips using scribing equipment, these chips were mounted with the flip-chip configuration using gold bumps. We prepared two samples with and without underfill as shown in Fig. 2. The underfill (U8437-2) was used to fill the gap between a device and a submount. Here, the major component of the underfill is epoxy resin. To remove the sapphire substrate, the LLO technique was used. An ArF pulsed excimer laser with a wavelength of 193 nm and pulse width of 15 ns was directed through the back of the transparent sapphire substrate. The laser light was absorbed at the interface between the AlN and the sapphire, and it will induce the decomposition of the AlN. The laser beam spot size was  $1 \times 2 \text{ mm}^2$ , which was slightly larger than the size of the flip-chip UV LED. Figure 3 shows the irradiated energy density vs yield rate. The yield rate was obtained from the result of experiments by changing the irradiated energy density per ten samples each. The best yield rate was obtained in the range where the irradiated energy density was higher than  $1.0 \text{ J/cm}^2$ . In this study, we employed the irradiated energy density was  $1.0 \text{ J/cm}^2$ , which was sufficiently high to perform LLO with one laser pulse. The devices were separated between the substrate and device only by the irradiation of the laser, unlike in the case of GaN/sapphire. Moreover, the radiation energy required to perform LLO of GaN has been reported that approximately  $0.26 \text{ J/cm}^2$  [11]. This difference in energy density are probably due to the decomposition temperature of AlN and GaN.

After the LLO, surface texturing will be carried out on the backside surface by hot aqueous potassium hydroxide (KOH) wet etching for the improvement of LEE. The wet etching condition was 100 °C for 1 min.

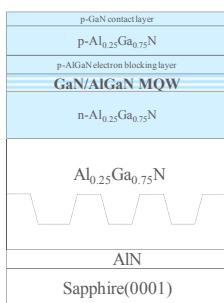


Figure 1 Structure of UV LED.

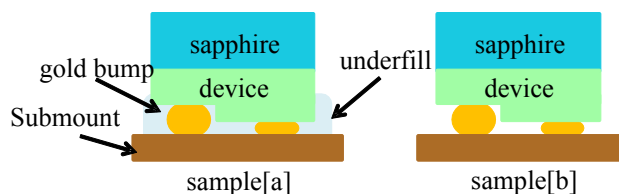


Figure 2 Flip-chip configuration with and without underfill.

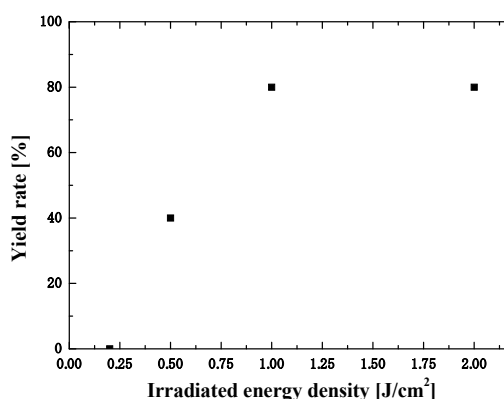


Figure 3 Irradiated energy density vs yield rate.

### 3 Results and discussion

Figures 4(a) and 4(b) show photographs of the sample after the LLO with and without the underfill, respectively. These results clearly show a significant difference between the samples with and without the underfill. While the sample without underfill was unintentionally chipped, the sample with underfill was successfully peeled off the sapphire substrate. We suspect that the physical shock by decomposition causes chip damage in the case without underfill. On the other hand, in the case with underfill, the device had no mechanical damage, because the UV LED had been completely fixed to the mounting substrate. Therefore, the underfill is useful to successfully perform the LLO.

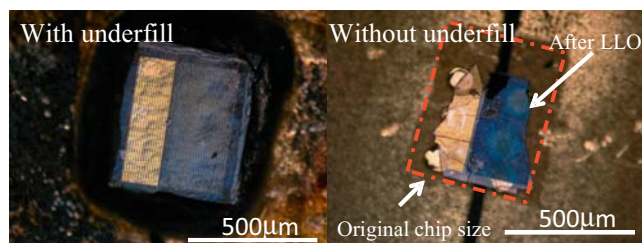
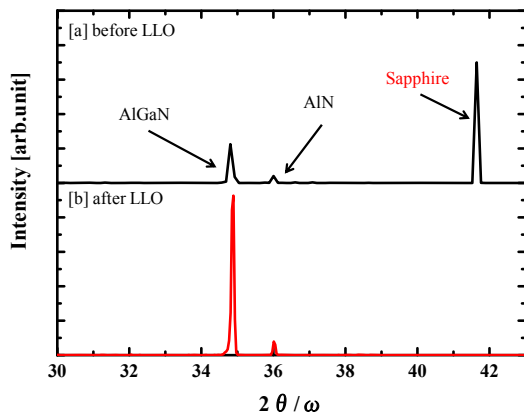


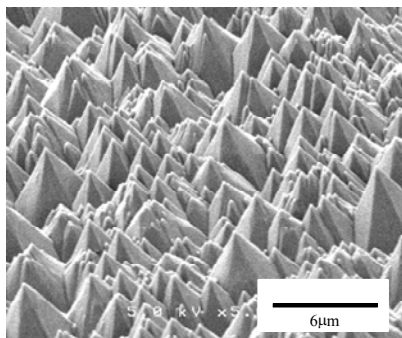
Figure 4 Photograph of UV-LED after LLO [left] with and [right] without underfill.



**Figure 5** (a) and (b) show  $2\theta$ - $\omega$  scan data from XRD before LLO and after LLO.

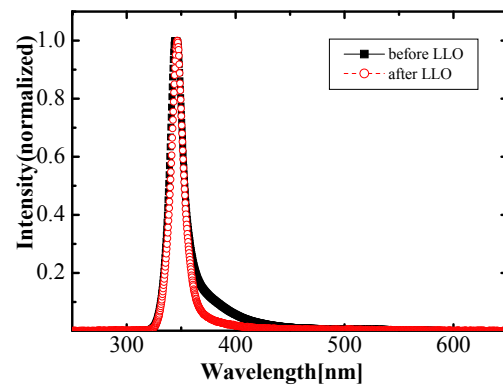
To confirm the backside materials before and after LLO, we measured X-ray diffraction (XRD) of the sample backside surfaces. Figures 5(a) and 5(b) show  $2\theta/\omega$  scan data from XRD before and after LLO, respectively. A strong peak from the sapphire substrate was observed in Fig. 5(a). In contrast, after LLO, no peak from the sapphire substrate was observed and intense AlGaIn and AlN peaks were observed. This XRD result indicates no sapphire was remained on the backside after the LLO.

Figure 6 shows an SEM image of an AlN surface of our samples after hot KOH wet etching at 100 °C. A large triangular texture was obtained. This texture structure is expected to improve the LLE in UV-LED.



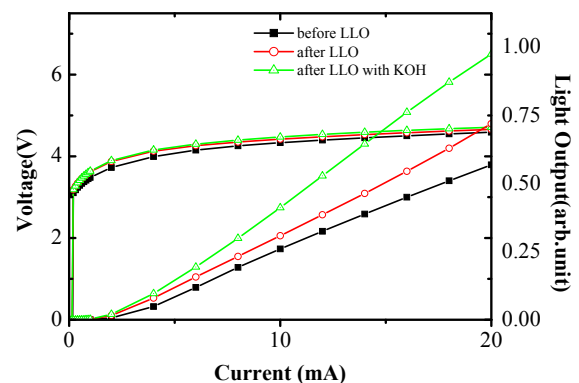
**Figure 6** SEM image of exfoliated AlN plane after KOH etching.

Figure 7 shows normalized electroluminescence (EL) spectra of UV LEDs before and after the LLO. The EL emission peaks from each device were 343 nm. The peak position and FWHM of the EL spectra are almost the same before and after the LLO. This result indicates that serious damage to the active layer was not introduced by the LLO.



**Figure 7** Normalized EL spectra before and after the LLO.

Figure 8 shows I-V and L-I curves of UV LEDs before the LLO, after the LLO, and after the LLO with KOH wet etching under DC bias condition. While the operating voltages are almost the same, the light output power after the LLO is 1.3 times higher than that before the LLO. This improvement probably comes from the surface roughness after the LLO, as shown in the SEM image (Fig. 9). As a result, we did not clearly observe the damage in the performances of the UV LED. Also, the light output power after the LLO with KOH wet etching is 1.7 times higher than that before the LLO at 20 mA current injection. This result indicates that the LLE was improved and no damage was introduced by LLO and KOH etching.



**Figure 8** V-I and L-I curves of UV LEDs before LLO, after LLO, and after the LLO with KOH wet etching.

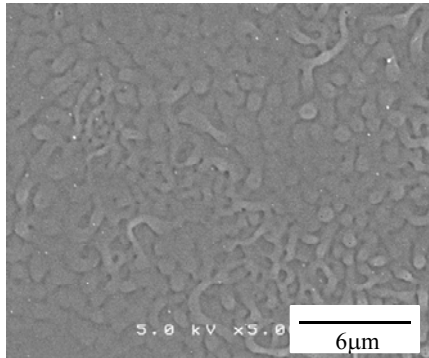


**Figure 9** Surface SEM image of exfoliated AlN plane after the LLO.

#### 4 Conclusions

We have achieved the LLO of AlN/sapphire and the surface texture fabricated by wet etching for higher extraction efficiency. Underfill is a key to successfully implement the LLO of AlN/sapphire. The light extraction efficiency of the UV-LEDs was also improved by 1.7 times by a combination of LLO and KOH etching.

#### References

- [1] H. Hirayama, *J. Appl. Phys.* **97**, 091101 (2005).
- [2] C. Pernot, M. Kim, S. Fukahori, T. Inazu, T. Fujita, Y. Nagasawa, A. Hirano, M. Ippommatsu, M. Iwaya, S. Kamiyama, I. Akasaki, and H. Amano, *Appl. Phys. Express* **3**, 061004(2010).
- [3] H. Tsuzuki, F. Mori, K. Takeda, M. Iwaya, S. Kamiyama, H. Amano, I. Akasaki, H. Yoshida, M. Kuwabara, Y. Yamashita, and H. Kan, *J. Cryst. Growth* **311**, 2860 (2009).
- [4] Y. Taniyasu, M. Kasu, and T. Makimoto, *Nature* **441**, 325 (2006).
- [5] D. Morita, M. Sano, M. Yamamoto, T. Murayama, S. Nagahama, and T. Mukai, *Jpn. J. Appl. Phys.* **41**, L 1434 (2002).
- [6] A. Khan, K. Balakrishnan, and T. Katona, *Nature Photon.* **2**, 77 (2008).
- [7] K. Ban, J. Yamamoto, K. Takeda, K. Ide, M. Iwaya, T. Takeuchi, S. Kamiyama, I. Akasaki, and H. Amano, *Appl. Phys. Express* **4**, 052101 (2011).
- [8] T. Fujii, Y. Gao, R. Sharma, E. L. Hu, S. P. DenBaars, and S. Nakamura, *Appl. Phys. Lett.* **84**, 855 (2004).
- [9] S. Hwang, D. Morgan, A. Kesler, M. Lachab, B. Zhang, A. Heidari, H. Nazir, I. Ahmad, J. Dion, Q. Fareed, V. Adivarahan, M. Islam, and A. Khan, *Appl. Phys. Express* **4**, 032102 (2011).
- [10] V. Adivarahan, A. Heidari, B. Zhang, Q. Fareed, M. Islam, S. Hwang, K. Balakrishnan, and A. Khan, *Appl. Phys. Express* **2**, 092102 (2009).
- [11] T. Ueda, M. Ishida, S. Tamura, Y. Fujimoto, M. Yuri, T. Saito, and D. Ueda, *Phys. Status Solidi C* **0**(7), 2219 (2003).

## Study on Efficiency Component Estimation of 405 nm Light Emitting Diodes from Electroluminescence and Photoluminescence Intensities

This content has been downloaded from IOPscience. Please scroll down to see the full text.

2013 Jpn. J. Appl. Phys. 52 08JL16

(<http://iopscience.iop.org/1347-4065/52/8S/08JL16>)

View [the table of contents for this issue](#), or go to the [journal homepage](#) for more

Download details:

IP Address: 202.11.1.201

This content was downloaded on 03/03/2017 at 06:55

Please note that [terms and conditions apply](#).

You may also be interested in:

[Improvement of Light Extraction Efficiency for AlGaIn-Based Deep Ultraviolet Light-Emitting Diodes](#)

Tetsuhiko Inazu, Shinya Fukahori, Cyril Pernot et al.

[Investigation of Light Extraction Efficiency and Internal Quantum Efficiency in High-Power Vertical Blue Light-Emitting Diode with 3.3 W Output Power](#)

Tak Jeong, Jong-Hyeob Baek, Ki Chang Jeong et al.

[Stress Engineering by Controlling Sapphire Substrate Thickness in 520 nm GaN-Based Light-Emitting Diodes](#)

Wael Z. Tawfik, Seo-Jung Bae, Seung Bae Yang et al.

[AlGaIn Deep-Ultraviolet Light-Emitting Diodes with External Quantum Efficiency above 10%](#)

Max Shatalov, Wenhong Sun, Alex Lunev et al.

[High Power Efficiency AlGaIn-Based Ultraviolet Light-Emitting Diodes](#)

Thorsten Passow, Richard Gutt, Michael Kunzer et al.

[Effect of Internal Electric Field in Well Layer of InGaIn/GaN Multiple Quantum Well Light-Emitting Diodes on Efficiency Droop](#)

Sang-Heon Han, Dong-Yul Lee, Jin-Young Lim et al.

[Mechanism on Effect of Surface Plasmons Coupling with InGaIn/GaN Quantum Wells: Enhancement and Suppression of Photoluminescence Intensity](#)

Zengli Huang, Jianfeng Wang, Zhenghui Liu et al.

[Quantum Efficiency Analysis of Near-Ultraviolet Emitting AlGaIn and AlInGaIn Structures](#)

Carsten Netzel, Arne Knauer and Markus Weyers

## Study on Efficiency Component Estimation of 405 nm Light Emitting Diodes from Electroluminescence and Photoluminescence Intensities

Kazuki Aoyama<sup>1\*</sup>, Atsushi Suzuki<sup>2</sup>, Tsukasa Kitano<sup>2</sup>, Satoshi Kamiyama<sup>1</sup>, Tetsuya Takeuchi<sup>1</sup>, Motoaki Iwaya<sup>1</sup>, and Isamu Akasaki<sup>1,3</sup>

<sup>1</sup>Faculty of Science and Technology, Meijo University, Nagoya 468-0073, Japan

<sup>2</sup>El-seed, Nagoya 468-0073, Japan

<sup>3</sup>Akasaki Research Center, Nagoya University, Nagoya 464-8603, Japan

Received October 24, 2012; revised March 21, 2013; accepted March 22, 2013; published online July 22, 2013

The Shockley–Read–Hall (SRH) model was applied to the determination of photoluminescence (PL) and electroluminescence (EL) characteristics. From the ratio of the internal quantum efficiency (IQE) obtained from the PL and EL intensities, the carrier injection efficiencies (CIE) for 405 nm LEDs were derived. All the efficiency components including the IQE, CIE, and light extraction efficiency for 405 nm LEDs were obtained for various structural parameters by fitting the experimental data to theoretical equations of the SRH model.

© 2013 The Japan Society of Applied Physics

### 1. Introduction

The external quantum efficiency (EQE) of LEDs is the most commonly used and important value, because it can be easily measured. However, it is a product of the internal quantum efficiency (IQE), carrier injection efficiency (CIE), and light extraction efficiency (LEE). Therefore, each of them should be properly clarified to understand the physics of device operation. For the estimation of IQE, the determination of temperature-dependent PL intensity<sup>1)</sup> and the application of the Shockley–Read–Hall (SRH) model to the evaluation of EL intensity versus current characteristic<sup>2)</sup> have been reported. In the former approach, the determination of PL excitation similarly to that in LED operation is difficult. For the latter case, the obtained IQE is a type of nominal IQE including CIE. Therefore, the components of the actual IQE and CIE cannot be derived. Estimation of CIE as the ratio of the IQE for electroluminescence (EL) to that for photoluminescence (PL) obtained using the SRH model has been reported for an AlGaIn/GaN ultraviolet laser diode.<sup>3)</sup>

However, the CIE for visible LEDs has not been investigated because it is not thought to be a significant issue. For the optimization of device structures, understanding of the CIE and other efficiency components will be very useful.

In this study, we applied the SRH model to determination of PL and EL characteristics, and derived the IQE, CIE, and LEE in 405 nm LEDs for various AlN molar fractions in the p-AlGaIn electron-blocking layer.

### 2. Estimation of CIE by SRH Model

In the SRH model, the nonradiative recombination factor  $A$ , radiative recombination factor  $B$ , and droop factor  $C$  are included as functions of the carrier density  $n$ .  $C$  is the droop factor including the carrier overflow and Auger recombination. However, it is known that the droop is negligibly small in optimized 405 nm LEDs;<sup>4)</sup> therefore, the droop is thought to be only caused by the carrier overflow in unoptimized heterostructures in 405 nm devices. In the case of EL, electron excitation is calculated from the current injection as follows:<sup>2)</sup>

$$\frac{J}{qd} = An + Bn^2 + Cn^3, \quad (1)$$

where  $J$  is the injected current density into the device,  $q$  is the electron charge, and  $d$  is the total width of the quantum well (QW). Optical excitation is used for the determination of PL characteristic, where the rate of generation ( $G$ ) by photo excitation is expressed by<sup>5)</sup>

$$G = An + Bn^2. \quad (2)$$

The third component in Eq. (1) is neglected, because there is no carrier overflow in photo excitation. The light intensities of EL and PL are defined as

$$L = k_c B, \quad (3)$$

$$I_{\text{PL}} = \eta Bn^2, \quad (4)$$

where  $k_c$  and  $\eta$  are the sensitivity and a proportional constant, respectively. Substituting Eqs. (3) and (4) into Eqs. (1) and (2), respectively, the following equations are obtained:

$$J = \alpha L^{1/2} + \beta L + \gamma L^{3/2}, \quad (5a)$$

$$G = P_1 \sqrt{I_{\text{PL}}} + P_2 I_{\text{PL}}, \quad (6a)$$

where

$$\alpha = \frac{qdA}{(k_c B)^{1/2}}, \quad \beta = \frac{qd}{k_c}, \quad \gamma = \frac{qdC}{(k_c B)^{3/2}}, \quad (5b)$$

$$P_1 = \frac{A}{\sqrt{B\eta}}, \quad P_2 = \frac{1}{\eta}. \quad (6b)$$

In the case of experimental PL, a nominal generation rate  $G$  is expressed by

$$G = \frac{P_{\text{laser}}(1-R)\alpha l}{A_{\text{spot}}h\nu} = \frac{P_{\text{laser}}(1-R)\alpha}{A_{\text{spot}}h\nu}, \quad (7)$$

where  $P_{\text{laser}}$  is the excitation power density,  $R$  is the Fresnel reflectivity,  $\alpha$  is the absorption coefficient,  $l$  is the total width of the QW, and  $h\nu$  is the photon energy of the excitation source. These parameters such as  $\alpha$ ,  $\beta$ ,  $\gamma$ ,  $P_1$ , and  $P_2$ , were obtained by fitting of theoretical and experimental curves of the output versus carrier density characteristic for EL and the light output versus generation rate characteristic for PL. The absorption coefficients for GaN and InN were assumed to be  $2.0 \times 10^5 \text{ cm}^{-1}$  (Ref. 6) and  $1.5 \times 10^5 \text{ cm}^{-1}$  (Ref. 7), respectively. That of the GaInN QW active layer was  $1.29 \times 10^5 \text{ cm}^{-2}$ , obtained from Vegard's law using the values of the binary materials. Since the excitation source

was a He–Cd laser with a wavelength of 325 nm, carriers were generated not only in the QWs but also in the whole layer, and carriers flow into QWs from neighboring layers. Therefore, Eq. (7) could not be used for the estimation of net  $G$  and related parameters. However, we used the nominal  $G$  to draw the curves of  $I_{PL}$  as a function of  $G$ , and fit Eq. (6a) to the curve to obtain the parameters  $P_1$  and  $P_2$ , which are also the nominal values. In this fitting, these curves are almost identical in the lower carrier density range because of the small contribution of the  $C$  component in Eq. (1). Then, the IQEs for EL and PL excitation were calculated by substitution of the parameters as described above into

$$IQE_{EL} = \frac{Bn^2}{An + Bn^2 + Cn^2} = \beta \frac{L}{J}, \quad (8)$$

$$IQE_{PL} = \frac{Bn^2}{An + Bn^2} = \frac{Bn^2}{G} = P_2 \frac{I_{PL}}{G}. \quad (9)$$

Although  $G$  and  $P_2$  are nominal values, as mentioned above, the ratio of  $P_2$  to  $G$  in Eq. (9) does not include the uncertainty of the excitation. The ratio of  $IQE_{EL}$  to  $IQE_{PL}$  represents CIE. LEE was calculated as the ratio of the experimental EQE to  $IQE_{EL}$ .

### 3. Experimental Procedure

Firstly, the estimation of efficiency components for two types of 405 nm LED with different LEEs was examined. From the same LED epitaxial wafer, an LED with Ni/Au as a p-type electrode and an LED with ITO<sup>8)</sup> as a p-type electrode were fabricated.

Secondly, 405 nm LEDs with an ITO electrode and different AlN molar fractions of 0, 15, and 25% in the p-AlGaIn electron-blocking layer (EBL) were fabricated,<sup>9)</sup> and the efficiency components of the devices were examined. All the LED samples have a multiple quantum well (MQW) active layer composed of five QWs, where the widths of the QW and barrier layer are fixed at 2.8 and 12 nm, respectively. In addition, the samples with AlN molar fractions of 15 and 25% have an EBL with a thickness of 30 nm.

The LED chips were mounted on TO headers without resin encapsulation, as shown in Fig. 1, and their EL properties were measured using an integrated sphere. Their PL properties were measured using the excitation source of a 325 nm He–Cd laser and a cooled Si-CCD-type photodetector.

### 4. Results and Discussion

Figures 2(a) and 2(b) show the curve-fitting results of EL and PL measurements for LEDs with ITO and Ni/Au p-electrodes, respectively. The theoretical curves obtained with Eqs. (5a) and (5b) can be made to closely fit the experimental ones by adjusting the fitting parameters  $\alpha$ ,  $\beta$ ,  $\gamma$ ,  $P_1$ , and  $P_2$ . The modified carrier density in the PL measurement is determined by fitting the curve of  $IQE_{PL}$  versus carrier density to the curve of  $IQE_{EL}$  versus carrier density in the low-excitation range as shown in Fig. 3. Also, Fig. 3 shows the fitting results of samples with AlN molar fractions of 0, 15, and 25%. From these results, the efficiency components when the carrier density was injected at 50 mA in this sample structure were obtained, as shown in Table I. The LEE of the ITO device is about 15%, which

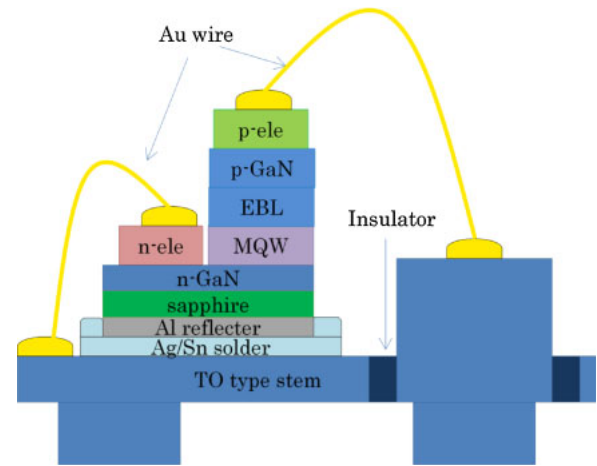
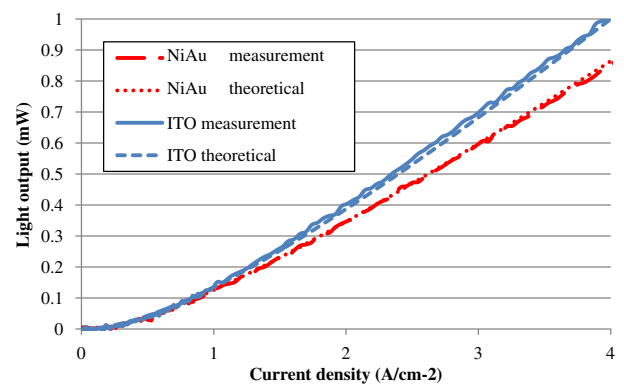
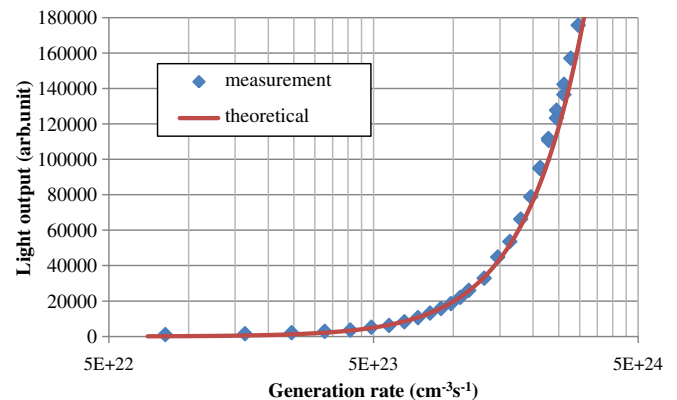


Fig. 1. (Color online) Samples structure.



(a)



(b)

Fig. 2. (Color online) Fitting results for (a) EL and (b) PL.

is much higher than that of the Ni/Au device. This is reasonable because ITO has a very low light absorption. The values of  $IQE_{EL}$  and CIE for the two types of LED were consistent because they originated from the same epitaxial wafer. Accordingly, these efficiency components are thought to be reasonable, indicating the usefulness of our estimation model.

For the LEDs with different AlN molar fractions, the same procedure as above was carried out. Figure 4 shows the CIEs of the three LEDs as a function of carrier density. For the devices with AlN molar fractions of 15 and 25%, the CIE at

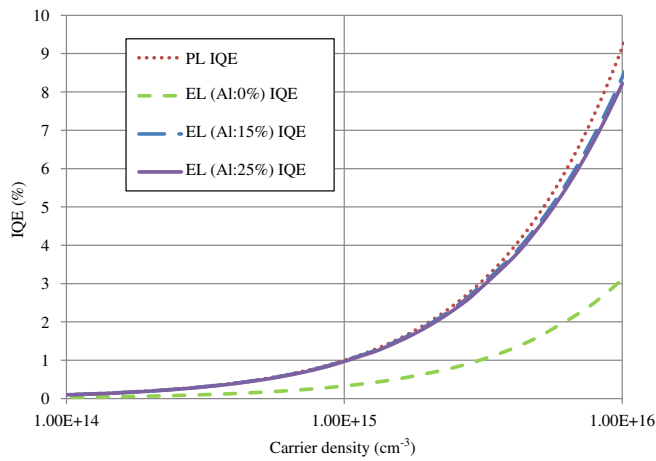


Fig. 3. (Color online) Fitting results for  $IQE_{EL}$  and  $IQE_{PL}$ .

Table I. Comparison of EQE,  $IQE \times CIE$ , and LEE for LEDs with ITO electrode and Ni/Au electrode as p-electrode (injection current is 50 mA).

	ITO device	Ni/Au device
EQE	9.1	7.1
$IQE_{EL}$	57.1	56.3
$IQE_{PL}$	94.8	94.8
LEE	15.9	12.5
CIE	62.6	61.0

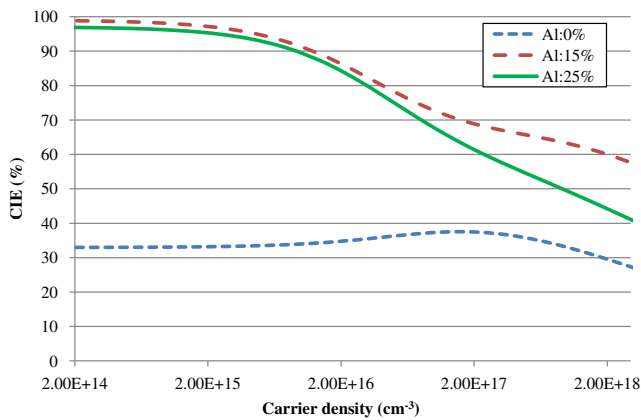


Fig. 4. (Color online) Carrier density dependence of CIE.

a low carrier density was almost 100% and decreased with increasing carrier density. The CIE of the LED with an AlN molar fraction of 15% slowly decreases with increasing carrier density. However, the LED with an AlN molar fraction of 0% exhibits a very low CIE even at low carrier densities. This may contain some measurement error. The PL measurement was carried out for only one sample, since the active layer is assumed to be uniform over the 2-in. LED wafer. However,  $IQE_{EL}$  and  $IQE_{PL}$  were not thought to be agreed with each other, indicating that fitting errors may be involved. At high carrier densities, the CIE of this device is considered to be reliable. All the efficiency components in this series of LEDs when the carrier density was injected at

Table II. Comparison of efficiency components for LEDs with AlN molar fractions of 0, 15, and 25% in p-AlGaIn electron-blocking layer (injection current is 50 mA).

	AlN 0%	AlN 15%	AlN 25%
EQE	3.7	9.1	6.1
$IQE_{EL}$	23.3	57.1	39.6
$IQE_{PL}$	94.8	94.8	94.8
LEE	15.9	15.9	15.4
CIE	30.1	62.6	45.0

50 mA in this sample structure are summarized in Table II. Although the CIE is strongly dependent on the AlN molar fraction in the p-AlGaIn electron-blocking layer, the LEEs in this series are almost the same. This result is also reasonable. Our estimation model for the efficiency components appears to be reliable for various types of LED.

### 5. Conclusions

The SRH model was applied to 405 nm LEDs. The CIE was derived from the ratio of the two types of IQE for the EL and PL intensities. These efficiency components were estimated for two series of LEDs. The efficiency components of LEDs with Ni/Au and ITO electrodes as p-electrodes were compared. It was found that the LEE of the LED with the ITO electrode was higher than that of the device with the Ni/Au electrode, while  $IQE_{EL}$  and CIE for the two types of LED were consistent. The efficiency components of LEDs with AlN molar fractions of 0, 15, and 25% in the p-AlGaIn electron-blocking layer were also compared. Although CIE is strongly dependent on the AlN molar fraction in the p-AlGaIn electron-blocking layer. The LEEs in this series are almost the same. These results are reasonable. Therefore, derivation of the efficiency components by this approach is considered to be useful for understanding device physics.

### Acknowledgment

This study was supported by Ministry of Education, Culture, Sports, Science and Technology Supported Program for the Strategic Research Foundation at Private Universities, 2012–2016.

- 1) Y.-L. Li, Y.-R. Huang, and Y.-H. Lai: *Appl. Phys. Lett.* **91** (2007) 181113.
- 2) H. Yoshida, M. Kuwabara, Y. Yamashita, K. Uchiyama, and H. Kan: *Appl. Phys. Lett.* **96** (2010) 211122.
- 3) K. Nagata, K. Takeda, Y. Oshimura, K. Takehara, H. Aoshima, S. Ito, M. Iwaya, T. Takeuchi, S. Kamiyama, I. Akasaki, H. Amano, H. Yoshida, M. Kuwabara, Y. Yamashita, and H. Kan: *Phys. Status Solidi C* **8** (2011) 2384.
- 4) Y. Narukawa, I. Niki, K. Izuno, M. Yamada, Y. Murazaki, and T. Mukai: *Jpn. J. Appl. Phys.* **41** (2002) L371.
- 5) Q. Dai, M. F. Schubert, M. H. Kim, J. K. Kim, E. F. Schubert, D. D. Koleske, M. H. Crawford, S. R. Lee, A. J. Fischer, G. Thaler, and M. A. Banas: *Appl. Phys. Lett.* **94** (2009) 111109.
- 6) J. F. Muth, J. H. Lee, I. K. Shmagin, R. M. Kolbas, H. C. Casey, Jr., B. P. Keller, U. K. Mishra, and S. P. DenBaars: *Appl. Phys. Lett.* **71** (1997) 2572.
- 7) J. W. Trainor and K. Rose: *J. Electron. Mater.* **3** (1974) 821.
- 8) A. El Amrani, F. Hijazi, B. Lucas, J. Bouclé, and M. Aldissi: *Thin Solid Films* **518** (2010) 4582.
- 9) O. Svensk, P. T. Törmä, S. Suihkonen, M. Ali, H. Lipsanen, M. Sopanen, M. A. Odnoblyudov, and V. E. Bougrov: *J. Cryst. Growth* **310** (2008) 5154.

## Room-temperature CW operation of a nitride-based vertical-cavity surface-emitting laser using thick GaInN quantum wells

This content has been downloaded from IOPscience. Please scroll down to see the full text.

2016 Jpn. J. Appl. Phys. 55 05FJ11

(<http://iopscience.iop.org/1347-4065/55/5S/05FJ11>)

View [the table of contents for this issue](#), or go to the [journal homepage](#) for more

Download details:

IP Address: 219.127.71.134

This content was downloaded on 03/03/2017 at 06:42

Please note that [terms and conditions apply](#).

You may also be interested in:

[GaN-based vertical cavity surface emitting lasers with periodic gain structures](#)

Kenjo Matsui, Yugo Kozuka, Kazuki Ikeyama et al.

[Room-temperature continuous-wave operation of GaN-based vertical-cavity surface-emitting lasers with n-type conducting AlInN/GaN distributed Bragg reflectors](#)

Kazuki Ikeyama, Yugo Kozuka, Kenjo Matsui et al.

[Room-temperature continuous-wave operation of GaN-based vertical-cavity surface-emitting lasers fabricated using epitaxial lateral overgrowth](#)

Shouichiro Izumi, Noriyuki Fuutagawa, Tatsushi Hamaguchi et al.

[Lateral carrier confinement of GaN-based vertical-cavity surface-emitting diodes using boron ion implantation](#)

Tatsushi Hamaguchi, Hiroshi Nakajima, Masamichi Ito et al.

[Self-consistent model of 650 nm GaInP/AlGaInP QW VCSELs](#)

ukasz Piskorski, Robert P Sarzaa and Wodzimierz Nakwaski

[InGaN light-emitting diodes with embedded nanoporous GaN distributed Bragg reflectors](#)

Bing-Cheng Shieh, Yuan-Chang Jhang, Kun-Pin Huang et al.

[InGaN-based violet laser diodes](#)

S Nakamura

[Investigation of the effect of nitride-based LEDs fabricated using hole injection layer at different growth temperatures](#)

Shih-Wei Wang, Chun-Kai Wang, Shoou-Jinn Chang et al.



## Room-temperature CW operation of a nitride-based vertical-cavity surface-emitting laser using thick GaInN quantum wells

Takashi Furuta<sup>1\*</sup>, Kenjo Matsui<sup>1</sup>, Kosuke Horikawa<sup>1</sup>, Kazuki Ikeyama<sup>1</sup>, Yugo Kozuka<sup>1</sup>, Shotaro Yoshida<sup>1</sup>, Takanobu Akagi<sup>1</sup>, Tetsuya Takeuchi<sup>1</sup>, Satoshi Kamiyama<sup>1</sup>, Motoaki Iwaya<sup>1</sup>, and Isamu Akasaki<sup>1,2</sup>

<sup>1</sup>Faculty of Science and Technology, Meijo University, Nagoya 468-8502, Japan

<sup>2</sup>Graduate School of Engineering and Akasaki Research Center, Nagoya University, Nagoya 464-8603, Japan

Received November 5, 2015; accepted January 22, 2016; published online April 19, 2016

We demonstrated a room-temperature (RT) continuous-wave (CW) operation of a GaN-based vertical-cavity surface-emitting laser (VCSEL) using a thick GaInN quantum well (QW) active region and an AlInN/GaN distributed Bragg reflector. We first investigated the following two characteristics of a 6 nm GaInN 5 QWs active region in light-emitting diode (LED) structures. The light output power at a high current density ( $\sim 10$  kA/cm<sup>2</sup>) from the 6 nm GaInN 5 QWs was the same or even higher than that from standard 3 nm 5 QWs. In addition, we found that hole injection into the farthest QW from a p-layer was sufficient. We then demonstrated a GaN-based VCSEL with the 6 nm 5 QWs, resulting in the optical confinement factor of 3.5%. The threshold current density under CW operation at RT was 7.5 kA/cm<sup>2</sup> with a narrow (0.4 nm) emission spectrum of 413.5 nm peak wavelength. © 2016 The Japan Society of Applied Physics

### 1. Introduction

III-nitrides and their alloys with direct bandgaps cover a broad range of operating wavelengths. After the first demonstration of nitride-based pn-junction LEDs in 1989, GaInN-based LEDs and lasers were successively achieved.<sup>1–3</sup> Now, GaInN-based edge-emitting lasers are operating from ultraviolet to green regions.<sup>4–7</sup> On the other hand, vertical-cavity surface-emitting lasers (VCSELs) were invented by Soda et al. in 1979, and the advantages of the VCSELs are low power consumption and two-dimensional arrays.<sup>8</sup> Thus far, the power conversion efficiency of infrared VCSELs reached 62%.<sup>9</sup> Recently, nitride-based VCSELs have also been achieved,<sup>10–16</sup> and expected to be utilized in retinal scanning displays, adaptive laser headlights, and visible light communication systems. However, further improvements of nitride-based VCSELs are required for practical use. The nitride-based VCSELs still have a much higher threshold current density than the infrared VCSELs.<sup>17</sup>

One of the possible reasons for the high threshold current density is the low optical confinement factor caused by thin quantum wells (QWs) in the nitride-based VCSELs. Generally, in infrared VCSELs, an 8 nm 3 QW active region is used within a  $1\lambda$ -cavity, resulting in a more than 3% optical confinement factor.<sup>17</sup> On the other hand, in nitride-based light-emitting devices, a thin (less than 3 nm) GaInN QW active region has been typically used to prevent a small overlap between electron and hole wave functions due to piezoelectric polarization fields in the wells.<sup>18</sup> If the active region with 3 nm GaInN 5 QWs is used in a  $4\lambda$ -cavity, the optical confinement factor is calculated to be only 2%. Note that such a large cavity length should be used for the nitride-based VCSELs since an intracavity contact structure must be used owing to the absence of conductive distributed Bragg reflectors (DBRs), and this situation aggravates the low optical confinement factor. The use of thick GaInN QWs certainly results in the improvement of the optical confinement factor, but also leads to a couple of issues related to carrier injections. One of the issues is the small overlap between electron and hole wave functions in the GaInN QWs as mentioned above. Another is poor carrier injections, especially hole injections, into the farthest QW from a

p-layer.<sup>19–22</sup> Nitride-based materials have largely asymmetric carrier properties, such as effective mass and mobility, between electrons and holes; thus, the issue is more serious than in the case of the other III–V semiconductor materials.

In this study, we first calculated the GaInN well width dependence on the optical confinement factor in the nitride-based VCSELs. Then, we experimentally measured the light output power of 6 nm GaInN 5 QWs in an LED structure in comparison with that of 3 nm 5 QWs to investigate the effect of thick QWs on the light output power, in other words, the overlap between electron and hole wave functions in the QWs. We also prepared an LED with specific 6 nm GaInN 5 QWs in which 4 QWs were emitting 405 nm wavelength and the farthest QW from a p-layer was emitting 425 nm wavelength. This is to determine whether the hole injection into the farthest QW was sufficient by comparing the 425 and 405 nm intensities from the LED. The device characteristic measurements were carried out at a very high current density to investigate the situation under a possible VCSEL operation. Finally, we demonstrated a room-temperature (RT) continuous-wave (CW) operation of a nitride-based VCSEL containing 6 nm GaInN 5 QWs and a  $4\lambda$ -cavity with an AlInN/GaN DBR.

### 2. Experimental methods

Figure 1 shows calculated optical confinement factors as a function of GaInN well width. A VCSEL structure in the calculation consisted of a GaN substrate, a 40-pair AlInN/GaN DBR, a  $4\lambda$ -cavity, and an 8-pair SiO<sub>2</sub>/Nb<sub>2</sub>O<sub>5</sub> DBR. The  $4\lambda$ -cavity contained a 300 nm n-GaN layer, GaInN/6 nm GaN 5 QWs, a 15 nm p-AlGaIn electron-blocking (EB) layer, a 60 nm p-GaN layer, a 10 nm p<sup>++</sup>-GaN contact, a 20 nm indium–tin oxide (ITO) p-contact, and a 30 nm Nb<sub>2</sub>O<sub>5</sub> spacer. The thicknesses of the layers were designed for a wavelength of 410 nm. Note that this structure is identical to that of a VCSEL fabricated and measured later. We calculated the optical power distribution in the cavity and DBRs, and then estimated the ratio of optical power in all the QWs to that in the cavity/DBRs. A 2.0% optical confinement factor was estimated in the case of 3 nm 5 QWs, while a 3.5% optical confinement factor was obtained in the case of 6 nm 5 QWs. Thus, the calculation result suggests that 6 nm QWs have a

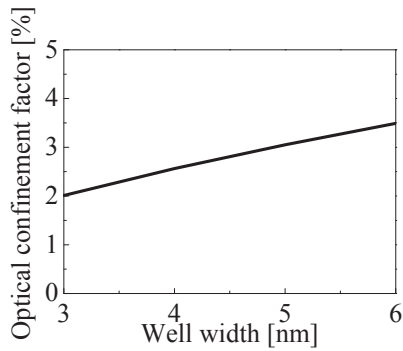


Fig. 1. Calculated optical confinement factors of a nitride-based VCSEL as a function of well width.

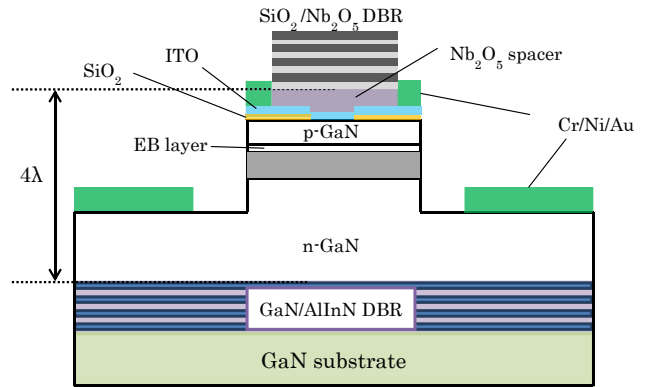


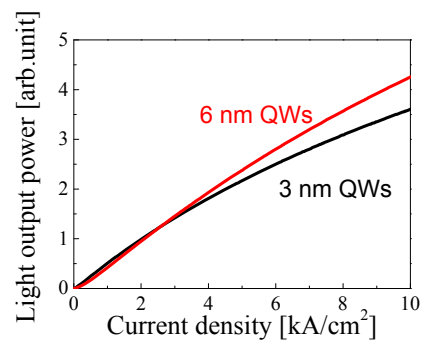
Fig. 2. (Color online) Schematic view of our VCSEL with 6 nm 5 QWs and an AlInN/GaN DBR.

high optical confinement factor, which is comparable to that of infrared VCSELs (~4%).<sup>17)</sup> Thus, we decided to use 6 nm 5 QWs in the following experiments.

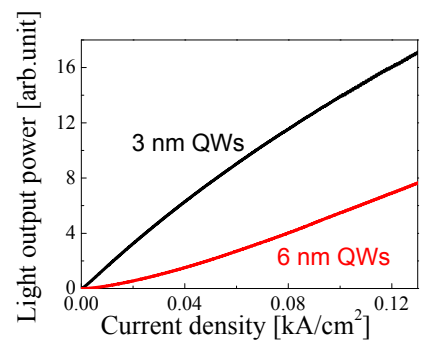
Next, we fabricated two LED test structures (Samples A and B) in order to investigate the effect of thick well width on light output power, in other words, an overlap between electron and hole wave functions. In this study, the LED test structures were grown on *c*-plane sapphire substrates by metal-organic chemical vapor deposition (MOCVD). The test structure consisted of a 30 nm low-temperature-deposited buffer layer, a 2 μm undoped GaN layer, a 0.4 μm n-type GaN layer, a GaInN/GaN 5 QW active region, a 15 nm p-type AlGaIn EB layer, a 60 nm p-type GaN layer, and a 10 nm p<sup>++</sup>-GaN contact. Sample A contained 6 nm GaInN/6 nm GaN 5 QWs and Sample B contained 3 nm GaInN/6 nm GaN 5 QWs. The peak wavelengths of both the 5 QWs were adjusted to be 405 nm. After the epitaxial growth, LEDs were fabricated with the wafers by our standard fabrication process. The emission area of the LEDs was 15 μm in diameter for the LED characteristic measurements under high current densities, which is comparable to that in a possible VCSEL operation. A transparent 20 nm ITO p-electrode was formed on top of the p-GaN contact layer, while a Cr/Ni/Au multilayer was used as both an n-electrode and a p-pad electrode. Standard 300 μm<sup>2</sup> LEDs were also fabricated for measurement under low current densities.

Another LED test structure (Sample C) with specific 6 nm GaInN 5 QWs was also prepared.<sup>19–23)</sup> The specific GaInN 5 QWs consisted of 4 QWs emitting a 405 nm peak wavelength and the remaining QW emitting a 425 nm peak wavelength, which is located at the farthest position from the p-AlGaIn EB layer (nearest to the n-GaN layer) in order to evaluate hole injection into the farthest QW by monitoring an emission intensity of not only 405 nm but also 425 nm. The two differently sized LEDs mentioned above were also prepared.

Finally, we fabricated VCSELs with 6 nm GaInN 5 QWs as shown in Fig. 2. The VCSEL structure was grown on a GaN substrate by MOCVD, in the same manner as that described in the optical confinement factor calculation. Note that the 40-pair AlInN/GaN DBR showed 99.7% reflectivity at around 410 nm as measured with an absolute reflectivity measurement system. The size of the VCSEL was defined by an 8-μm-diameter SiO<sub>2</sub> aperture. A transparent 20 nm ITO p-electrode was formed on the SiO<sub>2</sub> aperture. In addition, a Nb<sub>2</sub>O<sub>5</sub> spacer layer and an 8-pair SiO<sub>2</sub>/Nb<sub>2</sub>O<sub>5</sub> DBR were deposited on the ITO p-electrode to form the VCSEL cavity.



(a)



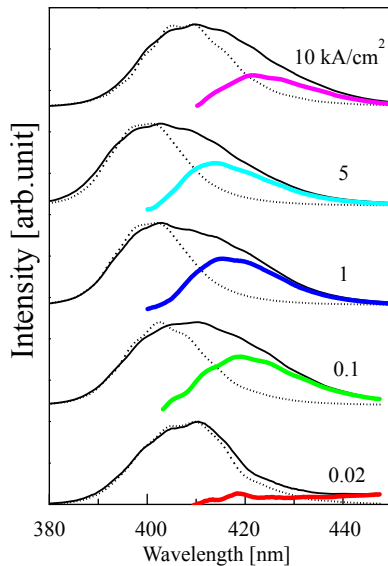
(b)

Fig. 3. (Color online) *J*-*V*-*L* characteristics of Samples A (6 nm 5 QWs) and B (3 nm 5 QWs) at (a) high and (b) at low current densities.

The reflectivity of the 8-pair SiO<sub>2</sub>/Nb<sub>2</sub>O<sub>5</sub> DBR was measured to be over 99.9% at around 410 nm.

### 3. Results and discussion

The current density–light output power (*J*-*L*) characteristics of Samples A (6 nm QWs) and B (3 nm QWs) are shown in Fig. 3(a) under high current densities up to 10 kA/cm<sup>2</sup> and (b) under low current densities up to 100 A/cm<sup>2</sup>. The *J*-*L* characteristics under high current densities clearly show that the light output power from the 6 nm QWs is comparable to or even higher than that from the 3 nm QWs. At the same time, the light output power from the 3 nm QWs was much higher than that from the 6 nm QWs under low current densities as typically observed in standard LED operations. Thus, we conclude that the overlap between electron and hole wave functions in the 6 nm QWs is sufficiently high under



**Fig. 4.** (Color online) Emission spectra of Sample C (specific 6 nm 5 QWs) under various current densities. Emission spectra of Sample A (uniform 6 nm 5 QWs) and emission spectra only from the farthest QW in Sample C were also plotted.

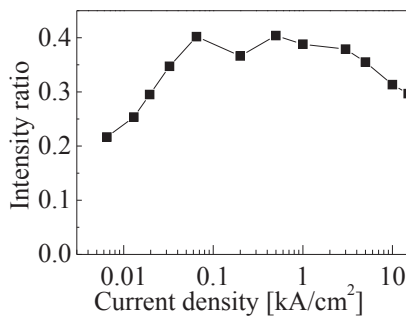


**Fig. 5.** Ratio of emission intensity from the farthest QW to total emission intensity from specific 5 QWs as a function of current density.

high current densities, like in the VCSEL operating range. It seems that the screening of the piezoelectric polarization field by the injected carriers is sufficient under such high current densities.

Figure 4 shows emission spectra of Sample C (specific 6 nm 5 QWs) under various current densities. In addition, emission spectra of Sample A, in which all the 6 nm QWs were identical and emitting 405 nm peak wavelength, are plotted with black dotted lines for comparison. Here, the intensities of all the spectra were normalized in their peak intensities. It is possible to estimate the emission spectra only from the farthest QW emitting 425 nm peak wavelength in Sample C by subtracting the spectra of Sample A from those of Sample C. Then, the spectra only from the farthest QW are also plotted with colored lines. Figure 5 then shows the ratio of the integral intensity of the emission spectra from the farthest QW (shown with colored lines in Fig. 4) to the integral intensity of the emission spectra from Sample C (shown with black solid lines in Fig. 4) as a function of current density. As intensity ratio of more than 35% was observed from 50 A/cm<sup>2</sup> to 5 kA/cm<sup>2</sup>. In principle, a 20% intensity ratio is expected in the case of a uniform carrier injection into 5 QWs, and the measured value here was

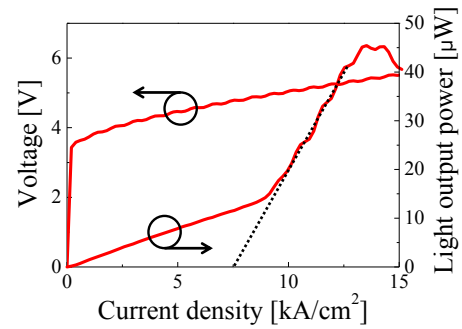


**Fig. 6.** (Color online)  $J$ - $V$ - $L$  characteristics of a VCSEL with 6 nm QWs and an AlInN/GaN DBR under RT CW operation. The threshold current density was 7.5 kA/cm<sup>2</sup>.

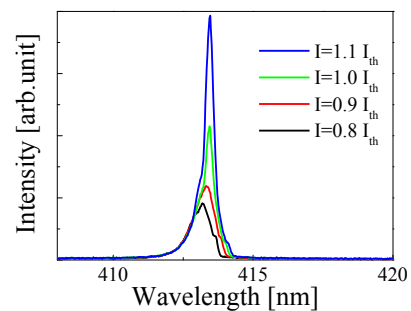


**Fig. 7.** (Color online) Emission spectra before and after the threshold. After the threshold, a narrow peak with 0.4 nm FWHM at 413.5 nm was observed.

higher than the expected value. We consider that the higher value could come from a smaller bandgap of the farthest QW, which should cause a larger carrier capture. In addition, we observed that the ratio was relatively low when the current density was less than 50 A/cm<sup>2</sup> and more than 5 kA/cm<sup>2</sup>. The low carrier injections into the farthest QW should be due to low hole injections. Such low hole injections may be caused by the existence of large piezoelectric fields at the low current density resulting from the small screening of the fields and by carrier overflow, in other words, a poor hole injection, at the high current density. Eventually, we conclude that the carrier injection into the 6 nm 5 QWs is sufficiently uniform.

Figure 6 shows the  $J$ - $V$ - $L$  characteristics of the VCSEL with 6 nm GaInN 5 QWs under CW operation at RT. The threshold current density is 7.5 kA/cm<sup>2</sup>, and the operating voltage at the threshold is 4.8 V. The differential quantum efficiency ( $\eta_d$ ) is still low, 0.46%, with the maximum output power of 45  $\mu$ W at 14 kA/cm<sup>2</sup>. At this moment, the maximum output power could be limited owing to the self-heating of the VCSEL, considering the low thermal conductivity ( $\sim 5$  W m<sup>-1</sup> K<sup>-1</sup>) of AlInN layers.<sup>24)</sup> Figure 7 shows emission spectra before and after the threshold. After the threshold, a narrow (0.4 nm full width at half maximum) peak at 413.5 nm was clearly observed. We previously reported a pulsed operation of a nitride-based VCSEL with the 3 nm GaInN 5 QWs, showing a threshold current density of 17 kA/cm<sup>2</sup>.<sup>25)</sup> A higher optical confinement factor with thick QWs is one of the reasons for the low threshold current density.

#### 4. Conclusions

We have achieved a RT CW operation of a nitride-based VCSEL using 6 nm GaInN 5 QWs and a  $4\lambda$ -cavity with a 40-pair AlInN/GaN DBR. The threshold current density under CW operation at RT was  $7.5 \text{ kA/cm}^2$  with a narrow (0.4 nm) emission spectrum of 413.5 nm peak wavelength. We also showed that the 6 nm GaInN 5 QWs provided a high optical confinement factor, a sufficient overlap between electron and hole wave functions, and uniform carrier injections under high current densities.

#### Acknowledgment

This study was supported by the MEXT Program for the Strategic Research Foundation at Private Universities, 2012–2016.

- 1) H. Amano, M. Kito, K. Hiramatsu, and I. Akasaki, *Jpn. J. Appl. Phys.* **28**, L2112 (1989).
- 2) S. Nakamura, T. Mukai, and M. Senoh, *Appl. Phys. Lett.* **64**, 1687 (1994).
- 3) S. Nakamura, M. Senoh, S. Nagahama, N. Iwasa, T. Yamada, T. Matsushita, H. Kiyoku, and Y. Sugimoto, *Jpn. J. Appl. Phys.* **35**, L74 (1996).
- 4) S. Nagahama, N. Iwasa, M. Senoh, T. Matsushita, Y. Sugimoto, H. Kiyoku, T. Kozaki, M. Sano, H. Matsumura, H. Umemoto, K. Chocho, and T. Mukai, *Jpn. J. Appl. Phys.* **39**, L647 (2000).
- 5) S. Nagahama, T. Yanamoto, M. Sano, and T. Mukai, *Appl. Phys. Lett.* **79**, 1948 (2001).
- 6) S. Masui, Y. Matsuyama, T. Yanamoto, T. Kozaki, S. Nagahama, and T. Mukai, *Jpn. J. Appl. Phys.* **42**, L1318 (2003).
- 7) T. Miyoshi, T. Yanamoto, T. Kozaki, S. Nagahama, Y. Narukawa, M. Sano, T. Yamada, and T. Mukai, *Proc. SPIE* **6894**, 689414 (2008).
- 8) H. Soda, K. Iga, C. Kinoshita, and Y. Suematsu, *J. Appl. Phys.* **18**, 2329 (1979).
- 9) K. Takaki, N. Iwai, K. Hiraiwa, S. Imai, H. Shimizu, T. Kageyama, Y. Kawakita, N. Tsukiji, and A. Kasukawa, 21st Int. Semiconductor Laser Conf., 2008, PDP1.
- 10) D. Kasahara, D. Morita, T. Kosugi, K. Nakagawa, J. Kawamata, Y. Higuchi, H. Matsumura, and T. Mukai, *Appl. Phys. Express* **4**, 072103 (2011).
- 11) T. C. Lu, S. W. Chen, T. T. Wu, P. M. Tu, C. K. Chen, C. H. Chen, Z. Y. Li, H. C. Kuo, and S. C. Wang, *Appl. Phys. Lett.* **97**, 071114 (2010).
- 12) T. Onishi, O. Imafuji, K. Nagamatsu, M. Kawaguchi, K. Yamanaka, and S. Takigawa, *IEEE J. Quantum Electron.* **48**, 1107 (2012).
- 13) C. Holder, J. S. Speck, S. P. DenBaars, S. Nakamura, and D. Feezell, *Appl. Phys. Express* **5**, 092104 (2012).
- 14) G. Cosendey, A. Castiglia, G. Rossbach, J. F. Carlin, and N. Grandjean, *Appl. Phys. Lett.* **101**, 151113 (2012).
- 15) J. T. Leonard, D. A. Cohen, B. P. Yonkee, R. M. Farrell, T. Margalith, S. Lee, S. P. DenBaars, J. S. Speck, and S. Nakamura, *Appl. Phys. Lett.* **107**, 011102 (2015).
- 16) J. T. Leonard, E. C. Young, B. P. Yonkee, D. A. Cohen, T. Margalith, S. P. DenBaars, J. S. Speck, and S. Nakamura, *Appl. Phys. Lett.* **107**, 091105 (2015).
- 17) L. A. Coldren and S. W. Corzine, *Diode Lasers and Photonic Integrated Circuits* (Wiley, New York, 1995) Chap. 5.
- 18) T. Takeuchi, S. Sota, M. Katsuragawa, M. Komori, H. Takeuchi, H. Amano, and I. Akasaki, *Jpn. J. Appl. Phys.* **36**, L382 (1997).
- 19) T. H. Wang and Y. K. Kuo, *Appl. Phys. Lett.* **102**, 171112 (2013).
- 20) Y. D. Qi, H. Liang, W. Tang, Z. D. Lu, and K. M. Lau, *J. Cryst. Growth* **272**, 333 (2004).
- 21) Y.-L. Li, Th. Gessmann, E. F. Schubert, and J. K. Sheu, *J. Appl. Phys.* **94**, 2167 (2003).
- 22) R. Charash, P. P. Maaskant, L. Lewis, C. McAleese, M. J. Kappers, C. J. Humphreys, and B. Corbett, *Appl. Phys. Lett.* **95**, 151103 (2009).
- 23) J. Y. Zhang, L. E. Cai, B. P. Zhang, X. L. Hu, F. Jiang, J. Z. Yu, and Q. M. Wang, *Appl. Phys. Lett.* **95**, 161110 (2009).
- 24) H. Tong, J. Zhang, G. Liu, J. A. Herbsommer, G. S. Huang, and N. Tansu, *Appl. Phys. Lett.* **97**, 112105 (2010).
- 25) Y. Kozuka, K. Ikeyama, T. Yasuda, T. Takeuchi, S. Kamiyama, M. Iwaya, and I. Akasaki, presented at MRS Fall Meet., 2014, T13.07.

## Microstructure Analysis of AlGa<sub>N</sub> on AlN Underlying Layers with Different Threading Dislocation Densities

This content has been downloaded from IOPscience. Please scroll down to see the full text.

2013 Jpn. J. Appl. Phys. 52 08JE22

(<http://iopscience.iop.org/1347-4065/52/8S/08JE22>)

View [the table of contents for this issue](#), or go to the [journal homepage](#) for more

Download details:

IP Address: 202.11.1.201

This content was downloaded on 03/03/2017 at 06:50

Please note that [terms and conditions apply](#).

You may also be interested in:

[Microstructures of GaInN/GaN Superlattices on GaN Substrates](#)

Toru Sugiyama, Yosuke Kuwahara, Yasuhiro Isobe et al.

[AlGa<sub>N</sub>-Based Deep Ultraviolet Light-Emitting Diodes Fabricated on Patterned Sapphire Substrates](#)

Myunghee Kim, Takehiko Fujita, Shinya Fukahori et al.

[Strain Relaxation Mechanisms in AlGa<sub>N</sub> Epitaxy on AlN Templates](#)

Zhihao Wu, Kentaro Nonaka, Yohjiro Kawai et al.

[Correlation between Device Performance and Defects in GaInN-Based Solar Cells](#)

Mikiko Mori, Shinichiro Kondo, Shota Yamamoto et al.

[Spatial Inhomogeneity of Aluminum Content in Air-Bridged Lateral Epitaxially Grown AlGa<sub>N</sub> Ternary Alloy Films Probed by Cross-Sectional Scanning Near-Field Optical Microscopy](#)

Akihiko Ishibashi, Hideaki Murotani, Toshiya Yokogawa et al.

[High Power Efficiency AlGa<sub>N</sub>-Based Ultraviolet Light-Emitting Diodes](#)

Thorsten Passow, Richard Gutt, Michael Kunzer et al.

[Growth of High-Quality Si-Doped AlGa<sub>N</sub> by Low-Pressure Metalorganic Vapor Phase Epitaxy](#)

Yuki Shimahara, Hideto Miyake, Kazumasa Hiramatsu et al.

## Microstructure Analysis of AlGa<sub>0.5</sub>N on AlN Underlying Layers with Different Threading Dislocation Densities

Kimiyasu Ide<sup>1</sup>, Yuko Matsubara<sup>1</sup>, Motoaki Iwaya<sup>1</sup>, Satoshi Kamiyama<sup>1</sup>, Tetsuya Takeuchi<sup>1</sup>, Isamu Akasaki<sup>1,3</sup>, and Hiroshi Amano<sup>2,3</sup>

<sup>1</sup>Faculty of Science and Technology, Meijo University, Nagoya 468-8502, Japan

<sup>2</sup>Graduate School of Engineering, Nagoya University, Nagoya 464-8603, Japan

<sup>3</sup>Akasaki Research Center, Nagoya University, Nagoya 464-8603, Japan

Received October 13, 2012; accepted May 1, 2013; published online August 20, 2013

Using the epitaxial lateral growth technique, we compared the crystallinity and relaxation ratio of 3- $\mu\text{m}$ - and 200-nm-thick Al<sub>0.5</sub>Ga<sub>0.5</sub>N on an AlN template and AlN grown by epitaxial lateral overgrowth (ELO-AlN), both of which were grown on a sapphire substrate. Although the relaxation ratios of 3- $\mu\text{m}$ -thick Al<sub>0.5</sub>Ga<sub>0.5</sub>N were almost the same, the misfit dislocation density at the interface and the density of threading dislocations reaching the surface of Al<sub>0.5</sub>Ga<sub>0.5</sub>N were significantly different. Also, the increase in the density of newly generated misfit dislocations was found to be highly dependent on the quality of the AlN underlying layer. We also discuss the difference in the initial growth mode of each Al<sub>0.5</sub>Ga<sub>0.5</sub>N sample. © 2013 The Japan Society of Applied Physics

### 1. Introduction

High-crystalline-quality AlGa<sub>0.5</sub>N is essential for realizing high-performance UV/deep UV light emitters.<sup>1–3</sup> The direct growth of an AlGa<sub>0.5</sub>N film on a sapphire substrate leads to poor material quality.<sup>4–6</sup> When AlGa<sub>0.5</sub>N is grown on GaN, because of the substantial lattice mismatch between AlGa<sub>0.5</sub>N and GaN, tensile stress in AlGa<sub>0.5</sub>N is released through crack generation when the critical thickness is exceeded.<sup>7</sup> Moreover, the light extraction efficiency of UV light-emitting diodes (UV-LEDs) with an emission wavelength of lower than 360 nm on GaN is much lower than that of UV-LEDs on AlN, because GaN absorbs UV light. Thus, the majority of UV-LEDs<sup>8–10</sup> and laser diodes<sup>11</sup> have been fabricated on a thick AlGa<sub>0.5</sub>N/AlN template.

However, there is a lattice mismatch as large as 2.4% between GaN and AlN. Therefore, the generation of misfit dislocations cannot be avoided when AlGa<sub>0.5</sub>N is grown on AlN. It has been reported that the AlN molar fraction density of dislocations generated in AlGa<sub>0.5</sub>N on underlying AlN depends on the AlN molar fraction.<sup>12,13</sup> These reports suggest that the highest dislocation density occurs in AlGa<sub>0.5</sub>N with an AlN molar fraction of approximately 0.5. Furthermore, the microstructure and relaxation process of Al<sub>0.5</sub>Ga<sub>0.5</sub>N on AlN with threading dislocation densities (TDDs) of approximately  $1 \times 10^9$  and  $3 \times 10^{10} \text{ cm}^{-2}$  have been reported.<sup>14–16</sup> These reports show that the relaxation mechanism of AlGa<sub>0.5</sub>N changes with the TDD of the AlN underlying layer. In the case of Al<sub>0.5</sub>Ga<sub>0.5</sub>N on AlN with a TDD of approximately  $3 \times 10^{10} \text{ cm}^{-2}$ , AlGa<sub>0.5</sub>N films are relaxed by the inclination of *a*-type pure edge threading dislocations (TDs) with Burgers vector  $\mathbf{b} = (1/3)(11\bar{2}0)$ .

AlN films with a low dislocation density of approximately  $2 \times 10^8 \text{ cm}^{-2}$  grown by epitaxial lateral overgrowth (ELO) have been reported.<sup>17</sup> Using this technique, an improvement in the internal quantum efficiency of UV-LEDs has been reported.<sup>18</sup> As can be seen from the above, the relaxation process in AlGa<sub>0.5</sub>N on an AlN template varies with differences in the underlying layer such as the difference in dislocation density. Therefore, there may be a different relaxation process for AlGa<sub>0.5</sub>N grown on an ELO-AlN. However, there have been no reports on the

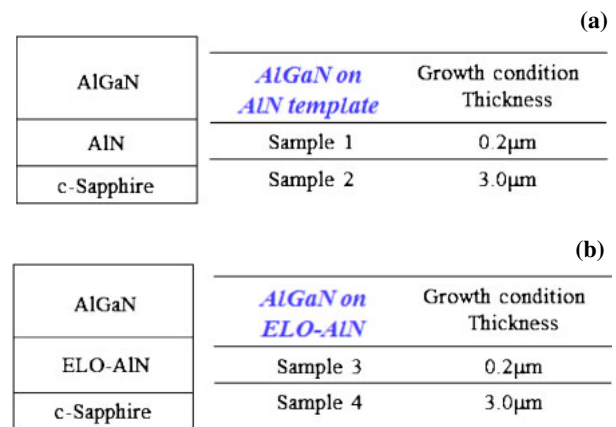


**Fig. 1.** (Color online) Schematic views of (a) 200-nm- and 3- $\mu\text{m}$ -thick Al<sub>0.5</sub>Ga<sub>0.5</sub>N grown on AlN template, and (b) 200-nm- and 3- $\mu\text{m}$ -thick Al<sub>0.5</sub>Ga<sub>0.5</sub>N grown on ELO-AlN.

relaxation process of AlGa<sub>0.5</sub>N on an ELO-AlN underlying layer.

In this study, we characterized Al<sub>0.5</sub>Ga<sub>0.5</sub>N on an ELO-AlN underlying layer by transmission electron microscopy (TEM), X-ray diffraction reciprocal lattice space mapping (XRD mapping) method, and atomic force microscopy (AFM). We compared the crystallinity and relaxation ratio of 3- $\mu\text{m}$ - and 200-nm-thick Al<sub>0.5</sub>Ga<sub>0.5</sub>N on an AlN template and ELO-AlN, both of which were grown on a sapphire substrate.

### 2. Experimental Procedure

Figures 1(a) and 1(b) show schematic views of the sample structures. All samples were grown on a *c*-plane sapphire substrate using a customized high-temperature-growth metalorganic vapor phase epitaxy (HT-MOVPE) system, which had a horizontal flow channel configuration and a face-down substrate setup. First, 4- $\mu\text{m}$ -thick AlN was grown on the sapphire substrate at a high growth temperature of 1,400 °C<sup>19,20</sup> at 100 Torr. The total TDD of the AlN film used in this work was approximately  $1 \times 10^9 \text{ cm}^{-2}$ . Periodic grooves along the  $\langle 1\bar{1}00 \rangle$  axis, where the width, spacing, and

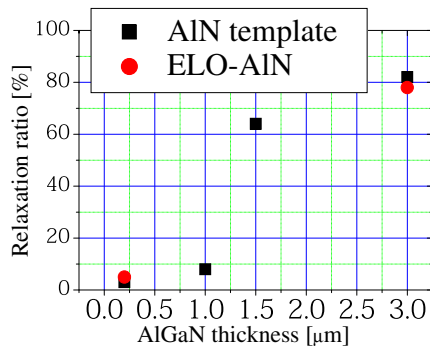


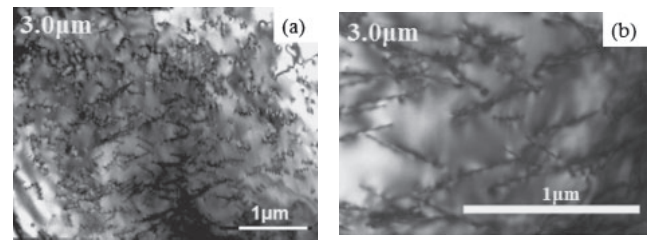
**Fig. 2.** (Color online) Relaxation ratio in  $\text{Al}_{0.5}\text{Ga}_{0.5}\text{N}$  as a function of  $\text{Al}_{0.5}\text{Ga}_{0.5}\text{N}$  thickness grown on AlN template and ELO-AIN.

depth are 3, 3, and 1  $\mu\text{m}$ , respectively, were formed on the AlN. Then, the AlN grooves were embedded in an approximately 20- $\mu\text{m}$ -thick ELO-AIN layer. We succeeded in growing a low-dislocation-density AlN template with an almost uniform dislocation density of  $2 \times 10^8 \text{ cm}^{-2}$ , which was confirmed by plan-view TEM and from the full widths at half maximums (FWHMs) of the measured X-ray rocking curve (XRC). Then, 200-nm- and 3- $\mu\text{m}$ -thick  $\text{Al}_{0.5}\text{Ga}_{0.5}\text{N}$  layers were grown on the ELO-AIN underlying layer. We also fabricated 200-nm- and 3- $\mu\text{m}$ -thick  $\text{Al}_{0.5}\text{Ga}_{0.5}\text{N}$  on AlN templates with an average TDD of  $1 \times 10^9 \text{ cm}^{-2}$  as shown in Fig. 1(a). The AlN molar fraction in AlGaIn was estimated from the lattice constants  $a$  and  $c$  determined by X-ray diffraction measurements.<sup>21–23</sup> Cross-sectional TEM specimens of  $\text{Al}_{0.5}\text{Ga}_{0.5}\text{N}$  samples were prepared using the focused ion beam technique with low-energy  $\text{Ar}^+$ -ion milling. Plan-view TEM specimens were prepared from the  $\text{Al}_{0.5}\text{Ga}_{0.5}\text{N}$  samples by standard mechanical polishing and  $\text{Ar}^+$ -ion milling techniques. The microstructure of the  $\text{Al}_{0.5}\text{Ga}_{0.5}\text{N}$  films was analyzed by TEM operating at 300 kV. All observation directions were parallel to the  $(1\bar{1}00)$  direction. We also used the  $g \cdot b$  method<sup>24</sup> in order to determine the components of the dislocations. The relaxation ratio and surface condition of each sample were characterized by XRD mapping around the  $(20\bar{2}4)$  diffraction and by AFM, respectively.

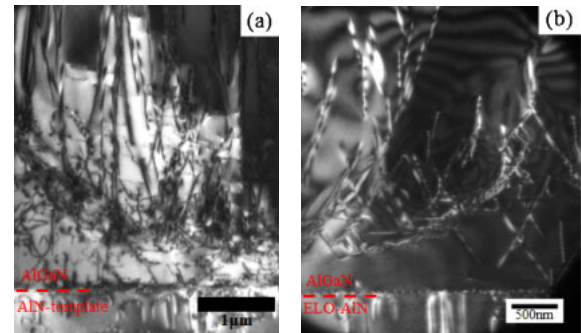
### 3. Results and Discussion

Figure 2 shows the relaxation ratio in  $\text{Al}_{0.5}\text{Ga}_{0.5}\text{N}$  as a function of  $\text{Al}_{0.5}\text{Ga}_{0.5}\text{N}$  thickness characterized by XRD mapping around the  $(20\bar{2}4)$  diffraction. From this figure, there was almost no dependence of the relaxation ratio on the underlying layer. Moreover, we observed similar lattice constants  $a$  and  $c$  for the AlGaIn films on AlN template and ELO-AIN. We concluded that AlGaIn samples with almost the same relaxation ratio and AlN molar fraction can be obtained even on different underlying layers.

Figure 3 shows bright-field plan-view TEM images of (a) 3- $\mu\text{m}$ -thick  $\text{Al}_{0.5}\text{Ga}_{0.5}\text{N}$  on an AlN template and (b) 3- $\mu\text{m}$ -thick  $\text{Al}_{0.5}\text{Ga}_{0.5}\text{N}$  on ELO-AIN. From these figures, the TDDs of the  $\text{Al}_{0.5}\text{Ga}_{0.5}\text{N}$  samples were approximately  $8.3 \times 10^9$  and  $2.6 \times 10^9 \text{ cm}^{-2}$ , respectively. It was clear that the TDDs at the surface of these two samples were different. That is, although the relaxation ratios of the  $\text{Al}_{0.5}\text{Ga}_{0.5}\text{N}$  samples were almost the same, the densities of misfit



**Fig. 3.** Plan-view TEM images and TDs at the surface: (a) 3- $\mu\text{m}$ -thick  $\text{Al}_{0.5}\text{Ga}_{0.5}\text{N}$  grown on AlN template and (b) 3- $\mu\text{m}$ -thick  $\text{Al}_{0.5}\text{Ga}_{0.5}\text{N}$  grown on ELO-AIN.



**Fig. 4.** (Color online) Dark-field cross-sectional TEM images of (a) 3- $\mu\text{m}$ -thick  $\text{Al}_{0.5}\text{Ga}_{0.5}\text{N}$  grown on AlN template and (b) 3- $\mu\text{m}$ -thick  $\text{Al}_{0.5}\text{Ga}_{0.5}\text{N}$  grown on ELO-AIN, taken along the  $[1\bar{1}00]$  projection with diffraction vector of  $g = [11\bar{2}0]$ .

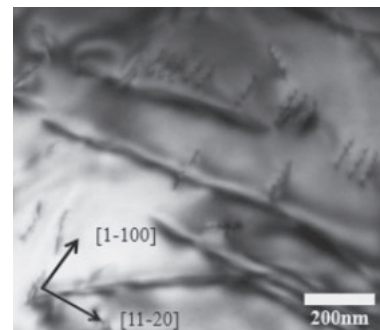


**Fig. 5.** Plan-view TEM image of 3- $\mu\text{m}$ -thick  $\text{Al}_{0.5}\text{Ga}_{0.5}\text{N}$  grown on ELO-AIN near the interface, taken along the  $[0001]$  projection.

dislocations of  $\text{Al}_{0.5}\text{Ga}_{0.5}\text{N}$  on the AlN template and ELO-AIN were significantly different.

Figure 4 shows dark-field cross-sectional TEM images of (a) 3- $\mu\text{m}$ -thick  $\text{Al}_{0.5}\text{Ga}_{0.5}\text{N}$  grown on the AlN template and (b) 3- $\mu\text{m}$ -thick  $\text{Al}_{0.5}\text{Ga}_{0.5}\text{N}$  grown on ELO-AIN, taken along the  $[1\bar{1}00]$  projection with a diffraction vector of  $g = [11\bar{2}0]$ . The inclination of  $a$ -type dislocations at the AlGaIn film was confirmed as shown in Figs. 4(a) and 4(b). Similar results have been reported in Refs. 14 and 15. Therefore, it was necessary to investigate the behavior of misfit dislocations at the interface between  $\text{Al}_{0.5}\text{Ga}_{0.5}\text{N}$  and AlN. Figure 5 shows a bright-field plan-view TEM image at the  $\text{Al}_{0.5}\text{Ga}_{0.5}\text{N}$ /ELO-AIN interface extracted from 3- $\mu\text{m}$ -thick  $\text{Al}_{0.5}\text{Ga}_{0.5}\text{N}$  grown on ELO-AIN. From this figure, the misfit dislocation density (MDD) generated at the interface between AlGaIn

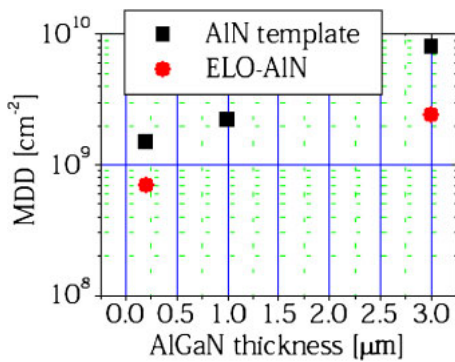


Fig. 6. (Color online) MDD at the interface as a function of thickness of Al<sub>0.5</sub>Ga<sub>0.5</sub>N grown on AlN template and ELO-AlN.

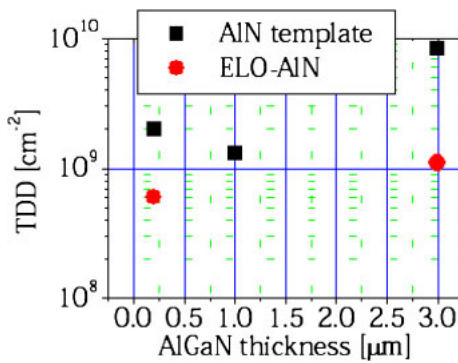


Fig. 7. (Color online) TDD at the surface as a function of thickness of Al<sub>0.5</sub>Ga<sub>0.5</sub>N grown on AlN template and ELO-AlN.

and AlN in this sample is approximately  $2.6 \times 10^9 \text{ cm}^{-2}$ . In contrast, the MDD of the 3- $\mu\text{m}$ -thick Al<sub>0.5</sub>Ga<sub>0.5</sub>N grown on the AlN template is approximately  $7.9 \times 10^9 \text{ cm}^{-2}$ . That is, there were significant differences in MDD depending on the underlying AlN layer.

Figures 6 and 7 show the MDD and TDD of Al<sub>0.5</sub>Ga<sub>0.5</sub>N as a function of the Al<sub>0.5</sub>Ga<sub>0.5</sub>N thickness, respectively. From these figures, the TDD of Al<sub>0.5</sub>Ga<sub>0.5</sub>N on the AlN template is almost the same as the MDD, but the TDD of Al<sub>0.5</sub>Ga<sub>0.5</sub>N on ELO-AlN is lower than the MDD. Next, we performed AFM observation of the 200-nm-thick Al<sub>0.5</sub>Ga<sub>0.5</sub>N on an AlN template and ELO-AlN to investigate the initial growth modes in Al<sub>0.5</sub>Ga<sub>0.5</sub>N. Figure 8 shows AFM images of (a) 200-nm-thick Al<sub>0.5</sub>Ga<sub>0.5</sub>N grown on an AlN template and (b) 200-nm-thick Al<sub>0.5</sub>Ga<sub>0.5</sub>N grown on ELO-AlN. From these figures, we confirmed that the growth modes of AlGa<sub>n</sub> on the AlN template and ELO-AlN are significantly different and involve two-dimensional growth and three-dimensional growth, respectively. We also characterized the surface structure of ELO-AlN from the AFM and TEM images. From these images, small steps of approximately 40 nm at intervals of 6  $\mu\text{m}$  were confirmed. The difference in growth mode was due to the difference in surface structure.

We propose a mechanism as illustrated in Fig. 9. The initial growth of Al<sub>0.5</sub>Ga<sub>0.5</sub>N on an AlN template is two-dimensional, as observed from the initial growth of Al<sub>0.5</sub>Ga<sub>0.5</sub>N. In contrast, the initial growth of Al<sub>0.5</sub>Ga<sub>0.5</sub>N on ELO-AlN was three-dimensional via the nucleation of

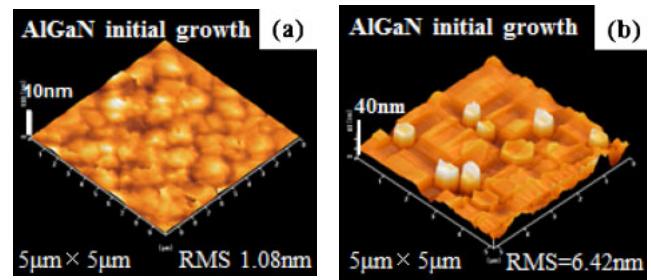


Fig. 8. (Color online) AFM images of (a) 200-nm-thick Al<sub>0.5</sub>Ga<sub>0.5</sub>N grown on AlN-template and (b) 200-nm-thick Al<sub>0.5</sub>Ga<sub>0.5</sub>N grown on ELO-AlN.

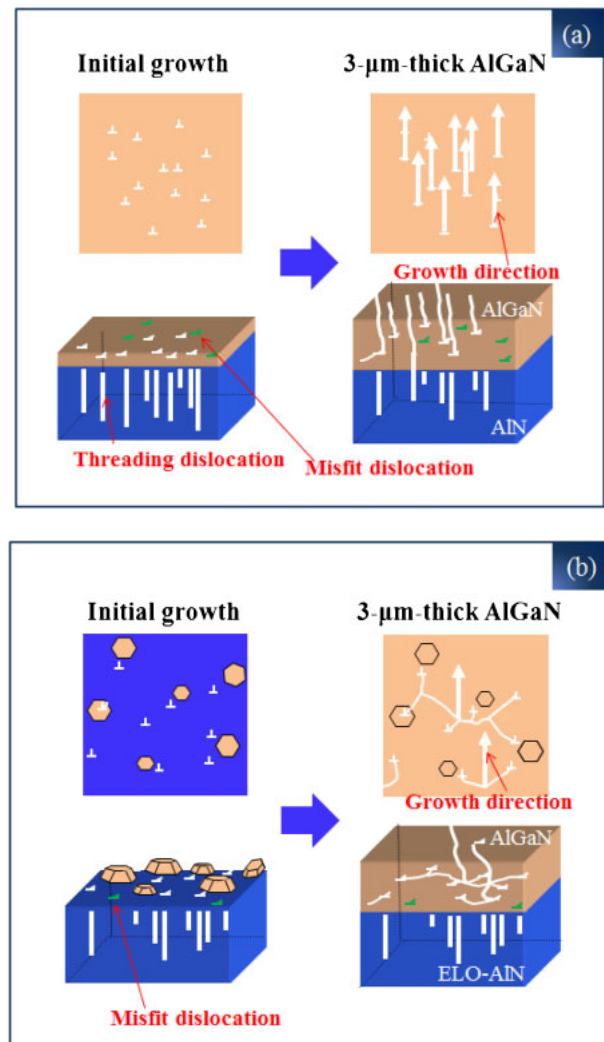


Fig. 9. (Color online) Modes of initial growth and growth at a thickness of 3  $\mu\text{m}$  for (a) Al<sub>0.5</sub>Ga<sub>0.5</sub>N grown on AlN-template and (b) Al<sub>0.5</sub>Ga<sub>0.5</sub>N grown on ELO-AlN.

Al<sub>0.5</sub>Ga<sub>0.5</sub>N. In Al<sub>0.5</sub>Ga<sub>0.5</sub>N on the AlN template, most of the misfit dislocations generated at the Al<sub>0.5</sub>Ga<sub>0.5</sub>N/AlN interface will thread to the surface since the initial growth mode is two-dimensional. In contrast, lattice relaxation can also be realized by changing the growth mode to be three-dimensional.<sup>25,26)</sup> Thus, we consider that the three-dimensional growth contributes to the relaxation in Al<sub>0.5</sub>Ga<sub>0.5</sub>N on ELO-AlN, in addition to the generation of the misfit

dislocations. Therefore, the MDD in  $\text{Al}_{0.5}\text{Ga}_{0.5}\text{N}$  on ELO-AIN is less than that of  $\text{Al}_{0.5}\text{Ga}_{0.5}\text{N}$  on the AIN template. In addition, the misfit dislocations are bent laterally by three-dimensional growth. Many threading dislocations do not reach the surface owing to their termination by loop formation. This mechanism explains the significant difference in the TDD of  $\text{Al}_{0.5}\text{Ga}_{0.5}\text{N}$  on an AIN template and ELO-AIN, even though the relaxation ratios of the  $\text{Al}_{0.5}\text{Ga}_{0.5}\text{N}$  are almost the same.

#### 4. Conclusions

We compared the crystallinity and relaxation ratio of 3- $\mu\text{m}$ - and 200-nm-thick  $\text{Al}_{0.5}\text{Ga}_{0.5}\text{N}$  on AIN templates and ELO-AIN grown on sapphire substrates. Although the relaxation ratios were almost the same, the increases in the misfit dislocation densities of the  $\text{Al}_{0.5}\text{Ga}_{0.5}\text{N}$  on the AIN template and ELO-AIN were significantly different. We also confirmed that the growth modes of  $\text{Al}_{0.5}\text{Ga}_{0.5}\text{N}$  on the AIN template and ELO-AIN are significantly different and exhibit two-dimensional growth and three-dimensional growth, respectively.

#### Acknowledgement

This study was supported by the Ministry of Education, Culture, Sports, Science and Technology Supported Program for the Strategic Research Foundation at Private Universities, 2012–2016.

- 1) T. Inazu, S. Fukahori, C. Pernot, M. H. Kim, T. Fujita, Y. Nagasawa, A. Hirano, M. Ippommatsu, M. Iwaya, T. Takeuchi, S. Kamiyama, M. Yamaguchi, Y. Honda, H. Amano, and I. Akasaki: *Jpn. J. Appl. Phys.* **50** (2011) 122101.
- 2) C. Pernot, S. Fukahori, T. Inazu, T. Fujita, M. Kim, Y. Nagasawa, A. Hirano, M. Ippommatsu, M. Iwaya, S. Kamiyama, I. Akasaki, and H. Amano: *Phys. Status Solidi A* **208** (2011) 1594.
- 3) M. Kim, T. Fujita, S. Fukahori, T. Inazu, C. Pernot, Y. Nagasawa, A. Hirano, M. Ippommatsu, M. Iwaya, T. Takeuchi, S. Kamiyama, M. Yamaguchi, Y. Honda, H. Amano, and I. Akasaki: *Appl. Phys. Express* **4** (2011) 092102.
- 4) Y. Koide, N. Itoh, K. Itoh, N. Sawaki, and I. Akasaki: *Jpn. J. Appl. Phys.* **27** (1988) 1156.
- 5) H. Amano, M. Iwaya, N. Hayashi, T. Kashima, S. Nitta, C. Wetzel, and I. Akasaki: *Phys. Status Solidi B* **216** (1999) 683.
- 6) N. Kuwano, T. Tsuruda, Y. Adachi, S. Terao, S. Kamiyama, H. Amano, and I. Akasaki: *Phys. Status Solidi A* **192** (2002) 366.
- 7) K. Ito, K. Hiramatsu, H. Amano, and I. Akasaki: *J. Cryst. Growth* **104** (1990) 533.
- 8) H. Amano, N. Sawaki, I. Akasaki, and Y. Toyoda: *Appl. Phys. Lett.* **48** (1986) 353.
- 9) H. Amano, M. Kito, K. Hiramatsu, and I. Akasaki: *Jpn. J. Appl. Phys.* **28** (1989) L2112.
- 10) H. Amano and I. Akasaki: Ext. Abstr. Materials Research Society, 1990, p. 165.
- 11) H. Amano, S. Takanami, M. Iwaya, S. Kamiyama, and I. Akasaki: *Phys. Status Solidi A* **195** (2003) 491.
- 12) T. Mori, K. Nagamatsu, K. Nonaka, K. Takeda, M. Iwaya, S. Kamiyama, H. Amano, and I. Akasaki: *Phys. Status Solidi C* **6** (2009) 2621.
- 13) N. Kuwano, T. Tsuruda, Y. Kida, H. Miyake, K. Hiramatsu, and T. Shibata: *Phys. Status Solidi C* **0** (2003) 2444.
- 14) Z. Wu, K. Nonaka, Y. Kawai, T. Asai, F. A. Ponce, C. Chen, M. Iwaya, S. Kamiyama, H. Amano, and I. Akasaki: *Appl. Phys. Express* **3** (2010) 111003.
- 15) D. M. Follstaedt, S. R. Lee, P. P. Provencio, A. A. Allerman, J. A. Floro, and M. H. Crawford: *Appl. Phys. Lett.* **87** (2005) 121112.
- 16) P. Cantu, F. Wu, P. Waltereit, S. Keller, A. E. Romanov, U. K. Mishra, S. P. DenBaars, and J. S. Speck: *Appl. Phys. Lett.* **83** (2003) 674.
- 17) M. Imura, K. Nakano, T. Kitano, N. Fujimoto, G. Narita, N. Okada, K. Balakrishnan, M. Iwaya, S. Kamiyama, H. Amano, I. Akasaki, K. Shimono, T. Noro, T. Takagi, and A. Bandoh: *Appl. Phys. Lett.* **89** (2006) 221901.
- 18) H. Hirayama, S. Fujikawa, J. Norimatsu, T. Takano, K. Tsubaki, and N. Kamata: *Phys. Status Solidi C* **6** (2009) S356.
- 19) N. Okada, N. Fujimoto, T. Kitano, G. Narita, M. Imura, K. Balakrishnan, M. Iwaya, S. Kamiyama, H. Amano, I. Akasaki, K. Shimono, T. Noro, T. Takagi, and A. Bandoh: *Jpn. J. Appl. Phys.* **45** (2006) 2502.
- 20) N. Kato, S. Sato, H. Sugimura, T. Sumii, N. Okada, M. Imura, M. Iwaya, S. Kamiyama, H. Amano, I. Akasaki, H. Maruyama, T. Takagi, and A. Bandoh: *Phys. Status Solidi C* **5** (2008) 1559.
- 21) D. Sun and E. Towe: *IEEE J. Quantum Electron.* **30** (1994) 466.
- 22) T. Takeuchi, S. Sota, M. Katsuragawa, M. Komori, H. Takeuchi, H. Amano, and I. Akasaki: *Jpn. J. Appl. Phys.* **36** (1997) L382.
- 23) A. F. Wright: *J. Appl. Phys.* **82** (1997) 2833.
- 24) B. Fultz and J. M. Howe: *Transmission Electron Microscopy and Diffractometry of Materials* (Springer, New York, 2002) 3rd ed., p. 362.
- 25) Z. Ren, Q. Sun, S.-Y. Kwon, J. Han, K. Davitt, Y. K. Song, A. V. Nurmikko, H.-K. Cho, W. Liu, J. A. Smart, and L. J. Schowalter: *Appl. Phys. Lett.* **91** (2007) 051116.
- 26) N. Gogneau, D. Jalabert, E. Monroy, T. Shibata, M. Tanaka, and B. Daudin: *J. Appl. Phys.* **94** (2003) 2254.

# Analysis of strain relaxation process in GaInN/GaN heterostructure by in situ X-ray diffraction monitoring during metalorganic vapor-phase epitaxial growth

Daisuke Iida<sup>1</sup>, Yasunari Kondo<sup>1</sup>, Mihoko Sowa<sup>1</sup>, Toru Sugiyama<sup>1</sup>, Motoaki Iwaya<sup>\*1</sup>, Tetsuya Takeuchi<sup>1</sup>, Satoshi Kamiyama<sup>1</sup>, and Isamu Akasaki<sup>1,2</sup>

<sup>1</sup> Faculty of Science and Technology, Meijo University, Nagoya 468-8502, Japan

<sup>2</sup> Akasaki Research Center, Nagoya University, Nagoya 464-8603, Japan

Received 18 January 2013, revised 24 January 2013, accepted 25 January 2013

Published online 30 January 2013

**Keywords** GaInN, heterostructures, in situ XRD, relaxation, pits, misfit dislocation

\* Corresponding author: e-mail [iwaya@meijo-u.ac.jp](mailto:iwaya@meijo-u.ac.jp)

Strain relaxation in a GaInN/GaN heterostructure is analyzed by combining *in situ* X-ray diffraction (XRD) monitoring and *ex situ* observations. Two different characteristic thicknesses of GaInN films are defined by the evolution of *in situ* XRD from the full width at half-maximum of symmetric (0002) diffraction as a function of GaInN thickness. This *in situ*

XRD measurement enables to clearly observe the critical thicknesses corresponding to strain relaxation in the GaInN/GaN heterostructure caused by the formation of surface pits with bent threading dislocations and the generation of misfit dislocations on GaInN during growth.

© 2013 WILEY-VCH Verlag GmbH & Co. KGaA, Weinheim

**1 Introduction** GaInN is widely used as an active layer in high-brightness blue and green light-emitting diodes (LEDs) and violet laser diodes [1]. The application of GaInN films in high-efficiency solar cells is also expected [2]. The bandgap of GaInN alloys ranges from 0.65 to 3.43 eV, making them suitable for the design of high-conversion-efficiency multijunction solar cells [3]. So far, we have succeeded in fabricating GaInN-based solar cells [4–6]. As a result, we have obtained solar cells with up to 4% conversion efficiency by irradiating concentrated sunlight with intensity up to 300 suns [6]. To realize high-performance GaInN-based solar cells with a high open-circuit voltage and fill factor, it is essential to realize a low surface pit density of less than  $10^7 \text{ cm}^{-2}$  [4, 5]. Moreover, GaInN-based green/yellow/red LEDs still have low internal quantum efficiency compared with blue LEDs [7]. The internal quantum efficiency of these LEDs decreases with increasing InN molar fraction in GaInN, which is caused by the generation of misfit dislocations (MDs) at the GaInN/GaN interface and built-in electrostatic fields [8, 9]. GaInN films with a high InN molar fraction on GaN have

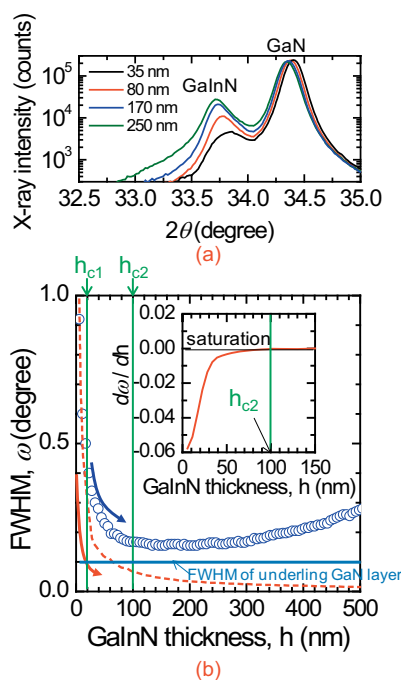
already been used to analyze the relaxation mechanism by which defects are formed by strain relaxation [10–14]. However, the sequence of relaxation in the GaInN/GaN heterostructure remains to be clarified. Moreover, an understanding of the critical layer thickness at which MDs and surface pits are introduced in the GaInN/GaN heterostructure is essential for the realization of high-performance devices.

In this study, we examined the application of the *in situ* XRD observation to GaInN/GaN heterostructures. As a result, we found that this method is useful for analyzing the relaxation process in GaInN/GaN heterostructures by *in situ* XRD monitoring of the full width at half-maximum (FWHM).

**2 Experimental procedure** All the samples were grown by metalorganic vapor phase epitaxy in a face-down  $2'' \times 3''$  wafer horizontal-flow reactor. After the growth of a 3- $\mu\text{m}$ -thick GaN template at 1050 °C on *c*-plane sapphire covered with a low-temperature buffer layer [15], it was cooled to 755–790 °C. Then, GaInN films of approxi-

mately 500 nm thickness with various InN molar fractions were grown on the GaN template. The threading dislocation (TD) density of the GaN template was approximately  $3 \times 10^8 \text{ cm}^{-2}$ , which was characterized by plan-view transmission electron microscopy (TEM). We evaluated GaInN films with symmetric (0002) Bragg diffraction using an *in situ* XRD system. *In situ* X-ray was focused on the sample surface using a Johansson curved crystal mirror, and the diffracted X-ray was detected by a one-dimensional charge-coupled device [16, 17]. This system realized the equivalent of a (0002)  $2\theta/\omega$  scan without any analyzer crystal in 1 s during rotation of the wafers. In this system, the tilt component and the distribution of the lattice constant  $c$  can be simultaneously characterized from the FWHM [18]. We observed the GaInN surface structure and defects close to the GaInN/GaN heterointerface by scanning electron microscopy (SEM) and TEM, respectively. Strain relaxation was also evaluated by a typical *ex situ* XRD reciprocal space mapping.

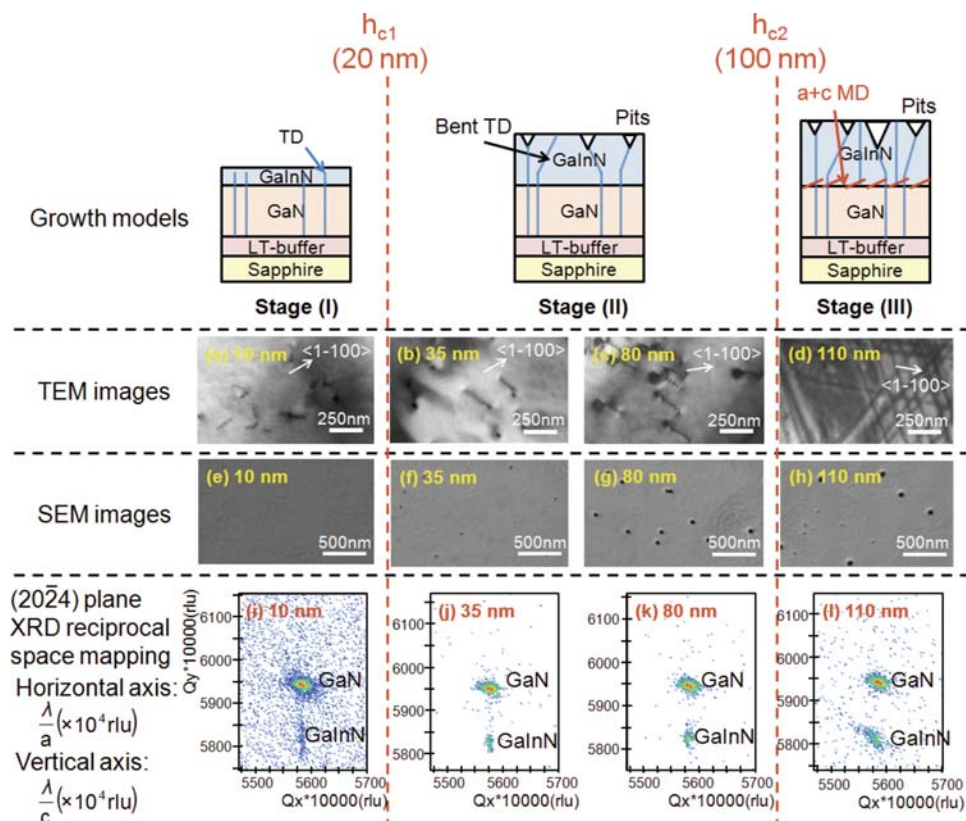
**3 Results and discussion** The *in situ* XRD spectra of  $\text{Ga}_{0.87}\text{In}_{0.13}\text{N}/\text{GaN}$  heterostructures are shown in Fig. 1(a); the InN molar fraction in GaInN can be determined from each peak of the spectrum, and its value corresponds exactly to the value estimated by *ex situ* XRD. Also,



**Figure 1** (online colour at: [www.pss-rapid.com](http://www.pss-rapid.com)) *In situ* XRD (a) spectrum and FWHM (b) as a function of  $\text{Ga}_{0.87}\text{In}_{0.13}\text{N}$  film thickness. The experimental FWHMs include the tilt distribution of (0002) diffraction. This indicates that the critical thickness for the strain relaxation process,  $h_{c1}$ , can be obtained by comparing the results of experiments and simulations. The inset of (b) shows the derivative of the FWHM with respect to  $\text{Ga}_{0.87}\text{In}_{0.13}\text{N}$  film thickness.

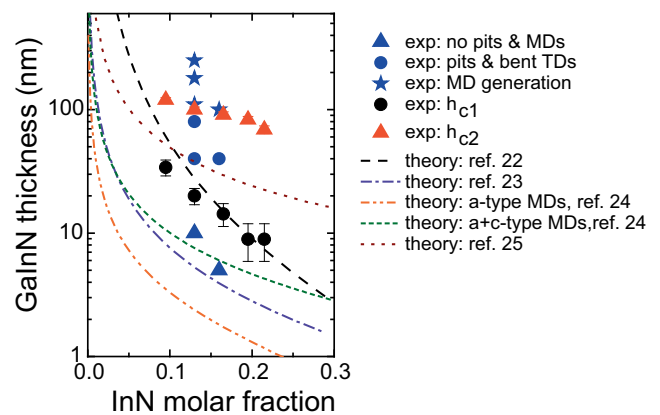
we confirmed that the peak positions of GaInN and GaN slightly shifted by the influence of the warpage of the sample. Figure 1(b) shows typical *in situ* XRD FWHMs of the  $\text{Ga}_{0.87}\text{In}_{0.13}\text{N}$  films during growth. The FWHM of the  $\text{Ga}_{0.87}\text{In}_{0.13}\text{N}$  films decreases with increasing film thickness, as determined using a pseudo-Voigt function [16]. The inset in Fig. 1(b) shows the derivative of the FWHM with respect to GaInN thickness. We confirm the existence of a difference between the experimental results and simulation values. The simulated XRD spectra were obtained using X'pert Epitaxy 4.0a, a typical X-ray analysis software [19]. The simulated FWHM was then determined using the same pseudo-Voigt function. Normally, the FWHM decreased to the same extent as the underlying GaN layer with increasing film thickness; however, this markedly changes for a small film thickness. The experimental and simulated FWHMs were shown to similarly decrease with increasing  $\text{Ga}_{0.87}\text{In}_{0.13}\text{N}$  film thickness up to approximately 20 nm. However, the FWHMs of the  $\text{Ga}_{0.87}\text{In}_{0.13}\text{N}$  films with thicknesses exceeding 20 nm tended to deviate from the simulation values. Then, the FWHM started to saturate at a GaInN thickness of approximately 100 nm in spite of decreasing simulation values. These behaviors suggest that the FWHM increases via the generation of MDs and pits owing to strain relaxation in  $\text{Ga}_{0.87}\text{In}_{0.13}\text{N}$  films. Therefore, we defined  $h_{c1}$  and  $h_{c2}$  to be approximately  $20 \pm 3 \text{ nm}$  and  $100 \pm 5 \text{ nm}$ , respectively.

Figure 2 shows a summary of the growth models along with bright-field TEM images, plan-view SEM images, and XRD (20 $\bar{2}$ 4) reciprocal space maps of 10-, 35-, 80-, and 110-nm-thick  $\text{Ga}_{0.87}\text{In}_{0.13}\text{N}$  films grown on GaN layers. The TDs almost reached the surfaces of the  $\text{Ga}_{0.87}\text{In}_{0.13}\text{N}$  films grown on the GaN layers in stage (I). We found that the  $\text{Ga}_{0.87}\text{In}_{0.13}\text{N}$  films formed surface pits at the ends of the TDs with increasing  $\text{Ga}_{0.87}\text{In}_{0.13}\text{N}$  film thickness in stage (II). In general, surface pits are formed along an inclined  $\{1\ 101\}$  plane [20]. Here, TDs appear to laterally extend with increasing  $\text{Ga}_{0.87}\text{In}_{0.13}\text{N}$  film thickness, as shown in Fig. 2(a) and (b). This suggests that TDs are bent during growth by in-plane compressive stress between  $\text{Ga}_{0.87}\text{In}_{0.13}\text{N}$  and GaN. Then, the surface pits expand with increasing  $\text{Ga}_{0.87}\text{In}_{0.13}\text{N}$  film thickness, as shown in Fig. 2(f) and (g). It is considered that this promotes the fluctuation of the InN molar fraction in GaInN films by the composition pulling effect [11, 12]. Therefore,  $h_{c1}$  is associated with bent TDs, which form surface pits at the ends of TDs. It was clarified that the deviation between the experimental results and simulation values for the FWHM above a thickness of  $h_{c1}$  increases with increasing apparent FWHM. Moreover, the density of surface pits increased with increasing  $\text{Ga}_{0.87}\text{In}_{0.13}\text{N}$  film thickness, as shown in Fig. 2(h). The formation of additional surface pits on the  $\text{Ga}_{0.87}\text{In}_{0.13}\text{N}$  films was mainly caused by TDs induced via the generation of MDs with strain relaxation in the  $\text{Ga}_{0.87}\text{In}_{0.13}\text{N}/\text{GaN}$  heterostructure in stage (III). We found that a network of MDs was generated along the  $\langle 1\ \bar{1}00 \rangle$  direction close to the  $\text{Ga}_{0.87}\text{In}_{0.13}\text{N}/\text{GaN}$  heterointerface; such



**Figure 2** (online colour at: [www.pss-rapid.com](http://www.pss-rapid.com)) Summary of several *ex situ* measurements of  $\text{Ga}_{0.87}\text{In}_{0.13}\text{N}$  films with various thicknesses showing plan-view (a)–(d) bright-field TEM and (e)–(h) SEM images, and XRD reciprocal space maps (i)–(l) around (2024) diffraction. Schematic views of the growth models in stages (I)–(III) are also shown. These stages involve completely coherent growth, the bending of TDs and the formation of surface pits, and the introduction of MDs, respectively.

dislocations were induced via slips along the  $\{1\bar{1}23\}$  direction in the  $\{1\bar{1}22\}$  plane system [21], as shown in Fig. 2(d). This result suggests that  $(a+c)$ -type MDs were induced at the  $\text{Ga}_{0.87}\text{In}_{0.13}\text{N}/\text{GaN}$  interface with strain relaxation in  $\text{Ga}_{0.87}\text{In}_{0.13}\text{N}$ . Therefore, although FWHMs by this *in situ* XRD do not give any direct information on relaxation,  $h_{c1}$  and  $h_{c2}$  were indicated as two different critical thicknesses at which the strain relaxation results in the formation of surface pits with bending TDs and the introduction of  $(a+c)$ -type MDs, respectively. The GaInN films are almost perfectly coherently grown on GaN, as indicated by the results of XRD mapping shown in Fig. 2(i)–(k). Although strain relaxation was evaluated by conventional *ex situ* XRD reciprocal space mapping [21], this method cannot be used to clearly show the relaxation of bent TDs with the formation of surface pits on  $\text{Ga}_{0.87}\text{In}_{0.13}\text{N}$  films. At thicknesses exceeding  $h_{c2}$ , we only observed the relaxation of MD generation at the heterointerface by *ex situ* XRD reciprocal space mapping as shown in Fig. 2(l). That is, relaxation in GaInN can only be confirmed by XRD reciprocal space maps above a thickness of  $h_{c2}$ . Therefore, *in situ* XRD monitoring was shown to be a useful method for evaluating  $h_{c1}$  in the thin-film growth stage.



**Figure 3** (online colour at: [www.pss-rapid.com](http://www.pss-rapid.com)) Summary of GaInN critical thicknesses  $h_{c1}$  and  $h_{c2}$  for various InN molar fractions. The black circles and red triangles indicate the value of  $h_{c1}$  and  $h_{c2}$ , respectively, obtained by *in situ* XRD measurements. Blue triangles, circles, and stars indicate *ex situ* measurement results for the cases of no pits or misfit dislocations, the appearance of pits and TD bending, and the appearance of misfit dislocations, respectively. The results obtained *in situ* and *ex situ* were in good agreement. Theoretical values were taken from Refs. [22–25].

We also investigated the values of  $h_{c1}$  and  $h_{c2}$  for various InN molar fractions from the behavior of the FWHMs by *in situ* XRD and *ex situ* measurements, as shown in Fig. 3. The results obtained *in situ* and *ex situ* were in good agreement. We also compared our experimental results with the results of theoretical calculations in Refs. [22–25]. Theoretical models of the critical thickness are generally based on lattice relaxation due to the introduction of misfit dislocations at the heterointerface. However, the experimental results indicate that the MDs are introduced by strain relaxation after the formation of bent TDs and that surface pits start to open up at a thickness exceeding  $h_{c1}$ . Therefore, our experimental results are not in good agreement with previous theoretical models. It is considered that the difference between the experimental and theoretical results for the generation of MDs in GaInN films is caused by the formation of bent TDs and the opening up of surface pits. We also observed the behavior of defects in GaInN/GaN heterostructures with several GaInN thicknesses by TEM. We found that the estimated critical thicknesses were in good agreement with those obtained by TEM observation. This indicates that the results of *in situ* and *ex situ* observations are in relatively good agreement.

**4 Summary** We observed strain relaxation in GaInN films during growth by *in situ* XRD monitoring. The evolutions of XRD peaks and FWHMs were obtained as functions of the GaInN film thickness. Two different features of strain relaxation were found: the formation of surface pits with bending TDs and the introduction of ( $a + c$ )-type MDs. The *in situ* XRD monitoring system proposed here enabled us to indicate the lattice properties and observe several strain relaxation features of GaInN films during growth. This is considered to be very helpful for growing high-performance device structures while suppressing the formation of surface pits and MDs.

**Acknowledgements** This study was supported by the Ministry of Education, Culture, Sports, Science and Technology of Japan through the Supported Program for the Strategic Research Foundation at Private Universities, 2012–2016.

## References

- [1] I. Akasaki and H. Amano, *Jpn. J. Appl. Phys.* **36**, 5393 (1997).
- [2] J. Wu, W. Walukiewicz, K. M. Yu, W. Shan, J. W. Ager, E. E. Haller, H. Lu, W. J. Schaff, W. K. Metzger, and S. Kurtz, *J. Appl. Phys.* **94**, 6477 (2003).
- [3] A. Devos, *Endoreversible Thermodynamics of Solar Energy Conversion* (Oxford University Press, New York, 1992).
- [4] Y. Kuwahara, T. Fujii, Y. Fujiyama, T. Sugiyama, M. Iwaya, T. Takeuchi, S. Kamiyama, I. Akasaki, and H. Amano, *Appl. Phys. Express* **3**, 111001 (2010).
- [5] M. Mori, S. Kondo, S. Yamamoto, T. Nakao, T. Fujii, M. Iwaya, T. Takeuchi, S. Kamiyama, I. Akasaki, and H. Amano, *Appl. Phys. Express* **5**, 082301 (2012).
- [6] M. Mori, S. Kondo, S. Yamamoto, T. Nakao, T. Fujii, M. Iwaya, T. Takeuchi, S. Kamiyama, I. Akasaki, and H. Amano, to be published in *Jpn. J. Appl. Phys.*
- [7] Y. Narukawa, M. Ichikawa, D. Sanga, M. Sano, and T. Mukai, *J. Phys. D, Appl. Phys.* **43**, 354002 (2010).
- [8] W. Lü, D. B. Li, C. R. Li, and Z. Zhang, *J. Appl. Phys.* **96**, 5267 (2004).
- [9] T. Takeuchi, H. Amano, and I. Akasaki, *Jpn. J. Appl. Phys.* **39**, 413 (2000).
- [10] N. A. El-Masry, E. L. Piner, S. X. Liu, and S. M. Bedair, *Appl. Phys. Lett.* **68**, 3269 (1996).
- [11] Y. Kawaguchi, M. Shimizu, K. Hiramatsu, and N. Sawaki, *Mater. Res. Soc. Symp. Proc.* **449**, 89 (1997).
- [12] K. Hiramatsu, Y. Kawaguchi, M. Shimizu, N. Sawaki, T. Zheleva, R. F. Davis, H. Tsuda, W. Taki, N. Kuwano, and K. Oki, *MRS Internet J. Nitride Semicond. Res.* **2**, 6 (1997).
- [13] R. Liu, J. Mei, S. Srinivasan, H. Omiya, F. A. Ponce, D. Cherns, Y. Narukawa, and T. Mukai, *Jpn. J. Appl. Phys.* **45**, L549 (2006).
- [14] S. Srinivasan, L. Geng, R. Liu, F. A. Ponce, Y. Narukawa, and S. Tanaka, *Appl. Phys. Lett.* **83**, 5187 (2003).
- [15] H. Amano, N. Sawaki, I. Akasaki, and Y. Toyoda, *Appl. Phys. Lett.* **48**, 353 (1986).
- [16] C. Simbrunner, K. Schmidegg, A. Bonanni, A. Kharchenko, J. Bethke, J. Woitok, K. Lischka, and H. Sitter, *Phys. Status Solidi A* **203**, 1704 (2006).
- [17] T. Sasaki, H. Suzuki, A. Sai, J.-H. Lee, M. Takahashi, S. Fujikawa, K. Arafune, I. Kamiya, Y. Ohshita, and M. Yamaguchi, *Appl. Phys. Express* **2**, 085501 (2009).
- [18] D. Iida, M. Sowa, Y. Kondo, D. Tanaka, M. Iwaya, T. Takeuchi, S. Kamiyama, and I. Akasaki, *J. Cryst. Growth* **361**, 1 (2012).
- [19] <http://www.panalytical.com/index.cfm?pid=354>
- [20] F. A. Ponce, S. Srinivasan, A. Bell, L. Geng, R. Liu, M. Stevens, J. Cai, H. Omiya, H. Marui, and S. Tanaka, *Phys. Status Solidi B* **240**, 273 (2003).
- [21] T. Sugiyama, Y. Kuwahara, Y. Isobe, T. Fujii, K. Nonaka, M. Iwaya, S. Kamiyama, H. Amano, and I. Akasaki, *Appl. Phys. Express* **4**, 015701 (2011).
- [22] R. People and J. C. Bean, *Appl. Phys. Lett.* **47**, 322 (1985).
- [23] J. W. Matthews, A. E. Blakeslee, and S. Mader, *Thin Solid Films* **33**, 253 (1976).
- [24] D. Holec, Y. Zhang, D. V. S. Rao, M. J. Kappers, C. McAleese, and C. J. Humphreys, *J. Appl. Phys.* **104**, 123514 (2008).
- [25] A. Fischer, H. Kühne, and H. Richter, *Phys. Rev. Lett.* **73**, 2712 (1994).

## Room-temperature continuous-wave operation of GaN-based vertical-cavity surface-emitting lasers with n-type conducting AlInN/GaN distributed Bragg reflectors

This content has been downloaded from IOPscience. Please scroll down to see the full text.

2016 Appl. Phys. Express 9 102101

(<http://iopscience.iop.org/1882-0786/9/10/102101>)

View [the table of contents for this issue](#), or go to the [journal homepage](#) for more

Download details:

IP Address: 219.127.71.134

This content was downloaded on 03/03/2017 at 06:38

Please note that [terms and conditions apply](#).

You may also be interested in:

[Room-temperature continuous-wave operation of GaN-based vertical-cavity surface-emitting lasers fabricated using epitaxial lateral overgrowth](#)

Shouichiro Izumi, Noriyuki Fuutagawa, Tatsushi Hamaguchi et al.

[Vertical-conducting InGaN/GaN multiple quantum wells LEDs with AlN/GaN distributed Bragg reflectors on Si\(111\) substrate](#)

Yibin Yang, Yan Lin, Peng Xiang et al.

[Electron and hole accumulations at GaN/AlInN/GaN interfaces and conductive n-type AlInN/GaN distributed Bragg reflectors](#)

Shotaro Yoshida, Kazuki Ikeyama, Toshiki Yasuda et al.

[Room-temperature CW operation of a nitride-based vertical-cavity surface-emitting laser using thick GaInN quantum wells](#)

Takashi Furuta, Kenjo Matsui, Kosuke Horikawa et al.

[High-reflectivity AlN/GaN distributed Bragg reflectors grown on sapphire substrates by MOCVD](#)

C M Wu, B P Zhang, J Z Shang et al.

[Characteristics of MOCVD- and MBE-grown InGa\(N\)As VCSELs](#)

H-P D Yang, C Lu, R Hsiao et al.

[Demonstration of Blue and Green GaN-Based Vertical-Cavity Surface-Emitting Lasers by Current Injection at Room Temperature](#)

Daiji Kasahara, Daisuke Morita, Takao Kosugi et al.

[InGaN light-emitting diodes with embedded nanoporous GaN distributed Bragg reflectors](#)

Bing-Cheng Shieh, Yuan-Chang Jhang, Kun-Pin Huang et al.

## Room-temperature continuous-wave operation of GaN-based vertical-cavity surface-emitting lasers with n-type conducting AlInN/GaN distributed Bragg reflectors

Kazuki Ikeyama<sup>1</sup>, Yugo Kozuka<sup>1</sup>, Kenjo Matsui<sup>1</sup>, Shotaro Yoshida<sup>1</sup>, Takanobu Akagi<sup>1</sup>, Yasuto Akatsuka<sup>1</sup>, Norikatsu Koide<sup>1</sup>, Tetsuya Takeuchi<sup>1\*</sup>, Satoshi Kamiyama<sup>1</sup>, Motoaki Iwaya<sup>1</sup>, and Isamu Akasaki<sup>1,2</sup>

<sup>1</sup>Faculty of Science and Technology, Meijo University, Nagoya 468-8502, Japan

<sup>2</sup>Graduate School of Engineering and Akasaki Research Center, Nagoya University, Nagoya 464-8603, Japan

\*E-mail: take@meijo-u.ac.jp

Received July 18, 2016; accepted August 13, 2016; published online September 1, 2016

The room-temperature continuous-wave operation of a 1.5 $\lambda$ -cavity GaN-based vertical-cavity surface-emitting laser with an n-type conducting AlInN/GaN distributed Bragg reflector (DBR) was achieved. A peak reflectivity of over 99.9% was obtained in the n-type conducting AlInN/GaN DBR so that the current was injected through the DBR for the operation. The threshold current was 2.6 mA, corresponding to the threshold current density of 5.2 kA/cm<sup>2</sup>, and the operating voltage was 4.7 V. A lasing spectrum with a peak wavelength of 405.1 nm and a full-width at half maximum of 0.08 nm was also observed. © 2016 The Japan Society of Applied Physics

**G**aN-based vertical-cavity surface-emitting lasers (VCSELs) are expected to be adopted in various applications, such as retinal scanning displays, adaptive headlights, and high-speed visible-light communication systems. Recently, the lasing operations of GaN-based VCSELs with a combination of two dielectric distributed Bragg reflectors (DBRs)<sup>1–10</sup> or a combination of a top dielectric DBR and a bottom undoped GaN-based DBR<sup>11–16</sup> have been demonstrated. Although most of the commercialized infrared VCSELs utilize conducting GaAs-based DBRs,<sup>17</sup> most of the GaN-based VCSELs reported so far have no other choice but to rely on double intracavity contact structures due to such insulating DBRs. The double intracavity contacts typically lead to current crowding at current aperture edges, low optical confinement factors due to a large cavity length, and complexities of fabrication processes, resulting in high threshold current densities and low slope efficiencies. If at least an n-type conducting GaN-based DBR is successfully developed, such as the n-type conducting GaAs-based DBR, a very short ( $\sim 1\lambda$ ) cavity structure with a simple back-side n-electrode is possible, leading to high-performance and low-cost GaN-based VCSELs.

There are few reports on the n-type conducting GaN-based DBRs. Arita et al. fabricated a 26-pair n-type Al<sub>0.4</sub>Ga<sub>0.6</sub>N/GaN DBR, showing a peak reflectivity of 91% at 400 nm and a series resistance of 180  $\Omega$  in a microcavity LED configuration.<sup>18</sup> Then, a 20.5-pair n-type AlN/GaN DBR grown on a SiC substrate by MBE showed a peak reflectivity of 99% at 450 nm and a specific series resistance of  $2 \times 10^{-3} \Omega \text{cm}^2$ .<sup>19</sup> Also, a 40-pair n-type Al<sub>0.12</sub>Ga<sub>0.88</sub>N/GaN DBR showed a peak reflectivity of 91.6% at 368 nm and a bulk resistivity of 0.52  $\Omega \text{cm}$ .<sup>20</sup> However, so far, there has been no report on the laser operation of a GaN-based VCSEL with a conducting DBR. We have been developing insulating and n-type conducting Al<sub>0.82</sub>In<sub>0.18</sub>N/GaN DBRs.<sup>21,22</sup> AlInN is lattice-matched with GaN, so that the AlInN/GaN DBRs have potentials of higher material quality and reflectivity than the AlGaIn/GaN DBRs,<sup>23,24</sup> possibly comparable to the GaAs-based DBRs.<sup>25</sup> A negative aspect of AlInN was the very low growth rate, but we have optimized the growth conditions for AlInN with a growth rate of over 0.5  $\mu\text{m}/\text{h}$ .<sup>21</sup> Regarding the conductivity, it must be considered that the large polarization charges induced at the AlInN/GaN inter-

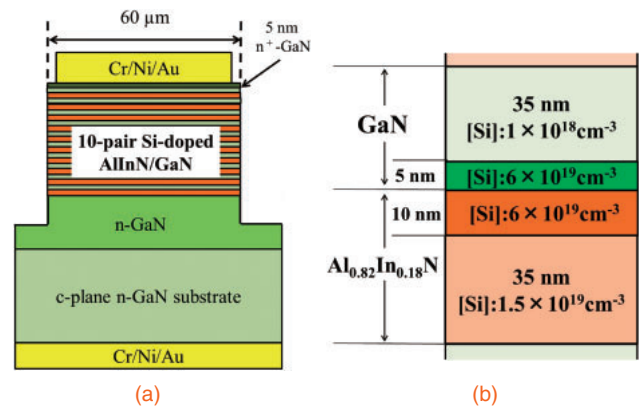


**Fig. 1.** (a) Schematic of a 10-pair Si-doped AlInN/GaN DBR structure for vertical current injection and (b) a Si-doping profile in a pair of AlInN/GaN layers.

faces markedly affect the vertical conductivity through the interfaces.<sup>26</sup> We then proposed and developed a new concept of modulation doping for a nitride-based DBR to neutralize the large polarization charges with ionized donors.<sup>22,27</sup> In this study, we developed n-type conducting AlInN/GaN DBRs and demonstrated the room-temperature continuous-wave (CW) operation of a GaN-based VCSEL utilizing the n-type conducting AlInN/GaN DBR.

We prepared four different samples on free-standing (0001) n-GaN substrates (carrier concentration:  $1 \times 10^{18} \text{cm}^{-3}$ , thickness: 330  $\mu\text{m}$ ) by metalorganic vapor phase epitaxy. The first three samples were AlInN/GaN DBRs. As shown in Fig. 1(a), a 10-pair Si-doped AlInN/GaN DBR with a 5 nm n<sup>+</sup>-GaN contact layer was prepared in order to investigate vertical current injection. A 1.0  $\mu\text{m}$  n-GaN buffer layer with a Si concentration of  $6.0 \times 10^{18} \text{cm}^{-3}$  was grown before the DBR growth. The thicknesses of AlInN and GaN were 40–45 nm, designed as a peak reflectivity wavelength of 405 nm. After the DBR growth, the 5 nm n<sup>+</sup>-GaN contact layer with a Si concentration of  $1 \times 10^{20} \text{cm}^{-3}$  was capped. On the other hand, as described in Fig. 1(b), a specific modulation doping with Si was formed in the DBR based on our previous results.<sup>22</sup> Although the Si concentrations in most regions were in the range of  $10^{18}$ – $10^{19} \text{cm}^{-3}$ , a very high Si concentration ( $6 \times 10^{19} \text{cm}^{-3}$ ) was doped in 15 nm regions including

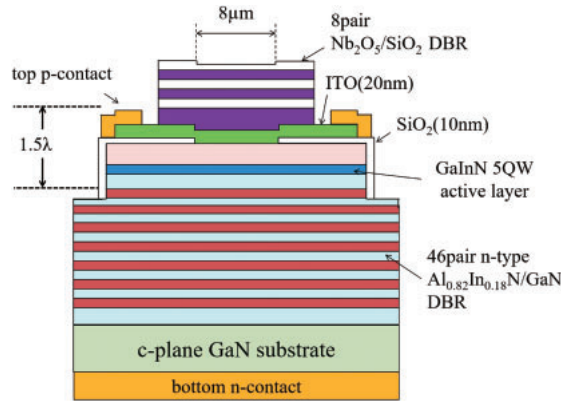


**Fig. 2.** Schematic of a  $1.5\lambda$ -cavity GaN-based VCSEL with vertical current injection through the n-type conducting AlInN/GaN DBR.

the top AlInN interfaces with GaN at which a large negative polarization charge concentration ( $3 \times 10^{13} \text{ cm}^{-2}$ ) was generated. Note that Si could be ionized and positively charged with the concentration of  $6 \times 10^{19} \text{ cm}^{-3}$  in the 15 nm regions corresponding to a sheet concentration of  $9 \times 10^{13} \text{ cm}^{-2}$ . Therefore, the Si concentration around the interface should be sufficiently high to completely neutralize the high negative polarization charge concentration. This is a concept that we previously proposed, sufficiently eliminating energy spikes in the band diagram at the GaN/AlInN interfaces due to the polarization charges in order to obtain a low vertical resistance through the interfaces.<sup>22,27</sup> A 60- $\mu\text{m}$ -diameter mesa was formed by dry etching, and Cr/Ni/Au contacts were deposited on the top of the mesa and on the back side of the substrate. Current density–voltage ( $J$ – $V$ ) characteristics under a vertical current injection through the DBR were measured.

The second DBR sample was a 46-pair Si-doped AlInN/GaN DBR for reflectivity and surface morphology measurements. The same modulation doping with Si was performed, but no contact layer was grown on the DBR. For comparison, a 40-pair undoped AlInN/GaN DBR, which was used in our previous VCSELs showing room-temperature CW operations,<sup>15,16</sup> was also prepared as the third DBR sample. Reflectivity spectra of the DBRs were measured with an absolute reflectivity measurement system, and the surface morphology was observed by atomic force microscopy.

The fourth sample was a GaN-based VCSEL with the 46-pair Si-doped AlInN/GaN DBR as shown in Fig. 2. After growing the AlInN/GaN DBR, a  $1.25\lambda$ -cavity containing 50 nm n-GaN, five 3 nm GaInN/6 nm GaN quantum wells, a 20 nm p- $\text{Al}_{0.2}\text{Ga}_{0.8}\text{N}$  electron blocking layer, 60 nm p-GaN, and a 10 nm  $\text{p}^+$ -GaN contact were continuously grown on the DBR. Next, a 39  $\mu\text{m}$  mesa of 200 nm height was formed on the wafer for device isolation by dry etching. Note that the Si-doped AlInN/GaN DBR was hardly etched out in the VCSEL structure. Then, 10 nm  $\text{SiO}_2$  with an 8- $\mu\text{m}$ -diameter aperture, a 20 nm indium–tin oxide (ITO) p-electrode, and a 32 nm  $\text{Nb}_2\text{O}_5$  spacer layer were deposited, forming a  $1.5\lambda$ -cavity. The emission area was defined by the 8- $\mu\text{m}$ -diameter aperture of  $\text{SiO}_2$ . Next, an 8-pair  $\text{Nb}_2\text{O}_5/\text{SiO}_2$  top DBR, showing a 99.9% reflectivity, was also deposited. Finally, a p-pad on the ITO layer and an n-electrode on the n-GaN substrate back side were deposited. Current–voltage–light output power ( $I$ – $V$ – $L$ ) characteristics were measured under

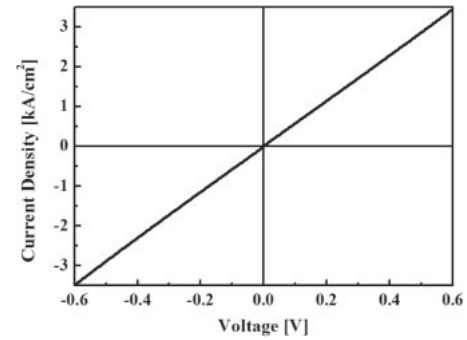


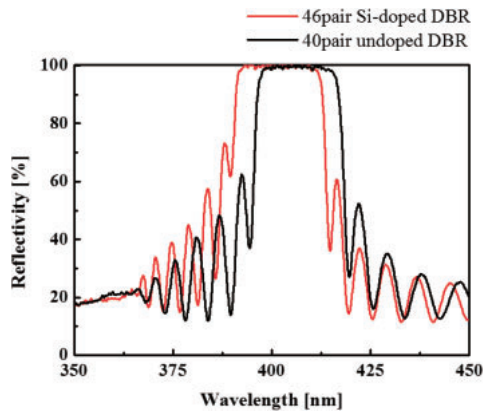
**Fig. 3.**  $J$ – $V$  characteristics of a 10-pair Si-doped AlInN/GaN DBR.

CW operation at room temperature. Emission spectra and polarization characteristics were also measured. The light output power was coupled to a fiber cable in the above measurements.

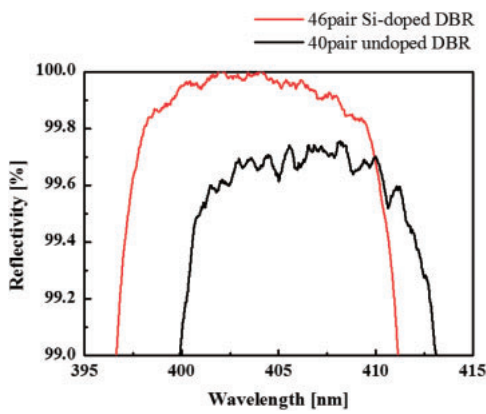
Figure 3 shows the  $J$ – $V$  characteristics of the 10-pair Si-doped AlInN/GaN DBR for the vertical current injection. The positive voltage in the figure means that a positive voltage was applied to the top n-electrode on the mesa. A linear relationship between current density and voltage was clearly observed in both forward and reverse directions. A specific series resistance of  $1.7 \times 10^{-4} \Omega \text{ cm}^2$  was obtained. Considering the number of pairs and the contribution of n-electrode contact resistances, the resistance of a 46-pair DBR is estimated to be  $7.8 \times 10^{-4} \Omega \text{ cm}^2$  or lower, which is lower than that previously reported for the GaN-based DBR,<sup>19</sup> but still higher than that reported for a p-type GaAs-based DBR ( $6.2 \times 10^{-5} \Omega \text{ cm}^2$ ).<sup>17</sup>

Figures 4(a) and 4(b) show wide-range and narrow-range reflectivity spectra of the 46-pair Si-doped and 40-pair undoped AlInN/GaN DBRs, respectively. A large stopband width (22 nm) above a 90% reflectivity and many sharp side lobes were consistently observed from both the DBRs as shown in Fig. 4(a). Furthermore, the 46-pair Si-doped AlInN/GaN DBR showed a peak reflectivity of over 99.9% at 404 nm, which was clearly higher than that of the 40-pair undoped AlInN/GaN DBR. These results suggest that our modulation doping with Si in the AlInN/GaN DBR does not adversely affect the reflectivity characteristics. The higher reflectivity of the 46-pair DBR was mainly due to 6 additional pairs. We also observed a well-ordered surface morphology of the Si-doped DBR covered with atomic layer steps in Fig. 5, suggesting that a small surface roughness (RMS value: 0.08 nm) led to a low scattering loss as a reflector. As indicated above, we have obtained the 46-pair Si-doped AlInN/GaN DBR showing the very high reflectivity and reasonably good electrical conductivity simultaneously.

Figures 6(a) and 6(b) show the  $I$ – $L$ – $V$  characteristics and emission spectra of the  $1.5\lambda$ -cavity GaN-based VCSEL with the n-type conducting AlInN/GaN bottom DBR under CW operation at room temperature. A marked increase in light output power was clearly observed at 2.6 mA, and also a very narrow emission spectrum (FWHM: 0.08 nm) at 405.1 nm was observed. In Fig. 6(b), a redshift of the emission peak was also observed with an increase of the injected current. At this moment we believe the shift was caused by heating due to a low thermal conductivity of AlInN layers.<sup>28</sup> Figure 7 shows light output power as a function of polarizer angle at



(a)



(b)

**Fig. 4.** (a) Wide-range and (b) narrow-range reflectivity spectra of a 46-pair n-type conducting AlInN/GaN DBR and a 40-pair undoped AlInN/GaN DBR.

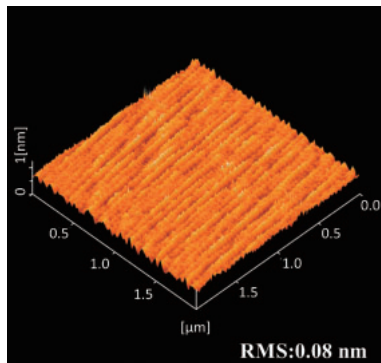
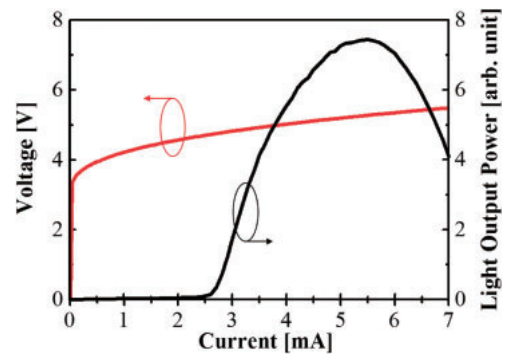
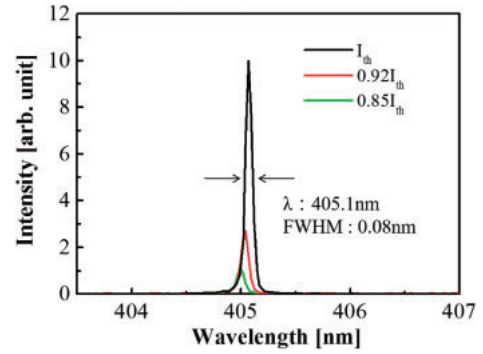


**Fig. 5.**  $2 \times 2 \mu\text{m}^2$  AFM image of a 46-pair n-type conducting AlInN/GaN DBR.

5.0 mA, indicating that the emission light was linearly polarized. Thus, we concluded that the GaN-based VCSEL with the vertical current injection through the conducting bottom DBR showed a room-temperature CW operation with a threshold current of 2.6 mA, corresponding to a threshold current density of  $5.2 \text{ kA/cm}^2$ . The operating voltage and differential device resistance at the threshold current were 4.7 V and  $250 \Omega$ , respectively. Previously, we demonstrated the  $4\lambda$ -cavity GaN-based VCSEL containing the double intracavity contacts with the insulating AlInN/GaN DBR. The VCSEL showed a  $7.5 \text{ kA/cm}^2$  threshold current density and a 4.8 V operating voltage.<sup>16)</sup> Thus, we concluded that the



(a)



(b)

**Fig. 6.** (a)  $I$ - $L$ - $V$  characteristics and (b) emission spectra of the  $1.5\lambda$ -cavity GaN-based VCSEL with the 46-pair n-type conducting AlInN/GaN DBR.

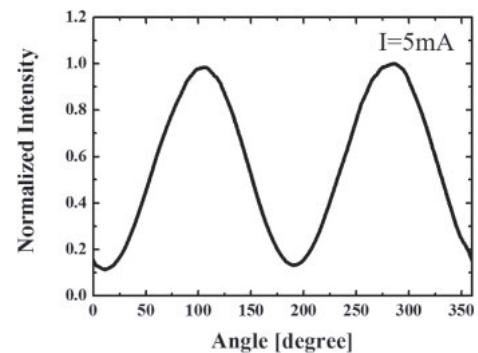


**Fig. 7.** Light output power of a VCSEL as a function of polarizer angle at 5.0 mA.

characteristics of our GaN-based VCSEL with the n-type conducting bottom DBR were comparable to or even better than those of the GaN-based VCSEL with the insulating DBR. Further improvements of the characteristics of the GaN-based VCSELs with the n-type conducting DBRs are expected with the further optimization of the modulation doping of Si in terms of not only resistivity but also the absorption and appropriate design/control of layer thicknesses in the VCSELs.

In summary, a room-temperature CW operation of the  $1.5\lambda$ -cavity GaN-based VCSEL with an n-type conducting AlInN/GaN bottom DBR was achieved. The n-type conducting AlInN/GaN DBR simultaneously showed an ohmic behavior and a high reflectivity (99.9%). As a result, the GaN-based VCSEL showed a threshold current density of

5.2kA/cm<sup>2</sup> and an operating voltage of 4.7V at a lasing wavelength of 405.1 nm. These results indicate the feasibility of high-performance and low-cost GaN-based VCSELs with vertical current injections through conducting DBRs.

**Acknowledgment** This study was supported by the MEXT-Supported Program for Strategic Research Foundation at Private Universities, 2012–2016.

- 1) Y. Higuchi, K. Omae, H. Matsumura, and T. Mukai, *Appl. Phys. Express* **1**, 121102 (2008).
- 2) K. Omae, Y. Higuchi, K. Nakagawa, H. Matsumura, and T. Mukai, *Appl. Phys. Express* **2**, 052101 (2009).
- 3) D. Kasahara, D. Morita, T. Kosugi, K. Nakagawa, J. Kawamata, Y. Higuchi, H. Matsumura, and T. Mukai, *Appl. Phys. Express* **4**, 072103 (2011).
- 4) T. Onishi, O. Imafuji, K. Nagamatsu, M. Kawaguchi, K. Yamanaka, and S. Takigawa, *IEEE J. Quantum Electron.* **48**, 1107 (2012).
- 5) W. J. Liu, X. L. Hu, L. Y. Ying, J. Y. Zhang, and B. P. Zhang, *Appl. Phys. Lett.* **104**, 251116 (2014).
- 6) S. Izumi, N. Fuutagawa, T. Hamaguchi, M. Murayama, M. Kuramoto, and H. Narui, *Appl. Phys. Express* **8**, 062702 (2015).
- 7) T. Hamaguchi, N. Fuutagawa, S. Izumi, M. Murayama, and H. Narui, *Phys. Status Solidi A* **213**, 1170 (2016).
- 8) C. Holder, J. S. Speck, S. P. DenBaars, S. Nakamura, and D. Feezell, *Appl. Phys. Express* **5**, 092104 (2012).
- 9) J. T. Leonard, D. A. Cohen, B. P. Yonkee, R. M. Farrell, T. Margalith, S. Lee, S. P. DenBaars, J. S. Speck, and S. Nakamura, *Appl. Phys. Lett.* **107**, 011102 (2015).
- 10) J. T. Leonard, E. C. Young, B. P. Yonkee, D. A. Cohen, T. Margalith, S. P. DenBaars, and S. Nakamura, *Appl. Phys. Lett.* **107**, 091105 (2015).
- 11) T.-C. Lu, C.-C. Kao, H.-C. Kuo, G.-S. Huang, and S.-C. Wang, *Appl. Phys. Lett.* **92**, 141102 (2008).
- 12) T.-C. Lu, S. W. Chen, T. T. Wu, P. M. Tu, C. K. Chen, C. H. Chen, Z. Y. Li, H. C. Kuo, and S. C. Wang, *Appl. Phys. Lett.* **97**, 071114 (2010).
- 13) D. H. Hsieh, A. J. Tzou, T. S. Kao, F. I. Lai, D. W. Lin, B. C. Lin, T. C. Lu, W. C. Lai, C. H. Chen, and H. C. Kuo, *Opt. Express* **23**, 27145 (2015).
- 14) G. Cosendey, A. Castiglia, G. Rossbach, J.-F. Carlin, and N. Grandjean, *Appl. Phys. Lett.* **101**, 151113 (2012).
- 15) K. Matsui, Y. Kozuka, K. Ikeyama, K. Horikawa, T. Furuta, T. Akagi, T. Takeuchi, S. Kamiyama, M. Iwaya, and I. Akasaki, *Jpn. J. Appl. Phys.* **55**, 05FJ08 (2016).
- 16) T. Furuta, K. Matsui, K. Horikawa, K. Ikeyama, Y. Kozuka, S. Yoshida, T. Akagi, T. Takeuchi, S. Kamiyama, M. Iwaya, and I. Akasaki, *Jpn. J. Appl. Phys.* **55**, 05FJ11 (2016).
- 17) K. Tai, L. Yang, Y. H. Wang, J. D. Wynn, and A. Y. Cho, *Appl. Phys. Lett.* **56**, 2496 (1990).
- 18) M. Arita, M. Nishioka, and Y. Arakawa, *Phys. Status Solidi A* **194**, 403 (2002).
- 19) T. Ive, O. Brandt, H. Kostial, T. Hesjedal, M. Ramsteiner, and K. H. Ploog, *Appl. Phys. Lett.* **85**, 1970 (2004).
- 20) Y.-S. Liu, A. F. M. S. Haq, T.-T. Kao, K. Mehta, S.-C. Shen, T. Detchprohm, P. D. Yoder, and R. D. Dupuis, *J. Cryst. Growth* **443**, 81 (2016).
- 21) Y. Kozuka, K. Ikeyama, T. Yasuda, T. Takeuchi, S. Kamiyama, M. Iwaya, and I. Akasaki, *MRS Proc.* **1736**, mrsf14-1736-t13-08 (2015).
- 22) S. Yoshida, K. Ikeyama, T. Yasuda, T. Furuta, T. Takeuchi, M. Iwaya, S. Kamiyama, and I. Akasaki, *Jpn. J. Appl. Phys.* **55**, 05FD10 (2016).
- 23) J.-F. Carlin and M. Ilegems, *Appl. Phys. Lett.* **83**, 668 (2003).
- 24) J.-F. Carlin, J. Dorsaz, E. Feltin, R. Butté, N. Grandjean, M. Ilegems, and M. Lüti, *Appl. Phys. Lett.* **86**, 031107 (2005).
- 25) M. C. Y. Huang, Y. Zhou, and C. J. Chang-Hasnain, *Nat. Photonics* **1**, 119 (2007).
- 26) R. Charash, H. Kim-Chauveau, A. Vajpeyi, M. Akther, P. P. Maaskant, E. Frayssinet, P. de Mierry, J.-Y. Duboz, and B. Corbett, *Phys. Status Solidi C* **8**, 2378 (2011).
- 27) T. Yasuda, K. Hayashi, S. Katsuno, T. Takeuchi, S. Kamiyama, M. Iwaya, I. Akasaki, and H. Amano, *Phys. Status Solidi A* **212**, 920 (2015).
- 28) H. Tong, J. Zhang, G. Liu, J. A. Herbsommer, G. S. Huang, and N. Tansu, *Appl. Phys. Lett.* **97**, 112105 (2010).

## Control of the Detection Wavelength in AlGaN/GaN-Based Hetero-Field-Effect-Transistor Photosensors

This content has been downloaded from IOPscience. Please scroll down to see the full text.

2013 Jpn. J. Appl. Phys. 52 08JF02

(<http://iopscience.iop.org/1347-4065/52/8S/08JF02>)

View [the table of contents for this issue](#), or go to the [journal homepage](#) for more

Download details:

IP Address: 202.11.1.201

This content was downloaded on 03/03/2017 at 06:56

Please note that [terms and conditions apply](#).

You may also be interested in:

[High-photosensitivity AlGaN-based UV heterostructure-field-effect-transistor-type photosensors](#)

Akira Yoshikawa, Yuma Yamamoto, Takuya Murase et al.

[Realization of high-performance hetero-field-effect-transistor-type ultraviolet photosensors using p-type GaN comprising three-dimensional island crystals](#)

Yuma Yamamoto, Akira Yoshikawa, Toshiki Kusafuka et al.

[Concentrating Properties of Nitride-Based Solar Cells Using Different Electrodes](#)

Mikiko Mori, Shinichiro Kondo, Shota Yamamoto et al.

[Microstructure Analysis of AlGaN on AlN Underlying Layers with Different Threading Dislocation Densities](#)

Kimiyasu Ide, Yuko Matsubara, Motoaki Iwaya et al.

[Improvement of Light Extraction Efficiency for AlGaN-Based Deep Ultraviolet Light-Emitting Diodes](#)

Tetsuhiko Inazu, Shinya Fukahori, Cyril Pernot et al.

[Correlation between Device Performance and Defects in GaInN-Based Solar Cells](#)

Mikiko Mori, Shinichiro Kondo, Shota Yamamoto et al.

[AlGaN/GaN Heterostructure Field-Effect Transistors on Fe-Doped GaN Substrates with High Breakdown Voltage](#)

Yoshinori Oshimura, Takayuki Sugiyama, Kenichiro Takeda et al.

[Laser Operation of Nitride Laser Diodes with GaN Well Layer in 340 nm Band](#)

Masakazu Kuwabara, Yoji Yamashita, Kousuke Torii et al.

## Control of the Detection Wavelength in AlGaIn/GaN-Based Hetero-Field-Effect-Transistor Photosensors

Mami Ishiguro<sup>1\*</sup>, Kazuya Ikeda<sup>1</sup>, Masataka Mizuno<sup>1</sup>, Motoaki Iwaya<sup>1</sup>, Tetsuya Takeuchi<sup>1</sup>, Satoshi Kamiyama<sup>1</sup>, and Isamu Akasaki<sup>1,2</sup>

<sup>1</sup>Faculty of Science and Technology, Meijo University, Nagoya 468-8502, Japan

<sup>2</sup>Akasaka Research Center, Nagoya University, Nagoya 464-8603, Japan

E-mail: 123434004@c alumni.meijo-u.ac.jp

Received October 12, 2012; accepted February 13, 2013; published online May 31, 2013

We examined the control of the detection wavelength in AlGaIn/GaN-based hetero-field-effect-transistor (HFET) photosensors. The detection wavelength of these devices can be controlled by using the p-GaInN optical gate or inserting a GaInN channel layer between AlGaIn and GaN. In addition, the photosensitivity of AlGaIn/GaN HFET photosensors with a p-GaInN optical gate was more than two orders of magnitude higher than that of the AlGaIn/GaN HFET photosensor with a GaInN channel layer. Moreover, the photosensitivity of the AlGaIn/GaN HFET photosensor with a p-GaInN optical gate greatly surpassed those of commercially available Si pin and Si avalanche photodiodes, and was comparable to those of photomultiplier tubes. © 2013 The Japan Society of Applied Physics

### 1. Introduction

Since group-III-nitride semiconductors, i.e., InN, GaN, AlN, and their alloys, have direct wide band gaps ranging from 0.67 to 6.2 eV,<sup>1-3</sup> they are suitable materials for optical devices for light in the UV to near-infrared range, which includes the entire visible region. High-performance emitters, such as UV-,<sup>4,5</sup> blue-, green-, and white-light-emitting diodes<sup>6</sup> and UV-<sup>7</sup> violet-,<sup>8</sup> blue-,<sup>9</sup> and green<sup>10</sup>-laser diodes, have already been achieved using these materials.

In contrast, the physical properties of nitride semiconductors are expected to be applied to other devices, such as hetero-field-effect-transistors<sup>11,12</sup> and solar cells.<sup>13,14</sup> Moreover, the nitride-based photosensors in the UV-region have also attracted attention for such applications as flame detection and biosensors.<sup>14-19</sup> The nitride-based photosensors are also promising as a technology for frontier applications, such as wireless visible-light communication. Wireless visible-light communication has attracted attention, for example, for use in the optical bus of computers and for wireless access in vehicles, because it has major advantages such as no effect of electromagnetic radiation, low cost, and high directionality. In wireless visible-light communication, Si-based photosensors, such as pin diodes, are used. However, the communication speed of such a system is limited to several hundred kbps because of the low performance of the photosensors. To increase the communication speed, the photosensor used must have a high photosensitivity, a high ratio of photocurrent to dark current (high S/N ratio), and a high response speed.

Recently, we have reported novel high-performance nitride-based AlGaIn/GaN hetero-field-effect-transistor-type (HFET-type) photosensors with a p-GaInN optical gate.<sup>20</sup> These photosensors employ a two-dimensional electron gas at the heterointerface between AlGaIn and GaN as a highly conductive channel with a high electron mobility. The photosensitivity of these devices greatly surpassed those of commercially available Si pin and Si avalanche photodiodes, and was comparable to those of photomultiplier tubes.<sup>21</sup>

Figure 1 shows schematic diagrams of the operating principle of this device. Such devices take advantage of the

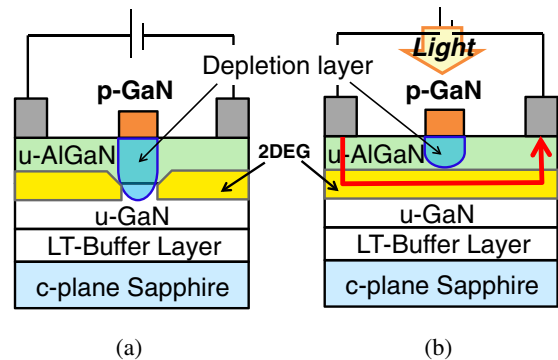


Fig. 1. (Color online) Schematic diagrams of the operating principle of HFET-type photosensor with p-GaInN optical gate (a) with no irradiation of light and (b) with irradiation of light.

two-dimensional electron gas (2DEG) by means of the AlGaIn/GaN heterostructure and depletion layer formed by the p-GaInN optical gate. In Fig. 1(a), a 2DEG is formed at the AlGaIn/GaN heterointerface region without the p-GaInN. Thus, contact and sheet resistances in this region are very small. In contrast, because the depletion layer is formed immediately beneath the p-GaInN, sheet resistance in this region is very high. According to the concept of the voltage divider circuit, most of the voltage is applied immediately beneath the p-GaInN. Because this distance is several micrometers, an electric field as high as  $10^4$  V/cm is applied only immediately beneath the p-GaInN, when a voltage of several volts is applied between the anode and cathode electrodes. In addition, the electron mobility of the 2DEG in the AlGaIn/GaN heterointerface is approximately  $1000 \text{ cm}^2 \text{ V}^{-1} \text{ s}^{-1}$ . When electron-hole pairs are formed in the p-GaInN optical gate by irradiating light, the conduction band edge in the AlGaIn/GaN heterostructure is considered to change. The drift current density is determined as the product of the elementary charge, electron concentration, electron mobility, and electric field. Accordingly, a large photocurrent can be obtained by irradiating weak light to the AlGaIn/GaN heterostructure, as shown in Fig. 1(b). Therefore, this structure can be expected to have an extremely

high photosensitivity and a high S/N ratio. However, there are many unclear points in the operating principle of these devices. In particular, control of the detection wavelength in these devices is unknown.

In this study, we examined the control of the detection wavelength in the AlGaInN/GaN-based HFET photosensors. We also discuss the performance of these devices.

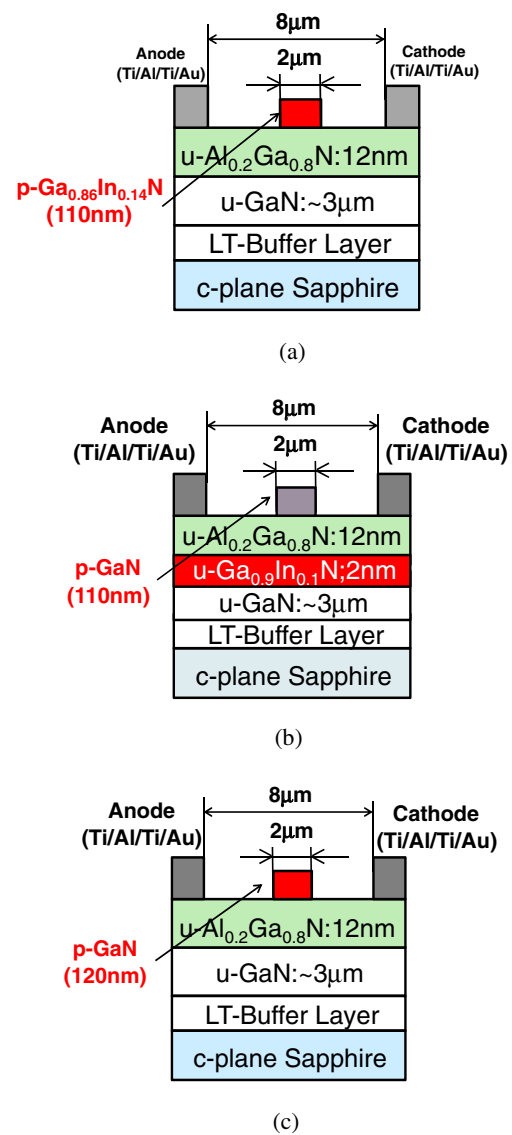
### 2. Experimental Procedure

Figure 2 shows a schematic view of the HFET-type photosensor with a p-layer optical gate. The device was grown by metalorganic vapor phase epitaxy on a sapphire (0001) substrate covered with a low-temperature-deposited (LT-) buffer layer.<sup>22)</sup> In this study, we fabricated three samples for controlling the detection wavelength. In type I [Fig. 2(a)], we fabricated an AlGaInN/GaN HFET-type photosensor with a p-GaInN optical gate. This structure is a stack comprising a 3.0- $\mu\text{m}$ -thick unintentionally doped GaN (u-GaN) layer, a 12-nm-thick unintentionally doped  $\text{Al}_{0.2}\text{Ga}_{0.8}\text{N}$  (u- $\text{Al}_{0.2}\text{Ga}_{0.8}\text{N}$ ) barrier layer, and a 110-nm-thick Mg-doped p- $\text{Ga}_{0.86}\text{In}_{0.14}\text{N}$  layer with a Mg concentration of approximately  $3 \times 10^{19} \text{ cm}^{-3}$ . In type II [Fig. 2(b)], we fabricated the AlGaInN/GaN HFET with a GaInN channel layer inserted between AlGaInN and GaN with a p-GaN optical gate. This structure is stacked with a 3.0- $\mu\text{m}$ -thick u-GaN layer, a 2-nm-thick u- $\text{Ga}_{0.9}\text{In}_{0.1}\text{N}$  channel layer, a 12-nm-thick u- $\text{Al}_{0.2}\text{Ga}_{0.8}\text{N}$  barrier layer, and a 110-nm-thick Mg-doped p-GaN layer with a Mg concentration of approximately  $3 \times 10^{19} \text{ cm}^{-3}$ . In type III [Fig. 2(c)], we fabricated the AlGaInN/GaN HFET with a 120-nm-thick p-GaN optical gate as a reference. The AlN molar fraction and thickness of the AlGaInN barrier layer were determined by X-ray diffraction  $2\theta/\omega$  scans with (0002) diffraction. The hole concentrations in the p- $\text{Ga}_{0.86}\text{In}_{0.14}\text{N}$  and p-GaN optical gates were approximately  $2 \times 10^{18}$  and  $1 \times 10^{18} \text{ cm}^{-3}$  at room temperature (RT), respectively.

After the activation of Mg acceptors by heating at 525 °C for 4 min in  $\text{N}_2$ , mesa isolation was performed by  $\text{Cl}_2$  reactive ion etching (RIE). Next, the p-layers were etched by RIE, except in the light-receiving area. Then, Ti/Al/Ti/Au was deposited as the anode and cathode contacts on the u- $\text{Al}_{0.2}\text{Ga}_{0.8}\text{N}$  layer. The length and width of the p-GaInN optical gate were 2 and 100  $\mu\text{m}$ , respectively, and the interval between the anode and cathode contacts was 8  $\mu\text{m}$ . No antireflection coating was used for any of the devices in this study. The photocurrent at each light wavelength was measured with a semiconductor parameter analyzer (Agilent Technologies HP-4155C). The photosensitivity of each photosensor was calculated from the photocurrent measured at light wavelength intervals of 5 nm using a spectroscope with a Xe lamp at RT. The intensity of the spectral radiance was measured at each wavelength. The monochromatic light irradiation densities of the spectroscope-measured photosensitivity ranged from 200 to 220  $\mu\text{W}/\text{cm}^2$ . Since the light-receiving area was 200  $\mu\text{m}^2$ , the amount of received light was very small and equivalent to approximately several hundred picowatts.

### 3. Results and Discussion

Figure 3 shows the monochromatic photosensitivity of each HFET-type photosensor with a driving voltage between



**Fig. 2.** (Color online) Schematic views of device structures: (a) HFET-type photosensor with p-GaInN optical gate, (b) HFET-type photosensor with GaInN channel layer, and (c) HFET-type photosensor with p-GaN optical gate.

the anode and cathode ( $V_{AC}$ ) of 5 V obtained using a Xe lamp and a spectrometer. Figure 4 also shows the normalized monochromatic photosensitivity of each photosensor. The absorption edge wavelengths of the photosensors with the p-GaInN optical gate, the GaInN channel, and the p-GaN optical gate were approximately 450, 410, and 375 nm, respectively, as shown in Fig. 4. From this result, we concluded that the detection wavelength of the photosensitivity of the HFET-type photosensor can be controlled by controlling the InN molar fraction in the p-GaInN optical gate or the GaInN channel layer. In addition, the photosensor with the p- $\text{Ga}_{0.8}\text{In}_{0.2}\text{N}$  optical gate exhibits photosensitivity up to a longer wavelength of 450 nm. This is considered to be due to the difference in the InN molar fraction in the p-GaInN optical gate and the GaInN channel. Moreover, the maximum photosensitivity of the photosensor with the p-GaInN optical gate is three orders of magnitude higher than that of the GaInN-channel sample. Since the mobility of the HFET with a GaInN channel is about two orders of

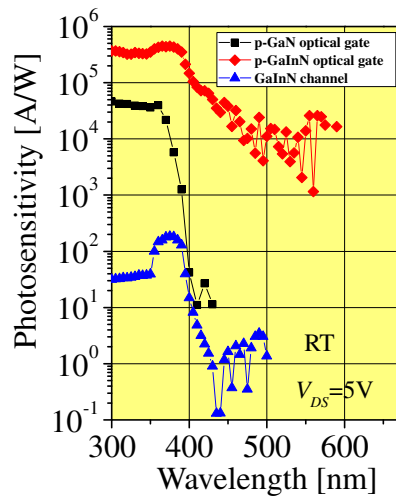


Fig. 3. (Color online) Monochromatic photosensitivity of each HFET-type photosensor.

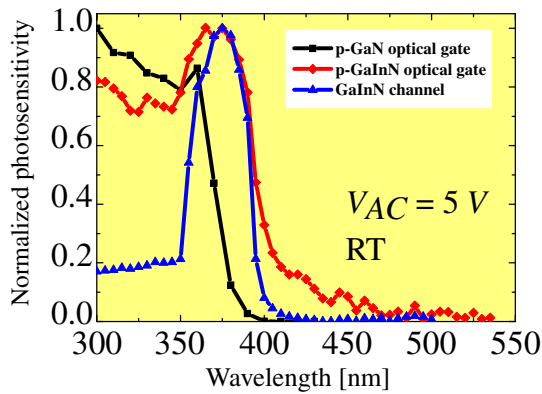


Fig. 4. (Color online) Normalized monochromatic photosensitivity of each HFET-type photosensor.

magnitude lower than that of the AlGaIn/GaN HFET,<sup>23)</sup> we inferred that such a difference in photosensitivity indeed exists in these devices. Therefore, we concluded that the p-GaInN optical gate is the best structure for controlling the detection wavelength of the AlGaIn/GaN HFET-type photosensors. The photocurrent-to-dark current (S/N) ratios of the p-GaInN optical gate and the GaInN channel were on the order of  $10^2$  and  $10^4$ , respectively.

Table I summarizes the photosensitivity, detection wavelength, and dark current of each photosensor. We also included the photosensitivity of our photosensors and those of commercial Si p-i-n photodiodes (Hamamatsu Photonics S2387-1010R),<sup>24)</sup> Si avalanche photodiodes (APD; Hamamatsu Photonics S8664-55),<sup>25)</sup> and photomultiplier tubes (Hamamatsu Photonics H7421-40, H7421-50, R928, and R3896).<sup>26)</sup> The photosensitivity of the HFET-type photosensor with a p-GaInN optical gate greatly surpassed those of the Si pin photodiode and Si APD and was comparable to those of the photomultiplier tubes. In addition, the dark currents of the HFET-type photosensor using a p-GaInN optical gate and GaInN channel layer are higher than those of other devices. We thought that this is caused by an insufficient depletion layer in the 2DEG in a p-GaInN optical gate and GaInN channel devices. Therefore,

Table I. Photosensitivity, detection wavelength, and dark current of commercial Si pin photodiode, Si APD, photomultiplier tubes, and HFET photosensors in this work.

Structure	Detection wavelength (nm)	Maximum photosensitivity (A/W)	Dark current (A)
HFET-type photosensor with p-GaInN optical gate	~450	$4 \times 10^5$	$10^{-5}$
HFET-type photosensor with GaInN channel layer	~410	$1 \times 10^2$	$10^{-5}$
HFET-type photosensor with p-GaN optical gate	~375	$4 \times 10^4$	$10^{-9}$
Si p-i-n photodiode <sup>19)</sup>	320–1100	$4 \times 10^{-1}$	$2.0 \times 10^{-10}$
Si APD <sup>19)</sup>	320–1000	$4 \times 10^1$	$5.0 \times 10^{-8}$
Photomultiplier tube <sup>19)</sup>	185–900	$9 \times 10^5$	$1.0 \times 10^{-8}$

we believe that the dark current is possible to be reduced by optimizing the device structure.<sup>27,28)</sup>

In addition to the high sensitivity, a high-speed response can be expected, because the response of this device is thought to be determined by the transit time of the 2DEG under the optical gate or the photocarrier recombination time in the p-GaInN optical gate, which are both estimated to be less than 1 ns.<sup>29,30)</sup> The dynamic performance of this device will be examined in the near future.

#### 4. Conclusions

We fabricated high-performance HFET-type photosensors for the detection of visible light. The detection wavelength of the photosensitivity of the HFET-type photosensor can be controlled by controlling the InN molar fraction in the p-GaInN optical gate or GaInN channel layer. Since the maximum photosensitivity of a photosensor with the p-GaInN optical gate is three orders of magnitude higher than that of the GaInN-channel sample, we concluded that the p-GaInN optical gate for controlling the detection wavelength of the AlGaIn/GaN HFET-type photosensors is the best structure. The photosensitivity of the HFET-type photosensors with a p-GaInN optical gate greatly surpassed those of the commercially available Si pin photodiode and Si APD and was comparable to those of photomultiplier tubes.

#### Acknowledgments

This study was supported by the Ministry of Education, Culture, Sports, Science and Technology of Japan, through the Supported Program for the Strategic Research Foundation at Private Universities, 2012–2016, and the Knowledge Cluster Initiative (Second Stage) of the Tokai Region Nanotechnology Manufacturing Cluster.

- 1) V. Yu. Davydov, A. A. Klochikhin, R. P. Seisyan, V. V. Emtsev, S. V. Ivanov, F. Bechstedt, J. Furthmüller, H. Harima, A. V. Mudryi, J. Aderhold, O. Semchinova, and J. Graul: *Phys. Status Solidi B* **229** (2002) r1.
- 2) H. Yamashita, K. Fukui, S. Misawa, and S. Yoshida: *J. Appl. Phys.* **50** (1979) 896.
- 3) B. Monemar: *Phys. Rev. B* **10** (1974) 676.
- 4) C. Pernot, M. Kim, S. Fukahori, T. Inazu, T. Fujita, Y. Nagasawa, A. Hirano, M. Ippommatsu, M. Iwaya, S. Kamiyama, I. Akasaki, and H.

- Amano: *Appl. Phys. Express* **3** (2010) 061004.
- 5) M. Shatalov, W. Sun, A. Lunev, X. Hu, A. Dobrinsky, Y. Bilenko, J. Yang, M. Shur, R. Gaska, C. Moe, G. Garrett, and M. Wraback: *Appl. Phys. Express* **5** (2012) 082101.
  - 6) I. Akasaki and H. Amano: *Jpn. J. Appl. Phys.* **45** (2006) 9001.
  - 7) K. Iida, T. Kawashima, A. Miyazaki, H. Kasugai, S. Mishima, A. Honshio, Y. Miyake, M. Iwaya, S. Kamiyama, H. Amano, and I. Akasaki: *Jpn. J. Appl. Phys.* **43** (2004) L499.
  - 8) I. Akasaki, H. Amano, S. Sota, H. Sakai, T. Tanaka, and M. Koike: *Jpn. J. Appl. Phys.* **34** (1995) L1517.
  - 9) S. Nagahama, T. Yanamoto, M. Sano, and T. Mukai: *Jpn. J. Appl. Phys.* **40** (2001) 3075.
  - 10) T. Miyoshi, S. Masui, T. Okada, T. Yanamoto, T. Kozaki, S. Nagahama, and T. Mukai: *Appl. Phys. Express* **2** (2009) 062201.
  - 11) M. A. Khan, M. S. Shur, Q. Chen, J. N. Kuznia, and C. J. Sun: *Electron. Lett.* **31** (1995) 398.
  - 12) Y. Kuwahara, T. Fujii, Y. Fujiyama, T. Sugiyama, M. Iwaya, T. Takeuchi, S. Kamiyama, I. Akasaki, and H. Amano: *Appl. Phys. Express* **3** (2010) 111001.
  - 13) M. Mori, S. Kondo, S. Yamamoto, T. Nakao, T. Fujii, M. Iwaya, T. Takeuchi, S. Kamiyama, I. Akasaki, and H. Amano: *Appl. Phys. Express* **5** (2012) 082301.
  - 14) C. Pernot, A. Hirano, M. Iwaya, T. Detchprohm, H. Amano, and I. Akasaki: *Jpn. J. Appl. Phys.* **39** (2000) L387.
  - 15) C. Pernot, A. Hirano, M. Iwaya, T. Detchprohm, H. Amano, and I. Akasaki: *Phys. Status Solidi A* **176** (1999) 147.
  - 16) D. Walker, X. Zhang, P. Kung, A. Saxler, S. Javadpour, J. Xu, and M. Razeghi: *Appl. Phys. Lett.* **68** (1996) 2100.
  - 17) E. Monroy, F. Calle, E. Muñoz, F. Omnès, P. Gibart, and J. A. Muñoz: *Appl. Phys. Lett.* **73** (1998) 2146.
  - 18) R. Mouillet, A. Hirano, M. Iwaya, T. Detchprohm, H. Amano, and I. Akasaki: *Jpn. J. Appl. Phys.* **40** (2001) L498.
  - 19) J. D. Brown, J. Li, P. Srinivasan, J. Matthews, and J. F. Schetzina: *MRS Internet J. Nitride Semicond. Res.* **5** (2000) 1.
  - 20) M. Iwaya, S. Miura, T. Fujii, S. Kamiyama, H. Amano, and I. Akasaki: *Phys. Status Solidi C* **6** (2009) S972.
  - 21) M. Ishiguro, K. Ikeda, M. Mizuno, M. Iwaya, T. Takeuchi, S. Kamiyama, and I. Akasaki: *Phys. Status Solidi: Rapid Res. Lett.* **7** (2013) 215.
  - 22) H. Amano, N. Sawaki, I. Akasaki, and Y. Toyoda: *Appl. Phys. Lett.* **48** (1986) 353.
  - 23) H. Ikki, Y. Isobe, D. Iida, M. Iwaya, T. Takeuchi, S. Kamiyama, I. Akasaki, H. Amano, A. Bandoh, and T. Udagawa: *Phys. Status Solidi A* **208** (2011) 1614.
  - 24) Web [[http://jp.hamamatsu.com/products/sensor-ssd/pd041/pd042/pd045/S2387-1010R/index\\_en.html](http://jp.hamamatsu.com/products/sensor-ssd/pd041/pd042/pd045/S2387-1010R/index_en.html)].
  - 25) Web [[http://jp.hamamatsu.com/products/\\_virtual/se/ssd\\_apd\\_s2/S8664-55/index\\_en.html](http://jp.hamamatsu.com/products/_virtual/se/ssd_apd_s2/S8664-55/index_en.html)].
  - 26) Web [[http://sales.hamamatsu.com/assets/pdf/catsandguides/p-dev\\_2009\\_TOH0017E01.pdf](http://sales.hamamatsu.com/assets/pdf/catsandguides/p-dev_2009_TOH0017E01.pdf)].
  - 27) T. Fujii, N. Tsuyukuchi, Y. Hirose, M. Iwaya, S. Kamiyama, H. Amano, and I. Akasaki: *Jpn. J. Appl. Phys.* **46** (2007) 115.
  - 28) T. Fujii, N. Tsuyukuchi, M. Iwaya, S. Kamiyama, H. Amano, and I. Akasaki: *Jpn. J. Appl. Phys.* **45** (2006) L1048.
  - 29) M. Shimizu, G. Piao, M. Inada, S. Yagi, Y. Yano, and N. Akutsu: *Jpn. J. Appl. Phys.* **47** (2008) 2817.
  - 30) M. Smith, G. D. Chen, J. Y. Lin, H. X. Jiang, A. Salvador, B. N. Sverdlov, A. Botchkarev, H. Morkoc, and B. Goldenberg: *Appl. Phys. Lett.* **68** (1996) 1883.

# Nitride-based hetero-field-effect-transistor-type photosensors with extremely high photosensitivity

Mami Ishiguro<sup>1</sup>, Kazuya Ikeda<sup>1</sup>, Masataka Mizuno<sup>1</sup>, Motoaki Iwaya<sup>\*1</sup>, Tetsuya Takeuchi<sup>1</sup>, Satoshi Kamiyama<sup>1</sup>, and Isamu Akasaki<sup>1,2</sup>

<sup>1</sup> Faculty of Science and Technology, Meijo University, Nagoya 468-8502, Japan

<sup>2</sup> Akasaki Research Center, Nagoya University, Nagoya 464-8603, Japan

Received 13 November 2012, revised 16 January 2013, accepted 17 January 2013

Published online 22 January 2013

**Keywords** GaInN, photosensors, HFET, field-effect transistors, two-dimensional electron gases

\* Corresponding author: e-mail [iwaya@meijo-u.ac.jp](mailto:iwaya@meijo-u.ac.jp)

AlGaIn/GaN hetero-field-effect-transistor-type (HFET-type) photosensors are fabricated with a p-GaInN optical gate for the detection of visible light. These photosensors employ a two-dimensional electron gas at the heterointerface between AlGaIn and GaN as a highly conductive channel with a high electron mobility. By changing the InN molar fraction in the

p-GaInN optical gate, the wavelength range of the photosensitivity of the HFET-type photosensors can be controlled. The photosensitivity of the AlGaIn/GaN HFET-type photosensors with a p-GaInN optical gate greatly surpassed those of commercially available Si pin and Si avalanche photodiodes, and was comparable to those of photomultiplier tubes.

© 2013 WILEY-VCH Verlag GmbH & Co. KGaA, Weinheim

**1 Introduction** Wireless visible-light communication has attracted attention for use in the optical bus in computers, for wireless access in vehicles, and so forth, because it has major advantages such as no effect of electromagnetic radiation, low cost, and high directionality. For these applications, the photosensor used must have a high photosensitivity, a high ratio of photocurrent to dark current (high S/N ratio), and a high response speed. However, no appropriate devices with a high photosensitivity and a high S/N ratio in the visible region have been developed. For instance, although a photomultiplier tube is able to detect light with an externally high photosensitivity, it is breakable, expensive, has a short lifetime, and requires a high operation voltage exceeding several hundred volts. Moreover, the photosensitivities of Si pin and avalanche photodiodes are up to four orders of magnitude lower than that of a photomultiplier tube.

Since group-III-nitride semiconductors, i.e., InN, GaN, AlN, and their alloys, have direct wide band gaps ranging from 0.67 to 6.2 eV [1–3], they are suitable materials for optical devices ranging from UV to near-infrared light, which includes the entire visible region. High-performance emitters, such as UV- [4], blue-, green-, and white-light-

emitting diodes and violet-, blue-, and green-laser diodes [5], have already been achieved using these materials. In contrast, although there have been several reports of nitride-based photodetectors, such as photoconductors [6], Schottky photovoltaic detectors [7], pin photodiodes [8], solar cells [9, 10], and photo field-effect transistors [11], no appropriate devices with both a high photosensitivity and a high S/N ratio have been realized. In addition, with the exception of solar cells, most devices only exhibit photosensitivity in the UV region, and cannot detect light in the visible region. Therefore, there are no suitable photosensors for application to wireless visible-light communication.

In this study, we fabricated high-performance nitride-based AlGaIn/GaN heterostructure-field-effect-transistor-type (HFET-type) photosensors with a p-GaInN optical gate for the detection of visible light. These photosensors employ a two-dimensional electron gas (2DEG) at the heterointerface between AlGaIn and GaN as a highly conductive channel with a high electron mobility. In addition, a p-GaInN layer ensures a high photosensitivity in the visible region and a high S/N ratio. The obtained results are very promising for the development of high-performance photosensors for wireless visible-light communication.

**2 Experimental procedure** Figure 1 shows a schematic view and a microscopic top-view image of an HFET-type photosensor with p-GaInN optical gate. The device was grown by metalorganic vapor phase epitaxy on a sapphire (0001) substrate covered with a low-temperature-deposited (LT-)buffer layer [12]. After depositing the 20-nm-thick LT-buffer layer at 500 °C, a 3.0- $\mu\text{m}$ -thick unintentionally doped GaN (u-GaN) layer, a 12-nm-thick unintentionally doped  $\text{Al}_{0.2}\text{Ga}_{0.8}\text{N}$  ( $\text{u-Al}_{0.2}\text{Ga}_{0.8}\text{N}$ ) barrier layer, and a Mg-doped p-GaInN layer with a Mg concentration of approximately  $3 \times 10^{19} \text{ cm}^{-3}$  were grown. We fabricated two devices with p-GaInN layer having InN molar fractions of 0.14 and 0. The AlN molar fraction and thickness of the AlGaN barrier layer were determined by X-ray diffraction  $2\theta/\omega$  scans with (0002) diffraction. The hole concentrations in the p-Ga<sub>0.86</sub>In<sub>0.14</sub>N and p-GaN optical gate, which were determined by Hall effect measurement, were approximately  $2 \times 10^{18}$  and  $3 \times 10^{18} \text{ cm}^{-3}$  at room temperature (RT), respectively.

After the activation of Mg acceptors by heating to 525 °C for 4 min in N<sub>2</sub>, mesa isolation was performed by Cl<sub>2</sub> reactive ion etching (RIE). Next, the p-GaInN optical gate was etched by RIE, except in the light-receiving area. Then, Ti/Al/Ti/Au was deposited as the anode and cathode contacts on the u-Al<sub>0.2</sub>Ga<sub>0.8</sub>N layer. The length and the width of p-GaInN optical gate were 2  $\mu\text{m}$  and 100  $\mu\text{m}$ , respectively, and the interval between the anode and cathode contacts was 8  $\mu\text{m}$ . No antireflection coating was used for any of the devices in this study.

In these devices, in absence of any p-layer, a 2DEG is formed at the AlGaN/GaN heterointerface region. Thus, contact and sheet resistances in this region are very small. The electron mobility is approximately 1000 cm<sup>2</sup>/Vs. However, in presence of a p-GaInN layer directly on top of the depletion layer, the sheet resistance in this region is very high. Therefore, whenever, a voltage of several volts is applied between the anode and cathode electrodes, an electric field as high as 10<sup>4</sup> V/cm acts across the depletion layer. Next, however, when by the irradiation of light onto the p-GaInN optical gate, electron–hole pairs are generated and the conduction band edge in the AlGaN/GaN heterostructure is considered to change. The drift current density depends on the product of the elementary charge, electron concentration, electron mobility, and electric field. Accordingly, a large photocurrent can be obtained by irra-

diation of weak light in the AlGaN/GaN heterostructure. Therefore, this structure can be expected to have an extremely high photosensitivity and a high S/N ratio.

The photosensitivity of each photosensor was calculated from the photocurrent measured at light wavelength intervals of 5 nm using a spectroscope with a Xe lamp at RT. The photocurrent at each light wavelength was measured by a semiconductor parameter analyzer (Agilent Technologies, Inc.: HP-4155B). The monochromatic light irradiation densities of the spectroscope-measured photosensitivity ranged from 200 to 220  $\mu\text{W}/\text{cm}^2$ . Since the light-receiving area was 200  $\mu\text{m}^2$ , the amount of received light was very small and equivalent to approximately several hundred picowatts.

**3 Results and discussion** Figure 2(a) and (b), respectively, show the monochromatic photosensitivity of HFET-type photosensors with p-Ga<sub>0.86</sub>In<sub>0.14</sub>N and p-GaN optical gates with a driving voltage between the anode and the cathode ( $V_{AC}$ ) of 5 V obtained using a Xe lamp and spectrometer. Figure 3 shows the normalized monochromatic photosensitivity of each photosensor. From these figures, although there are differences in the photosensitivity of each device, the photosensors can achieve a high external photosensitivity, exceeding 10<sup>4</sup> A/W. Also, dark current densities of the photosensors with the p-Ga<sub>0.86</sub>In<sub>0.14</sub>N and p-GaN optical gates of approximately 1  $\mu\text{A}/\text{mm}$  and lower than 10 nA/mm, respectively, were obtained at  $V_{AC} = 5 \text{ V}$ . The S/N ratios of the photocurrent to dark current of each sample were on the order of 10<sup>2</sup> and 10<sup>4</sup>, respectively. The dark current of such HFET-type photosensors using a p-GaInN optical gate is higher than those using a p-GaN optical gate. We believe that this is caused by an insufficient depletion of the 2DEG in the case of the p-GaInN optical gate and optimization should allow a further reduction of the dark current. Although the device structure needs to be optimized to maximize the photosensitivity and S/N ratio of the device, we have shown that a photosensor with a high external photosensitivity can be achieved. In addition, Fig. 3 shows normalized monochromatic photosensitivities of HFET-type photosensors. From this figure, the absorption edge wavelengths of the photosensors with p-Ga<sub>0.86</sub>In<sub>0.14</sub>N and p-GaN optical gates

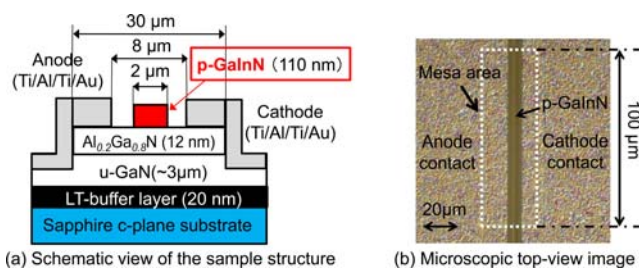


**Figure 1** (online colour at: www.pss-rapid.com) Schematic view and top-view microscopic image of HFET-type photosensor.

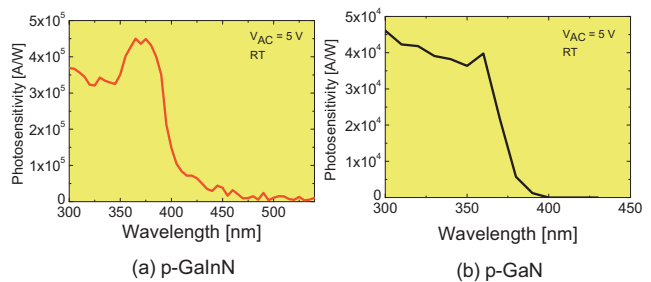


**Figure 2** (online colour at: www.pss-rapid.com) Monochromatic photosensitivity of HFET-type photosensors with (a) p-Ga<sub>0.86</sub>In<sub>0.14</sub>N and (b) p-GaN optical gates.

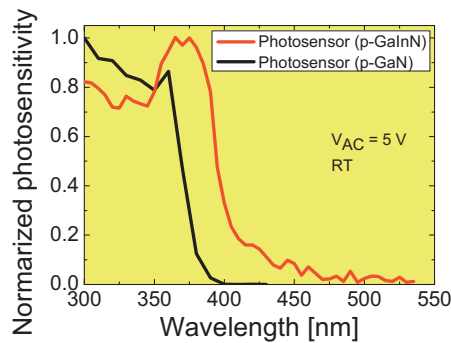


**Figure 3** (online colour at: [www.pss-rapid.com](http://www.pss-rapid.com)) Normalized monochromatic photosensitivity of HFET-type photosensors.

were approximately 420 nm and 375 nm, respectively. From this result, we concluded that the wavelength range of photosensitivity of the HFET-type photosensor can be controlled by controlling the InN molar fraction in the p-GaInN optical gate. In addition, the photosensor with the p-Ga<sub>0.86</sub>In<sub>0.14</sub>N optical gate exhibits photosensitivity up to a longer wavelength of 450 nm. This is considered to be due to the fluctuation in the InN molar fraction of p-GaInN since this device has a thick GaInN film [13].

We also compared the photosensitivity of our photosensors with those of commercially available Si pin photodiodes (Hamamatsu Photonics K.K.: S2387-1010R) [14], Si avalanche photodiodes (Si APD) (Hamamatsu Photonics K.K.: S8664-55) [14], and photomultiplier tubes (Hamamatsu Photonics K.K.: H7421-40, H7421-50, R928, and R3896) [14]. Figure 4 shows a summary of the monochromatic photosensitivity of each photosensor. The photosensitivity of the HFET-type photosensor with a p-GaInN optical gate greatly surpassed those of the Si pin photodiode and Si APD and was comparable to those of the photomultiplier tubes.

Moreover, the response time of this device is thought to be determined by transit time of 2DEG under the optical gate or photocarrier recombination time in p-GaInN opti-

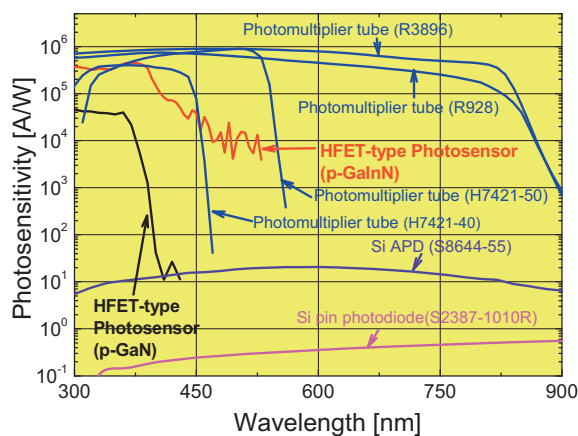


**Figure 4** (online colour at: [www.pss-rapid.com](http://www.pss-rapid.com)) Monochromatic photosensitivity of commercially Si pin photodiode, Si APD, photomultiplier tubes and HFET photosensors of this work.

cal gate. In a previous report, cutoff frequency of junction HFET using p-GaInN has been reported to reach more than 6 GHz [15]. Thus, we consider that it is possible to further shorten the transit time of electrons under the optical gate. Moreover, since the minority carrier lifetime in p-GaInN has been reported to be 0.3 ns [16], photocarrier recombination time in p-GaInN estimated to be less than 1 ns. Therefore, in addition to the high sensitivity, high-speed response can be expected. Dynamic performance of this device will be examined in the near future.

**4 Summary** We fabricated high-performance HFET-type photosensors for the detection of visible light. By changing the InN molar fraction of the p-GaInN optical gate, the wavelength range of photosensitivity of the HFET-type photosensors can be controlled. The photosensitivity of the HFET-type photosensors with a p-GaInN optical gate greatly surpassed those of the commercially available Si pin photodiode and Si APD and was comparable to those in photomultiplier tube.

**Acknowledgements** This study was supported by the Ministry of Education, Culture, Sports, Science and Technology of Japan, through the Supported Program for the Strategic Research Foundation at Private Universities, 2012–2016, and the Knowledge Cluster Initiative (Second Stage) of Tokai Region Nanotechnology Manufacturing Cluster.

## References

- [1] V. Yu. Davydov et al., *Phys. Status Solidi B* **229**, R1 (2002).
- [2] H. Yamashita, K. Fukui, S. Misawa, and S. Yoshida, *J. Appl. Phys.* **50**, 896 (1979).
- [3] B. Monemar, *Phys. Rev. B* **10**, 676 (1974).
- [4] C. Pernot et al., *Phys. Status Solidi A* **208**, 1594 (2011).
- [5] I. Akasaki and H. Amano, *Jpn. J. Appl. Phys.* **45**, 9001 (2006).
- [6] V. Lebedev, G. Cherkashinin, G. Ecke, I. Cimalla, and O. Ambacher, *J. Appl. Phys.* **101**, 033705 (2007).
- [7] M. A. Khan, J. N. Kuznia, D. T. Olson, M. Blasingame, and A. R. Bhattarai, *Appl. Phys. Lett.* **63**, 2455 (1993).
- [8] D. G. Zhao, S. Zhang, D. S. Jiang, J. J. Zhu, Z. S. Liu, H. Wang, S. M. Zhang, B. S. Zhang, and H. Yang, *J. Appl. Phys.* **110**, 053701 (2011).
- [9] Y. Kuwahara, T. Fujii, Y. Fujiyama, T. Sugiyama, M. Iwaya, T. Takeuchi, S. Kamiyama, I. Akasaki, and H. Amano, *Appl. Phys. Express* **3**, 111001 (2010).
- [10] S. Yamamoto, M. Mori, Y. Kuwahara, T. Fujii, T. Nakao, S. Kondo, M. Iwaya, T. Takeuchi, S. Kamiyama, I. Akasaki, and H. Amano, *Phys. Status Solidi RRL* **6**, 145 (2012).
- [11] M. A. Khan, M. S. Shur, Q. Chen, J. N. Kuznia, and C. J. Sun, *Electron. Lett.* **31**, 398 (1995).
- [12] H. Amano, N. Sawaki, I. Akasaki, and Y. Toyoda, *Appl. Phys. Lett.* **48**, 353 (1986).
- [13] M. Shimizu, Y. Kawaguchi, K. Hiramatsu, and N. Sawaki, *J. Appl. Phys.* **36**, 3381 (1997).
- [14] <http://jp.hamamatsu.com/en/index.html>
- [15] M. Shimizu, G. Piao, M. Inada, S. Yagi, Y. Yano, and N. Akutsu, *Jpn. J. Appl. Phys.* **47**, 2817 (2008).
- [16] M. Smith, G. D. Chen, J. Y. Lin, H. X. Jiang, A. Salvador, B. N. Sverdlov, A. Botchkarev, H. Morkoc, and B. Goldenberg, *Appl. Phys. Lett.* **68**, 1883 (1996).

# Growth of GaN and AlGa<sub>N</sub> on (100) $\beta$ -Ga<sub>2</sub>O<sub>3</sub> substrates

Shun Ito<sup>\*1</sup>, Kenichiro Takeda<sup>1</sup>, Kengo Nagata<sup>1</sup>, Hiroki Aoshima<sup>1</sup>, Kosuke Takehara<sup>1</sup>, Motoaki Iwaya<sup>1</sup>, Tetsuya Takeuchi<sup>1</sup>, Satoshi Kamiyama<sup>1</sup>, Isamu Akasaki<sup>1,3</sup>, and Hiroshi Amano<sup>2,3</sup>

<sup>1</sup> Faculty of Science and Technology, Meijo University, Nagoya 468-8502, Japan

<sup>2</sup> Department of Electrical Engineering and Computer Science, Nagoya University, Nagoya 464-8603, Japan

<sup>3</sup> Akasaki Research Center, Nagoya University, Nagoya 464-8603, Japan

Received 1 August 2011, revised 8 November 2011, accepted 8 November 2011

Published online 25 January 2012

**Keywords**  $\beta$ -Ga<sub>2</sub>O<sub>3</sub>(100), thermal annealing, GaN, AlGa<sub>N</sub>, MOVPE

\* Corresponding author: e-mail 103434008@ccalumni.meijo-u.ac.jp

The crystalline quality of GaN and Al<sub>0.08</sub>Ga<sub>0.92</sub>N epitaxial layers on (100)  $\beta$ -Ga<sub>2</sub>O<sub>3</sub> substrates was significantly improved by the facet-controlled growth method. The facets were controlled by changing the nitrogen ambient thermal annealing temperature. We demonstrated the high-crystalline-quality GaN and Al<sub>0.08</sub>Ga<sub>0.92</sub>N on  $\beta$ -Ga<sub>2</sub>O<sub>3</sub>

substrates, which were comparable to GaN and AlGa<sub>N</sub> on sapphire substrates using low-temperature buffer layers. This method is useful for the fabrication of vertical-type ultraviolet (UV) light-emitting diodes (LEDs) on  $\beta$ -Ga<sub>2</sub>O<sub>3</sub> substrates.

© 2012 WILEY-VCH Verlag GmbH & Co. KGaA, Weinheim

**1 Introduction** Group III-nitride-based UV LEDs are expected in many applications such as excitation sources of white LED lamps, material processing, healthcare field, and sterilization. There have been many reports on high-efficiency UV LEDs on sapphire substrates [1, 2]. However, the wall plug efficiency of UV LEDs is still lower than that of GaInN-based blue LEDs [3]. One of the major causes of such low-wall-plug efficiency in the UV LEDs is the current crowding effect caused by the combination of insulating sapphire substrates and an n-type AlGa<sub>N</sub> cladding layer with a relatively higher sheet resistance than that of GaN. One of the best methods to solve this problem is to use a vertical conductive device structure. Thus far, GaInN-based vertical visible and near-UV LEDs were grown on GaN and SiC conductive substrates [4, 5]. However, there is no report on AlGa<sub>N</sub>-based vertical UV LEDs on conductive transparent substrates.  $\beta$ -Ga<sub>2</sub>O<sub>3</sub> is one of the most attractive substrates for AlGa<sub>N</sub>-based vertical UV LEDs. It has a transparency of up to 260 nm and n-type high conductivity [6]. These properties can lead to a small absorption of UV light in  $\beta$ -Ga<sub>2</sub>O<sub>3</sub> and make it possible to realize vertical conductive LEDs. Therefore,  $\beta$ -Ga<sub>2</sub>O<sub>3</sub> is a promising material for the substrate of vertical UV LEDs. Several groups have reported the GaN epitaxial growth on  $\beta$ -Ga<sub>2</sub>O<sub>3</sub> and GaInN-based blue LEDs [7, 8]. Moreover,

our group has reported AlGa<sub>N</sub> with mirror surfaces on  $\beta$ -Ga<sub>2</sub>O<sub>3</sub> using low-temperature GaN buffer layers (LT-GaN), which is essential for UV LEDs [9]. However, the crystalline quality of these epitaxial layers was poorer than that on sapphire substrates. Thus, high-quality AlGa<sub>N</sub> films on  $\beta$ -Ga<sub>2</sub>O<sub>3</sub> substrates have been urgently required to achieve high-performance UV LEDs. In this study, to obtain high-crystalline-quality GaN and AlGa<sub>N</sub> epitaxial layers on (100)  $\beta$ -Ga<sub>2</sub>O<sub>3</sub> substrates, GaN and AlGa<sub>N</sub> were grown using facet layers reported previously [10]. The thermal annealing temperature of  $\beta$ -Ga<sub>2</sub>O<sub>3</sub> substrates was used as a parameter to control the facet formation.

**2 Experimental procedure** In this study, crystal growth was performed by metal organic vapor phase epitaxy. The aluminium and gallium sources were trimethylaluminium and trimethylgallium, respectively. The nitrogen source was NH<sub>3</sub>. Moreover, the thermal annealing and growth of GaN and Al<sub>0.08</sub>Ga<sub>0.92</sub>N were carried out in nitrogen ambient, because  $\beta$ -Ga<sub>2</sub>O<sub>3</sub> substrates were etched using hydrogen. The GaN and Al<sub>0.08</sub>Ga<sub>0.92</sub>N growths were carried out using LT-GaN. Al<sub>x</sub>Ga<sub>1-x</sub>N (0001) films grow epitaxially on (100)  $\beta$ -Ga<sub>2</sub>O<sub>3</sub> substrates with an in-plane epitaxial relationship of Al<sub>x</sub>Ga<sub>1-x</sub>N [1-100]|| $\beta$ -Ga<sub>2</sub>O<sub>3</sub>[001] [11].

Figure 1 shows the timing charts of the growth temperatures of GaN and Al<sub>0.08</sub>Ga<sub>0.92</sub>N without facet Al<sub>x</sub>Ga<sub>1-x</sub>N layers. After performing the thermal annealing for 3 min at 1100 °C and deposition of LT-GaN at 550 °C, GaN and Al<sub>0.08</sub>Ga<sub>0.92</sub>N of approximately 2.0- $\mu$ m-thick were grown at 1080 °C.

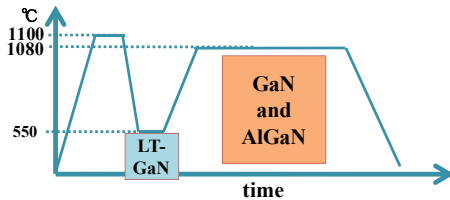


**Figure 1** Timing chart of the growth temperatures of GaN and AlGaN.

Figure 2 shows the timing charts of the growth temperatures of GaN and Al<sub>0.08</sub>Ga<sub>0.92</sub>N grown with facet-Al<sub>x</sub>Ga<sub>1-x</sub>N layers. The thermal annealing for 3 min and deposition of LT-GaN at 550 °C were performed in the same manner as for the samples without facet-Al<sub>x</sub>Ga<sub>1-x</sub>N layers. In addition, approximately 300-nm-thick facet-GaN or Al<sub>0.08</sub>Ga<sub>0.92</sub>N was grown at 1020 and 950 °C. The growth temperatures of the GaN and Al<sub>0.08</sub>Ga<sub>0.92</sub>N facets were lower than those of conventional GaN and Al<sub>0.08</sub>Ga<sub>0.92</sub>N layers to enhance island growth. Finally, GaN and Al<sub>0.08</sub>Ga<sub>0.92</sub>N of approximately 2.0- $\mu$ m-thick were grown on facet-GaN and Al<sub>0.08</sub>Ga<sub>0.92</sub>N at 1080 °C. In this case, the thermal annealing temperature was changed from 600 to 1100 °C.

Samples were characterized by atomic force microscopy (AFM), scanning electron microscopy (SEM), X-ray rocking curve (XRC), and photoluminescence (PL) measurement using a He-Cd laser (325 nm) at room temperature.

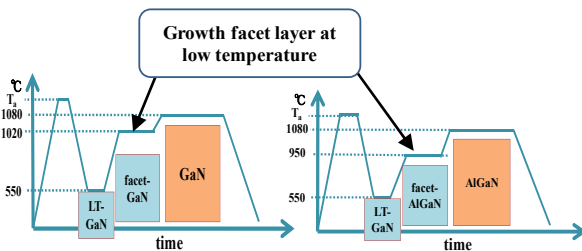
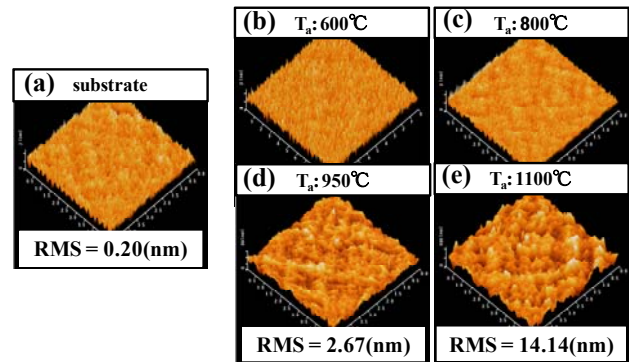


**Figure 2** Timing charts of growth temperatures of (a) GaN and (b) AlGaN using facet layers.

### 3 Results

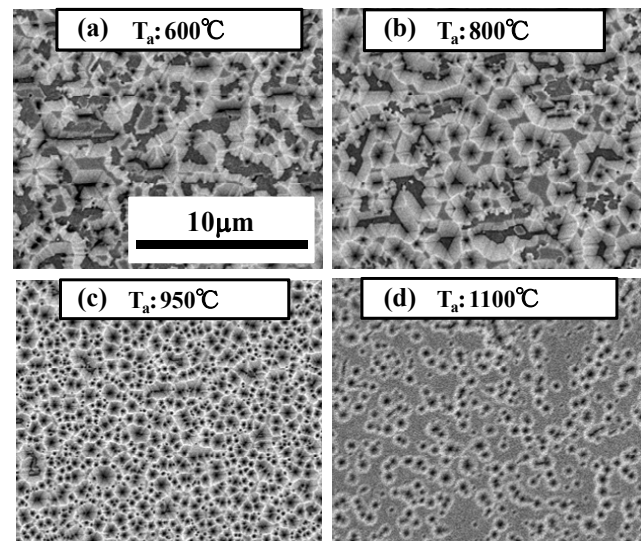
**3.1 Impact of thermal annealing temperature on  $\beta$ -Ga<sub>2</sub>O<sub>3</sub>** Figure 3 shows AFM images of (a) (100)  $\beta$ -Ga<sub>2</sub>O<sub>3</sub> substrate and (100)  $\beta$ -Ga<sub>2</sub>O<sub>3</sub> substrates annealed at (b) 600 °C, (c) 800 °C, (d) 950 °C, and (e) 1100 °C for 3 min. From these figures, the surface roughness of  $\beta$ -Ga<sub>2</sub>O<sub>3</sub> increases with increasing annealing temperature. By annealing at 1100 °C, the root mean square (RMS) roughness was increased from 0.20 to 14 nm.

**3.2 Fabrication of facet-GaN** Figure 4 shows plan-view SEM images of samples after substrate annealing and



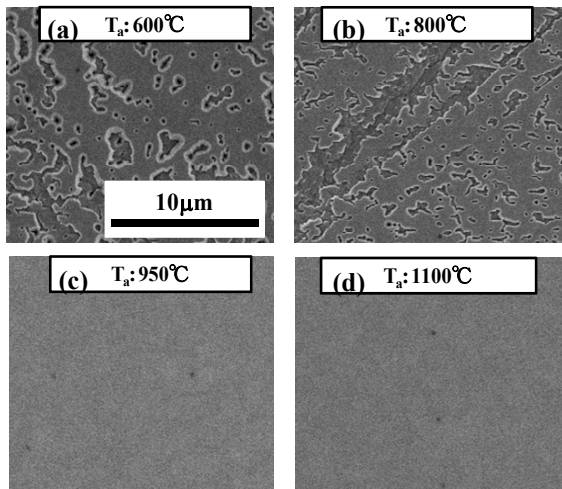
**Figure 3** Plan-view AFM images of (a) (100)  $\beta$ -Ga<sub>2</sub>O<sub>3</sub> substrate and (100)  $\beta$ -Ga<sub>2</sub>O<sub>3</sub> substrate thermal-annealed at (b) 600 °C, (c) 800 °C, (d) 950 °C, and (e) 1100 °C for 3 min.

subsequent deposition of LT-GaN at 550 °C and growth of approximately 300-nm-thick GaN facet layers at 1020 °C. From these figures, the GaN islands with inclined facets were grown, and the area of the surface covered by the facets was controlled by adjusting the thermal annealing temperature.



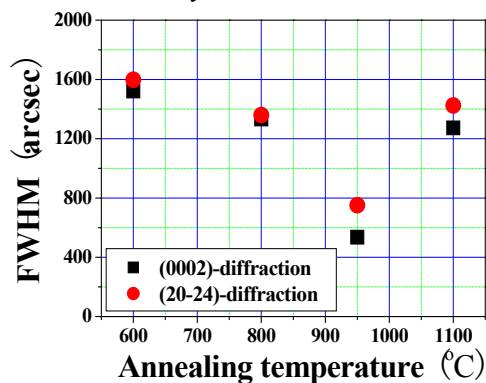
**Figure 4** Plan-view SEM images of substrates thermal-annealed at (a) 600 °C, (b) 800 °C, (c) 950 °C, and (d) 1100 °C followed by deposition of low-temperature GaN buffer layer and growth of approximately 300-nm-thick GaN layer at 1020 °C.

**3.3 Growth of GaN on facet layers** Figure 5 shows plan-view SEM images of approximately 2.0- $\mu$ m-thick GaN layers grown at 1080 °C on each facet-GaN sample. The surfaces of the GaN films on thermal-annealed substrates at (a) 600 °C and (b) 800 °C were not smooth. However the surfaces of the GaN films on samples thermal-annealed at (c) 950 °C and (d) 1100 °C were smooth and crack-free.



**Figure 5** Plan-view SEM images of 2.0- $\mu\text{m}$ -thick GaN grown at 1080  $^{\circ}\text{C}$  on substrates thermal-annealed at (a) 600  $^{\circ}\text{C}$ , (b) 800  $^{\circ}\text{C}$ , (c) 950  $^{\circ}\text{C}$ , and (d) 1100  $^{\circ}\text{C}$  followed by growth of approximately 300-nm-thick GaN facet layers at 1020  $^{\circ}\text{C}$ .

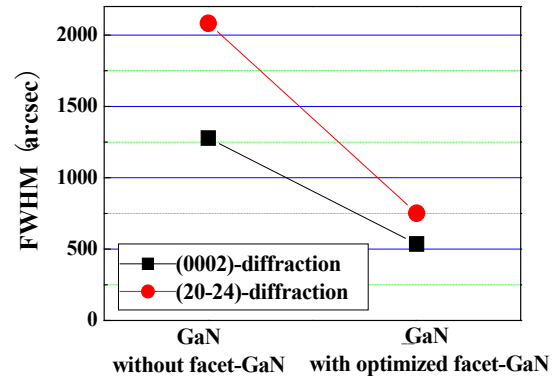
Figure 6 shows the full width at half maximum (FWHM) of XRC of GaN. Figure 4 indicates that the facet-GaN covered the whole surface when the thermal annealing temperature was 950  $^{\circ}\text{C}$ , and the flat surfaces remain when it was higher and lower than 950  $^{\circ}\text{C}$ . As mentioned in reference [10], the dislocations existing in the facet regions bend and do not glide to the surface. Therefore, the crystalline quality of GaN was highest when the annealing temperature is 950  $^{\circ}\text{C}$ . The formation of facets was related to the adequate roughness of the  $\beta\text{-Ga}_2\text{O}_3$  substrates. Further evaluation is necessary.



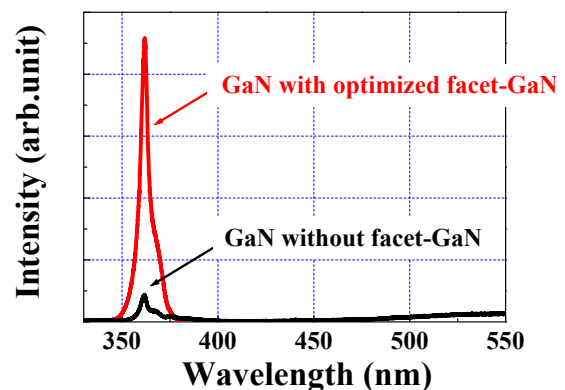
**Figure 6** XRC FWHM of GaN for various thermal annealing temperatures.

Figure 7 shows the comparison of XRC FWHM between the GaN without and with the facet-GaN layer by thermal annealing at 950  $^{\circ}\text{C}$ . The threading dislocation densities of the GaN films were estimated from the FWHM values [12]. The calculated dislocation densities of GaN without and with the facet-GaN layer were  $1.9 \times 10^{10}$  and  $2.5 \times 10^9$   $\text{cm}^{-2}$ , respectively. The threading dislocation den-

sity of GaN on (100)  $\beta\text{-Ga}_2\text{O}_3$  substrate was successfully decreased by almost one order of magnitude. Figure 8 shows the PL spectra of the GaN with and without the facet-GaN layer. These results indicated that the facet-GaN layer improves the crystalline quality and optical property of GaN on (100)  $\beta\text{-Ga}_2\text{O}_3$  substrate.



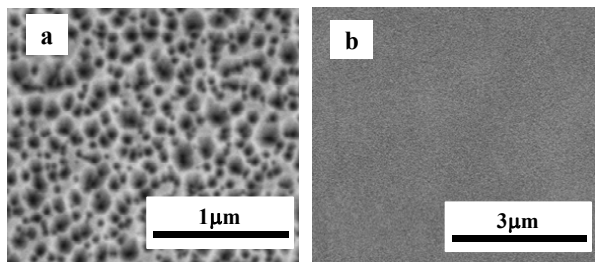
**Figure 7** XRC FWHM of GaN without and with facet sample formed by thermal annealing at 950  $^{\circ}\text{C}$ .



**Figure 8** PL spectra of GaN without and with facet sample formed by thermal annealing at 950  $^{\circ}\text{C}$ .

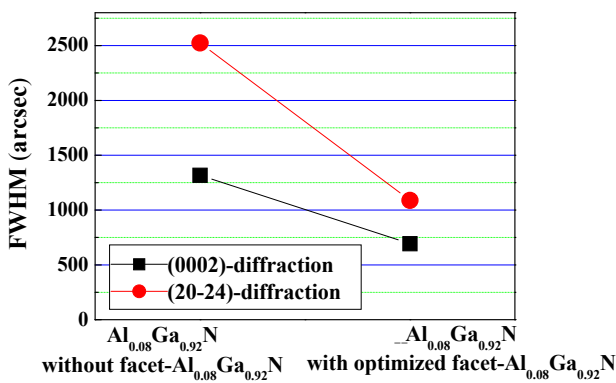
**3.4 Result of  $\text{Al}_{0.08}\text{Ga}_{0.92}\text{N}$**  The  $\text{Al}_{0.08}\text{Ga}_{0.92}\text{N}$  was grown under the same growth conditions of GaN. Only the facet- $\text{Al}_{0.08}\text{Ga}_{0.92}\text{N}$  growth temperature was changed to 950  $^{\circ}\text{C}$ . Figure 9 shows a plan-view SEM images of facet- $\text{Al}_{0.08}\text{Ga}_{0.92}\text{N}$  and an approximately 2.0- $\mu\text{m}$ -thick  $\text{Al}_{0.08}\text{Ga}_{0.92}\text{N}$  layer grown on facet- $\text{Al}_{0.08}\text{Ga}_{0.92}\text{N}$  samples at 1080  $^{\circ}\text{C}$ . Moreover, facet- $\text{Al}_{0.08}\text{Ga}_{0.92}\text{N}$  made it possible to obtain a smooth surface.

Figure 10 shows the XRC FWHM of  $\text{Al}_{0.08}\text{Ga}_{0.92}\text{N}$  without and with the facet- $\text{Al}_{0.08}\text{Ga}_{0.92}\text{N}$  layer. The calculated dislocation densities of GaN without and with the facet-GaN layer were  $2.6 \times 10^{10}$  and  $4.9 \times 10^9$   $\text{cm}^{-2}$ , respectively.



**Figure 9** Plan-view SEM images of (a) facet-Al<sub>0.08</sub>Ga<sub>0.92</sub>N and (b) approximately 2.0-μm-thick Al<sub>0.08</sub>Ga<sub>0.92</sub>N layer grown on facet-Al<sub>0.08</sub>Ga<sub>0.92</sub>N samples at 1080 °C.

Figure 11 shows the PL spectra of the samples without and with the facet-Al<sub>0.08</sub>Ga<sub>0.92</sub>N layer. These results show that the facet-Al<sub>0.08</sub>Ga<sub>0.92</sub>N layer is useful for growing high-quality Al<sub>0.08</sub>Ga<sub>0.92</sub>N on (100) β-Ga<sub>2</sub>O<sub>3</sub> substrate.



**Figure 10** XRC FWHM of Al<sub>0.08</sub>Ga<sub>0.92</sub>N without and with facet-Al<sub>0.08</sub>Ga<sub>0.92</sub>N formed by substrate thermal annealing at 950 °C.

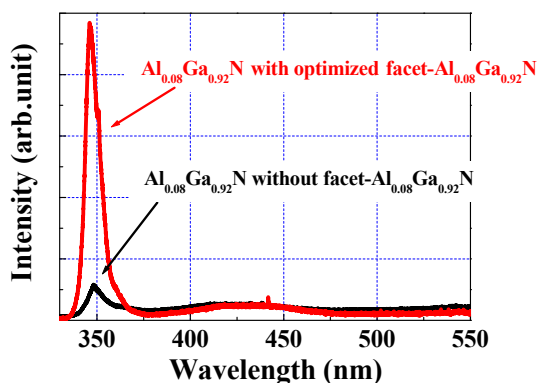


**Figure 11** PL spectra of Al<sub>0.08</sub>Ga<sub>0.92</sub>N without and with facet sample formed by thermal annealing at 950 °C.

**4 Conclusion** The thermal annealing of β-Ga<sub>2</sub>O<sub>3</sub> substrate at 950 °C led to the formation of GaN and Al<sub>0.08</sub>Ga<sub>0.92</sub>N having an inclined facet covering whole surfaces, resulting in high-quality GaN and Al<sub>0.08</sub>Ga<sub>0.92</sub>N on β-Ga<sub>2</sub>O<sub>3</sub> substrates. The facet-controlled method with β-

Ga<sub>2</sub>O<sub>3</sub> substrates is useful for high-efficiency vertical UV LEDs in the future.

**Acknowledgements** This work was partially supported by a Grant-in-Aid for Scientific Research in Priority Area "Optoelectronics Frontier by Nitride Semiconductor-Ultimate Utilization of Nitride Semiconductor Material Potential" (No. 18069011) of the Ministry of Education, Culture, Sports, Science and Technology.

## References

- [1] H. Tsuzuki, F. Mori, K. Takeda, T. Ichikawa, M. Iwaya, S. Kamiyama, H. Amano, I. Akasaki, H. Yoshida, M. Kuwabara, Y. Yamashita, and H. Kan, *Phys. Status Solidi A* **206**, 1199 (2009).
- [2] C. Pernot, M. Kim, S. Fukahori, T. Inazu, T. Fujita, Y. Nagasawa, A. Hirano, M. Ippommatsu, M. Iwaya, S. Kamiyama, I. Akasaki, and H. Amano, *Appl. Phys. Express* **3**, 061004 (2010).
- [3] X. A. Cao and S. D. Arthur, *Appl. Phys. Lett.* **85**, 3971 (2004).
- [4] J. Edmond, A. Abare, M. Bergman, J. Bharathan, K. L. Bunker, D. Emerson, K. Haberern, J. Ibbetson, M. Leung, P. Russel, and D. Slater, *J. Cryst. Growth* **272**, 242 (2004).
- [5] Y. Narukawa, M. Ichikawa, D. Sanga, M. Sano, and T. Mukai, *J. Phys. D: Appl. Phys.* **43**, 354002 (2010).
- [6] H. Aida, K. Nishiguchi, H. Takeda, N. Aota, K. Sunakawa, and Y. Yaguchi, *Jpn. J. Appl. Phys.* **47**, L11 (2008).
- [7] K. Shimamura, E. G. Villora, K. Domen, K. Yui, K. Aoki, and N. Ichinose, *Jpn. J. Appl. Phys.* **44**, L7 (2005).
- [8] X. Zi-Li, Z. Rong, X. Chang-Tai, X. Xiang-Qian, H. Ping, L. Bin, Z. Hong, J. Ruo-Lian, S. Yi, and Z. You-Dou, *Chin. Phys. Lett.* **25**, 2185 (2008).
- [9] Y. Kawai, S. Ito, K. Takeda, M. Iwaya, S. Kamiyama, H. Amano, and I. Akasaki, *Ext. Abst. of ISPlasma 2010*, **PB-56B** (2010).
- [10] S. Nitta, J. Yamamoto, Y. Koyama, Y. Ban, K. Wakao, and K. Takahashi, *J. Cryst. Growth* **272**, 438 (2004).
- [11] S. Ohira, N. Suzuki, H. Minami, K. Takahashi, T. Araki, and Y. Nanishi, *Phys. Status Solidi C* **4**, 2306 (2007).
- [12] S. R. Lee, A. M. West, A. A. Allenman, K. E. Waldrip, D. M. Follstaedt, P. P. Provencio, and D. D. Koleske, *Appl. Phys. Lett.* **86**, 241904 (2005).

## Relationship between misfit-dislocation formation and initial threading-dislocation density in GaInN/GaN heterostructures

This content has been downloaded from IOPscience. Please scroll down to see the full text.

2015 Jpn. J. Appl. Phys. 54 115501

(<http://iopscience.iop.org/1347-4065/54/11/115501>)

View [the table of contents for this issue](#), or go to the [journal homepage](#) for more

Download details:

IP Address: 219.127.71.134

This content was downloaded on 03/03/2017 at 06:46

Please note that [terms and conditions apply](#).

You may also be interested in:

[GaN barrier layer dependence of critical thickness in GaInN/GaN superlattice on GaN characterized by in situ X-ray diffraction](#)

Junya Osumi, Koji Ishihara, Taiji Yamamoto et al.

[Multijunction GaInN-based solar cells using a tunnel junction](#)

Hironori Kurokawa, Mitsuru Kaga, Tomomi Goda et al.

[Materials and growth issues for high-performance nonpolar and semipolar LEDs](#)

R M Farrell, E C Young, F Wu et al.

[Improved Strain-Free GaN Growth with a Nearly Lattice-Matched AlInN Interlayer by Metalorganic Chemical Vapor Deposition](#)

Tae Su Oh, Hyun Jeong, Tae Hoon Seo et al.

[Realization of Nitride-Based Solar Cell on Freestanding GaN Substrate](#)

Yosuke Kuwahara, Takahiro Fujii, Yasuharu Fujiyama et al.

[Reduction of V-pit and threading dislocation density in InGaN/GaN heterostructures grown on cracked AlGaN templates](#)

C B Soh, S Y Chow, S Tripathy et al.

[Strain Relaxation Mechanisms in AlGaN Epitaxy on AlN Templates](#)

Zhihao Wu, Kentaro Nonaka, Yohjiro Kawai et al.

[Fabrication of low-curvature 2 in. GaN wafers by Na-flux coalescence growth technique](#)

Mamoru Imade, Masayuki Imanishi, Yuma Todoroki et al.

## Relationship between misfit-dislocation formation and initial threading-dislocation density in GaInN/GaN heterostructures

Motoaki Iwaya<sup>1</sup>, Taiji Yamamoto<sup>1</sup>, Daisuke Iida<sup>1</sup>, Yasunari Kondo<sup>1</sup>, Mihoko Sowa<sup>1</sup>, Hiroyuki Matsubara<sup>1</sup>, Koji Ishihara<sup>1</sup>, Tetsuya Takeuchi<sup>1</sup>, Satoshi Kamiyama<sup>1</sup>, and Isamu Akasaki<sup>1,2</sup>

<sup>1</sup>Faculty of Science and Technology, Meijo University, Nagoya 468-8502, Japan

<sup>2</sup>Akasaki Research Center, Nagoya University, Nagoya 464-8603, Japan

Received July 21, 2015; accepted August 12, 2015; published online October 1, 2015

The dependence of the critical thickness for the introduction of misfit dislocations in a GaInN/GaN heterostructure system on the dislocation density in the underlying GaN layer was investigated using in situ X-ray diffraction (XRD), ex situ scanning electron microscopy, and transmission electron microscopy analyses. The critical thickness for the introduction of misfit dislocations in the GaInN layer was found to significantly depend on the dislocation density in the underlying GaN layer. Notably, on the basis of the in situ XRD results, a reliable critical thickness for obtaining misfit-dislocation-free growth was determined. © 2015 The Japan Society of Applied Physics

### 1. Introduction

GaInN ternary alloys have bandgaps extending from less than 0.65 to 3.4 eV, and therefore are used as active layers in commercially available visible-light-emitting devices.<sup>1)</sup> There are many interesting features that render these nitride semiconductor alloys particularly useful as efficient light emitters. In addition, these materials are also useful in high-conversion-efficiency solar cells.<sup>2–5)</sup> Most devices employing GaInN films are fabricated on GaN, because the growth of thick GaInN films with high crystallinity on substrates other than GaN is very difficult. Several studies were previously conducted to elucidate the mechanism by which defects form via strain relaxation in GaInN/GaN heterostructures,<sup>6–11)</sup> because it is necessary to minimize defect formation in order to improve device performance. However, current understanding of the critical layer thickness at which misfit dislocations (MDs) are introduced in GaInN/GaN heterostructures is insufficient. For example, the reported values for the critical thickness in GaInN/GaN heterostructure systems vary widely. In addition, the relationship between the threading dislocation (TD) density in the underlying layer and critical thickness is unclear. We previously reported the results of in situ X-ray diffraction (XRD) analyses of GaInN films during metal organic vapor phase epitaxy (MOVPE).<sup>12,13)</sup> By comparing these results with ex situ characterization data, such as transmission electron microscopy (TEM), cathode luminescence, atomic force microscopy, scanning electron microscopy (SEM), and XRD reciprocal mapping results, we found that it is possible to accurately observe the relaxation process that occurs in GaInN by analyzing the full width at half maximum (FWHM) of the in situ GaInN XRD spectrum.

In the present study, the critical thickness of introduced MDs in GaInN/GaN heterostructure systems as a function of the TD density in the underlying GaN layers was investigated using in situ XRD and ex situ analyses. The results indicated that the critical thickness for the introduction of MDs in the GaInN films depended significantly on the dislocation density in the underlying GaN layers.

### 2. Experimental procedure

GaInN samples were grown on *c*-plane sapphire and freestanding GaN substrates by MOVPE (Taiyo Nippon

Sanso GRC-230X) with a face down 2-in. × 3-wafer system (horizontal flow). Trimethylgallium, triethylgallium (TEG), trimethylindium (TMI), and ammonia were used as the Ga, In, and N source materials for the growth of GaN and GaInN. For the sapphire substrate (~330 μm), the GaInN samples were fabricated on an approximately 3-μm-thick GaN template grown using a low-temperature buffer layer. The TD densities of the GaN template and free standing GaN substrate (~330 μm) were approximately  $3 \times 10^8 \text{ cm}^{-2}$  and less than  $3 \times 10^6 \text{ cm}^{-2}$ , respectively. After the growth of a 1-μm-thick homoepitaxial GaN layer at 1,050 °C on the GaN substrate or template using H<sub>2</sub> as the carrier gas at 933 hPa, each sample was cooled to 730–800 °C and the carrier gas was changed to N<sub>2</sub>. A GaInN layer was then grown on each homoepitaxial GaN layer. The InN mole fraction in the GaInN film was varied from 0.1 to 0.22 by adjusting the growth temperature. The mole ratio of TMI to TEG during GaInN growth was fixed at approximately 0.67.

The GaInN films with symmetric (0002) Bragg diffractions were evaluated using an in situ XRD system. The MOVPE apparatus was equipped with a Be window that served as a viewport for the passage of X-rays, which were focused on the sample surface using a Johansson curved crystal mirror. Using this method, the incidence angle of X-rays could be changed without moving the X-ray source. Moreover, the diffracted X-rays were detected using a one-dimensional charge-coupled device, allowing for the detection of the scattered X-rays without moving the substrate or detector. With this configuration, the system realized the equivalent of a (0002)  $2\theta/\omega$  scan in 1 s during the rotation of the wafers without requiring the use of an analyzer crystal. Furthermore, the  $2\theta$  value was calibrated on the basis of the GaN peak. Although the resolution slightly decreased compared with that of a conventional XRD system, the equivalent of a (0002)  $2\theta/\omega$  scan at a resolution of 1 arcsec was possible. It is also noteworthy that the tilt mosaicity of the crystals was reflected in the spectrum because an analyzer crystal was not used. Therefore, the evaluation of the FWHM data obtained for crystalline dislocations using this in situ XRD system provided information on both dispersion in the lattice constant *c* and tilt mosaicity. The GaInN surface structures and defects close to the GaInN/GaN heterointerface were also evaluated using SEM and TEM, respectively.

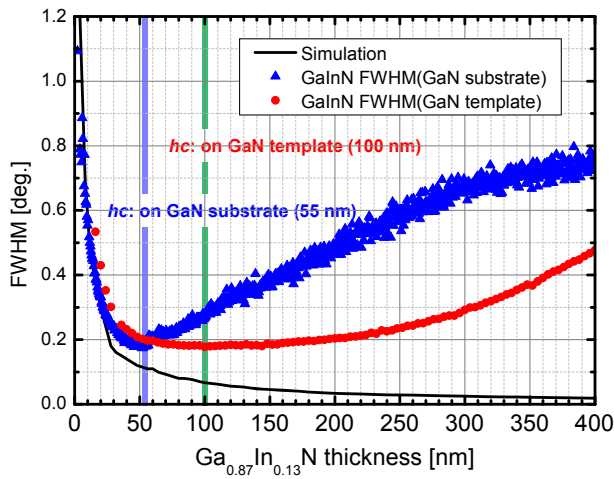


Fig. 1. (Color online) Typical in situ XRD FWHMs of the  $\text{Ga}_{0.87}\text{In}_{0.13}\text{N}$  films on GaN templates and substrates.

### 3. Results and discussion

Figure 1 shows typical in situ XRD FWHMs for the  $\text{Ga}_{0.87}\text{In}_{0.13}\text{N}$  films on the GaN templates and substrates. Each FWHM was determined by fitting a pseudo-Voigt function for each in situ XRD spectrum. The simulated FWHM values obtained using the X'pert Epitaxy 4.0a program<sup>14)</sup> (typical X-ray analysis software) are also presented. The FWHMs for the  $\text{Ga}_{0.87}\text{In}_{0.13}\text{N}$  films decreased with increasing film thickness during the initial growth stage. This result nearly matched the simulated results. However, the experimental results deviated from the simulated results with respect to the increase in film thickness. Inflection points were also observed in the experimental data. To clarify these inflection points, which are hereafter referred to as *hc*, each FWHM curve was differentiated as a function of film thickness. The behavior of the FWHM for the  $\text{Ga}_{0.87}\text{In}_{0.13}\text{N}$

film on the GaN template was considerably ably different from that for the film on the GaN substrate; the *hc* for the GaInN film on the GaN substrate (100 nm) was approximately twice that for the GaInN film on the GaN template (55 nm).

To investigate these phenomena,  $\text{Ga}_{0.87}\text{In}_{0.13}\text{N}$  samples with different thicknesses on GaN templates and substrates were investigated using ex situ characterization techniques. Figures 2 and 3 show the plan-view TEM images, plan-view SEM images, and proposed growth models for the  $\text{Ga}_{0.87}\text{In}_{0.13}\text{N}$  samples of different thicknesses on the GaN templates and substrates, respectively. As can be seen in these figures, significant differences were observed with increasing film thickness.

In the  $\text{Ga}_{0.87}\text{In}_{0.13}\text{N}$  samples on the GaN templates, many growth pits were observed in the plan-view SEM images from the initial growth stage. In addition, many TDs in the GaInN sample were observed in the GaN underlying layer in the plan-view TEM images. However, no MDs were detected in the 40- and 80-nm-thick  $\text{Ga}_{0.87}\text{In}_{0.13}\text{N}$  films on the GaN templates in the plan-view TEM images. Note that it was possible to observe the GaN/GaInN interface because the thickness of each TEM sample was approximately 250 nm. The lack of any MDs in the 80-nm-thick  $\text{Ga}_{0.87}\text{In}_{0.13}\text{N}$  film on the GaN template was also confirmed via cross-sectional TEM analysis. Therefore, lattice relaxation introduced by MDs did not occur in the  $\text{Ga}_{0.87}\text{In}_{0.13}\text{N}$  films on GaN templates with thicknesses up to 80 nm. Moreover, the origin of the growth pits was found to be the TDs in the underlying GaN layer, as reported in Refs. 7 and 15. In contrast, only *a + c*-type MDs along the  $\langle 1\bar{1}00 \rangle$  direction close to the  $\text{Ga}_{0.87}\text{In}_{0.13}\text{N}/\text{GaN}$  heterointerface, which were induced by slips along the  $\langle 11\bar{2}3 \rangle$  direction in the  $\{11\bar{2}2\}$  plane system,<sup>16)</sup> were observed in the 110-nm-thick  $\text{Ga}_{0.87}\text{In}_{0.13}\text{N}$  sample. The components of the MDs were characterized via dark-field cross-sectional TEM analysis. Only these *a + c*-

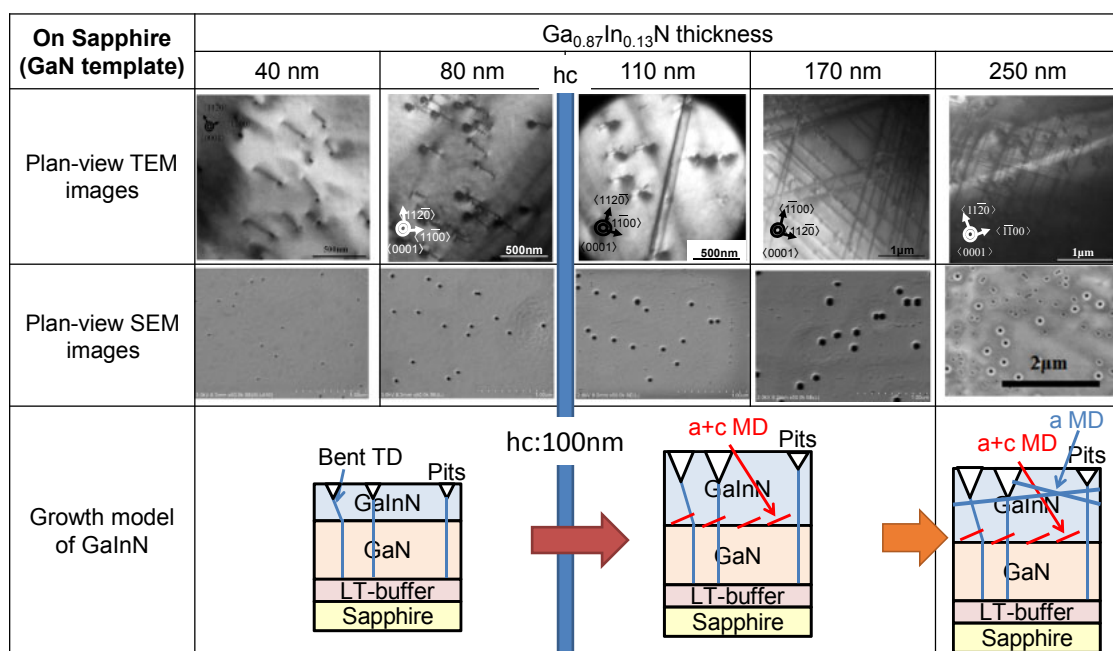
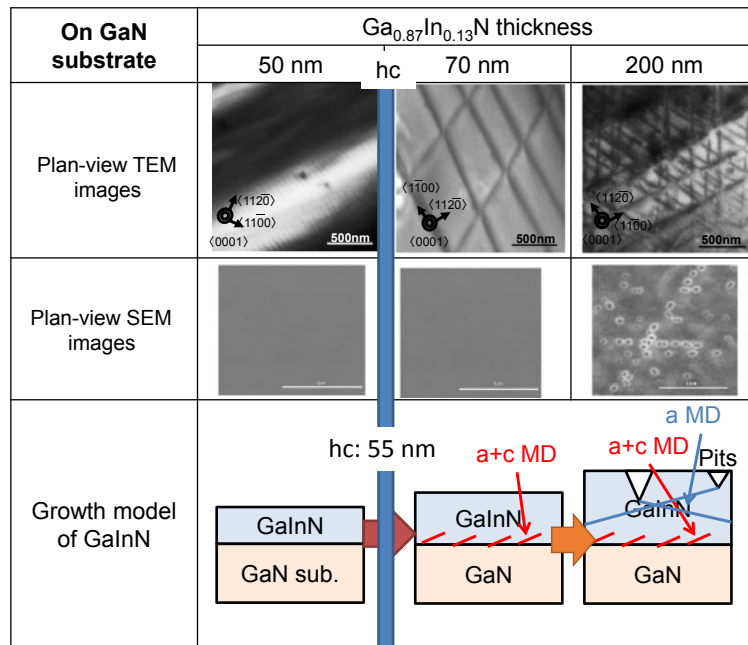


Fig. 2. (Color online) Plan-view TEM images, plan-view SEM images, and proposed growth model for  $\text{Ga}_{0.87}\text{In}_{0.13}\text{N}$  samples of different thicknesses on GaN templates.



**Fig. 3.** (Color online) Plan-view TEM images, plan-view SEM images, and proposed growth model for  $\text{Ga}_{0.87}\text{In}_{0.13}\text{N}$  samples of different thicknesses on GaN substrates.

type MDs were also observed in the 170-nm-thick  $\text{Ga}_{0.87}\text{In}_{0.13}\text{N}$  sample, although at a higher density than that in the 110-nm-thick film. Both *a*-type and *a + c*-type MDs were observed in the 250-nm-thick  $\text{Ga}_{0.87}\text{In}_{0.13}\text{N}$  sample. Notably, the *hc* identified in the in situ XRD analysis matched the appearance of the *a + c*-type MDs. Finally, these trends and relaxation processes were similar even when the InN molar fraction in the GaInN film was 0.17 (see below).

Notably, for the  $\text{Ga}_{0.87}\text{In}_{0.13}\text{N}$  samples on the GaN substrate, growth pits and MDs were not observed during the initial growth stage up to a  $\text{Ga}_{0.87}\text{In}_{0.13}\text{N}$  thickness of 50 nm. The growth pits did not appear because the TD density in the GaN substrate was much lower. On the other hand, *a + c*-type MDs were observed in the 70-nm-thick  $\text{Ga}_{0.87}\text{In}_{0.13}\text{N}$  sample, and *a*-type MDs were detected in addition to *a + c*-type MDs in the 200-nm-thick  $\text{Ga}_{0.87}\text{In}_{0.13}\text{N}$  sample. In addition, many growth pits were seen in the plan-view SEM image of this  $\text{Ga}_{0.87}\text{In}_{0.13}\text{N}$  sample. Also, the photoluminescence intensity from GaInN films at room temperature rapidly decreased after the introduction of MDs in both cases on the GaN substrate and template.

These results indicated that the GaInN films on the GaN substrates underwent a relaxation process similar to that for the films on the GaN templates, even though the growth pits appeared at the initial growth stage for the GaInN films on the GaN templates. Notably, the appearance of *hc* was consistent with the introduction of the *a + c*-type MDs in both GaN templates and substrates. Note that the symmetric (0002) Bragg diffraction was measured via in situ XRD. Because the FWHM of this diffraction is dependent on the tilt component, it is reasonable for the FWHM to increase when *a + c* type-MDs are introduced. Thus, we concluded that *hc* indicates the critical thickness at which *a + c* type-MDs are introduced.

Next, the critical thickness for the introduction of *a + c* type-MDs for various InN molar fractions was investigated. Figure 4 shows the critical thickness for the introduction

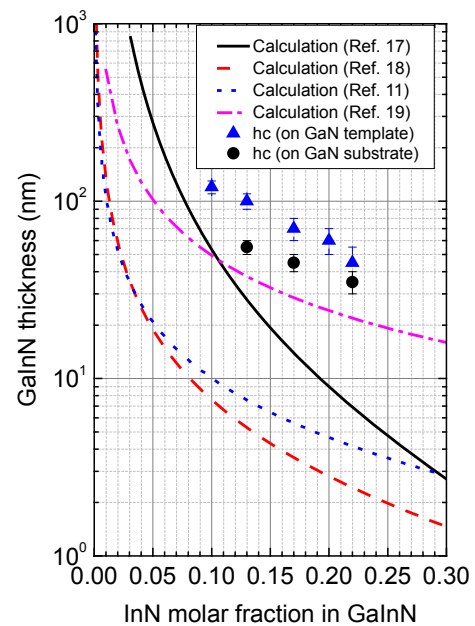


**Fig. 4.** (Color online) *hc* of GaInN films on GaN templates and substrates as a function of InN molar fraction. The results of theoretical calculations performed using data in Refs. 11, 17–19 are also shown.

of *a + c* type-MDs (*hc*) in the GaInN films on both GaN templates and substrates as a function of InN molar fraction. The results of theoretical calculations obtained using the data in Refs. 11, 17–19 are also included in the figure. It can be seen that the critical thickness for the introduction of *a + c* type-MDs in the GaInN films depended strongly on the dislocation density of the underlying GaN layer. This difference is due to the appearance of the growth pits in the case of the GaN template. It is possible that a fraction of the strain energy is released as a consequence of the formation of the growth pits, because it is thought that the strain energy required for the introduction of the MDs in the GaN template

increased with critical thickness. However, note that the growth pits generated thinner films on the GaN templates. In addition, because the growth pits cause significant negative effects with respect to device performance, GaN substrates are advantageous when fabricating devices. Furthermore, the experimental results for the GaInN films on the GaN substrates closely agreed with the calculated results obtained using the theory of Fischer et al.<sup>19)</sup> This theory considers the interaction between dislocations, in contrast to the other theories. Therefore, we concluded that this theory is the most applicable since GaN films have many dislocations. Therefore, it is preferable to use this theory when designing GaInN/GaN heterostructure systems for device applications based on the introduction of  $a + c$  type-MDs.

#### 4. Conclusions

We investigated GaInN/GaN heterostructures on underlying GaN layers with different dislocation densities using both in situ XRD and ex situ characterization techniques. It was demonstrated that the critical thickness for the introduction of  $a + c$  type-MDs can be obtained via in situ XRD analysis. In addition, the critical thickness for the introduction of  $a + c$  type-MDs in GaInN was found to depend strongly on the dislocation density in the underlying GaN layer.

#### Acknowledgments

This study was partially supported by the Program for the Strategic Research Foundation at Private Universities (2012–2016) supported by the Ministry of Education, Culture, Sports, Science and Technology (MEXT), the MEXT Grant-in-Aid for Specially Promoted Research Grant No. 25000011, and the MEXT Grant-in-Aid for Scientific Research A Grant No. 15H02019.

- 1) I. Akasaki and H. Amano, *Jpn. J. Appl. Phys.* **36**, 5393 (1997).
- 2) J. Wu, W. Walukiewicz, K. M. Yu, W. Shan, J. W. Ager, E. E. Haller, H. Lu, W. J. Schaff, W. K. Metzger, and S. Kurtz, *J. Appl. Phys.* **94**, 6477 (2003).
- 3) A. Vos, *Endoreversible Thermodynamics of Solar Energy Conversion* (Oxford University Press, New York, 1992) p. 29.
- 4) Y. Kuwahara, T. Fujii, Y. Fujiyama, T. Sugiyama, M. Iwaya, T. Takeuchi, S. Kamiyama, I. Akasaki, and H. Amano, *Appl. Phys. Express* **3**, 111001 (2010).
- 5) M. Mori, S. Kondo, S. Yamamoto, T. Nakao, T. Fujii, M. Iwaya, T. Takeuchi, S. Kamiyama, I. Akasaki, and H. Amano, *Appl. Phys. Express* **5**, 082301 (2012).
- 6) N. A. El-Masry, E. L. Piner, S. X. Liu, and S. M. Bedair, *Appl. Phys. Lett.* **68**, 3269 (1996).
- 7) Y. Kawaguchi, M. Shimizu, K. Hiramoto, and N. Sawaki, *MRS Proc.* **449**, 89 (1996).
- 8) K. Hiramoto, Y. Kawaguchi, M. Shimizu, N. Sawaki, T. Zheleva, R. F. Davis, H. Tsuda, W. Taki, N. Kuwano, and K. Oki, *MRS Internet J. Nitride Semicond. Res.* **2**, e6 (1997).
- 9) R. Liu, J. Mei, S. Srinivasan, H. Omiya, F. A. Ponce, D. Cherns, Y. Narukawa, and T. Mukai, *Jpn. J. Appl. Phys.* **45**, L549 (2006).
- 10) S. Srinivasan, L. Geng, R. Liu, F. A. Ponce, Y. Narukawa, and S. Tanaka, *Appl. Phys. Lett.* **83**, 5187 (2003).
- 11) D. Holec, Y. Zhang, D. V. S. Rao, M. J. Kappers, C. McAleese, and C. J. Humphreys, *J. Appl. Phys.* **104**, 123514 (2008).
- 12) D. Iida, Y. Kondo, M. Sowa, T. Sugiyama, M. Iwaya, T. Takeuchi, S. Kamiyama, and I. Akasaki, *Phys. Status Solidi: Rapid Res. Lett.* **7**, 211 (2013).
- 13) T. Yamamoto, D. Iida, Y. Kondo, M. Sowa, S. Umeda, M. Iwaya, T. Takeuchi, S. Kamimaya, and I. Akasaki, *J. Cryst. Growth* **393**, 108 (2014).
- 14) Web [<http://www.panalytical.com/index.cfm?pid=354>].
- 15) F. A. Ponce, S. Srinivasan, A. Bell, L. Geng, R. Liu, M. Stevens, J. Cai, H. Omiya, H. Marui, and S. Tanaka, *Phys. Status Solidi B* **240**, 273 (2003).
- 16) T. Sugiyama, Y. Kuwahara, Y. Isobe, T. Fujii, K. Nonaka, M. Iwaya, S. Kamiyama, H. Amano, and I. Akasaki, *Appl. Phys. Express* **4**, 015701 (2011).
- 17) R. People and J. C. Bean, *Appl. Phys. Lett.* **47**, 322 (1985).
- 18) J. W. Matthews, A. E. Blakeslee, and S. Mader, *Thin Solid Films* **33**, 253 (1976).
- 19) A. Fischer, H. Kühne, and H. Richter, *Phys. Rev. Lett.* **73**, 2712 (1994).

## GaNN-Based Tunnel Junctions in n–p–n Light Emitting Diodes

This content has been downloaded from IOPscience. Please scroll down to see the full text.

2013 Jpn. J. Appl. Phys. 52 08JH06

(<http://iopscience.iop.org/1347-4065/52/8S/08JH06>)

View [the table of contents for this issue](#), or go to the [journal homepage](#) for more

Download details:

IP Address: 202.11.1.201

This content was downloaded on 03/03/2017 at 06:54

Please note that [terms and conditions apply](#).

You may also be interested in:

[GaN-Based Light Emitting Diodes with Tunnel Junctions](#)

Tetsuya Takeuchi, Ghulam Hasnain, Scott Corzine et al.

[Lateral Hydrogen Diffusion at p-GaN Layers in Nitride-Based Light Emitting Diodes with Tunnel Junctions](#)

Yuka Kuwano, Mitsuru Kaga, Takatoshi Morita et al.

[GaNN-based tunnel junctions with graded layers](#)

Daiki Takasuka, Yasuto Akatsuka, Masataka Ino et al.

[Concentrating Properties of Nitride-Based Solar Cells Using Different Electrodes](#)

Mikiko Mori, Shinichiro Kondo, Shota Yamamoto et al.

[Improvement of Light Extraction Efficiency for AlGaN-Based Deep Ultraviolet Light-Emitting Diodes](#)

Tetsuhiko Inazu, Shinya Fukahori, Cyril Pernot et al.

[Investigations of Polarization-Induced Hole Accumulations and Vertical Hole Conductions in GaN/AlGaN Heterostructures](#)

Toshiki Yasuda, Kouta Yagi, Tomoyuki Suzuki et al.

[Correlation between Device Performance and Defects in GaInN-Based Solar Cells](#)

Mikiko Mori, Shinichiro Kondo, Shota Yamamoto et al.

## GaNN-Based Tunnel Junctions in n-p-n Light Emitting Diodes

Mitsuru Kaga<sup>1</sup>, Takatoshi Morita<sup>1</sup>, Yuka Kuwano<sup>1</sup>, Kouji Yamashita<sup>1</sup>, Kouta Yagi<sup>1</sup>, Motoaki Iwaya<sup>1</sup>, Tetsuya Takeuchi<sup>1</sup>, Satoshi Kamiyama<sup>1</sup>, and Isamu Akasaki<sup>1,2</sup>

<sup>1</sup>Faculty of Science and Technology, Meijo University, Nagoya 468-8502, Japan

<sup>2</sup>Graduate School of Engineering, Akasaki Research Center, Nagoya University, Nagoya 464-8603, Japan

Received October 12, 2012; accepted December 10, 2012; published online May 31, 2013

We optimized p<sup>++</sup>-GaNN/n<sup>++</sup>-GaN tunnel junctions grown on conventional light-emitting diodes, corresponding to n-p-n structures. We investigated two dependences at the tunnel junctions, the InN mole fraction dependence and a doping dependence. The lowest voltage drop at the reverse-biased tunnel junction was 0.68 V at 20 mA with a 3 nm p<sup>++</sup>-Ga<sub>0.8</sub>In<sub>0.2</sub>N (Mg: 1 × 10<sup>20</sup> cm<sup>-3</sup>)/30 nm n<sup>++</sup>-GaN (Si: 4 × 10<sup>20</sup> cm<sup>-3</sup>) structure. We then found that the Mg memory effect was reasonably suppressed by using the p<sup>++</sup>-GaNN instead of a p<sup>++</sup>-GaN. At the same time, the amount of Si doping in the following n<sup>++</sup>-GaN should be substantially high to overcome the Mg memory effect.

© 2013 The Japan Society of Applied Physics

### 1. Introduction

The tunnel diode was invented by Esaki in 1958.<sup>1)</sup> While the diode shows a negative resistance under forward bias, the diode shows an ohmic characteristic, not a rectification characteristic under reverse bias. Therefore, the reverse-biased tunnel junction can be a low-resistive-current path from an n-layer to a p-layer, resulting in greater flexibilities for current injection. There are some devices utilizing the reverse-biased tunnel junctions. For example, multijunction solar cells,<sup>2,3)</sup> multijunction LEDs,<sup>4,5)</sup> and vertical cavity surface-emitting lasers<sup>6-9)</sup> with current confinement are realized.

In nitride semiconductors, one of the remaining issues is a low hole concentration, resulting in a high resistivity of p-type layers.<sup>10,11)</sup> A typical hole concentration in p-GaN is at most 1 × 10<sup>18</sup> cm<sup>-3</sup>,<sup>12)</sup> and the resistivity is over 1 Ω cm, which is 100 times higher than the resistivity of n-GaN. These poor characteristics cause high operating voltages and low hole injection efficiencies, leading to poor device performances. This situation is even worse for larger band-gap materials, e.g., AlGaIn, which are important materials for UV regions.<sup>13,14)</sup> Therefore, if nitride semiconductor tunnel junctions are obtained, extensive performance improvements of nitride semiconductor devices are expected. So far, a few reports on the nitride semiconductor tunnel junctions have been published.<sup>15-19)</sup> The voltage drop at the tunnel junction is still high, over 1 V for some current flow, and there are no systematic reports on the optimum structure of the nitride semiconductor tunnel junctions. We then focus our attention to GaInN because GaInN has a small band gap energy, a high hole concentration,<sup>20-23)</sup> and potentially large polarization field due to the piezoelectric effect.<sup>24-26)</sup> In this study, we investigate the InN mole fraction dependence of p<sup>++</sup>-GaNN layers in the tunnel junctions. The reverse-biased tunnel junctions are characterized with n-p-n LED structures consisting of the tunnel junctions and the conventional LEDs. In addition, Mg and Si doping dependences of the voltage drops at the tunnel junctions are investigated. On the basis of obtained results, influences of a Mg memory effect on the tunnel junction characteristics are discussed.

### 2. Experimental Methods

All the samples were grown on c-plane sapphire (0001) substrates by low-pressure metal organic vapor phase

n <sup>+</sup> -GaN contact layer
top n-GaN (500nm)
n <sup>++</sup> -GaN (30nm)
p <sup>++</sup> -Ga <sub>1-x</sub> In <sub>x</sub> N (3 or 7.5nm)
p-GaN (100nm)
p-AlGaIn electron-blocking layer. (20nm)
GaInN/GaN MQW
bottom n-GaN(3μm)
u-GaN(3μm)
LT-GaN
c-plane sapphire(0001) substrate

**Fig. 1.** (Color online) Schematics of the n-p-n LED structure with the tunnel junction.

epitaxy (MOVPE). For the growth of the nitride semiconductor tunnel junctions, triethylgallium (TEGa), trimethylindium (TMIn), ammonia (NH<sub>3</sub>), and nitrogen were used as the Ga, In, and N sources and a carrier gas, respectively. We also used ethyl-bis(cyclopentadienyl)magnesium (Et-Cp2Mg), and silane (SiH<sub>4</sub>) as dopant precursors for p- and n-type layers.

As shown in Fig. 1, the n-p-n structure where the tunnel junction was grown on the conventional LED structure was fabricated to evaluate the reverse-biased tunnel junction in a device geometry. The structure consists of a GaN low-temperature-deposited buffer layer (LT-GaN),<sup>27)</sup> an undoped GaN layer, a bottom n-GaN layer, GaInN/GaN multiple quantum wells (MQWs), a p-AlGaIn electron blocking layer, a p-GaN layer, the tunnel junction (p<sup>++</sup>-Ga<sub>1-x</sub>In<sub>x</sub>N/30 nm n<sup>++</sup>-GaN), a top n-GaN layer, and a n<sup>+</sup>-GaN contact layer. We prepared a total of seven different samples as shown in Table I. The first sample series (Sample 1 to Sample 3) is for the study of InN mole fraction dependence in the p<sup>++</sup>-GaNN layers. The InN mole fraction was controlled by TMIn supply on/off and growth temperature, and calibrated by X-ray diffraction pattern measurements. Furthermore, the thickness of the p<sup>++</sup>-GaNN layer was adjusted according to the InN mole fractions to satisfy the condition of below the critical thickness.<sup>28,29)</sup> The second sample series (Sample 3

**Table 1.** InN mole fractions, thicknesses, and Mg concentrations of the p<sup>++</sup>-GaInN in the tunnel junctions. Si concentrations in n<sup>++</sup>-GaInN are also shown.

	InN mole fraction	Thickness (nm)	Si concentration (cm <sup>-3</sup> )	Mg concentration (cm <sup>-3</sup> )
Sample 1	0	7.5	3 × 10 <sup>20</sup>	1 × 10 <sup>20</sup>
Sample 2	0.1	7.5	3 × 10 <sup>20</sup>	1 × 10 <sup>20</sup>
Sample 3	0.2	3	3 × 10 <sup>20</sup>	1 × 10 <sup>20</sup>
Sample 4	0.2	3	3 × 10 <sup>20</sup>	2 × 10 <sup>20</sup>
Sample 5	0.2	3	3 × 10 <sup>20</sup>	5 × 10 <sup>19</sup>
Sample 6	0.2	3	6 × 10 <sup>20</sup>	1 × 10 <sup>20</sup>
Sample 7	0.2	3	1.5 × 10 <sup>20</sup>	1 × 10 <sup>20</sup>

to Sample 7) is for the Mg and Si doping dependences in the tunnel junctions. Doping concentration was controlled by adjusting the SiH<sub>4</sub> and Et-Cp2Mg flows, and calibrated by secondary ion mass spectrometry (SIMS).

A specific thermal annealing for Mg activation in the samples was carried out in the LED fabrication process. High temperature (725 °C) and a long (30 min) thermal annealing from etched sidewalls of the p-layers under oxygen ambient were required for sufficient Mg activation. Details can be found elsewhere.<sup>30)</sup> After the annealing, top and bottom n-electrode pads (Ti/Al/Ti/Au) were evaporated simultaneously by a standard lift-off technique. Since a low-resistivity top n-GaN layer exists at the surface unlike the conventional LED, no conductive transparent electrode is required. A conventional LED with a p-contact layer and a Ni/Au semitransparent electrode was also prepared to compare it with the LEDs containing the tunnel junctions.

The Mg and Si doping depth profiles of the samples were measured by SIMS. Surface morphologies of the LEDs with the tunnel junctions were characterized by an atomic force microscope (AFM). In addition, interfaces at the tunnel junctions were observed by scanning transmission electron microscope (STEM). Current–voltage (*I*–*V*) characteristics were then measured with 300 μm<sup>2</sup> LEDs. Emission patterns of the LEDs were also observed at the injected current of 50 mA.

### 3. Results and Discussion

#### 3.1 InN mole fraction dependence of p<sup>++</sup>-GaInN in tunnel junctions

Figures 2(a)–2(c) show bird’s-eye-view AFM images of the LEDs with tunnel junctions having different InN mole fractions in p<sup>++</sup>-GaInN layers (Samples 1–3). The InN mole fractions in Figs. 2(a)–2(c) are 0, 0.1, and 0.2, respectively. Surface roughness values of these samples are lower than 0.2 nm as the root-mean-square value. This value is similar to that of the conventional LED. In addition, Fig. 3 shows a cross-sectional STEM image of the LED with the 3 nm p<sup>++</sup>-Ga<sub>0.8</sub>In<sub>0.2</sub>N tunnel junction (Sample 3). Even though the tunnel junction was heavily doped (more than 1 × 10<sup>20</sup> cm<sup>-3</sup>), smooth interfaces similar to those of the MQWs were obtained.

Figure 4 shows *I*–*V* characteristics of the three LEDs with the tunnel junctions and the conventional LED. The operating voltages of the LEDs with the tunnel junctions were 6.20, 4.60, and 4.38 V at 20 mA for 0, 0.1, and 0.2 InN mole fractions in the p<sup>++</sup>-GaInN layers, respectively, while

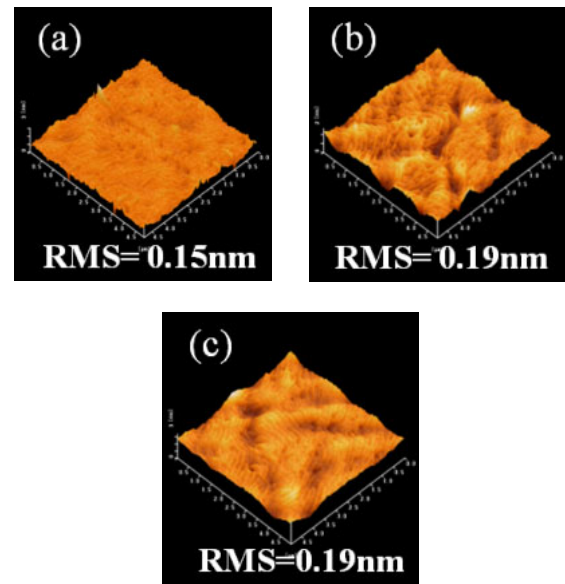


**Fig. 2.** (Color online) Bird’s-eye-view AFM images (5 × 5 μm<sup>2</sup>) of the surface for the LEDs with the p<sup>++</sup>-GaInN tunnel junctions with different InN mole fractions: (a) 0, (b) 0.1, and (c) 0.2.

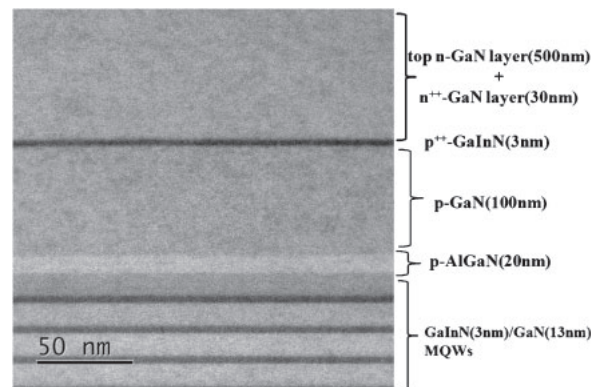


**Fig. 3.** Cross-sectional STEM image of the LED with the 3 nm p<sup>++</sup>-Ga<sub>0.8</sub>In<sub>0.2</sub>N tunnel junction.

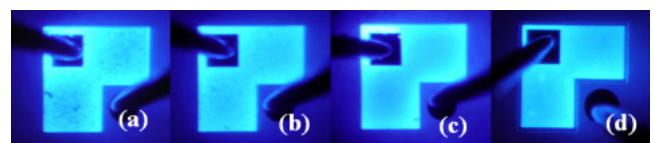


**Fig. 4.** (Color online) Emission patterns of the LEDs with the p<sup>++</sup>-GaInN tunnel junctions with different InN mole fractions: (a) 0, (b) 0.1, and (c) 0.2. The case of conventional LED is also shown for comparison.

that of the conventional LED was 3.60 V. Since the structures underneath the tunnel junctions are the same as the conventional LED structure, the differences in voltages from the conventional LED correspond to the voltage drops at the reverse-biased tunnel junctions. Therefore the voltage drops at the tunnel junctions are 2.65, 1.03, and 0.78 V at 20 mA for 0, 0.1, and 0.2 InN mole fractions in the p<sup>++</sup>-GaInN layers, respectively. The results clearly indicate that the p<sup>++</sup>-GaInN layers contribute to the drastic reductions in voltage drops at the tunnel junctions. Figure 5 shows the

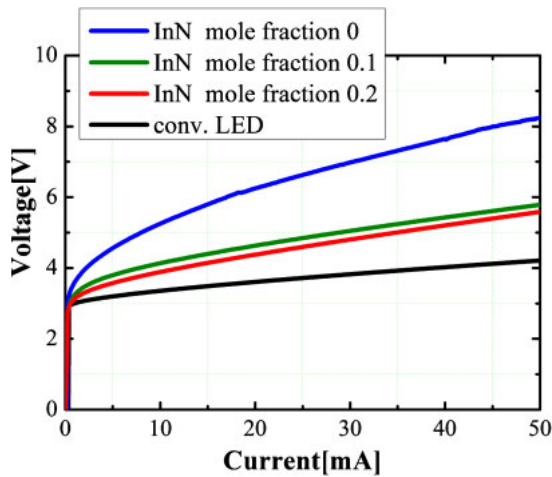


Fig. 5. (Color online)  $I$ - $V$  characteristics of the three LEDs with  $p^{++}$ -GaInN tunnel junctions with different InN mole fractions. The conventional LED result is also plotted.

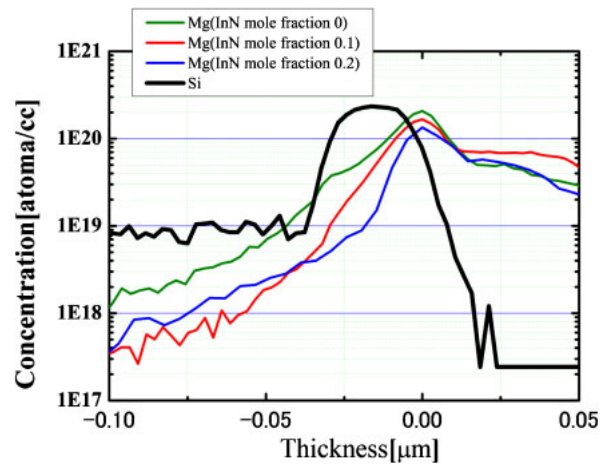


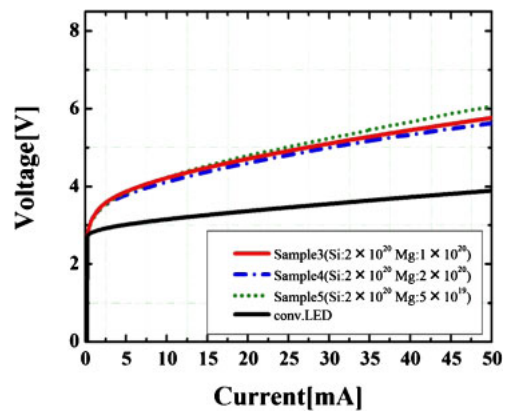
Fig. 6. (Color online) Mg and Si doping profiles measured by SIMS in the LEDs with  $p^{++}$ -GaInN tunnel junctions with different InN mole fractions.

emission patterns of the three LEDs with the tunnel junctions and the conventional LED. The conventional LED shows a uniform emission pattern since the current is spreading at the semitransparent electrode. Similar uniform emission patterns were also observed from the LEDs with the tunnel junctions. The result indicates that good current spreading at the top n-GaN was achieved and uniform tunnel junctions were formed.

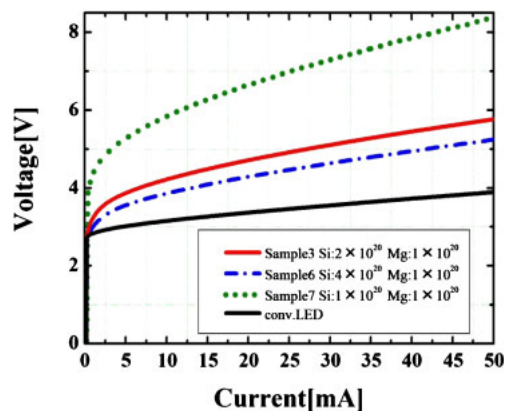
Figure 6 shows Si and Mg doping profiles measured by SIMS at the tunnel junctions of Samples 1–3.  $(1-2) \times 10^{20} \text{ cm}^{-3}$  of Mg and  $2 \times 10^{20} \text{ cm}^{-3}$  of Si were confirmed. We then found that residual Mg concentrations in the following  $n^{++}$ -layers, so-called Mg memory effect, were suppressed using GaInN as the Mg-doped p-layers in the tunnel junctions. When the InN mole fraction is 0, the residual Mg concentration in the  $n^{++}$ -layer remained high, about  $5 \times 10^{19} \text{ cm}^{-3}$ . On the other hand, with the Mg-doped  $p^{++}$ -GaInN layers, the residual Mg concentration steeply decreased to  $1 \times 10^{19} \text{ cm}^{-3}$  in the subsequent  $n^{++}$ -GaIn layers. At least we can say that the existence of the In atoms on the surface should play an important role in the suppression of the residual Mg incorporation. Further investigation is necessary to clarify the mechanism.

### 3.2 Doping concentration dependence in tunnel junction

In order to further investigate the influences of the Mg memory effect, additional LEDs with  $\times 2$  and  $\times 1/2$  doping concentrations (Samples 3 to 7) were characterized. Figures 7(a) and 7(b) show  $I$ - $V$  characteristics of the Si and Mg doping dependences for the LEDs with the tunnel junctions. The operating voltages of the LEDs are greatly influenced by the amount of Si doping. Especially in the case of  $\times 1/2$  Si doping case (Sample 7, Si:  $1 \times 10^{20} \text{ cm}^{-3}$ ), the voltage drop at the tunnel junction was markedly increased. Note that the residual Mg concentration in the  $n^{++}$ -GaIn was still high especially at the interface, some amount of Si could be easily compensated, resulting in the high voltage drop due to the wider depletion region. Actually, the  $\times 2$  Si doping sample (Sample 6, Si:  $4 \times 10^{20} \text{ cm}^{-3}$ ) showed further improvement, indicating that a higher Si concentration within the range used in the



(a)



(b)

Fig. 7. (Color online)  $I$ - $V$  characteristics of (a) Mg and (b) Si doping dependences for the LEDs with the tunnel junctions.

experiment is better. Interestingly, the voltage drop was almost independent of the amount of Mg doping within the range in the experiment. Several reasons are considered. A larger Et-Cp2Mg flow could result in a large amount of Mg incorporated, but with a more severe Mg memory effect at the same time. Alternatively, the polarization field due to the piezoelectric effect may be more dominant than the built-in

field with the impurity doping. Further investigation will be necessary to clarify the reason.

Eventually, the lowest voltage drop at the tunnel junction was 0.68 V at 20 mA obtained by optimizing the InN mole fraction and doping concentration, at which the resistance corresponds to 34  $\Omega$ . This is one of the lowest values of the nitride-based tunnel junctions reported so far. It is still necessary to further reduce the voltage drop for practical uses. A couple of further optimizations, such as reduction of hetero barrier spikes between GaInN and GaN with graded layers, the position of GaInN layer (currently only the p<sup>++</sup>-side), and the profile of the Si doping, are expected.

#### 4. Summary

In summary, we have demonstrated the n-p-n LED structures with the p<sup>++</sup>-GaInN/n<sup>++</sup>-GaN tunnel junctions. By employing the 3 nm p<sup>++</sup>-Ga<sub>0.8</sub>In<sub>0.2</sub>N/heavily Si-doped 30 nm n<sup>++</sup>-GaN tunnel junction, we obtained a very low voltage drop at the tunnel junction (0.68 V at 20 mA). We found that the Mg memory effect was reasonably suppressed using the p<sup>++</sup>-GaInN layer in the tunnel junctions. At the same time, the amount of Si doping in the subsequent n<sup>++</sup>-GaN should be substantially high to overcome the Mg memory effect. We found that it is essential to suppress the Mg memory effect in order to obtain low-resistivity tunnel junctions.

#### Acknowledgements

This work was supported by a Grant-in-Aid for Scientific Research (C) (No. 23560015) and the Ministry of Education, Culture, Sports, Science, and Technology Supported Program for the Strategic Research Foundation at Private Universities, Japan, 2012–2016. The SIMS measurements were carried out by courtesy of Toray Research Center, Inc. STEM was performed by courtesy of JFE Techno-Research Corporation.

- 1) L. Esaki: *Phys. Rev.* **109** (1958) 603.
- 2) T. Takamoto, E. Ikeda, H. Kurita, and M. Ohmori: *Appl. Phys. Lett.* **70** (1997) 381.
- 3) H. Sugiura, C. Amano, A. Yamamoto, and M. Yamaguchi: *Jpn. J. Appl. Phys.* **27** (1988) 269.
- 4) I. Ozden, E. Makarona, A. V. Nurmikko, T. Takeuchi, and M. Krames: *Appl. Phys. Lett.* **79** (2001) 2532.
- 5) J. K. Kim, S. Nakagawa, E. Hall, and L. A. Coldren: *Appl. Phys. Lett.* **77**

- (2000) 3137.
- 6) M. Diagne, Y. He, H. Zhou, E. Makarona, A. V. Nurmikko, J. Han, K. E. Waldrip, J. J. Figiel, T. Takeuchi, and M. Krames: *Appl. Phys. Lett.* **79** (2001) 3720.
- 7) S. R. Jeon, C. S. Oh, J. W. Yang, G. M. Yang, and B. S. Yoo: *Appl. Phys. Lett.* **80** (2002) 1933.
- 8) M. Mehta, D. Feezell, D. A. Buell, A. W. Jackson, L. A. Coldren, and J. E. Bowers: *IEEE J. Quantum Electron.* **42** (2006) 675.
- 9) D. Feezell, D. A. Buell, D. Lofgreen, M. Mehta, and L. A. Coldren: *IEEE J. Quantum Electron.* **42** (2006) 494.
- 10) H. Amano, M. Kito, K. Hiramatsu, and I. Akasaki: *Jpn. J. Appl. Phys.* **28** (1989) L2112.
- 11) S. Nakamura, M. Senoh, and T. Mukai: *Jpn. J. Appl. Phys.* **30** (1991) L1708.
- 12) H. Alves, M. Böhm, A. Hofstaetter, H. Amano, S. Einfeldt, D. Hommel, D. M. Hofmann, and B. K. Meyer: *Physica B* **308–310** (2001) 38.
- 13) M. Kim, T. Fujita, S. Fukahori, T. Inazu, C. Pernot, Y. Nagasawa, A. Hirano, M. Ippommatsu, M. Iwaya, T. Takeuchi, S. Kamiyama, M. Yamaguchi, Y. Honda, H. Amano, and I. Akasaki: *Appl. Phys. Express* **4** (2011) 092102.
- 14) K. Takehara, K. Takeda, S. Ito, H. Aoshima, M. Iwaya, T. Takeuchi, S. Kamiyama, I. Akasaki, and H. Amano: *Jpn. J. Appl. Phys.* **51** (2012) 042101.
- 15) S. R. Jeon, Y. H. Song, H. J. Jang, G. M. Yang, S. W. Hwang, and S. J. Son: *Appl. Phys. Lett.* **78** (2001) 3265.
- 16) T. Takeuchi, G. Hasnain, S. Corzine, M. Hueschen, R. P. Schneider, Jr., C. Kocot, M. Blomqvist, Y. Chang, D. Lefforge, M. R. Krames, L. W. Cookand, and S. A. Stockman: *Jpn. J. Appl. Phys.* **40** (2001) L861.
- 17) S. Krishnamoorthy, D. N. Nath, F. Akyol, P. S. Park, M. Esposto, and S. Rajan: *Appl. Phys. Lett.* **97** (2010) 203502.
- 18) J. Simon, Z. Zhang, K. Goodman, H. Xing, T. Kosel, P. Fay, and D. Jena: *Phys. Rev. Lett.* **103** (2009) 026801.
- 19) S. Krishnamoorthy, P. S. Park, and S. Rajan: *Appl. Phys. Lett.* **99** (2011) 233504.
- 20) K. Kumakura, T. Makimoto, and N. Kobayashi: *J. Cryst. Growth* **221** (2000) 267.
- 21) K. Kumakura, T. Makimoto, and N. Kobayashi: *Jpn. J. Appl. Phys.* **39** (2000) L337.
- 22) K. Kumakura, T. Makimoto, and N. Kobayashi: *J. Appl. Phys.* **93** (2003) 3370.
- 23) B. N. Pantha, A. Sedhain, J. Li, J. Y. Lin, and H. X. Jiang: *Appl. Phys. Lett.* **95** (2009) 261904.
- 24) T. Takeuchi, C. Wetzel, S. Yamaguchi, H. Sakai, H. Amano, I. Akasaki, Y. Kaneko, S. Nakagawa, Y. Yamaoka, and N. Yamada: *Appl. Phys. Lett.* **73** (1998) 1691.
- 25) T. Takeuchi, S. Sota, M. Komori, M. Katsuragawa, H. Takeuchi, H. Amano, and I. Akasaki: *Jpn. J. Appl. Phys.* **36** (1997) L382.
- 26) C. Wetzel, T. Takeuchi, H. Amano, and I. Akasaki: *J. Appl. Phys.* **85** (1999) 3786.
- 27) H. Amano, N. Sawaki, I. Akasaki, and Y. Toyoda: *Appl. Phys. Lett.* **48** (1986) 353.
- 28) D. Holec, Y. Zhang, D. V. S. Rao, M. J. Kappers, C. M. Aleese, and C. J. Humphreys: *Jpn. J. Appl. Phys.* **104** (2008) 123514.
- 29) W. Zhao, L. Wang, J. Wang, Z. Hao, and Y. Luo: *J. Cryst. Growth* **327** (2011) 202.
- 30) Y. Kuwano, K. Yamashita, M. Kaga, T. Morita, M. Iwaya, T. Takeuchi, S. Kamiyama, and I. Akasaki: submitted to *Jpn. J. Appl. Phys.*

## High quality $\text{Al}_{0.99}\text{Ga}_{0.01}\text{N}$ layers on sapphire substrates grown at 1150 °C by metalorganic vapor phase epitaxy

This content has been downloaded from IOPscience. Please scroll down to see the full text.

2017 Jpn. J. Appl. Phys. 56 015504

(<http://iopscience.iop.org/1347-4065/56/1/015504>)

View [the table of contents for this issue](#), or go to the [journal homepage](#) for more

Download details:

IP Address: 219.127.71.134

This content was downloaded on 03/03/2017 at 06:37

Please note that [terms and conditions apply](#).

You may also be interested in:

[Recent progress in metal-organic chemical vapor deposition of \(0001\) N-polar group-III nitrides](#)

Stacia Keller, Haoran Li, Matthew Laurent et al.

[Epitaxy of an Al-Droplet-Free AlN Layer with Step-Flow Features by Molecular Beam Epitaxy](#)

Pan Jian-Hai, Wang Xin-Qiang, Chen Guang et al.

[High Quality AlN with a Thin Interlayer Grown on a Sapphire Substrate by Plasma-Assisted Molecular Beam Epitaxy](#)

Ren Fan, Hao Zhi-Biao, Zhang Chen et al.

[Modified pulse growth and misfit strain release of an AlN heteroepilayer with a Mg–Si codoping pair by MOCVD](#)

Abdul Majid Soomro, Chenping Wu, Na Lin et al.

[MBE-grown high-quality \(Al,Ga\)N/GaN distributed Braggreflectors for resonant cavity LEDs](#)

S Fernández, F B Naranjo, F Calle et al.

[Effect of stress on the Al composition evolution in AlGaIn grown using metal organic vapor phase epitaxy](#)

Chenguang He, Zhixin Qin, Fujun Xu et al.

[Flat Surfaces and Interfaces in AlN/GaN Heterostructures and Superlattices Grown by Flow-Rate Modulation Epitaxy](#)

Masanobu Hiroki and Naoki Kobayashi

[Control of growth mode in Mg-doped GaN/AlN heterostructure](#)

Tomohiro Morishita, Kosuke Sato, Motoaki Iwaya et al.



# High quality $\text{Al}_{0.99}\text{Ga}_{0.01}\text{N}$ layers on sapphire substrates grown at 1150 °C by metalorganic vapor phase epitaxy

Shota Katsuno<sup>1</sup>, Toshiki Yasuda<sup>1</sup>, Koudai Hagiwara<sup>1</sup>, Norikatsu Koide<sup>1</sup>, Motoaki Iwaya<sup>1</sup>, Tetsuya Takeuchi<sup>1\*</sup>, Satoshi Kamiyama<sup>1</sup>, Isamu Akasaki<sup>1,2</sup>, and Hiroshi Amano<sup>2,3</sup>

<sup>1</sup>Faculty of Science and Technology, Meijo University, Nagoya 468-8502, Japan

<sup>2</sup>Akasaka Research Center, Nagoya 464-8603, Japan

<sup>3</sup>Institute of Materials and Systems for Sustainability, Nagoya University, Nagoya 464-8603, Japan

\*E-mail: take@meijo-u.ac.jp

Received October 19, 2016; revised November 9, 2016; accepted November 10, 2016; published online December 16, 2016

We systematically investigated metalorganic vapor phase epitaxy (MOVPE) growths of AlN layers with trimethylgallium (TMGa) supply on sapphire substrates at 1100–1250 °C. We found that Ga incorporations into the AlN layers contributed to smooth surfaces covered with step terraces at the early stage of the Al(Ga)N growth. In addition, a GaN mole fraction leading to the smooth surfaces was found to be around 2–3% at the beginning of growth. The Ga supply during the AlN layer growth at 1150 °C provided very smooth  $\text{Al}_{0.99}\text{Ga}_{0.01}\text{N}$  layers on sapphire substrates.

© 2017 The Japan Society of Applied Physics

## 1. Introduction

Nitride-based deep ultraviolet light-emitting diodes (DUV-LEDs) are expected to be utilized in various applications of medical and industrial fields. In order to fabricate the DUV-LEDs, an AlN layer on a sapphire substrate is used as a template. Originally the AlN epitaxial growths were performed around 1100 °C,<sup>1–3</sup> but later on high quality AlN templates for efficient DUV-LEDs have been achieved by growing at above 1400 °C.<sup>4–11</sup> At the same time, some issues have been arose related to such a high growth temperature for AlN. First, the wafer bowing caused by the high growth temperature, deteriorates wafer uniformity and yield.<sup>12,13</sup> Second, metalorganic vapor phase epitaxy (MOVPE) reactors require specialized heaters and growth chambers for the high growth temperature. In addition to that, some quartz and carbon parts in the reactor must be frequently replaced due to the damages caused by the high growth temperature.

If high quality AlN layers can be grown at low temperature, the above issues will be solved. So far high quality AlN layers grown at temperatures below 1200 °C have been attempted with various methods,<sup>14–20</sup> such as  $\text{NH}_3$  pulsed injection and/or migration enhanced epitaxy (MEE).<sup>21–24</sup> Recently, it was also reported that a Ga supply during the AlN growth contributed to smooth surfaces of the AlN layers.<sup>25–27</sup> The Ga supply during the AlN growth could enhance surface migration of surface adatoms which leads to the two dimensional growths. However, only a single sample was investigated in each case, and so far systematic investigations, such as growth parameter dependences or mechanism regarding the effect of Ga in the AlN layer, have not been carried out.

In this study, we systematically investigated growths of AlN layers under low growth temperature down to 1100 °C by supplying Ga with various Ga/III supply ratios. The  $\text{Al}_{0.97}\text{Ga}_{0.03}\text{N}$  layers with smooth surfaces were obtained by growing even at low growth temperature, 1100–1200 °C. A correlation between the smooth surface of the AlGa<sub>x</sub>N layer and the GaN mole fraction was clarified. We also evaluated the material qualities of the  $\text{Al}_{0.99}\text{Ga}_{0.01}\text{N}$  layers.

## 2. Experimental methods

All the samples in this study were grown on *c*-plane sapphire

substrates with a nitridation process by MOVPE.<sup>28–30</sup> The nitridation process was carried out along the following procedure. First,  $\text{NH}_3$  was introduced into the MOVPE reactor when a substrate temperature was room temperature. Then the substrate temperature was ramping up from room temperature to 1100 °C for 10 min and was held for 1 min with the  $\text{NH}_3$  flow. Note that no thermal etching under hydrogen was done for a sapphire substrate. After the nitridation, a 50 nm AlN buffer layer and an 80 nm AlN intermediate layer were grown at 1100 °C and 1100–1250 °C, respectively. The intermediate layer was used in order to obtain better crystal quality of a main AlN layer grown on the intermediate layer.<sup>14</sup> While the growth rate and the V/III ratio for the buffer layer were 3.0 μm/h and 3.9, those for the intermediate layer were 0.4 μm/h and 62, respectively. Finally a 1.8 μm main AlN layer was grown at the same temperature of the intermediate layer (1100–1250 °C) with and without trimethylgallium (TMGa) supply. The growth rate of the main AlN layer was 1.8 μm/h. The Ga/III supply ratio was varied from 0 to 0.3. In addition, in order to investigate the surface morphology evolution during the main AlN growth, the samples with various thicknesses of the main AlN layer (from 0 to 4.3 μm) grown at 1150 °C were also prepared.

Surface morphologies of the samples were observed by atomic force microscopy (AFM). A Ga depth profile in the 4.3 μm Al(Ga)N layer with TMGa supply was measured by secondary ion mass spectrometry (SIMS). GaN mole fractions and crystal qualities in the samples were estimated by X-ray diffraction (XRD) patterns. Threading dislocations in the 4.3 μm AlN layer with TMGa supply were observed by transmission electron microscopy (TEM).

## 3. Results and discussion

Figure 1(a) shows the  $10 \times 10 \mu\text{m}^2$  AFM images of the main AlN layers grown under various growth temperatures (1100, 1150, 1200, and 1250 °C) with various Ga/III supply ratios (0, 0.1, 0.18, and 0.3). Figure 1(b) also shows the AFM images of the main AlN layers grown at 1100 °C with small Ga/III supply ratios (0.01–0.03). It was found in the case without TMGa supply that the low growth temperatures (1100 and 1150 °C) resulted in rough surfaces with small

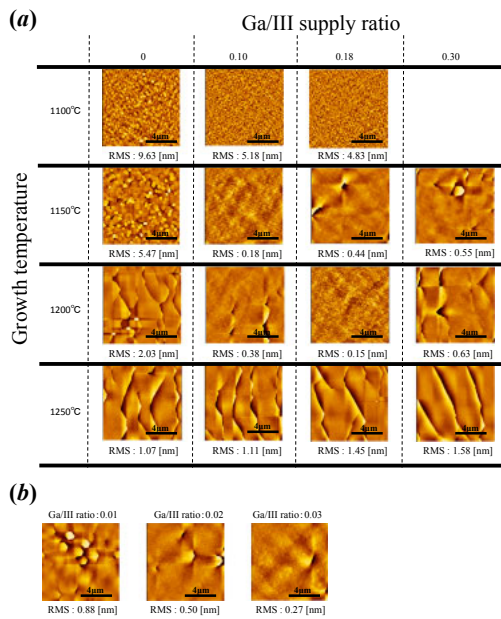


**Fig. 1.** (Color online) (a)  $10 \times 10 \mu\text{m}^2$  AFM images of the main AlN layers grown under various growth temperatures (1100, 1150, 1250, and 1250 °C) with various Ga/III supply ratios (0, 0.1, 0.18, and 0.3), and (b)  $10 \times 10 \mu\text{m}^2$  AFM images of the main AlN layers grown at 1100 °C with small Ga/III supply ratios (0.01–0.03).

columnar crystals with hexagonal (1150 °C) or circular (1100 °C) shapes, and high growth temperatures (1200 and 1250 °C) resulted in step bunching with wide flat terraces. While no effect of TMGa supply was observed on the surfaces of the samples grown at 1250 °C, very smooth surfaces were obtained from the samples grown at 1100, 1150, and 1200 °C with different Ga/III supply ratios, 0.03, 0.10, and 0.18, respectively. The images showed atomically flat surfaces with the steps but almost no columnar crystals or step bunching, which RMS values were less than 0.3 nm. Interestingly, too large Ga/III ratios also caused rough surfaces.

We then investigated surface morphology evolutions during the growth of the main AlN layer up to 4.3 μm, respectively. Figures 2(a) and 2(b) show a GaN mole fraction profile measured by SIMS in the 4.3 μm main AlN layer grown at 1150 °C with 0.10 Ga/III supply ratio, and AFM images of the surfaces of the main AlN layers with different layer thicknesses from 0 to 4.3 μm. Note that the 0 μm sample corresponded to the sample showing the AlN intermediate layer surface [Fig. 2(b)(i)]. The SIMS result reveals that the GaN mole fraction at the very beginning of the AlN main layer was high, 2.1%. Then the GaN mole fraction was decreased down to 1.2% within the first 1.3 μm thickness, resulting in a graded layer. After that, the GaN mole fraction remained constant, 1.2%. In other words, the two AlGaN layers, (the graded layer and the constant layer), were automatically formed even under the same growth condition. In addition, AFM images indicated that the surfaces became smooth (RMS values: 8.57 to 0.13 nm) during the first 1.3 μm layer, which was coincident with the thickness of the graded AlGaN layer. After the first 1.3 μm layer, the surface smoothness was kept to be the same up to 4.3 μm. These results suggest that TMGa supply was very useful to form smooth surface of the main Al(Ga)N layer.

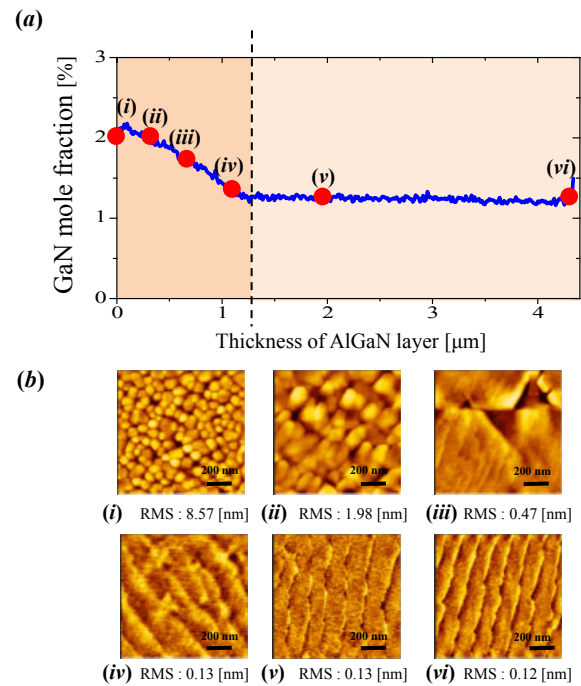


**Fig. 2.** (Color online) (a) a GaN mole fraction profile measured by SIMS in the 4.3 μm main AlN layer grown at 1150 °C with 0.10 Ga/III supply ratio, and (b)  $1 \times 1 \mu\text{m}^2$  AFM images of the surfaces of the main AlN layers with different layer thicknesses, (i) 0 μm (the intermediate layer), (ii) 0.5 μm, (iii) 0.9 μm, (iv) 1.2 μm, (v) 2 μm, and (vi) 4.3 μm.

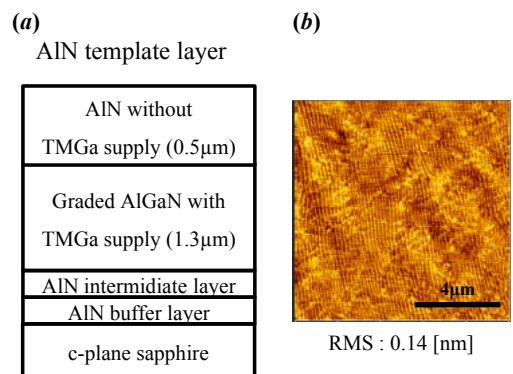


**Fig. 3.** (Color online) (a) the sample structure and (b) a  $10 \times 10 \mu\text{m}^2$  AFM image of the sample.

In order to further investigate the effect of Ga atoms for the growth of the smooth AlGaN layer, another sample consisting of the first 1.3 μm main graded AlGaN with TMGa supply and the second 0.5 μm main AlN without TMGa supply was prepared. Figures 3(a) and 3(b) show the sample structure and the AFM image of the sample. We clearly observed a very flat surface which was similar to that of the sample with TMGa supply during all the growth of the main AlN layer [Fig. 1(a) 1150 °C for growth temperature and 0.10 for Ga/III supply ratio], indicating that TMGa supply plays an important role in the first 1.3 μm layer for the smooth surface.

Next, we estimated the GaN mole fractions in the main AlN layers grown under various growth temperatures and various Ga/III supply ratios. Figure 4(a) shows (0002)  $2\theta/\omega$  XRD patterns of the main Al(Ga)N layers grown at 1150 °C with various Ga/III supply ratios. While a single main peak

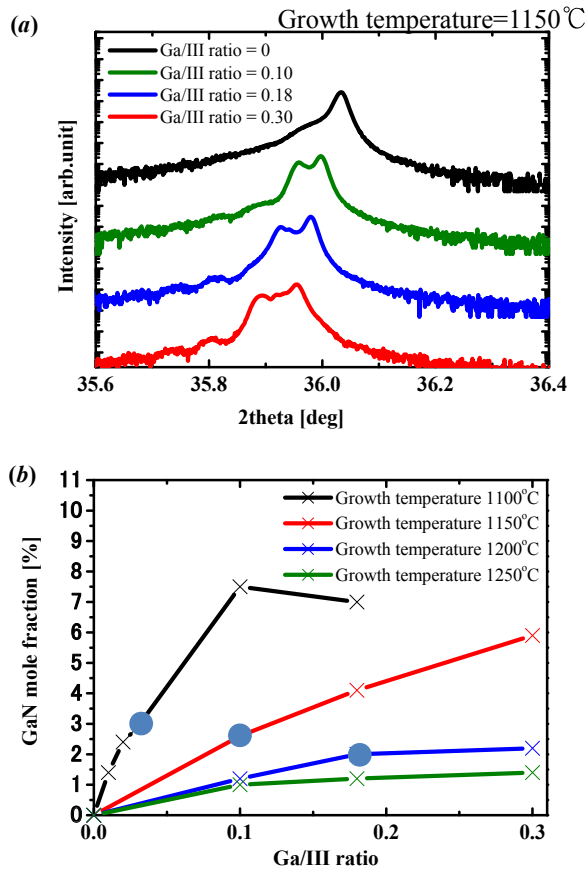


**Fig. 4.** (Color online) (a) (0002)  $2\theta/\omega$  XRD patterns of the main AlN layers grown at 1150°C with various Ga/III supply ratios, and (b) GaN mole fractions of the very bottom part in the graded AlGaIn layer as a function of Ga/III ratio and growth temperatures.

was observed from the AlN layer grown without TMGa supply, two peaks were observed from the main AlN layers grown with TMGa supplies. From the SIMS results shown in Fig. 2(a), the two peaks of XRD patterns should correspond to the two AlGaIn layers, the first 1.3 μm graded AlGaIn layer and the second 0.5 μm constant AlGaIn layer. A peak at a larger angle (lower GaN mole fraction) should correspond to the second constant AlGaIn layer and a peak at a smaller angle (higher GaN mole fraction) should correspond to the part of the highest GaN mole fraction in the first graded AlGaIn layer, that is the very bottom part of the graded AlGaIn layer. Furthermore, with an increase of the Ga/III supply ratios, the two peaks were shifted to a lower angle side, meaning that larger Ga incorporation was obtained with an increase of the Ga/III supply ratio. We then plotted the GaN mole fractions of the very bottom part in the graded AlGaIn layer as a function of Ga/III ratio and growth temperatures in Fig. 4(b). Coincidentally the three smooth surfaces observed by AFM were obtained in the case that the GaN mole fractions were within 2–3% (indicated with solid circles) regardless of the growth conditions. In other words, the results implies that not growth conditions but a certain GaN mole fraction value seems key factor to obtain smooth surfaces in the case of adding Ga in the AlN layer.

Finally we investigated material qualities of AlGaIn main layers. Figures 5(a) and 5(b) show XRD  $\omega$  scans of (20 $\bar{2}$ 4) and (10 $\bar{1}$ 5) planes of two different samples, respectively. Sample A is the sample grown at 1150°C, consisting of the

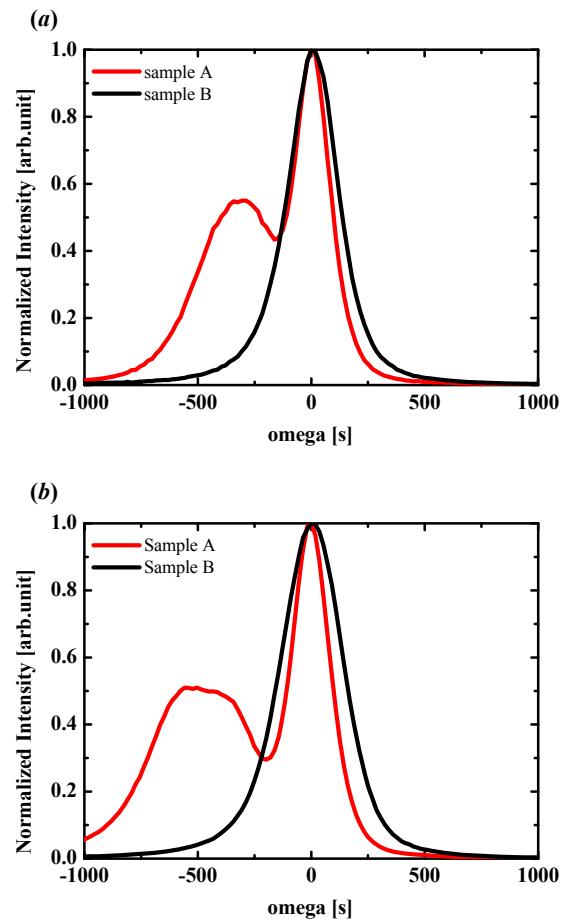


**Fig. 5.** (Color online) XRD  $\omega$  scans of (a) (20 $\bar{2}$ 4) and (b) (10 $\bar{1}$ 5) planes of two different samples.

first 1.3 μm graded AlGaIn with TMGa supply and the second 0.5 μm main AlN without TMGa supply shown in Fig. 3. Sample B consisted of the 1.8 μm main AlN layer grown at 1250°C without Ga supply shown in Fig. 1(a). Two peaks were clearly observed in Sample A due to the existence of the two layers, the 1.3 μm graded AlGaIn and the 0.5 μm AlN, and the narrower peak on the right side corresponds to the 0.5 μm AlN. The FWHMs of the peak from the AlN layer in Sample A are narrower than those of the peaks obtained from the Sample B. Figure 6 shows a cross-sectional TEM image of the 4.3 μm AlN layer with TMGa supply (the same as the SIMS sample in Fig. 2), taken with the reflection of  $g = [11\bar{2}0]$ . In the image, pure edge dislocations and edge/screw-mixed dislocations are observed, and the estimated dislocation density was approximately  $5 \times 10^9 \text{ cm}^{-2}$ , which is comparable to that of the AlN layer grown at 1300°C or higher.<sup>31)</sup> These results clearly suggest that Ga supply during the AlN layer growth at less than 1200°C is very useful to obtain reasonably high quality AlN layer on sapphire.

#### 4. Conclusions

We investigated an epitaxial growth of AlN layer with Ga supply on sapphire at relatively low growth temperature. Smooth surfaces of the AlGaIn layers with the small amount of GaN mole fractions were obtained even with the low growth temperature, such as 1100–1150°C. Such smooth surfaces have been formed during the initial growth of the

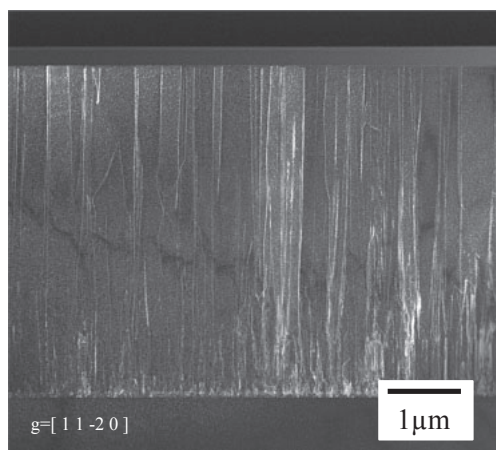


**Fig. 6.** A cross-sectional TEM image of the 4.3  $\mu\text{m}$  AlN layer with TMGa supply (the same as the SIMS sample), taken with the reflections of  $g = [11\bar{2}0]$ .

AlN filmy layer with the TMGa supply. The Ga incorporation could contribute to the promotion of lateral growth in the initial growth. We also found that the samples with smooth surfaces contained 2–3% GaN mole fractions regardless of the growth conditions.

#### Acknowledgments

This work was supported by Technology Supported Program for the Strategic Research Foundation at Private Universities (2012–2016), MEXT Grant-in-Aid for Specially Promoted Research (No. 25000011), and Grant-in-Aid for Scientific Research (B) (No. 26286045).

- 1) S. Nitta, M. Kariya, T. Kashima, S. Yamaguchi, H. Amano, and I. Akasaki, *Appl. Surf. Sci.* **159–160**, 421 (2000).
- 2) S. Nitta, Y. Yukawa, Y. Watanabe, S. Yamaguchi, H. Amano, and I. Akasaki, *Phys. Status Solidi A* **194**, 485 (2002).
- 3) S. Nitta, Y. Yukawa, Y. Watanabe, M. Kosaki, M. Iwaya, S. Yamaguchi, H. Amano, and I. Akasaki, *Mater. Sci. Eng. B* **93**, 139 (2002).
- 4) M. Imura, H. Sugimura, N. Okada, M. Iwaya, S. Kamiyama, H. Amano, I. Akasaki, and A. Bandoh, *J. Cryst. Growth* **310**, 2308 (2008).
- 5) M. Imura, K. Nakano, N. Fujimoto, N. Okada, K. Balakrishnan, M. Iwaya, S. Kamiyama, H. Amano, I. Akasaki, T. Noro, T. Takagi, and A. Bandoh, *Jpn. J. Appl. Phys.* **46**, 1458 (2007).
- 6) M. Imura, K. Nakano, N. Fujimoto, N. Okada, K. Balakrishnan, M. Iwaya, S. Kamiyama, H. Amano, I. Akasaki, T. Noro, T. Takagi, and A. Bandoh, *Jpn. J. Appl. Phys.* **45**, 8639 (2006).
- 7) R. Miyagawa, S. Yang, H. Miyake, and K. Hiramatsu, *Phys. Status Solidi C* **9**, 499 (2012).
- 8) N. Fujimoto, T. Kitano, G. Narita, N. Okada, K. Balakrishnan, M. Iwaya, S. Kamiyama, H. Amano, I. Akasaki, K. Shimono, T. Noro, T. Takagi, and A. Bandoh, *Phys. Status Solidi C* **3**, 1617 (2006).
- 9) M. Imura, N. Fujimoto, N. Okada, K. Balakrishnan, M. Iwaya, S. Kamiyama, H. Amano, I. Akasaki, T. Noro, T. Takagi, and A. Bandoh, *J. Cryst. Growth* **300**, 136 (2007).
- 10) F. Brunner, H. Protzmann, M. Heuken, A. Knauer, M. Weyers, and M. Kneissl, *Phys. Status Solidi C* **5**, 1799 (2008).
- 11) O. Reentilä, F. Brunner, A. Knauer, A. Mogilatenko, W. Neumann, H. Protzmann, M. Heuken, M. Kneissl, M. Weyers, and G. Tränkle, *J. Cryst. Growth* **310**, 4932 (2008).
- 12) V. Hoffmann, A. Knauer, C. Brunner, S. Einfeldt, M. Weyers, G. Tränkle, K. Haberland, J.-T. Zettler, and M. Kneissl, *J. Cryst. Growth* **315**, 5 (2011).
- 13) N. Kato, S. Sato, H. Sugimura, T. Sumii, N. Okada, M. Imura, M. Iwaya, S. Kamiyama, H. Amano, I. Akasaki, H. Maruyama, T. Takagi, and A. Bandoh, *Phys. Status Solidi C* **5**, 1559 (2008).
- 14) S. Nikishin, B. Borisov, M. Pandikunta, R. Dahal, J. Y. Lin, H. X. Jiang, H. Harris, and M. Holtz, *Appl. Phys. Lett.* **95**, 054101 (2009).
- 15) X. H. Li, S. Wang, H. Xie, Y. O. Wei, T. T. Kao, Md. M. Satter, S. C. Shen, P. D. Yoder, T. Detchprohm, R. D. Dupuis, A. M. Fischer, and F. A. Ponce, *Phys. Status Solidi B* **252**, 1089 (2015).
- 16) Z. Chen, S. Newman, D. Brown, R. Chung, S. Keller, U. K. Mishra, S. P. Denbaars, and S. Nakamura, *Appl. Phys. Lett.* **93**, 191906 (2008).
- 17) Y. A. Xi, K. X. Chen, F. Mont, K. Kim, C. Wetzel, E. F. Schubert, W. Liu, X. Li, and J. A. Smart, *Appl. Phys. Lett.* **89**, 103106 (2006).
- 18) Y. A. Xi, K. X. Chen, F. Mont, J. K. Kim, E. F. Schubert, C. Wetzel, W. Liu, X. Li, and J. A. Smart, *J. Electron. Mater.* **36**, 533 (2007).
- 19) J. Yan, J. Wang, Y. Zhang, P. Cong, L. Sun, Y. Tian, C. Zhao, and J. Li, *J. Cryst. Growth* **414**, 254 (2015).
- 20) A. Kakanakova-Georgieva, D. Nilsson, and E. Janzen, *J. Cryst. Growth* **338**, 52 (2012).
- 21) H. Hirayama, S. Fujikawa, N. Noguchi, J. Norimatsu, T. Takano, K. Tsubaki, and N. Kamata, *Phys. Status Solidi A* **206**, 1176 (2009).
- 22) H. Hirayama, N. Maeda, S. Fujikawa, S. Toyoda, and N. Kamata, *Jpn. J. Appl. Phys.* **53**, 100209 (2014).
- 23) R. G. Banal, M. Funato, and Y. Kawakami, *Appl. Phys. Lett.* **92**, 241905 (2008).
- 24) R. G. Banal, M. Funato, and Y. Kawakami, *J. Cryst. Growth* **311**, 2834 (2009).
- 25) T. M. Al tahtamouni, J. Li, J. Y. Lin, and H. X. Jiang, *J. Phys. D* **45**, 285103 (2012).
- 26) A. Dadgar, A. Krost, J. Christen, B. Bastek, F. Bertram, A. Krtischil, T. Hempel, J. Bläsing, U. Habocek, and A. Hoffmann, *J. Cryst. Growth* **297**, 306 (2006).
- 27) W. V. Lundin, A. E. Nikolaev, M. Yagovkina, P. N. Brunkov, M. M. Rozhavskaia, B. Ya. Ber, D. Yu. Kazantsev, A. F. Tsatsulnikov, A. V. Lobanova, and R. A. Talalaev, *J. Cryst. Growth* **352**, 209 (2012).
- 28) Y. Wu, A. Hanlon, J. F. Kaeding, R. Sharma, P. T. Fini, S. Nakamura, and J. S. Speck, *Appl. Phys. Lett.* **84**, 912 (2004).
- 29) Q. Paduano and D. Weyburne, *Jpn. J. Appl. Phys.* **42**, 1590 (2003).
- 30) R. G. Banal, Y. Akashi, K. Matsuda, Y. Hayashi, M. Funato, and Y. Kawakami, *Jpn. J. Appl. Phys.* **52**, 08JB21 (2013).
- 31) M. L. Nakarmi, B. Cai, J. Y. Lin, and H. X. Jiang, *Phys. Status Solidi A* **209**, 126 (2012).

## GaN<sub>1-x</sub>Sb<sub>x</sub> alloys grown with H<sub>2</sub> and N<sub>2</sub> carrier gases

This content has been downloaded from IOPscience. Please scroll down to see the full text.

2016 Jpn. J. Appl. Phys. 55 05FD01

(<http://iopscience.iop.org/1347-4065/55/5S/05FD01>)

View [the table of contents for this issue](#), or go to the [journal homepage](#) for more

Download details:

IP Address: 219.127.71.134

This content was downloaded on 03/03/2017 at 06:41

Please note that [terms and conditions apply](#).

You may also be interested in:

[Flat Surfaces and Interfaces in AlN/GaN Heterostructures and Superlattices Grown by Flow-Rate Modulation Epitaxy](#)

Masanobu Hiroki and Naoki Kobayashi

[Growth and properties of Al-rich In<sub>x</sub>Al<sub>1-x</sub>N ternary alloy](#)

Tae Su Oh, Jong Ock Kim, Hyun Jeong et al.

[Recent progress in metal-organic chemical vapor deposition of \(0001\) N-polar group-III nitrides](#)

Stacia Keller, Haoran Li, Matthew Laurent et al.

[Optical and structural properties of BGaN layers grown on different substrates](#)

A Kadys, J Mickevicius, T Malinauskas et al.

[Highly mismatched GaN<sub>1-x</sub>Sb<sub>x</sub> alloys: synthesis, structure and electronic properties](#)

K M Yu, W L Sarney, S V Novikov et al.

[Nucleus and spiral growth mechanisms of nitride semiconductors in metalorganic vapor phase epitaxy](#)

Tetsuya Akasaka and Hideki Yamamoto

[MBE-grown high-quality \(Al,Ga\)N/GaN distributed Braggreflectors for resonant cavity LEDs](#)

S Fernández, F B Naranjo, F Calle et al.



## GaN<sub>1-x</sub>Sb<sub>x</sub> alloys grown with H<sub>2</sub> and N<sub>2</sub> carrier gases

Daisuke Komori<sup>1\*</sup>, Kaku Takarabe<sup>1</sup>, Tetsuya Takeuchi<sup>1</sup>, Takao Miyajima<sup>1</sup>, Satoshi Kamiyama<sup>1</sup>, Motoaki Iwaya<sup>1</sup>, and Isamu Akasaki<sup>1,2</sup>

<sup>1</sup>Faculty of Science and Technology, Meijo University, Nagoya 468-8502, Japan

<sup>2</sup>Akasaki Research Center, Nagoya University, Nagoya 464-8603, Japan

\*E-mail: 143434022@c alumni.meijo-u.ac.jp

Received November 5, 2015; accepted November 8, 2015; published online February 26, 2016

We grew GaNSb layers with H<sub>2</sub> and N<sub>2</sub> carrier gases by metalorganic vapor phase epitaxy. We estimated the GaSb molar fraction in a GaNSb layer grown with H<sub>2</sub> by Rutherford backscattering spectroscopy. A 0.8% GaSb molar fraction was obtained, which was consistent with the value obtained by secondary ion mass spectroscopy. We correlated the obtained GaSb molar fraction with the *c*-axis lattice constant of GaSb estimated from an X-ray diffraction pattern. We investigated GaSb molar fractions in GaNSb grown with H<sub>2</sub> and N<sub>2</sub> at various growth temperatures. While GaSb molar fractions in the H<sub>2</sub> case showed a plateau at 0.8% at less than 800 °C, those in the N<sub>2</sub> case increased to 1.1% with a decrease in the growth temperature to 750 °C. Sb incorporation into GaNSb could be further improved by carrying out growth under N<sub>2</sub>, similar to the case of GaInN growth. © 2016 The Japan Society of Applied Physics

### 1. Introduction

Group-III nitride materials, such as AlN, GaN, InN, and related alloys, have been extensively investigated towards their use in various applications, such as optoelectronics and power electronics. For instance, light-emitting and light-detecting devices covering near-infrared, visible, and ultraviolet regions are expected since the materials have wide bandgap regions from 0.7 to 6.0 eV. Unfortunately, the material choices for high-quality nitride-based heterostructures have been limited because of large mismatches in the growth temperatures and lattice constants. Whereas a temperature of around 1400 °C is necessary for AlN growth by metalorganic vapor phase epitaxy (MOVPE),<sup>1-4</sup> In-containing nitride-based materials must be grown at less than 800 °C to enable reasonable amounts of In to be incorporated.<sup>5-8</sup> Such a huge temperature difference results in poor interface qualities of the heterostructures. Also, lattice mismatches for AlN/GaN and InN/GaN are 2.4 and 11%, respectively.<sup>9,10</sup> These values are too large to fabricate high-quality heterostructures without the generation of dislocations.

Under the circumstances, the use of GaNSb alloys could be considered to solve the above challenging issues. Antimony (Sb) is known as a surfactant that enhances the migration of surface species and increases the critical thickness of heteroepitaxy in several semiconductor materials. For instance, GaIn(N)As multiple quantum wells (MQWs) grown on GaAs with Sb supply showed larger critical thicknesses and better optical qualities.<sup>11</sup> Furthermore, GaN layers and GaInN MQWs grown with Sb supply showed an enhancement in the lateral growth and better optical qualities, respectively.<sup>12,13</sup> Thus, supplying Sb could be effective for growing high-quality nitride-based materials at low growth temperatures. Also, since AlGaInSb alloys have large lattice constants, AlGaInNSb alloys could be new candidates for lattice-matched heterostructures.

At the same time, group-III nitride alloys are generally formed by replacing the group-III elements, but research on nitride-based alloys replaced with other group-V elements is very limited.<sup>14-17</sup> Regarding GaSb molar fractions in GaNSb alloys, a 4% GaSb molar fraction in a GaNSb layer grown by molecular beam epitaxy was estimated by Rutherford backscattering spectrometry (RBS).<sup>18</sup> On the other hand, a 0.05%

GaSb molar fraction in a MOVPE-grown sample was estimated by secondary ion mass spectroscopy (SIMS) calibrated with an Sb-implanted Si standard sample.<sup>19</sup> Thus, a more precise evaluation of MOVPE-grown GaNSb is necessary.

In this study, we estimated the GaSb molar fraction in a MOVPE-grown GaNSb layer by Rutherford backscattering spectroscopy. Then, we correlated the molar fraction with the *c*-axis lattice constant of the same sample measured from X-ray diffraction (XRD) patterns. We systematically investigated the carrier gas dependence, H<sub>2</sub> or N<sub>2</sub>, of GaSb molar fractions in GaNSb layers grown at various temperatures. We found that the use of N<sub>2</sub> carrier gas led to some improvements in Sb incorporations into GaNSb layers, similar to the cause of GaInN. We also found that a Sb supply is effective for obtaining smooth surfaces even at a low growth temperature down to 750 °C.

### 2. Experimental procedure

All the samples in this study were grown on 3 μm GaN templates prepared on *c*-plane sapphire substrates with the buffer layers deposited at low temperatures by MOVPE.<sup>20</sup> Then, GaNSb layers were grown on the GaN templates by MOVPE with an Sb source. Trimethylgallium (TMGa), trimethylantimony (TMSb), and ammonia (NH<sub>3</sub>) were used as Ga, Sb, and N sources, respectively. During all the GaNSb epitaxial growths, supply rates of TMGa, TMSb, and NH<sub>3</sub> were fixed at 155 μmol/min, 548 μmol/min, and 152 mmol/min, respectively, resulting in a N/Ga ratio of 980 and an Sb/N ratio of 0.0036. In contrast, the carrier gas and growth temperature for GaNSb growth were changed. H<sub>2</sub> or N<sub>2</sub> carrier gas was used during the GaNSb growth. Also, the growth temperature was changed from 650 to 950 °C. The thicknesses of the GaNSb layer were 500 and 200 nm with H<sub>2</sub> and N<sub>2</sub> carrier gases, respectively. This difference was caused by the growth rate difference between H<sub>2</sub> and N<sub>2</sub> carrier gases.

We then measured the number of Sb atoms in the samples by RBS and SIMS. XRD patterns of the samples were also measured. Furthermore, images of the sample surfaces were obtained by atomic force microscopy (AFM).

### 3. Results and discussion

The composition of the GaNSb/GaN sample was measured

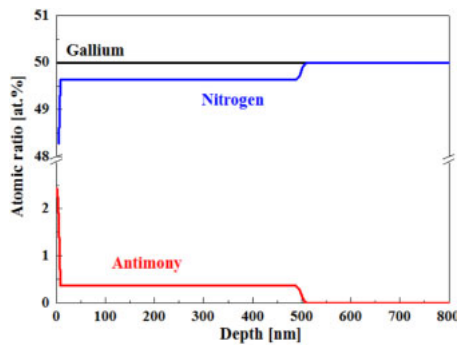


**Fig. 1.** (Color online) Depth profiles of Sb and Ga compositions in GaNSb/GaN measured by RBS. The GaNSb layer was grown at 800 °C with H<sub>2</sub>.

by RBS. For the measurement, a 500 nm GaNSb layer was grown on the 3 μm GaN template with H<sub>2</sub> carrier gas at 800 °C. Figure 1 shows the measured Ga, N, and Sb compositions in the GaNSb/GaN sample. Note that C and O compositions were less than the detection limits in both the GaNSb and GaN layers. The Ga, N, and Sb compositions in the GaNSb layer were 0.500 ± 0.005, 0.496 ± 0.025, and 0.004 ± 0.001, respectively. In the bottom GaN layer, Ga, N, and Sb compositions were 0.500 ± 0.005, 0.500 ± 0.025, and 0.000 ± 0.001, respectively. While the Ga composition was consistently 0.500 in both the GaN and GaNSb layers, the N composition was reduced from 0.500 in GaN to 0.496 in GaNSb. At the same time, the Sb composition was complementarily increased from 0 in GaN to 0.004 in GaNSb. Therefore, it is most likely that Sb atoms were replaced with N atoms in GaNSb. On the basis of these findings, the GaSb molar fraction in GaNSb was estimated to be 0.008 ± 0.002, in other words, 0.8%.

SIMS measurement was also performed on the same GaNSb layer. The Sb concentration was found to be 3.4 × 10<sup>21</sup> atoms/cm<sup>3</sup>, which corresponds to a 0.9% GaSb molar fraction. The value was calibrated with an Sb-implanted GaN standard sample and determined to be consistent with that obtained by RBS.

We then measured two XRD patterns of the same GaNSb sample. Figures 2(a) and 2(b) show a (0002) 2θ/ω XRD pattern and a (202̄4) reciprocal space mapping for GaNSb, respectively. A clear additional peak on the left side of the GaN peak was observed. Since GaSb has a large lattice constant, GaNSb should have a larger lattice constant than GaN, leading to a smaller diffraction angle of (0002) than that of GaN. Thus, this peak is assigned as a GaNSb peak. In addition, it is also found that the GaNSb layer was coherently grown on the bottom GaN template and still fully strained, as shown in Fig. 2(b). Thus, we determined that the *c*-axis lattice constant of the fully strained GaNSb with a 0.8% GaSb molar fraction on GaN was 5.196 Å. Also, the *c*-axis lattice constant of GaN was 5.189 Å. Note that a weak peak was also found on the right side of the GaN peak in Fig. 2(a). At the same time, no corresponding peak was found in Fig. 2(b). At this moment, the origin of the peak is unknown and further investigations are necessary. Assuming that there is a linear relationship between the GaSb molar fraction and the *c*-axis lattice constant, we derive

$$L_c = 5.189 + 0.875x. \quad (1)$$

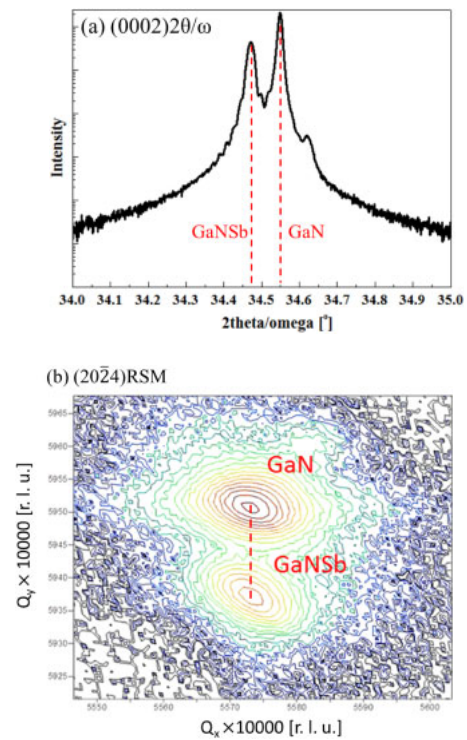


**Fig. 2.** (Color online) (a) (0002) 2θ/ω XRD pattern and (b) (202̄4) RSM of the GaNSb sample grown at 800 °C with H<sub>2</sub>.

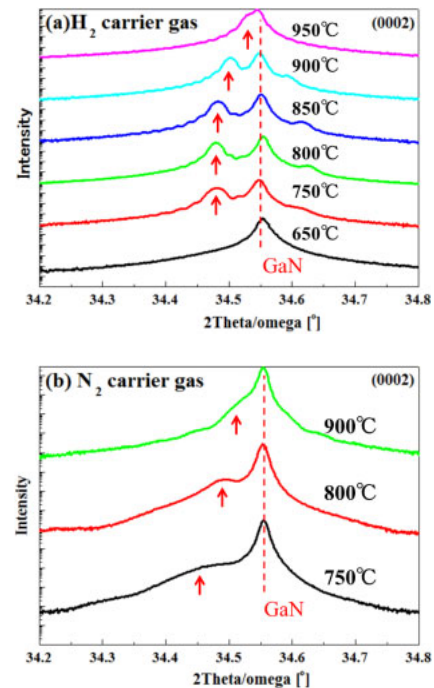


**Fig. 3.** (Color online) (0002) 2θ/ω XRD patterns of the GaNSb/GaN samples grown at various temperatures with (a) H<sub>2</sub> and (b) N<sub>2</sub>.

Here, *x* is the GaSb molar fraction and *L<sub>c</sub>* is the *c*-axis lattice constant of GaN<sub>1-*x*</sub>Sb<sub>*x*</sub>. We later use the equation to estimate GaSb molar fractions of GaNSb samples grown under various growth conditions.

Figures 3(a) and 3(b) show (0002) 2θ/ω XRD patterns of the GaNSb/GaN samples grown at various growth temperatures with H<sub>2</sub> and N<sub>2</sub> carrier gases, respectively. GaNSb peaks were clearly observed on the left side of the GaN peaks in the samples grown with H<sub>2</sub> carrier gas at 750 °C and higher.

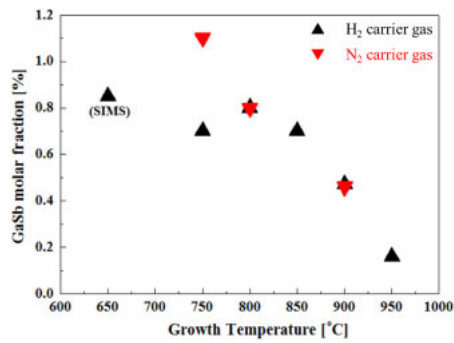


**Fig. 4.** (Color online) GaSb molar fractions estimated from *c*-axis lattice constants of GaNSb layers grown with H<sub>2</sub> and N<sub>2</sub>, as a function of growth temperature.

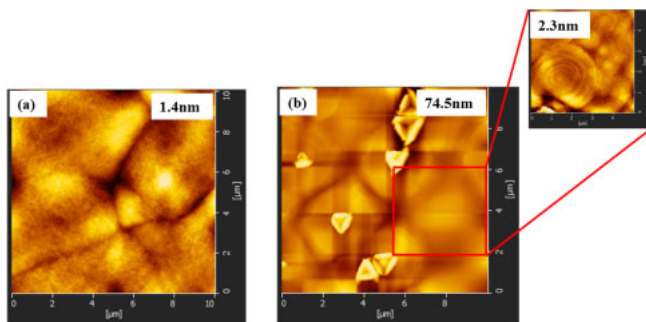


**Fig. 5.** (Color online) AFM images of GaNSb surfaces grown at 800 °C with (a) H<sub>2</sub> and (b) N<sub>2</sub>.

No peak other than the GaN peak was observed in the sample grown at 650 °C, meaning that the GaNSb quality was very poor. On the contrary, broad peaks related to GaNSb were observed in the samples grown under N<sub>2</sub> carrier gas. Even considering the difference in the GaNSb thickness between the cases of H<sub>2</sub> and N<sub>2</sub>, the quality of GaNSb grown with N<sub>2</sub> seemed to be poorer than that of GaNSb grown with H<sub>2</sub>.

Next, we estimated GaSb molar fractions from the measured *c*-axis lattice constants using the above-mentioned equation and plotted the results in the cases of H<sub>2</sub> and N<sub>2</sub> as a function of growth temperature in Fig. 4. The GaSb molar fraction in the case of 650 °C with H<sub>2</sub> was measured by SIMS. Basically, the GaSb molar fractions with H<sub>2</sub> and N<sub>2</sub> similarly increased with a decrease in growth temperature from 950 to 800 °C. This was probably due to lower Sb desorption from the growth surface at such low growth temperatures. However, the GaSb molar fraction under H<sub>2</sub> carrier gas became saturated at about 0.8% as the growth temperature was further decreased from 800 to 650 °C. On the contrary, the GaSb molar fraction with N<sub>2</sub> was monotonically increased to 1.1% at 750 °C. This value is the highest GaSb molar fraction obtained in this study. The result indicates that using N<sub>2</sub> carrier gas in GaNSb growth seems to be effective for obtaining higher GaSb molar fractions.

Finally, Fig. 5 shows AFM images of GaNSb surfaces grown at 800 °C with (a) H<sub>2</sub> and (b) N<sub>2</sub> carrier gases. Typically, many pits are observed on the GaN surface grown at 800 °C owing to insufficient migration. Here, significant differences appeared in the surface morphologies of the GaNSb layers. No pits but many hexagonal regions with spiral steps were covered on the GaNSb surfaces, resulting in relatively smooth surfaces. Actually, considering the low

growth temperature (800 °C), the surfaces were surprisingly smooth. Also, small grains were found on GaNSb grown with N<sub>2</sub> carrier gas. It seems that Sb acts as a surfactant on the GaN surface. Thus, further optimization of the growth conditions of nitride-based materials with Sb supply could lead to the possibility of high-quality nitride-based materials and heterostructures being grown at low temperatures.

#### 4. Conclusions

We have grown GaNSb layers with H<sub>2</sub> and N<sub>2</sub> carrier gases by MOVPE. A 0.8% GaSb molar fraction in one of the GaNSb layers was obtained by RBS. We correlated the obtained GaSb molar fraction with the *c*-axis lattice constant of GaNSb estimated from an X-ray diffraction (XRD) pattern. The maximum GaSb mole fraction in this study was 1.1% in GaNSb grown with N<sub>2</sub> carrier gas at 750 °C. Also, a relatively smooth surface of the GaNSb layer grown with H<sub>2</sub> was obtained, probably owing to an Sb surfactant effect. The use of GaNSb could open up the possibility of growing high-quality nitride-based heterostructures at relatively low temperatures.

#### Acknowledgements

This study was supported by the MEXT Program for the Strategic Research Foundation at Private Universities (2012–2016) and the Grant-in-Aid for Challenging Exploratory Research (No. 15K13959), and the Foundation for Promotion of Material Science and Technology of Japan (MST Foundation). Sb sources were provided by Japan Advanced Chemicals.

- 1) R. Miyagawa, S. Yang, H. Miyake, and K. Hiramoto, *Phys. Status Solidi C* **9**, 499 (2012).
- 2) A. V. Lobanova, E. V. Yakovlev, R. A. Talalaev, S. B. Thapa, and F. Scholz, *J. Cryst. Growth* **310**, 4935 (2008).
- 3) A. V. Lobanova, K. M. Mazaev, R. A. Talalaev, M. Leys, S. Boeykens, K. Cheng, and S. Degroote, *J. Cryst. Growth* **287**, 601 (2006).
- 4) Y. Ohba and R. Sato, *J. Cryst. Growth* **221**, 258 (2000).
- 5) M. Jamil, H. Zhao, J. B. Higgins, and N. Tansu, *J. Cryst. Growth* **310**, 4947 (2008).
- 6) Y. Zhang, Y. Liu, T. Kimura, M. Hirata, K. Prasertusk, S. Ji, R. Katayama, and T. Matsuoka, *Phys. Status Solidi C* **8**, 482 (2011).
- 7) Y. Huang, H. Wang, Q. Sun, J. Chen, D. Y. Li, Y. T. Wang, and H. Yang, *J. Cryst. Growth* **276**, 13 (2005).
- 8) S. Suihkonen, J. Sormunen, V. T. Rangel-Kuoppa, H. Koskenvaara, and M. Sopanen, *J. Cryst. Growth* **291**, 8 (2006).
- 9) J. Gleize, M. A. Renucci, J. Frandon, and F. Demangeot, *Phys. Rev. B* **60**, 15985 (1999).
- 10) B. Damilano, N. Grandjean, S. Dalmaso, and J. Massies, *Appl. Phys. Lett.* **75**, 3751 (1999).
- 11) H. Shimizu, K. Kumada, S. Uchiyama, and A. Kasukawa, *Electron. Lett.* **36**, 1379 (2000).
- 12) L. Zhang, H. F. Tang, and T. F. Kuecha, *Appl. Phys. Lett.* **79**, 3059 (2001).
- 13) M. Baranowski, M. Latkowska, R. Kudrawiec, M. Syperek, J. Misiewicz, K. Giri Sadasivam, J. Shim, and J. K. Lee, *Semicond. Sci. Technol.* **27**, 105027 (2012).
- 14) M. Weyers and M. Sato, *Appl. Phys. Lett.* **62**, 1396 (1993).
- 15) J. F. Geisz, R. C. Reedy, B. N. Keyes, and W. K. Metzger, *J. Cryst. Growth* **259**, 223 (2003).
- 16) A. Kimura, H. F. Tang, and T. F. Kuech, *J. Cryst. Growth* **265**, 71 (2004).
- 17) S. Yoshida, J. Kikawa, and Y. Itoh, *J. Cryst. Growth* **237–239**, 1037 (2002).
- 18) K. M. Yu, W. L. Sarney, S. V. Novikov, D. Detert, R. Zhao, and J. D. Denlinger, *Appl. Phys. Lett.* **102**, 102104 (2013).
- 19) S. H. Moon, H. A. Do, J. Park, and S. W. Ryu, *J. Mater. Res.* **24**, 3569 (2009).
- 20) H. Amano, N. Sawaki, I. Akasaki, and Y. Toyoda, *Appl. Phys. Lett.* **48**, 353 (1986).

# Advantages of the moth-eye patterned sapphire substrate for the high performance nitride based LEDs

Toshiyuki Kondo<sup>\*1,2</sup>, Tsukasa Kitano<sup>1</sup>, Atsushi Suzuki<sup>1</sup>, Midori Mori<sup>1</sup>, Koichi Naniwae<sup>1</sup>, Satoshi Kamiyama<sup>1,2</sup>, Motoaki Iwaya<sup>2</sup>, Tetsuya Takeuchi<sup>2</sup>, and Isamu Akasaki<sup>2</sup>

<sup>1</sup> EL-SEED Corp., Innovative Science and Technology Building 2F, Meijo University, 2-1522 Shiogamaguchi, Tenpaku-ku, Nagoya 468-0073, Japan

<sup>2</sup> Faculty of Science and Technology, Meijo University, 1-501 Shiogamaguchi, Tenpaku-ku, Nagoya 468-8502, Japan

Received 23 August 2013, revised 23 December 2013, accepted 20 January 2014

Published online 21 March 2014

**Keywords** moth-eye structure, sapphire, LED, nitride, light extraction, PSS

\* Corresponding author: e-mail toshiyuki\_kondo@elseed.com

We propose moth-eye patterned sapphire substrate (MPSS) as a solution to improve the light extraction efficiency and to reduce the production cost of LEDs. The MPSS samples' surfaces consisted of a triangular grid of about 375 nm high truncated cones with different pitches of 460 nm, 500 nm, 600 nm, 700 nm and 800 nm. A commercially available patterned sapphire substrate (PSS) and a flat sapphire substrate (FSS) was also used in the experiments for comparison. According to the cathode luminescence observation, the GaN template on MPSS with a thickness of 3  $\mu\text{m}$  showed a threading dislocation density (TDD) of around  $1.9 \times 10^8 \text{ cm}^{-2}$ . Transmission electron microscope observation revealed that

many of the dislocations were bent and disappeared as loops formed in the vicinity of MPSS cones. On the other hand, PSS required a GaN template thicker than  $5 \mu\text{m}$  to achieve a level of TDD equal to MPSS. The LED on MPSS with a pitch of 600 nm showed the highest light output power among the evaluated LEDs as it was 1.89 times higher than that on FSS and 1.05 times higher than that on PSS. The pitch dependence of the light output improvement agrees with the pitch dependence of the simulated transmissivity at the GaN/sapphire interface.

As a result of our comparison, we concluded that MPSS provides the most cost effective solution for high performance LEDs.

© 2014 WILEY-VCH Verlag GmbH & Co. KGaA, Weinheim

## 1 Introduction

General illuminations accounts for approximately 16% of all electricity consumption in households. It is expected that energy saving rates will increase by the replacement of existing illumination solutions with next-generation illumination, light emitting diodes (LED) and organic electroluminescence (OEL) that have high energy efficiency. This technique is necessary to make sure that the next-generation illumination solutions obtain about twice the luminous efficiency of current fluorescent lamps and to get the price reduction that is expected to be attained through the general technology development of next-generation illumination.

LED performance depends on internal quantum efficiency (IQE) and light extraction efficiency (LEE). As for the blue LEDs, a sufficiently high IQE has already been achieved. On the other hand, LEE is limited by the total in-

ternal reflection, which is caused by the large difference in the refractive indexes of the group III nitride based epitaxial film and the sapphire substrate. Patterned sapphire substrates (PSS) using micro-scale patterns and thin film technology are generally being used in order to address this problem. This technology is however plagued by wafer bowing problems that limit the possibility to increase substrate size and suffers from high production costs.

We have proposed that a new approach based on a sub-micron scale patterned sapphire substrate, the so-called "moth-eye patterned sapphire substrate" ("MPSS"), should be used instead. It is a very promising solution which improves the LEE of the nitride-based LEDs [1-6].

MPSS, with its sub-micron scale structure, can, in contrast to the PSS, be successfully planarized even when one uses a relatively thin GaN epitaxial layer.

In this paper, we will make a comprehensive comparison of LED performance and GaN layer quality on MPSS, PSS and flat sapphire substrate (FSS).

## 2 Experimental

The MPSS samples were fabricated by using nano-imprinting lithography and ICP dry etching. The nano-imprinting lithography can pattern wafers with a diameter of up to 6 inches in size. The surfaces of the samples used in our experiment consisted of a triangular grid of approximately 375 nm-high truncated cones with different pitches: 460 nm, 500 nm, 600 nm, 700 nm and 800 nm respectively. The top of the truncated cones were rounded by hot phosphoric acid etching to improve the crystalline quality of the GaN layers. A bird's-eye view SEM image of an MPSS sample with a 460 nm pitch is shown in Fig. 1. Commercially available PSS samples with a pitch of 3  $\mu\text{m}$  and 1.5  $\mu\text{m}$  high pointed cones as well as FSS were also used in the experiments for comparison.

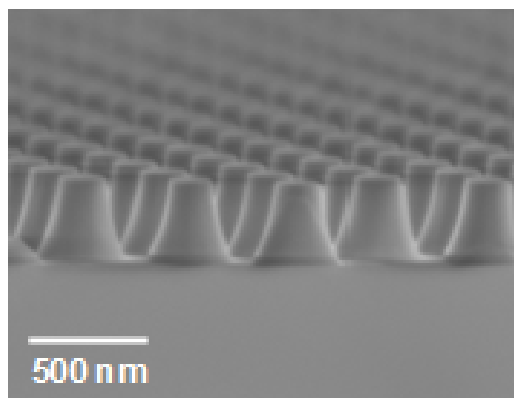


**Figure 1** Bird's-view SEM image of a MPSS with a pitch of 460 nm.

Metal organic vapor phase epitaxy (MOVPE) was used for the nitride layer growth and trimethylgallium, trimethylindium, and ammonia were used as source materials. Furthermore, magnesium and tetra methyl silane were used as p-type and n-type dopant sources respectively. Prior to growth, all of the MPSS, PSS and FSS samples were thermally cleaned at 1100  $^{\circ}\text{C}$  in hydrogen gas to get rid of surface contamination.

The GaN templates which consisted of a low temperature GaN buffer layer and high-temperature undoped GaN layer were grown on MPSS, PSS and FSS so that we could evaluate the crystalline quality of the GaN layer on each substrate. The thickness of the GaN template on MPSS and FSS was 3  $\mu\text{m}$  compared to 5  $\mu\text{m}$  on the PSS. The LED structures were also grown on the templates that consisted of 3  $\mu\text{m}$  thick n-type GaN:Si layer, and a 0.15  $\mu\text{m}$  thick p-type GaN layer. The MQW active layer consists of five pairs of 3 nm thick GaInN wells and 12 nm thick GaN barriers, respectively. Flip-chip type blue LEDs were fabricat-

ed with an area of 600  $\mu\text{m}$  x 500  $\mu\text{m}$ . A combination of an ITO and an Ag-Pd-Cu alloy (APC) was employed as a p-electrode and an n-electrode in order to obtain both low contact resistance and high reflectivity [4, 9].

The LED chips were mounted onto the header without resin encapsulation. The crystalline quality of the GaN templates was characterized using X-ray diffraction (XRD), cathode luminescence (CL) and transmission electron microscopy (TEM). The light output versus current (L-I) and the angular intensity distribution of the LEDs were evaluated at room temperature (RT). In addition, we simulated the transmissivity at the GaN/sapphire interface as a function of the incidence angle using rigorous coupled wave analysis (RCWA).

## 3 Results and discussion

The full width at half maximums (FWHMs) of the XRD for GaN(0002) and GaN(10-12) on each substrate were as follows: 236 arcsec and 320 arcsec in case of having a MPSS with a pitch of 460 nm; 192 arcsec and 290 arcsec in case of having a PSS; 216 arcsec and 314 arcsec in case of having a FSS. The thickness of the GaN template on the MPSS (3  $\mu\text{m}$ ) was thinner than that on the PSS and equal in thickness to that on the FSS, yet did not cause any adversary effects on the crystalline quality nor the surface morphology of the GaN. Having a thinner GaN layer reduces wafer bowing, which opens up for the possibility to enlarge the size of the wafer. Consequently, wafer bowing decreased by approximately 10% as we reduced the GaN thickness from 5  $\mu\text{m}$  to 3  $\mu\text{m}$  when growing GaN on sapphire substrates with a diameter of 4 inches. In addition, the epi cost can also be reduced by growing thinner GaN layers. Furthermore, Fig. 2 shows the CL results after GaN template growth on MPSS with a pitch of 460 nm and on PSS, respectively.

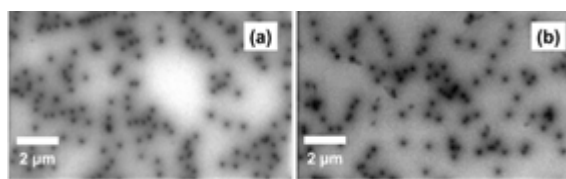


**Figure 2** Plan view CL image of GaN template on MPSS with a pitch of 460 nm (a) and that on PSS (b).

The threading dislocation density (TDD) in the GaN templates on MPSS and PSS were  $1.9 \times 10^8 \text{ cm}^{-2}$  and  $1.58 \times 10^8 \text{ cm}^{-2}$ , respectively. In addition, the TDD of the GaN templates on MPSS with a pitch of 500 nm, 600 nm and 800 nm were  $1.9 \times 10^8 \text{ cm}^{-2}$ ,  $2.0 \times 10^8 \text{ cm}^{-2}$  and  $2.1 \times 10^8 \text{ cm}^{-2}$ , respectively. However, if the bottom diameter of the MPSS cones with a pitch of 460 nm exceeds 360 nm, the GaN surface was getting roughened due to the difficulty to grow cores on c-plane areas. The crystalline quality of GaN templates on PSS was slightly better than that on MPSS and FSS substrates. However, it was necessary to

grow more than 5  $\mu\text{m}$  thick GaN layers on PSS in order to planarize the surface and keep a low dislocation density. Figure 3 shows a cross-sectional bright-field TEM image of the GaN template on MPSS with a pitch of 460 nm. Many of the dislocations were bent and disappeared as loops formed in the vicinity of MPSS cones. These observations clearly suggest that the MPSS can provide a quality equivalent to that of GaN templates with a thinner GaN-layer compared to that on the PSS.

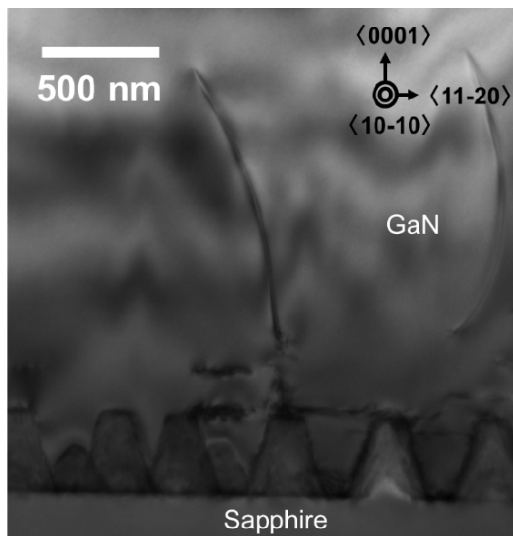


**Figure 3** Cross sectional TEM image of the GaN template on MPSS with a pitch of 460 nm.

MPSS has an optical wavelength order periodic structure on a sapphire substrate, utilizing the Bragg diffraction effect to not only suppress the occurrence of total reflection in the GaN/sapphire interface, but also extract light with an incident angle larger than the critical angle. Figure 4 shows the transmissivity at the GaN/sapphire interface as a function of the incidence angle simulated by using RCWA [1, 7, 8].

For this simulation we assumed that the cone pattern of the MPSS consisted of a periodic triangular grid consisting of fixed truncated cones with a height of 375 nm, a bottom-diameter of 350 nm and a top-diameter of 150 nm. We used different cone pitch parameters.

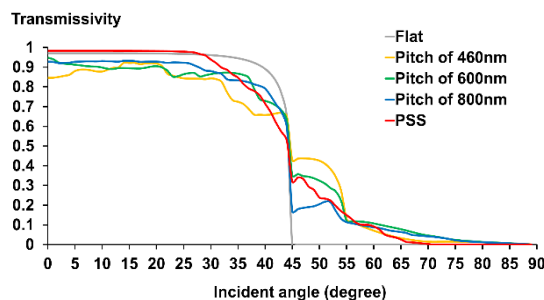


**Figure 4** Calculation of the transmissivity dependence on incident angle at the GaN/sapphire interface.

The distinct total internal reflection of the light entering into the moth-eye plane disappeared when the incident angle got higher than 46 degrees. The MPSS do however get a lower transmissivity within the critical angle, compared to the FSS and PSS since we get a diffractive reflectance at the GaN/MPSS interface. The transmissivity does, however, increase due to the diffraction effect we get at angles above the critical angle.

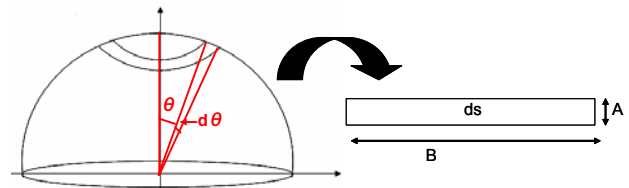


**Figure 5** A schematic hemisphere used to estimate light extraction efficiency, LEE.

The following Eq. (3) was used to calculate the overall transmissivity for each angle between the angles 0 degrees to 89 degrees. Each variables are described in Fig. 5.

$$ds = A \cdot B = 2\pi r^2 \cdot \sin\theta \cdot d\theta, \quad (1)$$

$$S = \int_{90^\circ}^0 2\pi r^2 \cdot \sin\theta \cdot d\theta = 2\pi r^2, \quad (2)$$

$$T = 1 / 2\pi r^2 \int_{\theta_1}^{\theta_2} T(\theta) \cdot 2\pi r^2 \cdot \sin\theta \cdot d\theta \\ = \int_{\theta_1}^{\theta_2} T(\theta) \cdot \sin\theta \cdot d\theta. \quad (3)$$

$r$  is the radius of a sphere,  $T$  is the transmissivity of the incident angle  $\theta$  calculated by simulation with RCWA.

The integrated transmissivity increased at incident angles higher than the critical angle due to Bragg's diffraction effect in cones with a pitch of up to 600 nm as shown in Fig. 6. On the other hand, the integrated transmissivity starts to decrease as the pitch reaches above 600 nm. This occurs due to the increase of internal total reflection intensity as the flat areas between the cones widen along with the increasing pitch.

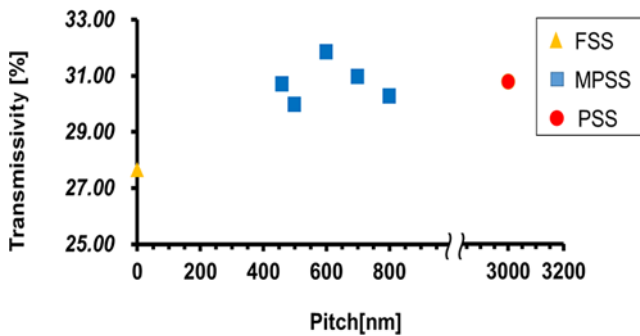


**Figure 6** Calculated transmissivity over the entire solid angle at the GaN/sapphire interface as a function of the pitch of the cones by RCWA simulation.

Flip-chip type blue LEDs on MPSS, PSS and FSS with an area of 600 μm x 500 μm were prepared in order to compare their light output. The light output improvement ratios of the blue LED on the FSS at 50 mA are summarized in Fig. 7. The blue LEDs on MPSS with a pitch of 600 nm had the highest light output power at 50 mA among the tested samples.

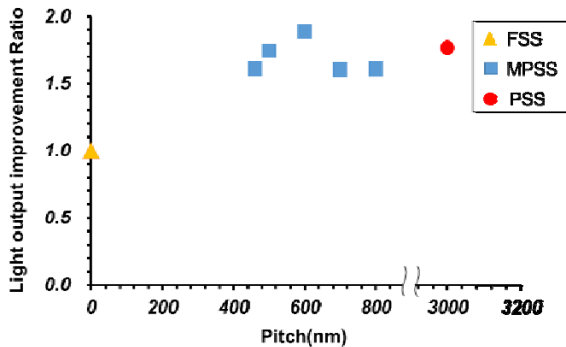


**Figure 7** Light output improvement ratios of the LEDs on MPSS and PSS compared to the LED on FSS

Furthermore, the blue LEDs on MPSS with a pitch of 600 nm had a light output power 1.89 times higher than that on the FSS, and a light output power 1.05 times higher than that on the PSS. However, since the GaN templates on each of the MPSS, PSS and FSS used in the experiments had nearly the same TDD, all the LEDs should have nearly the same IQE. Therefore the improvement of the MPSS should attribute to the enhancement of LEE by the diffraction effect.

The results show that the pitch dependence of the light output improvement is in good agreement with that of the simulated transmissivity at the GaN/sapphire interface.

On the other hand, the reason why the calculation values and the experiment results differ is that the RCWA simulation only shows results of a one-way transmissivity of the

GaN/sapphire interface whereas the experiment results show the impact on LEE.

#### 4 Conclusions

In this paper, we have presented the advantages of the MPSS over the existing PSS and FSS technology. The submicron-scale periodic cones of the MPSS can, according to the RCWA simulation, enhance the transmissivity at the GaN/sapphire interface thanks to the diffraction effect. TEM and CL observation results clearly show that the MPSS can provide a thinner GaN template of equal or higher quality than PSS. A 3 μm-thick high quality GaN template on the MPSS with a dislocation density of  $1.9 \times 10^8 \text{ cm}^{-2}$  has been demonstrated. And the LEDs on MPSS with a 600 nm pitch show the highest light output power among the evaluated LEDs on various types of substrates as it is 1.89 times higher than that on FSS and 1.05 times higher than that on PSS. The pitch dependence of the light output improvement is in excellent agreement with that of the simulated transmissivity at the GaN/sapphire interface. As a result of the comparisons made of the GaN templates and LEDs on MPSS, PSS and FSS, we have come to the conclusion that the MPSS does provide the most cost effective solution for high performance LEDs.

**Acknowledgements** This research has been supported by a NEDO project.

#### References

- [1] T. Seko, S. Mabuchi, F. Teramae, A. Suzuki, Y. Kaneko, R. Kawai, S. Kamiyama, M. Iwaya, H. Amano, and I. Akasaki, Proc. SPIE, Photonics West 2009, to be published.
- [2] C. C. Bernhard, Endeavour **26**, 79 (1967).
- [3] H. Toyota, K. Takahara, M. Okano, T. Yotsuya, and H. Kikuta, Jpn. J. Appl. Phys. **40**, L747 (2001).
- [4] R. Kawai, T. Mori, W. Ochiai, A. Suzuki, M. Iwaya, H. Amano, S. Kamiyama, and I. Akasaki, Phys. Status Solidi C **6**, S830 (2009).
- [5] H. J. Kang, S. U. Cho, E. S. Kim, and M. Y. Jeong, Proc. SPIE, Photonics West 2013, to be published, February 2013/Vol. **52**(2).
- [6] A. Ishihara, R. Kawai, T. Kitano, A. Suzuki, T. Kondo, M. Iwaya, H. Amano, S. Kamiyama, and I. Akasaki, Phys. Status Solidi C **7**, 2056 (2010).
- [7] M. G. Moharam, Proc. SPIE 883 (1988).
- [8] M. G. Moharam and T. K. Gaylord, J. Opt. Soc. Am. **71**, (1981).
- [9] H. Yoshida, M. Kuwabar, Y. Yamashita, K. Uchiyama, and H. Kan, Appl. Phys. Lett. **96**, 211122 (2010).

## Multijunction GaInN-based solar cells using a tunnel junction

This content has been downloaded from IOPscience. Please scroll down to see the full text.

2014 Appl. Phys. Express 7 034104

(<http://iopscience.iop.org/1882-0786/7/3/034104>)

View [the table of contents for this issue](#), or go to the [journal homepage](#) for more

Download details:

IP Address: 202.11.1.201

This content was downloaded on 03/03/2017 at 06:48

Please note that [terms and conditions apply](#).

You may also be interested in:

[Realization of Nitride-Based Solar Cell on Freestanding GaN Substrate](#)

Yosuke Kuwahara, Takahiro Fujii, Yasuharu Fujiyama et al.

[Concentrating Properties of Nitride-Based Solar Cells Using Different Electrodes](#)

Mikiko Mori, Shinichiro Kondo, Shota Yamamoto et al.

[GaInN-Based Solar Cells Using Strained-Layer GaInN/GaN Superlattice Active Layer on a Freestanding GaN Substrate](#)

Yosuke Kuwahara, Takahiro Fujii, Toru Sugiyama et al.

[GaN barrier layer dependence of critical thickness in GaInN/GaN superlattice on GaN characterized by in situ X-ray diffraction](#)

Junya Osumi, Koji Ishihara, Taiji Yamamoto et al.

[Relationship between misfit-dislocation formation and initial threading-dislocation density in GaInN/GaN heterostructures](#)

Motoaki Iwaya, Taiji Yamamoto, Daisuke Iida et al.

[Correlation between Device Performance and Defects in GaInN-Based Solar Cells](#)

Mikiko Mori, Shinichiro Kondo, Shota Yamamoto et al.

[Improved conversion efficiency of as-grown InGaN/GaN quantum-well solar cells for hybrid integration](#)

Sirona Valdueza-Felip, Anna Mukhtarova, Louis Grenet et al.

[GaInN-based tunnel junctions with graded layers](#)

Daiki Takasuka, Yasuto Akatsuka, Masataka Ino et al.

## Multijunction GaInN-based solar cells using a tunnel junction

Hironori Kurokawa<sup>1</sup>, Mitsuru Kaga<sup>1</sup>, Tomomi Goda<sup>1</sup>, Motoaki Iwaya<sup>1\*</sup>, Tetsuya Takeuchi<sup>1</sup>, Satoshi Kamiyama<sup>1</sup>, Isamu Akasaki<sup>1,2</sup>, and Hiroshi Amano<sup>2,3</sup>

<sup>1</sup>Faculty of Science and Technology, Meijo University, Nagoya 468-8502, Japan

<sup>2</sup>Akasaka Research Center, Nagoya University, Nagoya 464-8603, Japan

<sup>3</sup>Graduate School of Engineering, Nagoya University, Nagoya 464-8603, Japan

E-mail: iwaya@meijo-u.ac.jp

Received January 10, 2014; accepted February 14, 2014; published online March 3, 2014

We fabricated and characterized a two-junction GaInN-based solar cell using a tunnel junction fabricated by crystal growth. This solar cell has two active layers with a differing bandgap energy corresponding to blue or green light. We confirmed that the open-circuit voltage ( $V_{OC}$ ) in this solar cell was increased by the series connection using the tunnel junction. The short-circuit current density,  $V_{OC}$ , fill factor, and energy conversion efficiency of this solar cell were 0.28 mA/cm<sup>2</sup>, 3.0 V, 0.5, and 0.41%, respectively, under an air mass filter of 1.5 G at 1-sun irradiation and room temperature. © 2014 The Japan Society of Applied Physics

Group III nitride semiconductors are widely used in light-emitting diodes (LEDs)<sup>1–4</sup> and laser diodes.<sup>5,6</sup> Since the bandgap of GaInN ternary alloys covers a broad range of values from 0.65 to 3.43 eV,<sup>7</sup> these alloys are suitable for solar-cell applications.<sup>8–10</sup> In a multijunction solar cell, materials with a broad range of bandgap values offer many possibilities. To date, there have been several reports of nitride-based solar cells<sup>11,12</sup> and we have previously succeeded in fabricating GaInN-based solar cells.<sup>13–18</sup> By improving the crystal quality of GaInN through the application of GaInN superlattice (SL) structures,<sup>14,15</sup> the conversion efficiency of GaInN-based solar cells has been increased. Moreover, an energy-conversion efficiency ( $\eta$ ) of up to 4.0% for GaInN-based solar cells under an air mass filter of 1.5 G and 300 suns irradiation has been achieved at room temperature (RT).<sup>18</sup>

In contrast, the realization of multiple junctions in GaInN-based solar cells remains an important challenge. Tunnel-junction formation using crystal growth<sup>19,20</sup> and mechanical stack<sup>21</sup> methods has often been used to fabricate multiple junctions in material systems such as GaAs, Ge, and AlGaInP. In particular, tunnel-junction fabrication by crystal growth has achieved a high energy-conversion efficiency in solar cells. A multijunction GaInN-based solar cell was previously fabricated by the mechanical stack method.<sup>22</sup> On the other hand, there is no report of a multijunction nitride-based solar cell using a tunnel junction fabricated by crystal growth.

In this study, we devised a two-junction GaInN-based solar cell using a tunnel junction fabricated by crystal growth. We confirm that the open-circuit voltage ( $V_{OC}$ ) in this solar cell was increased by the series connection using the tunnel junction.

All samples were grown by metalorganic vapor-phase epitaxy (MOVPE). Figure 1 shows a schematic view of the sample structure. Trimethylindium, trimethylaluminum, trimethylgallium, triethylgallium, and ammonia were used as the source gases. We also used ethyl-bis(cyclopentadienyl)-magnesium (Et-Cp<sub>2</sub>Mg) and silane (SiH<sub>4</sub>) as dopant precursors for p- and n-type layers, respectively. C-plane sapphire was used as the substrate. The device structure was designed as a GaInN-based solar cell with two GaInN-based SL active layers on a sapphire substrate covered with a low-temperature buffer layer (LT-buffer layer) grown at 550 °C.<sup>23</sup> The device structure consisted of the LT-buffer layer, an unintentionally doped GaN underlying layer (~3 μm), a first

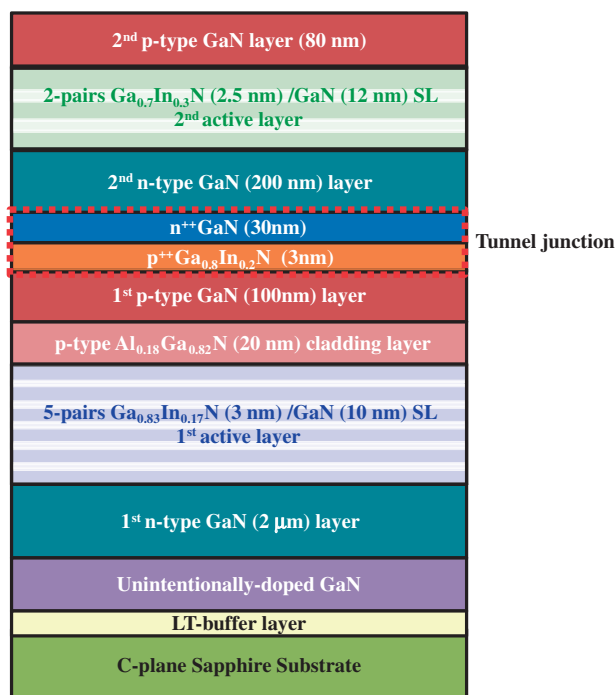


Fig. 1. Schematic view of the sample structure.

n-type GaN layer (~2 μm) grown at 1,050 °C, a 5-pair unintentionally doped Ga<sub>0.83</sub>In<sub>0.17</sub>N (3 nm)/GaN (10 nm) SL first active layer grown at 780 °C, a p-type Al<sub>0.18</sub>Ga<sub>0.82</sub>N cladding layer (20 nm) grown at 780 °C to suppress thermal damage at a second n-type GaN layer,<sup>24</sup> a first p-type GaN layer (100 nm) grown at 950 °C, the tunnel junction [p<sup>++</sup>-type Ga<sub>0.8</sub>In<sub>0.2</sub>N (3 nm) and n<sup>++</sup>-type GaN (30 nm)] grown at 780 °C, a second n-type GaN layer (200 nm) grown at 1,000 °C, a 2-pair unintentionally doped Ga<sub>0.70</sub>In<sub>0.30</sub>N (2.5 nm)/GaN (12 nm) SL second active layer grown at 730 °C, a second p-type GaN layer (80 nm) grown at 800 °C, and a p<sup>+</sup>-type GaN contact layer (5 nm) grown at 800 °C. The Si and Mg concentrations in the n<sup>++</sup>-type GaN and p<sup>++</sup>-type Ga<sub>0.8</sub>In<sub>0.2</sub>N layers were set to 4 × 10<sup>20</sup> and 1 × 10<sup>20</sup> cm<sup>-3</sup>, respectively. The properties of the tunnel junction, such as the doping concentrations, film thickness, and InN molar fraction, were based on the results of Ref. 25. Further, in order to obtain a high short-circuit current density ( $J_{SC}$ ) in GaInN-based solar cells, the thickness of the GaInN active layer was

required to be greater than 150 nm.<sup>13)</sup> Finally, a wide-gap material top cell is required to fabricate a high-performance multijunction solar cell.<sup>19,20)</sup> However, the growth conditions to achieve a high crystallinity in a GaInN-based active layer of such thickness are difficult to determine even in single-junction solar cells. Because the purpose of this study is the fabrication of a multijunction GaInN-based solar cell, we designed a structure with relatively few periods in the GaInN-based SL active layer. Similarly, we designed the InN molar fraction in the first SL active layer to be lower than that in the second SL active layer for ease of fabrication, because low-temperature growth is required to realize the high InN molar fraction GaInN in MOVPE. Moreover, the p<sup>+</sup>-type GaN contact layer, with a Mg concentration of approximately  $1 \times 10^{20} \text{ cm}^{-3}$ , was introduced to reduce the contact resistance between the p-type electrodes.<sup>26)</sup>

After annealing the samples at 550 °C for 10 min in ambient air to activate the p-type layer, we fabricated a face-up type solar cell. A 100-nm-thick indium tin oxide (ITO) p-type ohmic transparent electrode and a Ti (20 nm)/Au (150 nm) pad electrode were deposited onto the p<sup>+</sup>-type GaN contact layer. After annealing the ITO p-type electrode at 550 °C for 10 min in ambient N<sub>2</sub> to reduce the contact resistance between the p<sup>+</sup>-type GaN contact layer and the ITO p-type electrode, a Ti (30 nm)/Al (100 nm)/Ti (20 nm)/Au (150 nm) ohmic n-type electrode was deposited onto the first n-type GaN layer, which was exposed by inductively coupled plasma etching. Finally, we performed annealing at 525 °C for 10 min in ambient N<sub>2</sub> to reduce the contact resistance between the first n-type GaN layer and the Ti/Al/Ti/Au n-type electrode. In this study, the ITO p-type electrode was deposited by sputtering, while the other electrodes were deposited by electron-beam evaporation; no antireflection coating was used for this device. The device and p-type pad electrode dimensions in this two-junction GaInN-based solar cell were 350 × 350 and 100 × 100 μm<sup>2</sup>, respectively.

The current density versus voltage characteristics in solar-cell mode (*J-V* curve in solar-cell mode) of this device were measured using an air mass 1.5 G (AM 1.5 G) solar simulator (Asahi Spectra HAL-320) with a light intensity of 1 sun at RT. We also characterized the injection-current density versus voltage relation in LED mode (*J-V* curve in LED mode) and spectra from this device using a semiconductor parameter analyzer (Agilent Technologies 4156C) and spectrum analyzer (Hamamatsu Photonics TM-UV/VIS C100820AH). The concentrations of Mg and Si in the sample were measured by secondary-ion mass spectrometry. The thickness and InN molar fraction of each GaInN/GaN SL active layer were characterized by X-ray diffraction (XRD; Rigaku SmartLab) using an XRD simulator (Rigaku GlobalFit). The surface morphology of this device was characterized by atomic force microscopy (AFM) and scanning electron microscopy (SEM). In addition, interfaces at the tunnel junction were observed by cross-sectional transmission electron microscopy (TEM).

Figure 2 shows the XRD (0002)  $2\theta/\omega$  scan spectra obtained from this device and the simulation results using design values. This figure displays clear satellite peaks from the -4th to the +2nd order, indicating that the two SL active layers are relatively well formed even in the multijunction

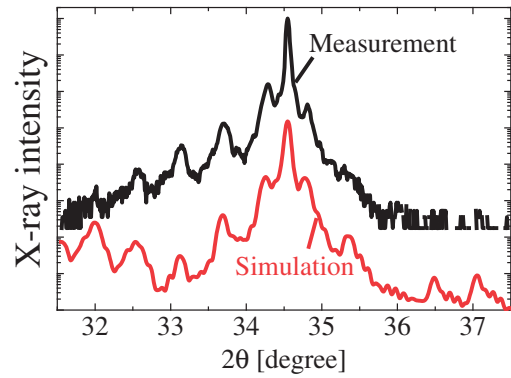
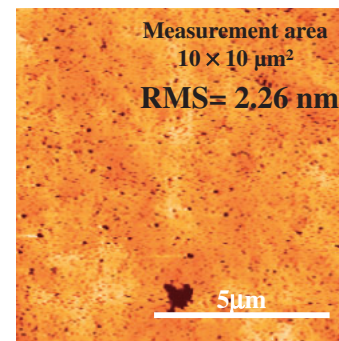
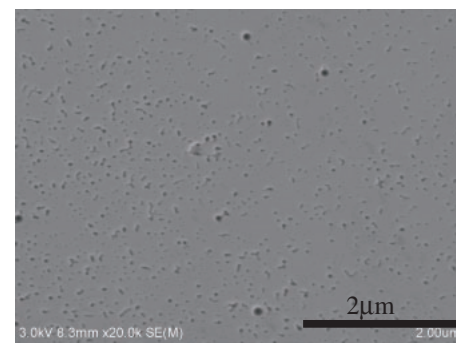


Fig. 2. XRD (0002)  $2\theta/\omega$  scan spectra obtained by measurement and simulation using the design values.



(a)



(b)

Fig. 3. Plan-view (a) AFM and (b) SEM images of the device.

region. Moreover, the consistency between the experimental XRD spectra and the simulation results confirm that this device was fabricated as designed. However, there were problems related to the surface structure. Figure 3 shows the plan-view AFM and SEM images, where a high density ( $1.6 \times 10^9 \text{ cm}^{-2}$ ) of growth pits is apparent on the device surface. Moreover, a root-mean-square (RMS) surface roughness of approximately 2.3 nm was measured by AFM. Considering the RMS surface roughness is usually lower than 1 nm in a blue LED, the measured RMS value of 2.3 nm is high. This results from deterioration by the multijunction formation. From the viewpoint of the surface morphology, because the largest pit diameter is of the order of several tens of nanometers, these pits are likely to have originated from the second p-type GaN layer. Figure 4 shows the cross-sectional bright-field TEM image of this device, confirming

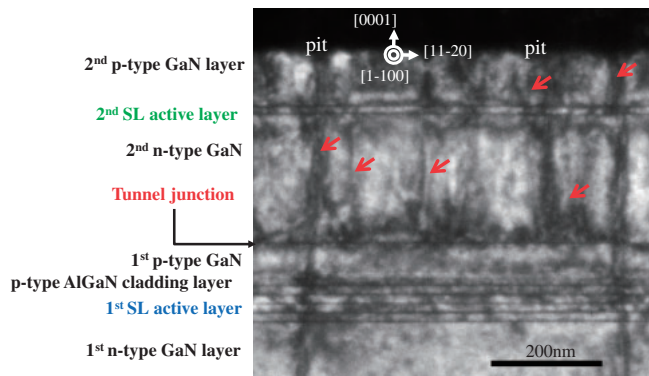


Fig. 4. Cross sectional bright-field TEM image of the device.

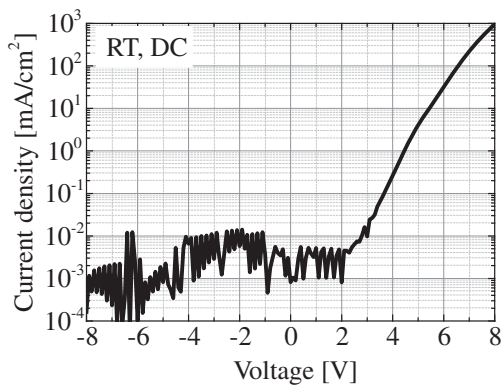


Fig. 5.  $J$ - $V$  curve for the device in LED mode.

that the thickness of each layer was as designed; we also confirmed that each SL structure was well formed. In contrast, many new dislocations were introduced near the tunnel junction, probably as a result of the high concentration of impurities in the tunnel junction. Further, growth pits were formed in the second p-type GaN layer, as observed in the TEM image (Fig. 4) as well as in the results of plan-view SEM and AFM (Fig. 3). Therefore, the optimization of the growth conditions is essential.

Figures 5 and 6 show, respectively, the  $J$ - $V$  curve in LED mode and the emission spectrum with an emission microscopic image from this device for an injection current of 20 mA (injection current density of  $\sim 1.8 \times 10^4$  mA/cm<sup>2</sup>) at RT. Two emission peaks at 436 and 516 nm, corresponding to the blue and green wavelengths, respectively, are clearly apparent in Fig. 6. These emissions presumably correspond to the first and second GaInN SL active layers, respectively. Moreover, the emission wavelengths closely match the wavelengths expected from each GaInN SL active layer. Therefore, we confirm that the carriers are injected, as expected, by the tunnel junction. In contrast, the reverse leakage-current density was lower than  $10^{-2}$  mA/cm<sup>2</sup> when a voltage of  $-8$  V was applied (see Fig. 5). The value of this reverse leakage current is normally very low in GaInN-based solar cells<sup>17)</sup> and growth pits generally act as leakage-current sources. However, we believe that the growth pits in this sample did not act as leakage-current sources, given that these were generated in the second p-type GaN layer and did not penetrate the second GaInN SL active layer. In addition, the forward operated voltage for an injection current density

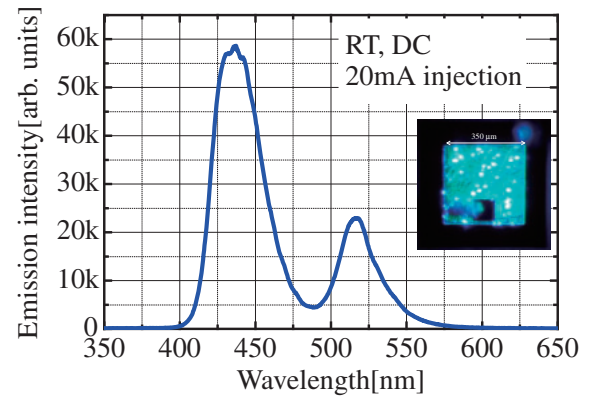
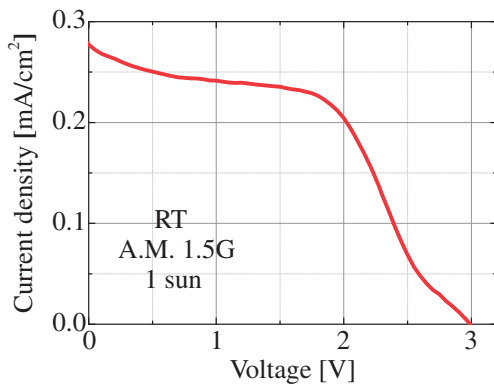


Fig. 6. Emission spectrum and emission microscopic image (inset) of the device for an injection current of 20 mA.

of 0.3 mA/cm<sup>2</sup>, a value that almost equals the  $J_{SC}$  of this device operated in solar-cell mode with an irradiation of 1 sun, was approximately 3.8 V. Since the turn-on voltage of typical green and blue LEDs is approximately 2 V, the turn-on voltage of this device connected in series is slightly lower than the theoretical expected value. This decrease in the turn-on voltage is correlated to many defects generated by the fabrication of the tunnel junction. Also, the differential resistance for an injection current density of 0.3 mA/cm<sup>2</sup> in LED mode was approximately 1.0 k $\Omega$ -cm<sup>2</sup>. Since the device resistance for that injection current in blue and green LEDs is as low as several tens of ohms centimeters squared, the differential resistance of this device is extremely high. Therefore, it is likely that the device resistance was increased by the high resistance of the tunnel junction. Further, we confirmed the presence of non-uniform emission-light-dots from Fig. 6. This effect is particularly significant in the blue region. We previously reported that hydrogen in p-type GaN diffuses laterally through the exposed portions of the p-type GaN and not vertically through the n-type GaN layer above it.<sup>27)</sup> Therefore, it is suggested that this is caused by insufficient activation of the p-type Al<sub>0.18</sub>Ga<sub>0.82</sub>N cladding layer, the first p-type GaN layer, and the p<sup>++</sup>Ga<sub>0.8</sub>In<sub>0.2</sub>N layer in the tunnel junction. Further, the device resistance was increased as a result of insufficient activation. In addition, since the growth pits and defects are present on the surface of this sample, it is considered that a non-uniform activation of the p-type AlGaIn cladding layer, the first p-type GaN layer, and the p<sup>++</sup>Ga<sub>0.8</sub>In<sub>0.2</sub>N layer is a consequence of these defects. For these reasons, the reduction of the resistance in the tunnel junction optimized by growth conditions and processing methods is essential.

Figure 7 shows the  $J$ - $V$  curves in solar-cell mode for this two-junction GaInN-based solar cell produced by the solar simulator (AM 1.5 G, 1 sun) at RT. Judging from this figure, the solar cell exhibited good characteristics. The  $\eta$ ,  $V_{OC}$ , fill factor,  $J_{SC}$ , shunt resistance ( $R_{SH}$ ), and series resistance ( $R_S$ ) of this solar cell were 0.41%, 3.0 V, 0.5, 0.28 mA/cm<sup>2</sup>, 2.8 k $\Omega$ -cm<sup>2</sup>, and 0.830 k $\Omega$ -cm<sup>2</sup> at 1-sun irradiation, respectively. From these results, the  $J_{SC}$  is lower than that of a common GaInN-based solar cell owing to a thin-film active layer in this solar cell. According to a simple calculation, the theoretical  $J_{SC}$  for a 1-sun irradiation of the active layer with an absorption edge of 516 or 436 nm is approximately 9.2 or



**Fig. 7.**  $J$ - $V$  curves in solar-cell mode of the two-junction GaInN-based solar cell, produced by the solar simulator (AM 1.5G, 1 sun) at RT.

4.1 mA/cm<sup>2</sup>, respectively. However, the active layer of this device is not thick enough to absorb light. Because the thicknesses of the GaInN layers are 5 and 15 nm, respectively, the absorbance of each GaInN layer was only 5 and 15%, respectively, assuming the absorption coefficient of GaInN to be 10<sup>5</sup> cm<sup>-1</sup>. Therefore, the theoretical  $J_{SC}$  for each GaInN active layer under a 1-sun irradiation was 0.45 and 0.61 mA/cm<sup>2</sup>, respectively. Thus, when considering the reflection of the semiconductor surface, it is reasonable that the resulting  $J_{SC}$  is close to the theoretical values. In addition, a relatively high  $R_{SH}$  is obtained because the leakage-current density in this device is small. However, because this value is insufficient, the reduction of pit and defect densities is required for the improvement of GaInN solar cells. In contrast,  $R_S$  is approximately one order of magnitude higher than that in the other GaInN-based solar cells. In addition, this  $R_S$  was almost identical to the value of the differential resistance evaluated in LED mode. Therefore, we concluded that  $R_S$  had increased as a result of the high tunnel-junction resistance and insufficient activation in the p-type layer. Moreover, we confirmed the presence of two inflection points in the  $J$ - $V$  curve. We think that these inflection points are due to the inactivation of carriers that produces a high resistance in the tunnel junction. Further, because  $R_S$  is high, the fill factor of the device is low and optimization of the process and crystal growth conditions to reduce  $R_S$  is required. The  $V_{OC}$  of GaInN-based single-junction solar cells is approximately 2 V. Therefore, the  $V_{OC}$  for the two-junction solar cell was increased by a factor of approximately 1.5 through the series connection using the tunnel junction. We previously reported a strong correlation between the pit density and  $V_{OC}$ .<sup>17)</sup> We also reported that a pit density below 10<sup>7</sup> cm<sup>-2</sup> is required to obtain a high  $V_{OC}$ .<sup>17)</sup> Therefore, the reduction of the pit density is essential for further increases in  $V_{OC}$ .

In conclusion, we designed and characterized a two-junction GaInN-based solar cell using a tunnel junction fabricated by crystal growth. We confirmed that the  $V_{OC}$  in this solar cell was increased by the series connection using the tunnel junction. Although a high resistance in the tunnel junction remains a problem, we demonstrated that multijunction GaInN-based solar cells are possible by tunnel-junction fabrication.

**Acknowledgments** This work was supported by a Grant-in-Aid for Scientific Research (C) No. 23560015, Grant-in-Aid for Young Scientists (A) No. 24686003, the New Energy and Industrial Technology Development Organization (NEDO) Project “Research and Development on Innovative Solar Cells”, and the Ministry of Education, Culture, Sports, Science and Technology Supported Program for the Strategic Research Foundation at Private Universities, Japan, 2012–2016.

- 1) H. Amano, M. Kito, K. Hiramatsu, and I. Akasaki, *Jpn. J. Appl. Phys.* **28**, L2112 (1989).
- 2) M. Koike, N. Koide, S. Asami, J. Umezaki, S. Nagai, S. Yamasaki, N. Shibata, H. Amano, and I. Akasaki, *Proc. SPIE* **3002**, 36 (1997).
- 3) S. Nakamura, M. Senoh, N. Iwasa, and S. Nagahama, *Jpn. J. Appl. Phys.* **34**, L797 (1995).
- 4) S. Nakamura, M. Senoh, N. Iwasa, S. Nagahama, T. Yamada, and T. Mukai, *Jpn. J. Appl. Phys.* **34**, L1332 (1995).
- 5) I. Akasaki, H. Amano, S. Sota, H. Sakai, T. Tanaka, and M. Koike, *Jpn. J. Appl. Phys.* **34**, L1517 (1995).
- 6) S. Nakamura, M. Senoh, S. I. Nagahama, N. Iwasa, T. Yamada, T. Matsushita, H. Kiyoku, and Y. Sugimoto, *Jpn. J. Appl. Phys.* **35**, L74 (1996).
- 7) V. Yu. Davydov, A. A. Klochikhin, R. P. Seisyan, V. V. Emtsev, S. V. Ivanov, F. Bechstedt, J. Furthmüller, H. Harima, A. V. Mudryi, J. Aderhold, O. Semchinova, and J. Graul, *Phys. Status Solidi B* **229**, r1 (2002).
- 8) R. Liu, J. Mei, S. Srinivasan, F. A. Ponce, H. Omiya, Y. Narukawa, and T. Mukai, *Appl. Phys. Lett.* **89**, 201911 (2006).
- 9) J. Wu, W. Walukiewicz, K. M. Yu, J. W. Ager, III, E. E. Haller, H. Lu, W. J. Schaff, Y. Saito, and Y. Nanishi, *Appl. Phys. Lett.* **80**, 3967 (2002).
- 10) H. Hamzaoui, A. S. Bouazzi, and B. Rezic, *Sol. Energy Mater. Sol. Cells* **87**, 595 (2005).
- 11) K. Y. Lai, G. J. Lin, Y.-L. Lai, Y. F. Chen, and J. H. He, *Appl. Phys. Lett.* **96**, 081103 (2010).
- 12) J. R. Lang, C. J. Neufeld, C. A. Humi, S. C. Cruz, E. Matioli, U. K. Mishra, and J. S. Speck, *Appl. Phys. Lett.* **98**, 131115 (2011).
- 13) Y. Kuwahara, Y. Fujiyama, M. Iwaya, S. Kamiyama, H. Amano, and I. Akasaki, *Phys. Status Solidi C* **7**, 1807 (2010).
- 14) T. Sugiyama, Y. Kuwahara, Y. Isobe, T. Fujii, K. Nonaka, M. Iwaya, T. Takeuchi, S. Kamiyama, I. Akasaki, and H. Amano, *Appl. Phys. Express* **4**, 015701 (2011).
- 15) Y. Kuwahara, T. Fujii, T. Sugiyama, D. Iida, Y. Isobe, Y. Fujiyama, Y. Morita, M. Iwaya, T. Takeuchi, S. Kamiyama, I. Akasaki, and H. Amano, *Appl. Phys. Express* **4**, 021001 (2011).
- 16) T. Nakao, T. Fujii, T. Sugiyama, S. Yamamoto, D. Iida, M. Iwaya, T. Takeuchi, S. Kamiyama, I. Akasaki, and H. Amano, *Appl. Phys. Express* **4**, 101001 (2011).
- 17) M. Mori, S. Kondo, S. Yamamoto, T. Nakao, T. Fujii, M. Iwaya, T. Takeuchi, S. Kamiyama, I. Akasaki, and H. Amano, *Appl. Phys. Express* **5**, 082301 (2012).
- 18) M. Mori, S. Kondo, S. Yamamoto, T. Nakao, M. Iwaya, T. Takeuchi, S. Kamiyama, I. Akasaki, and H. Amano, *Jpn. J. Appl. Phys.* **52**, 08JH02 (2013).
- 19) T. Takamoto, M. Kaneiwa, M. Imaizumi, and M. Yamaguchi, *Prog. Photovoltaics* **13**, 495 (2005).
- 20) T. Sasaki, K. Arafune, H. S. Lee, N. J. Ekins-Daukes, S. Tanaka, Y. Ohshita, and M. Yamaguchi, *Physica B* **376–377**, 626 (2006).
- 21) H. F. Macmillan, B.-C. Chung, H. C. Hamaker, N. R. Kaminar, M. S. Kuryla, M. Ladle Ristow, D. D. Liu, L. D. Partain, J. C. Schultz, G. F. Virshup, and J. G. Werthen, *Sol. Cells* **27**, 205 (1989).
- 22) N. Shigekawa, J. Liang, N. Watanabe, and A. Yamamoto, *Abstr. 10th Int. Conf. Nitride Semiconductors*, 2013, B6.06.
- 23) H. Amano, N. Sawaki, I. Akasaki, and Y. Toyoda, *Appl. Phys. Lett.* **48**, 353 (1986).
- 24) Y.-Y. Zhang and G.-R. Yao, *J. Appl. Phys.* **110**, 093104 (2011).
- 25) M. Kaga, T. Morita, Y. Kuwano, K. Yamashita, K. Yagi, M. Iwaya, T. Takeuchi, S. Kamiyama, and I. Akasaki, *Jpn. J. Appl. Phys.* **52**, 08JH06 (2013).
- 26) K. Kumakura, T. Makimoto, and N. Kobayashi, *Jpn. J. Appl. Phys.* **42**, 2254 (2003).
- 27) Y. Kuwano, M. Kaga, T. Morita, K. Yamashita, K. Yagi, M. Iwaya, T. Takeuchi, S. Kamiyama, and I. Akasaki, *Jpn. J. Appl. Phys.* **52**, 08JK12 (2013).

## Lateral Hydrogen Diffusion at p-GaN Layers in Nitride-Based Light Emitting Diodes with Tunnel Junctions

This content has been downloaded from IOPscience. Please scroll down to see the full text.

2013 Jpn. J. Appl. Phys. 52 08JK12

(<http://iopscience.iop.org/1347-4065/52/8S/08JK12>)

View [the table of contents for this issue](#), or go to the [journal homepage](#) for more

Download details:

IP Address: 202.11.1.201

This content was downloaded on 03/03/2017 at 06:55

Please note that [terms and conditions apply](#).

You may also be interested in:

[GaN-Based Light Emitting Diodes with Tunnel Junctions](#)

Tetsuya Takeuchi, Ghulam Hasnain, Scott Corzine et al.

[GaN-Based Tunnel Junctions in n-p-n Light Emitting Diodes](#)

Mitsuru Kaga, Takatoshi Morita, Yuka Kuwano et al.

[Hydrogen Dissociation from Mg-doped GaN](#)

Yoshinori Nakagawa, Masanobu Haraguchi, Masuo Fukui et al.

[Reduced Contact Resistance and Improved Surface Morphology of Ohmic Contacts on GaN Employing KrF Laser Irradiation](#)

Grace Huiqi Wang, Ting-Chong Wong, Xin-cai Wang et al.

[A Vertical InGaN/GaN Light-Emitting Diode Fabricated on a Flexible Substrate by a Mechanical Transfer Method Using BN](#)

Toshiki Makimoto, Kazuhide Kumakura, Yasuyuki Kobayashi et al.

[GaN-Based Laser Diodes Processed by Annealing with Minority-Carrier Injection](#)

Mamoru Miyachi, Hiroyuki Ota, Yoshinori Kimura et al.

[Photo-Enhanced Activation of Hydrogen-Passivated Magnesium in P-Type GaN Films](#)

Yoichi Kamiura, Yoshifumi Yamashita and Shuji Nakamura

[Concentrating Properties of Nitride-Based Solar Cells Using Different Electrodes](#)

Mikiko Mori, Shinichiro Kondo, Shota Yamamoto et al.

## Lateral Hydrogen Diffusion at p-GaN Layers in Nitride-Based Light Emitting Diodes with Tunnel Junctions

Yuka Kuwano<sup>1</sup>, Mitsuru Kaga<sup>1</sup>, Takatoshi Morita<sup>1</sup>, Kouji Yamashita<sup>1</sup>, Kouta Yagi<sup>1</sup>, Motoaki Iwaya<sup>1</sup>, Tetsuya Takeuchi<sup>1</sup>, Satoshi Kamiyama<sup>1</sup>, and Isamu Akasaki<sup>1,2</sup>

<sup>1</sup>Faculty of Science and Technology, Meijo University, Nagoya 468-8502, Japan

<sup>2</sup>Akasaki Research Center, Nagoya University, Nagoya 464-8603, Japan

Received October 13, 2012; accepted April 24, 2013; published online August 20, 2013

We demonstrated lateral Mg activation along p-GaN layers underneath n-GaN surface layers in nitride-based light emitting diodes (LEDs) with GaInN tunnel junctions. A high temperature thermal annealing was effective for the lateral Mg activation when the p-GaN layers were partly exposed to an oxygen ambient as etched sidewalls. The activated regions gradually extended from the etched sidewalls to the centers with an increase of annealing time, observed as emission regions with current injection. These results suggest that hydrogen diffuses not vertically through the above n-GaN but laterally through the exposed portions of the p-GaN. The lowest voltage drop at the GaInN tunnel junction was estimated to be 0.9 V at 50 mA with the optimized annealing condition. © 2013 The Japan Society of Applied Physics

### 1. Introduction

Nitride semiconductor materials are most promising materials for blue light-emitting diodes (LEDs), ultraviolet laser diodes, and high power electronic devices.<sup>1,2</sup> It had been very difficult to obtain p-type GaN until Amano et al. achieved p-type conduction in Mg-doped GaN treated with low-energy electron beam irradiation (LEEBI).<sup>3–5</sup> Since then, thermal annealing without hydrogen or ammonia ambient was also proposed to obtain p-type conduction in the Mg-doped GaN.<sup>6–8</sup> Several groups have reported that Mg acceptors are passivated with hydrogen atoms, resulting in Mg–H bond formation.<sup>9–13</sup> During LEEBI and thermal annealing, the Mg–H bonds are broken and the Mg acceptors are electrically activated.

Through the above studies, it have been also revealed that hydrogen atoms exist in Mg-doped GaN, but not in undoped or Si-doped GaN even after thermal annealing with hydrogen ambient.<sup>14</sup> This phenomena has been also observed in other semiconductor materials, such as Si and InP. Furthermore,<sup>15,16</sup> it has been suggested that hydrogen atoms can migrate only in p-type materials, but not in n-type materials.

Meanwhile, a novel current injection in GaInN-based LEDs using tunnel junctions was proposed in order to avoid the poor conductivity of the p-type GaN.<sup>17,18</sup> After a growth of a conventional GaInN-based LED, a p<sup>++</sup>-Ga(In)N/n<sup>++</sup>-GaIn tunnel junction and an n-GaN were successively grown on the LED structure. This structure is useful for higher light extraction in LEDs and current confinement in vertical cavity surface emitting lasers due to excellent current spreading in the top n-GaN layers. Interestingly, in this structure, p-type layers are fully covered with n-type layers, and hydrogen atoms in the p-type layers may not pass through the n-type layers from the p-type layers.

In this paper, we optimize thermal annealing conditions for Mg activation in such a LED structure with the tunnel junction and the n-GaN surface layer. We then demonstrate lateral Mg activation from etched sidewalls in the LED structure, indicating that hydrogen atom can only diffuse laterally in the p-GaN layers due to the n-GaN surface layers.

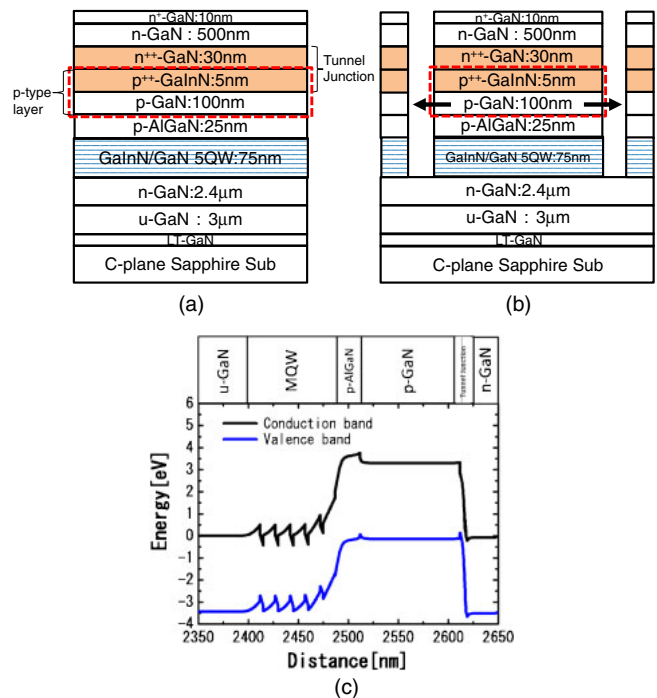
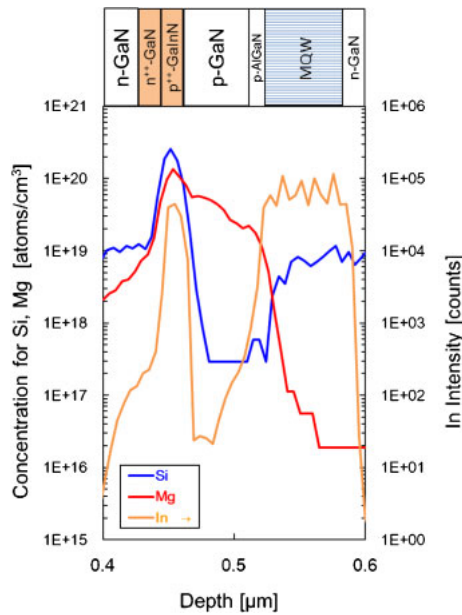


Fig. 1. (Color online) Schematics of (a) the wafer structure containing the tunnel junction and the LED structure and (b) the same wafer structure but after the etching. The arrows indicate potential hydrogen diffusion paths during the Mg activation.

### 2. Experiments

We prepared the wafer containing a tunnel junction structure and a LED structure in series as shown in Fig. 1(a). After deposited a 25-nm-thick GaN layer at low temperature on a sapphire substrate, a 3.0-μm-thick undoped GaN, a 2.4-μm-thick Si-doped GaN bottom contact layer, a multiple-quantum well active layer consisting of five periods of 3 nm GaInN/12 nm GaN (emission wavelength: 450 nm), a 25-nm-thick Mg-doped AlGaIn, and a 100-nm-thick Mg-doped GaN were grown by metalorganic vapor phase epitaxy. Up to the Mg-doped GaN layer, the structure is the same as a conventional LED structure. Additionally, a tunnel junction, a 500-nm-thick Si-doped GaN for lateral current spreading, and a 10-nm-thick highly Si-doped GaN



**Fig. 2.** (Color online) Mg, Si, and In depth profiles at the tunnel junctions measured by SIMS.

top contact layer were successively grown on the structure. The tunnel junction consists of a 5-nm-thick heavily Mg-doped  $\text{Ga}_{0.8}\text{In}_{0.2}\text{N}$  layer and a 30-nm-thick heavily Si-doped GaN layer. Triethylgallium (TEG), ammonia ( $\text{NH}_3$ ), ethyl-bis(cyclopentadienyl)magnesium ( $\text{Et-Cp}_2\text{Mg}$ ), and silane ( $\text{SiH}_4$ ) were used as Ga, N, Mg, and Si sources, respectively. Figure 2 shows depth profiles of Mg, Si, and In atoms in the wafer by Secondary Ion-microprobe Mass Spectrometry.  $1 \times 10^{20} \text{ cm}^{-3}$  Mg and  $3 \times 10^{20} \text{ cm}^{-3}$  Si were observed at the tunnel junction. A band diagram of structure of Fig. 1(a) shown in Fig. 1(c).

Then LEDs with tunnel junctions were fabricated from the wafer mentioned above by a newly modified process based on our standard LED process. In the modified process, two different parts exist comparing with the standard LED process. First, the thermal annealing was carried out after etching to expose the Si-doped GaN bottom layer surface for the bottom n-contact. Typically we perform the thermal annealing before the etching in a standard LED process. The reason for changing the order of these process steps is to expose a portion of the p-layers as an etched sidewall and form a potential hydrogen diffusion path during the Mg activation as shown in Fig. 1(b) by arrows. For the thermal annealing conditions, several annealing temperatures (525, 625, 725 °C) and holding times (4, 15, 30 min) were selected. Our typical annealing conditions in the standard process are 525 °C and 4 min. Oxygen gas was used as an ambient gas. Second, a single patterning process for forming metal electrodes was carried out since both the electrodes were n-contacts in the LEDs with tunnel junctions. Furthermore, no transparent electrode is required since the Si-doped GaN top layer act as current spreading layer, like a semi-transparent electrode. A size of the LED was  $300 \times 300 \mu\text{m}^2$ . A standard LED (without tunnel junction) with a semi-transparent Ni/Au electrode was also fabricated for comparison. Emission regions and current–voltage characteristics of the LEDs were measured under direct current conditions at

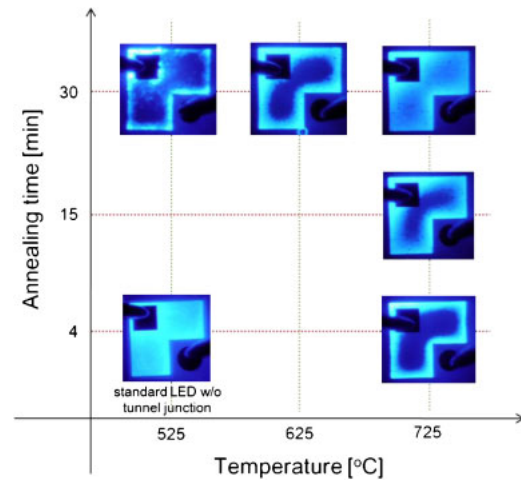


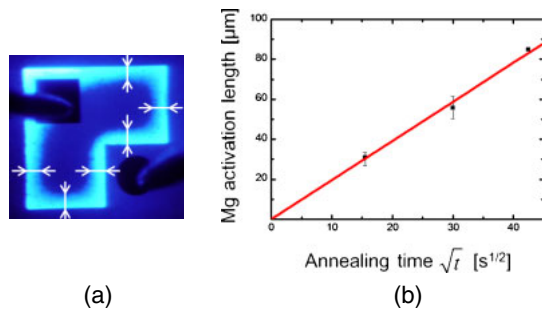
**Fig. 3.** (Color online) Emission regions of the LEDs with the tunnel junctions activated under the various thermal annealing conditions. The case of a standard LED without the tunnel junction but with a semi-transparent Ni/Au electrode annealed under the standard condition is also shown.

room temperature. Voltage drops at the tunnel junction regions were estimated by subtracting voltage drops of the standard LED from those of the LEDs with tunnel junctions.

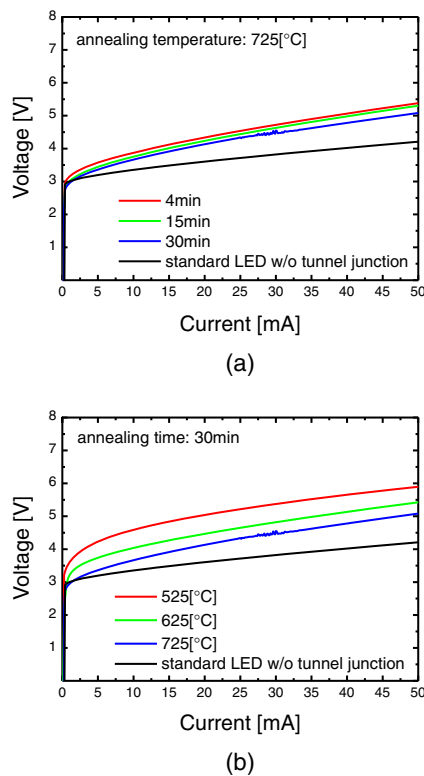
### 3. Results and Discussion

Figure 3 shows the emission regions of LEDs with the tunnel junctions activated under the various thermal annealing conditions. While a uniform emission region was obtained from the LED with the tunnel junction annealed at 725 °C for 30 min, the emission regions of the other LEDs with the tunnel junctions were restricted near the etched sidewall of the LEDs. More precisely narrower emission regions just adjacent to the etched sidewall of the LEDs were obtained in the cases of lower annealing temperature and shorter annealing time. Then with increases of annealing temperature and annealing time, the emission regions progressively extended to the center of the LEDs. We confirmed that the standard LED with a semi-transparent Ni/Au electrode showed uniform emission regions, so the active regions in all the LEDs should be uniform. Thus, the nonuniform emission should be caused by nonuniformity of current injections at the tunnel junctions. We then suppose that Mg acceptors are activated first at the etched sidewalls of the LEDs where Mg-doped layers are directly exposed to the oxygen ambient, and then Mg activation regions extend from the edge to the center.

To discuss the above point further, Mg activation length was plotted as a function of the square root of annealing time as shown in Fig. 4. Here Mg activation length is defined as shown in Fig. 4(a), corresponding to the length of the emission region. As shown in Fig. 4(a), we measured total six points which were away from the corners and the top n-electrode in order to minimize influences of the corners and the electrode. In the Fig. 4(b), the dots indicate the average values of the six points and the error bars indicate the range of the values. As shown in Fig. 4(b), the Mg activation length is proportional to the square root of annealing time. Therefore, the Mg activation length should be governed by some sort of diffusion process. The diffusion coefficient  $D$  was estimated to be  $9.6 \times 10^{-9} \text{ cm}^2/\text{s}$  from



**Fig. 4.** (Color online) (a) Mg activation length defined as shown with arrows. (b) Mg activation length as a function of square root of annealing time at 725 °C.



**Fig. 5.** (Color online) Current–voltage characteristics of the LEDs with the tunnel junction annealed under (a) various annealing times at 725 °C and (b) various annealing temperatures for 30 min. The case of a standard LED with a semi-transparent Ni/Au electrode is also plotted.

Fig. 4(b). At this moment we conclude that hydrogen atoms diffused only toward lateral direction through the etched sidewalls, but not vertically to the surface since the n-GaN surface layers blocked the hydrogen diffusion. The phenomena that n-layers block the hydrogen diffusion is already reported in the other semiconductor materials.<sup>9–11)</sup>

Figure 5 shows current–voltage characteristics of the LEDs with the tunnel junction under various thermal annealing conditions. Figure 5(a) shows an annealing time dependence under 725 °C and Fig. 5(b) shows an annealing temperature dependence for 30 min. The result of the standard LED with a semi-transparent Ni/Au electrode is also plotted for comparison. The voltage difference between the standard LED and the LED with tunnel junction corresponds to the voltage drop at the tunnel junction. When the annealing temperature was increased from 525 to

725 °C, the voltage drops at the tunnel junctions was clearly decreased. At the same time, no annealing time dependence of the voltage drop was observed within the range of the experiments. The lowest voltage drop at the GaInN tunnel junction is 0.9 V at 50 mA in the experiments.

#### 4. Conclusions

In summary, we have optimized thermal annealing conditions for the Mg activation in the LED structure with the tunnel junction and the n-GaN surface layer. We found that the p-GaN layers underneath the n-GaN surface layers were activated when the p-GaN layers were exposed to an oxygen ambient as etched sidewalls. Higher temperature and longer time for the thermal annealing resulted in an extension of Mg activated regions from the etched sidewall to the center. This result suggest that hydrogen diffused not through the above n-GaN layers but along p-GaN layers toward the etched sidewalls. We also found the annealing temperature affects a degree of the Mg activation and the annealing time affects a length of the Mg activation from the exposed portion. The lowest voltage drop at the GaInN tunnel junction was estimated to be 0.9 V at 50 mA with the optimized annealing condition.

#### Acknowledgements

This work was supported by Grant-in-Aid for Scientific Research (C) (No. 23560015), and the Ministry of Education, Culture, Sports, Science and Technology Supported Program for the Strategic Research Foundation at Private Universities, 2012–2016. The SIMS measurement was carried out by courtesy of Toray Research Center, Inc.

- 1) H. Amano, N. Sawaki, I. Akasaki, and Y. Toyoda: *Appl. Phys. Lett.* **48** (1986) 353.
- 2) S. Nakamura, T. Mukai, and M. Senoh: *Appl. Phys. Lett.* **64** (1994) 1687.
- 3) H. Amano, M. Kito, K. Hiramatsu, and I. Akasaki: *Jpn. J. Appl. Phys.* **28** (1989) L2112.
- 4) O. Gelhausen, H. N. Klein, M. R. Philips, and E. M. Goldys: *Appl. Phys. Lett.* **81** (2002) 3747.
- 5) Y. Okamoto, M. Saito, and A. Oshiyama: *Jpn. J. Appl. Phys.* **35** (1996) L807.
- 6) S. Nakamura, M. Senoh, and T. Mukai: *Jpn. J. Appl. Phys.* **30** (1991) L1708.
- 7) S. Nakamura, T. Mukai, and M. Senoh: *Jpn. J. Appl. Phys.* **30** (1991) L1998.
- 8) S. Nakamura, T. Mukai, M. Senoh, and N. Iwasa: *Jpn. J. Appl. Phys.* **31** (1992) L139.
- 9) W. Götz, N. M. Johnson, J. Walker, D. P. Bour, H. Amano, and I. Akasaki: *Appl. Phys. Lett.* **67** (1995) 2666.
- 10) W. Götz, N. M. Johnson, D. P. Bour, M. D. McCluskey, and E. E. Haller: *Appl. Phys. Lett.* **69** (1996) 3725.
- 11) S. Nakamura, N. Iwasa, M. Senoh, and T. Mukai: *Jpn. J. Appl. Phys.* **31** (1992) 1258.
- 12) B. A. Hull, S. E. Mohny, H. S. Venugopalan, and J. C. Ramer: *Appl. Phys. Lett.* **76** (2000) 2271.
- 13) D.-H. Youn, M. Lachab, M. Hao, T. Sugahara, H. Takenaka, Y. Naoi, and S. Sakai: *Jpn. J. Appl. Phys.* **38** (1999) 631.
- 14) A. Y. Polyakov, N. B. Smirnov, S. J. Pearton, F. Ren, B. Theys, F. Jomard, Z. Teukam, V. A. Dmitriev, A. E. Nikolaev, A. S. Usikov, and I. P. Nikitina: *Appl. Phys. Lett.* **79** (2001) 1834.
- 15) J. I. Pankove, C. W. Magee, and R. O. Wance: *Appl. Phys. Lett.* **47** (1985) 748.
- 16) G. R. Antell, A. T. R. Briggs, B. R. Butler, S. A. Kitching, J. P. Stagg, A. Chew, and D. E. Sykes: *Appl. Phys. Lett.* **53** (1988) 758.
- 17) S. Krishnamoorthy, D. N. Nath, F. Akyol, P. S. Park, M. Esposto, and S. Rajan: *Appl. Phys. Lett.* **97** (2010) 203502.
- 18) I. Ozden, E. Makarona, A. V. Nurmikko, T. Takeuchi, and M. Krames: *Appl. Phys. Lett.* **79** (2001) 2532.

# Dislocation density dependence of stimulated emission characteristics in AlGa<sub>N</sub>/Al multiquantum wells

Yuko Matsubara<sup>\*1</sup>, Tomoaki Yamada<sup>1</sup>, Kenichiro Takeda<sup>1</sup>, Motoaki Iwaya<sup>1</sup>, Tetsuya Takeuchi<sup>1</sup>, Satoshi Kamiyama<sup>1</sup>, Isamu Akasaki<sup>1,2</sup>, and Hiroshi Amano<sup>2,3</sup>

<sup>1</sup> Faculty of Science and Technology, Meijo University, Nagoya 468-8502, Japan

<sup>2</sup> Akasaki Research Center, Nagoya University, Nagoya 464-8062, Japan

<sup>3</sup> Graduate School of Engineering, Nagoya University, Nagoya 464-8062, Japan

Received 23 June 2013, revised 18 September 2013, accepted 25 September 2013

Published online 28 October 2013

**Keywords** stimulated emission characteristics, deep UV, AlGa<sub>N</sub>/AlN, dislocation density

\* Corresponding author: e-mail 123434041@ccalumni.meijo-u.ac.jp, Phone: +82 52 832 1151, Fax: +81 52 832 1244

We investigated dislocation density dependence on stimulated emission characteristics of AlGa<sub>N</sub>/AlN multiquantum wells (MQWs: emission wavelength of approximately 285 nm) on AlN templates with various dislocation densities. We found that the stimulated emission

characteristics of the deep UV MQWs were strongly dependent on the dislocation densities. A reduction of the dislocation densities is very important in order to realize good stimulated emission characteristics of deep UV MQWs.

© 2013 WILEY-VCH Verlag GmbH & Co. KGaA, Weinheim

**1 Introduction** AlGa<sub>N</sub> ternary nitride semiconductors have much potential for optoelectronic applications, particularly in the deep UV/UV region. Recently numerous reports on the deep UV/UV light emitting diodes have been published [1-5]. Especially the UV lasers are important in terms of many applications in the medical, chemical, and engineering fields. However, developments of the UV laser diodes [6-13] are hampered by poor material quality of AlGa<sub>N</sub>-based heterostructures and difficulty of current injection, especially with high AlN molar fraction. Optical pumping is a flexible and convenient excitation technique for investigation of stimulated emission characteristics compared to electrical injection. Most studies on the stimulated emission characteristics in AlGa<sub>N</sub> by optical pumping have been focused on the optimization of growth conditions and structure designs [14, 15], whereas the stimulated emission characteristics of the AlGa<sub>N</sub>-based active layer in conjunction with dislocation density have not been investigated in detail.

In this study, we investigated the dislocation density dependence on the stimulated emission characteristics of AlGa<sub>N</sub>/AlN multiquantum wells (MQWs) on a thick AlN templates with various dislocation densities by excita-

tion density dependent photoluminescence (PL) measurement.

## 2 Experiments and results

**2.1 MQWs on AlN** All samples were grown by high-temperature metalorganic vapor phase epitaxy [16] on a c-plane sapphire substrate. The epitaxial wafers were then polished and cleaved in the direction of the a-axis for AlN with a 500 μm cavity length. Figure 1 shows a schematic view of the sample structure. We prepared the samples with an emission wavelength of approximately 280 nm. The quantum well structures are 10-pairs of Al<sub>0.25</sub>Ga<sub>0.75</sub>N (4 nm)/AlN (8 nm) MQWs. The sapphire was polished to less than 100 μm in thickness, and then cleavages were made using a diamond scribe. The samples have cleaved mirror facets without coating.

We determined the layer thickness and the AlN molar fraction of each AlGaN MQWs from the satellite peaks of the  $2\theta/\omega$  scan X-ray diffraction profiles. The threading dislocation densities of AlN underlying layers were controlled from  $3 \times 10^9$  to  $1 \times 10^{10} \text{ cm}^{-2}$  by changing the growth condition. The value of the dislocation density of each sample was estimated from the values of full width half maximum (FWHMs) of the X-ray rocking curve (XRC)  $\omega$ -scan (0002) and (10-12) diffractions with the following formula [17]:

$$N = \frac{\beta^2}{4.35 |\bar{b}|^2}, \quad (1)$$

where  $N$  is the threading dislocation density,  $b$  is the magnitude of Burgers vector, and  $\beta$  is the half width by measuring the omega magnitude of XRC. Table 1 shows the dislocation density of each AlN template. We derived the density values of edge dislocations and mixed dislocations, which should act as non-radiative recombination centers [18]. Therefore, we here used the sum of both as dislocation

**Table 1** Dislocation density of AlN templates

	Sample A	Sample B	Sample C
Edge dislocation density [ $\text{cm}^{-2}$ ]	$2.95 \times 10^9$	$5.51 \times 10^9$	$1.00 \times 10^{10}$
Mixed dislocation density [ $\text{cm}^{-2}$ ]	$7.85 \times 10^7$	$2.31 \times 10^8$	$5.29 \times 10^7$

tion density values correlated with optical properties. Note that a cross-check was conducted using plan-view transmission electron microscopy and cathodoluminescence regarding the dislocation density.

**2.2 Measurement** We characterized the stimulated emission of the MQWs by excitation density dependent photoluminescence measurement at room temperature (RT). The samples were excited by the 4th harmonic (266 nm) of the Q-switched YAG:Nd laser radiation. The pulse width was 5 ns and the frequency was 10 Hz. A neutral density filter was used to control the excitation density. The stimulated emission measurements were performed in edge-detection mode. The light beam from the YAG laser was refracted by a prism and irradiated on the samples. The photoluminescence light emitting from the sample edge was passing through a receiving lens, and detected in the spectrometer (SPEC Miniature Fiber Optic Spectrometer). We focused the YAG laser on the sample surface. The irradiation area on the surface was about  $0.015 \text{ cm}^2$ , and the shape was circle. Note that in these samples only the well layers were selectively excited.

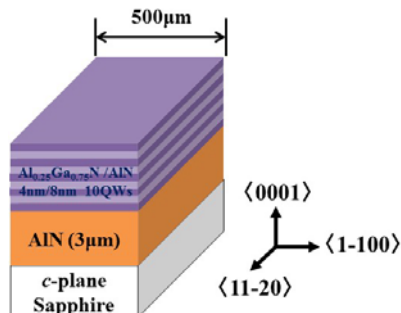


**Figure 1** Schematic view of sample structure.

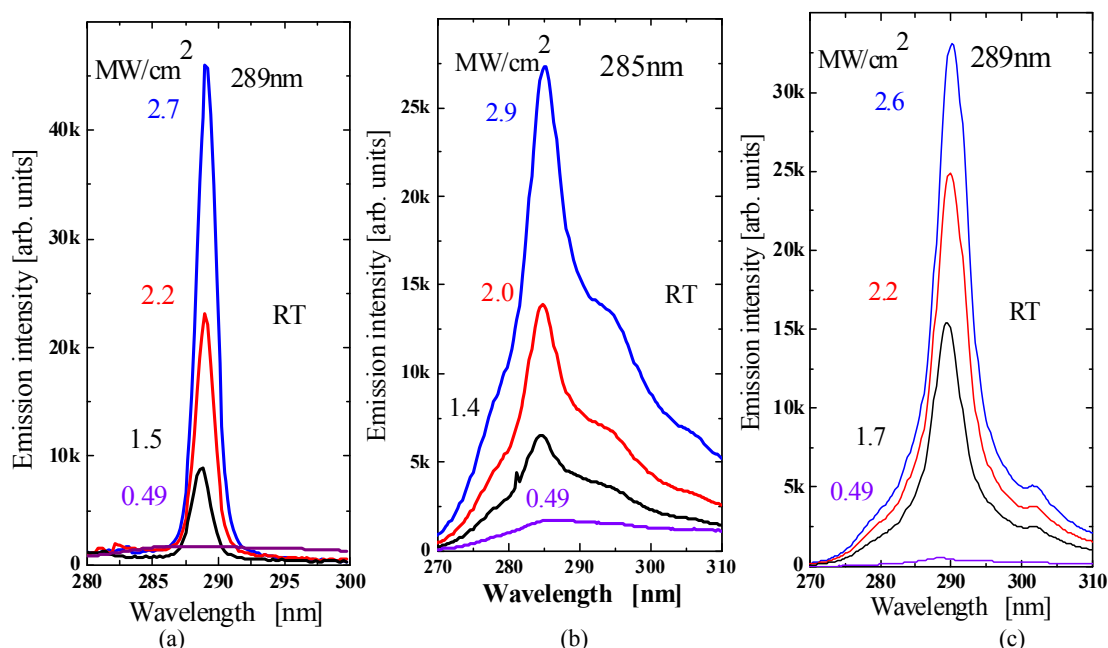


**Figure 2** PL spectra under different excitation power densities. (a) Dislocation density of  $3 \times 10^9 \text{ cm}^{-2}$ . (b) Dislocation density of  $5 \times 10^9 \text{ cm}^{-2}$ . (c) Dislocation density of  $1 \times 10^{10} \text{ cm}^{-2}$ .

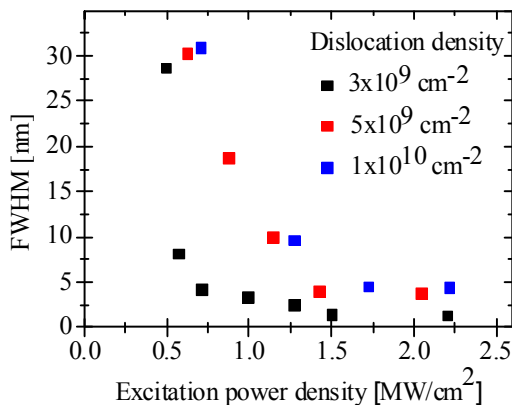


**Figure 3** FWHM of the PL emission intensity as a function of the excitation power density.

Figures 2(a)-(c) show the measured emission spectra under different excitation power densities, varying from 49 kW/cm<sup>2</sup> to about 3.0 MW/cm<sup>2</sup> at RT for each MQW. In the case of sample A, the FWHM was approximately 1.5 nm at pumping power of 2.7 MW/cm<sup>2</sup>. This FWHM value is limited by a resolution in our experiment equipment. Thus, we considered that the stimulated emission was observed from sample A even though the FWHM was not very narrow.

Figure 3 summarizes the FWHMs of the emission spectra as a function of the excitation power density. The FWHM of sample A reduced largely when excitation power density exceeded the threshold power density. From this figure, the FWHMs of sample B and C are similarly decreased to the FWHM of sample A. Thus, we concluded that these samples have reached the stimulated emission.

Figure 4 summarizes the PL emission peak intensity as a function of the excitation power density. For all samples, new narrow peaks appear in the spectra as the excitation power densities are increased above certain values. With the further increase in the excitation intensity, the intensity of the new peak increases superlinearly. We observed that the stimulated emission characteristics of the deep UV MQWs were strongly dependent on the dislocation densities. As the dislocation density decreased in AlN template, the threshold power density also decreased. The threshold power density of the stimulated emission from each AlGaIn MQW changes from approximately 500 kW/cm<sup>2</sup> to 5 MW/cm<sup>2</sup> when the dislocation density changes from 3×10<sup>9</sup> to 1×10<sup>10</sup> cm<sup>-2</sup>. Thus, a reduction of the dislocation densities is very important in order to realize superior stimulated emission characteristics of the deep UV MQWs.

**3 Summary** We analysed the stimulated emission characteristics of the AlGaIn/AlN MQWs on the AlN underlying layer with the various dislocation densities by excitation density dependent PL measurement. The threshold power density of each AlGaIn MQW changed when the dislocation density changed. Thus, it was found that, in or-

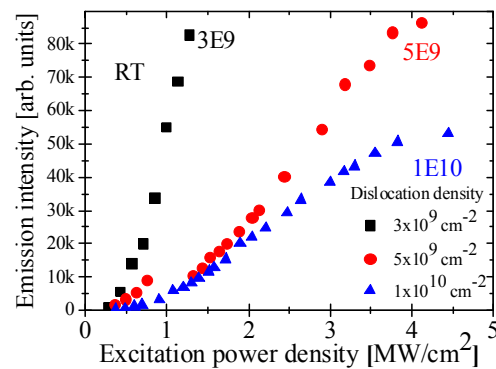


**Figure 4** PL emission peak intensity as a function of the excitation power density.

der to realize a low-threshold laser diode, a base layer with low dislocation density is required.

**Acknowledgements** This study was supported by the MEXT-Supported Program for the Strategic Research Foundation at Private Universities, 2012-2016, and the Adaptable and Seamless Technology Transfer Program through Target-driven R&D, JST (AS2421230J).

## References

- [1] C. Pernot, M. Kim, S. Fukahori, T. Inazu, T. Fujita, Y. Nagasawa, A. Hirano, M. Ippommatsu, M. Iwaya, S. Kamiyama, I. Akasaki, and H. Amano, *Appl. Phys. Express* **3**, 061004 (2010).
- [2] V. Adivarahan, J. Zhang, A. Chitnis, W. Shuai, J. Sun, R. Pachipulusu, M. Shatalov, and A. Khan, *Jpn. J. Appl. Phys.* **41**, 435 (2002).
- [3] H. Hirayama, N. Noguchi, and N. Kamata, *Appl. Phys. Express* **3**, 032102 (2010).
- [4] Z. Ren, Q. Sun, S.-Y. Kwon, J. Han, K. Davitt, Y. K. Song, A. V. Nurmikko, H.-K. Cho, W. Liu, J. A. Smart, and L. J. Schowalter, *Appl. Phys. Lett.* **91**, 051116 (2007).
- [5] M. Iwaya, S. Terao, T. Sano, S. Takanami, T. Ukai, R. Nakamura, S. Kamiyama, H. Amano, and I. Akasaki, *Phys. Status Solidi A* **188**, 117 (2001).
- [6] S. Masui, Y. Matsuyama, T. Yanamoto, T. Kozaki, S. Nagahama, and T. Mukai, *Jpn. J. Appl. Phys.* **42**, L1318 (2003).
- [7] K. Iida, T. Kawashima, A. Miyazaki, H. Kasugai, S. Mishima, A. Honshio, Y. Miyake, M. Iwaya, S. Kamiyama, H. Amano, and I. Akasaki, *Jpn. J. Appl. Phys.* **43**, L499 (2004).
- [8] J. Edmond, A. Abare, M. Bergman, J. Bharathan, K. L. Bunker, D. Emerson, K. Haberern, J. Ibbetson, M. Leung, P. Russel, and D. Slater, *J. Cryst. Growth* **272**, 242 (2004).
- [9] M. Kneissl, Z. Yang, M. Teepe, C. Knollenberg, O. Schmidt, P. Kiesel, and N. M. Johnson, *J. Appl. Phys.* **101**, 123103 (2007).
- [10] H. Yoshida, Y. Yamashita, M. Kuwabara, and H. Kan, *Appl. Phys. Lett.* **93**, 241106 (2008).

- [11] H. Tsuzuki, F. Mori, K. Takeda, M. Iwaya, S. Kamiyama, H. Amano, I. Akasaki, H. Yoshida, M. Kuwabara, Y. Yamashita, and H. Kan, *J. Cryst. Growth* **311**, 2860 (2009).
- [12] K. Nagata, K. Takeda, K. Nonaka, T. Ichikawa, M. Iwaya, T. Takeuchi, S. Kamiyama, I. Akasaki, H. Amano, H. Yoshida, M. Kuwabara, Y. Yamashita, and H. Kan, *Phys. Status Solidi C* **8**, 1564 (2011).
- [13] J. Xie, S. Mita, Z. Bryan, W. Guo, L. Hussey, B. M. Raoul Schlessler, R. Kirste, M. Gerhold, R. Collazo, and Z. Sitar, *Appl. Phys. Lett.* **102**, 171102 (2013).
- [14] T. Takano, Y. Narita, A. Horiuchi, and H. Kawanishi, *Appl. Phys. Lett.* **84**, 3567 (2004).
- [15] M. Shatalov, M. Gaevski, V. Adivarahan, and A. Khan, *Jpn. J. Appl. Phys.* **45**, L1286 (2006).
- [16] M. Imura, K. Nakano, N. Fujimoto, N. Okada, K. Balakrishnan, M. Iwaya, S. Kamiyama, H. Amano, I. Akasaki, T. Noro, T. Takagi, and A. Bandoh, *Jpn. J. Appl. Phys.* **45**, 8639 (2006).
- [17] T. Metzger, R. Höppler, E. Born, O. Ambacher, M. Stutzmann, R. Stommer, M. Schuster, H. Gobeli, S. Christiansen, M. Albrecht, and H. P. Strunk, *Philos. Mag. A* **77**, 1013 (1998).
- [18] K. Ban, J. Yamamoto, K. Takeda, K. Ide, M. Iwaya, T. Takeuchi, S. Kamiyama, I. Akasaki, and H. Amano, *Appl. Phys. Express* **4**, 052101 (2011).

## Carrier Injections in Nitride-Based Light Emitting Diodes Including Two Active Regions with Mg-Doped Intermediate Layers

This content has been downloaded from IOPscience. Please scroll down to see the full text.

2013 Jpn. J. Appl. Phys. 52 08JG02

(<http://iopscience.iop.org/1347-4065/52/8S/08JG02>)

View [the table of contents for this issue](#), or go to the [journal homepage](#) for more

Download details:

IP Address: 202.11.1.201

This content was downloaded on 03/03/2017 at 06:58

Please note that [terms and conditions apply](#).

You may also be interested in:

[GaN-based vertical cavity surface emitting lasers with periodic gain structures](#)

Kenjo Matsui, Yugo Kozuka, Kazuki Ikeyama et al.

[GaN-Based Green-Light-Emitting Diodes with InN/GaN Growth-Switched InGaN Wells](#)

Wei-Chih Lai, Cheng-Hsiung Yen and Shoou-Jinn Chang

[Improvements in Optical Power and Emission Angle of Blue Light Emitting Diodes Using Patterned Sapphire Substrates with Low Threading Dislocation Densities](#)

Seong-Muk Jeong, Suthan Kissinger, Yong-Ho Ra et al.

[Formation of Selective High Barrier Region by Inductively Coupled Plasma Treatment on GaN-Based Light-Emitting Diodes](#)

Ting-Wei Kuo, Shi-Xiong Lin, Pin-Kun Hung et al.

[Enhanced Electro-Static Discharge Endurance of GaN-Based Light-Emitting Diodes with Specially Designed Electron Blocking Layer](#)

Chunxia Wang, Xiong Zhang, Hao Guo et al.

[Lateral Hydrogen Diffusion at p-GaN Layers in Nitride-Based Light Emitting Diodes with Tunnel Junctions](#)

Yuka Kuwano, Mitsuru Kaga, Takatoshi Morita et al.

[The Light Extraction Efficiency of p-GaN Patterned InGaN/GaN Light-Emitting Diodes Fabricated by Size-Controllable Nanosphere Lithography](#)

Jae In Sim, Byoung Gyu Lee, Ji Won Yang et al.

[Red-Light-Emitting Diodes with Site-Selective Eu-Doped GaN Active Layer](#)

Hiroto Sekiguchi, Yasufumi Takagi, Tatsuki Otani et al.

## Carrier Injections in Nitride-Based Light Emitting Diodes Including Two Active Regions with Mg-Doped Intermediate Layers

Kenjo Matsui<sup>1\*</sup>, Koji Yamashita<sup>1</sup>, Mitsuru Kaga<sup>1</sup>, Takatoshi Morita<sup>1</sup>, Tomoyuki Suzuki<sup>1</sup>, Tetsuya Takeuchi<sup>1</sup>, Satoshi Kamiyama<sup>1</sup>, Motoaki Iwaya<sup>1</sup>, and Isamu Akasaki<sup>1,2</sup>

<sup>1</sup>Faculty of Science and Technology, Meijo University, Nagoya 468-8502, Japan

<sup>2</sup>Akasaki Research Center, Nagoya University, Nagoya 464-8603, Japan

Received October 13, 2012; revised December 6, 2012; accepted December 7, 2012; published online May 20, 2013

We achieved simultaneous two emissions from a single light emitting diode containing violet and blue GaInN/GaN quantum well active regions separated with an intermediate layer. By adjusting a thickness of a Mg-doped region in the intermediate layer, an intensity ratio between violet and blue emissions was changed, caused by different carrier distributions in the two active regions. The intensity ratio from two active regions was also changed by changing an amount of current injection. An unintentional Mg incorporation into the active region above the Mg-doped intermediate layer was observed, which is due to Mg memory effect. © 2013 The Japan Society of Applied Physics

### 1. Introduction

Optoelectronic devices handling with broad spectra, like solar light, have been demanded, such as solid state lighting and solar cells. GaN-based material system is most promising to cover the solar spectrum by using a mixed crystal of AlN, GaN, and InN.<sup>1)</sup> However semiconductor optoelectronic devices, such as light emitting diodes (LEDs), laser diodes, and photodiodes fundamentally deal with just narrow spectra corresponding to bandgaps at active regions. Thus a practical white LED has been fabricated by a combination of a blue LED and a yellow phosphor material.<sup>2)</sup>

Recently multi-color LEDs with multiple peak wavelengths have been demonstrated on target to a monolithic white LED. Various approaches and structures for the multiple peak emissions have been proposed, such as a tandem structure with a tunnel junction,<sup>3,4)</sup> an active region consisting of various quantum wells (QWs),<sup>5–11)</sup> and a QW on various micro facets.<sup>12,13)</sup> In any case, these devices have a single active region in a single pn junction in principle, like a conventional LED.

Here we are interested in multiple active regions in a single pn junction. The multiple active regions consist of two or more active regions separated with intermediate layers which thickness is comparable to that of the active region. This structure is useful not only for multi-color LEDs but also other light emitting devices. For instance, the structure has been used as a periodic gain structure (PGS) in a vertical cavity surface emitting laser (VCSEL) to increase an optical confinement factor.<sup>14)</sup> Also, the structure should be useful to suppress the efficiency droop issue typically observed in GaN-based LEDs by diluting carrier concentrations with the thick active regions.<sup>5)</sup> Note that in the above examples the active regions have the same peak wavelength. So far the structure has been applied to GaAs-based and InP-based device structures mostly as the PGSs in the VCSELs.<sup>15)</sup> There are almost no attempts to investigate the two active region structures with GaN-based materials. This seems reasonable in a way since holes in GaN-based materials have very heavy mass and short diffusion length which lead to poor carrier injection into the thick active region.

In this paper, we demonstrate simultaneous two emissions by current injection from two GaInN QW active regions separated with a Mg-doped intermediate layer. We found

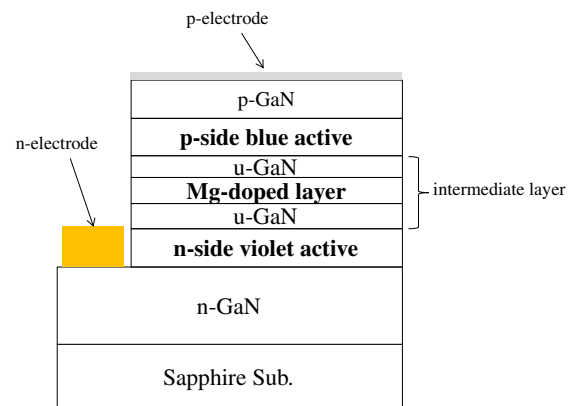
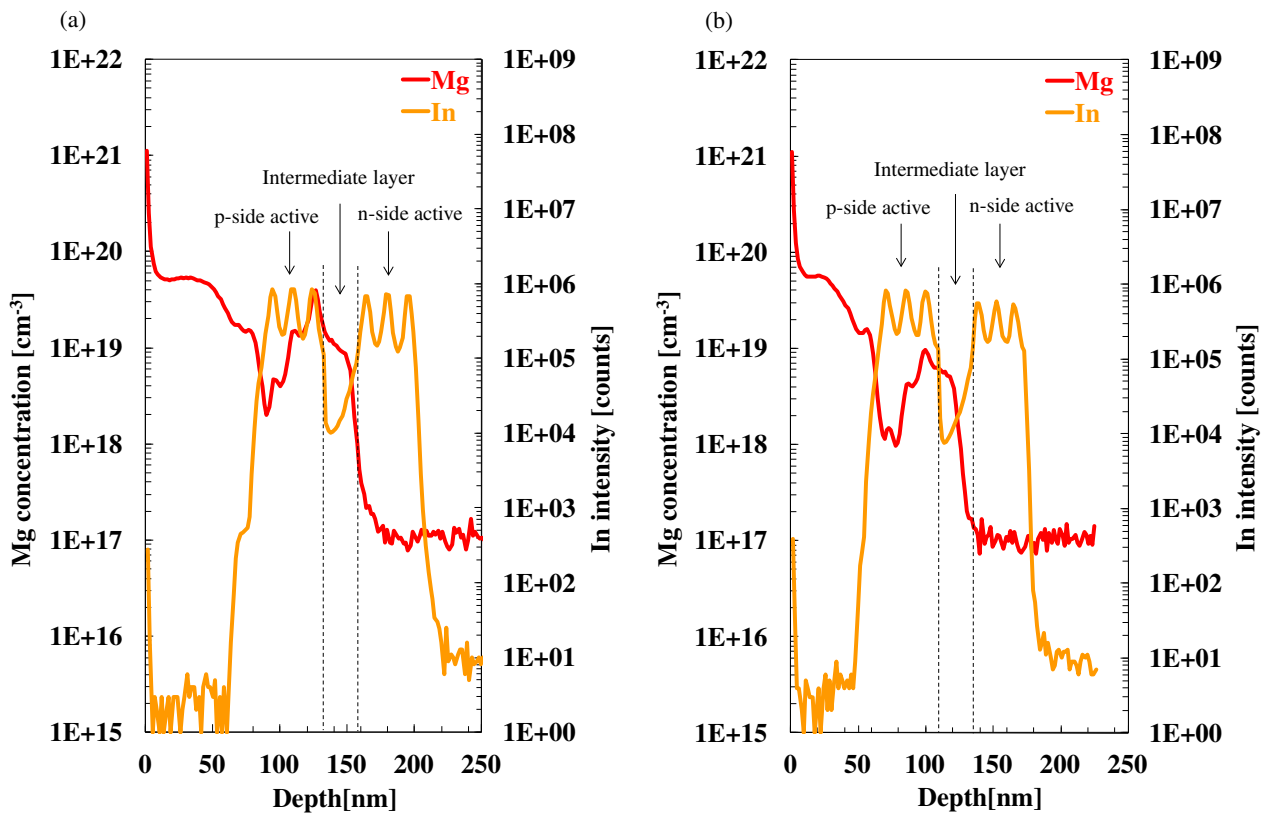


Fig. 1. (Color online) Schematic view of the two wavelength violet/blue LED, containing the two active regions separated with the intermediate layer.

that the Mg doping level in the intermediate layer is a key to obtain the simultaneous emissions. Furthermore current injection dependences on emission intensities and spectrum patterns are discussed.

### 2. Experiments

All the samples used in this study are LED structures grown on *c*-plane sapphire substrates by metalorganic vapor phase epitaxy. The sample structure is shown in Fig. 1. Before the LED structure growth, a 25-nm-thick low-temperature-deposited buffer layer and a 3- $\mu$ m-thick undoped GaN template were grown first. Following the growth of the GaN template, a 2.5- $\mu$ m-thick n-GaN layer, a three-period of undoped Ga<sub>0.88</sub>In<sub>0.12</sub>N/GaN QWs as an “n-side” violet active region, a 45-nm-thick GaN/p-GaN/GaN intermediate layer, a three-period of undoped Ga<sub>0.8</sub>In<sub>0.2</sub>N/GaN QWs as a “p-side” blue active region, a 20-nm-thick p-type AlGaIn electron blocking layer, a 80-nm-thick p-GaN layer, and a 10-nm p<sup>+</sup>-GaIn contact layer were grown. Each GaInN/GaN 3QW active region is composed by 2.5-nm-thick GaInN wells and 13-nm-thick GaN barriers. Regarding the GaN/p-GaN/GaN intermediate layer, an intentionally Mg-doped region is located at the center of the intermediate layer. In this study, the thickness of the Mg-doped region in the intermediate layer was changed while supplying the same



**Fig. 2.** (Color online) Mg and In depth profiles measured by SIMS for the samples (a) with the 14 nm Mg-doped layer and (b) with the 1.6 nm Mg-doped layer.

amount of bis(ethylcyclopentadienyl) magnesium (Et-Cp<sub>2</sub>Mg) flow in order to change a total amount of Mg in the intermediate layer. Five different samples were prepared in which the Mg-doped layer thickness was changed, 14, 4, 1.6, 0.8, and 0 (corresponding to undoped) nm. At the same time, the total thickness of the intermediate layers was kept as 45 nm. After the epitaxial growth, all the samples were fabricated by our standard LED process. A size of LEDs was 300 × 300 μm<sup>2</sup>. A semi-transparent p-electrode at the top of the device was formed by Ni/Au, while Ti/Al/Ti/Au was used as an n-electrode.

Mg and In atom depth profiles of the samples were measured by secondary ion mass spectrometry (SIMS). Room temperature photoluminescence (PL) spectra from the LED structures were measured to confirm emission wavelengths and intensities of the active regions, which were independent on a carrier distribution imbalance caused by a current injection. Then emission spectra with several current injection levels were measured from the same LED structures at room temperature. In addition current–light output power (*I*–*L*) characteristics were measured under direct current condition at room temperature.

### 3. Results and Discussion

Mg and In atom depth profiles of the samples with the 14 and 1.6 nm Mg-doped layers were shown in Figs. 2(a) and 2(b), respectively. Even though the Et-Cp<sub>2</sub>Mg flows were fixed among the two samples, the Mg concentrations at the intermediate layers were different in the two samples, 1 × 10<sup>19</sup> cm<sup>-3</sup> in the sample with the 14 nm Mg-doped layer and 5 × 10<sup>18</sup> cm<sup>-3</sup> in the sample with the 1.6 nm Mg-doped

layer. This could be attributed to Mg turn-on delay due to the Mg memory effect. In addition, a considerable amount of Mg atoms in the range of more than 1 × 10<sup>18</sup> cm<sup>-3</sup> were incorporated into the p-side active regions. This Mg turn-off delay also came from the Mg memory effect. Note that Mg incorporation in the GaInN well looks higher than that of GaN barrier, but this behavior may be caused by a sensitivity difference of Mg atoms in GaN and GaInN. At this moment it is hard to estimate the difference in the Mg incorporation between GaInN and GaN.

Room temperature PL spectra of all the samples consisting of the LED structures are shown in Fig. 3. An excitation source was a 325 nm He–Cd laser. As shown in Fig. 3, all the samples basically showed similar spectrum patterns with intensities in the twofold range. Weak peaks indicated by solid arrows around 400 to 430 nm from the n-side active regions and strong peaks indicated by dashed arrows around 450 to 470 nm from the p-side active regions were consistently observed. Note that the sample-to-sample variations of the PL peak wavelength correspond to run-to-run variations of growth temperatures at the active regions. Since the similar PL intensities were obtained from all the samples, the optical qualities of the active regions among all the samples could be similar. The reason for much weaker PL intensity from the n-side violet active region compared to that from the p-side blue active region is a lower excitation intensity due to a deeper position of the n-side violet active region from the surface.

Next, room temperature emission spectra by a current injection of 20 mA were plotted in Fig. 4. Interestingly, the spectra are very different among the samples, and also

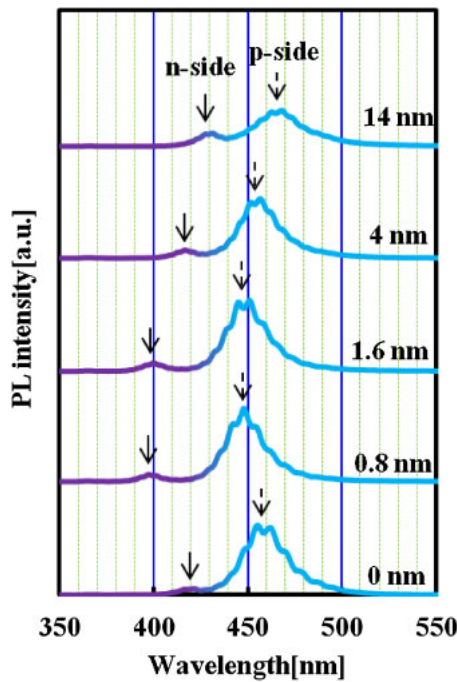


**Fig. 3.** (Color online) Room temperature PL spectra of all the samples with the LED structures. PL peak positions from the n- and p-side active regions are indicated by the solid and dashed arrows, respectively.

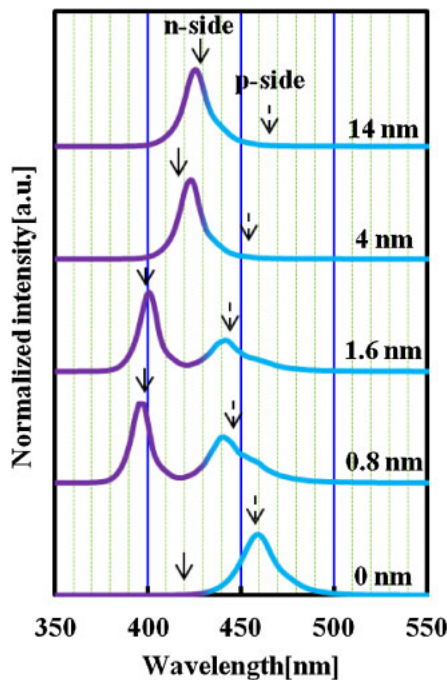


**Fig. 4.** (Color online) Room temperature emission spectra of all the samples at a current injection of 20 mA. For comparison, the PL peak positions from n-side active regions and p-side active regions are indicated by the solid and dashed arrows, respectively.

different from the PL spectra. For comparison between the emission peak positions by current injections and the PL peak positions shown in Fig. 3, the PL peak positions are also indicated in Fig. 4 by the solid (for n-side active) and the dashed (for p-side active) arrows. The sample with the 0 nm Mg-doped layer showed only a blue emission from the

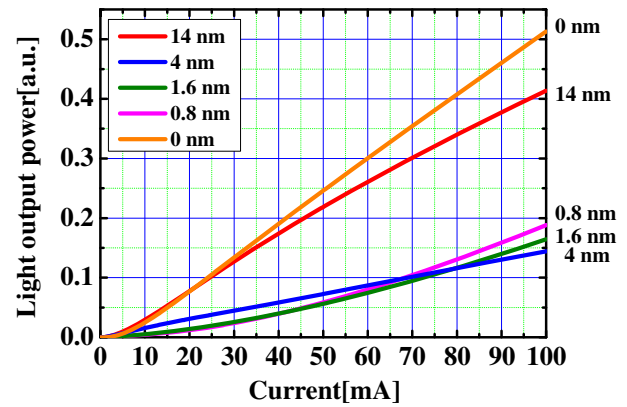


**Fig. 5.** (Color online) Room temperature  $I$ - $L$  characteristics for all the samples.

p-side active region. This seems reasonable because holes are only injected into the p-side active region due to much heavier mass and shorter diffusion length of the holes. Then the samples with the 0.8 and 1.6 nm Mg-doped layers clearly showed a violet and a blue emissions simultaneously from the n- and p-side active regions. On the contrary, the samples with the 4 and 14 nm Mg-doped layers showed only a violet emission from the n-side active regions. These results suggest that appropriate Mg doping at the intermediate layer, corresponding to the cases of the 0.8 and 1.6 nm Mg-doped layers, should supply enough holes even into the n-side violet active region. In other words, distributions of holes and electrons are well-balanced in both the n- and p-side active regions, so that two reasonable peak intensities were obtained. On the other hands, more Mg doping, such as 4 and 14 nm Mg-doped layer cases, should not only enhance a hole injection into the n-side violet active region but also suppress an electron injection into the p-side blue active region, resulting in a single violet emission. These results indicate that the balance of the emission intensities between the two active regions can be designed by the Mg doping level at the intermediate layer.

Figure 5 shows  $I$ - $L$  characteristics of all the samples. We found that the light output intensities of the samples with the 0.8, 1.6, and 4 nm Mg-doped layers were less than half of those of the samples with 0 and 14 nm Mg-doped layers. This result most likely came from an influence of the unintentional Mg incorporation into the p-side active regions shown in Fig. 2. Since Mg acts as a nonradiative center, then the radiative efficiency of the p-side active region should be decreased. At this moment our explanation for the above result is as follows. Obviously the sample with 0 nm Mg-doped layer was not influenced by the unintentional Mg incorporation, resulting in the strong emission from the p-side active region. In the case of the 14 nm Mg-doped layer, not only the intermediate layer but also the p-side active region are probably p-type due to the unintentional Mg incorporation, so most electrons and holes are efficiently injected into the n-side active region. On the contrary, the samples with 0.8, 1.6, and 4 nm Mg-doped layers could contain moderate Mg concentrations in the intermediate layer, so electrons and holes are injected to both the p- and n-side active regions. Then some carriers in the p-side active regions recombine through the Mg-related nonradiative

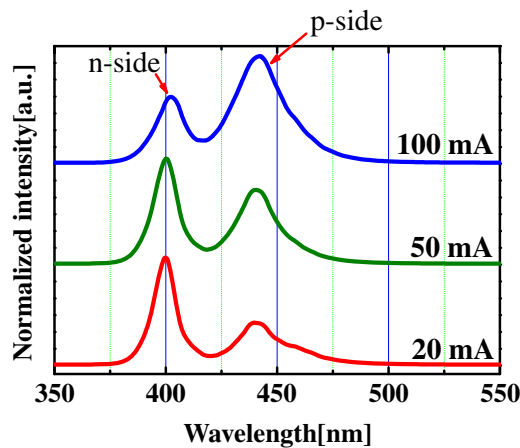


Fig. 6. (Color online) Current injection dependence of emission spectra of the sample with the 1.6 nm Mg-doped layer.

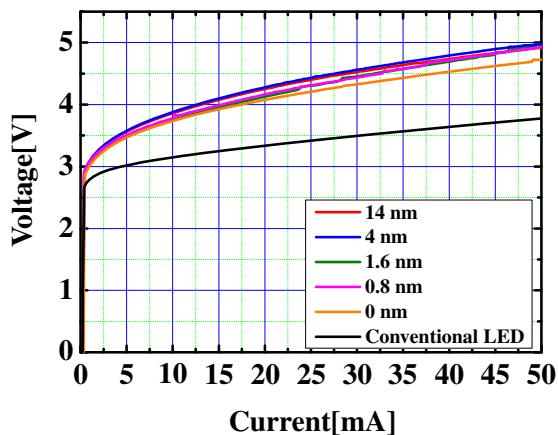


Fig. 7. (Color online) Room temperature  $I$ - $V$  characteristics for all the samples and a conventional LED.

centers, leading to the poor intensities. Actually it seems that all the injected carriers in the p-type active region recombine as nonradiative in the case of the 4 nm. Based on the above consideration, it seems very important to suppress the Mg incorporation into the p-side active regions for further improvements.

Figure 6 shows current injection dependence of emission spectra of the sample with the 1.6 nm Mg-doped layer. An intensity ratio of the p-side blue active region to the n-side violet active region was increased with an increase of a current injection up to 100 mA. Two possibilities are considered. One is that holes are built up at the p-side active region with the increase of the current injection due to heavy mass and short diffusion length. The other is that the nonradiative recombinations in the p-type active are saturated with the increase of the current injection.

Figure 7 shows  $I$ - $V$  characteristics of all the samples. For comparison, the case of our conventional GaInN/Si-doped GaN 5QW blue LED are also plotted. The forward voltages were about 4.07–4.17 at 20 mA for all the samples contain-

ing two active regions with the intermediate layer, while that of our conventional LED were 3.33 V. The high forward voltages for the samples with the two active regions are presumably due to the thicker total thicknesses (135 nm instead of 75 nm in the conventional LED) of the active regions and also undoped barriers of the MQWs.

#### 4. Summary

We have grown the two different active regions separated with the Mg-doped intermediate layer placed in the single pn-junction. Room temperature PL spectra of all the samples basically showed similar spectrum patterns, meaning that the active region qualities were similar. At the same time, very different emission spectra by current injection of 20 mA were observed among the samples. The samples with the 0.8 and 1.6 nm Mg-doped layers in the intermediate layers clearly showed the two different emissions simultaneously from the n- and p-side active regions. At the same time, the samples showing two emissions resulted in lower light output intensities by current injection, possibly caused by the unintentional Mg incorporation in one of the active regions. The intensity ratio between the two emissions was changed by changing the current injection.

#### Acknowledgments

This work was partly supported by the Hibi Science Foundation and Ministry of Education, Culture, Sports, Science and Technology Supported Program for the Strategic Research Foundation at Private Universities, 2012–2016. The SIMS measurements were carried out by courtesy of Toray Research Center, Inc.

- 1) R. Dahal, B. Pantha, J. Y. Lin, and H. X. Jiang: *Appl. Phys. Lett.* **94** (2009) 063505.
- 2) S. Nakamura, M. Senoh, S. Nagahama, N. Iwasa, T. Yamada, T. Mukai, Y. Sugimoto, and H. Kiyoku: *Appl. Phys. Lett.* **69** (1996) 4056.
- 3) I. Ozden, E. Makarona, A. V. Nurmikko, T. Takeuchi, and M. Krames: *Appl. Phys. Lett.* **79** (2001) 2532.
- 4) C. H. Chen, S. J. Chang, Y. K. Su, J. K. Sheu, J. F. Chen, C. H. Kuo, and Y. C. Lin: *IEEE Photonics Technol. Lett.* **14** (2002) 908.
- 5) R. Charash, P. P. Maaskant, L. Lewis, C. McAleese, M. J. Kappers, C. J. Humphreys, and B. Corbett: *Appl. Phys. Lett.* **95** (2009) 151103.
- 6) Z. Y. Zhang, L. E. Cai, B. P. Zhang, X. L. Hu, F. Jiang, J. Z. Yu, and Q. M. Wang: *Appl. Phys. Lett.* **95** (2009) 161110.
- 7) Y. D. Qi, H. Liang, W. Tang, Z. D. Lu, and K. M. Lau: *J. Cryst. Growth* **272** (2004) 333.
- 8) I.-K. Park, J.-Y. Kim, M.-K. Kwon, C.-Y. Cho, J.-H. Lim, and S.-J. Park: *Appl. Phys. Lett.* **92** (2008) 091110.
- 9) S.-C. Shei, J.-K. Sheu, C.-M. Tsai, W.-C. Lai, M.-L. Lee, and C.-H. Kuo: *Jpn. J. Appl. Phys.* **45** (2006) 2463.
- 10) C.-F. Huang, T.-Y. Tang, J.-J. Huang, W.-Y. Shiao, and C. C. Yang: *Appl. Phys. Lett.* **89** (2006) 051913.
- 11) Y.-L. Li, Th. Gessmann, E. F. Schubert, and J. K. Sheu: *J. Appl. Phys.* **94** (2003) 2167.
- 12) M. Funato, T. Kondou, K. Hayashi, S. Nishiura, M. Ueda, Y. Kawakami, Y. Narukawa, and T. Mukai: *Appl. Phys. Express* **1** (2008) 011106.
- 13) C.-Y. Cho, I.-K. Park, M.-K. Kwon, J.-Y. Kim, S.-J. Park, D.-R. Jung, and K.-W. Kwon: *Appl. Phys. Lett.* **93** (2008) 241109.
- 14) S. W. Corzine, R. S. Geels, R. H. Yan, J. W. Scott, L. A. Coldren, and P. L. Gourley: *IEEE Photonics Technol. Lett.* **1** (1989) 52.
- 15) C. Ellmers, M. R. Hofmann, D. Karaiskaj, S. Lew, W. Stolz, W. W. Ruhle, and M. Hilpert: *Appl. Phys. Lett.* **74** (1999) 1367.

## Concentrating Properties of Nitride-Based Solar Cells Using Different Electrodes

This content has been downloaded from IOPscience. Please scroll down to see the full text.

2013 Jpn. J. Appl. Phys. 52 08JH02

(<http://iopscience.iop.org/1347-4065/52/8S/08JH02>)

View [the table of contents for this issue](#), or go to the [journal homepage](#) for more

Download details:

IP Address: 202.11.1.201

This content was downloaded on 03/03/2017 at 06:58

Please note that [terms and conditions apply](#).

You may also be interested in:

[Correlation between Device Performance and Defects in GaInN-Based Solar Cells](#)

Mikiko Mori, Shinichiro Kondo, Shota Yamamoto et al.

[GaInN-Based Solar Cells Using Strained-Layer GaInN/GaInN Superlattice Active Layer on a Freestanding GaN Substrate](#)

Yousuke Kuwahara, Takahiro Fujii, Toru Sugiyama et al.

[Realization of Nitride-Based Solar Cell on Freestanding GaN Substrate](#)

Yosuke Kuwahara, Takahiro Fujii, Yasuharu Fujiyama et al.

[InGaN/GaN Multiple Quantum Well Solar Cells with Good Open-Circuit Voltage and Concentrator Action](#)

Xue-Fei Li, Xin-He Zheng, Dong-Yan Zhang et al.

[Barrier Thickness Dependence of Photovoltaic Characteristics of InGaN/GaN Multiple Quantum Well Solar Cells](#)

Noriyuki Watanabe, Haruki Yokoyama, Naoteru Shigekawa et al.

[Photovoltaic Response of InGaN/GaN Multiple-Quantum Well Solar Cells](#)

Sirona Valdueza-Felip, Anna Mukhtarova, Qing Pan et al.

[Multijunction GaInN-based solar cells using a tunnel junction](#)

Hironori Kurokawa, Mitsuru Kaga, Tomomi Goda et al.

## Concentrating Properties of Nitride-Based Solar Cells Using Different Electrodes

Mikiko Mori<sup>1</sup>, Shinichiro Kondo<sup>1</sup>, Shota Yamamoto<sup>1</sup>, Tatsuro Nakao<sup>1</sup>, Motoaki Iwaya<sup>1</sup>,  
Tetsuya Takeuchi<sup>1</sup>, Satoshi Kamiyama<sup>1</sup>, Isamu Akasaki<sup>1,2</sup>, and Hiroshi Amano<sup>2,3</sup>

<sup>1</sup>Faculty of Science and Technology, Meijo University, Nagoya 468-8502, Japan

<sup>2</sup>Akasaka Research Center, Nagoya University, Nagoya 464-8603, Japan

<sup>3</sup>Graduate School of Engineering, Nagoya University, Nagoya 464-8603, Japan

Received October 11, 2012; accepted December 14, 2012; published online May 20, 2013

We investigated the concentration properties of GaInN-based solar cells using different window electrodes. A significant difference was observed between the concentrating properties of the window electrode structures. It was clearly found that indium tin oxide (ITO) is suitable as an electrode. The short-circuit current density, open-circuit voltage, fill factor, and energy conversion efficiency of nitride-based solar cells fabricated using an ITO electrode were  $7.1 \times 10^2$  mA/cm<sup>2</sup>, 2.2 V, 79%, and 4.0%, respectively, under an air mass filter of 1.5G at 300 suns and at room temperature. © 2013 The Japan Society of Applied Physics

### 1. Introduction

Nitride material systems including AlN, GaN, InN, and their alloys are widely used as light-emitting diodes and laser diodes.<sup>1-4</sup> Since the band gap of GaInN ternary alloys covers a broad range from 0.65 to 3.43 eV,<sup>5</sup> these alloys are suitable for solar cell applications.<sup>6-8</sup> Up to now, a few studies on III-nitride solar cells have been reported.<sup>9-11</sup> We have previously reported the fabrication of GaInN-based solar cells.<sup>12-16</sup> By improving the crystal quality of GaInN with a low InN molar fraction by applying GaInN superlattice (SL) structures,<sup>13</sup> the conversion efficiency of nitride-based solar cells has been improved. We also reported that it is essential to realize a low pit density, which should be lower than  $10^7$  cm<sup>-2</sup>, to realize high-performance GaInN-based solar cells with a high open-circuit voltage ( $V_{OC}$ ) and fill factor (FF) at 1 sun.<sup>14</sup>

However, when GaInN-based solar cells with a high InN molar fraction were fabricated, favorable performance was not observed because of the increase in the leakage current. Furthermore, there are several disadvantages of nitride-based solar cells. One of the disadvantages of compound semiconductor solar cells is their high cost compared with Si and organic solar cells. This problem can be solved by using a solar concentrator. Furthermore, a condenser can be designed to lower the production cost. The performances of the solar cells using other material systems such as AlGaInP and GaInAs have been improved by the concentration of sunlight.<sup>17-20</sup> Although we have reported the properties of nitride-based solar cells under a concentrated light illumination,<sup>16</sup> they have not been analyzed in detail. In particular, the window electrode pattern under concentration light has not been discussed in detail. In nitride semiconductor solar cells, the resistivity of p-GaN is high, making it difficult to form a satisfactory ohmic contact with the material. In addition, there are few metals with a high work function comparable to the work function of p-GaN that can also form a low-resistance interface with GaN. The structure of most nitride-based solar cells reported so far has been p-side-up, because it is difficult to realize a p-type ohmic contact when p-GaN is etched by dry etching. In general, the resistivity of p-GaN is two orders of magnitude higher than that of n-GaN. Therefore, the p-electrode of nitride-based solar cells may be an essential feature of the high current

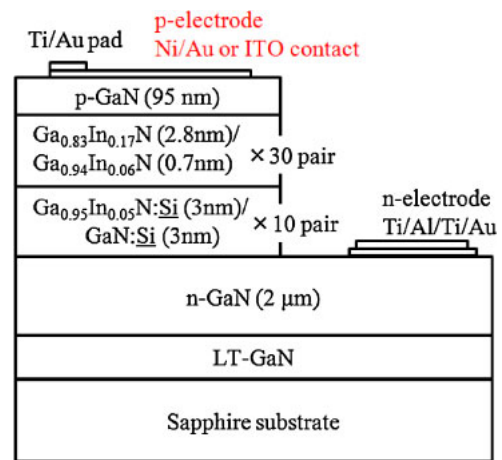


Fig. 1. (Color online) Schematic view of device structure.

spreading. Generally, a grid electrode is used in solar cells based on other material systems. Probably, there is a suitable electrode structure for each material. It is important to investigate the electrode structure to improve the conversion efficiency of nitride-based solar cells.

In this study, we optimized the window electrode pattern for GaInN-based solar cells. We also investigated the concentrating properties of such nitride-based solar cells at light intensities of up to 300 suns.

### 2. Experimental Methods

Figure 1 shows a schematic view of the device structure. The device structure is a GaInN-based solar cell with a GaInN/GaInN superlattice active layer on a sapphire substrate covered with a low-temperature buffer layer.<sup>21</sup> We grew 50 pairs of unintentionally doped Ga<sub>0.83</sub>In<sub>0.17</sub>N (3 nm)/Ga<sub>0.93</sub>In<sub>0.07</sub>N (0.6 nm) superlattice layers as active layers on freestanding GaN substrates. Another 10 pairs of Si-doped Ga<sub>0.90</sub>In<sub>0.10</sub>N (3 nm)/GaN (3 nm) superlattice layers were inserted beneath the active layers. The Si concentration in the 10 pairs of superlattice layers was  $3 \times 10^{18}$  cm<sup>-3</sup>. The role of the additional Si-doped superlattice layers was to suppress the generation and growth of V-shaped pits.<sup>22</sup> The density of V-shaped pits in this sample is lower than  $1 \times 10^7$  cm<sup>-2</sup>, which is sufficient to achieve

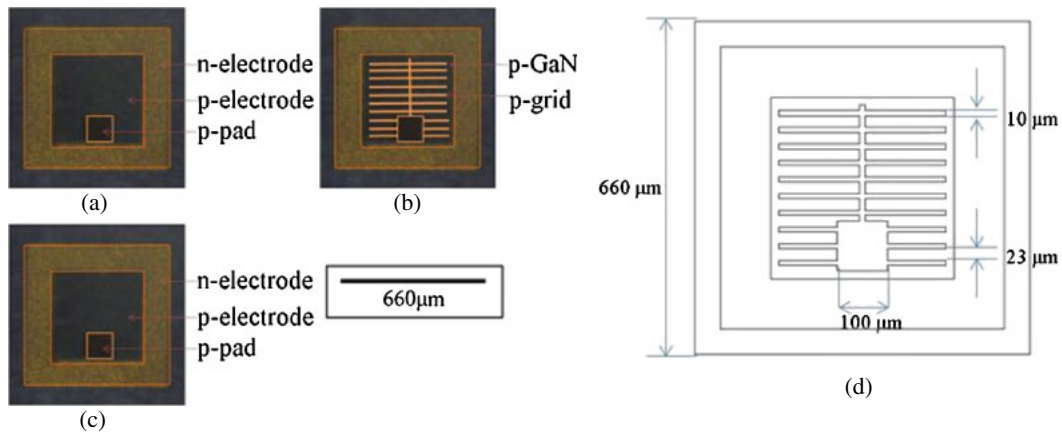


**Fig. 2.** (Color online) (a)–(c) Schematic views of electrode structure: (a) Ni/Au, (b) Ni/Au grid, and (c) ITO. (Orange line is auxiliary line of contact area.) (d) Size of the grid electrode in detail.

high-performance nitride-based solar cells with high  $V_{OC}$  and FF at 1 sun.

Figures 2(a)–2(c) show microscopy images observed from the top of each device. Figure 2(d) also shows the dimensions of the Ni/Au grid electrode in detail. Three samples with different p-electrodes were investigated. In the type I sample [Fig. 2(a)], Ni/Au whole-area electrodes (5 nm/5 nm) were deposited on a p-GaN layer by electron beam evaporation, and rapid thermal annealing was performed at 525 °C in oxygen for 5 min. This electrode structure is often used in typical nitride-based LEDs. In the type II sample [Figs. 2(b) and 2(d)], Ni/Au (5 nm/5 nm) grid electrodes were deposited on p-GaN layers by electron beam evaporation. This structure is often used in solar cells based on other material systems. Details of the electrode structure such as the sizes of finger and bus-bar electrodes are shown in Fig. 2(d). In the type III sample [Fig. 2(c)], indium tin oxide (ITO) whole-area electrodes (100 nm) were deposited on p-GaN layers by sputtering, and rapid thermal annealing was performed at 550 °C in nitrogen for 10 min. An ITO electrode has commonly been used in recent blue LEDs. Ti/Al/Ti/Au (30 nm/100 nm/20 nm/150 nm) electrodes were deposited by electron beam evaporation as ohmic contacts to the n-GaN layers.

Figure 3 shows the transmittances of the Ni/Au and ITO electrodes. Table I also summarizes the transmittances of these electrodes and the specific contact resistance between p-GaN and these electrodes.<sup>23)</sup> Although the transmittance of the ITO electrode in the visible region is higher than that of the Ni/Au electrode, the contact resistance and specific contact resistance between p-GaN are higher than those for the Ni/Au electrode. In addition, the transmittance of the ITO electrode in the UV region (300 nm or less) is lower than that of the Ni/Au electrode. In this study, the structure of the Ni/Au grid electrode and the thickness of the ITO electrode were optimized at 1 sun.

The conversion efficiencies of these devices were measured using an air mass 1.5 G (AM 1.5G) solar simulator (Asahi Spectra HAL-320). Both the irradiation area and the light intensity were varied to concentrate the light. The current density versus voltage characteristics of each device were measured at light intensities from 1 to 300 suns at room

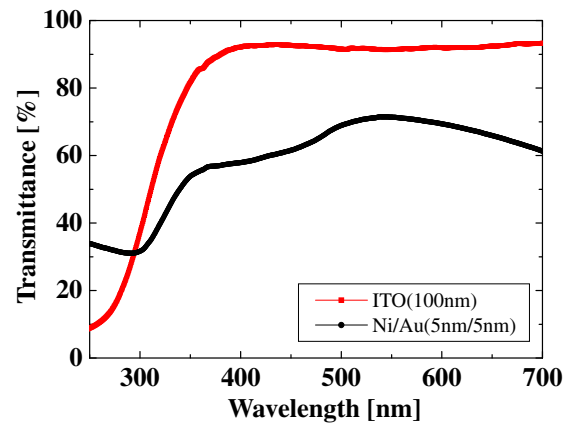


**Fig. 3.** (Color online) Transmittances of ITO and Ni/Au electrodes.

**Table I.** Characteristics of Ni/Au and ITO electrodes.

Material	Thickness (nm)	Sheet resistance ( $\Omega/\square$ )	Specific contact resistance ( $\Omega\cdot\text{cm}^2$ )	Transmittance (400 nm) (%)
Ni/Au (5 nm/5 nm)	10	14	$5.3 \times 10^{-4}$	58
ITO (100 nm)	$1.0 \times 10^2$	$2.9 \times 10^2$	$2.6 \times 10^{-3}$	92

temperature (RT). We investigated the concentrating properties of such nitride-based solar cells at light intensities of up to 300 suns.

### 3. Results and Discussion

Figure 4 shows the current density versus voltage characteristics of the nitride-based solar cells under the solar simulator (AM 1.5G, 1 to 300 suns) at RT. The solar cells exhibited good characteristics from 1 to 300 suns. We found that  $J_{SC}$  and  $V_{OC}$  for the nitride-based solar cells increased with increasing concentration ratio.

The short-circuit current density ( $J_{SC}$ ),  $V_{OC}$ , series resistance ( $R_S$ ), shunt resistance ( $R_{SH}$ ), FF, and energy conversion efficiency ( $\eta$ ) at 1 and 300 suns for each sample

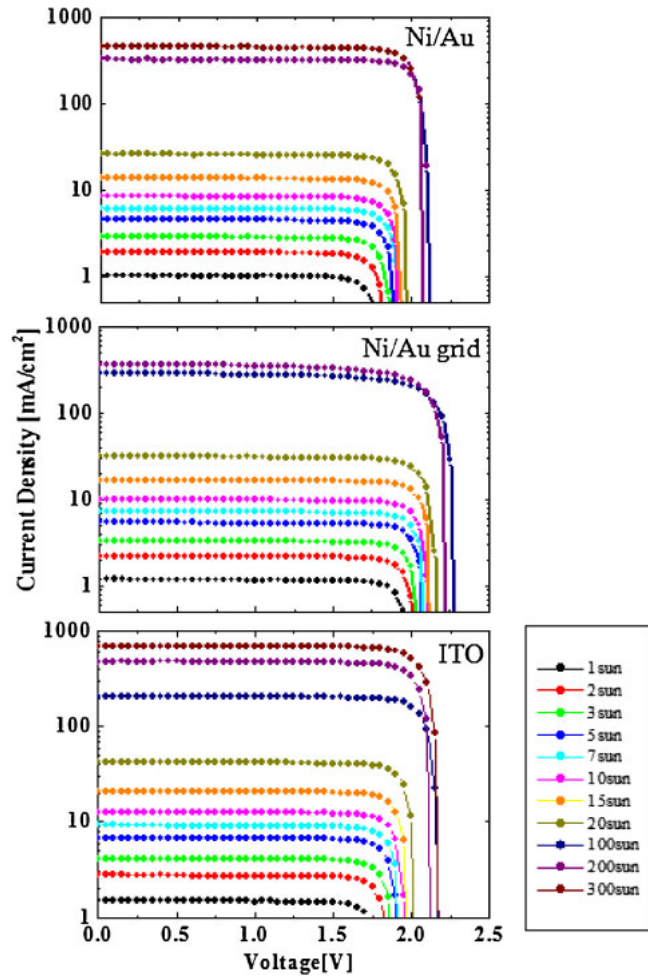


Fig. 4. (Color online)  $I$ - $V$  curves of solar cells using each electrode under solar simulator (AM 1.5G, 1 to 300 suns) at RT.

Table II. Device performance characteristics under solar simulator (AM 1.5G, 1 sun) at RT.

p-electrode	$V_{OC}$ (V)	FF (%)	$J_{SC}$ (mA/cm <sup>2</sup> )	$\eta$ (%)	$R_S$ ( $\Omega$ -cm <sup>2</sup> )	$R_{SH}$ ( $\Omega$ -cm <sup>2</sup> )
Ni/Au	1.8	82	1.0	1.5	$1.7 \times 10^2$	$3.4 \times 10^4$
Ni/Au grid	2.0	82	1.2	1.9	$4.9 \times 10^2$	$3.9 \times 10^4$
ITO	1.8	82	1.5	2.2	$2.1 \times 10^2$	$3.4 \times 10^4$

Table III. Device performance characteristics under solar simulator (AM 1.5G, 300 suns) at RT.

p-electrode	$V_{OC}$ (V)	FF (%)	$J_{SC}$ (mA/cm <sup>2</sup> )	$\eta$ (%)	$R_S$ ( $\Omega$ -cm <sup>2</sup> )	$R_{SH}$ ( $\Omega$ -cm <sup>2</sup> )
Ni/Au	2.1	81	$4.5 \times 10^2$	2.5	1.0	34
Ni/Au grid	2.2	64	$3.7 \times 10^2$	1.8	3.2	85
ITO	2.2	79	$7.1 \times 10^2$	4.0	0.8	50

using different electrodes are summarized in Tables II and III, respectively.

Figure 5 shows  $J_{SC}$  and  $V_{OC}$  as a function of the concentration ratio. We compared these results with the solar cell characteristics of other material systems. In theory,  $J_{SC}$  for solar cells should increase linearly with increasing concentration ratio. From Fig. 5,  $J_{SC}$  for all samples

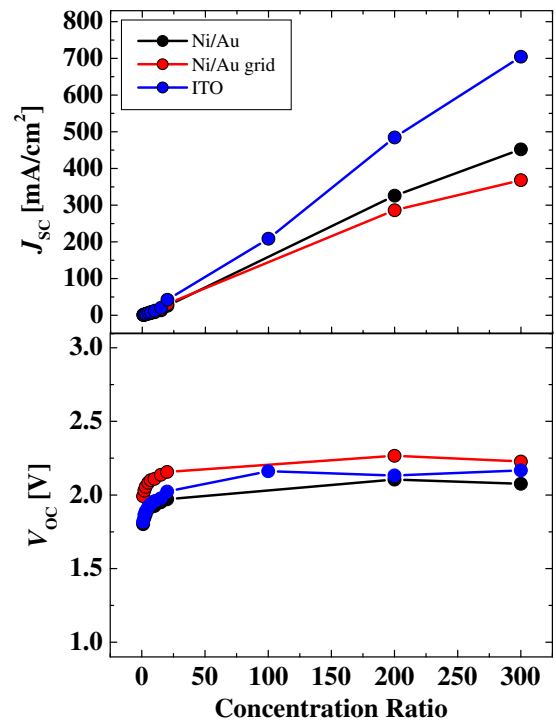


Fig. 5. (Color online)  $J_{SC}$  and  $V_{OC}$  as a function of concentration ratio.

increased linearly with increasing concentration ratio. Among the three types of electrode structure,  $J_{SC}$  is highest for the ITO electrodes. This is because the transmittance of ITO electrodes is higher than that of Ni/Au electrodes.

Next, we consider  $V_{OC}$ , where  $V_{OC}$  for a condenser can be defined as follows:<sup>24)</sup>

$$V_{OC} = \frac{nkT}{q} \ln\left(\frac{J_{SC}}{J_0} + 1\right). \quad (1)$$

Here,  $J_0$ ,  $n$ ,  $k$ ,  $T$ , and  $q$  are the reverse saturation current, nonideality factor, Boltzmann constant, temperature, and elementary charge, respectively. According to Eq. (1),  $V_{OC}$  should increase logarithmically with the increased condensations of light. The results for all samples almost match the theory from 1 to 300 suns. Moreover, among the three types of electrode structure,  $V_{OC}$  for the solar cell using a Ni/Au grid electrode was slightly higher. This slight difference is caused by the small coverage of pits by the Ni/Au grid electrode, because the contact area of the Ni/Au grid electrode is narrower than that of the other electrodes.

Figure 6 shows FF and  $\eta$  as a function of the concentration ratio. Although FF for the solar cells using ITO and Ni/Au whole-area electrodes remained constant upon changing the concentration ratio, that of the solar cell using a Ni/Au grid electrode was greatly reduced with increasing concentration ratio. As a result,  $\eta$  for the solar cell using the Ni/Au grid electrode showed almost no increase with increasing concentration ratio. We next discuss the cause of the difference in the concentrating characteristics of FF in each solar cell.

Figure 7 shows  $R_S$  and  $R_{SH}$  for each solar cell as a function of the concentration ratio. Although  $R_S$  and  $R_{SH}$  for all samples decrease with increasing concentration ratio, the rate of decrease of  $R_S$  in the solar cells using a Ni/Au grid

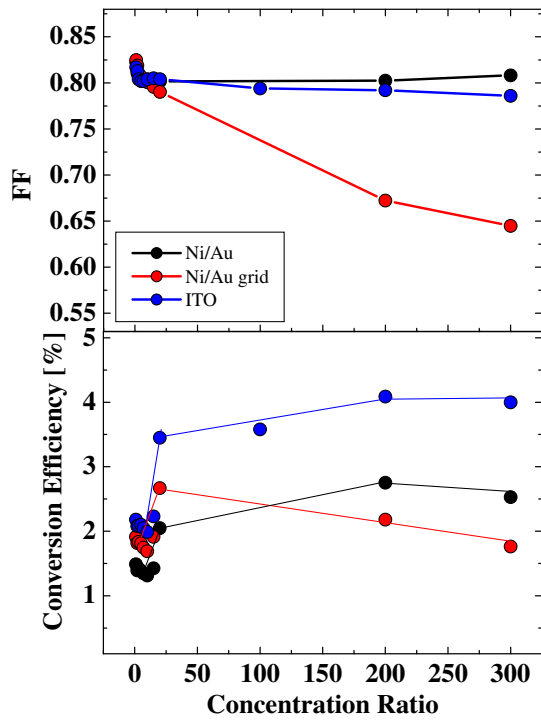


Fig. 6. (Color online) FF and  $\eta$  as a function of concentration ratio.

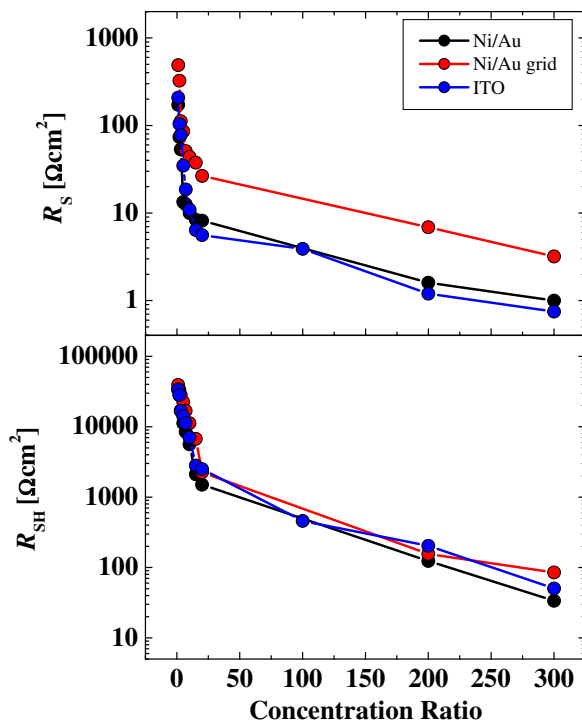


Fig. 7. (Color online)  $R_S$  and  $R_{SH}$  as a function of concentration ratio.

electrode is lower than that of other samples. The high resistance of p-GaN may affect the solar cell using the Ni/Au grid electrode. From the equivalent circuit of the solar cell shown in Fig. 8,<sup>25)</sup> the energy loss ( $P_{loss}$ ) due to the series resistance of the solar cell can be represented as follows:

$$P_{loss} = I_C^2 R_S, \tag{2}$$

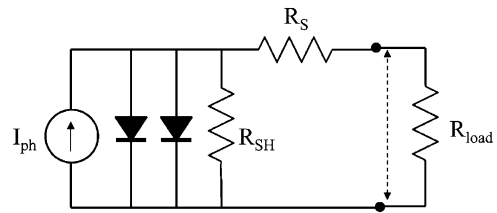


Fig. 8. Equivalent circuit of solar cell.  $I_{ph}$  and  $R_{load}$  are photocurrent and external resistance, respectively.

where  $I_C$  is the circuit current flowing to  $R_{load}$ . Therefore, the extraction of energy from the solar cell using the Ni/Au grid electrode is decreased with increasing circuit current owing to the high concentration ratio. Since the resistivity of the p-type nitride semiconductor layer is higher than that of other material systems, we concluded that the grid electrode is not suitable for GaInN-based solar cells with the p-side-up structure. Therefore, we concluded that the ITO whole-area electrode is suitable as an electrode for GaInN-based solar cells with the p-side-up structure, although there is an issue regarding the cost due to the scarcity of indium.<sup>26)</sup> We also believe that in the future there will be a need to consider GaInN-based solar cells with the n-side-up structure<sup>27,28)</sup> fabricated using the laser liftoff method<sup>29,30)</sup> and other methods. To realize high-performance GaInN-based solar cells, it is necessary to achieve good current spreading of the p-electrode.  $V_{OC}$ ,  $J_{SC}$ , FF, and  $\eta$  for the solar cell with the ITO whole-area contacts were 2.2 V,  $7.1 \times 10^2$  mA/cm<sup>2</sup>, 79%, and 4.0% at 300 suns, respectively.

#### 4. Conclusions

We investigated the correlation between the device performance and the window electrode pattern for GaInN-based solar cells. To realize high-performance GaInN-based solar cells with a high  $V_{OC}$  and FF, it is essential to realize a low  $R_S$  and high  $R_{SH}$ .  $V_{OC}$  and  $\eta$  for the cells were found to increase with increasing light intensity. The conversion efficiency of the solar cell using an ITO p-electrode was the highest at light intensities from 1 to 300 suns because of its good performance in increasing the concentration of incident light and its low  $R_S$ . As a result, we obtained  $\eta$  of up to 4.0% by irradiating concentrated sunlight with a light intensity of up to 300 suns.

#### Acknowledgments

This study was partially supported by the New Energy and Industrial Technology Development Organization (NEDO) Project, “Research and Development on Innovative Solar Cells” and the Program for the Strategic Research Foundation at Private Universities, 2012–2016, supported by the Ministry of Education, Culture, Sports, Science and Technology, Japan (MEXT).

- 1) H. Amano, A. Miyazaki, K. Iida, T. Kawashima, M. Iwaya, S. Kamiyama, I. Akasaki, R. Liu, A. Bell, F. A. Ponce, S. Sahonta, and D. Cherns: *Phys. Status Solidi A* **201** (2004) 2679.
- 2) Q. Dai, M. F. Schubert, M. H. Kim, J. K. Kim, E. F. Schubert, D. D. Koleske, M. H. Crawford, S. R. Lee, A. J. Fischer, G. Thaler, and M. A. Banas: *Appl. Phys. Lett.* **94** (2009) 111109.
- 3) I. Akasaki and H. Amano: *Jpn. J. Appl. Phys.* **45** (2006) 9001.

- 4) C. Pernot, M. Kim, S. Fukahori, T. Inazu, T. Fujita, Y. Nagasawa, A. Hirano, M. Ippommatsu, M. Iwaya, S. Kamiyama, I. Akasaki, and H. Amano: *Appl. Phys. Express* **3** (2010) 061004.
- 5) V. Yu. Davydov, A. A. Klochikhin, R. P. Seisyan, V. V. Emtsev, S. V. Ivanov, F. Bechstedt, J. Furthmüller, H. Harima, A. V. Mudryi, J. Aderhold, O. Semchinova, and J. Graul: *Phys. Status Solidi B* **229** (2002) r1.
- 6) R. Liu, J. Mei, S. Srinivasan, F. A. Ponce, H. Omiya, Y. Narukawa, and T. Mukai: *Appl. Phys. Lett.* **89** (2006) 201911.
- 7) J. Wu, W. Walukiewicz, K. M. Yu, J. W. Ager, III, E. E. Haller, H. Lu, W. J. Schaff, Y. Saito, and Y. Nanishi: *Appl. Phys. Lett.* **80** (2002) 3967.
- 8) H. Hamzaoui, A. S. Bouazzi, and B. Rezig: *Sol. Energy Mater. Sol. Cells* **87** (2005) 595.
- 9) C. J. Neufeld, N. G. Toledo, S. C. Cruz, M. Iza, S. P. DenBaars, and U. K. Mishra: *Appl. Phys. Lett.* **93** (2008) 143502.
- 10) K. Y. Lai, G. J. Lin, Y. L. Lai, Y. F. Chen, and J. H. He: *Appl. Phys. Lett.* **96** (2010) 081103.
- 11) J. R. Lang, C. J. Neufeld, C. A. Hurni, S. C. Cruz, E. Matioli, U. K. Mishra, and J. S. Speck: *Appl. Phys. Lett.* **98** (2011) 131115.
- 12) Y. Kuwahara, Y. Fujiyama, M. Iwaya, S. Kamiyama, H. Amano, and I. Akasaki: *Phys. Status Solidi C* **7** (2010) 1807.
- 13) T. Sugiyama, Y. Kuwahara, Y. Isobe, T. Fujii, K. Nonaka, M. Iwaya, T. Takeuchi, S. Kamiyama, I. Akasaki, and H. Amano: *Appl. Phys. Express* **4** (2011) 015701.
- 14) M. Mori, S. Kondo, S. Yamamoto, T. Nakao, T. Fujii, M. Iwaya, T. Takeuchi, S. Kamiyama, I. Akasaki, and H. Amano: *Appl. Phys. Express* **5** (2012) 082301.
- 15) Y. Kuwahara, T. Fujii, T. Sugiyama, D. Iida, Y. Isobe, Y. Fujiyama, Y. Morita, M. Iwaya, T. Takeuchi, S. Kamiyama, I. Akasaki, and H. Amano: *Appl. Phys. Express* **4** (2011) 021001.
- 16) S. Yamamoto, M. Mori, Y. Kuwahara, T. Fujii, T. Nakao, S. Kondo, M. Iwaya, T. Takeuchi, S. Kamiyama, I. Akasaki, and H. Amano: *Phys. Status Solidi: Rapid Res. Lett.* **6** (2012) 145.
- 17) A. Braun, N. Szabó, K. Schwarzburg, T. Hannappel, E. A. Katz, and J. M. Gordon: *Appl. Phys. Lett.* **98** (2011) 223506.
- 18) M. A. Steiner and J. F. Geisz: *Appl. Phys. Lett.* **100** (2012) 251106.
- 19) S. Ma, H. Sodabanlu, K. Watanabe, M. Sugiyama, and Y. Nakano: *Jpn. J. Appl. Phys.* **51** (2012) 10ND09.
- 20) Y. Wen, Y. Wang, and Y. Nakano: *Appl. Phys. Lett.* **100** (2012) 053902.
- 21) H. Amano, N. Sawaki, I. Akasaki, and Y. Toyoda: *Appl. Phys. Lett.* **48** (1986) 353.
- 22) T. Fujii, Y. Kuwahara, D. Iida, Y. Fujiyama, Y. Morita, T. Sugiyama, Y. Isobe, M. Iwaya, T. Takeuchi, S. Kamiyama, I. Akasaki, and H. Amano: *Phys. Status Solidi C* **8** (2011) 2463.
- 23) K. Takehara, K. Takeda, N. Kengo, H. Sakurai, S. Ito, M. Iwaya, S. Kamiyama, H. Amano, and I. Akasaki: *Phys. Status Solidi C* **8** (2011) 2375.
- 24) J. Nelson: *The Physics of Solar Cells* (Imperial College Press, London, 2003) p. 142.
- 25) C. Chibbaro, M. Zimbone, G. Litrico, P. Baeri, M. L. Lo Trovato, and F. Aleo: *Jpn. J. Appl. Phys.* **110** (2011) 044505.
- 26) J.-P. Shim, M. Choe, S.-R. Jeon, D. Seo, T. Lee, and D.-S. Lee: *Appl. Phys. Express* **4** (2011) 052302.
- 27) T. Gu, M. A. El-Emawy, K. Yang, A. Stintz, and L. F. Lester: *Appl. Phys. Lett.* **95** (2009) 261106.
- 28) V. Smirnov, O. Astakhov, R. Carius, B. E. Pieters, Y. Petrusenko, V. Borysenko, and F. Finger: *Appl. Phys. Lett.* **101** (2012) 143903.
- 29) T. Fujii, Y. Gao, R. Sharma, E. L. Hu, S. P. DenBaars, and S. Nakamura: *Appl. Phys. Lett.* **84** (2004) 855.
- 30) T. Ueda, M. Ishida, and M. Yuri: *Jpn. J. Appl. Phys.* **50** (2011) 041001.

## Low-ohmic-contact-resistance V-based electrode for n-type AlGa<sub>N</sub> with high AlN molar fraction

This content has been downloaded from IOPscience. Please scroll down to see the full text.

2016 Jpn. J. Appl. Phys. 55 05FL03

(<http://iopscience.iop.org/1347-4065/55/5S/05FL03>)

View [the table of contents for this issue](#), or go to the [journal homepage](#) for more

Download details:

IP Address: 219.127.71.134

This content was downloaded on 03/03/2017 at 06:40

Please note that [terms and conditions apply](#).

You may also be interested in:

[Electrical properties of n-type AlGa<sub>N</sub> with high Si concentration](#)

Kunihiro Takeda, Motoaki Iwaya, Tetsuya Takeuchi et al.

[Development of nanoscale Ni-embedded single-wall carbon nanotubes by electroless plating for transparent conductive electrodes of 375 nm AlGa<sub>N</sub>-based ultraviolet light-emitting diodes](#)

Jun-Beom Park, Hyung-Jo Park, Hyojung Bae et al.

[Realization of high-performance hetero-field-effect-transistor-type ultraviolet photosensors using p-type GaN comprising three-dimensional island crystals](#)

Yuma Yamamoto, Akira Yoshikawa, Toshiki Kusafuka et al.

[Thermally stable Ti/Al-based ohmic contacts to N-polar n-GaN by using an indium interlayer](#)

Sung Ki Kim, Jae Chun Han and Tae-Yeon Seong

[High Output Power 365 nm Ultraviolet Light Emitting Diode of GaN-Free Structure](#)

Daisuke Morita, Masahiko Sano, Masashi Yamamoto et al.

[Watt-Class High-Output-Power 365 nm Ultraviolet Light-Emitting Diodes](#)

Daisuke Morita, Masashi Yamamoto, Kazuyuki Akaishi et al.

[Hexagonal boron nitride for deep ultraviolet photonic devices](#)

H X Jiang and J Y Lin

[Investigation of V-Ti/Al/Ni/Au Ohmic contact to AlGa<sub>N</sub>/GaN heterostructures with a thin GaN cap layer](#)

Sang Min Jung, Chang Taek Lee and Moo Whan Shin



## Low-ohmic-contact-resistance V-based electrode for n-type AlGa<sub>N</sub> with high AlN molar fraction

Kazuki Mori<sup>1\*</sup>, Kunihiro Takeda<sup>1</sup>, Toshiki Kusafuka<sup>1</sup>, Motoaki Iwaya<sup>1</sup>, Tetsuya Takeuchi<sup>1</sup>, Satoshi Kamiyama<sup>1</sup>, Isamu Akasaki<sup>1,2</sup>, and Hiroshi Amano<sup>2,3</sup>

<sup>1</sup>Faculty of Science and Technology, Meijo University, Nagoya 468-0073, Japan

<sup>2</sup>Akasaka Research Center, Nagoya University, Nagoya 464-8603, Japan

<sup>3</sup>Graduate School of Engineering, Nagoya University, Nagoya 464-8603, Japan

\*E-mail: 143434035@c alumni.meijo-u.ac.jp

Received December 29, 2015; accepted February 23, 2016; published online April 25, 2016

We investigated a V-based electrode for the realization of low ohmic-contact resistivity in n-type AlGa<sub>N</sub> with a high AlN molar fraction characterized by the circular transmission line model. The contact resistivity of n-type Al<sub>0.62</sub>Ga<sub>0.38</sub>N prepared using the V/Al/Ni/Au electrode reached  $1.13 \times 10^{-6} \Omega \text{ cm}^2$ . Using this electrode, we also demonstrated the fabrication of UV light-emitting diodes (LEDs) with an emission wavelength of approximately 300 nm. An operating voltage of LED prepared using a V/Al/Ni/Au electrode was 1.6 V lower at 100 mA current injection than that prepared using a Ti/Al/Ti/Au electrode, with a specific contact resistance of approximately  $2.36 \times 10^{-4} \Omega \text{ cm}^2$  for n-type Al<sub>0.62</sub>Ga<sub>0.38</sub>N.  
© 2016 The Japan Society of Applied Physics

### 1. Introduction

Ultraviolet (UV) light has been used in various fields, such as medicine, chemical treatment, light sensing, and semiconductor manufacturing processes. AlGa<sub>N</sub>-based deep-UV light-emitting diodes (UV LEDs) are expected to be used as the next-generation UV-light emitters that will replace conventional UV lights such as mercury lamps. UV LEDs have many advantages over mercury lamps, such as their small size, long lifetime, and high efficiency. Currently, high external quantum efficiencies of UV LEDs ranging between UV-B (emission wavelength 280–315 nm) and UV-C (emission wavelength: lower than 280 nm) have already been reached.<sup>1–9</sup> From a practical viewpoint, improvement of wall plug efficiency (WPE) of these LEDs is essential. A decrease in device resistance, including the sheet and specific contact resistances ( $\rho_c$ ) of n- and p-type layers, is important for WPE improvement. In particular, the  $\rho_c$  of the n-type AlGa<sub>N</sub> layer with a high AlN molar fraction accounts for a large component of device resistance in these LEDs. Thus, a reduction in  $\rho_c$  in the n-type AlGa<sub>N</sub> layer with a high AlN molar fraction is important.

Many groups have reported the fabrication of an electrode for n-type GaN with good ohmic contact using Ti-, Mo-, and Cr-based four-metal-layer structures.<sup>10–12</sup> The first-layer metal in this electrode is Ti, Mo, or Cr. The metal reacts with GaN to form a nitride metal and generates N vacancies in GaN as donors, thereby increasing the doping level at the metal–semiconductor interface. The second layer is almost always Al, which ensures that the aforementioned doping-level increase does not occur by impeding the out-diffusion of Ga.<sup>13,14</sup> The third layer is a barrier layer that stabilizes the electrode and prevents second-layer oxidation and melting. The fourth layer is a cap layer that prevents the oxidation of the underlying layers.

Ti-based electrodes can form good ohmic contact with n-type AlGa<sub>N</sub> with an AlN molar fraction of up to 0.5.<sup>15–19</sup> However, Ti-based electrodes increase specific contact resistance, thereby increasing the AlN molar fraction. Ti-based electrodes have high specific contact resistance to n-type AlGa<sub>N</sub> with AlN molar fractions above 0.6.<sup>20</sup>

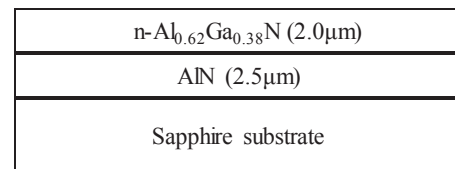


Fig. 1. Schematic structure of n-Al<sub>0.62</sub>Ga<sub>0.38</sub>N.

Recently, France et al. reported a low specific contact resistance of n-type AlGa<sub>N</sub> using a V/Al/V/Au electrode with an AlN molar fraction of 0.6.<sup>21</sup> However, we have found no report on the application of this electrode for UV LEDs, because this electrode has low repeatability. The V/Al bilayers are unreliable after high-temperature annealing because of the propensity for V/Al oxidation to occur and the tendency of Al to melt and ball up. Thus, the barrier layer is important for improving the thermal stability of contacts.

In this study, we investigated the barrier layer of a V-based electrode to improve its stabilization against high-temperature annealing. We evaluated the contact characteristics of each barrier layer under various annealing conditions. Moreover, we demonstrated the fabrication of UV LEDs with 300 nm emission wavelengths using this electrode.

### 2. Experimental procedure

Figure 1 shows a schematic view of the sample structure. The samples were epitaxially grown on a *c*-plane sapphire substrate by metal–organic vapor phase epitaxy. An unintentionally doped, 2.5-μm-thick AlN layer was grown at 1,180 °C and a 2.0-μm-thick Si-doped Al<sub>0.62</sub>Ga<sub>0.38</sub>N layer was sequentially grown. The free-electron concentration in Si-doped Al<sub>0.62</sub>Ga<sub>0.38</sub>N was determined to be approximately  $1.9 \times 10^{18} \text{ cm}^{-3}$  at room temperature (RT) by Hall-effect measurements using the van der Pauw method. Moreover, the resistivity and mobility of this Al<sub>0.62</sub>Ga<sub>0.38</sub>N were  $6.9 \times 10^{-2} \Omega \text{ cm}$  and  $49 \text{ cm}^2 \text{ V}^{-1} \text{ s}^{-1}$ , respectively.

After cleaning with an organic solvent, aqua regia, and hydrogen fluoride, the V (20 nm)/Al (80 nm)/barrier layer (40 nm)/Au (100 nm) electrodes were deposited on this n-type Al<sub>0.62</sub>Ga<sub>0.38</sub>N. Thus far, a Ti-based electrode has been

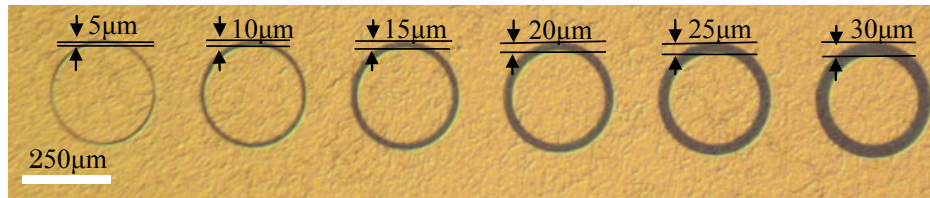
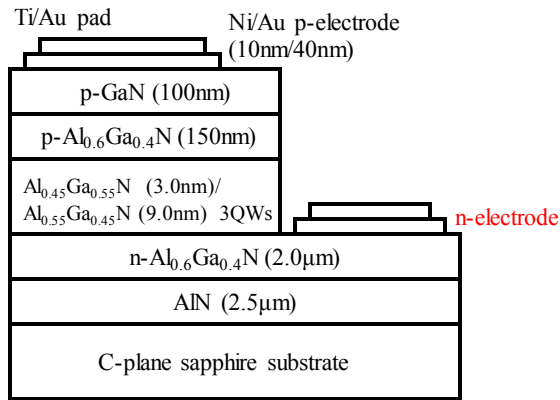
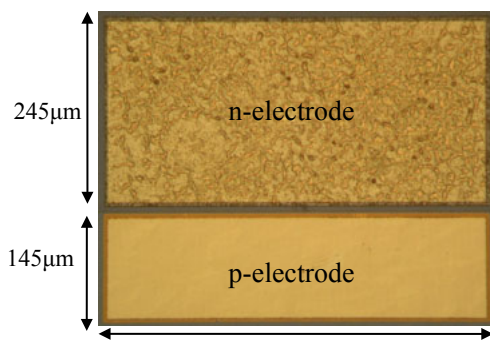


Fig. 2. (Color online) Microscopy image of the electrode patterns for measurements.



(a)



(b)

Fig. 3. (Color online) (a) Structure of UV LEDs with an emitting peak wavelength of 300 nm and (b) Plane view of the electrode pattern.

reported to be introduced into the barrier layer (Ni, Ti, and Mo) between the Ti/Al and Au layers. Therefore, we investigated the dependence of barrier layers on V, Mo, Ti, and Ni. After electrode deposition, the samples were annealed for various times from 1 to 7 min under ambient N<sub>2</sub> at 900 °C. We also prepared a sample using a Ti/Al/Ti/Au electrode as a reference.

Contact characteristics were measured using the circular transmission line model (CTLM) at RT.<sup>22</sup> Figure 2 shows the CTLM patterns obtained in this study. The electrode intervals were 5, 10, 15, 20, 25, and 30 μm. The propagation length ( $L_c$ ) and sheet resistance ( $R_{SH}$ ) were calculated from this measurement. Therefore,  $\rho_c$  was derived from

$$\rho_c = R_{SH} \cdot L_t^2. \quad (1)$$

The structure of UV LEDs with an emitting peak wavelength of 300 nm is shown in Figs. 3(a) and 3(b). UV LEDs were composed of a 2.5-μm-thick AlN template, a 2.0-μm-thick n-type Al<sub>0.6</sub>Ga<sub>0.4</sub>N cladding layer, three pairs of unintentionally doped Al<sub>0.45</sub>Ga<sub>0.55</sub>N/Al<sub>0.55</sub>Ga<sub>0.45</sub>N multi-

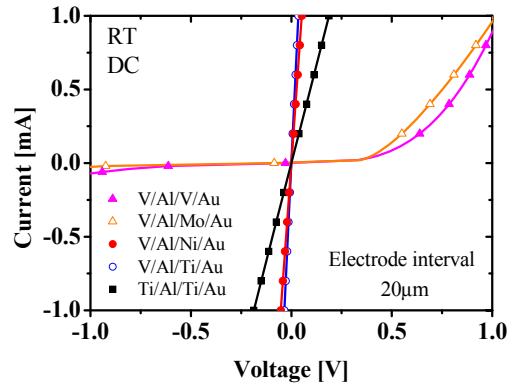


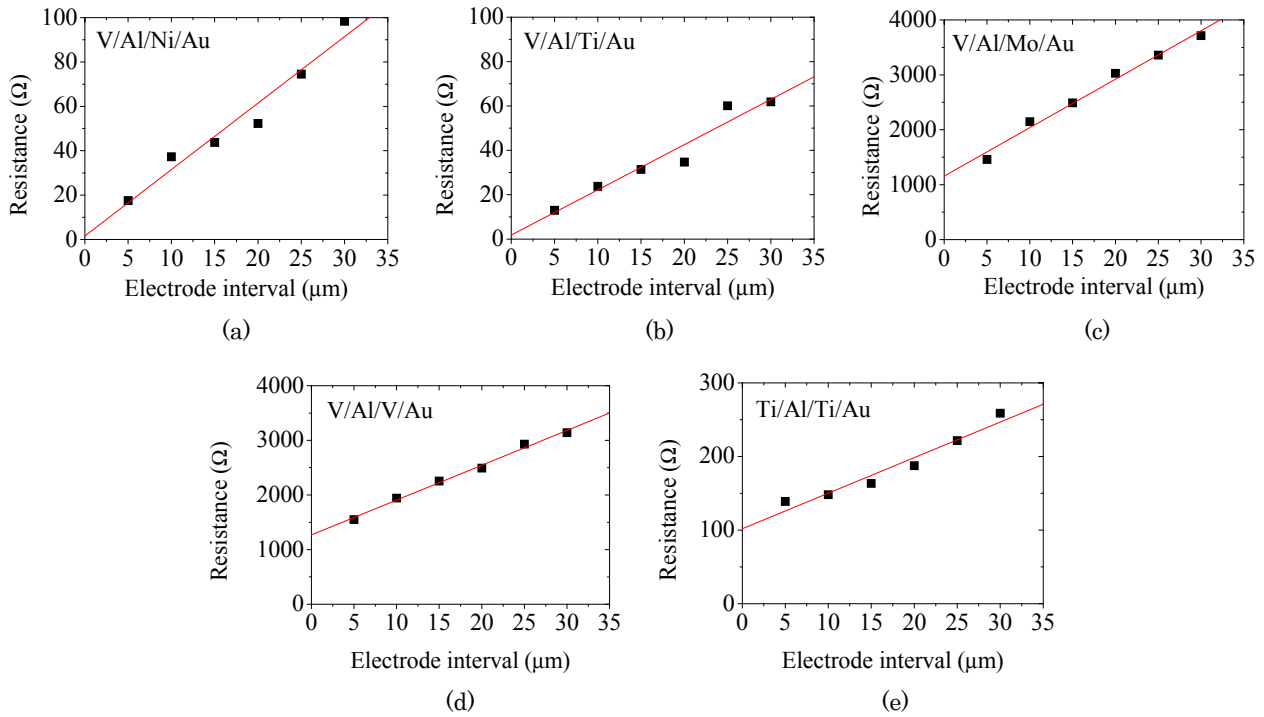
Fig. 4. (Color online)  $I$ - $V$  characteristics of each electrode at an electrode interval of 20 μm.

quantum wells (3QW), a 150-nm-thick p-type Al<sub>0.6</sub>Ga<sub>0.4</sub>N cladding layer, and a 100-nm-thick p-type GaN contact layer. These samples were annealed at 800 °C for 5 min in ambient N<sub>2</sub> for p-type activation. These samples were etched up to n-type AlGa<sub>0.4</sub>N by inductively coupled plasma reactive-ion etching. Then, the n-type electrodes were deposited on the n-type AlGa<sub>0.4</sub>N layer by electron-beam evaporation. The size of the n-type electrode was 500 × 245 μm<sup>2</sup>. After the deposition of these electrodes, they were annealed at 900 °C for 5 min in ambient N<sub>2</sub> to induce ohmic contact to the n-type AlGa<sub>0.4</sub>N layer. Ni/Au (10/40 nm) was deposited on the p-type GaN layer and annealed at 550 °C for 3 min in ambient O<sub>2</sub> to induce ohmic contact to the p-type GaN layer. The size of the p-type electrode was 500 × 140 μm<sup>2</sup>. In addition, Ti/Au (10/200 nm) pad electrodes were formed on all electrodes for implementation. Injection voltage–current ( $V$ - $I$ ) characteristics were measured using a semiconductor parameter analyzer (Agilent 4156C) at RT and DC.

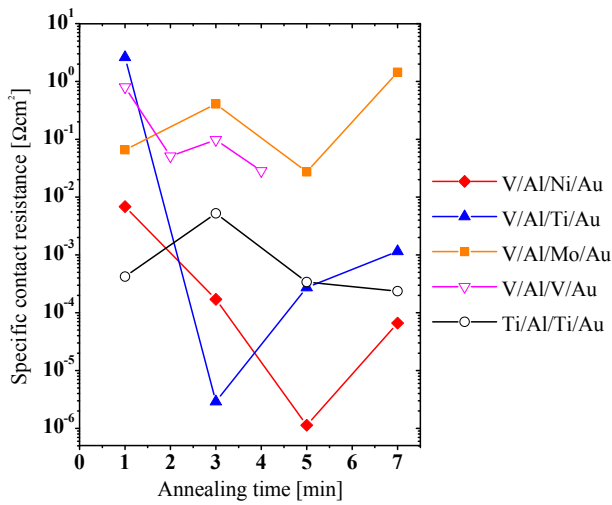
### 3. Results and discussion

Figure 4 shows the current–voltage ( $I$ - $V$ ) characteristics at 20 μm intervals between the Ti/Al/Ti/Au electrodes and V-based electrodes with different barrier layers. For this figure, we describe only the result of optimizing the annealing conditions for each electrode. The optimized annealing times of V/Al/Ti/Au, V/Al/V/Au, V/Al/Ni/Au, and V/Al/Mo/Au electrodes were 3, 4, 5, and 5 min, respectively.

As shown in the figure, the V/Al/V/Au and V/Al/Mo/Au electrodes exhibited nonlinear  $I$ - $V$  characteristics. Introducing V or Mo as a barrier layer formed a Schottky contact. In contrast, the V/Al/Ni/Au and V/Al/Ti/Au electrodes were shown to have good ohmic-contact characteristics. Moreover, the slopes of the  $I$ - $V$  characteristics of the V/Al/Ni/Au and V/Al/Ti/Au electrodes were larger than that of the Ti/Al/Ti/Au electrode. Introducing Ni or Ti as a barrier layer formed



**Fig. 5.** (Color online) Resistance at each electrode interval and optimized annealing time: (a) V/Al/Ni/Au, (b) V/Al/Ti/Au, (c) V/Al/Mo/Au, (d) V/Al/V/Au, and (e) Ti/Al/Ti/Au.



**Fig. 6.** (Color online)  $\rho_c$  of each barrier layer depending on the annealing conditions.

better ohmic contact to the V/Al/Ni/Au and V/Al/Ti/Au electrodes than to the Ti/Al/Ti/Au electrode.

For calculating  $\rho_c$ , resistances between electrodes were measured at each electrode interval. Figures 5(a)–5(e) show the resistance plots at the electrode interval from 5 to 30  $\mu\text{m}$ . Since the resistance plots almost agree with the fitting line, the specific contact resistances obtained are considered reliable in this investigation.

Figure 6 shows the annealing-time dependence of  $\rho_c$  at each electrode at 900  $^\circ\text{C}$  in ambient  $\text{N}_2$ . The  $\rho_c$  values of the V/Al/V/Au and V/Al/Mo/Au electrodes were higher than  $2.84 \times 10^{-2}$  and  $2.73 \times 10^{-2} \Omega\text{cm}^2$ , respectively, even when the annealing time was changed from 1 to 7 min. This is due to the Schottky contact. In contrast to each electrode, the  $\rho_c$

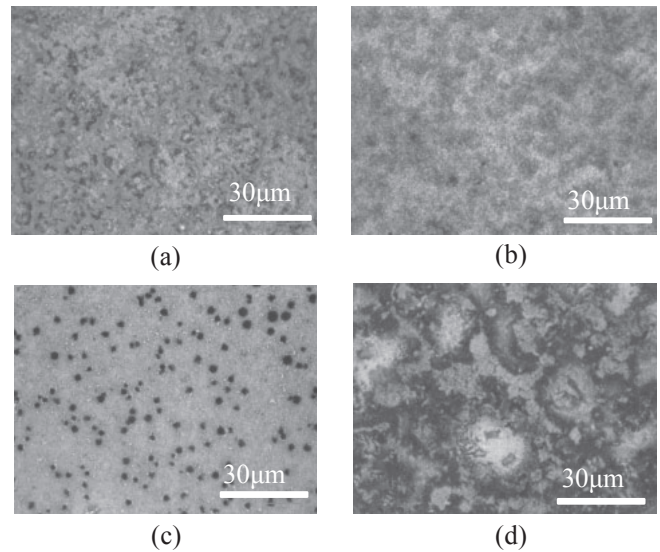


**Fig. 7.** Differential interference microscopy images of (a) V/Al/Ni/Au, (b) V/Al/Ti/Au, (c) V/Al/Mo/Au, and (d) V/Al/V/Au after annealing.

values of V/Al/Ti/Au and V/Al/Ni/Au electrodes were as low as  $2.90 \times 10^{-6}$  and  $1.13 \times 10^{-6} \Omega\text{cm}^2$ , respectively. We found that these two electrodes exhibit low contact resistances for deep UV LEDs, because the  $\rho_c$  value of the Ti/Al/Ti/Au electrode was  $2.36 \times 10^{-4} \Omega\text{cm}^2$  for an annealing time of 5 min. Therefore, we found that Ni and Ti are promising barrier metals for V-based electrodes.

Next, we investigated the mechanism under lying the effect of each barrier metal by the differential interference microscopy method and Auger electron spectroscopy (AES). Figures 7(a)–7(d) show the differential interference microscopy images of each electrode after annealing. We found

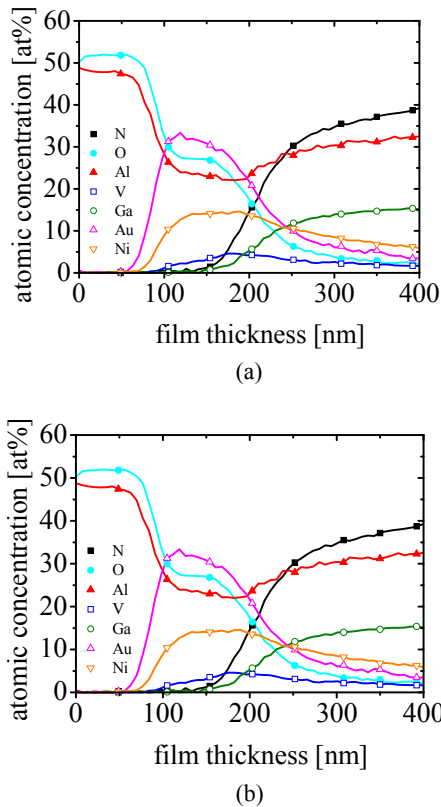


**Fig. 8.** (Color online) Atomic concentrations analyzed by AES: (a) V/Al/V/Au and (b) V/Al/Mo/Au.

a significant difference in surface morphology of each electrode. The surface roughness of the electrode fabricated using V and Mo barrier metals was much larger than that fabricated using Ni and Ti barrier metals. In particular, we found protruding portions on the surfaces of both samples, which were confirmed by the laser microscopy method. We also measured the atomic concentration by AES of two samples fabricated using Ni and V barrier metals. These two samples show significant differences in surface roughness and contact resistance. Figures 8(a) and 8(b) show the depth profiles of the V/Al/Ni/Au and V/Al/V/Au electrodes. From these figures, although the outermost surface was Au before thermal annealing, the V/Al/Ni/Au electrode until a depth of 50 nm from the surface was composed almost entirely of Al and O, i.e., the V/Al/Ni/Au electrode was formed with an  $\text{AlO}_x$  oxide layer as a result of thermal annealing. The Ni–Al alloy formed by thermal annealing confined the stable oxide film and the control of oxidation to the underlying metals.<sup>23)</sup> Thus, the oxygen concentration at the contact interface was 8.14%. We initially thought that this result reflected incipient layer composition. However, the V/Al/V/Au electrode is composed almost entirely of Al and O, with only small amounts of Au and Ga at the surface. Thus, the  $\text{AlO}_x$  oxide layer is degraded by high-temperature annealing. Also, the  $\text{VO}_x$  oxide layer is formed by the reaction between V and O at the barrier layer.  $\text{VO}_x$  induces the high-temperature corrosion phenomenon.<sup>24)</sup> Thus, the metal composition exhibits notable interdiffusion because of it, the underlying layers of the electrode were rapidly oxidized. The oxygen concentration of the electrode was 17.0% at the contact interface. For high-temperature anneal-

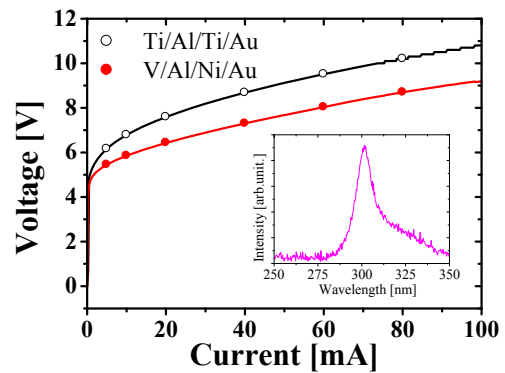


**Fig. 9.** (Color online)  $V$ - $I$  characteristics of UV LEDs emitting at 300 nm prepared using Ti/Al/Ti/Au and V/Al/Ni/Au n-type contacts.

ing, the barrier layer in the V-based electrode is important for meeting the requirement for the control of the degree of oxidation.

We also fabricated UV LEDs with an emission wavelength of 300 nm with V/Al/Ni/Au as the n-type electrode, which exhibited a  $\rho_c$  value of approximately  $1.13 \times 10^{-6} \Omega \text{ cm}^2$  for the n-type  $\text{Al}_{0.62}\text{Ga}_{0.38}\text{N}$ . We prepared the same LEDs using a Ti/Al/Ti/Au electrode, which exhibited a  $\rho_c$  value of approximately  $2.36 \times 10^{-4} \Omega \text{ cm}^2$  for the n-type  $\text{Al}_{0.62}\text{Ga}_{0.38}\text{N}$ . Figure 9 shows the  $V$ - $I$  curves of each LED. In this figure, we inserted the typical spectrum of this UV LED. According to this figure, the operating voltage of the LED prepared using a V/Al/Ni/Au electrode was reduced by 1.6 V at 100 mA current injection, compared with that prepared using a Ti/Al/Ti/Au electrode.

#### 4. Conclusions

In this study, we investigated the V-based electrode for low  $\rho_c$  in n- $\text{Al}_{0.62}\text{Ga}_{0.38}\text{N}$ . We found it advantageous to fabricate the V-based electrode with low  $\rho_c$  using Ni or Ti as a barrier metal. The minimum  $\rho_c$  value of n-type  $\text{Al}_{0.62}\text{Ga}_{0.38}\text{N}$  prepared using the V/Al/Ni/Au electrode reached  $1.13 \times 10^{-6} \Omega \text{ cm}^2$ . We also demonstrated the fabrication of a UV LED with an emission wavelength of approximately 300 nm using this electrode.

#### Acknowledgments

This study was partially supported by the Program for the Strategic Research Foundation at Private Universities, 2012–2016; by a MEXT Grant-in-Aid for Specially Promoted Research (No. 2500011), and by a MEXT Grant-in-Aid for Scientific Research A (No. 15H02019).

- 1) H. Hirayama, *J. Appl. Phys.* **97**, 091101 (2005).
- 2) J. R. Grandusky, S. R. Gibb, M. C. Mendrick, and L. J. Schowalter, *Appl. Phys. Express* **3**, 072103 (2010).
- 3) C. Pernot, M. Kim, S. Fukahori, T. Inazu, T. Fujita, Y. Nagasawa, A. Hirano, M. Ippommatsu, M. Iwaya, and S. Kamiyama, *Appl. Phys. Express* **3**, 061004 (2010).
- 4) T. Inazu, S. Fukahori, C. Pernot, M. Hee, T. Fujita, Y. Nagasawa, A. Hirano, M. Ippommatsu, M. Iwaya, T. Takeuchi, S. Kamiyama, M. Yamaguchi, Y. Honda, H. Amano, and I. Akasaki, *Jpn. J. Appl. Phys.* **50**, 122101 (2011).
- 5) G. Tamulaitis, *Lith. J. Phys.* **51**, 177 (2011).
- 6) C. Pernot, S. Fukahori, T. Inazu, T. Fujita, M. Kim, Y. Nagasawa, A. Hirano, M. Ippommatsu, M. Iwaya, S. Kamiyama, I. Akasaki, and H.

- Amano, *Phys. Status Solidi A* **208**, 1594 (2011).
- 7) M. Kim, T. Fujita, S. Fukahori, T. Inazu, C. Pernot, Y. Nagasawa, A. Hirano, M. Ippommatsu, M. Iwaya, T. Takeuchi, S. Kamiyama, M. Yamaguchi, Y. Honda, H. Amano, and I. Akasaki, *Appl. Phys. Express* **4**, 092102 (2011).
- 8) M. Shatalov, W. Sun, R. Jain, A. Lunev, X. Hu, A. Dobrinsky, Y. Bilenko, J. Yang, G. A. Garrett, L. E. Rodak, M. Wraback, M. Shur, and R. Gaska, *Semicond. Sci. Technol.* **29**, 084007 (2014).
- 9) K. Yamada, Y. Furusawa, S. Nagai, A. Hirano, M. Ippommatsu, K. Aosaki, N. Morishima, H. Amano, and I. Akasaki, *Appl. Phys. Express* **8**, 012101 (2015).
- 10) N. A. Papanicolaou and K. Zekentes, *Solid-State Electron.* **46**, 1975 (2002).
- 11) X. A. Cao, H. Piao, and S. F. LeBoeuf, *Appl. Phys. Lett.* **89**, 082109 (2006).
- 12) D. Selvanathan, F. M. Mohammed, A. Tesfayesys, and I. Adesida, *J. Vac. Sci. Technol. B* **22**, 2409 (2004).
- 13) S. J. Fonash, S. Ashok, and R. Singh, *Appl. Phys. Lett.* **39**, 423 (1981).
- 14) B. Van Daele, G. Van Tendeloo, W. Ruythooren, J. Derluyn, M. R. Leys, and M. Germain, *Appl. Phys. Lett.* **87**, 061905 (2005).
- 15) J. Burm, K. Chu, W. A. Davis, W. J. Schaff, T. J. Eustis, and L. F. Eastman, *Appl. Phys. Lett.* **70**, 464 (1997).
- 16) S. H. Lim, W. Swider, J. Washburn, and Z. L. Weber, *J. Appl. Phys.* **88**, 6364 (2000).
- 17) S. Murai, H. Masuda, Y. Koide, and M. Murakami, *Appl. Phys. Lett.* **80**, 2934 (2002).
- 18) X. A. Cao, H. Piao, S. F. LeBoeuf, J. Li, J. Y. Lin, and H. X. Jiang, *Appl. Phys. Lett.* **89**, 082109 (2006).
- 19) W. Zhang, J. Zhang, Z. Wu, S. Chen, Y. Li, Y. Tian, J. Dai, C. Chen, and Y. Fang, *J. Appl. Phys.* **113**, 094503 (2013).
- 20) UV Craftory Co, Ltd, Japan Patent 236690 (2010).
- 21) R. France, T. Xu, P. Chen, R. Chandrasekaran, and T. D. Moustakas, *Appl. Phys. Lett.* **90**, 062115 (2007).
- 22) L. W. C. Janis, *Metal Contacts to P-Type Gallium Nitride* (NUS Press, Singapore, 2005) Chap. 2.
- 23) E. P. George, C. T. Liu, and D. P. Pope, *Scr. Metall. Mater.* **30**, 37 (1994).
- 24) Web [<http://www.nipponyuka.jp/category/1756170.html>].

## Control of growth mode in Mg-doped GaN/AlN heterostructure

This content has been downloaded from IOPscience. Please scroll down to see the full text.

2014 Jpn. J. Appl. Phys. 53 030305

(<http://iopscience.iop.org/1347-4065/53/3/030305>)

View [the table of contents for this issue](#), or go to the [journal homepage](#) for more

Download details:

IP Address: 202.11.1.201

This content was downloaded on 03/03/2017 at 06:48

Please note that [terms and conditions apply](#).

You may also be interested in:

[Recent progress and future prospects of AlGaIn-based high-efficiency deep-ultraviolet light-emitting diodes](#)

Hideki Hirayama, Noritoshi Maeda, Sachie Fujikawa et al.

[GaN-based light-emitting diodes on various substrates: a critical review](#)

Guoqiang Li, Wenliang Wang, Weijia Yang et al.

[Hexagonal boron nitride for deep ultraviolet photonic devices](#)

H X Jiang and J Y Lin

[Advances in group III-nitride-based deep UV LED technology](#)

M Kneissl, T Kolbe, C Chua et al.

[Multijunction GaInN-based solar cells using a tunnel junction](#)

Hironori Kurokawa, Mitsuru Kaga, Tomomi Goda et al.

[Recent progress in metal-organic chemical vapor deposition of \(0001\) N-polar group-III nitrides](#)

Stacia Keller, Haoran Li, Matthew Laurent et al.

[Electrical properties of n-type AlGaIn with high Si concentration](#)

Kunihiro Takeda, Motoaki Iwaya, Tetsuya Takeuchi et al.

[Topical Review: Development of overgrown semi-polar GaN for high efficiency green/yellow emission](#)

T Wang

[Prospects of III-nitride optoelectronics grown on Si](#)

D Zhu, D J Wallis and C J Humphreys

## Control of growth mode in Mg-doped GaN/AlN heterostructure

Tomohiro Morishita<sup>1,2\*</sup>, Kosuke Sato<sup>1</sup>, Motoaki Iwaya<sup>2</sup>, Tetsuya Takeuchi<sup>2</sup>, Satoshi Kamiyama<sup>2</sup>, and Isamu Akasaki<sup>2,3</sup>

<sup>1</sup>Asahi Kasei Corporation, Fuji, Shizuoka 416-8501, Japan

<sup>2</sup>Faculty of Science and Technology, Meijo University, Nagoya 468-8502, Japan

<sup>3</sup>Akasaki Research Center, Nagoya University, Nagoya 464-8603, Japan

E-mail: morishita.tc@om.asahi-kasei.co.jp

Received November 18, 2013; accepted December 23, 2013; published online February 14, 2014

We investigated the effect of carrier gas on the growth mode of Mg-doped GaN on AlN layers. The growth mode of Mg-doped GaN strongly depends on the type of carrier gas used. In H<sub>2</sub> carrier gas, Mg-doped GaN on AlN layers is grown in the shape of an island. In contrast, in N<sub>2</sub> carrier gas, Mg-doped GaN on AlN layers shows a two-dimensional growth different from the initial growth mode. We observed that the type of carrier gas used has a significant impact on the electrical conductivity of Mg-doped GaN owing to the difference in surface flatness.

© 2014 The Japan Society of Applied Physics

**A**lGaIn ternary nitride semiconductors show great potential for optoelectronic applications, particularly in deep UV (DUV)/UV light-emitting diodes (LEDs). These devices have many applications such as in air/water sterilization and can be used as a substitute of mercury lamps from the viewpoint of environmental burden. However, the external quantum efficiency (EQE) of DUV/UV LEDs is much lower than that of blue LEDs.<sup>1,2</sup> There are many studies on the increase in internal quantum efficiency (IQE) by reducing the dislocation density<sup>3–5</sup> such as that using free standing AlN substrates, an epitaxial lateral overgrowth method, and so on.<sup>6–8</sup> Because the relatively high IQE of the AlGaIn active layer in DUV/UV LEDs has already been realized by these studies, light extraction efficiency (LEE) is one of the most important factors for the improvement of EQE in DUV/UV LEDs.

The LEE of flip-chip visible LEDs can be improved by using high-reflectivity electrodes based on Ag<sup>9</sup> or Rh<sup>10</sup> on the back surface of the LEDs. Furthermore, the sapphire substrate is removed by laser lift-off (LLO)<sup>11</sup> and flip-chip visible LEDs are sealed with resin or silicone.<sup>12</sup> By combining these methods, the LEE of visible LEDs reached ~80%.<sup>13</sup> Thus far, we have reported highly reflective p-type electrodes formed by combining indium ITO and Al,<sup>14</sup> which are highly reflective in the UV region. We have also reported the application of LLO to UV LEDs.<sup>15</sup> However, the most significant issue is the absorption of light by a p-type GaN layer for the improvement of LEE in DUV/UV-LEDs. To decrease the absorption of light by a Mg-doped p-type GaN layer, the thickness of the p-type GaN layer must be reduced or the layer must be replaced with a high-AlN-molar-fraction p-type AlGaIn layer. However, this method is very difficult. The resistivity of the p-type AlGaIn layer increases with AlN molar fraction, because the activation energy of the acceptor increases with the AlN molar fraction.<sup>16</sup> In addition, the contact resistivity between the p-type AlGaIn layer and the electrode also increases markedly.<sup>17</sup> Thus, such a method is not practical because the operating voltage of DUV/UV LEDs increases significantly. Therefore, Mg-doped p-type GaN is used as a p-type layer for almost all DUV/UV LEDs.<sup>18,19</sup> In contrast, the decrease in the thickness of the p-type GaN layer is also difficult because GaN grown on an AlN layer shows three-dimensional growth.<sup>20</sup> Thus, in most DUV/UV LEDs, p-type GaN layers with a thickness of more than 100 nm have been used, resulting in the absorption of most light by Mg-doped p-type

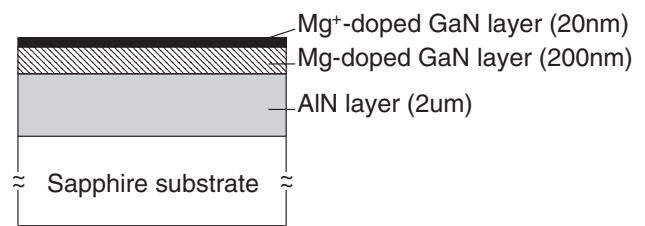


Fig. 1. Schematic view of the sample structure.

GaN layers. To decrease the absorption of light by a Mg-doped GaN layer, it is very important for GaN on AlN layers to be grown in two-dimensional modes and to decrease the thickness of the Mg-doped GaN layer.

In this study, we investigated the growth mode of Mg-doped GaN on an AlN layer. As a result, we found that there is a significant difference in initial growth mode caused by the difference in the type of carrier gas used. Moreover, such a difference had a significant impact on the electrical conductivity of p-GaN.

The AlN layers were grown on (0001) c-plane sapphire substrates. After the growth of 2- $\mu$ m-thick AlN layers at 1,250 °C, Mg-doped GaN layers were grown by a metal-organic vapor phase epitaxial (MOVPE) reactor. Trimethylaluminum (TMAI), trimethylgallium (TMGa), bis(ethylcyclopentadienyl)magnesium (Et-Cp<sub>2</sub>Mg), and ammonia (NH<sub>3</sub>) were used as the sources of Al, Ga, Mg, and N, respectively. The growth temperature was controlled by direct measurements of the substrate surface using a pyrometer. Figure 1 shows a schematic view of the sample structure. The sapphire substrates were thermally cleaned in H<sub>2</sub> ambient at approximately 1,250 °C. Subsequently, AlN layers with a thickness of approximately 2  $\mu$ m were grown at a temperature of 1,250 °C and a pressure of 30 Torr using hydrogen (H<sub>2</sub>) carrier gas. Then, the substrate temperature was decreased to approximately 1,030 °C and the MOVPE reactor pressure was increased to 200 Torr. Moreover, p-type Mg-doped GaN layers with a thickness of approximately 200 nm and a higher-Mg-concentration-doped (Mg<sup>+</sup>-) GaN contact layer with a thickness of approximately 20 nm were grown with H<sub>2</sub> or N<sub>2</sub>. The V/III ratio was 1,000, which is a typical value of the p-type Mg-doped GaN grown by MOVPE. The Mg concentrations in Mg- and Mg<sup>+</sup>-doped GaN layers had set the growth conditions to be  $3 \times 10^{19}$  and  $2 \times 10^{20}$  cm<sup>-3</sup>, respectively.

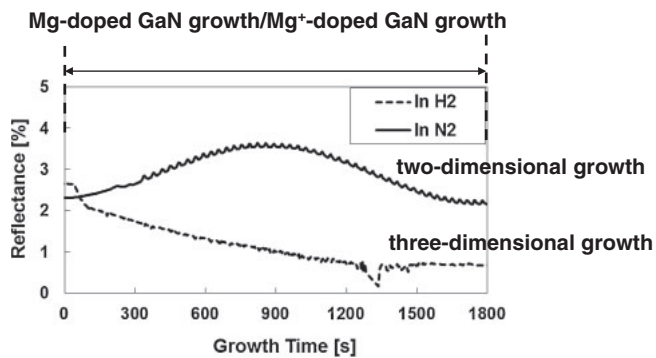


Fig. 2. In situ reflectance measurement results of Mg- and Mg<sup>+</sup>-doped GaN layers grown on AlN layers in H<sub>2</sub> and N<sub>2</sub> carrier gases.

To characterize the growth mode and thickness of Mg-doped GaN layers, we used a real-time in situ optical reflectometer. This reflectometer consisted of a semiconductor laser ( $\lambda = 650 \text{ nm}$ ) as the light source. The reflected light was detected via the same probe, a semitransparent mirror, and a photodiode. We also observed the surface morphology by Nomarski interference and cross-sectional scanning electron microscopies. Moreover, we characterized the crystallinity and strain in Mg-doped GaN layers by a typical X-ray diffraction (XRD) measurement. We measured the Van der Pauw Hall effect with a magnetic field of 1,000 G to determine the hole concentration, mobility, and resistivity of each sample at room temperature (RT). A Ni/Au ohmic electrode was deposited by electron beam evaporation on a Mg<sup>+</sup>-GaN layer for Van der Pauw Hall effect measurement. Note that the resistivity of the Mg<sup>+</sup>-GaN layer was ignored because this layer was very thin and showed high resistivity.

Figure 2 shows in situ reflectance measurement results of Mg-doped GaN layers grown with H<sub>2</sub> and N<sub>2</sub> carrier gases. From this figure, we confirmed the significant difference in reflectance between the samples. In H<sub>2</sub> carrier gas, the reflectance from the Mg-doped GaN layer monotonically decreased. In addition, we could not confirm the interference from this figure. Therefore, it is suggested that the Mg-doped GaN layer in H<sub>2</sub> carrier gas shows a three-dimensional growth mode rather than a two-dimensional growth mode. In contrast, we confirmed the interference from the reflection of the Mg-doped GaN layer from the initial growth stage in N<sub>2</sub> carrier gas. Therefore, it is suggested that the Mg-doped GaN layer in N<sub>2</sub> carrier gas shows a two-dimensional growth mode different from the initial growth mode, and that the growth mode of the p-type Mg- and Mg<sup>+</sup>-doped GaN layers on AlN layers strongly depends on the type of carrier gas used.

For further analysis, we obtained Nomarski interference microscopic and cross-sectional SEM images of Mg-doped GaN layers in H<sub>2</sub> and N<sub>2</sub> carrier gases as shown in Figs. 3 and 4, respectively. These figures revealed a significant difference in surface structure depending on the type of carrier gas used. In H<sub>2</sub> carrier gas, Mg-doped GaN layers were grown in the shape of islands. The height of each island was approximately 500 nm, which is approximately two times larger than the designed value. In addition, there were no GaN layer growth areas. On the other hand, although the surface morphology was slightly worse, no island growth and two-dimensional growth were observed in N<sub>2</sub> carrier gas.

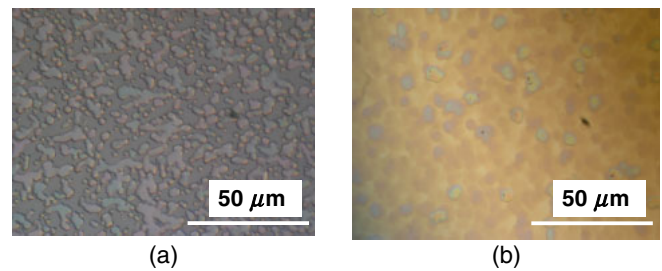


Fig. 3. (Color online) Nomarski interference microscopic images of Mg- and Mg<sup>+</sup>-doped GaN layers on AlN layers in (a) H<sub>2</sub> and (b) N<sub>2</sub> carrier gases.

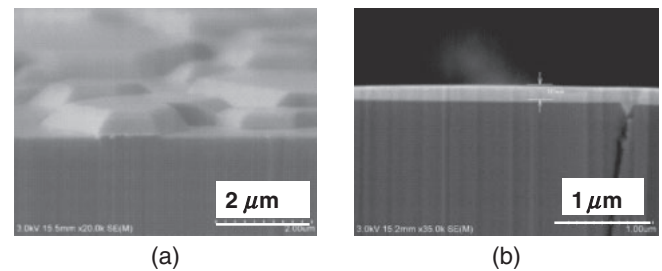
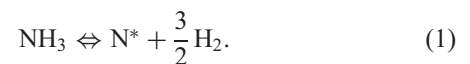


Fig. 4. Nomarski surface and cross-sectional SEM images of Mg- and Mg<sup>+</sup>-doped GaN layers on AlN layers in (a) H<sub>2</sub> and (b) N<sub>2</sub> carrier gases. The photograph was slightly tilted in order to clarify the structure in (b).

The thickness of Mg- and Mg<sup>+</sup>-doped GaN layers was approximately 180 nm, which is almost the same as the designed value. From these results, the Mg-doped GaN layer was grown in the three-dimensional mode in H<sub>2</sub> carrier gas and in the two-dimensional mode in N<sub>2</sub> carrier gas. A different growth mode was assumed during the initial growth. The equation for the decomposition of NH<sub>3</sub> is



From Eq. (1), the reaction of equilibrium moves to the left-hand side easily in H<sub>2</sub> carrier gas; thus, it is difficult to decompose NH<sub>3</sub>. In contrast, there is no difficulty in the decomposition of NH<sub>3</sub> in N<sub>2</sub> carrier gas. This means that the number of N atoms contributing to the growth of the Mg-doped GaN layer at the surface varies even if the same quantity of NH<sub>3</sub> as the gas phase is supplied.

Hypothetical models for different growth modes are shown in Fig. 5. In H<sub>2</sub> carrier gas, the number of N atoms at the AlN surface is low and the migration of Ga atoms is sufficient. Therefore, the Mg-doped GaN layer was grown in the three-dimensional mode after nucleation, as shown in Fig. 5(a). To suppress the three-dimensional growth, the Mg-doped GaN layer was grown at a lower growth temperature and a higher V/III ratio; however, no two-dimensional growth was observed. On the other hand, in N<sub>2</sub> carrier gas, the number of N atoms at the AlN surface is sufficient, there are many opportunities for Ga atoms to interact with N atoms, and the migration of Ga atoms is suppressed. Thus, many small crystal nuclei were generated and the initial growth of the Mg-doped GaN layer was in the two-dimensional mode as observed by in situ monitoring, as shown in Fig. 5(b).

For further analysis, the XRD reciprocal space mapping image around the (20 $\bar{2}$ 4) diffraction was obtained and is

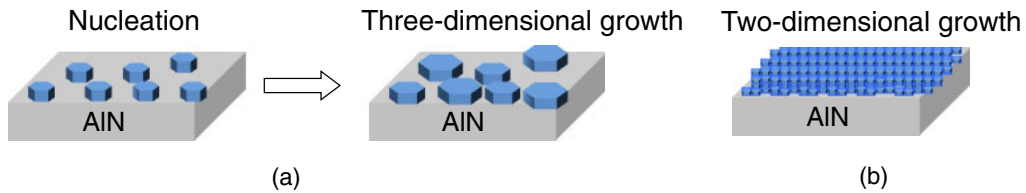


Fig. 5. (Color online) Hypothetical models for growth modes of Mg-doped GaN layers in  $H_2$  and  $N_2$  carrier gases.

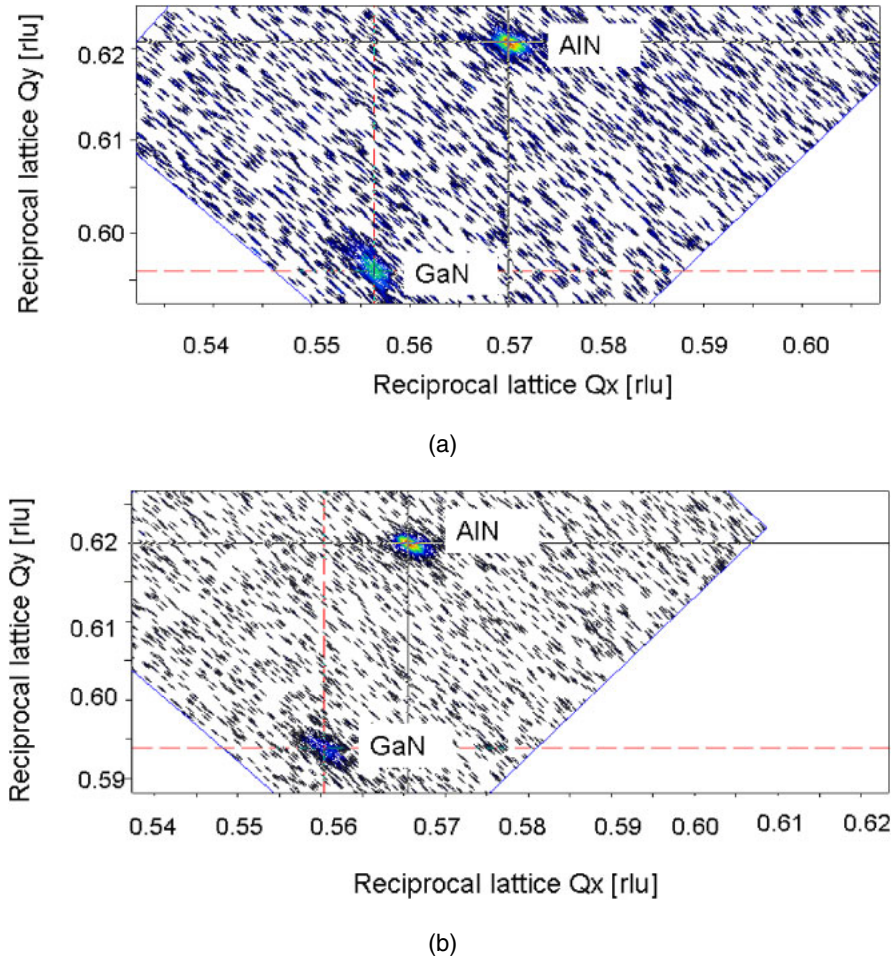


Fig. 6. (Color online) XRD reciprocal space mapping around  $(20\bar{2}4)$ : (a) Mg- and  $Mg^+$ -doped GaN layers in  $H_2$  carrier gas, and (b) Mg- and  $Mg^+$ -doped GaN layers in  $N_2$  carrier gas.

shown in Fig. 6. As shown in Fig. 6(a), the Mg-doped GaN layer in  $H_2$  carrier gas was almost 100% relaxed in contrast to that in  $N_2$  carrier gas, which was approximately 75% relaxed as shown in Fig. 6(b). This is because Ga atoms migrated easily in  $H_2$  carrier gas and the Mg-doped GaN layer exhibited the lattice constant of GaN through lattice relaxation.

Finally, we examined the electrical properties of the Mg-doped GaN layers grown in  $H_2$  and  $N_2$  carrier gases by using the Van der Pauw Hall effect measurement method. For the Mg-doped GaN layer grown in  $H_2$  carrier gas, no current flow was observed, even when the voltage was increased up to 5 V because of island growth. In contrast, the Mg-doped GaN layer grown in  $N_2$  carrier gas showed good electrical properties. From the Hall measurements, the hole concen-

tration, mobility, and resistivity at RT were determined to be approximately  $5 \times 10^{17} \text{ cm}^{-3}$ ,  $6 \text{ cm}^2 \text{ V}^{-1} \text{ s}^{-1}$ , and  $1.3 \Omega \text{ cm}$ , respectively, as shown in Table I. Moreover, the Mg concentration in this Mg-doped GaN layer characterized by secondary ion mass spectrometry was  $3 \times 10^{19} \text{ cm}^{-3}$ , and the activation rate was approximately 1.7%, which is almost the same as the typical value because the activation ratio of the p-type impurity (Mg) in GaN at RT is generally about 2 to 5%.<sup>21)</sup>

From the surface morphology and electrical properties, Mg-doped GaN growth in  $N_2$  carrier gas was considered to be very useful for forming DUV/UV-LEDs on AlN layers and the obtained results encourage the use of thinner p-type Mg-doped GaN layers and promise an increase in the efficiency of DUV/UV LEDs.

**Table I.** Hall effect measurement results of Mg-doped GaN in N<sub>2</sub> carrier gas.

Mobility (cm <sup>2</sup> V <sup>-1</sup> s <sup>-1</sup> )	Resistivity (Ω cm)	Hole concentration (cm <sup>-3</sup> )
6	2.2	5 × 10 <sup>17</sup>

In conclusion, we investigated the effect of carrier gas on the growth of GaN layers on AlN underlying layers. The growth mode of Mg-doped GaN strongly depends on the type of carrier gas used. In H<sub>2</sub> carrier gas, Mg-doped GaN on AlN layers is grown in the shape of an island. In contrast, in N<sub>2</sub> carrier gas, Mg-doped GaN on AlN layers shows a two-dimensional growth mode. In addition, Mg-doped GaN grown in N<sub>2</sub> carrier gas shows good electrical characteristics. Therefore, the growth of Mg-doped GaN in N<sub>2</sub> carrier gas is very useful for forming DUV/UV LEDs on AlN from the viewpoint of both two-dimensional growth and electrical properties compared with the growth of Mg-doped GaN in H<sub>2</sub> carrier gas. These results promise an increase in the efficiency of DUV/UV LEDs through a decrease in the absorption of Mg-doped GaN.

- 1) M. A. Khan, M. Shatalov, H. P. Maruska, H. M. Wang, and E. Kuokstis, *Jpn. J. Appl. Phys.* **44**, 7191 (2005).
- 2) M. Shatalov, W. Sun, Y. Bilenko, A. Sattu, X. Hu, J. Deng, J. Yang, M. Shur, C. Moe, M. Wraback, and R. Gaska, *Appl. Phys. Express* **3**, 062101 (2010).
- 3) C. Pernot, M. Kim, S. Fukahori, T. Inazu, T. Fujita, Y. Nagasawa, A. Hirano, M. Ippommatsu, M. Iwaya, S. Kamiyama, I. Akasaki, and H. Amano, *Appl. Phys. Express* **3**, 061004 (2010).
- 4) H. Hirayama, N. Noguchi, and N. Kamata, *Appl. Phys. Express* **3**, 032102 (2010).
- 5) S. Masui, Y. Matsuyama, T. Yanamoto, T. Kozaki, S. Nagahama, and T. Mukai, *Jpn. J. Appl. Phys.* **42**, L1318 (2003).
- 6) H. J. Kim, S. Choi, D. Yoo, J.-H. Ryou, R. D. Dupuis, R. F. Dalmau, P. Lu, and Z. Sitar, *Appl. Phys. Lett.* **93**, 022103 (2008).
- 7) Z. Ren, Q. Sun, S.-Y. Kwon, J. Han, K. Davitt, Y. K. Song, A. V. Nurmikko, H.-K. Cho, W. Liu, J. A. Smart, and L. J. Schowalter, *Appl. Phys. Lett.* **91**, 051116 (2007).
- 8) T. Kinoshita, K. Hironaka, T. Obata, T. Nagashima, R. Dalmau, R. Schlessler, B. Moody, J. Xie, S. Inoue, Y. Kumagai, A. Koukitsu, and Z. Sitar, *Appl. Phys. Express* **5**, 122101 (2012).
- 9) D. S. Leem, T. Lee, and T. Y. Seong, *Electron. Mater. Lett.* **1**, 115 (2005).
- 10) M. Yamada, T. Mitani, Y. Narukawa, S. Shioji, I. Niki, S. Sonobe, K. Deguchi, M. Sano, and T. Mukai, *Jpn. J. Appl. Phys.* **41**, L1431 (2002).
- 11) T. Ueda, M. Ishida, S. Tamura, Y. Fujimoto, M. Yuri, T. Saito, and D. Ueda, *Phys. Status Solidi C* **0**, 2219 (2003).
- 12) C. C. Lin and R.-S. Liu, *J. Phys. Chem. Lett.* **2**, 1268 (2011).
- 13) Y. Narukawa, M. Ichikawa, D. Sanga, M. Sano, and T. Mukai, *J. Phys. D* **43**, 354002 (2010).
- 14) K. Takehara, K. Takeda, S. Ito, H. Aoshima, M. Iwaya, T. Takeuchi, S. Kamiyama, I. Akasaki, and H. Amano, *Jpn. J. Appl. Phys.* **51**, 042101 (2012).
- 15) H. Aoshima, K. Takeda, K. Takehara, S. Ito, M. Mori, M. Iwaya, T. Takeuchi, S. Kamiyama, I. Akasaki, and H. Amano, *Phys. Status Solidi C* **9**, 753 (2012).
- 16) M. L. Nakarmi, K. H. Kim, M. Khizar, Z. Y. Fan, J. Y. Lin, and H. X. Jiang, *Appl. Phys. Lett.* **86**, 092108 (2005).
- 17) N. Maeda and H. Hirayama, *Phys. Status Solidi C* **10**, 1521 (2013).
- 18) J. Li, T. N. Oder, M. L. Nakarmi, J. Y. Lin, and H. X. Jiang, *Appl. Phys. Lett.* **80**, 1210 (2002).
- 19) M. L. Nakarmi, N. Nepal, C. Ugolini, T. M. Altahtamouni, J. Y. Lin, and H. X. Jiang, *Appl. Phys. Lett.* **89**, 152120 (2006).
- 20) D. Morita, A. Fujioka, T. Mukai, and M. Fukui, *Jpn. J. Appl. Phys.* **46**, 2895 (2007).
- 21) D. Iida, M. Iwaya, S. Kamiyama, H. Amano, and I. Akasaki, *Phys. Status Solidi B* **246**, 1188 (2009).

# Reduction of contact resistance in V-based electrode for high AlN molar fraction n-type AlGaN by using thin SiN<sub>x</sub> intermediate layer

Noriaki Nagata<sup>\*1</sup>, Takashi Senga<sup>1</sup>, Motoaki Iwaya<sup>1</sup>, Tetsuya Takeuchi<sup>1</sup>, Satoshi Kamiyama<sup>1</sup>, and Isamu Akasaki<sup>1,2</sup>

<sup>1</sup> Faculty of Science and Technology, Meijo University, Nagoya 468-0073, Japan

<sup>2</sup> Akasaki Research Center, Nagoya University, Nagoya 464-8603, Japan

Received 4 November 2016, revised 23 November 2016, accepted 23 November 2016

Published online 1 March 2017

**Keywords** contact resistance, D-UV LED, high AlN molar fraction, n-AlGaN

\* Corresponding author: e-mail 153434027@c alumni.meijo-u.ac.jp

We found out the reduction of contact resistance in V-based electrode for high AlN molar fraction n-type AlGaN by using thin SiN<sub>x</sub> intermediate layer. The contact resistivity for n-type Al<sub>0.70</sub>Ga<sub>0.30</sub>N with the V/Al/Ni/Au electrode using SiN<sub>x</sub> intermediated layer reached  $1.13 \times 10^{-6} \Omega \text{ cm}^2$ . Moreover, contact resistivity using SiN<sub>x</sub> intermediated layer had been reduced more than one order of magnitude in all AlN molar

fractions from 0.62 to 0.87. Using this electrode, we also demonstrated UV light-emitting diodes (LEDs) on n-type Al<sub>0.70</sub>Ga<sub>0.30</sub>N underlying layer with an emission wavelength of approximately 283 nm. An operating LED voltage using a V/Al/Ni/Au electrode with SiN<sub>x</sub> intermediated layer was 3.3 V lower at 100 mA current injection than that without SiN<sub>x</sub> intermediated layer.

© 2017 WILEY-VCH Verlag GmbH & Co. KGaA, Weinheim

**1 Introduction** AlGaN-based UV light-emitting diodes (UV LEDs) have many advantages, such as compactness, high efficiency, and wavelength selectivity, these devices are expected to replace conventional UV-light sources based on glass lamps. So far, a high external quantum efficiency of deep UV LEDs ranging between UV-B (emission wavelength 280–315 nm) and UV-C (emission wavelength: lower than 280 nm) has already been reached [1–9]. However, there are several issues in UV LEDs. Especially, an improvement in wall plug efficiency (WPE) in these LEDs is one of the most important issues in AlGaN-based UV LEDs. For increase of WPE, reduction of operating voltage in deep UV LED is essential. The contact resistance of n-AlGaN accounts for large component of the device resistance in LEDs, because low ohmic contact resistivity electrode for n-AlGaN is difficult with increase of AlN molar fraction. Therefore, a reduction of contact resistance in the n-type AlGaN layer with a high AlN molar fraction is important.

Many other groups have reported the fabrication of an electrode for n-type GaN with good Ohmic contact using Ti-based, Mo-based, Cr-based, V-based four-metal-layer structures [10–15]. The Ti-based electrodes can form good low Ohmic contact ( $\sim 10^{-6} \Omega \text{ cm}^2$ ) with n-type AlGaN with an AlN molar fraction of up to 0.4. However, Ti-based electrodes increase specific contact resistance ( $\rho_c$ ), thereby increasing the AlN molar fraction. In addition, Ti-based electrodes have high  $\rho_c$  to n-type AlGaN with AlN molar fractions above 0.6 [16]. We reported that V/Al/Ni/Au electrode realized low contact resistivity ( $\sim 10^{-6} \Omega \text{ cm}^2$ ) with n-type AlGaN with AlN molar fraction of 0.62 [17]. However, we confirmed contact resistivity for AlGaN with AlN molar fraction of 0.7 rapidly increased to  $10^{-3} \Omega \text{ cm}^2$  order. Therefore, it is essential for realization of low ohmic contact electrode with AlN molar fraction of more than 0.7. So far, it has achieved the reduction of  $\rho_c$  by insertion of thin SiN<sub>x</sub> intermediate layer in AlGaN/GaN heterostructure field-effect-transistors [18]. However, there are no reports of

reduction of  $\rho_c$  in high AlN molar fraction AlGaIn single layer by using SiN<sub>x</sub> intermediate layer.

In this study, we found out the reduction of  $\rho_c$  in V-based electrode for high AlN molar fraction n-type AlGaIn by using thin SiN<sub>x</sub> intermediate layer. We evaluated the contact characteristics of using thin SiN<sub>x</sub> layer depending on the thickness. Moreover, we demonstrated UV LEDs with 283-nm emission wavelengths using this electrode.

**2 Experimental** The samples were epitaxially grown on a *c*-plane sapphire substrate by metal-organic vapor phase epitaxy. Figure 1 is a schematic view of the sample structure. After baking the sapphire substrate at 1180 °C, an unintentionally doped 2.5- $\mu\text{m}$ -thick AlN layer was grown at 1180 °C and a 2.0- $\mu\text{m}$ -thick Si-doped Al<sub>x</sub>Ga<sub>1-x</sub>N layer was sequentially grown. The free-electron concentrations in Si-doped Al<sub>x</sub>Ga<sub>1-x</sub>N were measured to be approximately  $2.0 \times 10^{18} \text{ cm}^{-3}$  at room temperature (RT) by Hall-effect measurements using the van der Pauw method. We prepared the Al<sub>x</sub>Ga<sub>1-x</sub>N samples with different AlN molar fraction *x* from 0.62 to 0.87.

After cleaning with an organic solvent, *aqua regia*, and hydrogen fluoride, SiN<sub>x</sub> thin layer on this n-type Al<sub>0.70</sub>Ga<sub>0.30</sub>N were deposited by electron beam evaporation method, and the V (20 nm)/Al (80 nm)/Ni(40 nm)/Au (100 nm) electrodes were deposited by electron beam evaporation method. We also investigated the dependence of thickness of SiN<sub>x</sub> intermediated layers. The thickness of the SiN<sub>x</sub> intermediated layer was adjusted by the both of deposition time and the deposition rate. In this experiment, the deposition rate using the deposition conditions of  $0.5 \text{ \AA s}^{-1}$ . In addition, we did not flow any other gases for suppression of decompose the SiN<sub>x</sub> intermediated layer.

After electrode deposition, the samples were annealed for 5 min under ambient N<sub>2</sub> at 900 °C. We also prepared the sample using a Ti/Al/Ti/Au electrode as a reference.

The contact characteristics were measured using the circular transmission line model (CTLM) at RT [19]. Figure 2 shows the CTLM patterns in this study. The electrode intervals were 5, 10, 15, 20, 25, and 30  $\mu\text{m}$ . The propagation length (*L<sub>t</sub>*) and sheet resistance (*R<sub>SH</sub>*) were computed from this measurement. Therefore,  $\rho_c$  was derived from

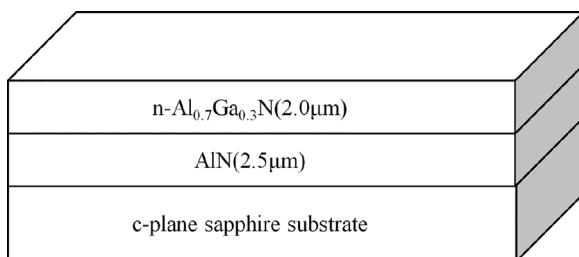


**Figure 1** Schematic structure of n-Al<sub>x</sub>Ga<sub>1-x</sub>N.

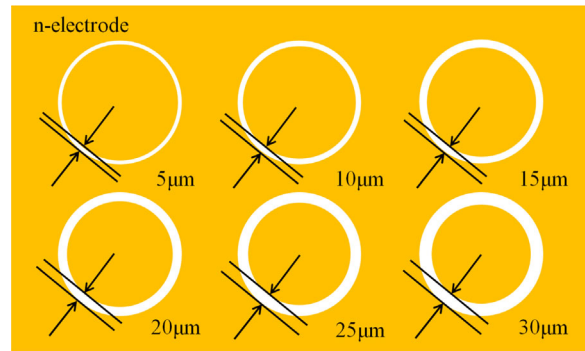


**Figure 2** Schematic views of the electrode patterns for measurements.

$$\rho_c = R_{SH} \cdot L_t^2. \quad (1)$$

The structure of UV LEDs with an emitting peak wavelength of 283 nm is shown in Fig. 3. UV LEDs were composed of a 2.5- $\mu\text{m}$ -thick AlN template, a 2.0- $\mu\text{m}$ -thick n-type Al<sub>0.7</sub>Ga<sub>0.3</sub>N cladding layer, three pairs of unintentionally doped Al<sub>0.4</sub>Ga<sub>0.6</sub>N/GaN multi-quantum wells (3QWs), a 150-nm-thick *p*-type Al<sub>0.7</sub>Ga<sub>0.4</sub>N cladding layer, and a 100-nm-thick *p*-type GaN contact layer. These samples were annealed at 800 °C for 5 min in ambient N<sub>2</sub> for *p*-type activation. These samples were etched up to n-type AlGaIn by inductively coupled plasma reactive ion etching. Then, the V (20 nm)/Al (80 nm)/Ni(40 nm)/Au (100 nm) n-type electrodes with and without SiN<sub>x</sub> intermediated layer were deposited on the n-type AlGaIn layer by electron-beam evaporation for current injection. The size of the n-type electrode was  $500 \times 245 \mu\text{m}^2$ . After the deposition of these electrodes, annealing was performed at 900 °C for 5 min under ambient N<sub>2</sub> for inducing Ohmic contact to the n-type AlGaIn layer. Ni/Au (10/40 nm) was deposited on the *p*-type GaN layer and annealed at 550 °C for 3 min under ambient O<sub>2</sub> for inducing Ohmic contact to the *p*-type GaN layer. The size of the *p*-type electrode was  $500 \times 140 \mu\text{m}^2$ . In addition, Ti/Au (10/200 nm) pad electrodes were formed on all electrodes for implementation. Injection voltage–current

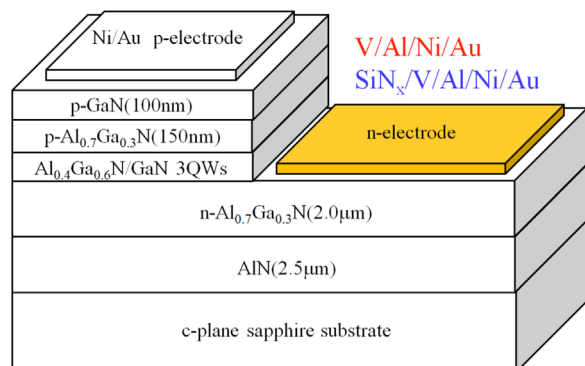


**Figure 3** Structure of UV LEDs with an emitting peak wavelength of 283 nm.

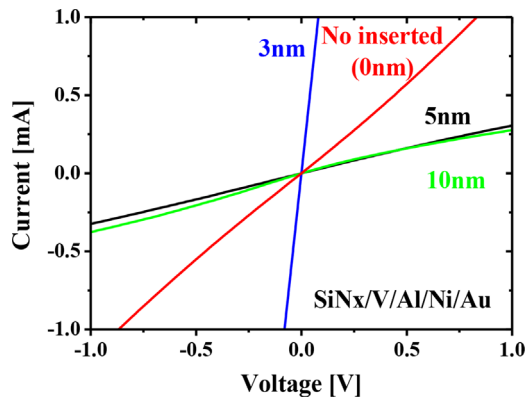


**Figure 4**  $I$ - $V$  characteristics with different thickness of  $\text{SiN}_x$  intermedated layer at an electrode interval of  $20\ \mu\text{m}$ .

( $V$ - $I$ ) characteristics were measured using a semiconductor parameter analyzer (Agilent 4156C) at RT and direct current (DC).

**3 Results and discussion** Figure 4 shows the current-voltage ( $I$ - $V$ ) characteristics at  $20\text{-}\mu\text{m}$  intervals between the V (20 nm)/Al (80 nm)/Ni (40 nm)/Au (100 nm) electrodes on n-type  $\text{Al}_{0.7}\text{Ga}_{0.3}\text{N}$  inserted with different thickness of  $\text{SiN}_x$  intermedated layer. As shown in the figure, all samples were shown to have good Ohmic-contact characteristics. However, the slopes of the  $I$ - $V$  characteristics in V/Al/Ni/Au electrode inserted with 3-nm-thick  $\text{SiN}_x$  intermedated layer were larger than that in the 0-nm-thick  $\text{SiN}_x$  (no insertion  $\text{SiN}_x$  layer). In contrast, the slope of  $I$ - $V$  characteristics rapidly decreased, when the  $\text{SiN}_x$  thickness was increased to 5 nm. Therefore, it is confirmed that the improvement of  $I$ - $V$  characteristics when  $\text{SiN}_x$  intermedated layers were the thin films. Although the optimum conditions of  $\text{SiN}_x$  thickness is limited, the effect of the insertion 3-nm-thick  $\text{SiN}_x$  was high reproducible result. Therefore, we evaluated the detailed contact characteristics in  $\text{SiN}_x$  thickness of 0 (no insertion sample) and 3 nm.

For calculating the  $\rho_c$ , resistances between each electrode were measured at each electrode interval. Figure 5 (a) and (b) shows the resistance plots of the electrode interval from 5 to  $30\ \mu\text{m}$ . Since the resistance plots almost

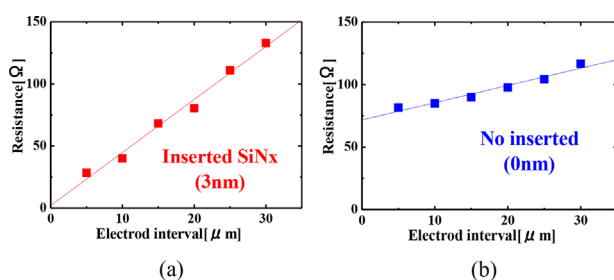


**Figure 5** Resistance at each electrode interval: (a)  $\text{SiN}_x/\text{V}/\text{Al}/\text{Ni}/\text{Au}$ , (b)  $\text{V}/\text{Al}/\text{Ni}/\text{Au}$ .

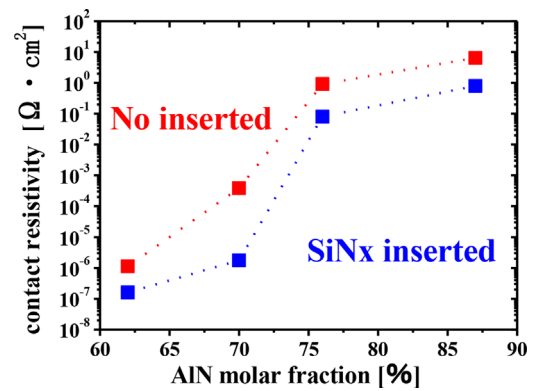


**Figure 6** The  $\rho_c$  of each AlN molar fraction AlGa<sub>N</sub> determined by the TLM method.

agree with the fitting line, the  $\rho_c$  obtained are considered reliable in this investigation. The  $\rho_c$  values for the V/Al/Ni/Au electrodes with and without  $\text{SiN}_x$  intermedated layer were  $1.76 \times 10^{-6}$  and  $6.75 \times 10^{-3}\ \Omega\text{cm}^2$ , respectively. Therefore, we succeeded the  $\rho_c$  was reduced approximately three order magnitudes by the insertion of the  $\text{SiN}_x$  intermedated layer between n-type  $\text{Al}_{0.7}\text{Ga}_{0.3}\text{N}$  and V/Al/Ni/Au electrode. We also investigated the AlN molar fraction dependence of the  $\rho_c$ . Figure 6 shows the  $\rho_c$  of each AlN molar fraction AlGa<sub>N</sub> determined by the TLM method. The  $\rho_c$  had been reduced more than one order of magnitude by insertion of  $\text{SiN}_x$  intermedated layer in all AlN molar fractions.

Next, we investigated the mechanism of the  $\rho_c$  reduction by insertion of  $\text{SiN}_x$  intermedated layer. Figure 7(a) and (b) shows the cross-sectional transmission electron microscopic image and Si concentration mapping image characterized by energy dispersive X-ray spectrometry (EDX) of vicinity of the electrode. In order from the bottom,  $\text{Al}_{0.7}\text{Ga}_{0.3}\text{N}$  and the electrode can be confirmed. However, the layer of  $\text{SiN}_x$  was not confirmed. Although clear diffusion into the  $\text{Al}_{0.7}\text{Ga}_{0.3}\text{N}$  layer was unable to verify, diffusion of Si to the electrode was able to confirm. Therefore, it will be considered that Si concentration of the electrode interface is

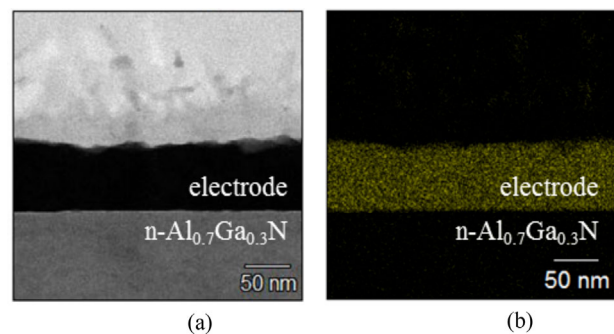


**Figure 7** Reaction of electrode n- $\text{Al}_{0.7}\text{Ga}_{0.3}\text{N}$  interface of vicinity of the electrode. (a) The cross-sectional transmission electron microscopic image, (b) Si concentration mapping image characterized by energy dispersive X-ray spectrometry (EDX).

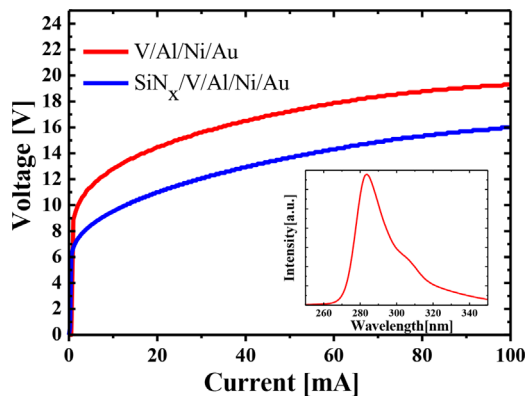


**Figure 8**  $V$ - $I$  characteristics of UV LEDs emitting at 283 nm.

increasing. So, it is estimated that the contact resistance is reduced by increasing the Si concentration in the vicinity of the electrode.

We also fabricated UV LEDs with emission wavelength of 283 nm with V/Al/Ni/Au with and without 3-nm-thick  $\text{SiN}_x$  intermediated layer, respectively, as the n-type electrode. Figure 8 shows the  $V$ - $I$  curves of each LED. In this figure, we inserted the typical spectra of this UV LED. According to this figure, the operating voltage of the LED using a V/Al/Ni/Au electrode with insertion of 3-nm-thick  $\text{SiN}_x$  intermediated layer was reduced by 3.3 V at 100 mA current injection compared to that without  $\text{SiN}_x$  intermediated layer.

**4 Conclusions** We present novel method for realization of low ohmic contact electrode by using thin  $\text{SiN}_x$  intermediate layer. As a result, contact resistivity are reduced from  $6.75 \times 10^{-3}$  to  $1.76 \times 10^{-6} \Omega\text{cm}^2$  by using V-based electrode with  $\text{SiN}_x$  intermediated layer for n-type  $\text{Al}_{0.70}\text{Ga}_{0.30}\text{N}$  layer. We also confirmed that reduction of the operating voltage in 283-nm-emission deep UV-LED at 100 mA was 3.3 V by insertion of  $\text{SiN}_x$  intermediate layer.

**Acknowledgements** This study was partially supported by the MEXT Program for the Strategic Research Foundation at Private Universities (2012–2016), JSPS Grant-in-Aid for Scientific Research A (no. 15H02019), JSPS Grant-in-Aid for Scientific Research B (no. 26286045), JSPS KAKENHI (no. 16H06416), and JST CREST (no. 16815710).

## References

- [1] H. Hirayama, *J. Appl. Phys.* **97**, 091101 (2005).
- [2] J. R. Grandusky, S. R. Gibb, M. C. Mendrick, and L. J. Schowalter, *Appl. Phys. Express* **3**, 072103 (2010).
- [3] C. Pernot, M. Kim, S. Fukahori, T. Inazu, T. Fujita, Y. Nagasawa, A. Hirano, M. Ippommatsu, M. Iwaya, and S. Kamiyama, *Appl. Phys. Express* **3**, 061004 (2010).
- [4] T. Inazu, S. Fukahori, C. Pernot, M. Hee, T. Fujita, Y. Nagasawa, A. Hirano, M. Ippommatsu, M. Iwaya, T. Takeuchi, S. Kamiyama, M. Yamaguchi, Y. Honda, H. Amano, and I. Akasaki, *Jpn. J. Appl. Phys.* **50**, 122101 (2011).
- [5] G. Tamulaitis, *Lith. J. Phys.* **51**, 177 (2011).
- [6] C. Pernot, S. Fukahori, T. Inazu, T. Fujita, M. Kim, Y. Nagasawa, A. Hirano, M. Ippommatsu, M. Iwaya, S. Kamiyama, I. Akasaki, and H. Amano, *Phys. Status Solidi A* **208**, 1594 (2011).
- [7] M. Kim, T. Fujita, S. Fukahori, T. Inazu, C. Pernot, Y. Nagasawa, A. Hirano, M. Ippommatsu, M. Iwaya, T. Takeuchi, S. Kamiyama, M. Yamaguchi, Y. Honda, H. Amano, and I. Akasaki, *Appl. Phys. Express* **4**, 092102 (2011).
- [8] M. Shatalov, W. Sun, R. Jain, A. Lunev, X. Hu, A. Dobrinsky, Y. Bilenko, J. Yang, G. A. Garrett, L. E. Rodak, M. Wraback, M. Shur, and R. Gaska, *Semicond. Sci. Technol.* **29**, 084007 (2014).
- [9] K. Yamada, Y. Furusawa, S. Nagai, A. Hirano, M. Ippommatsu, K. Aosaki, N. Morishima, H. Amano, and I. Akasaki, *Appl. Phys. Express* **8**, 012101 (2015).
- [10] N. A. Papanicolaou and K. Zekentes, *Solid-State Electron.* **46**, 1975 (2002).
- [11] X. A. Cao, H. Piao, and S. F. LeBoeuf, *Appl. Phys. Lett.* **89**, 082109 (2006).
- [12] D. Selvanathan, F. M. Mohammed, A. Tesfayesys, and I. Adesida, *J. Vac. Sci. Technol. B* **22**, 2409 (2004).
- [13] M. A. Millera, S. E. Mohny, A. Nikiforov, G. S. Cargill III, and K. H. A. Bogart, *Appl. Phys. Lett.* **89**, 132114 (2006).
- [14] R. France, T. Xu, P. Chen, R. Chandrasekaran, and T. D. Moustakas, *Appl. Phys. Lett.* **90**, 062115 (2007).
- [15] M. A. Miller, B. H. Koo, K. H. A. Bogart, and S. E. Mohny, *J. Electron. Mater.* **37**, 5 (2008).
- [16] UV Craftory Co., Ltd., Japan Patent 236690 (2010).
- [17] K. Mori, K. Takeda, T. Kusafuka, M. Iwaya, T. Takeuchi, S. Kamiyama, I. Akasaki, and H. Amano, *Jpn. J. Appl. Phys.* **55**, 05FL03 (2016).
- [18] B. Van Daelea, G. Van Tendeloo, J. Derluyn, P. Shrivastava, A. Lorenz, M. R. Leys, and M. Germain, *Appl. Phys. Lett.* **89**, 201908 (2006).
- [19] L. W. C. Janis, *Metal Contacts to p-Type Gallium Nitride* (NUS Press, Singapore, 2005), chap. 2.

## Combination of Indium–Tin Oxide and SiO<sub>2</sub>/AlN Dielectric Multilayer Reflective Electrodes for Ultraviolet-Light-Emitting Diodes

This content has been downloaded from IOPscience. Please scroll down to see the full text.

2013 Jpn. J. Appl. Phys. 52 08JG07

(<http://iopscience.iop.org/1347-4065/52/8S/08JG07>)

View [the table of contents for this issue](#), or go to the [journal homepage](#) for more

Download details:

IP Address: 202.11.1.201

This content was downloaded on 03/03/2017 at 06:57

Please note that [terms and conditions apply](#).

You may also be interested in:

[Indium–Tin Oxide/Al Reflective Electrodes for Ultraviolet Light-Emitting Diodes](#)

Kosuke Takehara, Kenichiro Takeda, Shun Ito et al.

[Improvement of Light Extraction Efficiency for AlGa<sub>N</sub>-Based Deep Ultraviolet Light-Emitting Diodes](#)

Tetsuhiko Inazu, Shinya Fukahori, Cyril Pernot et al.

[High Power Efficiency AlGa<sub>N</sub>-Based Ultraviolet Light-Emitting Diodes](#)

Thorsten Passow, Richard Gutt, Michael Kunzer et al.

[Substrate Lifted-off AlGa<sub>N</sub>/AlGa<sub>N</sub> Lateral Conduction Thin-Film Light-Emitting Diodes Operating at 285 nm](#)

Fatima Asif, Hung-Chi Chen, Antwon Coleman et al.

[Investigation of Light Extraction Efficiency in AlGa<sub>N</sub> Deep-Ultraviolet Light-Emitting Diodes](#)

Han-Youl Ryu, Il-Gyun Choi, Hyo-Sik Choi et al.

[Microstructure Analysis of AlGa<sub>N</sub> on AlN Underlying Layers with Different Threading Dislocation Densities](#)

Kimiyasu Ide, Yuko Matsubara, Motoaki Iwaya et al.

[AlGa<sub>N</sub>-Based 355 nm UV Light-Emitting Diodes with High Power Efficiency](#)

Richard Gutt, Thorsten Passow, Michael Kunzer et al.

[Concentrating Properties of Nitride-Based Solar Cells Using Different Electrodes](#)

Mikiko Mori, Shinichiro Kondo, Shota Yamamoto et al.

## Combination of Indium–Tin Oxide and SiO<sub>2</sub>/AlN Dielectric Multilayer Reflective Electrodes for Ultraviolet-Light-Emitting Diodes

Tsubasa Nakashima<sup>1\*</sup>, Kenichiro Takeda<sup>1</sup>, Hiroshi Shinzato<sup>1</sup>, Motoaki Iwaya<sup>1</sup>, Satoshi Kamiyama<sup>1</sup>, Tetsuya Takeuchi<sup>1</sup>, Isamu Akasaki<sup>1,2</sup>, and Hiroshi Amano<sup>2,3</sup>

<sup>1</sup>Faculty of Science and Technology, Meijo University, Nagoya 468-8502, Japan

<sup>2</sup>Akasaka Research Center, Nagoya University, Nagoya 464-8062, Japan

<sup>3</sup>Graduate School of Engineering, Nagoya University, Nagoya 464-8062, Japan

E-mail: 123434034@columni.meijo-u.ac.jp

Received October 13, 2012; revised January 25, 2013; accepted March 12, 2013; published online May 31, 2013

We have investigated novel reflective electrodes by combining an indium–tin oxide (ITO) layer and a SiO<sub>2</sub>/AlN dielectric multilayer (DM) for UV-light-emitting diodes (LEDs). The reflectance of 10 pairs of SiO<sub>2</sub>/AlN DM reached 98.5% at 350 nm. As a result, the ITO/DM electrodes simultaneously satisfied the requirements of high reflectivity in the UV region, good contact characteristics, and current spreading. The light output power of the UV LED with an ITO/DM electrode is 1.2 and 1.6 times higher than those of LEDs with ITO/Al and Ni/Au electrodes, respectively.  
© 2013 The Japan Society of Applied Physics

### 1. Introduction

UV-light sources have been used in various fields, such as medicine, biochemistry and photolithography, in semiconductor device fabrication process.<sup>1)</sup> Since AlGaIn-based UV-light-emitting diodes (UV LEDs) have many advantages, such as compactness, high efficiency, and wavelength selectivity, these devices are expected to replace conventional UV-light sources based on glass lamps. Thus far, there have been many reports on the improvement in the device performance of UV LEDs.<sup>2–10)</sup> However, the external quantum efficiency (EQE) of UV LEDs is still lower than those of visible LEDs.

To improve the EQE of UV LEDs, light extraction efficiency (LEE) is one of the most important factors when the internal quantum efficiency (IQE) of the active layer in the UV LED is high.<sup>11)</sup> In general, the LEE of flip-chip visible LEDs can be improved using high-reflectivity electrodes based on Ag or Rh on the back surface of the LEDs.<sup>12–14)</sup> However, the reflectivities of Ag and Rh in the UV region are very low.<sup>15)</sup> Recently, we have reported highly reflective electrodes that are combinations of indium–tin oxide (ITO) and Al.<sup>15)</sup> Although Al is highly reflective in the UV region, it is difficult to form an ohmic contact with p-GaN. Therefore, we proposed a high-reflectance ohmic electrode of ITO, to form good ohmic contact with p-GaN with high transmittance, combined with highly reflective Al. By using this bilayer electrode, the light output of UV-LEDs was improved 1.2 times compared with that when using the conventional Ni/Au electrode. Because the reflectivity of Al in the UV region is about 90%, further improvements in device performance can be expected if an electrode with a much higher reflectance is realized.

In this study, we propose a novel highly reflective p-electrode of a SiO<sub>2</sub>/AlN dielectric multilayer (DM) combined with ITO for UV LEDs. We fabricated and characterized 350 nm UV LEDs with this proposed electrode.

### 2. Experiments

The structure of UV LEDs with an emission peak wavelength of 350 nm is shown in Fig. 1. The samples were epitaxially grown on sapphire substrates by metalorganic

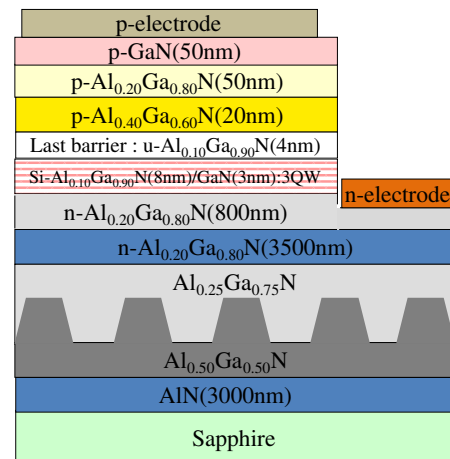
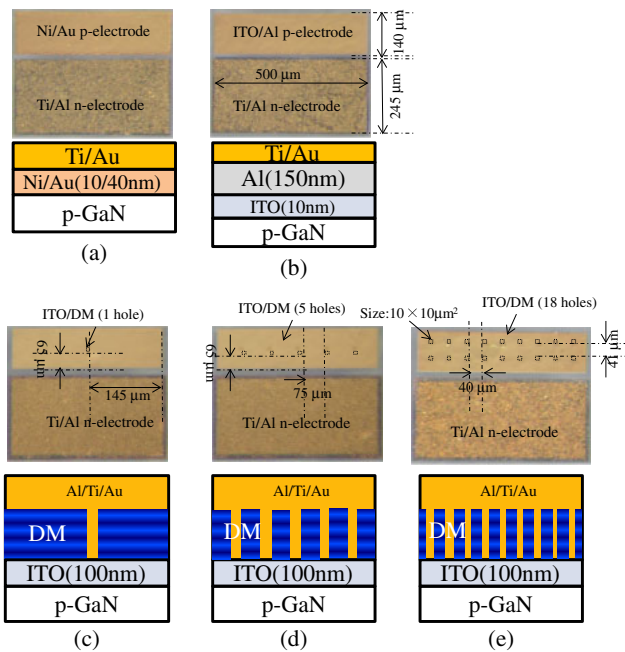


Fig. 1. (Color online) Schematic diagram of the UV-LED.

vapor phase epitaxy. The UV LED structure was fabricated on low-dislocation-density Al<sub>0.20</sub>Ga<sub>0.75</sub>N grown on a grooved Al<sub>0.25</sub>Ga<sub>0.75</sub>N/AlN template.<sup>16)</sup> The UV LED structure was composed of a 3.5- $\mu$ m-thick n-Al<sub>0.2</sub>Ga<sub>0.8</sub>N cladding layer, three pairs of unintentionally doped GaN (3 nm)/Si-doped Al<sub>0.1</sub>Ga<sub>0.9</sub>N (8 nm) multi-quantum wells (MQWs) with a 4-nm-thick unintentionally doped Al<sub>0.1</sub>Ga<sub>0.9</sub>N last barrier, a 20-nm-thick p-Al<sub>0.4</sub>Ga<sub>0.6</sub>N electron-blocking layer, a 50-nm-thick p-Al<sub>0.2</sub>Ga<sub>0.8</sub>N cladding layer, and a 50-nm-thick p-GaN contact layer. The samples were annealed at 800 °C for 5 min in N<sub>2</sub> ambient for p-type activation. A Ti/Al/Ti/Au ohmic contact with the n-AlGaIn layer exposed by reactive ion etching was deposited by electron beam evaporation. After the evaporation, annealing was performed at 850 °C for 30 s in N<sub>2</sub> ambient.

Then, three samples with different p-electrodes were prepared. In type I [Fig. 2(a)], Ni (10 nm)/Au (40 nm) whole-area electrodes were deposited on the p-GaN layer by electron beam evaporation. This electrode structure was used as the control sample. In type II [Fig. 2(b)], ITO (10 nm)/Al (150 nm) whole-area electrodes were deposited on p-GaN by sputtering. Details of the fabrication conditions



**Fig. 2.** (Color online) Top views and cross sectional views of each electrode structure: (a) Ni/Au, (b) ITO/Al, (c) ITO/DM (1 hole), (d) ITO/DM (5 holes), and (e) ITO/DM (18 holes). Ti/Au pad electrodes were formed on all electrodes. Black lines are auxiliary conductors.

of Ni/Au and ITO/Al electrode have been reported in Ref. 15. In type III [Figs. 2(c)–2(e)], a combination of ITO (100 nm) and 10 pairs of SiO<sub>2</sub> (60 nm)/AlN (41 nm) DM with many holes, which were formed by a lift-off method, as shown in Figs. 2(c)–2(e), was deposited on p-GaN by sputtering. By forming holes and filling them with metal, current injection can be achieved. In this study, we used a 100-nm-thick ITO film, because the transmittance of this layer is higher than 90% at 350 nm and its sheet resistance is as low as 300 Ω/□. In order to increase the reflectance of the hole portions, a 200-nm-thick Al metal layer was deposited in the hole. Then, a Ti (10 nm)/Au (240 nm) bilayer was deposited by electron beam evaporation for current injection. The size of the p-electrode was 500 × 140 μm<sup>2</sup>. The number of holes in SiO<sub>2</sub>/AlN DM was varied at 1, 5, and 18, and the size was the fixed at 10 × 10 μm<sup>2</sup>. Ratios of the area occupied by the holes in the p-electrode are approximately 0.02, 0.08, and 2.5%. In addition, Ti (10 nm)/Au (240 nm) pad electrodes were formed on all electrodes for implementation.

The voltage–injection current (*V–I*) and light output power–injection current (*L–I*) characteristics of the UV LEDs were measured using a semiconductor parameter analyzer (Agilent 4156C). The light output powers and EQEs of each device were measured by the power meter and integrating sphere. Moreover, IQEs, which include current injection efficiency in the active layer and LEEs of each sample were determined by the Shockley Read Hall model method.<sup>17–20</sup>

**3. Results and Discussion**

Figure 3 shows the reflectance spectrum of the SiO<sub>2</sub>/AlN DM film. In this figure, we have also included the simulation results. From this figure, the reflectance of the SiO<sub>2</sub>/AlN DM film at 350 nm was found to be approximately 98.5%.

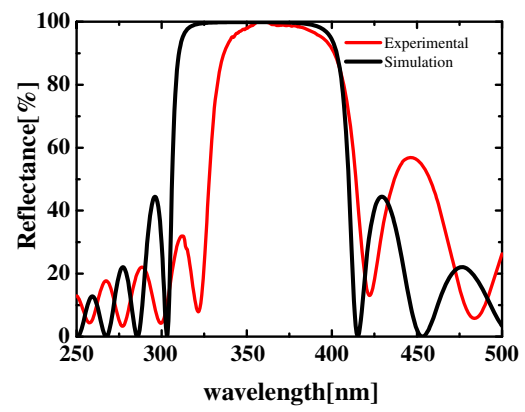


**Fig. 3.** (Color online) Wavelength dispersion of the reflectance of the SiO<sub>2</sub>/AlN DM film. In this figure, we have also included the simulation results calculated by the matrix method.

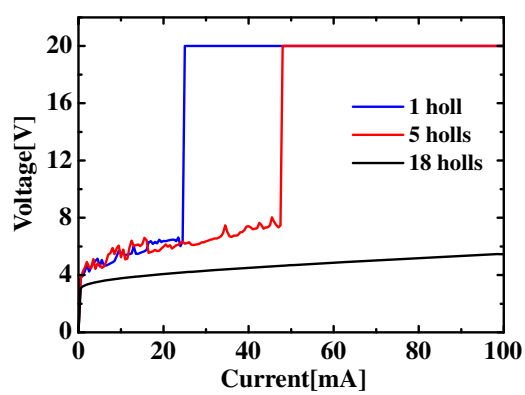


**Fig. 4.** (Color online) *V–I* characteristic of UV-LEDs with ITO/DM p-electrodes with three different numbers of holes.

Although there is a slight deviation between the simulation and experimental results, the reflectance of the SiO<sub>2</sub>/AlN DM film is found to be higher than that of Al.

Figure 4 shows the *V–I* characteristics of UV LEDs with ITO/DM p-electrodes with three different numbers of holes. With 18 holes, satisfactory current injection can be confirmed. Therefore, we have compared the UV LEDs with Ni/Au, ITO/Al, and ITO/DM 18-hole electrodes in this study.

A simple calculation based on the reflectivity results indicates that the light output powers for the ITO/DM electrodes are approximately 1.1 and 1.5 times higher than those for the ITO/Al and Ni/Au electrode assuming no absorption, respectively. Figure 5 shows the *V–I* and *L–I* characteristics of the 350-nm-emission UV LEDs nm with the three different p-electrodes. Table I also was summarized the light output powers and operating voltages of each samples at operation currents of 40 and 80 mA. The light output power of the UV LED with the ITO/DM p-electrode was 14 mW at 100 mA. The *L–I* characteristic shows that the light output power of UV LEDs with the ITO/DM electrode was 1.17 and 1.6 times higher than those of UV LEDs with ITO/Al and Ni/Au electrodes, respectively. These improvements are caused by the increase in the amount of reflected light at the p-electrode. However, the operating voltage at 100 mA of the UV LED with the SiO<sub>2</sub>/

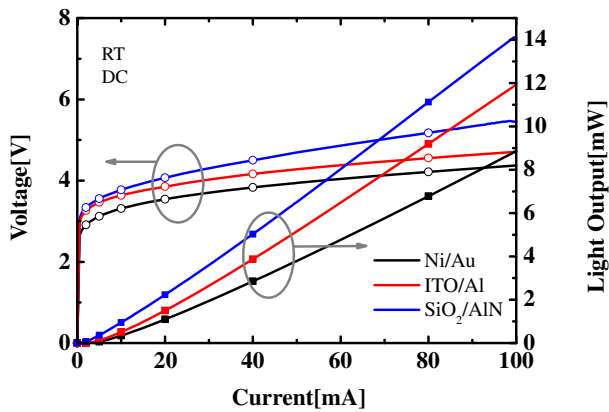


**Fig. 5.** (Color online)  $V$ - $I$  and  $L$ - $I$  characteristics of UV LED with ITO/DM, ITO/Al, and Ni/Au p-electrodes.

**Table I.** Characteristics of the UV-LEDs with three different p-electrodes.

p-electrode	Operating current = 40 mA		Operating current = 80 mA	
	Voltage (V)	Light output (mW)	Voltage (V)	Light output (mW)
Ni/Au	3.8	2.8	4.2	6.7
ITO/Al	4.1	3.8	4.5	9.2
ITO/DM	4.5	5.0	5.1	11.1

**Table II.** EQEs, IQEs including IE, and LEEs of the UV-LEDs with three different p-electrodes.

p-electrode	EQE (%)	IQE <sup>a)</sup> (%)	LEE (%)	WPE (%)
Ni/Au	2.3	28	8	1.9
ITO/Al	2.9	29	10	2.7
ITO/DM	3.4	29	11	2.6

a) including IE.

AlN dielectric multilayer p-electrode was 1.1 V higher than that of the UV LED with the Ni/Au p-electrode. The increase in the operating voltage can be reduced by optimizing the number and size of holes in SiO<sub>2</sub>/AlN DM. Table II shows the EQE, IQE including injection efficiency (IE), LEE, and wall plug efficiency (WPE) of each LED. The EQE of LED with the ITO/DM p-electrode was 3.4%. This value was the highest among the three LEDs. Since the IQEs of the three LEDs are almost the same, we concluded that the EQE of the UV LED with the ITO/DM p-electrode is improved by increasing LEE.

#### 4. Summary

We have investigated a novel ITO/DM reflective p-electrode for UV LEDs. The ITO/DM electrode with holes

filled with metal, exhibited high reflectivity in the UV region, good contact characteristics, and current spread, simultaneously. The light output power of the UV LED with the ITO/DM electrode is 1.2 and 1.6 times higher than those of the ITO/Al and Ni/Au electrodes, respectively.

#### Acknowledgements

This study was partially supported by the Program for the Strategic Research Foundation at Private Universities, 2012–2016, supported by the Ministry of Education, Culture, Sports, Science and Technology.

- 1) Web [http://www.iwasaki.co.jp/chishiki/uv/01.html].
- 2) M. Kim, T. Fujita, S. Fukahori, T. Inazu, C. Pernot, Y. Nagasawa, A. Hirano, M. Ippommatsu, M. Iwaya, T. Takeuchi, S. Kamiyama, M. Yamaguchi, Y. Honda, H. Amano, and I. Akasaki: *Appl. Phys. Express* **4** (2011) 092102.
- 3) M. Shatalov, W. Sun, A. Lunev, X. Hu, A. Dobrinsky, Y. Bilenko, J. Yang, M. Shur, R. Gaska, C. Moe, G. Garrett, and M. Wraback: *Appl. Phys. Express* **5** (2012) 082101.
- 4) H. Tsuzuki, F. Mori, K. Takeda, M. Iwaya, S. Kamiyama, H. Amano, I. Akasaki, H. Yoshida, M. Kuwabara, Y. Yamashita, and H. Kan: *J. Cryst. Growth* **311** (2009) 2860.
- 5) C. Pernot, S. Fukahori, T. Inazu, T. Fujita, M. Kim, Y. Nagasawa, A. Hirano, M. Ippommatsu, M. Iwaya, S. Kamiyama, I. Akasaki, and H. Amano: *Phys. Status Solidi A* **208** (2011) 1594.
- 6) H. Hirayama: *J. Appl. Phys.* **97** (2005) 091101.
- 7) W. H. Sun, J. P. Zhang, V. Adivarahan A. Chitnis, M. Shatalov, S. Wu, V. Mandavilli, J. W. Yang, and M. A. Khan: *Appl. Phys. Lett.* **85** (2004) 531.
- 8) Y. Liao, C. Thomidis, C. Kao, and T. D. Moustakas: *Appl. Phys. Lett.* **98** (2011) 081110.
- 9) R. Gutt, T. Passow, M. Kunzer, W. Pletschen, L. Kirste, K. Forghani, F. Scholz, K. Köhler, and J. Wagner: *Appl. Phys. Express* **5** (2012) 032101.
- 10) J. R. Grandusky, S. R. Gibb, M. C. Mendrick, C. Moe, M. Wraback, and L. J. Schowalter: *Appl. Phys. Express* **4** (2011) 082101.
- 11) K. Ban, J. Yamamoto, K. Takeda, K. Ide, M. Iwaya, T. Takeuchi, S. Kamiyama, I. Akasaki, and H. Amano: *Appl. Phys. Express* **4** (2011) 052101.
- 12) T. Fujii, Y. Gao, R. Sharma, E. L. Hu, S. P. DenBaars, and S. Nakamura: *Appl. Phys. Lett.* **84** (2004) 855.
- 13) T. Jeong, H. H. Lee, S.-H. Park, J. H. Baek, and J. K. Lee: *Jpn. J. Appl. Phys.* **47** (2008) 8811.
- 14) N. Lobo, H. Rodriguez, A. Knauer, M. Hoppe, S. Einfeldt, P. Vogt, M. Weyers, and M. Kneissl: *Appl. Phys. Lett.* **96** (2010) 081109.
- 15) K. Takehara, K. Takeda, S. Ito, H. Aoshima, M. Iwaya, T. Takeuchi, S. Kamiyama, I. Akasaki, and H. Amano: *Jpn. J. Appl. Phys.* **51** (2012) 042101.
- 16) H. Tsuzuki, F. Mori, K. Takeda, T. Ichikawa, M. Iwaya, S. Kamiyama, H. Amano, I. Akasaki, H. Yoshida, M. Kuwabara, Y. Yamashita, and H. Kan: *Phys. Status Solidi A* **206** (2009) 1199.
- 17) W. Shockley and T. Read: *Phys. Rev.* **87** (1952) 835.
- 18) Q. Dai, M. F. Schubert, M. H. Kim, J. K. Kim, E. F. Schubert, D. D. Koleske, M. H. Crawford, S. R. Lee, A. J. Fischer, G. Thaler, and M. A. Banas: *Appl. Phys. Lett.* **94** (2009) 111109.
- 19) K. Takeda, F. Mori, Y. Ogiso, T. Ichikawa, K. Nonaka, M. Iwaya, S. Kamiyama, H. Amano, and I. Akasaki: *Phys. Status Solidi C* **7** (2010) 1916.
- 20) K. Nagata, K. Takeda, K. Nonaka, T. Ichikawa, M. Iwaya, T. Takeuchi, S. Kamiyama, I. Akasaki, H. Amano, H. Yoshida, M. Kuwabara, Y. Yamashita, and H. Kan: *Phys. Status Solidi C* **8** (2011) 1564.

# Improvement of light extraction efficiency of 350-nm emission UV light-emitting diodes

Tsubasa Nakashima<sup>\*1</sup>, Kenichiro Takeda<sup>1</sup>, Motoaki Iwaya<sup>1</sup>, Tetsuya Takeuchi<sup>1</sup>, Satoshi Kamiyama<sup>1</sup>, Isamu Akasaki<sup>1,2</sup>, and Hiroshi Amano<sup>2,3</sup>

<sup>1</sup> Faculty of Science and Technology, Meijo University, 468-8502 Nagoya, Japan

<sup>2</sup> Akasaki Research Center, Nagoya University, 464-8062 Nagoya, Japan

<sup>3</sup> Graduate School of Engineering, Nagoya University, 464-8062 Nagoya, Japan

Received 19 September 2013, revised 6 December 2013, accepted 16 January 2014

Published online 12 March 2014

**Keywords** UV-LED, AlGaIn, ITO, LLO

\* Corresponding author: e-mail 123434034@ccalumni.meijo-u.ac.jp, Phone: +81-52-832-1151, Fax: +81-52-832-1244

In this study, we have aimed to improve the light extraction efficiency by using p- and n- high-reflectivity indium tin oxide (ITO)/Al electrodes with a reflectivity of ~77% at 350 nm, laser lift-off (LLO) method, and silicone sealing. By a combination of these three methods,

the light output power and operating voltage of UV LEDs were improved to 23.8 mW and 6.6 V at 100 mA. Furthermore, the external quantum efficiency and light extraction efficiency were improved to 6.6 and 25.3% at 100 mA.

© 2014 WILEY-VCH Verlag GmbH & Co. KGaA, Weinheim

**1 Introduction** UV light is widely used in the fields of medicine, biochemistry, and photolithography and in semiconductor device fabrication [1]. In particular, AlGaIn-based UV-light-emitting diodes (UV LEDs) afford many advantages such as compactness, high efficiency, and wavelength selectivity, and therefore, these devices are expected to replace conventional UV-light sources based on glass lamps. Recently, many studies have reported new techniques to achieve higher-performance AlGaIn-based UV LEDs [2-10]. However, the external quantum efficiency (EQE) of UV LEDs remains lower than those of visible LEDs.

Light extraction efficiency (LEE) is one of the most important factors for the improvement of EQE in UV LEDs, because the internal quantum efficiency (IQE) of the active layer in UV LEDs has already been improved as much as is possible [11]. The LEE of flip-chip visible LEDs can be improved by using high-reflectivity electrodes based on Ag [12] or Rh [13] on the back surface of the LEDs. The LEE can also be improved by the laser lift-off (LLO) method [14] and by sealing using resin or silicone [15]. By a combination of these methods, the LEE of visible LEDs was improved to ~80% [16]. However, these approaches cannot be applied to UV LEDs.

Thus far, we have reported p- high-reflectivity electrodes made of indium tin oxide (ITO) and Al, which is highly reflective in the UV region [17]. We have also reported the application of LLO to UV LEDs [18]. However, no study has reported on the combination of these methods to improve the device performance of UV LEDs. In addition, UV LEDs sealed by resin or silicone have not yet been reported.

In this study, we propose the application of a combination of p- and n-type ITO/Al reflective electrodes, LLO, and silicone sealing for improving the device performance of UV LEDs. Toward this end, we fabricated and characterized 350-nm UV LEDs.

## 2 Experiments

UV LEDs with an emission peak wavelength of 350 nm were epitaxially grown on sapphire substrates by metalorganic vapor phase epitaxy. The samples of low-dislocation-density Al<sub>0.25</sub>Ga<sub>0.75</sub>N grown on grooved Al<sub>0.5</sub>Ga<sub>0.5</sub>N/AlN/sapphire comprised a 2.8- $\mu$ m-thick n-Al<sub>0.2</sub>Ga<sub>0.8</sub>N cladding layer, three pairs of unintentionally doped GaN (3 nm), Si-doped Al<sub>0.1</sub>Ga<sub>0.9</sub>N (8 nm) multiple quantum wells (MQWs) with a 4-nm-thick unintentionally doped Al<sub>0.1</sub>Ga<sub>0.9</sub>N last barrier, a 20-nm-thick p-Al<sub>0.4</sub>Ga<sub>0.6</sub>N

electron blocking layer, a 50-nm-thick p-Al<sub>0.2</sub>Ga<sub>0.8</sub>N cladding layer, and a 50-nm-thick p-GaN contact layer. The samples were annealed at 800 °C for 5 min in N<sub>2</sub> ambient for p-type activation. A contact with the n-AlGaIn layer exposed by reactive ion etching was deposited by electron beam evaporation.

We fabricated and characterized five types of flip-chip LEDs with different device structures. Samples A–C were fabricated to understand the usefulness of a high-reflectivity electrode. Samples D and E were fabricated to investigate the usefulness of LLO and resin sealing. The details of the structure of each sample are as follows:

1. Sample A:

This UV LED has a conventional Ni (10 nm)/Au (40 nm) p-electrode that was annealed at 550 °C for 3 min in O<sub>2</sub> ambient and a Ti (30 nm)/Al (100 nm)/Ti/Au n-electrode that was annealed at 850 °C for 30 s in N<sub>2</sub> ambient.

2. Sample B:

This UV LED has a high-reflectivity ITO (10 nm)/Al (150 nm) p-electrode of which only ITO was annealed at 600 °C for 5 min in N<sub>2</sub> ambient and a Ti (30 nm)/Al (100 nm) n-electrode that was annealed at 850 °C for 30 s in N<sub>2</sub> ambient.

3. Sample C:

This UV LED has both high-reflectivity ITO (10 nm)/Al (150 nm) p- and n-electrodes that were annealed at 600 °C for 5 min in N<sub>2</sub> ambient.

Samples E and D were used to examine the effect of LLO and silicone sealing. We processed sample C for use

in these investigations. Sample D was subjected to LLO by irradiating a 193-nm ArF laser (pulse width: 1.5 ns, energy: 1.5 J/cm<sup>2</sup>) one time. Next, KOH wet etching was performed at 100 °C for 1 min. Figure 2 shows the scanning electron microscopy (SEM) image of the N-face of GaN after LLO and KOH wet etching. It is observed that the KOH-etched N-face GaN surfaces show hexagonal cone-like features with a size and height of 100–1,000 nm and 500–1,000 nm, respectively. In addition, sample E was subjected to silicone sealing at the sample D. The silicone sealing was of the chip-on-board type. The silicone sealing was processed into a semi-spherical form with a diameter of 1 mm. It involved heat treatment at 150 °C for 30 min.

The voltage-injection current (V-I) and light output power-injection current (L-I) characteristics of the LEDs were measured using a semiconductor parameter analyzer (Agilent 4156C). The light output powers and wall plug efficiencies (WPEs) of each device were respectively measured using a power meter and an integrating sphere. Then, the IQEs, including current injection efficiency (IE) in the active layer, and the LEEs of each sample were determined by the Shockley–Read–Hall model method [18–21].

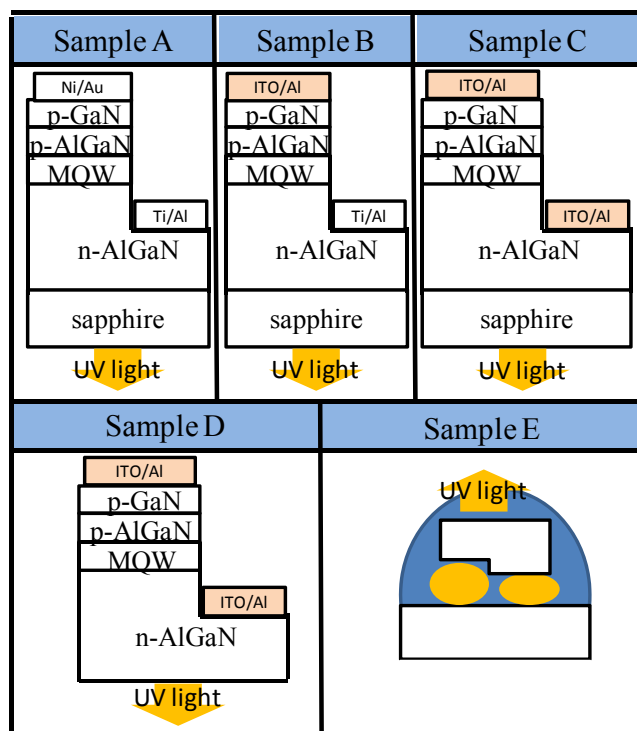


Figure 1 Five types of flip-chip LEDs.

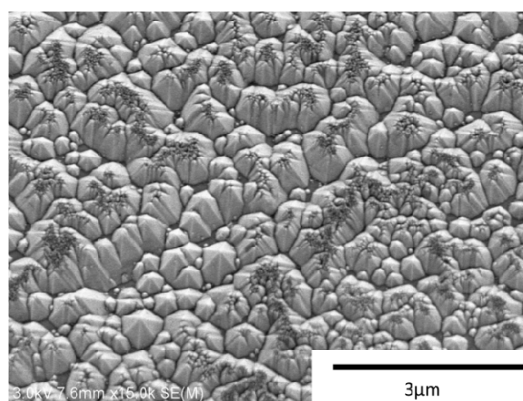


Figure 2 Scanning electron microscopy image of AlN after KOH wet etching.

**3 Results and discussion** Figure 3 shows the V-I and L-I characteristics of samples A–C. Table 1 summarizes the light output powers and operating voltages of each sample at operation currents of 50 and 100 mA. From the L-I characteristic, the light output power of sample C was 1.2 and 1.3 times higher than that of samples A and B, respectively. This improvement is caused by the increase in the amount of reflected light at the p-type electrode.

Because GaN has a large absorption coefficient of  $\sim 1 \times 10^5 \text{ cm}^{-1}$  at 350 nm, approximately 60% of the reflected light is absorbed in the p-GaN layer. Nevertheless, we confirmed that the high reflectivity electrode is effective enough to increase the LEE. Figure 4 shows the reflectance of each electrode. Considering this absorption and these electrode reflectances, the calculated results for samples B and C were approximately 1.3 and 1.4 times higher than that for sample A. These calculations are in good agreement with the experimental result. However, the op-

erating voltage of the UV LED with a high-reflectivity n-electrode at 100 mA was 1.6 V higher than that of the UV LED with the Ti/Al n-electrode. This is because the ITO and n-AlGaIn formed a Schottky contact. Although the optimization of the high-reflectivity n-electrode is essential, we found that a highly reflective n-type electrode is also useful for improving the light output power.

Figure 5 shows the V-I and L-I characteristics of samples C–E. Because the V-I curves of each LED are almost the same, it is suggested that there is no damage on each LED by LLO and silicone sealing. In contrast, the light output power of samples D and E was 1.5 and 2.0 times higher than that of sample C, respectively. These results suggest that LLO and silicone sealing effectively improve the LEE in the 350-nm wavelength region. LLO increased the light output power by more than 2.0 times in visible LEDs [14]. However, in this experiment, the increase was by 1.5 times, because the absorption of p-GaN occurs by multiple reflection. We thought that this decrease in the rate of increase of the light output power was affected by the decrease in the multiple reflection effect owing to the absorption in p-type GaN. Therefore, further improvement of the LEE can be expected if the p-type GaN layer is removed. Table 2 summarizes the EQE, IQE including IE, LEE, and WPE of each device. The EQE and LEE of the UV LED of sample E was 6.6 and 25.3% at 100 mA.

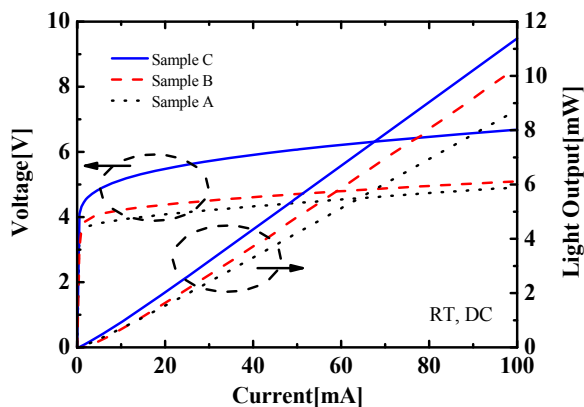


**Figure 3** V-I and L-I characteristics of flip-chip UV LEDs of samples A, B, and C.

**4 Summary** In this study, we demonstrated the use of a reflective electrode, LLO, and silicone sealing to improve the LEE of UV LEDs. The EQE and LEE of a 350-nm-emission UV LED were improved to 6.6 and 25.3% by a combination of both p- and n- high-reflectivity electrodes, LLO, and silicone sealing.

**Acknowledgements** This study was partially supported by the Program for the Strategic Research Foundation at Private Universities, 2012–2016, supported by the Ministry of Education, Culture, Sports, Science and Technology (MEXT) and a MEXT Grant-in-Aid for Specially Promoted Research #25000011.

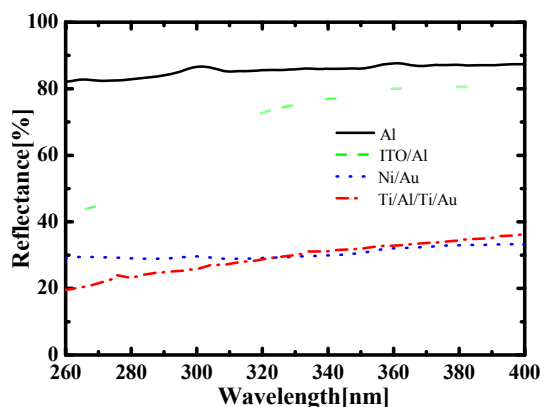


**Figure 4** The reflectance of Al, ITO/Al and Ni/Au electrode.

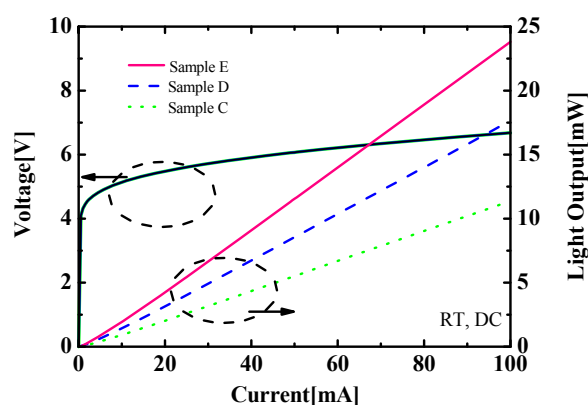


**Figure 5** V-I and L-I characteristics of flip-chip UV LEDs of samples C, D, and E.

**Table 1** Characteristics of flip-chip UV LEDs.

	Operating Current = 50mA		Operating Current = 100mA	
	Voltage [V]	Light output [mW]	Voltage [V]	Light output [mW]
Sample A	4.4	4.2	4.9	8.7
Sample B	4.7	4.8	5.1	10.3
Sample C	6.1	5.5	6.6	11.4
Sample D	6.1	8.6	6.6	17.6
Sample E	6.1	11.5	6.6	23.8

**Table 2** EQEs, IQEs including IE, and LEEs of flip-chip UV LEDs.

	EQE [%]	IQE <sup>a)</sup> [%]	LEE [%]	WPE [%]
Sample A	1.9	26	7.6	1.7
Sample B	2.6	26	10.0	2.1
Sample C	3.1	26	11.9	1.7
Sample D	4.9	26	18.8	2.7
Sample E	6.6	26	25.3	3.6

a) Including IE

## References

- [1] M. Kim, T. Fujita, S. Fukahori, T. Inazu, C. Pernot, Y. Nagasawa, A. Hirano, M. Ippommatsu, M. Iwaya, T. Takeuchi, S. Kamiyama, M. Yamaguchi, Y. Honda, H. Amano, and I. Akasaki, *Appl. Phys. Express* **4**, 092102 (2011).
- [2] M. Shatalov, W. Sun, A. Lunev, X. Hu, A. Dobrinsky, Y. Bilenko, J. Yang, M. Shur, R. Gaska, C. Moe, G. Garrett, and M. Wraback, *Appl. Phys. Express* **5**, 082101 (2012).
- [3] H. Tsuzuki, F. Mori, K. Takeda, M. Iwaya, S. Kamiyama, H. Amano, I. Akasaki, H. Yoshida, M. Kuwabara, Y. Yamashita, and H. Kan, *J. Cryst. Growth* **311**, 2860 (2009).
- [4] C. Pernot, S. Fukahori, T. Inazu, T. Fujita, M. Kim, Y. Nagasawa, A. Hirano, M. Ippommatsu, M. Iwaya, S. Kamiyama, I. Akasaki, and H. Amano, *Phys. Status Solidi A* **208**, 1594 (2011).
- [5] H. Hirayama, *J. Appl. Phys.* **97**, 091101 (2005).
- [6] W. H. Sun, J. P. Zhang, V. Adivarahan, A. Chitnis, M. Shatalov, S. Wu, V. Mandavilli, J. W. Yang, and M. A. Khan, *Appl. Phys. Lett.* **85**, 531 (2004).
- [7] Y. Liao, C. Thomidis, C. Kao, and T. D. Moustakas, *Appl. Phys. Lett.* **98**, 081110 (2011).
- [8] C. Pernot, M. Kim, S. Fukahori, T. Inazu, T. Fujita, Y. Nagasawa, A. Hirano, M. Ippommatsu, M. Iwaya, S. Kamiyama, I. Akasaki, and H. Amano, *Appl. Phys. Express* **3**, 061004 (2010).
- [9] H. Hirayama, Y. Tsukada, T. Maeda, and N. Kamata, *Appl. Phys. Express* **3**, 031002 (2010).
- [10] J. R. Grandusky, S. R. Gibb, M. C. Mendrick, and L. J. Schowalter, *Appl. Phys. Express* **3**, 072103 (2010).
- [11] K. Ban, J. Yamamoto, K. Takeda, K. Ide, M. Iwaya, T. Takeuchi, S. Kamiyama, I. Akasaki, and H. Amano, *Appl. Phys. Express* **4**, 052101 (2011).
- [12] T. Mukai, S. Nagahama, T. Kozaki, M. Sano, D. Morita, T. Yanamoto, M. Yamamoto, K. Akashi, and S. Masui, *Phys. Status Solidi A* **201**, 2712 (2004).
- [13] M. Yamada, T. Mitani, Y. Narukawa, S. Shioji, I. Niki, S. Sonobe, K. Deguchi, M. Sano, and T. Mukai, *Jpn. J. Appl. Phys.* **41**, L1431 (2002).
- [14] T. Fujii, Y. Gao, R. Sharma, E. L. Hu, S. P. DenBaars, and S. Nakamura, *Appl. Phys. Lett.* **84**, 855 (2004).
- [15] M. Funato, M. Ueda, Y. Kawakami, Y. Narukawa, T. Kosugi, M. Takahashi, and T. Mukai, *Jpn. J. Appl. Phys.* **45**, L659 (2006).
- [16] Y. Narukawa, M. Ichikawa, D. Sanga, M. Sano, and T. Mukai, *J. Phys. D, Appl. Phys.* **43**, 354002 (2010).
- [17] H. Aoshima, K. Takeda, K. Takehara, S. Ito, M. Mori, M. Iwaya, T. Takeuchi, S. Kamiyama, I. Akasaki, and H. Amano, *Phys. Status Solidi C* **9**, 753 (2012).
- [18] W. Shockley and T. Read, *Phys. Rev.* **87**, 835 (1952).
- [19] Q. Dai, M. F. Schubert, M. H. Kim, J. K. Kim, E. F. Schubert, D. D. Koleske, M. H. Crawford, S. R. Lee, A. J. Fischer, G. Thaler, and M. A. Banas, *Appl. Phys. Lett.* **94**, 111109 (2009).
- [20] K. Takeda, F. Mori, Y. Ogiso, T. Ichikawa, K. Nonaka, M. Iwaya, S. Kamiyama, H. Amano, and I. Akasaki, *Phys. Status Solidi C* **7**, 1916 (2010).
- [21] K. Nagata, K. Takeda, K. Nonaka, T. Ichikawa, M. Iwaya, T. Takeuchi, S. Kamiyama, I. Akasaki, H. Amano, H. Yoshida, M. Kuwabara, Y. Yamashita, and H. Kan, *Phys. Status Solidi C* **8**, 1564 (2011).

## GaN barrier layer dependence of critical thickness in GaInN/GaN superlattice on GaN characterized by in situ X-ray diffraction

This content has been downloaded from IOPscience. Please scroll down to see the full text.

2016 Jpn. J. Appl. Phys. 55 05FD11

(<http://iopscience.iop.org/1347-4065/55/5S/05FD11>)

View [the table of contents for this issue](#), or go to the [journal homepage](#) for more

Download details:

IP Address: 219.127.71.134

This content was downloaded on 03/03/2017 at 06:40

Please note that [terms and conditions apply](#).

You may also be interested in:

[Relationship between misfit-dislocation formation and initial threading-dislocation density in GaInN/GaN heterostructures](#)

Motoaki Iwaya, Taiji Yamamoto, Daisuke Iida et al.

[Multijunction GaInN-based solar cells using a tunnel junction](#)

Hironori Kurokawa, Mitsuru Kaga, Tomomi Goda et al.

[Realization of Nitride-Based Solar Cell on Freestanding GaN Substrate](#)

Yosuke Kuwahara, Takahiro Fujii, Yasuharu Fujiyama et al.

[Microstructures of GaInN/GaN Superlattices on GaN Substrates](#)

Toru Sugiyama, Yosuke Kuwahara, Yasuhiro Isobe et al.

[GaInN-Based Solar Cells Using Strained-Layer GaInN/GaN Superlattice Active Layer on a Freestanding GaN Substrate](#)

Yosuke Kuwahara, Takahiro Fujii, Toru Sugiyama et al.

[Growth of 2 m Crack-Free GaN on Si\(111\) Substrates by Metal Organic Chemical Vapor Deposition](#)

Wei Meng, Wang Xiao-Liang, Xiao Hong-Ling et al.

[V-pit to truncated pyramid transition in AlGaInN-based heterostructures](#)

A Mogilatenko, J Enslin, A Knauer et al.

[Reduction of V-pit and threading dislocation density in InGaInN/GaN heterostructures grown on cracked AlGaInN templates](#)

C B Soh, S Y Chow, S Tripathy et al.



## GaN barrier layer dependence of critical thickness in GaInN/GaN superlattice on GaN characterized by in situ X-ray diffraction

Junya Osumi<sup>1\*</sup>, Koji Ishihara<sup>1</sup>, Taiji Yamamoto<sup>1</sup>, Motoaki Iwaya<sup>1</sup>, Tetsuya Takeuchi<sup>1</sup>, Satoshi Kamiyama<sup>1</sup>, and Isamu Akasaki<sup>1,2</sup>

<sup>1</sup>Faculty of Science and Technology, Meijo University, Nagoya 468-8502, Japan

<sup>2</sup>Akasaki Research Center, Nagoya University, Nagoya 464-8603, Japan

\*E-mail: 153434005@ccalumni.meijo-u.ac.jp

Received December 29, 2015; revised February 18, 2016; accepted February 23, 2016; published online April 22, 2016

We investigated the critical thickness dependence on the GaN barrier layer thickness in a GaInN/GaN superlattice (SL). The characterization was done by combining an in situ X-ray diffraction (XRD) system attached to a metalorganic vapor phase epitaxy reactor and ex situ analyses such as scanning electron microscopy and transmission electron microscopy. The critical thickness required for the introduction of *a* + *c*-type misfit dislocations (MDs) in the GaInN/GaN SL was determined by analyzing the full width at half maximum of the in situ XRD spectrum from a GaInN/GaN SL as a function of SL periods, and we successfully found the critical thicknesses of specific different SLs.

© 2016 The Japan Society of Applied Physics

### 1. Introduction

GaInN ternary alloys have bandgaps ranging from 0.65 to 3.43 eV, and are therefore used as active layers in violet, blue, and green light-emitting diodes (LEDs).<sup>1–3</sup> In addition, these materials can theoretically be used in the design of a multijunction solar cell that covers the infrared to the ultraviolet regions of the solar spectrum.<sup>4–10</sup> In general, most GaInN-based solar cells are fabricated on a GaN template or a freestanding GaN substrate because the growth of a thick GaInN layer is quite difficult. Many previous studies have revealed the mechanism by which defects form via strain relaxation in GaInN/GaN heterostructures<sup>11–15</sup> in order to minimize defect formation and improve device performance. We have previously reported that the superlattice (SL) is useful for improving the crystallinity of the GaInN/GaN SL active layer.<sup>9,10,16–19</sup> The increases in the SL periods and InN molar fraction in the GaInN/GaN SL active layer are required for realizing high-conversion-efficiency GaInN-based solar cells. However, the crystallinity of the GaInN/GaN SL deteriorates rapidly upon the introduction of misfit dislocations (MDs) and growth pits if the layer thickness exceeds the critical thickness.<sup>4,12,13</sup> Thus, the determination of the structure and growth conditions that suppress the generated MDs in a GaInN/GaN SL is important. Therefore, several experiments are needed to explore the optimal structures unless in situ observations are employed.

In situ monitoring in metal–organic vapor phase epitaxy (MOVPE) is the key process in device manufacturing. In fact, the information given by this monitoring can be fed back into the growth condition setup, and therefore, helps us to understand the growth mechanism. We have already reported on the novel X-ray in situ measurements in Refs. 20 and 21. In situ monitoring using X-rays yields a measure of the lattice constant, the nanostructure of the thin film, and the crystalline quality, for example. So far, we have reported that the use of this in situ X-ray diffraction (XRD). It makes possible to accurately follow the relaxation process that occurs in a GaInN/GaN heterostructure by analyzing the full width at half maximum (FWHM) of the spectrum of the GaInN layers. Moreover, we have reported the determination

of a reliable critical thickness in GaInN/GaN heterostructures to obtain MD-free growth.<sup>22</sup>

In the present study, we analyzed a GaInN/GaN SL using an in situ XRD system attached to the MOVPE reactor, and then, compared the results with those of ex situ characterization techniques such as scanning electron microscopy (SEM) and transmission electron microscopy (TEM). Thus, we investigated the critical thickness of MDs introduced in to the GaInN/GaN SL on GaN systems as a function of GaN barrier layer thickness. The results indicate that the critical thickness required for the introduction of MDs in the GaInN/GaN SL depends on the GaN barrier layer for the GaInN/GaN SL on GaN.

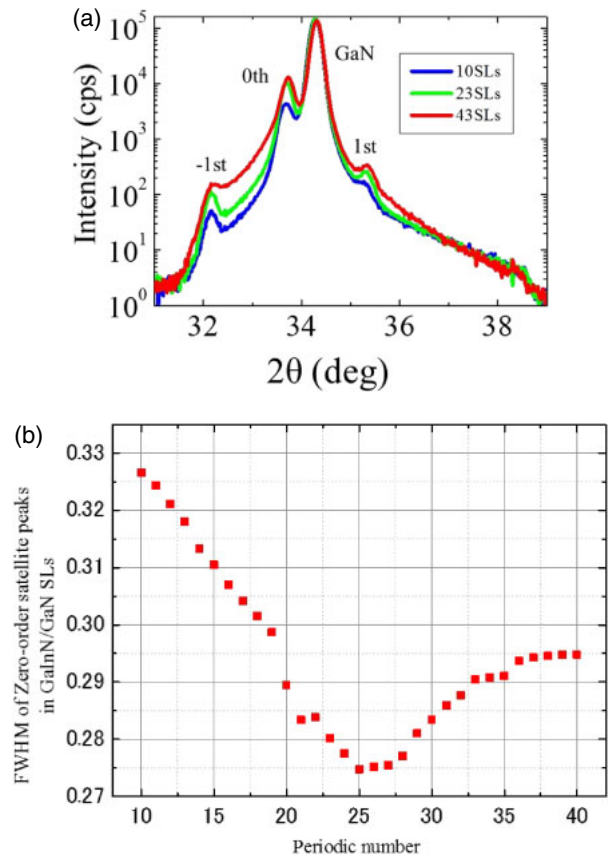
### 2. Experimental methods

All samples were grown on *c*-plane sapphire and freestanding GaN substrates using MOVPE with a horizontal face-down 2-in. × 3-wafer reactor system (Taiyo Nippon Sanso EMC GRC-230X). Trimethylgallium (TMGa), triethylgallium (TEGa), trimethylindium (TMIn), and ammonia (NH<sub>3</sub>) were used as Ga, In, and N source materials for the growth of GaN and GaInN, respectively. Hydrogen (H<sub>2</sub>) and nitrogen (N<sub>2</sub>) were used as the carrier gases. The rotational speed of the substrate was 5 rpm. For the sapphire substrate (~430 μm), the GaInN/GaN SL samples were fabricated on an ~3-μm-thick GaN template grown using a low-temperature buffer layer.<sup>23</sup> For the GaN substrate (~330 μm), the GaInN/GaN SL samples were fabricated after the growth of an ~1-μm-thick homoepitaxial GaN layer. The threading dislocation (TD) densities of the GaN template and freestanding GaN substrate were ~3 × 10<sup>8</sup> cm<sup>-2</sup> and less than 3 × 10<sup>6</sup> cm<sup>-2</sup>, respectively. After the growth of the homoepitaxial GaN layer at 1,050 °C on the GaN template or substrate using H<sub>2</sub> as the carrier gas at 933 hPa, each sample was cooled to 720–750 °C and the carrier gas was changed to N<sub>2</sub>. Then, a Ga<sub>1-x</sub>In<sub>x</sub>N (2 nm)/GaN (*y* nm) SL was grown on the GaN template and GaN substrate. The InN mole fraction in the GaInN layer was varied from 0.20 to 0.25 by adjusting the growth temperature, and the GaN barrier thickness in the GaN layer was varied from 3 to 11 nm by adjusting the growth time. The thickness of the GaInN well layer was set to 2 nm for all samples. We observed the GaInN/GaN SL with

symmetric (0002) Bragg diffraction using the in situ XRD system attached to the MOVPE. The MOVPE apparatus was equipped with two beryllium (Be) windows, which served as viewports for the passage of X-rays focused on the sample surface using a Johansson curved crystal mirror. By using this method, the incidence angle of the X-rays can be changed independently from the X-ray source. The X-rays diffracted on the sample surface were detected by a one-dimensional charge-coupled device (1D CCD) without moving the substrate or the detector. This system executed the equivalent of a (0002)  $2\theta/\omega$  scan in one second during the sample rotation without requiring the use of an analyzer crystal. Furthermore, the  $2\theta$  value was calibrated using on the GaN peak. Although the resolution slightly decreased compared with that of a conventional XRD system, the equivalent of a (0002)  $2\theta/\omega$  scan at a resolution of 1 arcsec was possible. Therefore, in this system, both the tilt component and distribution of the lattice constant  $c$  can be characterized from the FWHM. Furthermore, FWHMs of the in situ XRD spectrum were analyzed by a Gaussian fitting method. We observed the GaInN surface structure and defects by SEM and TEM, respectively.

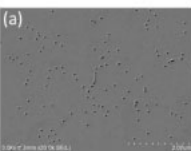
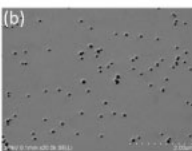
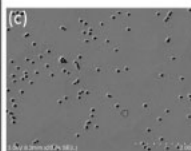
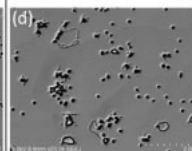
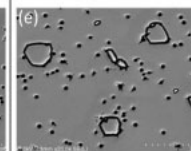
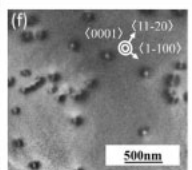
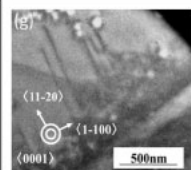
**3. Results and discussion**

The in situ XRD spectra of Ga<sub>0.80</sub>In<sub>0.20</sub>N (2 nm)/GaN (3 nm) SL are shown in Fig. 1(a). The FWHM obtained from the in situ XRD signal for the Ga<sub>0.80</sub>In<sub>0.20</sub>N (2 nm)/GaN (3 nm) SL on a GaN template in the zero-order satellite peak region is shown in Fig. 1(b). The FWHM was determined by fitting the pseudo-Voigt function for the in situ XRD spectrum. The FWHMs for the Ga<sub>0.80</sub>In<sub>0.20</sub>N (2 nm)/GaN (3 nm) SL decreased with increasing number of periods of SL up to 25 periods. The decrease in the FWHM is attributed to the increase in the intensity of the satellite peak with an increasing diffraction surface for the X-rays through the periods of the GaInN/GaN SL. Hereafter, the minimum value of FWHM was observed and the FWHM increased after this minimum value. However, it is observed that after the minimum point, crystal defects appeared in the GaInN/GaN SL. To investigate this phenomenon, Ga<sub>0.80</sub>In<sub>0.20</sub>N (2 nm)/GaN (3 nm) SL samples on GaN templates with different periods were investigated by ex situ characterization



**Fig. 1.** (Color online) (a) In situ XRD spectra of Ga<sub>0.80</sub>In<sub>0.20</sub>N (2 nm)/GaN (3 nm) SL. (b) Typical FWHMs from the Ga<sub>0.80</sub>In<sub>0.20</sub>N/GaN SL on the GaN template as a function of number of SL periods.

techniques. Plan-view SEM and TEM images for the Ga<sub>0.80</sub>In<sub>0.20</sub>N (2 nm)/GaN (3 nm) SL samples on GaN templates are shown in Fig. 2. The number of periods ranges from 10 to 40. The plan-view SEM images show significant differences in the size of v-pits with increasing GaInN/GaN SL periods. The v-pit increases in size for additional periods, as shown in Figs. 2(a)–2(c), and is homogenous for each sample. However, the v-pits are no longer homogenous and their size increases with higher number of periods, as shown in Figs. 2(d) and 2(e). Note that those smaller than 200 nm

On GaN template	10 periods	20 periods	25 periods	30 periods	40 periods
Plan-view SEM images	(a)  $4.2 \times 10^8 \text{ cm}^{-2}$	(b)  $3.9 \times 10^8 \text{ cm}^{-2}$	(c)  $4.5 \times 10^8 \text{ cm}^{-2}$	(d)  $9.8 \times 10^8 \text{ cm}^{-2}$	(e)  $9.5 \times 10^8 \text{ cm}^{-2}$
Plan-view TEM images		(f) 	(g) 		

**Fig. 2.** (Color online) Plan-view SEM images and plan-view TEM images for Ga<sub>0.80</sub>In<sub>0.20</sub>N/GaN SL samples of different periods on GaN templates. The v-pit density is shown below the SEM images.

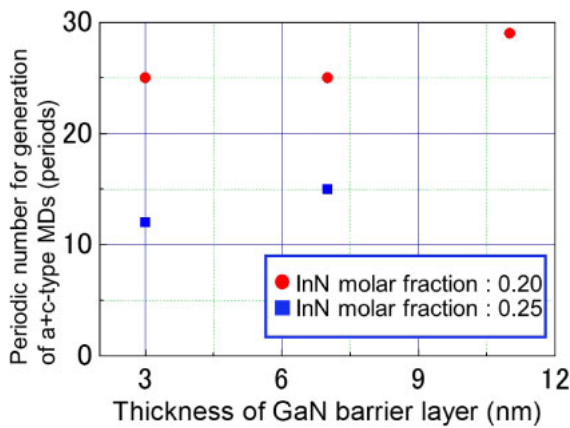


**Fig. 3.** (Color online) GaN barrier layer thickness as a function of the number of periods required for the generation of *a + c*-type MDs for different InN molar fractions.

appear as *v*-pits after the minimum point. It is reported elsewhere that the *v*-pits are created by the TDs originating from the underlying GaN template.<sup>13)</sup> The pit density of each sample is almost comparable to the TD density. However, after 30 periods, as shown in Figs. 2(d) and 2(e), pits with different diameters and trenches are observed. It is suggested that the larger pits originate in deeper interfaces. The *a + c*-type MDs were observed after 25 periods, as shown in Fig. 2(g), in contrast to the cases with fewer than 25 periods. Therefore, in situ XRD measures the critical thickness for the introduction of *a + c*-type MDs in the GaInN/GaN SL on the GaN system through only one-time crystal growth.

The number of periods required for the generation of *a + c*-type MDs with different InN molar fractions in GaInN layers as a function of thickness in the GaN barrier layer are shown in Fig. 3. For the InN molar fraction of 0.25, the number of periods required for the generation of *a + c*-type MDs increases from 12 to 15 on changing from the 3- to the 7-nm-thick GaN barrier layer. Also, for the InN molar fraction of 0.20, the number of periods required for the generation of *a + c*-type MDs increases from 25 to 29 on changing from the 3- to the 11-nm-thick GaN barrier layer. In contrast, it did not change in the case of 3- and 7-nm-thick GaN barrier layers. In general, the critical thickness in the SL increases with increasing barrier layer thickness because of the reduction of compression stress in the GaInN well layer upon increasing the GaN barrier layer thickness. Bykhovski et al. reported the calculation of stress in the SL structure. In this report, the ratio of barrier to well layer thickness is largely dependent on the critical thickness.<sup>24)</sup> Therefore, it is considered to be intended to suggest these results. Also, in the case of an InN molar fraction of 0.20 with 3 and 7 nm thicknesses of the GaN barrier layer, since the strain in Ga<sub>0.80</sub>In<sub>0.20</sub>N is less than that in Ga<sub>0.85</sub>In<sub>0.25</sub>N, it is considered that the effect of the GaN barrier layer is weak on a thin film. Moreover, on the basis of the in situ XRD results, a reliable critical thickness for obtaining *a + c*-type MD-free growth was determined.

Because we compared with a GaInN single layer on GaN, the critical thickness of the sum of GaInN and GaN as a function of average InN molar fraction of GaInN/GaN SL is shown in Fig. 4. We also plot the data of the critical thickness

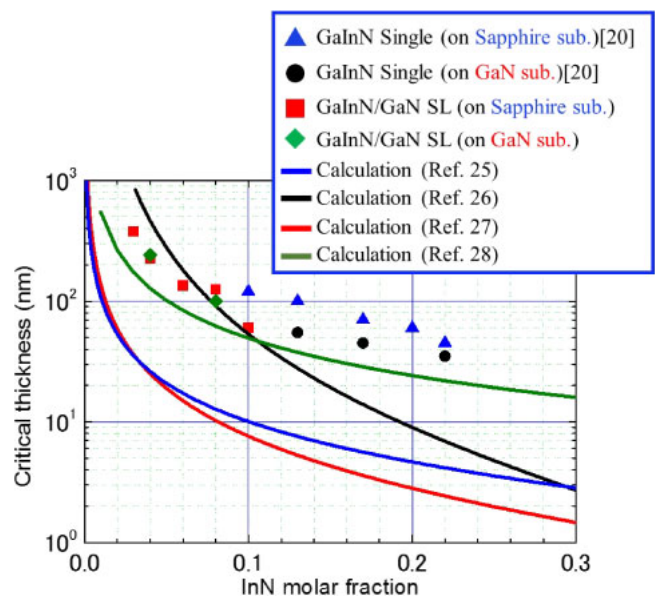


**Fig. 4.** (Color online) Critical thickness of the sum of GaInN and GaN as a function of average InN molar fraction of GaInN/GaN SL. The data for the GaInN single layer on GaN template and GaN substrate of critical thickness are taken from Ref. 20. The results of theoretical calculations performed using data in Refs. 25–28 are also shown.

of the GaInN single layer on the GaN template and GaN substrate from Ref. 20. The critical thickness required for the introduction of *a + c*-type MDs in the GaInN single layer depended strongly on the TD density of the underlying GaN layer. In contrast, for the GaInN/GaN SL on the GaN template and GaN substrate with the same InN molar fraction, there is no dependence of the critical thickness on the TD density of the underlying GaN layer. We compared our results with theoretical calculations for GaInN/GaN heterostructures and the critical thickness required for the introduction of *a + c*-type MDs in the GaInN/GaN SL on the GaN template and GaN substrate. These theoretical calculations, as obtained from the data in Refs. 25–28, are also included in Fig. 4. The critical thickness of the SL behaves in accordance with the theoretical formula in Ref. 28. The theory presented in this reference considers the interaction between dislocations, in contrast to other theories. In the case of the underlying GaN layer with a high TD density, it is believed that the critical thickness increases with the bending of the TD. Therefore, it is considered that the critical thickness is affected by the difference in the TD density of the underlying GaN layer. In contrast to the GaInN/GaN SL on GaN, the critical thickness of *a + c*-type MDs did not change with the TD density in the underlying GaN layer. It is thought that because of the greater stress reduction effect of the barrier layer than the stress relaxation due to the bending of the TD.

#### 4. Conclusions

We investigated GaInN/GaN SLs with different GaN barrier layer thicknesses by both in situ XRD and ex situ characterization techniques. It was demonstrated that the critical thickness required for the introduction of *a + c*-type MDs can be obtained via in situ XRD analysis. In addition, the critical thickness required for the introduction of *a + c*-type MDs in the GaInN/GaN SL was found to depend strongly on the

GaN barrier layer thickness. For the GaInN/GaN SL on the GaN template and GaN substrate with the same InN molar fraction, there is no dependence of the critical thickness on the TD density of the underlying GaN layer.

### Acknowledgments

This study was partially supported by the Program for the Strategic Research Foundation at Private Universities, 2012–2016, supported by the Ministry of Education, Culture, Sports, Science and Technology (MEXT), the MEXT Grant-in-Aid for Specially Promoted Research No. 25000011, and the MEXT Grant-in-Aid for Scientific Research A No. 15H02019.

- 1) I. Akasaki and H. Amano, *Jpn. J. Appl. Phys.* **36**, 5393 (1997).
- 2) V. Y. Davydov, A. A. Klochikhin, R. P. Seisyan, V. V. Emtsev, S. V. Ivanov, F. Bechstedt, J. Furthmüller, H. Harima, A. V. Mudryi, J. Aderhold, O. Semchinova, and J. Graul, *Phys. Status Solidi B* **229**, r1 (2002).
- 3) B. Monemar, *Phys. Rev. B* **10**, 676 (1974).
- 4) R. Liu, J. Mei, S. Srinivasan, F. A. Ponce, H. Omiya, Y. Narukawa, and T. Mukai, *Appl. Phys. Lett.* **89**, 201911 (2006).
- 5) J. Wu, W. Walukiewicz, K. M. Yu, J. W. Ager, III, E. E. Haller, H. Lu, W. J. Schaff, Y. Saito, and Y. Nanishi, *Appl. Phys. Lett.* **80**, 3967 (2002).
- 6) H. Hamzaoui, A. S. Bouazzi, and B. Rezig, *Sol. Energy Mater. Sol. Cells* **87**, 595 (2005).
- 7) J. Wu, W. Walukiewicz, K. M. Yu, W. Shan, J. W. Ager, E. E. Haller, H. Lu, W. J. Schaff, W. K. Metzger, and S. Kurtz, *J. Appl. Phys.* **94**, 6477 (2003).
- 8) A. Vos, *Endoreversible Thermodynamics of Solar Energy Conversion* (Oxford University Press, New York, 1992) p. 29.
- 9) Y. Kuwahara, T. Fujii, Y. Fujiyama, T. Sugiyama, M. Iwaya, T. Takeuchi, S. Kamiyama, I. Akasaki, and H. Amano, *Appl. Phys. Express* **3**, 111001 (2010).
- 10) M. Mori, S. Kondo, S. Yamamoto, T. Nakao, T. Fujii, M. Iwaya, T. Takeuchi, S. Kamiyama, I. Akasaki, and H. Amano, *Appl. Phys. Express* **5**, 082301 (2012).
- 11) N. A. El-Masry, E. L. Piner, S. X. Liu, and S. M. Bedair, *Appl. Phys. Lett.* **72**, 40 (1998).
- 12) Y. Kawaguchi, M. Shimizu, K. Hiramatsu, and N. Sawaki, *MRS Proc.* **449**, 89 (1996).
- 13) K. Hiramatsu, Y. Kawaguchi, M. Shimizu, N. Sawaki, T. Zheleva, R. F. Davis, H. Tsuda, W. Taki, N. Kuwano, and K. Oki, *MRS Internet J. Nitride Semicond. Res.* **2**, e6 (1997).
- 14) R. Liu, J. Mei, S. Srinivasan, H. Omiya, F. A. Ponce, D. Cherns, Y. Narukawa, and T. Mukai, *Jpn. J. Appl. Phys.* **45**, L549 (2006).
- 15) S. Srinivasan, L. Geng, R. Liu, F. A. Ponce, Y. Narukawa, and S. Tanaka, *Appl. Phys. Lett.* **83**, 5187 (2003).
- 16) Y. Kuwahara, Y. Fujiyama, M. Iwaya, S. Kamiyama, H. Amano, and I. Akasaki, *Phys. Status Solidi C* **7**, 1807 (2010).
- 17) T. Sugiyama, Y. Kuwahara, Y. Isobe, T. Fujii, K. Nonaka, M. Iwaya, T. Takeuchi, S. Kamiyama, I. Akasaki, and H. Amano, *Appl. Phys. Express* **4**, 015701 (2011).
- 18) Y. Kuwahara, T. Fujii, T. Sugiyama, D. Iida, Y. Isobe, Y. Fujiyama, Y. Morita, M. Iwaya, T. Takeuchi, S. Kamiyama, I. Akasaki, and H. Amano, *Appl. Phys. Express* **4**, 021001 (2011).
- 19) S. Yamamoto, M. Mori, Y. Kuwahara, T. Fujii, T. Nakao, S. Kondo, M. Iwaya, T. Takeuchi, S. Kamiyama, I. Akasaki, and H. Amano, *Phys. Status Solidi: Rapid Res. Lett.* **6**, 145 (2012).
- 20) D. Iida, Y. Kondo, M. Sowa, T. Sugiyama, M. Iwaya, T. Takeuchi, S. Kamiyama, and I. Akasaki, *Phys. Status Solidi: Rapid Res. Lett.* **7**, 211 (2013).
- 21) T. Yamamoto, D. Iida, Y. Kondo, M. Sowa, S. Umeda, M. Iwaya, T. Takeuchi, S. Kamimaya, and I. Akasaki, *J. Cryst. Growth* **393**, 108 (2014).
- 22) M. Iwaya, T. Yamamoto, D. Iida, Y. Kondo, M. Sowa, H. Matsubara, K. Ishihara, T. Takeuchi, S. Kamiyama, and I. Akasaki, *Jpn. J. Appl. Phys.* **54**, 115501 (2015).
- 23) H. Amano, N. Sawaki, I. Akasaki, and Y. Toyoda, *Appl. Phys. Lett.* **48**, 353 (1986).
- 24) D. Bykhovski, B. L. Gelmont, and M. S. Shur, *J. Appl. Phys.* **81**, 6332 (1997).
- 25) D. Holec, Y. Zhang, D. V. S. Rao, M. J. Kappers, C. McAleese, and C. J. Humphreys, *J. Appl. Phys.* **104**, 123514 (2008).
- 26) R. People and J. C. Bean, *Appl. Phys. Lett.* **47**, 322 (1985).
- 27) J. W. Matthews, A. E. Blakeslee, and S. Mader, *Thin Solid Films* **33**, 253 (1976).
- 28) A. Fischer, H. Kühne, and H. Richter, *Phys. Rev. Lett.* **73**, 2712 (1994).

## Extremely Low-Resistivity and High-Carrier-Concentration Si-Doped $\text{Al}_{0.05}\text{Ga}_{0.95}\text{N}$

This content has been downloaded from IOPscience. Please scroll down to see the full text.

2013 Appl. Phys. Express 6 121002

(<http://iopscience.iop.org/1882-0786/6/12/121002>)

View [the table of contents for this issue](#), or go to the [journal homepage](#) for more

Download details:

IP Address: 202.11.1.201

This content was downloaded on 03/03/2017 at 06:49

Please note that [terms and conditions apply](#).

You may also be interested in:

[Improvement of Light Extraction Efficiency for AlGaIn-Based Deep Ultraviolet Light-Emitting Diodes](#)

Tetsuhiko Inazu, Shinya Fukahori, Cyril Pernot et al.

[Microstructures of GaInN/GaN Superlattices on GaN Substrates](#)

Toru Sugiyama, Yosuke Kuwahara, Yasuhiro Isobe et al.

[GaInN-Based Solar Cells Using Strained-Layer GaInN/GaN Superlattice Active Layer on a Freestanding GaN Substrate](#)

Yosuke Kuwahara, Takahiro Fujii, Toru Sugiyama et al.

[Concentrating Properties of Nitride-Based Solar Cells Using Different Electrodes](#)

Mikiko Mori, Shinichiro Kondo, Shota Yamamoto et al.

[Correlation between Device Performance and Defects in GaInN-Based Solar Cells](#)

Mikiko Mori, Shinichiro Kondo, Shota Yamamoto et al.

[Lateral Hydrogen Diffusion at p-GaN Layers in Nitride-Based Light Emitting Diodes with Tunnel Junctions](#)

Yuka Kuwano, Mitsuru Kaga, Takatoshi Morita et al.

[Investigation of Dominant Nonradiative Mechanisms as a Function of Current in InGaIn/GaN Light-Emitting Diodes](#)

Il-Gyun Choi, Dong-Pyo Han, Joosun Yun et al.

[Study of GaN-based Laser Diodes in Near Ultraviolet Region](#)

Shin-ichi Nagahama, Tomoya Yanamoto, Masahiko Sano et al.

Extremely Low-Resistivity and High-Carrier-Concentration Si-Doped  $\text{Al}_{0.05}\text{Ga}_{0.95}\text{N}$ Toru Sugiyama<sup>1</sup>, Daisuke Iida<sup>1</sup>, Toshiki Yasuda<sup>1</sup>, Motoaki Iwaya<sup>1\*</sup>, Tetsuya Takeuchi<sup>1</sup>, Satoshi Kamiyama<sup>1</sup>, and Isamu Akasaki<sup>1,2</sup><sup>1</sup>Faculty of Science and Technology, Meijo University, Nagoya 468-8502, Japan<sup>2</sup>Akasaki Research Center, Nagoya University, Nagoya 464-8603, Japan

E-mail: iwaya@meijo-u.ac.jp

Received August 29, 2013; accepted November 7, 2013; published online November 27, 2013

We discovered that Si-doped  $\text{Al}_{0.05}\text{Ga}_{0.95}\text{N}$  can be used to realize an extremely low-resistivity n-type layer at room temperature. In Si-doped GaN, a resistivity of  $2.7 \times 10^{-3} \Omega \text{ cm}$  with a carrier concentration of  $4.0 \times 10^{19} \text{ cm}^{-3}$  was almost saturated. In contrast, Si-doped  $\text{Al}_{0.05}\text{Ga}_{0.95}\text{N}$  with a minimum resistivity of  $5.9 \times 10^{-4} \Omega \text{ cm}$  was produced with an electron concentration and electron mobility of  $1.4 \times 10^{20} \text{ cm}^{-3}$  and  $70 \text{ cm}^2/\text{V s}$ , respectively. We confirmed a reduction in the differential resistance of a violet light-emitting diode with a high external quantum efficiency by using this Si-doped  $\text{Al}_{0.05}\text{Ga}_{0.95}\text{N}$ . © 2013 The Japan Society of Applied Physics

Group-III nitride semiconductors are used as light-emitting diodes (LEDs)<sup>1–4</sup> and laser diodes<sup>5,6</sup> (LDs) having a wide wavelength range. High-brightness GaInN-based visible LEDs are presently commercialized worldwide,<sup>7–9</sup> but from a practical viewpoint, the wall plug efficiency (WPE) of such devices needs improvement. The external quantum efficiency (EQE) of these devices is already sufficiently high,<sup>10,11</sup> therefore, the device resistance, which includes the sheet, bulk, and contact resistances of n- and p-type layers, needs to be reduced to improve the WPE. In particular, the low-resistivity (low- $\rho$ ) n-type layer is important because commonly used nitride-based LEDs require for current spreading layers and for simple contacting. A number of studies have reported on the reduction of  $\rho$  in n-type GaN.<sup>12–16</sup> Fritze et al.<sup>16</sup> managed to reduce  $\rho$  for the Si doping of GaN to  $\sim 2.5 \times 10^{-3} \Omega \text{ cm}$  at room temperature (RT). They stated that a  $\rho$  and free electron concentration ( $n_e$ ) of less than  $\sim 2.5 \times 10^{-3} \Omega \text{ cm}$  and higher than  $\sim 1.9 \times 10^{19} \text{ cm}^{-3}$ , respectively, could not be achieved because 3D growth occurs by excess Si-doping. In contrast to Si-doping, a high- $n_e$  ( $\sim 2.9 \times 10^{20} \text{ cm}^{-3}$ ) and low- $\rho$  ( $\sim 6.3 \times 10^{-4} \Omega \text{ cm}$ ) GaN layer could be realized by Ge doping.<sup>16</sup>

In this study, we demonstrated n-type cladding layer of Si-doped  $\text{Al}_{0.05}\text{Ga}_{0.95}\text{N}$  with low- $\rho$  and high- $n_e$  with smooth surface. We improved the WPE of a violet LED by using this Si-doped  $\text{Al}_{0.05}\text{Ga}_{0.95}\text{N}$ .

All samples were grown by metal organic vapor-phase epitaxy. Figure 1 shows a schematic view of the sample structure. Trimethylindium, trimethylaluminum, trimethylgallium, triethylgallium, and ammonia were used as the source gases. C-plane sapphire was used as a substrate; it was covered with a low-temperature-deposited buffer layer.<sup>17</sup> An unintentionally doped  $\sim 3\text{-}\mu\text{m}$ -thick GaN layer and a  $1.5\text{-}\mu\text{m}$ -thick Si-doped  $\text{Al}_{0.05}\text{Ga}_{0.95}\text{N}$  layer or GaN layer were then sequentially grown. Silane ( $\text{SiH}_4$ , 50 ppm diluted by  $\text{H}_2$ ) was used as a dopant source.<sup>18</sup> The carrier concentration of the Si-doped  $\text{Al}_{0.05}\text{Ga}_{0.95}\text{N}$  and GaN was adjusted from  $8.0 \times 10^{18}$  to  $1.5 \times 10^{20} \text{ cm}^{-3}$ . We measured the van der Pauw Hall effect to determine  $n_e$ , mobility ( $\mu_e$ ), and  $\rho$  of each sample at RT. The two-dimensional electron gas at the heterointerface between  $\text{Al}_{0.05}\text{Ga}_{0.95}\text{N}$  and GaN was ignored because the sheet resistance of each sample was very low. We also characterized the surface morphology by scanning electron microscopy (SEM).

We fabricated a violet LED with a 390-nm-emission GaInN multiple quantum well (MQW) active layer on the

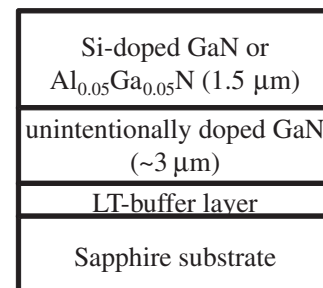


Fig. 1. Schematic view of the sample structure.

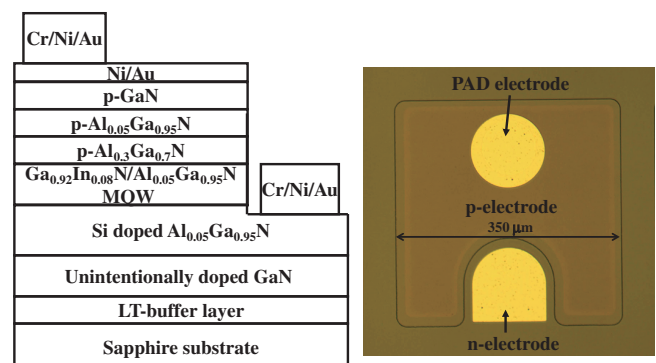
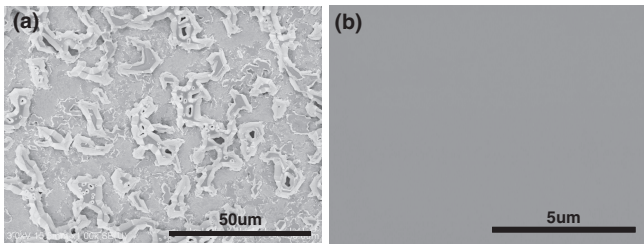


Fig. 2. Schematic structure and top view of the violet LED.

Si-doped  $\text{Al}_{0.05}\text{Ga}_{0.95}\text{N}$  layer. This LED structure was composed of a  $2.0\text{-}\mu\text{m}$ -thick Si-doped n- $\text{Al}_{0.05}\text{Ga}_{0.95}\text{N}$  layer, three pairs of unintentionally doped  $\text{Ga}_{0.92}\text{In}_{0.08}\text{N}$  (2.7 nm)/ $\text{Al}_{0.05}\text{Ga}_{0.95}\text{N}$  (12 nm) MQWs, a 20-nm-thick Mg-doped p- $\text{Al}_{0.3}\text{Ga}_{0.7}\text{N}$  electron-blocking layer, a 100-nm-thick p- $\text{Al}_{0.05}\text{Ga}_{0.95}\text{N}$  cladding layer, and a 10-nm-thick p-GaN contact layer. Figure 2 shows the schematic device structure and top view of this LED. After the samples were annealed at  $800^\circ\text{C}$  for 10 min in ambient air for p-type activation, we fabricated a face-up LED. A Cr/Ni/Au ohmic electrode was deposited by electron beam evaporation on the n- $\text{Al}_{0.05}\text{Ga}_{0.95}\text{N}$  layer, which was exposed by inductively coupled plasma etching. A Ni/Au ohmic semitransparent electrode and Cr/Ni/Au pad electrode were deposited on the p-GaN layer. We prepared two samples with different Si-doped  $\text{Al}_{0.05}\text{Ga}_{0.95}\text{N}$  ( $n_e = 1.0 \times 10^{19}$  and  $1.6 \times 10^{20} \text{ cm}^{-3}$ ). The



**Fig. 3.** Plan-view SEM image of (a) Si-doped GaN ( $n_e = 3.0 \times 10^{19} \text{ cm}^{-3}$ ) and (b) Si-doped AlGaIn ( $n_e = 1.4 \times 10^{20} \text{ cm}^{-3}$ ).

device size of each LED was  $350 \times 350 \mu\text{m}^2$ . The voltage–injection current ( $V$ – $I$ ) and light output power–injection current ( $L$ – $I$ ) characteristics of the LEDs were measured using a semiconductor parameter analyzer (Agilent 4156C). Each LED was characterized with a bare chip. The light output powers and WPEs of each device were measured using the photodiode.

Figure 3 shows the plan-view SEM image of the Si-doped (a) GaN ( $n_e = 3.0 \times 10^{19} \text{ cm}^{-3}$ ) and (b)  $\text{Al}_{0.05}\text{Ga}_{0.95}\text{N}$  ( $n_e = 4.0 \times 10^{20} \text{ cm}^{-3}$ ). Significant differences in surface morphology were identified through these figures. In Fig. 3(a), the Si-doped GaN showed island growth (size,  $1.5 \mu\text{m}$  to several tens of micrometers). Because  $n_e$  of Si-doped GaN up to  $1.0 \times 10^{19} \text{ cm}^{-3}$  can be obtained on a smooth surface, we concluded that the surface of this sample was rough because of excess Si. This result is almost in agreement with that reported in Ref. 16. In contrast, a smooth surface was obtained in  $\text{Al}_{0.05}\text{Ga}_{0.95}\text{N}$  despite the Si concentration being too high; we were unable to confirm the existence of cracks in all  $\text{Al}_{0.05}\text{Ga}_{0.95}\text{N}$  samples. We concluded that a smooth surface can be obtained by the addition of AlN even though for a high Si concentration.

Figures 4 and 5 show  $\rho$  as a function of  $n_e$  and  $\mu_e$  as a function of  $n_e$ , respectively, in Si-doped  $\text{Al}_{0.05}\text{Ga}_{0.95}\text{N}$  and GaN.  $n_e$  of the Si-doped GaN was unambiguously increased up to  $4.0 \times 10^{19} \text{ cm}^{-3}$ . However,  $\rho$  of  $2.7 \times 10^{-3} \Omega \text{ cm}$  with  $n_e$  of  $4.0 \times 10^{19} \text{ cm}^{-3}$  was close to saturation because  $\mu_e$  rapidly decreased with deteriorating surface roughness. These results are similar to those reported in Ref. 16. In contrast,  $n_e$  of  $\text{Al}_{0.05}\text{Ga}_{0.95}\text{N}$  continued to increase to  $10^{19} \text{ cm}^{-3}$  and further to  $1.4 \times 10^{20} \text{ cm}^{-3}$ . The minimum  $\rho$  in Si-doped  $\text{Al}_{0.05}\text{Ga}_{0.95}\text{N}$  was  $5.9 \times 10^{-4} \Omega \text{ cm}$ . This  $\rho$  is lower than that of GaN with Ge doping.<sup>16)</sup>  $n_e$  and  $\mu_e$  of n- $\text{Al}_{0.05}\text{Ga}_{0.95}\text{N}$  in the minimum- $\rho$  sample were  $1.4 \times 10^{20} \text{ cm}^{-3}$  and  $70 \text{ cm}^2/\text{Vs}$ , respectively. Because 3D growth is suppressed using  $\text{Al}_{0.05}\text{Ga}_{0.95}\text{N}$  even under high Si concentration,  $\mu_e$  of this n- $\text{Al}_{0.05}\text{Ga}_{0.95}\text{N}$  did not decrease significantly. This result shows the potential of realizing a low- $\rho$  n-type layer by using  $\text{Al}_{0.05}\text{Ga}_{0.95}\text{N}$ .

Figure 6 shows the measurement results of  $I$ – $L$  and  $I$ – $V$  of the violet LED on different Si-doped  $\text{Al}_{0.05}\text{Ga}_{0.95}\text{N}$  ( $n_e$ :  $1.0 \times 10^{19}$  and  $1.6 \times 10^{20} \text{ cm}^{-3}$ ). We confirmed a significant difference in the  $I$ – $V$  curve of each LED. By increasing the Si concentration ( $n_e$  in n- $\text{Al}_{0.05}\text{Ga}_{0.95}\text{N}$  was changed from  $1.0 \times 10^{19}$  and  $1.6 \times 10^{20} \text{ cm}^{-3}$ ), we found that the operating voltage was reduced by  $\sim 1 \text{ V}$  at  $100 \text{ mA}$  current injection. Moreover, the differential resistance at  $100 \text{ mA}$  current injection (series resistance) of each LED was reduced from  $14$  to  $7.2 \Omega$ . According to a simple calculation, approxi-

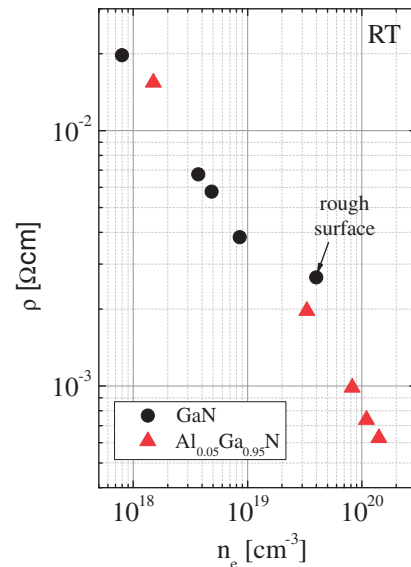


**Fig. 4.**  $n_e$  dependence of  $\rho$  in Si-doped GaN and  $\text{Al}_{0.05}\text{Ga}_{0.95}\text{N}$ .

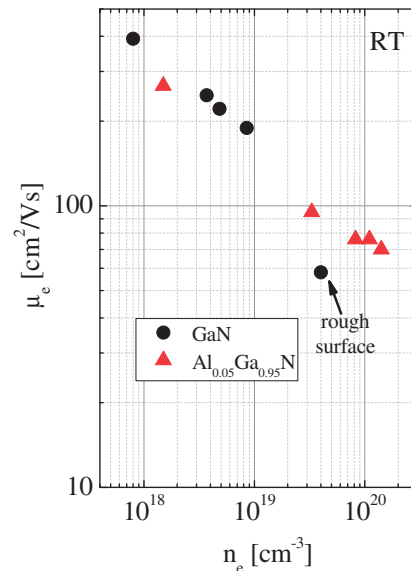


**Fig. 5.**  $n_e$  dependence of  $\mu_e$  in Si-doped GaN and  $\text{Al}_{0.05}\text{Ga}_{0.95}\text{N}$ .

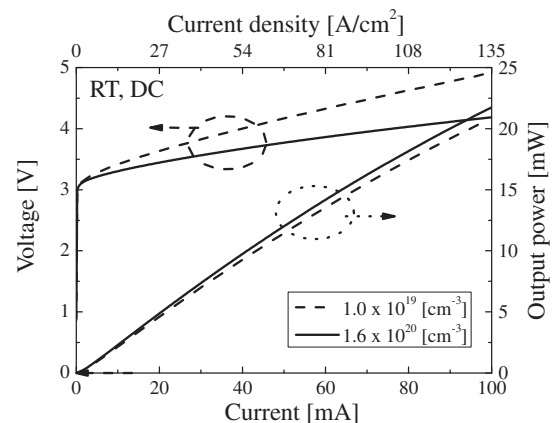


**Fig. 6.**  $I$ – $V$  and  $I$ – $L$  measurements of the LED on Si-doped  $\text{Al}_{0.05}\text{Ga}_{0.95}\text{N}$ .

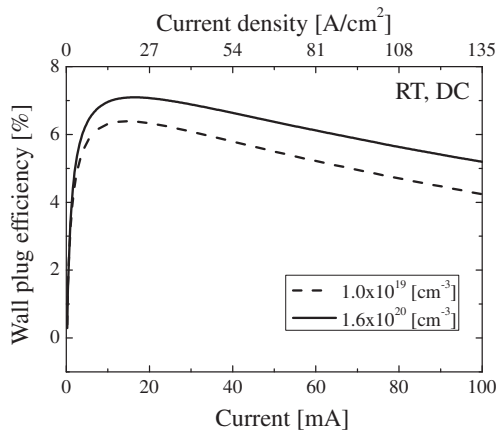


Fig. 7. WPEs for injection current.

mately  $4\ \Omega$  is caused by the p-type layer (contact and bulk resistance) among the series resistance. Because  $\rho$  was reduced to approximately 1/5 times by  $n_e$  increases from  $1.0 \times 10^{19}$  and  $1.6 \times 10^{20}\ \text{cm}^{-3}$ , this reduction in differential resistance can be partially explained by the decrease in the sheet resistance of the n-Al<sub>0.05</sub>Ga<sub>0.95</sub>N layer. Because the light output power of each LED for the low-current injection was almost the same, as indicated by the  $I$ - $L$  curves, the quality of the active layer is sufficiently high even when using an underlying layer with a high Si concentration. In contrast, the light output power in violet LEDs when using an underlying layer with a high Si concentration at a high-current injection was high approximately 5%. Cause of this difference can be considered heat generation,<sup>21)</sup> decrease of the current injection efficiency by current over flow,<sup>22)</sup> and droop.<sup>23)</sup> Among these, we considered the decrease of injection efficiency and droop are irrelevant, because structure of the p-type layer and the GaInN based active layer in both devices is the same. Also, since we have not seen a noticeable difference in the light emission pattern of each LEDs, we attributed this to the fact that heat generation is reduced by reductions in differential resistance. Therefore, this n-Al<sub>0.05</sub>Ga<sub>0.95</sub>N underlying layer with a high Si concentration is useful for a high-current-operation LED. Figure 7 shows the WPE as a function of the injection current. The WPE of the violet LED when using an underlying layer with a high carrier concentration was around 1.15 times as high as that when using an underlying layer with a low carrier concentration. Therefore, this Si-doped n-Al<sub>0.05</sub>Ga<sub>0.95</sub>N underlying layer is extremely useful for realizing high-performance GaInN-based LEDs. In addition, because AlGaIn is also useful as a UV light-emitting device material,<sup>19,20)</sup> we expect that our results can be applied to UV and deep-UV LEDs and laser diodes.

In conclusion, we discovered that Si-doped n-type Al<sub>0.05</sub>-Ga<sub>0.95</sub>N with extremely low resistivity ( $5.9 \times 10^{-4}\ \Omega\ \text{cm}$ )

can be realized at RT. In contrast,  $\rho$  and  $n_e$  in Si-doped n-type GaN of less than  $\sim 2.5 \times 10^{-3}\ \Omega\ \text{cm}$  and higher than  $\sim 1.9 \times 10^{19}\ \text{cm}^{-3}$ , respectively, could not be achieved because 3D growth occurs by excess Si-doping. Furthermore, the reduction of the series resistance of the LED with a high internal quantum efficiency was possible by using this underlying layer. Therefore, this Si-doped n-Al<sub>0.05</sub>Ga<sub>0.95</sub>N underlying layer is extremely useful for the realization of high-performance GaInN-based LEDs.

- 1) H. Amano, M. Kito, K. Hiramatsu, and I. Akasaki: *Jpn. J. Appl. Phys.* **28** (1989) L2112.
- 2) M. Koike, N. Koide, S. Asami, J. Umezaki, S. Nagai, S. Yamasaki, N. Shibata, H. Amano, and I. Akasaki: *Proc. SPIE* **3002** (1997) 36.
- 3) S. Nakamura, M. Senoh, N. Iwasa, and S. Nagahama: *Jpn. J. Appl. Phys.* **34** (1995) L797.
- 4) S. Nakamura, M. Senoh, N. Iwasa, S. Nagahama, T. Yamada, and T. Mukai: *Jpn. J. Appl. Phys.* **34** (1995) L1332.
- 5) I. Akasaki, H. Amano, S. Sota, H. Sakai, T. Tanaka, and M. Koike: *Jpn. J. Appl. Phys.* **34** (1995) L1517.
- 6) S. Nakamura, M. Senoh, S. Nagahama, N. Iwasa, T. Yamada, T. Matsushita, H. Kiyoku, and Y. Sugimoto: *Jpn. J. Appl. Phys.* **35** (1996) L74.
- 7) S. Watanabe, N. Yamada, M. Nagashima, Y. Ueki, C. Sasaki, Y. Yamada, T. Taguchi, K. Tadatomo, H. Okagawa, and H. Kudo: *Appl. Phys. Lett.* **83** (2003) 4906.
- 8) O. B. Shchekin, J. E. Epler, T. A. Trottier, T. Margalith, D. A. Steigerwald, M. O. Holcomb, P. S. Martin, and M. R. Krames: *Appl. Phys. Lett.* **89** (2006) 071109.
- 9) J. Baur, F. Baumann, M. Peter, K. Engl, U. Zehnder, J. Off, V. Kuemmler, M. Kirsch, J. Strauss, R. Wirth, K. Streubel, and B. Hahn: *Phys. Status Solidi C* **6** (2009) S905.
- 10) Y. Narukawa, J. Narita, T. Sakamoto, T. Yamada, H. Narimatsu, M. Sano, and T. Mukai: *Phys. Status Solidi A* **204** (2007) 2087.
- 11) Y. Narukawa, M. Ichikawa, D. Sanga, M. Sano, and T. Mukai: *J. Phys. D* **43** (2010) 354002.
- 12) N. Koide, H. Kato, M. Sassa, S. Yamasaki, K. Manabe, M. Hashimoto, H. Amano, K. Hiramatsu, and I. Akasaki: *J. Cryst. Growth* **115** (1991) 639.
- 13) J. Xie, S. Mita, A. Rice, J. Tweedie, L. Hussey, R. Collazo, and Z. Sitar: *Appl. Phys. Lett.* **98** (2011) 202101.
- 14) L. T. Romano, C. G. Van de Walle, J. W. Ager, W. Götz, and R. S. Kern: *J. Appl. Phys.* **87** (2000) 7745.
- 15) L. T. Romano, C. G. Van de Walle, B. S. Krusor, R. Lau, J. Ho, T. Schmidt, J. W. Ager, III, W. Götz, and R. S. Kern: *Physica B* **273–274** (1999) 50.
- 16) S. Fritze, A. Dadgar, H. Witte, M. Bügler, A. Rohrbeck, J. Bläsing, A. Hoffmann, and A. Krost: *Appl. Phys. Lett.* **100** (2012) 122104.
- 17) H. Amano, N. Sawaki, I. Akasaki, and Y. Toyoda: *Appl. Phys. Lett.* **48** (1986) 353.
- 18) I. Akasaki and H. Amano: *Jpn. J. Appl. Phys.* **45** (2006) 9001.
- 19) C. Pernot, M. Kim, S. Fukahori, T. Inazu, T. Fujita, Y. Nagasawa, A. Hirano, M. Ippommatsu, M. Iwaya, S. Kamiyama, I. Akasaki, and H. Amano: *Appl. Phys. Express* **3** (2010) 061004.
- 20) K. Ban, J. Yamamoto, K. Takeda, K. Ide, M. Iwaya, T. Takeuchi, S. Kamiyama, I. Akasaki, and H. Amano: *Appl. Phys. Express* **4** (2011) 052101.
- 21) A. A. Efremov, N. I. Bochkareva, R. I. Gorbunov, D. A. Lavrinovich, Yu. T. Rebane, D. V. Tarkhin, and Yu. G. Shreter: *Semiconductors* **40** (2006) 605.
- 22) A. Y. Kim, W. Götz, D. A. Steigerwald, J. J. Wierer, N. F. Gardner, J. Sun, S. A. Stockman, P. S. Martin, M. R. Krames, R. S. Kern, and F. M. Steranka: *Phys. Status Solidi A* **188** (2001) 15.
- 23) Y. C. Shen, G. O. Mueller, S. Watanabe, N. F. Gardner, A. Munkholm, and M. R. Krames: *Appl. Phys. Lett.* **91** (2007) 141101.

# Small current collapse in AlGaIn/GaN HFETs on a-plane GaN self-standing substrate

T. Sugiyama<sup>\*,1</sup>, Y. Honda<sup>1</sup>, M. Yamaguchi<sup>1</sup>, H. Amano<sup>1,3</sup>, Y. Isobe<sup>2</sup>, M. Iwaya<sup>2</sup>, T. Takeuchi<sup>2</sup>, S. Kamiyama<sup>2</sup>, I. Akasaki<sup>2,3</sup>, M. Imade<sup>4</sup>, Y. Kitaoka<sup>4</sup>, and Y. Mori<sup>4</sup>

<sup>1</sup> Graduate School of Engineering, Nagoya University, C3-1 Furo-cho, Chikusa-ku, Nagoya 464-8603, Japan

<sup>2</sup> Faculty of Science and Technology, Meijo University, 1-501 Shiogamaguchi, Tempaku-ku, Nagoya 468-8502, Japan

<sup>3</sup> Akasaki Research Center, Nagoya University, Furo-cho, Chikusa-ku, Nagoya 464-8603, Japan

<sup>4</sup> Graduate School of Electrical Engineering, Osaka University, Suita 565-0871, Japan

Received 8 July 2011, revised 20 December 2011, accepted 24 January 2012

Published online 17 February 2012

**Keywords** GaN, AlGaIn/GaN, HFET, nonpolar, a-plane, current collapse

\* Corresponding author: e-mail takayu\_s@nuee.nagoya-u.ac.jp

We measured drain bias stress effects and current collapse in AlGaIn/GaN heterostructure field-effect transistors (HFETs) on a-plane and c-plane GaN substrates. An a-plane AlGaIn/GaN HFET (a-HFET) shows small current collapse with a threshold voltage ( $V_{th} = -1.8$  V). On the other hand, a c-plane HFET (c-HFET) with the same barrier thickness (20 nm) shows a small current collapse, although  $V_{th}$  was negatively large ( $V_{th} = -4$  V).

Current collapse in a-HFET was not large compared with that in conventional c-HFET on GaN. A c-HFET on sapphire was also measured. The current collapses in HFETs on sapphire were larger than that in HFETs on a GaN substrate. The current collapses in the thin-barrier c-HFET ( $V_{th} = -1.8$  V) were particularly large. Therefore, an a-plane device is promising for a small or positive  $V_{th}$  with small current collapse.

© 2012 WILEY-VCH Verlag GmbH & Co. KGaA, Weinheim

**1 Introduction** AlGaIn/GaN HFETs are expected for high-efficiency and high-power switching devices in power inverter circuits. Normally off mode operation is necessary to realize a fail-safe operation in power switching applications. Studies on normally off operation have been reported by many groups [1–5]. Nonpolar AlGaIn/GaN HFETs are also expected as a structure to realize normally off operation. The heterojunction on a nonpolar plane (a-plane and m-plane) is not affected by piezoelectric and spontaneous polarizations. Therefore, two dimensional electron gases (2DEGs) channel at the hetero-interface can be controlled merely by Si doping. However, dislocation and stacking fault density in nonpolar GaN on a highly mismatched substrate are huge, which results in very low mobility. Recently, HFETs on m-plane and a-plane GaN substrates have been reported [5–7]. High drain current and small threshold voltage ( $V_{th}$ ) were realized using a nonpolar HFET on GaN substrates.

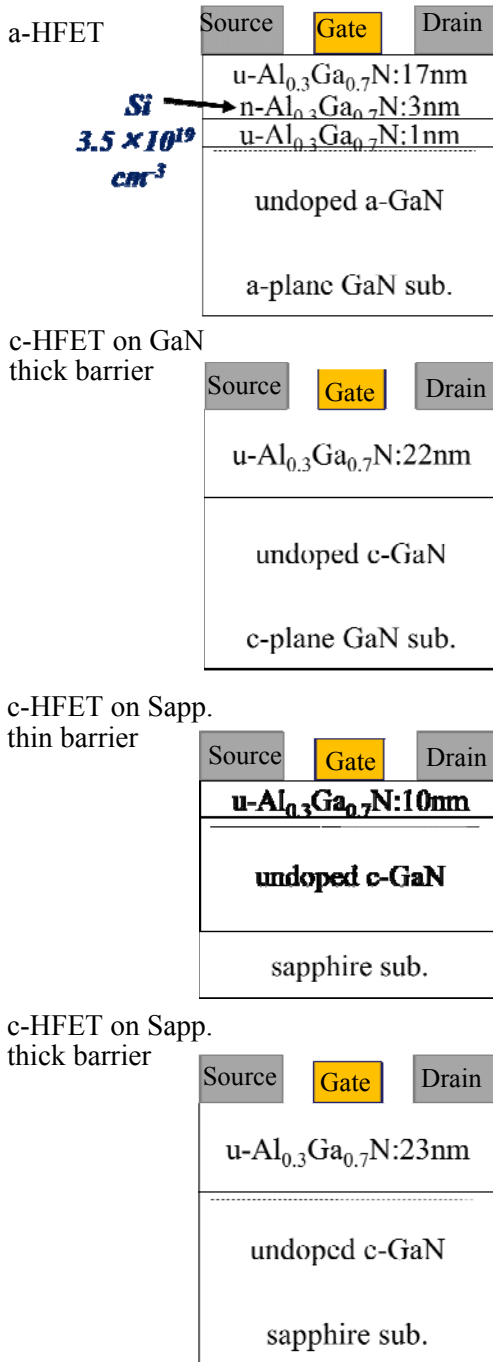
The current collapse in HFETs caused by electron traps has been reported [8, 9]. The surface states and carrier

generation mechanisms of c-plane and a-plane HFETs are different. Therefore, it is meaningful to characterize the current collapse property in a-plane HFETs (a-HFETs). In this study, we measured drain bias stress effects and current collapse in HFETs on a-plane and c-plane GaN substrates and conventional HFETs on sapphire. The relationships the FET characteristics, the substrate and device structure were measured.

## 2 Experiments

**2.1 Device structure** Figure 1 shows the device structures. We fabricated 4 samples. All the HFETs were grown by MOVPE. The a-HFET was grown on an a-plane GaN liquid phase epitaxial (LPE) substrate. An unintentionally doped thick GaN layer and an  $\text{Al}_{0.3}\text{Ga}_{0.7}\text{N}$  barrier of 21 nm thickness were grown. The AlGaIn barrier contained a Si-doped layer. As references, an  $\text{Al}_{0.3}\text{Ga}_{0.7}\text{N}$  (22 nm)/GaN HFET on a free-standing c-GaN substrate and conventional  $\text{Al}_{0.3}\text{Ga}_{0.7}\text{N}$  (10 and 23 nm)/GaN HFETs on c-sapphire were also grown. After the growth, the sam-

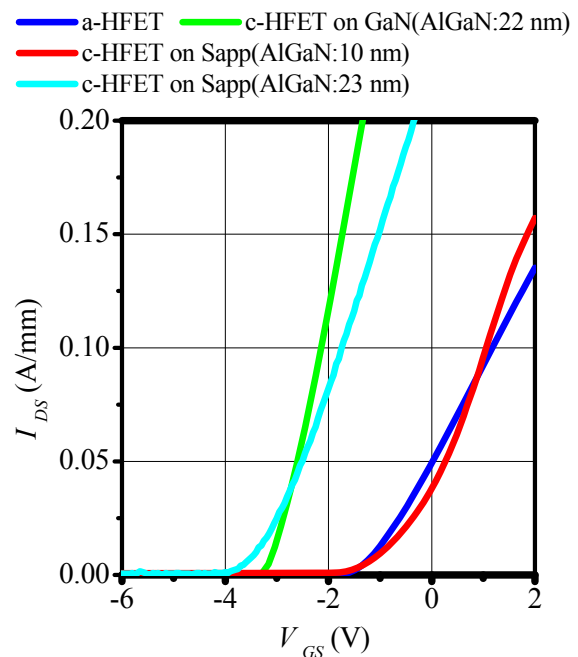
ple was etched for mesa isolation by Cl<sub>2</sub>-based reactive ion etching (RIE). Ti/Al/Ti/Au was used as the source-drain electrode, while Ni/Au was used as the schottky gate metal for the metal-semiconductor (MES) structure. The gate length (L<sub>G</sub>) and the distance between the source and drain (L<sub>GD</sub>) of all the devices were 2 and 8 μm, respectively. The current collapse in all the devices was measured without passivation.



**Figure 1** Schematic view of HFETs.

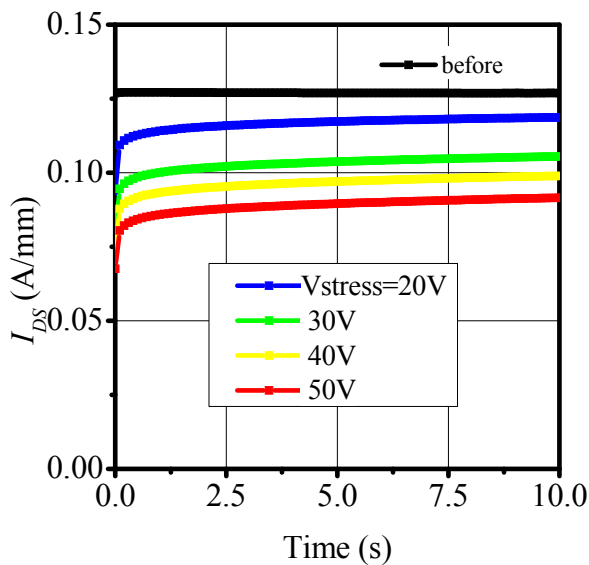
**2.2 Current collapse measurements** The drain stress effects and current collapse of HFETs were measured in a dark room. The current collapse measurements were done by placing the substrate on a quartz plate. A parameter analyzer 4155C (Agilent) was used for all the measurements.

Figure 2 shows the transfer characteristics ( $V_{GS}$ - $I_{DS}$ ) of 4 samples with  $V_{DS} = 5 \text{ V}$ .  $V_{th}$  and  $I_{DS}$  of the a-HFET and c-HFET (Al<sub>0.3</sub>Ga<sub>0.7</sub>N: 10 nm) were almost the same ( $V_{th} = -1.8 \text{ V}$ ). On the other hand, the c-HFETs with a thick AlGa<sub>0.3</sub>N barrier (Al<sub>0.3</sub>Ga<sub>0.7</sub>N: 22 and 23 nm) showed high  $I_{DS}$  but the  $V_{th}$  values were negatively large.



**Figure 2** Transfer characteristics ( $V_{GS}$ - $I_{DS}$ ) with  $V_{DS} = 5 \text{ V}$ .

**3 Results** The drain stress bias was maintained for 30 s with  $V_{GS} = -8 \text{ V}$ . The time shift of the drain current was measured when the gate and drain were turned on ( $V_{GS} = 0 \text{ V}$ ,  $V_{DS} = 5 \text{ V}$ ). Figure 3 shows the time shift of the drain current with stress bias in a-HFETs.  $I_{DS}$  decreased with increasing stress bias. The  $I_{DS}$  was not quickly recovered with a very long time constant. However, the  $I_{DS}$  was recovered by exposure to room light. Therefore, the origin of the current collapse is not device damage but the electron traps. This current collapse is considered to originate from deep traps as indicated by the long time constant [10]. Figure 4 shows the stress bias and stress time dependence of the normalized  $I_{DS}$  at 10 s after the stress bias. The  $I_{DS}$  and current collapses depend not on the stress time but on the stress voltage. This trend is the same in all HFETs. Thus, the following current collapse measurements were carried out with the stress time of 30 s.



**Figure 3** Time shift of  $I_{DS}$  in a-HFET.

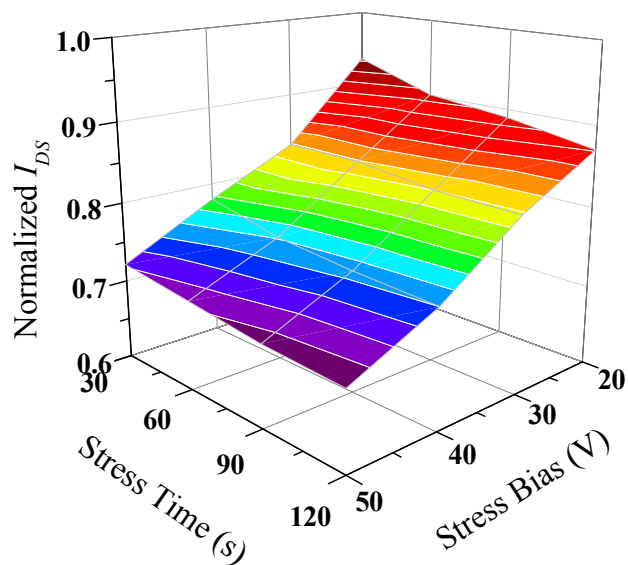


**Figure 4** Normalized  $I_{DS}$  at 10 s after the stress bias and stress time.

Figures 5 and 6 show the decrease in drain current in each HFET with stress bias. Figure 5 shows the normalized  $I_{DS}$  at 10 s after stress off and FET turn on. The decrease in  $I_{DS}$  in the a-HFET is small next to that in the c-HFET on GaN (AlGaIn: 22 nm), and the same as that in the c-HFET on sapphire (AlGaIn: 23 nm). In contrast, decrease in  $I_{DS}$  in the c-HFET on sapphire (AlGaIn: 10 nm) is very large. Figure 6 shows the normalized  $I_{DS}$  at 0.1 s. The difference of the normalized  $I_{DS}$  was large immediately after the

switching, by GaN substrates and a thick AlGaIn barrier. A small current collapse is very important in a high-speed switching device. The electric field was decreased by conductive GaN substrates, and the trapped electrons were also decreased [11]. A virtual gate is generated by the coulomb force of the trapped electrons. Therefore, the effects of current collapse in the HFET with a thin barrier layer are large.

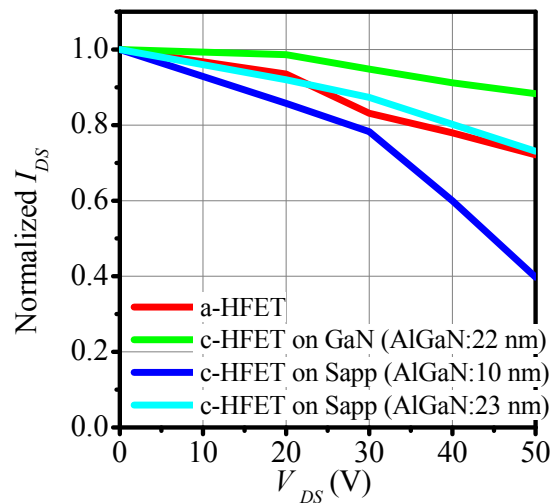


**Figure 5** Normalized  $I_{DS}$  at 10 s for each HFET.

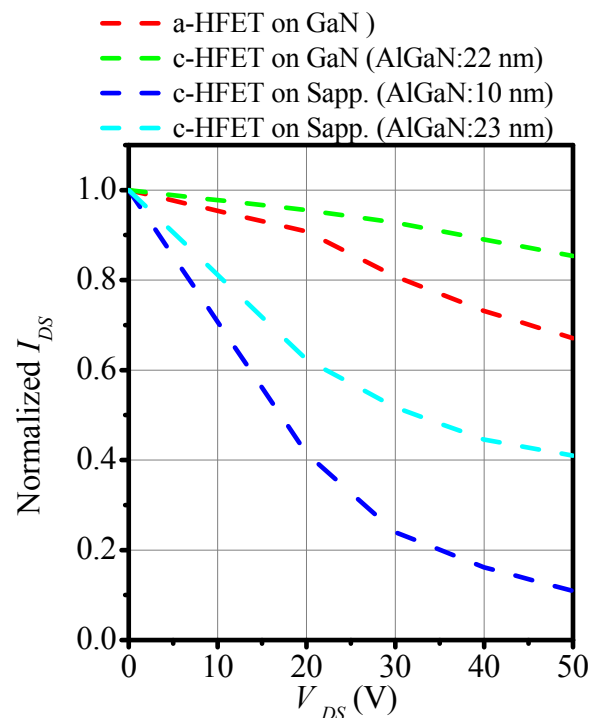


**Figure 6** Normalized  $I_{DS}$  at 0.1 s for each HFET.

The a-HFET with a conventional structure and without passivation showed a small  $V_{th}$  and a small current collapse compared with c-HFETs. Thus, improvements of the performance of the a-HFET are expected by passivation and with the reform of the device structure design [12, 13].

**4 Summary** The drain bias stress effects and current collapse in a-plane and c-plane HFETs were measured. The c-HFET with thick barrier thickness (22 nm) on GaN shows small current collapse; however,  $V_{th}$  was negatively large. On the other hand, a c-HFET with a thin AlGaIn barrier (10 nm) on sapphire shows a small  $V_{th}$  because the 2DEG sheet carrier density is small. However, in contrast, the current collapse in the thin-barrier c-HFET was large. Because the surface was very close to the 2DEG channel, maximum electric field concentration is high and the 2DEG sheet carrier density is low. Therefore, the effect of trapped electrons was large.

In contrast,  $V_{th}$  of a-HFETs were small, because carrier concentration in a-HFET structure was low, however the effects of current collapse were small. These characteristics in a-HFET are contrast with that in c-HFET. Moreover, there are differences in device structures, conductive substrates and Si delta-doped AlGaIn barrier layer. These differences also effected the current collapse [14].

The a-plane AlGaIn/GaN HFET on GaN substrates shows a small current collapse and  $V_{th}$ . Current collapse in a-HFET was not bad compared with that in the conventional c-HFET, in spite of a-HFETs were nonpolar plane growth which have a mixture surface of Ga and N. Thus, the a-plane device is promising for the realization of a small or positive  $V_{th}$  and small current collapse.

#### Acknowledgements

This work was supported by the New Energy and Industrial Technology Development Organization Project, Nanotechnology and Materials Technology, "Development of Nitride-Based Semiconductor Single Crystal Substrate and Epitaxial Growth Technology," and the second-stage Knowledge Cluster Initiative, Tokai Region Nanotechnology Manufacturing Cluster in Japan.

#### References

- [1] N. Tsuyukuchi, K. Nagamatsu, Y. Hirose, M. Iwaya, S. Kamiyama, H. Amano, and I. Akasaki, *Jpn. J. Appl. Phys.* **45**, 319-321 (2006).
- [2] Y. Uemoto, M. Hikita, H. Ueno, H. Matsuo, H. Ishida, M. Yanagihara, T. Ueda, T. Tanaka, and D. Ueda, *IEEE Trans. Electron Devices* **54**, 3393-3399 (2007).
- [3] T. Mizutani, M. Ito, S. Kishimoto, and F. Nakamura, *IEEE Electron Device Lett.* **28**, 549-551 (2007).
- [4] M. Kanamura, T. Ohki, T. Kikkawa, K. Imanishi, T. Imada, A. Yamada, and N. Hara, *IEEE Electron Device Lett.* **31**, 189-191 (2010).
- [5] T. Fujiwara, S. Rajan, S. Keller, M. Higashiwaki, J. S. Speck, S. P. DenBaars, and U. K. Mishra, *APEX* **2**, 011001 (2009).
- [6] T. Fujiwara, S. Keller, M. Higashiwaki, J. S. Speck, S. P. DenBaars, and U. K. Mishra, *APEX* **2**, 061003 (2009).
- [7] Y. Isobe, H. Ikki, T. Sakakibara, M. Iwaya, T. Takeuchi, S. Kamiyama, I. Akasaki, T. Sugiyama, H. Amano, M. Imade, Y. Kitaoka, and Y. Mori, *APEX* **4**, 064102 (2010).
- [8] R. Vetury, N. Q. Zhang, S. Keller, and U. K. Mishra, *IEEE Trans. Electron Devices* **48**, 560-566 (2001).
- [9] H. Hasegawa, T. Inagaki, S. Ootomo, and T. Hashizume, *J. Vac. Sci. Technol. B* **21**, 1844-1855 (2003).
- [10] J. Joh and J. del Alamo, *IEEE Trans. Electron Devices* **58**, 132-140 (2011).
- [11] W. Saito, T. Nitta, Y. Kakiuchi, Y. Saito, K. Tsuda, I. Omura, and M. Yamaguchi, *IEEE Electron Device Lett.* **28**, 523-525 (2007).
- [12] M. F. Romero, A. Jiménez, J. Miguel-Sánchez, A. F. Braña, F. González-Posada, R. Cuervo, F. Calle, and E. Muñoz, *IEEE Electron Device Lett.* **29**, 209-211 (2008).
- [13] N. Tsurumi, H. Ueno, T. Murata, H. Ishida, Y. Uemoto, T. Ueda, K. Inoue, and T. Tanaka, *IEEE Trans. Electron Devices* **57**, 980-985 (2010).
- [14] G. Meneghesso, G. Verzellesi, F. Danesin, F. Rampazzo, F. Zanon, A. Tazzoli, M. Meneghini, E. Zanoni, *IEEE Trans. Electron Devices* **53**, 332-343 (2008).

## Trench-Shaped Defects on AlGaIn Quantum Wells Grown under Different Growth Pressures

This content has been downloaded from IOPscience. Please scroll down to see the full text.

2013 Jpn. J. Appl. Phys. 52 08JB27

(<http://iopscience.iop.org/1347-4065/52/8S/08JB27>)

View [the table of contents for this issue](#), or go to the [journal homepage](#) for more

Download details:

IP Address: 202.11.1.201

This content was downloaded on 03/03/2017 at 06:57

Please note that [terms and conditions apply](#).

You may also be interested in:

[Influence of Growth Temperature on Quaternary AlInGaN Epilayers for Ultraviolet Emission Grown by Metalorganic Chemical Vapor Deposition](#)

Yang Liu, Takashi Egawa, Hiroyasu Ishikawa et al.

[Growth of High-Quality Si-Doped AlGaIn by Low-Pressure Metalorganic Vapor Phase Epitaxy](#)

Yuki Shimahara, Hideto Miyake, Kazumasa Hiramatsu et al.

[Ternary AlGaIn Alloys with High Al Content and Enhanced Compositional Homogeneity Grown by Plasma-Assisted Molecular Beam Epitaxy](#)

Vincent Fellmann, Périne Jaffrennou, Diane Sam-Giao et al.

[Pulsed Metalorganic Chemical Vapor Deposition of Quaternary AlInGaN Layers and Multiple Quantum Wells for Ultraviolet Light Emission](#)

Changqing Chen, Jinwei Yang, Mee-Yi Ryu et al.

[Light Improvement of Near Ultraviolet Light-Emitting Diodes by Utilizing Lattice-Matched InAlGaIn as Barrier Layers in Active Region](#)

Yu-Hsuan Lu, Yi-Keng Fu, Shyh-Jer Huang et al.

[Strain-Compensated Effect on the Growth of InGaIn/AlGaIn Multi-Quantum Well by Metalorganic Vapor Phase Epitaxy](#)

Tomohiro Doi, Yoshio Honda, Masahito Yamaguchi et al.

[AlGaIn/GaN Heterostructure Field-Effect Transistors on Fe-Doped GaN Substrates with High Breakdown Voltage](#)

Yoshinori Oshimura, Takayuki Sugiyama, Kenichiro Takeda et al.

## Trench-Shaped Defects on AlGaInN Quantum Wells Grown under Different Growth Pressures

Tomoyuki Suzuki<sup>1</sup>, Mitsuru Kaga<sup>1</sup>, Kouichi Naniwae<sup>2</sup>, Tsukasa Kitano<sup>2</sup>, Keisuke Hirano<sup>1</sup>, Tetsuya Takeuchi<sup>1</sup>, Satoshi Kamiyama<sup>1,2</sup>, Motoaki Iwaya<sup>1</sup>, and Isamu Akasaki<sup>1,3</sup>

<sup>1</sup>Faculty of Science and Technology, Meijo University, Nagoya 468-8502, Japan

<sup>2</sup>EL-SEED Corporation, Nagoya 468-0073, Japan

<sup>3</sup>Akasaki Research Center, Nagoya University, Nagoya 464-8603, Japan

Received October 13, 2012; revised March 11, 2013; accepted March 24, 2013; published online July 22, 2013

We obtained high-quality AlGaInN/GaN quantum wells (QWs) with a 385 nm emission by adding Al sources to GaInN QWs grown at a low growth pressure of 150 mbar. When AlGaInN QWs were grown at a relatively high growth pressure of 400 mbar, a considerable amount of peculiar trench-shaped defects were observed on the surface of the AlGaInN QWs. We found that the trench defects acted as nonradiative centers, leading to low photoluminescence (PL) intensities. Our experiments reveal that a low growth pressure is effective in suppressing the trench defect formation, resulting in high-quality AlGaInN QWs. © 2013 The Japan Society of Applied Physics

### 1. Introduction

AlGaInN quaternary alloy has an important flexibility in that the band-gap energy can be designed while the lattice matching condition is satisfied. This flexibility is very useful for obtaining high-quality heterointerfaces, which are commonly required in various semiconductor devices.<sup>1-3)</sup> However, it is difficult to grow the AlGaInN alloy since the typical growth conditions of AlN and InN are very different, such as growth temperature and pressure. A high growth temperature and a low growth pressure are necessary for the AlN growth to reduce parasitic reactions between Al sources and N sources and enhance Al adatom migrations on the surfaces.<sup>4-7)</sup> In contrast, a low growth temperature and a high growth pressure are required for the InN growth to incorporate In atoms into epitaxial layers.<sup>8-11)</sup> The two growth parameters are completely opposite.

Recently, a novel monolithic white LED fabricated using a combination of a fluorescent SiC substrate and a nitride semiconductor near UV-LED structure was proposed.<sup>12-15)</sup> The UV-LED should have a peak wavelength of 385 nm to excite carriers in the fluorescent SiC substrate. To obtain 385 nm emission, Ga<sub>0.95</sub>In<sub>0.05</sub>N quantum wells (QWs) are typically used.<sup>16)</sup> Unfortunately, the 0.05 InN mole fraction is too small to make the most of the In inhomogeneity for a higher radiative efficiency. The effect of In inhomogeneity has been observed in purple to blue GaInN-based LEDs in which the GaInN QWs contain more than 0.1 InN mole fractions. We then proposed to use AlGaInN QWs for 385 nm emission. AlGaInN with 385 nm emission should have relatively large (~0.1) InN and AlN mole fractions simultaneously. The concept is to obtain not only sufficient In inhomogeneity with about 0.1 InN mole fraction but also a large band-gap corresponding to 385 nm emission with about 0.1 AlN mole fraction. So far, the AlGaInN alloys with a few percent InN mole fractions have been investigated as active regions for the emission of less than 365 nm.<sup>17-22)</sup>

In this study, AlGaInN QWs targeting high-efficiency 385 nm emission are fabricated and characterized. Our approach to obtaining the AlGaInN QWs is to supply additional Al sources to our typical GaInN QW growth conditions. We found that peculiar trench-shaped defects

**Table I.** Materials of well/barrier and growth conditions at well layers.

Sample	Materials of well/barrier layers	Pressure (mbar)	TMIn (μmol/min)	TEGa (μmol/min)	TMAI (μmol/min)
A1	Ga <sub>0.9</sub> In <sub>0.1</sub> N/GaN	400	32	37	0
A2	AlGaInN/AlGaInN	400	32	37	9
B1	AlGaInN/GaN	400	4	37	9
B2	AlGaInN/GaN	400	1	37	9
B3	Al <sub>0.07</sub> Ga <sub>0.93</sub> N/GaN	400	0	37	9
C1	Ga <sub>0.87</sub> In <sub>0.13</sub> N/GaN	150	38	46	0
C2	AlGaInN/GaN	150	38	46	9
C3	Al <sub>0.86</sub> In <sub>0.14</sub> N/GaN	150	38	0	9

showing a strong correlation with nonradiative recombinations were observed on the surfaces of the AlGaInN QWs.<sup>23)</sup> A key growth parameter is discussed to suppress the formation of the trench-shaped defects.

### 2. Experimental Methods

A sample structure in the experiments is five QWs grown on a Si-doped GaN/undoped GaN/sapphire template by metalorganic vapor phase epitaxy (MOVPE). The well and barrier thicknesses were estimated to be about 3 and 12 nm, respectively, from X-ray diffraction patterns and growth time. For the five QW structures, trimethylaluminum (TMAI), triethylgallium (TEGa), trimethylindium (TMIn), ammonia (NH<sub>3</sub>), and nitrogen were used as Al, Ga, In, and N sources and a carrier gas, respectively. The growth temperature was 780 °C to obtain reasonably high In incorporation. A total of eight samples in three sets were prepared, as listed in Table I. The first set of two samples (A1 and A2) is for growing AlGaInN QWs on the basis of a standard GaInN QW. Sample A1 was our standard GaInN/GaN QWs grown at 400 mbar. Then, Sample A2 was grown under the same growth condition as Sample A1 but with an additional TMAI flow at the wells and barriers, resulting in AlGaInN/AlGaInN QWs. The second set of three samples (B1 to B3) is for growing AlGaInN/GaN QWs with smaller TMIn flows to observe the TMIn flow dependence of surface morphologies. Samples B1 to B3 were grown under the

same growth conditions as Sample A2 but with smaller TMIn flows. Actually, no TMIn flow was used for Sample B3, meaning that the nominal well material was AlGaIn. The third set of three samples (C1 to C3) is for growing AlGaInN QWs on the basis of another standard growth condition of GaInN QWs. Sample C1 was GaInN/GaN QWs grown under a lower growth pressure of 150 mbar. Samples C2 (AlGaInN/GaN) and C3 (AlInN/GaN) were grown under the same low growth pressure but with TMAI flows. In Sample C3, only TMIn and TMAI flows were supplied to the wells.

For the ternary alloys, such as Samples A1, B3, C1, and C3, the mole fractions were determined from X-ray diffraction patterns as listed in Table I. Even though the growth temperature and In/(Ga + In) supply ratio were the same between A1 and C1, the InN mole fractions were slightly different. This could be due to differences in the total flow rate as well as growth pressure.

For the quarternary alloys, such as A2, B1, B2, and C2, the mole fractions are unknown owing to insufficient information. However, note that the InN mole fractions of C1 (GaInN) and C3 (AlInN) are almost the same. The growth conditions of both the samples are the same in terms of growth temperature, growth pressure, and the amount of TMIn supply but differ in the amount of other group-III (Ga or Al) source supplies. Thus, in this experiment, the InN mole fractions of A2 and C2 (AlGaInN) may be similar to those of A1 and C1 (GaInN), respectively.

The surface morphologies of all the samples were characterized by atomic force microscopy (AFM). In addition, surface images were obtained by scanning electron microscopy (SEM) and room-temperature panchromatic (160–930 nm) cathodoluminescence (CL) analysis in the same areas to correlate the surface morphologies with luminescence intensities. Also, room temperature photoluminescence (PL) spectra were measured to evaluate the optical qualities of the QW samples.

### 3. Results and Discussion

Room temperature PL revealed that the AlGaInN QW Sample A2 showed a 385 nm peak wavelength as designed but also a much lower PL intensity than the standard GaInN QW Sample A1. Note that AlGaInN QW Sample A2 contains AlGaIn barrier layers, as listed in Table I, for an equivalent carrier confinement to that of GaInN QW Sample A1. Thus, the lower PL intensity of Sample A2 could suggest a poor quality of the AlGaInN QW material.

To investigate this further, surface morphology images obtained by AFM and SEM, and CL images were observed, as shown in Fig. 1(a) for the GaInN Sample A1 and Fig. 1(b) for AlGaInN Sample A2. The SEM and CL images were taken in the same regions. Some pits were found in GaInN QW Sample A1, which are typically observed in GaInN QWs. Also, even though some undulation in the CL image of GaInN QW Sample A1 was observed due to the In inhomogeneity, the CL image showed reasonably high intensity. In contrast, AlGaInN QW Sample A2 showed many defects on the surface. The inset of the AFM image in Fig. 1(b) revealed that each defect was surrounded with a trench, and the surrounded region was slightly higher than the other flat regions. The height and width of the region

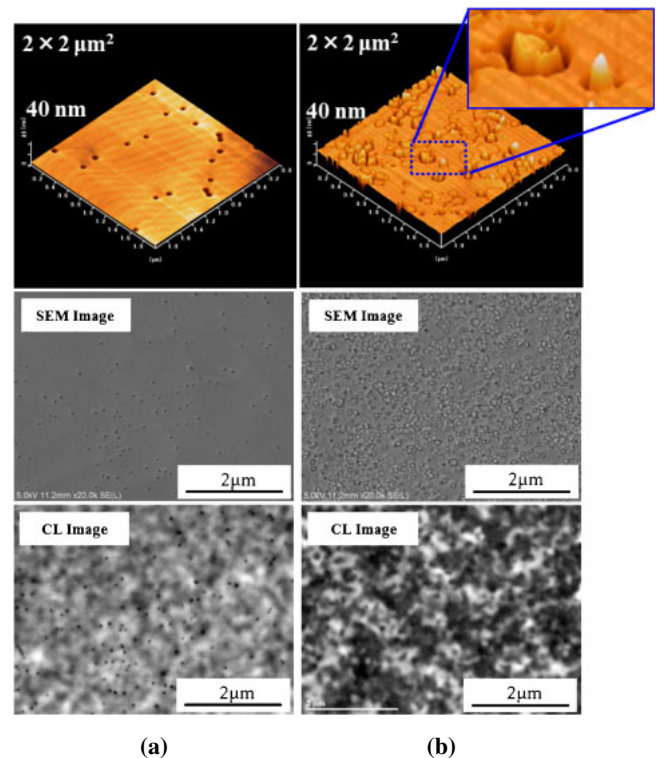


**Fig. 1.** (Color online) AFM, SEM, and CL images of (a) Ga<sub>0.90</sub>In<sub>0.10</sub>N QWs (Sample A1) and (b) AlGaInN QWs (Sample A2).

surrounded by the trench are about 4–13 and 60–200 nm, respectively. In addition, the CL image revealed that the areas of the trench defects were very dark, meaning that the trench defects should act as nonradiative centers. The trench defects are not typically observed in GaInN QWs, so the defects should result from the additional TMAI flow.

Next, to understand the origin of the trench defects, additional AlGaInN QW samples (B1 to B3) were grown and characterized. In the AlGaInN samples, various TMIn flows including zero flow were selected during the AlGaInN QW growths. Figures 2(a)–2(c) show the surface morphologies of AlGaInN QW Samples B1, B2, and B3 measured by AFM. As the TMIn flow was reduced, the trench defects were clearly reduced. Actually, no trench defects were observed in AlGaIn QW Sample B3, which was grown without TMIn flow. Therefore, the origin of the trench defects in this case should be related to the coexistence of Al and In at least.

We then grew QW samples at a lower growth pressure of 150 mbar. The purpose of using a lower growth pressure is to minimize potential parasitic reactions between TMAI, TMIn, and possibly NH<sub>3</sub> by increasing the flow velocity in the MOVPE reactor flow channel. Figures 3(a) and 3(b) show AFM, SEM, and CL images of GaInN QW Sample C1 and AlGaInN QW Sample C2 grown at 150 mbar, respectively. Clearly, AlGaInN QW Sample C2 shows almost no trench defects on the surface. Furthermore, a bright CL image was also obtained from AlGaInN QW Sample C2. This is attributed to the elimination of the trench defects on the surface. Another finding is that the size of the bright regions in the CL image of AlGaInN QW Sample C2 [Fig. 3(b)] was smaller than that of those in GaInN QW

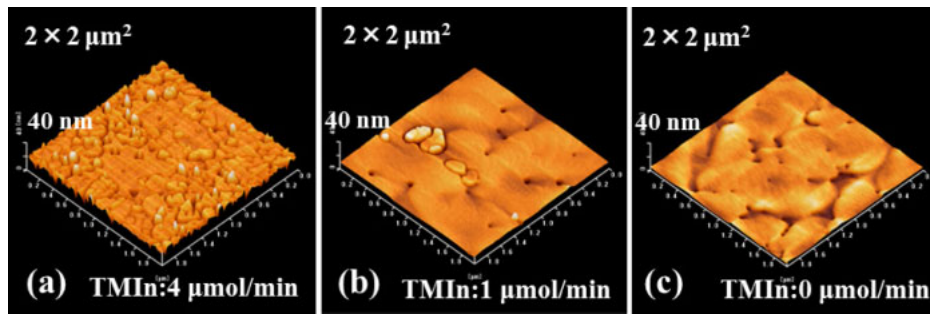


Fig. 2. (Color online) AFM images of (a) AlGaInN QWs (Sample B1), (b) AlGaInN QWs (Sample B2), and (c) Al<sub>0.07</sub>Ga<sub>0.93</sub>N QWs (Sample B3).

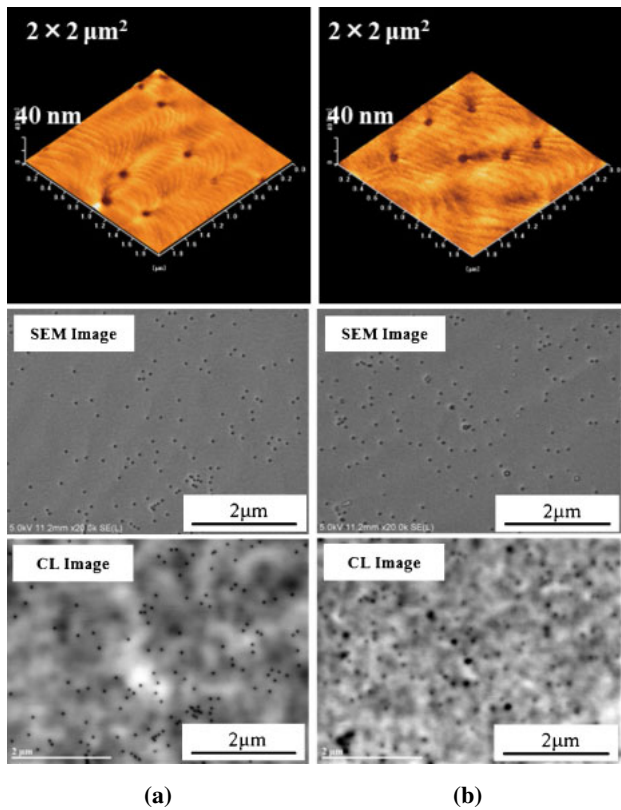


Fig. 3. (Color online) AFM, SEM, and CL images of (a) Ga<sub>0.87</sub>In<sub>0.13</sub>N QWs (Sample C1) and (b) AlGaInN QWs (Sample C2).

Sample C1 [Fig. 3(a)]. This should be one of the influences of adding Al atoms in the well layers, but the details are unknown at this moment.

PL spectra of AlGaInN QW Samples A2 and C2, and reference GaInN QW Samples A1 and C1 are plotted in Fig. 4. AlGaInN QW Sample C2 grown at 150 mbar clearly showed a drastic improvement of PL intensity compared with AlGaInN QW Sample A2, and almost comparable PL intensities to those of GaInN QW Samples A1 and C1. Also, the emission peak wavelength of AlGaInN QW Sample C2 showed a blue-shift from that of GaInN QW Sample C1, resulting in 385 nm emission. This result implies that some Al atoms incorporated in the well layer contributed to the blue-shift.

Additionally, for an extreme case with the coexistence of Al and In, AlInN QW Sample C3 was grown at 150 mbar. As shown in Fig. 5, no trench defects on the surface were

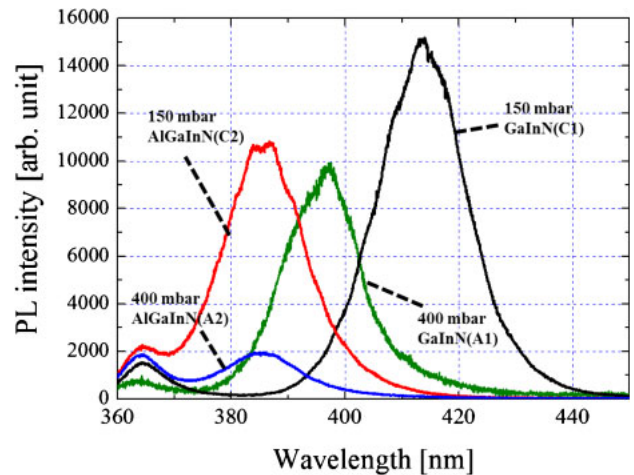


Fig. 4. (Color online) PL spectra of AlGaInN QWs (Samples A2 and C2) and reference GaInN QWs (Samples A1 and C1).

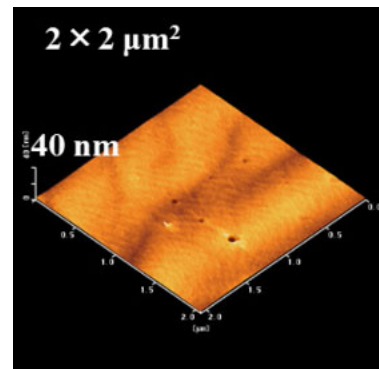


Fig. 5. (Color online) AFM image of Al<sub>0.86</sub>In<sub>0.14</sub>N QWs (Sample C3).

observed, so the low-pressure growth is confirmed to be a key technique for obtaining high-quality AlGaInN layers by suppressing the formation of trench defects. At this moment, we do not have direct evidence explaining why the low-pressure growth is effective for suppressing the trench defect formation. Further investigations will be necessary.

#### 4. Summary

We have grown AlGaInN QWs based on the growth conditions of GaInN QWs under different growth pressures, 400 and 150 mbar. When the AlGaInN QWs were grown at 400 mbar, a considerable amount of trench defects were

observed on the surface, which acted as nonradiative centers. The number of trench defects decreased with the decreasing amount of TMIn flow. When the AlGaInN QWs were grown at 150 mbar, AlGaInN QWs without trench defects were obtained, resulting in a high PL intensity with a 385 nm peak wavelength. We found that the low-pressure growth is a key technique for obtaining high-quality AlGaInN QWs by suppressing the trench defect formation.

### Acknowledgement

This study was supported by the MEXT-Supported Program for the Strategic Research Foundation at Private Universities, 2012–2016.

- 1) B. Reuters, A. Wille, B. Holländer, E. Sakalauskas, N. Ketteniss, C. Mauder, R. Goldhahn, M. Heuken, H. Kalisch, and A. Vescan: *J. Electron. Mater.* **41** (2012) 905.
- 2) Y. Yan, Q. Wang, W. Shu, Z. Jia, X. Ren, X. Zhang, and Y. Huang: *Physica B* **407** (2012) 4570.
- 3) M. Jetter, C. Wächter, A. Meyer, and P. Michler: *Phys. Status Solidi C* **8** (2011) 2163.
- 4) R. Miyagawa, S. Yang, H. Miyake, and K. Hiramatsu: *Phys. Status Solidi C* **9** (2012) 499.
- 5) A. V. Lobanova, E. V. Yakovlev, R. A. Talalaev, S. B. Thapa, and F. Scholz: *J. Cryst. Growth* **310** (2008) 4935.
- 6) A. V. Lobanova, K. M. Mazaev, R. A. Talalaev, M. Leys, S. Boeykens, K. Cheng, and S. Degroote: *J. Cryst. Growth* **287** (2006) 601.
- 7) Y. Ohba and R. Sato: *J. Cryst. Growth* **221** (2000) 258.
- 8) M. Jamil, H. Zhao, J. B. Higgins, and N. Tansu: *J. Cryst. Growth* **310** (2008) 4947.
- 9) Y. Zhang, Y. Liu, T. Kimura, M. Hirata, K. Prasertusk, S. Ji, R. Katayama, and T. Matsuoka: *Phys. Status Solidi C* **8** (2011) 482.
- 10) Y. Huang, H. Wang, Q. Sun, J. Chen, D. Y. Li, Y. T. Wang, and H. Yang: *J. Cryst. Growth* **276** (2005) 13.
- 11) S. Suihkonen, J. Sormunen, V. T. Rangel-Kuoppa, H. Koskenvaara, and M. Sopanen: *J. Cryst. Growth* **291** (2006) 8.
- 12) S. Kamiyama, T. Maeda, Y. Nakamura, M. Iwaya, H. Amano, I. Akasaki, H. Kinoshita, T. Furusho, M. Yoshimoto, T. Kimoto, J. Suda, A. Henry, I. G. Ivanov, J. P. Bergman, B. Monemar, T. Onuma, and S. F. Chichibu: *Jpn. J. Appl. Phys.* **99** (2006) 093108.
- 13) S. Kamiyama, M. Iwaya, T. Takeuchi, I. Akasaki, M. Syväjärvi, and R. Yakimova: *J. Semicond.* **32** (2011) 013004.
- 14) Y. Ou, V. Jokubavicius, S. Kamiyama, C. Liu, R. W. Berg, M. Linnarsson, R. Yakimova, M. Syväjärvi, and H. Ou: *Opt. Express* **1** (2011) 1439.
- 15) M. Syväjärvi, J. Müller, J. W. Sun, V. Grivickas, Y. Ou, V. Jokubavicius, P. Hens, M. Kaisr, K. Ariyawong, K. Gulbinas, P. Hens, R. Liljedahl, M. K. Linnarsson, S. Kamiyama, P. Wellmann, E. Spiecker, and H. Ou: *Phys. Scr.* **T148** (2012) 014002.
- 16) Y. Ohba, K. Kaneko, H. Katsuno, and M. Kushibe: *Appl. Phys. Express* **1** (2008) 101101.
- 17) X. A. Cao and Y. Yang: *Appl. Phys. Lett.* **96** (2010) 151109.
- 18) H. Hirayama, S. Fujikawa, N. Noguchi, J. Norimatsu, T. Takano, K. Tsubaki, and N. Kamata: *Phys. Status Solidi A* **206** (2009) 1176.
- 19) H. Hirayama, A. Kinoshita, A. Hirata, and Y. Aoyagi: *Phys. Status Solidi A* **188** (2001) 83.
- 20) E. Kuokstis, J. Zhang, J. W. Yang, G. Simin, M. A. Khan, R. Gaska, and M. Shur: *Phys. Status Solidi A* **228** (2001) 559.
- 21) V. Adivarahan, A. Chitnis, J. P. Zhang, M. Shatalov, J. W. Yang, G. Simin, M. A. Khan, R. Gaska, and M. S. Shur: *Appl. Phys. Lett.* **79** (2001) 4240.
- 22) H. Hirayama, A. Kinoshita, T. Yamabi, Y. Enomoto, A. Hirata, T. Araki, Y. Nanishi, and Y. Aoyagi: *Appl. Phys. Lett.* **80** (2002) 207.
- 23) F. C.-P. Massabuau, S.-L. Sahonta, L. Trinh-Xuan, S. Rhode, T. J. Puchtler, M. J. Kappers, C. J. Humphreys, and R. A. Oliver: *Appl. Phys. Lett.* **101** (2012) 212107.

## GaNN-based tunnel junctions with graded layers

This content has been downloaded from IOPscience. Please scroll down to see the full text.

2016 Appl. Phys. Express 9 081005

(<http://iopscience.iop.org/1882-0786/9/8/081005>)

View [the table of contents for this issue](#), or go to the [journal homepage](#) for more

Download details:

IP Address: 219.127.71.134

This content was downloaded on 03/03/2017 at 06:39

Please note that [terms and conditions apply](#).

You may also be interested in:

[GaN-Based Tunnel Junctions in n-p-n Light Emitting Diodes](#)

Mitsuru Kaga, Takatoshi Morita, Yuka Kuwano et al.

[Multijunction GaN-based solar cells using a tunnel junction](#)

Hironori Kurokawa, Mitsuru Kaga, Tomomi Goda et al.

[Over 1000 channel nitride-based micro-light-emitting diode arrays with tunnel junctions](#)

Masahiro Watanabe, Keisuke Nakajima, Mitsuru Kaga et al.

[Room-temperature continuous-wave operation of GaN-based vertical-cavity surface-emitting lasers with n-type conducting AlInN/GaN distributed Bragg reflectors](#)

Kazuki Ikeyama, Yugo Kozuka, Kenjo Matsui et al.

[Electron and hole accumulations at GaN/AlInN/GaN interfaces and conductive n-type AlInN/GaN distributed Bragg reflectors](#)

Shotaro Yoshida, Kazuki Ikeyama, Toshiki Yasuda et al.

[Lateral Hydrogen Diffusion at p-GaN Layers in Nitride-Based Light Emitting Diodes with Tunnel Junctions](#)

Yuka Kuwano, Mitsuru Kaga, Takatoshi Morita et al.

[Room-temperature CW operation of a nitride-based vertical-cavity surface-emitting laser using thick GaN quantum wells](#)

Takashi Furuta, Kenjo Matsui, Kosuke Horikawa et al.

[Hybrid tunnel junction contacts to III-nitride light-emitting diodes](#)

Erin C. Young, Benjamin P. Yonkee, Feng Wu et al.

## GaNN-based tunnel junctions with graded layers

Daiki Takasuka<sup>1</sup>, Yasuto Akatsuka<sup>1</sup>, Masataka Ino<sup>1</sup>, Norikatsu Koide<sup>1</sup>, Tetsuya Takeuchi<sup>1\*</sup>, Motoaki Iwaya<sup>1</sup>, Satoshi Kamiyama<sup>1</sup>, and Isamu Akasaki<sup>1,2</sup>

<sup>1</sup>Faculty of Science and Engineering, Meijo University, Nagoya 468-8502, Japan

<sup>2</sup>Graduate School of Engineering, Akasaki Research Center, Nagoya University, Nagoya 464-8601, Japan

\*E-mail: take@meijo-u.ac.jp

Received June 20, 2016; accepted July 7, 2016; published online July 22, 2016

We demonstrated low-resistivity GaInN-based tunnel junctions using graded GaInN layers. A systematic investigation of the samples grown by metalorganic vapor phase epitaxy revealed that a tunnel junction consisting of a 4 nm both-sides graded GaInN layer (Mg:  $1 \times 10^{20} \text{ cm}^{-3}$ ) and a 2 nm GaN layer (Si:  $7 \times 10^{20} \text{ cm}^{-3}$ ) showed the lowest specific series resistance of  $2.3 \times 10^{-4} \Omega \text{ cm}^2$  at  $3 \text{ kA/cm}^2$  in our experiment. The InN mole fraction in the 4 nm both-sides graded GaInN layer was changed from 0 through 0.4 to 0. The obtained resistance is comparable to those of standard p-contacts with Ni/Au and MBE-grown tunnel junctions. © 2016 The Japan Society of Applied Physics

The first GaInN-based tunnel junction for current injection from n-layers to p-layers was demonstrated in 2001.<sup>1)</sup> Because the tunnel junctions made of other III–V semiconductors have been adopted in various devices,<sup>2–4)</sup> such a GaInN-based tunnel junction is also expected to be utilized to improve device performance in not just tandem solar cells<sup>5)</sup> and cascaded LEDs,<sup>6–12)</sup> but also in micro-LEDs,<sup>13,14)</sup> their arrays,<sup>15)</sup> lasers,<sup>16,17)</sup> and vertical cavity surface emitting lasers (VCSELs).<sup>6,18)</sup> At that time, however, the voltage drop at the GaInN tunnel junction was high, about 0.6 V at  $50 \text{ A/cm}^2$ , and further reduction in tunnel junction resistance was demanded.

In 2010, a new concept to leverage polarization charges at the GaInN/GaN interfaces was proposed towards realizing low-resistivity GaInN-based tunnel junctions.<sup>19)</sup> Thus, the GaInN layer has been used in the tunnel junctions because of not only a narrower band gap<sup>20)</sup> with a lower ionized energy of a Mg acceptor<sup>21)</sup> but also the polarization doping. Since then, the GaInN-based tunnel junctions have shown marked improvements in their reverse-biased characteristics. In particular, a GaInN tunnel junction grown by MBE showed a very low specific series resistance of  $1.2 \times 10^{-4} \Omega \text{ cm}^2$ .<sup>22)</sup> On the other hand, a GaInN tunnel junction grown by metalorganic vapor phase epitaxy (MOVPE) showed a resistance of  $4.0 \times 10^{-4} \Omega \text{ cm}^2$  by using a very high InN mole fraction of 0.4 and lateral Mg activation.<sup>23–25)</sup> However, a large voltage drop at the GaInN tunnel junction of about 1 V was still observed under operation with a high current density of  $\sim 3 \text{ kA/cm}^2$ .

In this study, we paid attention to not only a tunneling probability component in the GaInN layer but also an energy spike component at the GaInN/GaN interfaces in terms of the resistance of the GaInN tunnel junction. The GaInN layer with the high InN mole fraction leads to a high tunneling probability owing to the small band gap, but at the same time generates large energy spikes at the GaInN/GaN interfaces, which result in a high resistance. Such energy spikes are notorious as a cause of the large resistance in semiconductor-based devices, such as distributed Bragg reflectors. In order to eliminate such energy spikes, graded layers were proposed and often used.<sup>26,27)</sup> Actually, the effect of the graded AlGaIn layers in a GaN/AlN tunnel junction was theoretically investigated by Schubert.<sup>28)</sup> Here, we experimentally investigated the impact of the graded GaInN layers on the resistance of the GaInN tunnel junctions. Various InN mole fraction profiles in

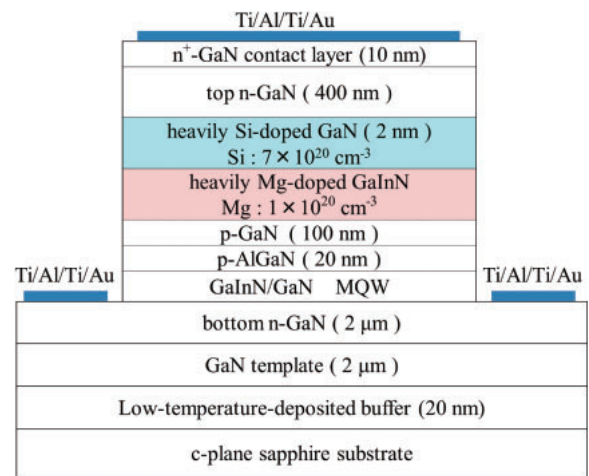


**Fig. 1.** Sample structure consisting of a standard blue LED structure, a GaInN-based tunnel junction, a 400-nm top n-GaN layer, and a 10-nm n<sup>+</sup>-GaN contact layer.

the graded GaInN tunnel junctions were also determined. As a result, we demonstrated a graded GaInN tunnel junction with a very low resistivity, the specific series resistance of which was  $2.3 \times 10^{-4} \Omega \text{ cm}^2$  at  $3 \text{ kA/cm}^2$ .

All the samples were grown by MOVPE on *c*-plane sapphire substrates using low-temperature-deposited buffer layers.<sup>29)</sup> As shown in Fig. 1, a sample structure consisted of a standard blue LED structure, a GaInN-based tunnel junction, a 400 nm top n-GaN layer, and a 10 nm n<sup>+</sup>-GaN contact layer. We prepared four samples containing different GaInN layers in the tunnel junctions. Figure 2 shows the designed InN mole fraction profiles in the GaInN layers. The first sample shown in Fig. 2(a) contained a 2 nm<sup>2</sup> Ga<sub>0.6</sub>In<sub>0.4</sub>N layer, which was the same layer that we previously optimized.<sup>24)</sup> The other three samples contained graded GaInN layers. The second sample shown in Fig. 2(b) had a 4 nm p-side graded GaInN layer in which the InN mole fraction was increased from 0 at the p-side (left) to 0.4 at the n-side (right). The third sample included the opposite n-side graded GaInN layer in which the InN mole fraction was decreased from 0.4 at the p-side to 0 at the n-side, as shown in Fig. 2(c). Finally, as shown in Fig. 2(d), the fourth sample contained a 4 nm both-sides graded GaInN layer in which the InN mole fraction was changed from 0 to 0.4 in a 2 nm p-side GaInN layer and from 0.4 to 0 in a 2 nm n-side GaInN layer. In other

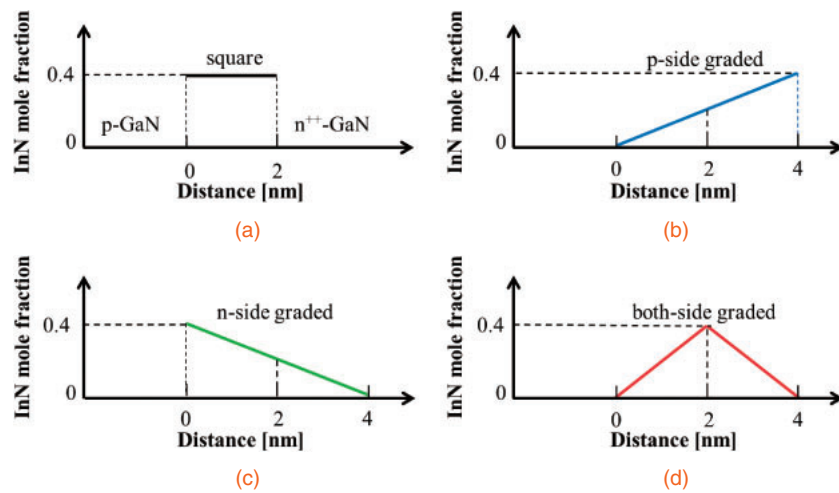


**Fig. 2.** Designed InN mole fraction profiles in the GaInN tunnel junctions: (a) a  $2\text{ nm}^2$   $\text{Ga}_{0.6}\text{In}_{0.4}\text{N}$ , (b) a 4 nm p-side graded GaInN, (c) a 4 nm n-side graded GaInN, and (d) a 4 nm both-sides graded GaInN.

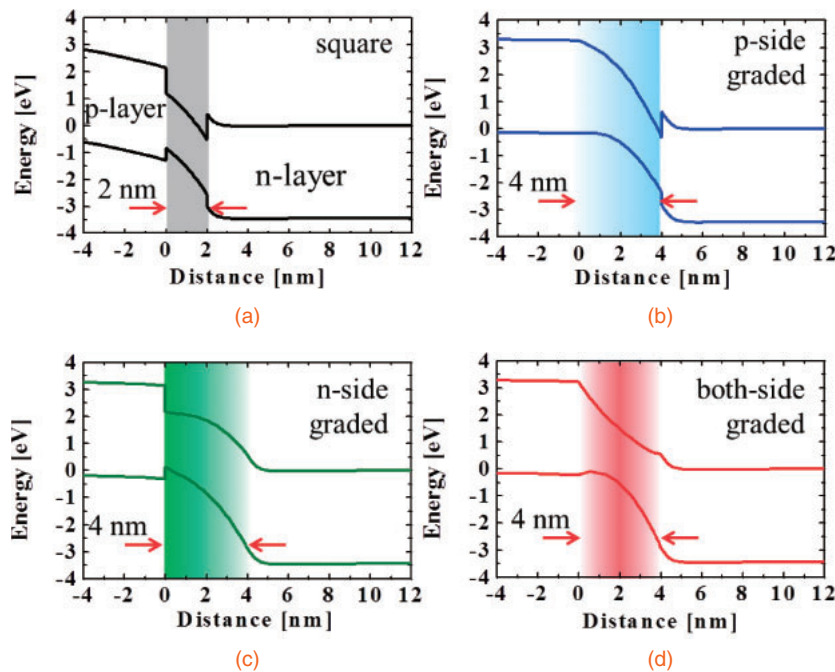


**Fig. 3.** Calculated band diagrams around the GaInN tunnel junctions: (a) a  $2\text{ nm}^2$   $\text{Ga}_{0.6}\text{In}_{0.4}\text{N}$ , (b) a 4 nm p-side graded GaInN, (c) a 4 nm n-side graded GaInN, and (d) a 4 nm both-sides graded GaInN.

words, the InN mole fraction profile of the both-sides graded GaInN layer was “Λ”-shaped. Here, the InN mole fractions were controlled by changing the TMIn flow rate during the graded GaInN layer growth while the growth temperature and TMGa flow rate remained constant. Note that the total amount of In in the tunnel junction was designed to be the same among all the samples. All the GaInN layers in the tunnel junctions were doped with Mg of  $1 \times 10^{20}\text{ cm}^{-3}$ . Then, 2 nm heavily Si-doped ( $7 \times 10^{20}\text{ cm}^{-3}$ ) GaN layers were grown on the GaInN layers to complete the tunnel junction structures.

A lateral Mg activation previously developed for the LEDs with the tunnel junctions was performed for all the samples.<sup>25)</sup> After forming device mesas of  $35\text{ }\mu\text{m}$  diameter, the wafers were thermally annealed under oxygen ambient at  $725\text{ }^\circ\text{C}$  for 30 min. Metal layers, Ti (30 nm)/Al (100 nm)/

Ti (20 nm)/Au (150 nm), for the top and bottom n-contacts were simultaneously formed. Since the small mesas were formed, we were able to measure the current density–voltage ( $j$ – $V$ ) and current density–light output power ( $j$ – $L$ ) characteristics of the LEDs with the tunnel junctions under a high current density of up to  $5\text{ kA/cm}^2$ . For comparison, we also prepared a small standard blue LED with a p-contact with Ni/Au.

Figure 3 shows calculated band diagrams around the tunnel junctions in the four samples. Commercial software (SiLENSe)<sup>30)</sup> was used for the calculation. Large energy spikes were clearly shown at the interfaces of the  $2\text{ nm}^2$  GaInN layer in Fig. 3(a). The energy heights of the spikes were 0.9 eV at the conduction band and 0.4 eV at the valence band. On the other hand, no energy spikes were shown at the p-side interface in the p-side graded GaInN tunnel junction

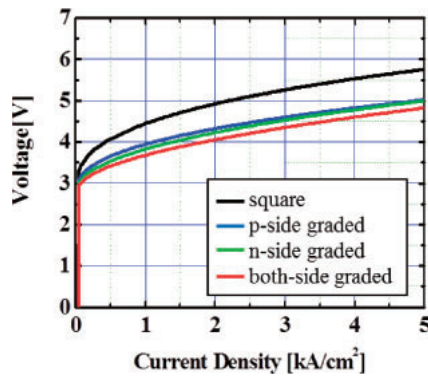
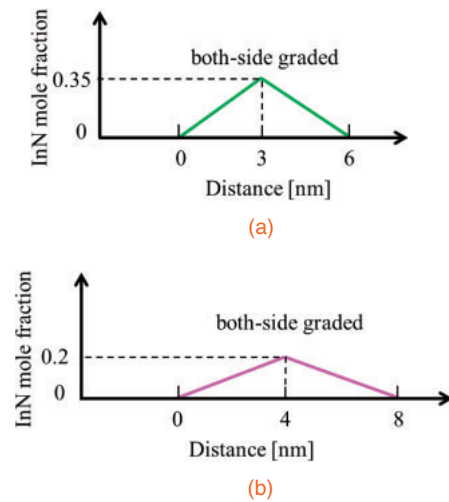


**Fig. 4.**  $j$ - $V$  characteristics of the four LEDs with the GaInN tunnel junctions containing the  $2\text{ nm}^2$   $\text{Ga}_{0.6}\text{In}_{0.4}\text{N}$ , 4 nm p-side graded GaInN, 4 nm n-side graded GaInN, or 4 nm both-sides graded GaInN.

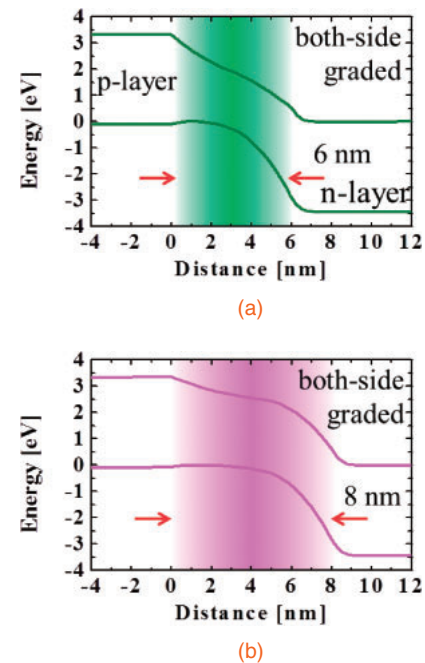
[Fig. 3(b)] and at the n-side interface in the n-side graded GaInN tunnel junction [Fig. 3(c)] owing to the graded layers. Interestingly, even with the very thin graded layers (2 nm) [Fig. 3(d)], a clear reduction in the number of energy spikes was also shown at both interfaces in the both-sides graded GaInN tunnel junction.<sup>28)</sup>

Figure 4 shows the  $j$ - $V$  characteristics of the four LEDs with the square GaInN tunnel junctions or various graded GaInN tunnel junctions. The operating voltage of the LED with the square GaInN tunnel junction was 5.3 V at  $3\text{ kA/cm}^2$ . On the other hand, all of the LEDs with the graded GaInN tunnel junctions showed lower operating voltages of 4.6 V or lower at  $3\text{ kA/cm}^2$ . The differential specific series resistance of the device was also estimated to be  $2.3 \times 10^{-4}\ \Omega\text{ cm}^2$  at  $3\text{ kA/cm}^2$ , suggesting that the tunnel junction resistance should be lower than this value, which is comparable to the best value of MBE-grown nitride-based tunnel junctions.<sup>22)</sup> These lines of evidence suggest that the energy spikes at the heterointerfaces have a considerable impact on the tunnel junction resistances. Note that the LED with the both-sides graded tunnel junction showed the lowest voltage of 4.3 V at  $3\text{ kA/cm}^2$ , but the value was not so low as expected in consideration of the results obtained from the single-side (the p- or n-side) graded tunnel junctions. One of the possible reasons is that the actual 2 nm graded GaInN layer could be too thin to eliminate the energy spike sufficiently.

Then, we attempted a larger graded layer thickness in the both-sides graded GaInN tunnel junction. We found that the sample surface deteriorated when we grew an 8 nm both-sides graded GaInN layer from 0 through 0.4 to 0 on the LED structure. It is difficult to obtain simultaneously a small band gap and thick graded layers with high InN mole fractions owing to the large lattice mismatch between GaInN and GaN. In other words, the choice of InN mole fraction in the graded GaInN tunnel junction affects two opposite aspects. One is the tunneling probability in which a “higher” InN mole fraction results in a lower resistance, and the other is the energy spike height in which a “lower” InN mole fraction results in a lower resistance. Therefore, an optimum InN mole fraction may exist in such a trade-off situation. We then prepared two additional LEDs with different both-sides graded GaInN tunnel junctions. As shown in Fig. 5, two different InN mole fraction profiles were obtained. The first one was a 6 nm both-sides graded GaInN layer with InN mole fractions from 0 through 0.35 to 0, as shown in Fig. 5(a). The second one



**Fig. 5.** Designed InN mole fraction profiles in the graded GaInN tunnel junctions: (a) a 6 nm both-sides graded  $\text{Ga}_{0.65}\text{In}_{0.35}\text{N}$  and (b) an 8 nm both-sides graded  $\text{Ga}_{0.8}\text{In}_{0.2}\text{N}$ .



**Fig. 6.** Calculated band diagrams around the graded GaInN tunnel junctions: (a) a 6 nm both-sides graded  $\text{Ga}_{0.65}\text{In}_{0.35}\text{N}$  and (b) an 8 nm both-sides graded  $\text{Ga}_{0.8}\text{In}_{0.2}\text{N}$ .

was an 8 nm both-sides graded GaInN layer with InN mole fractions from 0 through 0.2 to 0, as shown in Fig. 5(b).

Figure 6 shows calculated band diagrams around the tunnel junctions in the two samples. No energy spikes were found at both interfaces in the two samples. Actually, as compared with the above-mentioned 4 nm both-sides graded GaInN tunnel junction in Fig. 3(d), the additional two samples containing the wider graded layer with the lower InN mole fraction showed smoother potential profiles but slightly larger depletion lengths. Figure 7 shows the  $j$ - $V$  characteristics of the two additional both-sides graded GaInN tunnel junctions (6 and 8 nm) as well as the 4 nm both-sides graded GaInN tunnel junction. In this experiment, we found that the 4 nm graded GaInN layer with the 0.4 InN mole fraction still resulted in the lowest resistance.

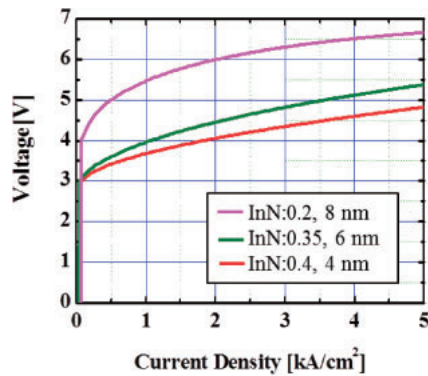


**Fig. 7.**  $j$ - $V$  characteristics of the three LEDs with the tunnel junctions containing the 4 nm both-sides graded  $\text{Ga}_{0.6}\text{In}_{0.4}\text{N}$ , 6 nm both-sides graded  $\text{Ga}_{0.65}\text{In}_{0.35}\text{N}$ , or 8 nm both-sides graded  $\text{Ga}_{0.8}\text{In}_{0.2}\text{N}$ .

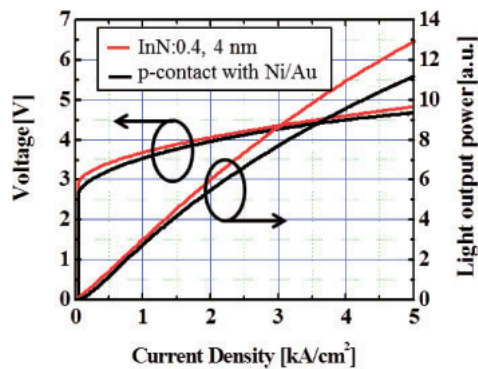


**Fig. 8.**  $j$ - $V$ - $L$  characteristics of the LED with the 4 nm both-sides graded  $\text{Ga}_{0.6}\text{In}_{0.4}\text{N}$  tunnel junction and a standard LED with p-contact and Ni/Au.

Eventually, we plotted the  $j$ - $V$ - $L$  characteristics of the LED with the 4 nm both-sides graded  $\text{Ga}_{0.6}\text{In}_{0.4}\text{N}$  tunnel junction showing the lowest resistance and the standard LED containing the p-contact with Ni/Au. Here, light output power was measured under the bottom emission configuration. As shown in Fig. 8, the operating voltage and light output power of the LED with the tunnel junction were comparable to those of the standard LED with p-contact.

In this study, we investigated the impact of the graded GaInN layers on the resistance of the GaInN tunnel junctions grown by MOVPE. The experimental results revealed that the graded GaInN layers resulted in lower voltage drops at the tunnel junctions. Our lowest specific series resistance of the graded GaInN tunnel junction was  $2.3 \times 10^{-4} \Omega \text{cm}^2$  at  $3 \text{ kA/cm}^2$  as obtained by using the 4 nm both-sides graded  $\text{Ga}_{0.6}\text{In}_{0.4}\text{N}$  layer. The value is now comparable to those of the standard p-contact with Ni/Au and the GaInN tunnel junction grown by MBE. Such a low-resistivity GaInN tunnel junction grown by MOVPE could open up great possibilities for high-performance nitride-based optoelectronic devices.

**Acknowledgments** This work was supported by a Grant-in-Aid for Scientific Research (B) (No. 26286045), a Grant-in-Aid for Challenging

Exploratory Research (No. 15K13959), and the Ministry of Education, Culture, Sports, Science and Technology (MEXT)-Supported Program for the Strategic Research Foundation at Private Universities, 2012–2016.

- 1) T. Takeuchi, G. Hasnain, S. Corzine, M. Hueschen, R. P. Schneider, Jr., C. Kocot, M. Blomqvist, Y.-L. Chang, D. Lefforge, M. Krames, L. W. Cook, and S. A. Stockman, *Jpn. J. Appl. Phys.* **40**, L861 (2001).
- 2) J. P. van der Ziel and W. T. Tsang, *Appl. Phys. Lett.* **41**, 499 (1982).
- 3) H. Sugiura, C. Amano, A. Yamamoto, and M. Yamaguchi, *Jpn. J. Appl. Phys.* **27**, 269 (1988).
- 4) J. J. Wierer, P. W. Evans, N. Holonyak, Jr., and D. A. Kelloff, *Appl. Phys. Lett.* **71**, 3468 (1997).
- 5) H. Kurokawa, M. Kaga, T. Goda, M. Iwaya, T. Takeuchi, S. Kamiyama, I. Akasaki, and H. Amano, *Appl. Phys. Express* **7**, 034104 (2014).
- 6) M. Diagne, Y. He, H. Zhou, E. Makarona, A. V. Nurmikko, J. Han, K. E. Waldrip, J. J. Figiel, T. Takeuchi, and M. Krames, *Appl. Phys. Lett.* **79**, 3720 (2001).
- 7) M. J. Grundmann and U. K. Mishra, *Phys. Status Solidi C* **4**, 2830 (2007).
- 8) F. Akyol, S. Krishnamoorthy, and S. Rajan, *Appl. Phys. Lett.* **103**, 081107 (2013).
- 9) J. Piprek, *Phys. Status Solidi: Rapid Res. Lett.* **8**, 424 (2014).
- 10) F. Akyol, S. Krishnamoorthy, Y. Zhang, and S. Rajan, *Appl. Phys. Express* **8**, 082103 (2015).
- 11) S.-J. Chang, W.-H. Lin, and C.-T. Yu, *IEEE Electron Device Lett.* **36**, 366 (2015).
- 12) S. M. Sadaf, Y.-H. Ra, H. P. T. Nguyen, M. Djavid, and Z. Mi, *Nano Lett.* **15**, 6696 (2015).
- 13) S.-R. Jeon, C. S. Oh, J.-W. Yang, G. M. Yang, and B.-S. Yoo, *Appl. Phys. Lett.* **80**, 1933 (2002).
- 14) M. Malinverni, D. Martin, and N. Grandjean, *Appl. Phys. Lett.* **107**, 051107 (2015).
- 15) M. Watanabe, K. Nakajima, M. Kaga, Y. Kuwano, D. Minamikawa, T. Suzuki, K. Yamashita, M. Iwaya, T. Takeuchi, S. Kamiyama, and I. Akasaki, *Jpn. J. Appl. Phys.* **53**, 05FL06 (2014).
- 16) B. P. Yonkee, E. C. Young, C. Lee, J. T. Leonard, S. P. DenBaars, J. S. Speck, and S. Nakamura, *Opt. Express* **24**, 7816 (2016).
- 17) M. X. Feng, J. P. Liu, S. M. Zhang, D. S. Jiang, Z. C. Li, K. Zhou, D. Y. Li, L. Q. Zhang, F. Wang, H. Wang, P. Chen, Z. S. Liu, D. G. Zhao, Q. Sun, and H. Yang, *Appl. Phys. Lett.* **103**, 043508 (2013).
- 18) J. T. Leonard, E. C. Young, B. P. Yonkee, D. A. Cohen, T. Margalith, S. P. DenBaars, J. S. Speck, and S. Nakamura, *Appl. Phys. Lett.* **107**, 091105 (2015).
- 19) S. Krishnamoorthy, D. N. Nath, F. Akyol, P. S. Park, M. Esposito, and S. Rajan, *Appl. Phys. Lett.* **97**, 203502 (2010).
- 20) N. Yoshimoto, T. Matsuoka, T. Sasaki, and A. Katsui, *Appl. Phys. Lett.* **59**, 2251 (1991).
- 21) S. Yamasaki, S. Asami, N. Shibata, M. Koike, K. Manabe, T. Tanaka, H. Amano, and I. Akasaki, *Appl. Phys. Lett.* **66**, 1112 (1995).
- 22) S. Krishnamoorthy, F. Akyol, P. S. Park, and S. Rajan, *Appl. Phys. Lett.* **102**, 113503 (2013).
- 23) M. Kaga, T. Morita, Y. Kuwano, K. Yamashita, K. Yagi, M. Iwaya, T. Takeuchi, S. Kamiyama, and I. Akasaki, *Jpn. J. Appl. Phys.* **52**, 08JH06 (2013).
- 24) D. Minamikawa, M. Ino, S. Kawai, T. Takeuchi, S. Kamiyama, M. Iwaya, and I. Akasaki, *Phys. Status Solidi B* **252**, 1127 (2015).
- 25) Y. Kuwano, M. Kaga, T. Morita, K. Yamashita, K. Yagi, M. Iwaya, T. Takeuchi, T. Takeuchi, S. Kamiyama, and I. Akasaki, *Jpn. J. Appl. Phys.* **52**, 08JK12 (2013).
- 26) P. Zhou, J. Cheng, C. F. Schaus, S. Z. Sun, K. Zheng, E. Armour, C. Hains, W. Hsin, D. R. Myers, and G. A. Vawter, *IEEE Photonics Technol. Lett.* **3**, 591 (1991).
- 27) E. F. Schubert, L. W. Tu, G. J. Zyzdzik, R. F. Kopf, A. Benvenuti, and M. R. Pinto, *Appl. Phys. Lett.* **60**, 466 (1992).
- 28) M. F. Schubert, *Phys. Rev. B* **81**, 035303 (2010).
- 29) H. Amano, N. Sawaki, I. Akasaki, and Y. Toyoda, *Appl. Phys. Lett.* **48**, 353 (1986).
- 30) Web [<http://www.str-soft.com/products/SiLENSe/index.htm>].

## Electrical properties of n-type AlGa<sub>N</sub> with high Si concentration

This content has been downloaded from IOPscience. Please scroll down to see the full text.

2016 Jpn. J. Appl. Phys. 55 05FE02

(<http://iopscience.iop.org/1347-4065/55/5S/05FE02>)

View [the table of contents for this issue](#), or go to the [journal homepage](#) for more

Download details:

IP Address: 219.127.71.134

This content was downloaded on 03/03/2017 at 06:41

Please note that [terms and conditions apply](#).

You may also be interested in:

[Low-ohmic-contact-resistance V-based electrode for n-type AlGa<sub>N</sub> with high AlN molar fraction](#)

Kazuki Mori, Kunihiro Takeda, Toshiki Kusafuka et al.

[Control of growth mode in Mg-doped GaN/AlN heterostructure](#)

Tomohiro Morishita, Kosuke Sato, Motoaki Iwaya et al.

[The doping process and dopant characteristics of GaN](#)

J K Sheu and G C Chi

[The effect of exciton localization on the optical and electrical properties of undoped and Si-doped Al<sub>x</sub>Ga<sub>1-x</sub>N](#)

G R James, A W R Leitch, F Omnès et al.

[MIT inn-type doped CuGaSe<sub>2</sub>](#)

J H Schön, Ch Kloc, E Arushanov et al.

[Multijunction GaInN-based solar cells using a tunnel junction](#)

Hironori Kurokawa, Mitsuru Kaga, Tomomi Goda et al.

[Hall-effect measurements of metalorganic vapor-phase epitaxy-grown p-type homoepitaxial GaN layers with various Mg concentrations](#)

Masahiro Horita, Shinya Takashima, Ryo Tanaka et al.

[Hexagonal boron nitride for deep ultraviolet photonic devices](#)

H X Jiang and J Y Lin

[Electrical Properties of p- and n-GaSe Doped with As and Ge](#)

Shigeru Shigetomi, Tetsuo Ikari and Hiroshi Nakashima



## Electrical properties of n-type AlGa<sub>N</sub> with high Si concentration

Kunihiro Takeda<sup>1\*</sup>, Motoaki Iwaya<sup>1</sup>, Tetsuya Takeuchi<sup>1</sup>, Satoshi Kamiyama<sup>1</sup>, and Isamu Akasaki<sup>1,2</sup>

<sup>1</sup>Faculty of Science and Technology, Meijo University, Nagoya 468-8502, Japan

<sup>2</sup>Akasaki Research Center, Nagoya University, Nagoya 464-8603, Japan

\*E-mail: 143434025@c alumni.meijo-u.ac.jp

Received November 5, 2015; accepted December 1, 2015; published online March 30, 2016

The electrical properties of Si-doped AlGa<sub>N</sub> layers (AlN molar fractions: 0.03–0.06) with the donor concentrations ( $N_D$ ) from  $8.8 \times 10^{17}$  to  $4.5 \times 10^{20} \text{ cm}^{-3}$  were investigated by variable-temperature Hall effect measurement using the van der Pauw method. A minimum resistivity of  $3.6 \times 10^{-4} \Omega \text{ cm}$  was obtained for Si-doped AlGa<sub>N</sub> with a smooth surface at room temperature. We found that the activation energy of the Si donor is affected by the Coulomb interaction in the AlGa<sub>N</sub> layer with  $N_D$  values from  $8.8 \times 10^{17}$  to  $2.5 \times 10^{20} \text{ cm}^{-3}$ . In several AlGa<sub>N</sub> layers, the free-electron concentration did not vary with sample temperature, as expected in the case of degeneracy. The localization of GaN in the AlGa<sub>N</sub> layer was speculated as a cause of degeneracy of samples. © 2016 The Japan Society of Applied Physics

### 1. Introduction

High-performance AlGaInN-based green, blue, and UV light-emitting diodes (LEDs) are commercialized worldwide.<sup>1–5)</sup> Nowadays, the external quantum efficiencies (EQEs) of blue and near-UV LEDs are already more than 80%<sup>4)</sup> and 40%,<sup>5,6)</sup> respectively. From a practical viewpoint, the improvement of wall plug efficiency (WPE) in these LEDs is essential. A decrease in device resistance including the sheet and contact resistances of n- and p-type layers is important for improving WPE.<sup>7)</sup> A reduction in resistivity ( $\rho$ ) in an n-type layer is important, because the layer has a role in current spreading and contact layers. Many studies have reported on the reduction of  $\rho$  in n-type GaN.<sup>8–11)</sup> Fritze et al. realized an n-type GaN layer with a high free electron concentration ( $n_e$ ) ( $\sim 2.9 \times 10^{20} \text{ cm}^{-3}$ ) and low  $\rho$  ( $\sim 6.3 \times 10^{-4} \Omega \text{ cm}$ ) at RT by Ge doping.<sup>10)</sup> Since Si is often used as an n-type dopant in nitride-based LED device manufacturing, low- $\rho$  Si-doped n-type layers are preferred. We have reported that high  $n_e$  ( $\sim 1.4 \times 10^{20} \text{ cm}^{-3}$ ) and low- $\rho$  ( $\sim 5.9 \times 10^{-4} \Omega \text{ cm}$ ) Si-doped Al<sub>0.05</sub>Ga<sub>0.95</sub>N films have been obtained at RT with an atomically flat surface.<sup>7)</sup> In addition, violet LEDs fabricated using a low- $\rho$  Si-doped n-type Al<sub>0.05</sub>Ga<sub>0.95</sub>N layer were realized to reduce device resistance and improve WPE.<sup>7)</sup> On the other hand, a number of studies have shown the activation energy ( $E_D$ ) of the Si donor in GaN.<sup>11–13)</sup> In these studies, the electrical conduction properties of Si-doped GaN with a Si concentration of approximately  $10^{19} \text{ cm}^{-3}$  have been shown to degenerate, which is defined as the Fermi level exit in the conduction band. Nevertheless, the detailed electrical properties and minimum  $\rho$  of Si-doped AlGa<sub>N</sub> with a low AlN molar fraction have not yet been elucidated.

In this study, we obtained the reduction bounds of resistivity and  $E_D$  in Si-doped AlGa<sub>N</sub> layers (AlN molar fractions: 0.03–0.06) with donor concentrations ( $N_D$ ) from  $8.8 \times 10^{17}$  to  $4.5 \times 10^{20} \text{ cm}^{-3}$  and a flat surface by variable-temperature Hall effect measurement. Moreover, the degeneracy of AlGa<sub>N</sub> layers with high  $N_D$  was investigated.

### 2. Experimental methods

All samples were grown using metal organic vapor-phase epitaxy (MOVPE) reactors. Figure 1 shows a schematic view of the sample structure. Trimethylaluminum, trimethylgallium, and ammonia (NH<sub>3</sub>) were used as the precursors of

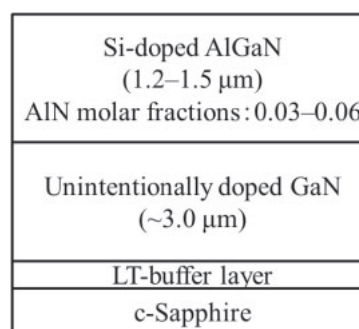


Fig. 1. Schematic view of the sample structure.

Al, Ga, and N, respectively. Silane (SiH<sub>4</sub>) or tetramethylsilane [Si(CH<sub>3</sub>)<sub>4</sub>] was used as a dopant source. A low-temperature (LT) buffer layer was used as a cover to obtain a high-crystalline-quality GaN underlying layer on a c-plane sapphire substrate. Thereafter, an unintentionally doped approximately 3-μm-thick GaN underlying layer and a Si-doped AlGa<sub>N</sub> (AlN molar fractions: 0.03–0.06) layer were sequentially grown. The thicknesses of AlGa<sub>N</sub> layers were from 1.2 to 1.5 μm. The AlGa<sub>N</sub> layers were grown at a constant pressure of 150 Torr. The growth temperature of AlGa<sub>N</sub> layers was set to be in the range from 1,050 to 1,080 °C and the V/III ratio was 3,400. The  $n_e$ , mobility ( $\mu_e$ ), and  $\rho$  in each sample were characterized by variable-temperature Hall effect measurement using the van der Pauw method.

### 3. Results and discussion

Figure 2 shows the Si/III ratio dependence of the  $n_e$  and  $\rho$  in Si-doped AlGa<sub>N</sub> at RT. The Si-doped AlGa<sub>N</sub> layers were grown at various Si/III ratios from  $6.5 \times 10^{-6}$  to  $5.2 \times 10^{-3}$ . The maximum  $n_e$  and minimum  $\rho$  of  $4.5 \times 10^{20} \text{ cm}^{-3}$  and  $3.6 \times 10^{-4} \Omega \text{ cm}$ , respectively, were obtained at a Si/III ratio of  $3.9 \times 10^{-3}$  and at RT. At Si/III ratios from  $6.5 \times 10^{-6}$  to  $3.9 \times 10^{-3}$ , the samples were observed to have a smooth surface by differential interference contrast microscopy measurement and also a root mean square (RMS) roughness of less than 0.31 nm at  $5 \times 5 \mu\text{m}^2$  measured by atomic force microscopy (AFM). The full width at half maximum (FWHM) values of AlGa<sub>N</sub>(0002) and the (10 $\bar{1}$ 2) X-ray

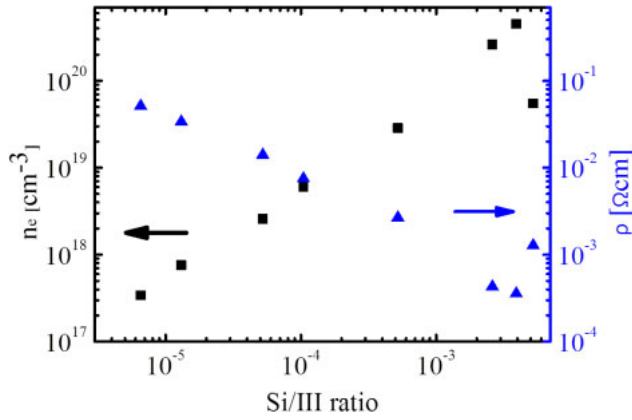


Fig. 2. (Color online) Si/III ratio dependence of  $n_e$  and  $\rho$  at RT.

rocking curve (XRC)  $\omega$ -scan were very much the same as those of the GaN underlying layer. FWHMs of approximately 290 arcsec for the AlGaIn(0002)  $\omega$ -scan and 330 arcsec for the AlGaIn(10 $\bar{1}2$ ) XRC  $\omega$ -scan were observed in these samples. In calculating  $E_D$ , the donor levels of defects and unexpected impurities were ignored, because  $n_e$  was almost proportional to the Si/III ratio in a range from  $6.5 \times 10^{-6}$  to  $3.9 \times 10^{-3}$ , as shown in Fig. 2.

In contrast, the decrease in  $n_e$  and increase in  $\rho$  were observed in Si-doped AlGaIn with a Si/III ratio of  $5.2 \times 10^{-3}$ , as shown in Fig. 2. The surface of this AlGaIn layer was quite rough and the FWHM value of AlGaIn(10 $\bar{1}2$ ) XRC  $\omega$ -scan was increased. The maximum  $n_e$  in Si-doped GaN with a smooth surface has been reported to be approximately  $2 \times 10^{19} \text{ cm}^{-3}$  at RT.<sup>10</sup> In contrast, we obtained an n-type layer with a smooth surface and  $n_e$  of  $4.5 \times 10^{20} \text{ cm}^{-3}$  at RT using GaN with addition of a small amount of AlN. Thus, we investigated the electrical properties of samples with the  $n_e$  of less than  $4.5 \times 10^{20} \text{ cm}^{-3}$  at RT.

Figures 3 and 4 show the results of variable-temperature Hall effect measurement of each sample. These figures show  $n_e$  as a function of reciprocal temperature. From the 12 grown samples, 4 showed electrical properties such as degeneracy. Accordingly, we classified the samples into two types from the temperature dependence of  $n_e$ . Group I showed  $n_e$  that varies with sample temperature, as shown in Fig. 3. In contrast, Group II showed  $n_e$  that did not vary with sample temperature in the range from 300 to 70 K, as shown in Fig. 4. This electrical property suggests degeneracy.<sup>11–13</sup>

First, we investigated the  $E_D$  of the Si donor in the AlGaIn layer from the samples in Group I. In Fig. 3, the samples with  $n_e$  values of more than  $6.0 \times 10^{18} \text{ cm}^{-3}$  at RT showed a variation of  $n_e$  at approximately RT and  $n_e$  saturation at 150 K or below. Since the C, O, H, Mg, and Zn impurity concentrations in the AlGaIn layer of each sample were determined to be below the secondary ion mass spectroscopy detection limits, the effect of donor impurities excluding Si was ignored. A two-band model that includes electron transport within a donor impurity band as well as in the conduction band should be considered to explain the occurrence of the variation and saturation of  $n_e$ .<sup>14–16</sup> Thus, the  $E_D$  values of the samples with  $n_e$  values of more than  $6.0 \times 10^{18} \text{ cm}^{-3}$  at RT were obtained by fitting the temperature dependence of  $n_e$  at approximately RT.

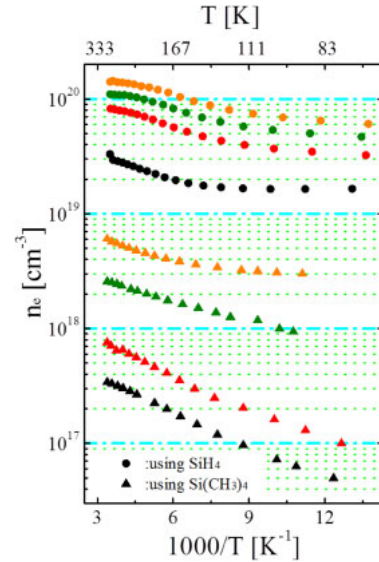


Fig. 3. (Color online)  $n_e$  in Si-doped AlGaIn (AlN molar fractions: 0.03–0.06) as a function of reciprocal temperature characterized by the variable-temperature Hall effect measurement. This figure only plotted the results of Group I. Circles and triangles in the figure indicate the samples grown in MOVPE reactors using  $\text{SiH}_4$  and  $\text{Si}(\text{CH}_3)_4$ , respectively.

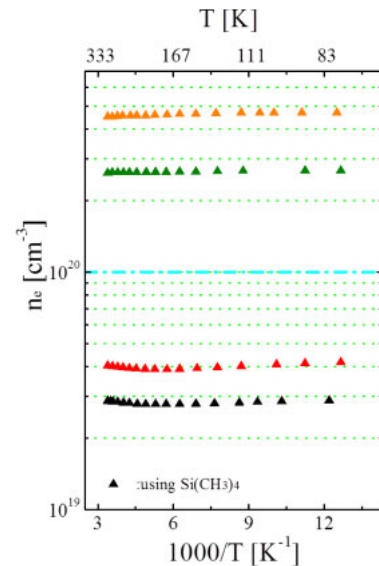


Fig. 4. (Color online)  $n_e$  in Si-doped AlGaIn (AlN molar fraction: 0.03) as a function of reciprocal temperature determined by variable-temperature Hall effect measurement. This figure only plotted the results of Group II. The samples in this figure were grown in MOVPE reactors using  $\text{Si}(\text{CH}_3)_4$ .

From Fig. 2,  $E_D$  was calculated as a single-donor level of the Si dopant. When the donor level is regarded as a single-impurity level, the activation energy of the dopant was calculated from the charge neutrality condition taking residual acceptors into consideration. In the charge neutrality equation for the n-type semiconductor,  $E_D$ ,  $N_D$ , and  $N_A$  are related through the equation<sup>11,17–20</sup>

$$\frac{n_e(n_e + N_A)}{N_D - N_A - n_e} = \frac{N_C}{2} \exp\left(-\frac{E_D}{kT}\right), \quad (1)$$

$$N_C = 2 \left( \frac{2\pi m_e^* kT}{h^2} \right)^{3/2}, \quad (2)$$

where  $N_C$  is the effective density of states in the conduction band,  $k$  is the Boltzmann constant,  $T$  is the temperature,  $m_e^*$  is

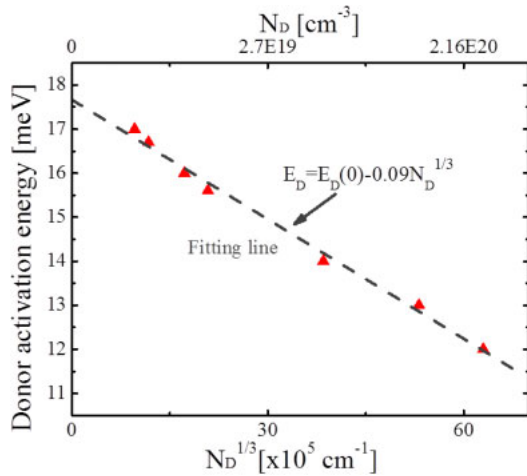


**Fig. 5.** (Color online)  $E_D$  of Si-doped AlGaN (AlN molar fractions: 0.03–0.06) as a function of  $N_D^{1/3}$ . The  $E_D$  values were obtained in the range between 12.0 and 17.0 meV. The fitting line is shown in the figure. From this fitting line, the inherent donor energy observed at very low donor concentrations was estimated to be approximately 17.6 meV.

the electron effective mass, and  $h$  is the Planck constant. The  $m_e^*$  in AlGaN of each sample were presumed by<sup>20,21)</sup>

$$m_e^* = (m_{e\perp}^2 \cdot m_{e\parallel})^{1/3} \cdot m_0. \quad (3)$$

$m_{e\parallel}$  and  $m_{e\perp}$  were 0.20 and 0.18 in GaN, and 0.33 and 0.25 in AlN, respectively.<sup>18,21)</sup> We obtained  $E_D$  by fitting using Eq. (1). Fit parameters were  $E_D$ ,  $N_D$ , and  $N_A$ .

Götz et al. have suggested a linear function for the acceptor activation energies ( $E_A$ ) in Mg-doped GaN.<sup>22)</sup> From this case, the donor activation energy ( $E_D$ ) and  $E_A$  should be described as<sup>17–19,23,24)</sup>

$$E_{D,A(N_{D,A})} = E_{D,A(0)} - f \frac{q^2}{4\pi\epsilon} N_{D,A}^{1/3}, \quad (4)$$

where  $f$  is a geometric factor of value  $\Gamma(2/3)(4\pi/3)^{1/3}$ ,  $q$  is the electronic charge,  $\epsilon$  is the dielectric constant,  $E_{D(0)}$  is an inherent donor energy that corresponds to hydrogen-like donors observed at very low  $N_D$ ,<sup>24)</sup> and  $N_A$  is the acceptor concentration. From Eq. (4), the  $E_{D,A}$  of the impurity semiconductor is affected by Coulomb interaction between band carriers and ionized impurities. From this theory,  $E_{D,A}$  is presumed to be proportional to the 1/3 power of  $N_{D,A}$ . Several impurity semiconductors have been fabricated on the basis of this theory,<sup>22,24–26)</sup> nevertheless, there has been no report in n-type nitride semiconductors.

Figure 5 shows a summary of the  $E_D$  of the Si donor in AlGaN layers as a function of  $N_D$ .  $E_D$  decreased from approximately 17.0 to 12.0 meV with increasing  $N_D$  from  $8.8 \times 10^{17}$  to  $2.5 \times 10^{20} \text{ cm}^{-3}$ .  $E_{D(0)}$  was estimated to be approximately 17.6 meV by fitting in Fig. 5. From a fitting line, the  $E_D$  of Si-doped AlGaN with a low AlN molar fraction was confirmed to vary proportionally to the 1/3 power of  $N_D$ . Therefore, we concluded that the  $E_D$  of Si-doped AlGaN (AlN molar fractions: 0.03–0.06) is affected by Coulomb interaction between conduction band electrons and ionized donors.

Next, we investigated the cause of electrical properties such as degeneracy in Group II. The samples with  $n_e$  values of more than  $3.3 \times 10^{19} \text{ cm}^{-3}$  at RT in Group I were grown using SiH<sub>4</sub> as the Si source. All the samples in Group II were

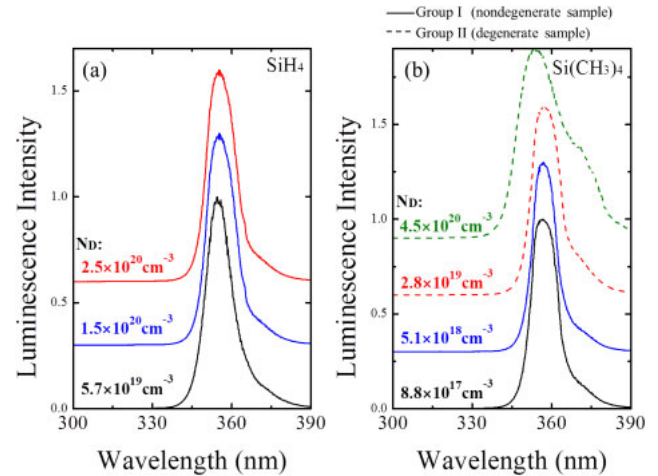


**Fig. 6.** (Color online) PL spectra from (a) AlGaN layer grown using SiH<sub>4</sub> and (b) AlGaN layer grown using Si(CH<sub>3</sub>)<sub>4</sub> obtained using a 266 nm third harmonics YAG laser at RT. The solid and dashed lines indicate samples of Group I and Group II, respectively.

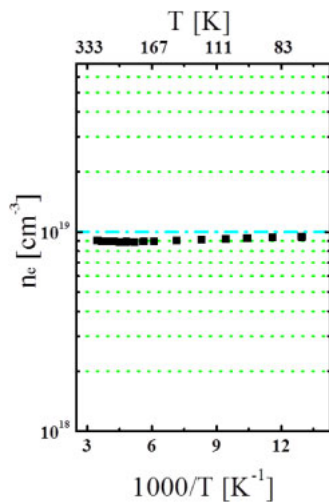
grown using Si(CH<sub>3</sub>)<sub>4</sub> as the Si source; therefore, the difference in the Si source is considered as the cause of the different electrical properties occurring in AlGaN layers of the same  $n_e$ .

Figure 6 shows the photoluminescence (PL) spectra obtained using a 266 nm third harmonics yttrium aluminum garnet (YAG) laser at RT. Figures 6(a) and 6(b) show the PL spectra of the AlGaN layer grown using SiH<sub>4</sub> and Si(CH<sub>3</sub>)<sub>4</sub>, respectively. In Fig. 6, the solid line and dashed line indicate PL spectra of nondegenerate and degenerate samples, respectively.

As shown in Fig. 6(b), the spectral patterns of the samples grown using Si(CH<sub>3</sub>)<sub>4</sub> showed that the peaks of AlGaN and approximately 365 nm in degenerate samples with  $N_D$  values of  $2.8 \times 10^{19}$  and  $4.5 \times 10^{20} \text{ cm}^{-3}$ , despite having approximately the same thickness. A particularly large change was observed in the sample with an  $N_D$  of  $4.5 \times 10^{20} \text{ cm}^{-3}$ . On the other hand, as shown in Fig. 6(a), even when  $N_D$  increased, the spectral patterns of the samples grown using SiH<sub>4</sub> did not show a peak of approximately 365 nm. From these different spectral patterns, the localization of GaN was observed in degenerate samples.

Figure 7 shows the Si-doped GaN layer with  $n_e$  of  $9.0 \times 10^{18} \text{ cm}^{-3}$  as a function of reciprocal temperature determined by the variable-temperature Hall effect measurement. This GaN layer was grown in the MOVPE reactor using SiH<sub>4</sub>. Similarly to Group II, this Si-doped GaN layer showed degeneracy. Regarding the results, Götz et al. have already reported that the  $n_e$  of Si-doped GaN with a Si concentration of  $2 \times 10^{19} \text{ cm}^{-3}$  does not vary with sample temperature, indicating a doping level above the degeneracy limit.<sup>11)</sup> From our results and the report,<sup>11)</sup> the electrical properties of Si-doped GaN with  $N_D$  of more than  $9.0 \times 10^{18} \text{ cm}^{-3}$  should change degeneracy.<sup>27)</sup>

The localization of GaN in the AlGaN layer can be considered as the cause of degeneracy. Because the bandgap energy of AlGaN with an AlN molar fraction of 0.03 is higher by more than 80 meV than that of GaN, the AlGaN layer with the  $N_D$  of approximately  $2 \times 10^{19} \text{ cm}^{-3}$  would not attain the degeneracy. The electrical properties of AlGaN



**Fig. 7.** (Color online)  $n_e$  in Si-doped GaN layer with  $n_e$  of  $9.0 \times 10^{18} \text{ cm}^{-3}$  as a function of reciprocal temperature determined by variable-temperature Hall effect measurement. Similarly to Fig. 3, this Si-doped GaN layer showed degeneracy.

and GaN can be obtained when GaN forms partially in the AlGaIn layer. When GaN localizes in AlGaIn, the sample with high  $N_D$  might show degeneracy in GaN, even when nondegenerate in AlGaIn. Since a peak of approximately 365 nm was observed in degenerate samples, as shown in Fig. 6(b), this assumption is possible. From the difference in luminescence intensity at approximately 365 nm in the PL spectra of the  $N_D$  values of  $2.8 \times 10^{19}$  and  $4.5 \times 10^{20} \text{ cm}^{-3}$ , there is a possibility that the localization of GaN is enhanced with the increase in  $\text{Si}(\text{CH}_3)_4$  supply. The samples were grown in two types of MOVPE reactor using  $\text{Si}(\text{CH}_3)_4$ . AlGaIn layers with  $N_D$  values of more than  $2.8 \times 10^{19} \text{ cm}^{-3}$  grown in each MOVPE reactor showed degeneracy. In particular, the Si-doped  $\text{Al}_{0.09}\text{Ga}_{0.91}\text{N}$  layer with  $N_D$  of  $4.8 \times 10^{19} \text{ cm}^{-3}$  in unintentionally doped AlN underlying layer grown in the MOVPE reactor using  $\text{Si}(\text{CH}_3)_4$  was confirmed to show degeneracy, and the PL spectral pattern measured using the 266 nm third harmonics YAG laser at RT showed that the peaks of AlGaIn and approximately 365 nm.

The localization of GaN might tend to occur when using  $\text{Si}(\text{CH}_3)_4$  as a dopant source. However, we are unable to conclude that the localization of GaN in AlGaIn is the cause of the degeneracy of samples with AlGaIn layers with an AlN molar fraction of 0.03 and  $N_D$  values of more than  $2.8 \times 10^{19} \text{ cm}^{-3}$ . Therefore, further studies are needed to determine the cause of degeneracy of samples.

#### 4. Conclusions

We grew Si-doped AlGaIn layers with  $N_D$  values from  $8.8 \times 10^{17}$  to  $4.5 \times 10^{20} \text{ cm}^{-3}$  using MOVPE reactors with  $\text{SiH}_4$  or  $\text{Si}(\text{CH}_3)_4$  as a dopant source. The minimum- $\rho$  ( $3.6 \times 10^{-4} \Omega \text{ cm}$ ) was obtained at the Si-doped AlGaIn layer with the  $n_e$  of  $4.5 \times 10^{20} \text{ cm}^{-3}$  and a flat surface. The samples were classified into two types from the temperature dependence of  $n_e$  by the variable-temperature Hall effect measurement. From the sample group in which  $n_e$  varies with sample temperature, the  $E_D$  of the Si donor in AlGaIn layers decreased from approximately 17.0 to 12.0 meV with increasing  $N_D$  from

$8.8 \times 10^{17}$  to  $2.5 \times 10^{20} \text{ cm}^{-3}$ ,  $E_{D(0)}$  was also estimated to be approximately 17.6 meV. We found that the  $E_D$  of the Si donor is affected by the Coulomb interaction in the AlGaIn layer with  $N_D$  values from  $8.8 \times 10^{17}$  to  $2.5 \times 10^{20} \text{ cm}^{-3}$ . In several AlGaIn layers with high  $N_D$  values,  $n_e$  did not vary with sample temperature, as expected in the case of degeneracy. The cause of the degeneracy of samples was assumed to be the localization of GaN in the AlGaIn layer.

#### Acknowledgments

This study was partially supported by the Program for the Strategic Research Foundation at Private Universities, 2012–2016, supported by the Ministry of Education, Culture, Sports, Science and Technology (MEXT), a MEXT Grant-in-Aid for Specially Promoted Research No. 25000011, and a MEXT Grant-in-Aid for Scientific Research A No. 15H02019.

- 1) H. Amano, M. Kito, K. Hiramatsu, and I. Akasaki, *Jpn. J. Appl. Phys.* **28**, L2112 (1989).
- 2) S. Nakamura, M. Senoh, N. Iwasa, and S. Nagahama, *Jpn. J. Appl. Phys.* **34**, L797 (1995).
- 3) S. Nakamura, M. Senoh, N. Iwasa, S. Nagahama, T. Yamada, and T. Mukai, *Jpn. J. Appl. Phys.* **34**, L1332 (1995).
- 4) Y. Narukawa, M. Ichikawa, D. Sanga, M. Sano, and T. Mukai, *J. Phys. D* **43**, 354002 (2010).
- 5) D. Morita, M. Yamamoto, K. Akashi, K. Matoba, K. Yasutomo, Y. Kasai, M. Sano, S. Nagahama, and T. Mukai, *Jpn. J. Appl. Phys.* **43**, 5945 (2004).
- 6) M. Kneissl, T. Kolbe, C. Chua, V. Kueller, N. Lobo, J. Stellmach, A. Knauer, H. Rodriguez, S. Einfeldt, Z. Yang, N. M. Johnson, and M. Weyers, *Semicond. Sci. Technol.* **26**, 014036 (2011).
- 7) T. Sugiyama, D. Iida, T. Yasuda, M. Iwaya, T. Takeuchi, S. Kamiyama, and I. Akasaki, *Appl. Phys. Express* **6**, 121002 (2013).
- 8) Z. Fan, S. N. Mohammad, W. Kim, Ö. Aktas, A. E. Botchkarev, and H. Morkoç, *Appl. Phys. Lett.* **68**, 1672 (1996).
- 9) C. Mavroidis, J. J. Harris, M. J. Kappers, C. J. Humphreys, and Z. Bougrioua, *J. Appl. Phys.* **93**, 9095 (2003).
- 10) S. Fritze, A. Dadgar, H. Witte, M. Bügler, A. Rohrbeck, J. Blasing, A. Hoffmann, and A. Krost, *Appl. Phys. Lett.* **100**, 122104 (2012).
- 11) W. Götz, N. M. Johnson, C. Chen, H. Liu, C. Kuo, and W. Imler, *Appl. Phys. Lett.* **68**, 3144 (1996).
- 12) R. C. Budhani, P. Pant, R. K. Rakshit, K. Senapati, S. Mandal, N. K. Pandey, and J. Kumar, *J. Phys.: Condens. Matter* **17**, 75 (2005).
- 13) S. K. V. Farahani, V. Muñoz-Sanjósé, J. Zúñiga-Pérez, C. F. McConville, and T. D. Veal, *Appl. Phys. Lett.* **102**, 022102 (2013).
- 14) R. J. Molnar, T. Lei, and T. D. Moustakas, *Appl. Phys. Lett.* **62**, 72 (1993).
- 15) H. Eshghi, D. Lancefield, B. Beaumont, and P. Gibart, *Phys. Status Solidi B* **216**, 733 (1999).
- 16) J. M. D. Coey, M. Venkatesan, and C. B. Fitzgerald, *Nat. Mater.* **4**, 173 (2005).
- 17) J. F. Woods and N. G. Ainslie, *J. Appl. Phys.* **34**, 1469 (1963).
- 18) Y. Taniyasu, M. Kasu, and N. Kobayashi, *Appl. Phys. Lett.* **81**, 1255 (2002).
- 19) S. M. Sze and K. K. Ng, *Physics of Semiconductor Devices* (Wiley, Hoboken, NJ, 2007) 3rd ed., p. 22.
- 20) W. Suttrop, G. Pensl, W. J. Choyke, R. Stein, and S. Leibenzeder, *J. Appl. Phys.* **72**, 3708 (1992).
- 21) M. Suzuki and T. Uenoyama, *J. Appl. Phys.* **80**, 6868 (1996).
- 22) W. Götz, R. S. Kern, C. H. Chen, H. Liu, D. A. Steigerwald, and R. M. Fletcher, *Mater. Sci. Eng.* **59**, 211 (1999).
- 23) M. Katsuragawa, S. Sota, M. Komori, C. Anbe, T. Takeuchi, H. Sakai, H. Amano, and I. Akasaki, *J. Cryst. Growth* **189–190**, 528 (1998).
- 24) P. Kozodoy, H. Xing, S. P. DenBaars, U. K. Mishra, A. Saxler, R. Perrin, S. Elhamri, and W. C. Mitchel, *J. Appl. Phys.* **87**, 1832 (2000).
- 25) P. P. Debye and E. M. Conwell, *Phys. Rev.* **93**, 693 (1954).
- 26) K. Nagamatsu, K. Takeda, M. Iwaya, S. Kamiyama, H. Amano, and I. Akasaki, *Phys. Status Solidi C* **6**, S437 (2009).
- 27) A. Wolos, Z. Wilamowski, M. Piersa, W. Stupinski, B. Lucznik, I. Grzegory, and S. Porowski, *Phys. Rev. B* **83**, 165206 (2011).

## Metal–Organic Vapor Phase Epitaxy Growth of Embedded Gallium Nitride Nanocolumn for Reduction in Dislocation Density

This content has been downloaded from IOPscience. Please scroll down to see the full text.

2013 Jpn. J. Appl. Phys. 52 08JE23

(<http://iopscience.iop.org/1347-4065/52/8S/08JE23>)

View [the table of contents for this issue](#), or go to the [journal homepage](#) for more

Download details:

IP Address: 202.11.1.201

This content was downloaded on 03/03/2017 at 06:57

Please note that [terms and conditions apply](#).

You may also be interested in:

[Drastic Reduction of Dislocation Density in Semipolar \(1122\) GaN Stripe Crystal on Si Substrate by Dual Selective Metal–Organic Vapor Phase Epitaxy](#)  
Tasuku Murase, Tomoyuki Tanikawa, Yoshio Honda et al.

[Improved Crystal Quality of \(1122\) Semi-Polar GaN Grown on A Nanorod Template](#)  
Kun Xing, Yipin Gong, Xiang Yu et al.

[GaN Nanowires Grown on a Graphite Substrate by Radio Frequency Molecular Beam Epitaxy](#)  
Shinta Nakagawa, Takuya Tabata, Yoshio Honda et al.

[Selective Growth of Microscale GaN Pyramids on Apex of GaN Pyramids](#)  
Dong Wan Jo, Jin Eun Ok, Wy il Yun et al.

[GaN Lateral Overgrowth by Hydride Vapor Phase Epitaxy through Nanometer-Size Channels Fabricated with Nanoimprint Lithography](#)  
Akira Usui, Toshiharu Matsueda, Hiroki Goto et al.

[Analysis of Dislocations Generated during Metal–Organic Vapor Phase Epitaxy of GaN on Patterned Templates](#)  
Sami Suihkonen, Muhammad Ali, Pekka T. Törmä et al.

[Growth of GaN Layer on Patterned Al/Ti Metal Mask by Metal–Organic Chemical Vapor Deposition](#)  
Jinsub Park, Daeyoung Moon, Sehun Park et al.

[Heteroepitaxial Lateral Overgrowth of GaN on Periodically Grooved Substrates: A New Approach for Growing Low-Dislocation-Density GaN Single Crystals](#)  
Theeradetch Detchprohm, Masahiro Yano, Shigekazu Sano et al.

## Metal–Organic Vapor Phase Epitaxy Growth of Embedded Gallium Nitride Nanocolumn for Reduction in Dislocation Density

Shinya Umeda<sup>1\*</sup>, Takahiro Kato<sup>1</sup>, Tsukasa Kitano<sup>2</sup>, Toshiyuki Kondo<sup>2</sup>, Hiroyuki Matsubara<sup>1</sup>, Satoshi Kamiyama<sup>1</sup>, Tetsuya Takeuchi<sup>1</sup>, Motoaki Iwaya<sup>1</sup>, and Isamu Akasaki<sup>1,3</sup>

<sup>1</sup>Department of Materials Science and Engineering, Meijo University, Nagoya 468-0073, Japan

<sup>2</sup>El-seed, Nagoya 468-0073, Japan

<sup>3</sup>Akasaki Research Center, Nagoya University, Nagoya 464-8603, Japan

E-mail: 123434006@ccalumni.meijo-u.ac.jp

Received October 14, 2012; accepted May 19, 2013; published online August 20, 2013

The use of nanocolumn crystals is thought to be effective in producing a low-dislocation-density GaN layers. In this paper, we propose a metal–organic vapor phase epitaxial (MOVPE) growth method for producing uniform GaN nanocolumns using deep through-holes in a thick SiO<sub>2</sub> selective growth mask. A SiO<sub>2</sub> film with a thickness of 500 nm was deposited by sputtering on an AlN buffer layer/SiC substrate. A nanoimprinting technique was applied to produce dot openings. Then, dry etching with CF<sub>4</sub> gas was carried out to form deep through-holes in the SiO<sub>2</sub> film. In the second MOVPE growth, individual GaN nanocolumns coalesced into a planarized GaN layer, after thinning the SiO<sub>2</sub> mask to 100 nm. A cathodoluminescence image of the GaN layer on a GaN nanocolumn template shows a low dislocation density of  $1.3 \times 10^8 \text{ cm}^{-2}$ , while that of a GaN layer directly grown on an AlN buffer layer shows a dislocation density of  $9.4 \times 10^8 \text{ cm}^{-2}$ . © 2013 The Japan Society of Applied Physics

### 1. Introduction

Nitride semiconductor nanocolumns are one-dimensional nanoscale crystals without dislocations. Such crystals are columnar materials with diameters of about several tens to several hundreds of nm, where threading dislocations penetrating along the growth direction bend horizontally and are terminated in the process.<sup>1)</sup> Owing to this advantage, studies of high-performance light-emitting devices with nanocolumn structures have been focused on.<sup>2,3)</sup> Nanocolumn materials are also promising for the growth of a high-quality nitride layer by nanoscale epitaxial lateral overgrowth (nano-ELO).<sup>4)</sup> Nano-ELO can significantly reduce the epilayer thickness for planarization, compared with conventional microscale ELO. Therefore, this approach may give a great advantage for GaN growth on foreign substrates such as Si and SiC,<sup>5–7)</sup> which have a thermal expansion mismatch with GaN and a thickness limitation due to crack formation. Moreover, the selective growth of alloys, such as AlGaIn and InGaIn, which is impossible in conventional microscale ELO, may be possible, because nano-ELO requires only a short migration distance of species on the growth surface. Similarly to the conventional microscale ELO, the use of nanocolumns may also allow heteroepitaxial growth without the formation of misfit dislocations and cracks, because the stress caused by lattice and thermal expansion mismatches at a heterointerface can be relaxed.

Nanocolumn crystals are prepared mainly by molecular beam epitaxial (MBE) growth,<sup>8,9)</sup> and only a limited number of reports on the metal–organic vapor phase epitaxial (MOVPE) growth of nanocolumns have been published.<sup>10–14)</sup> This may be due to the fact that the MOVPE growth of nanocolumns makes it difficult to control the in-plane uniformity under small-scale selective growth. Actually, there are no reports on the selective-area growth of nanocolumns by MOVPE, in terms of uniform growth over a wide area of several cm<sup>2</sup>. In our experiments using this approach, the uniformity of nanocolumns over a 2-in. wafer has not yet been achieved. Considering their device application, it is indispensable to grow uniform nanocolumns in a wide area.

In this study, we demonstrate a method of high-quality GaN layer growth on SiC, which is composed of deep through-holes in a SiO<sub>2</sub> film, embedded GaN nanocolumns, and a planarized GaN overlayer. The method of embedding nanocolumns deep into SiO<sub>2</sub> films makes it possible to show a high structural uniformity in a wafer with a wide area of over 2 in. In addition, the GaN layer grown on such nanocolumns with a low dislocation density of  $1.3 \times 10^8 \text{ cm}^{-2}$  has been achieved.

### 2. Experimental Procedure

Figure 1 shows the procedure for GaN nanocolumn growth by MOVPE. First, a 100-nm-thick AlN buffer layer was grown on a 2-in. SiC substrate. The AlN buffer layer is commonly used for growing a high-quality GaN crystal on a SiC substrate.<sup>15–17)</sup> A SiO<sub>2</sub> film with a thickness of 30 or 550 nm was then deposited by RF sputtering on this substrate. Nanoimprinting lithography was applied to the patterning of nanocolumns. A thermally cured resist was spin-coated on the substrate, and the pattern was transferred from a mold having pillars in a triangular arrangement with a pitch of 460 nm and a diameter of 250 nm to the substrate. Then, dry etching by CF<sub>4</sub> gas was carried out to form through-holes in the SiO<sub>2</sub> film. After removing the nanoimprinting resist, GaN nanocolumns were grown at a temperature of 950 °C, a V/III ratio of 1000, and a pressure of 100 mbar, which seem to be suitable for nanocolumn growth. These growth conditions tend to form {11̄01} facets. The two substrates with patterned 30 and 550-nm-thick SiO<sub>2</sub> films were simultaneously set in the MOVPE reactor, and GaN nanocolumns were grown under the same growth conditions. In the case of the 30-nm-thick SiO<sub>2</sub> film, a typical selective growth of GaN nanocolumns can be achieved.

The SiO<sub>2</sub> mask was then etched down to a thickness of 100 nm to expose the upper part of the nanocolumns in order to promote the lateral growth and planarization of the GaN layer. When the etching of SiO<sub>2</sub> was not achieved, large island crystals were grown, and as a result, the planarization of the overgrown GaN layer became difficult. On the other hand, a planarized GaN layer was easily obtained in the

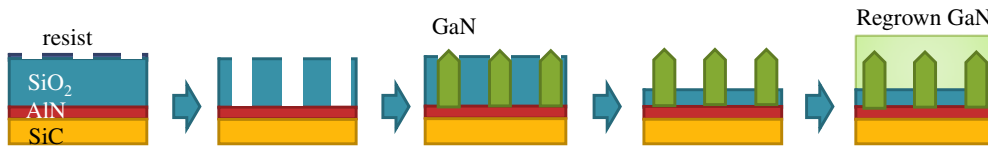


Fig. 1. (Color online) Growth procedure of GaN nanocolumns and regrowth of planarized GaN layer.

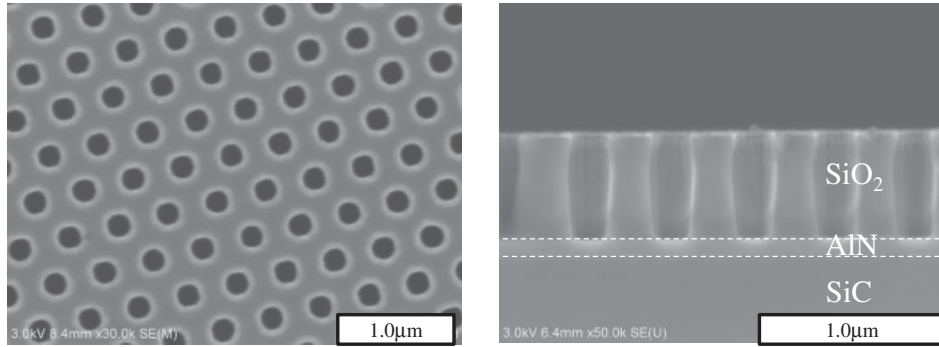


Fig. 2. SEM images of top and cross-sectional views of SiO<sub>2</sub> mask with deep through-holes.

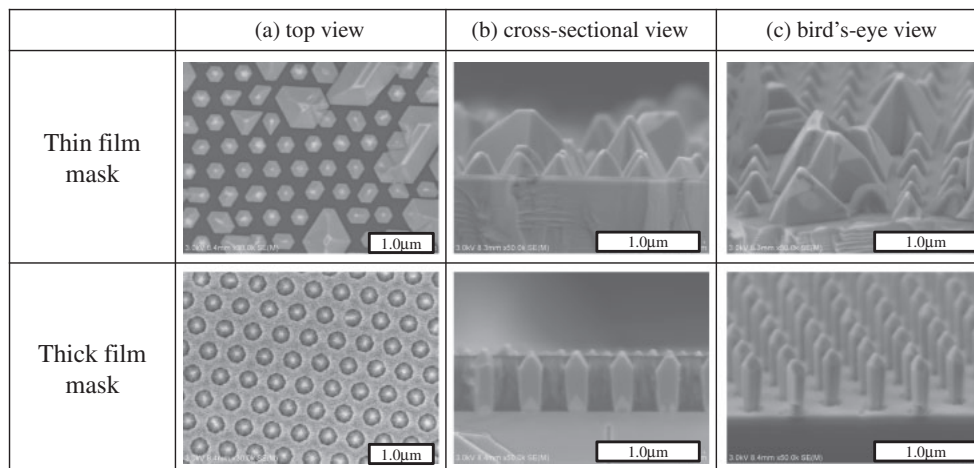


Fig. 3. SEM images of (a) top, (b) cross-sectional, and (c) bird's-eye views of GaN nanocolumns grown on thin and thick SiO<sub>2</sub> masks. For the observation of the bird's-eye view SEM image, the SiO<sub>2</sub> was removed.

case that all the SiO<sub>2</sub> was removed before the regrowth of GaN. However, no reduction in dislocation density was observed. Therefore, such a process using of SiO<sub>2</sub> masks suitable thickness is required for the planarized growth of GaN. After that, the regrowth of the GaN layer was performed on a GaN nanocolumn template. For comparison, the regrowth of the GaN layer was also carried out on a flat AlN/SiC substrate. The growth conditions of a temperature of 1050 °C, a pressure of 100 mbar, and a V/III ratio of 2700 were used for the planarized growth because of the enhancement of lateral growth.<sup>18)</sup> Dislocation densities were measured using the cathodoluminescence (CL) mapping images of these samples.

### 3. Results and Discussion

Figure 2 shows scanning electron microscopy (SEM) images of the top and cross-sectional views of the SiO<sub>2</sub> mask after achieving the through-hole arrangement. Uniform through-

holes were successfully obtained by our process, although their sidewalls were not perfectly smooth. From the images, a period of 460 nm and a hole diameter of 200 nm were confirmed. The etching of the SiO<sub>2</sub> mask was accurately terminated on the surface of the AlN buffer layer, and the depth of the through-holes was 550 nm. Figure 3 shows SEM images of the top, cross-sectional, and bird's-eye views of GaN nanocolumns. In the thin (30 nm) SiO<sub>2</sub> mask, small pyramids and large islands were randomly observed. Owing to the large diffusion length of Ga-containing species on the surface, large islands tended to form, interrupting nanocolumn growth. Under typical MOVPE growth conditions, the supply rate of precursors was considered to be very high against a small volume of nanocolumn crystals. Special techniques, such as the pulsed supply of precursors,<sup>13,14)</sup> may be indispensable in the MOVPE growth of nanocolumns. On the other hand, uniform nanocolumns with a height of 600 nm were obtained in through-holes in the thick

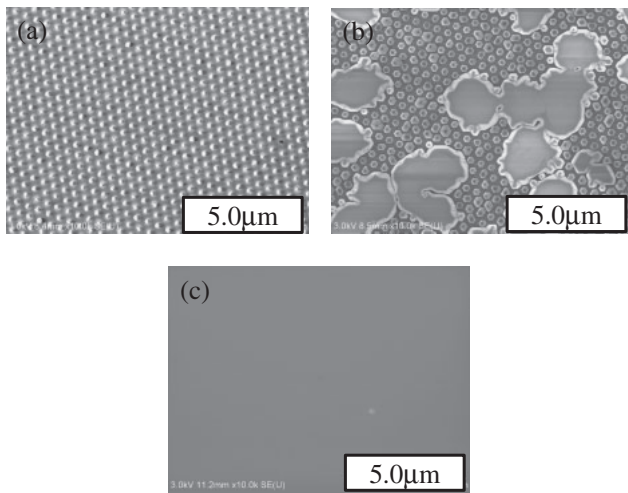


**Fig. 4.** Top SEM images at time of regrowth of GaN layer on nanocolumn substrate: (a) before growth, (b) during growth (10 min growth), and (c) after growth (180 min growth).

SiO<sub>2</sub> mask. Accordingly, we found that the deep-through-hole-patterned mask used in this experiment is effective for growing uniform nanocolumn crystals.

Then, a planarized GaN layer was regrown on the substrate with GaN nanocolumns, after etching the SiO<sub>2</sub> mask down to 100 nm thickness. Figure 4 shows the regrowth process of this sample. From (a) to (b), islands of GaN are randomly growing to form {1100} and {1101} facets from the side walls of the nanocolumns. Island crystals are formed in accordance with the variation in Ga diffusion length. Because the lateral growth is dominant in this situation, the height of the island crystals is almost kept constant at 500 nm from the mask level. From Fig. 4, the planarization of the regrown GaN is conducted by the coalescence of the island crystals growing in the lateral direction. A cross-sectional SEM image of the GaN layer is shown in Fig. 5. The thickness of the regrown GaN layer was 4.3 μm. A flat surface and the absence of void inclusions around the regrowth interface were observed.

Finally, CL mapping images of the GaN layers with and without GaN nanocolumns are shown in Fig. 6. The dark spots observed in the images correspond to threading dislocations. From the images, the dislocation density of the GaN layer directly grown on the flat AlN/SiC substrate was  $9.3 \times 10^8 \text{ cm}^{-2}$ , and that of the GaN layer grown on

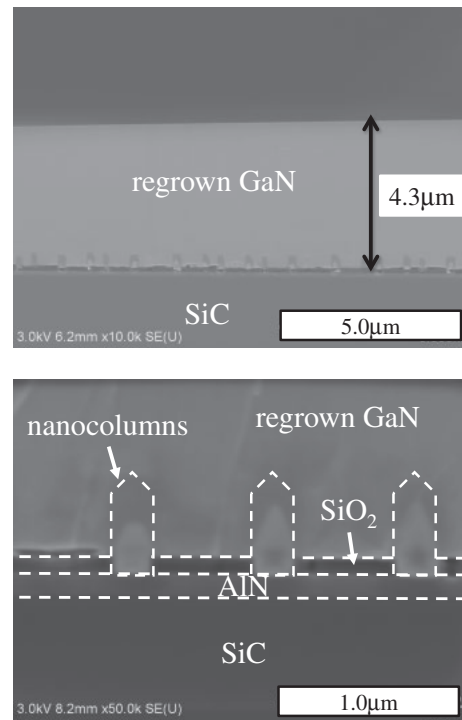


**Fig. 5.** Cross-sectional SEM image of regrown GaN layer with thickness of 4.3 μm and magnified view around nanocolumn interface.

the GaN nanocolumn template was  $1.3 \times 10^8 \text{ cm}^{-2}$ . A significant reduction in dislocation density was realized by nano-ELO.

The dislocation density of a commercial SiC substrate is about  $1.0 \times 10^5 \text{ cm}^{-2}$ . However, that of the AlN buffer layer grown on the SiC substrate is about  $10^{10} \text{ cm}^{-2}$ , owing to lattice mismatch. The number of dislocations decreases when a GaN layer is grown on the AlN buffer layer.

The reduction in dislocation density is thought to be due to the fact that nano-ELO prevents the propagation of internal dislocations existing in the AlN buffer layer. Furthermore, the GaN layer regrown by a lateral growth over the SiO<sub>2</sub> mask also has a small number of dislocations, similarly to the conventional ELO-grown GaN layer. The reduction in the number of dislocations in the overgrown GaN layer is partly thought to be caused by the initial GaN nanocolumn crystals with a low dislocation density. In the regrowth stage, island crystals are formed uniformly. These island crystals coalesce with the termination of dislocations

GaN layer	on AlN/SiC substrate	on GaN nanocolumn template
CL images		
Dislocation density [ $\text{cm}^{-2}$ ]	$9.4 \times 10^8$	$1.3 \times 10^8$

**Fig. 6.** CL mapping images of GaN layer on flat AlN/SiC substrate and GaN nanocolumn template.

and are eventually planarized, similarly to those in the conventional ELO with a micron scale pattern.<sup>19–21</sup> With the optimization of the conditions for the regrowth of GaN, further reduction in dislocation density can be expected.

#### 4. Conclusions

We demonstrate a new GaN nanocolumn growth method using deep SiO<sub>2</sub> through-holes. This gives reproducible and uniform GaN nanocolumn crystals under typical MOVPE growth conditions. By applying this method, the GaN layer regrown on the nanocolumns shows a low dislocation density of  $1.3 \times 10^8 \text{ cm}^{-2}$ , which is much lower than that  $9.3 \times 10^8 \text{ cm}^{-2}$  of the GaN layer grown on a flat AlN/SiC substrate.

- 1) K. Kishino, H. Sekiguchi, and A. Kikuchi: *J. Cryst. Growth* **311** (2009) 2063.
- 2) A. Kikuchi, M. Kawai, M. Tada, and K. Kishino: *Jpn. J. Appl. Phys.* **43** (2004) L1524.
- 3) K. Y. Zang, S. J. Chua, J. H. Teng, N. S. S. Ang, A. M. Yong, and S. Y. Chow: *Appl. Phys. Lett.* **92** (2008) 243126.
- 4) K. Kusakabe, A. Kikuchi, and K. Kishino: *J. Cryst. Growth* **237–239** (2002) 988.
- 5) A. Watanabe, T. Takeuchi, K. Hirosawa, H. Amano, K. Hiramatsu, and I. Akasaki: *J. Cryst. Growth* **128** (1993) 391.
- 6) H. Lahrière, P. Vennéguès, O. Tottereau, M. Laügt, P. Lorenzini, M. Leroux, B. Beaumont, and P. Gibart: *J. Cryst. Growth* **217** (2000) 13.
- 7) A. Kuramata, K. Domen, R. Soejima, K. Horino, S. Kubota, and T. Tanahashi: *J. Cryst. Growth* **189–190** (1998) 826.
- 8) H. Sekiguchi, K. Kishino, and A. Kikuchi: *Appl. Phys. Lett.* **96** (2010) 231104.
- 9) T. Gotschke, T. Schumann, F. Limbach, T. Stoica, and R. Calarco: *Appl. Phys. Lett.* **98** (2011) 103102.
- 10) W. Bergbauer, M. Strassburg, C. Kölper, N. Linder, C. Roder, J. Lähnemann, A. Trampert, S. Fündling, S. F. Li, H.-H. Wehmann, and A. Waag: *J. Cryst. Growth* **315** (2011) 164.
- 11) Z. Keyan, W. Yadong, and C. S. Jin: *Phys. Status Solidi C* **6** (2009) S514.
- 12) K. Choi, M. Arita, and Y. Arakawa: *J. Cryst. Growth* **357** (2012) 58.
- 13) S. D. Hersee, X. Sun, and X. Wang: *Nano Lett.* **6** (2006) 1808.
- 14) T.-W. Yeh, Y.-T. Lin, L. S. Stewart, P. D. Dapkus, R. Sarkissian, J. D. O'Brien, B. Ahn, and S. R. Nutt: *Nano Lett.* **12** (2012) 3257.
- 15) T. W. Weeks, Jr., M. D. Bremser, K. S. Ailey, E. Carlson, W. G. Perry, and R. F. Davis: *Appl. Phys. Lett.* **67** (1995) 401.
- 16) P. Waltereit, O. Brandt, A. Trampert, M. Ramsteiner, M. Reiche, M. Qi, and K. H. Ploog: *Appl. Phys. Lett.* **74** (1999) 3660.
- 17) T. Nishida and N. Kobayashi: *J. Cryst. Growth* **221** (2000) 297.
- 18) K. Hiramatsu, K. Nishiyama, M. Onishi, H. Mizutani, M. Narukawa, A. Motogaito, H. Miyake, Y. Iyechika, and T. Maeda: *J. Cryst. Growth* **221** (2000) 316.
- 19) A. Sakai, H. Sunakawa, and A. Usui: *Appl. Phys. Lett.* **71** (1997) 2259.
- 20) S. Tomiya, K. Funato, T. Asatsuma, T. Hino, S. Kijima, T. Asano, and M. Ikeda: *Appl. Phys. Lett.* **77** (2000) 636.
- 21) P. Vennéguès, B. Beaumont, V. Bousquet, M. Vaille, and P. Gibart: *Appl. Phys.* **87** (2000) 4175.



# Properties of nitride-based photovoltaic cells under concentrated light illumination

Shota Yamamoto<sup>1</sup>, Mikiko Mori<sup>1</sup>, Yosuke Kuwahara<sup>1</sup>, Takahiro Fujii<sup>1</sup>, Tatsuo Nakao<sup>1</sup>, Shinichiro Kondo<sup>1</sup>, Motoaki Iwaya<sup>\*1</sup>, Tetsuya Takeuchi<sup>1</sup>, Satoshi Kamiyama<sup>1</sup>, Isamu Akasaki<sup>1,3</sup>, and Hiroshi Amano<sup>2,3</sup>

<sup>1</sup> Faculty of Science and Technology, Meijo University, Nagoya 468-8502, Japan

<sup>2</sup> Graduate School of Engineering, Nagoya University, Nagoya 464-8603, Japan

<sup>3</sup> Akasaki Research Center, Nagoya University, Nagoya 464-8603, Japan

Received 31 January 2012, revised 7 March 2012, accepted 7 March 2012

Published online 13 March 2012

**Keywords** nitride semiconductors, solar cells, concentrator cells, GaInN

\* Corresponding author: e-mail [iwaya@meijo-u.ac.jp](mailto:iwaya@meijo-u.ac.jp)

We investigated the properties of nitride-based solar cells under concentrated light illumination from 1 to 200 suns. The conversion efficiency of our solar cells increased with increasing concentration up to 200 suns. The short-circuit cur-

rent density, open-circuit voltage, fill factor, and conversion efficiency were 510 mA/cm<sup>2</sup>, 1.9 V, 70%, and 3.4%, respectively, under an air mass filter of 1.5G at 200 suns and room temperature.

© 2012 WILEY-VCH Verlag GmbH & Co. KGaA, Weinheim

**1 General** Since the band gap of GaInN ternary alloys covers a broad range from 0.65 to 3.43 eV [1], these alloys are suitable for solar cell applications. So far, we have succeeded in fabricating GaInN-based solar cells [2, 3]. By reducing the pit density in the GaInN active layer using freestanding *c*-plane GaN substrates and applying GaInN superlattice structures, the conversion efficiency of our nitride-based solar cells has reached 2.9% [4].

One of the disadvantages of compound semiconductor solar cells is their high cost compared with that of Si or organic solar cells. This problem can be solved by using a condenser lens system. In general, a low-cost material can be used for the condenser lens system. Thus, if the solar cells can operate at 200 suns, for example, the cost per chip would be reduced almost 200-fold. In addition, the performances of solar cells using Si, InP, and GaAs are improved by focusing the sunlight [5], although the improvement in performance is limited depending on a material, a junction quality, a cell configuration, and an electrode pattern. The maximum efficiencies of Si and InP solar cells have been reported to be obtained at 90–95 suns [5]. In contrast, the maximum efficiency of GaAs solar cells has been reported to be obtained at over 200 suns [5]. On the other hand, photovoltaic cell characteristics of

GaInN-based solar cells have been investigated in concentration up to 30 suns only [6]. Details of nitride-based solar cell characteristics in concentration above 30 suns are still unknown.

In this study, we investigate the focusing properties of nitride-based solar cells up to 200 suns. We also discuss the dependence of the concentration ratio on the solar cell characteristics.

**2 Sample structure** Nitride-based solar cells were grown by metal organic vapour phase epitaxy. Trimethylindium, trimethylaluminium, trimethylgallium, triethylgallium, and ammonia were used as the source gases.

Figure 1 schematically shows the structure of the devices prepared in this study. We grew 50 pairs of unintentionally doped Ga<sub>0.83</sub>In<sub>0.17</sub>N (3 nm)/Ga<sub>0.93</sub>In<sub>0.07</sub>N (0.6 nm) superlattice layers as active layers on freestanding GaN substrates. Another 10 pairs of Si-doped Ga<sub>0.90</sub>In<sub>0.10</sub>N (3 nm)/GaN (3 nm) superlattice layers were inserted beneath the active layers. The Si concentration in the 10 pairs of superlattice layers was  $3 \times 10^{18} \text{ cm}^{-3}$ . The role of the additional Si-doped superlattice layers was to reduce the dislocation density and to obtain high-quality active layers with a higher InN mole fraction while maintaining a low

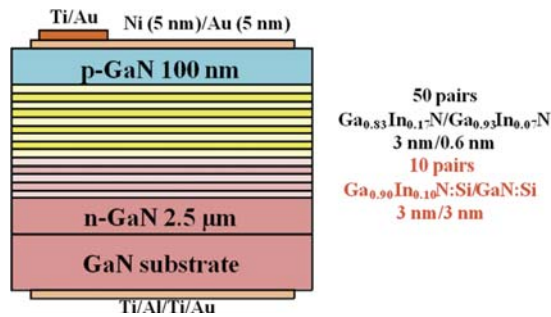


**Figure 1** (online colour at: www.pss-rapid.com) Schematic view of sample structure of nitride-based solar cells.

series resistance ( $R_S$ ) [3]. In addition, the numbers of superlattice layers are experimentally obtained. Dislocation density was reduced also by using the GaN substrate. A semitransparent Ni (5 nm)/Au (5 nm) ohmic contact and a Ti (30 nm)/Al (100 nm)/Ti (20 nm)/Au (150 nm) ohmic contact were formed on p-GaN (the surface of the device) and on n-GaN (the reverse side of the device) by electron beam evaporation, respectively. The devices had a vertical structure.

**3 Experimental conditions** The conversion efficiencies of the devices were measured using a solar simulator with an air mass (AM) filter of 1.5G (Asahi Spectra HAL-302). In this solar simulator, the infrared light was eliminated with a filter. Both the irradiation area and the photon density were changed to adjust the concentration of the light from 1 to 200 suns. The current density versus voltage characteristics of the devices were measured from 1 to 200 suns at room temperature (RT). No active temperature control of the devices was performed.

**4 Experimental result** Figure 2 shows the current density versus voltage characteristics of the nitride-based solar cells under the solar simulator (1 to 200 suns) at RT. We found that the open-circuit voltage ( $V_{OC}$ ) of the nitride-based solar cells was increased with increasing concentra-

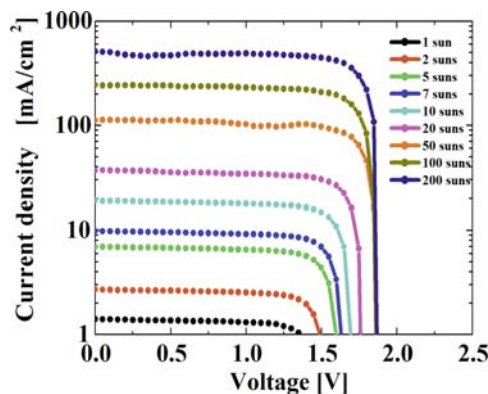


**Figure 2** (online colour at: www.pss-rapid.com) Current density versus voltage characteristics of nitride-based solar cells under the solar simulator (AM of 1.5G, 1 to 200 suns) at RT.

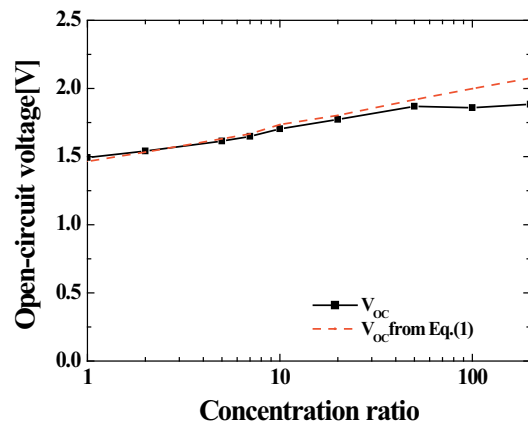


**Figure 3** (online colour at: www.pss-rapid.com)  $V_{OC}$  as function of concentration ratio. The red dashed line was obtained using Eq. (1).

tion ratio and appeared to saturate above 50 suns.  $V_{OC}$  is plotted as a function of concentration ratio in Fig. 3.

In general,  $V_{OC}$  can be expressed as [7]

$$V_{OC} = \frac{nkT}{q} \ln \left( \frac{J_{SC}CR}{J_0} + 1 \right), \quad (1)$$

where  $J_{SC}$ ,  $CR$ ,  $J_0$ ,  $n$ ,  $k$ ,  $T$ , and  $q$  are the short-circuit current density, concentration ratio, reverse saturation current,  $n$ -value (a correction value of the diode equation), Boltzmann constant, temperature, and elementary charge, respectively. Equation (1) shows that  $V_{OC}$  should increase logarithmically with increasing light intensity. The dashed line in Fig. 3 almost matches the experimental results for 1 to 200 suns.

Figure 4 shows the fill factor (FF) and  $J_{SC}$  as functions of the concentration ratio. FF only changed slightly, from 72 to 70%, when the concentration was increased from 1 to 200 suns. In general, FF under concentrated sunlight is affected by the enhanced carrier recombination in the inter-

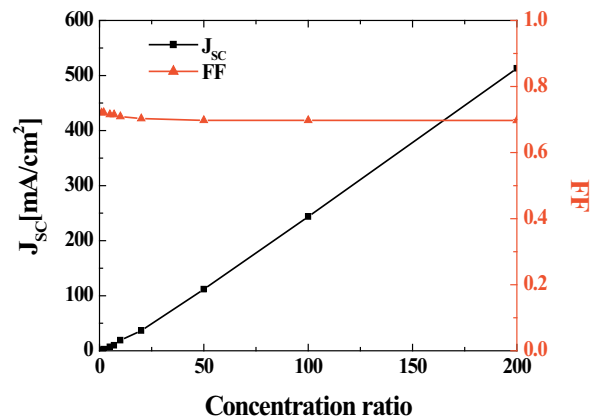


**Figure 4** (online colour at: www.pss-rapid.com)  $J_{SC}$  and FF as functions of concentration ratio.

**Table 1** Device performance characteristics of nitride-based solar cells under the solar simulator (AM of 1.5G, 1 and 200 suns).

	$V_{OC}$ [V]	FF [%]	$J_{SC}$ [mA/cm <sup>2</sup> ]	$\eta$ [%]	$R_S$ [ $\Omega$ cm <sup>2</sup> ]	$R_{SH}$ [ $\Omega$ cm <sup>2</sup> ]
1 sun	1.5	72	1.4	1.5	110	12000
200 suns	1.9	70	520	3.4	0.53	18

face region due to the high carrier density under concentrated sunlight [7].

In Ref. [6], FF decreased from 64% to 57% when the concentration ratio increased from 1 to 30 suns, whereas for the samples used in this study, FF did not decrease significantly when the concentration ratio increased. Previous reports concluded that the significant decrease in FF with increasing concentration was due to the poor crystal quality of the sample [6]. Our samples with the GaN substrate and superlattice structure have high crystallinity [3]. The dislocation density of this sample was approximately  $5 \times 10^7$  cm<sup>-2</sup>. Therefore, a high FF was maintained up to 200 suns.

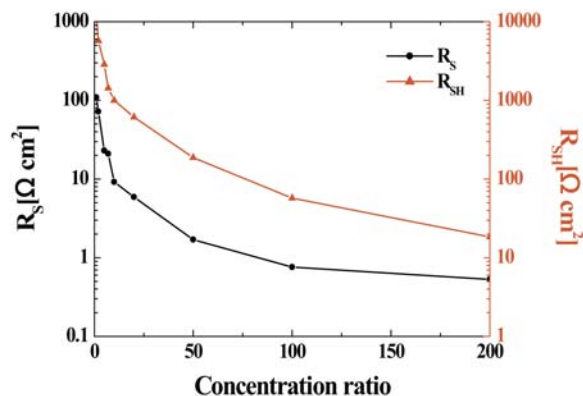


**Figure 5** (online colour at: www.pss-rapid.com)  $R_S$  and  $R_{SH}$  as functions of concentration ratio (1 to 200 suns).

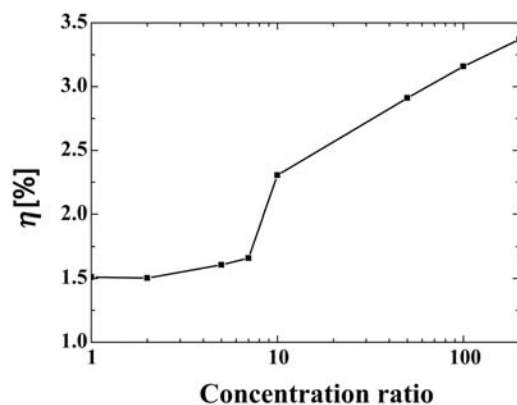


**Figure 6**  $\eta$  as a function of concentration ratio.

$J_{SC}$  was approximately proportional to the concentration ratio and increased 370-fold when the concentration ratio was increased from 1 to 200 suns (cf. Table 1).

Figure 5 shows the measured series resistance ( $R_S$ ) and shunt resistance ( $R_{SH}$ ) as functions of the concentration ratio. We calculated  $R_S$  and  $R_{SH}$  from the slope of the  $I$ - $V$  curves [8].  $R_S$  and  $R_{SH}$  rapidly decrease with increasing concentration ratio. Because the photo current of this solar cell is very small at low sun,  $R_S$  and  $R_{SH}$  appear larger. Thus,  $R_S$  and  $R_{SH}$  are rapidly reduced due to an increase in the photo current with high concentrated light illumination.

Figure 6 shows the power conversion efficiency  $\eta$  as a function of concentration ratio. We also summarize the values of  $J_{SC}$ ,  $V_{OC}$ ,  $R_S$ ,  $R_{SH}$ , FF, and  $\eta$  at 1 and 200 suns exposures in Table 1. The efficiency increases from 1.5% to 3.4% when the concentration ratio increases from 1 to 200 suns. The efficiency is increased by a factor of 2.3, whereas  $V_{OC}$  is increased by a factor of 1.3. The higher rate of increase of the ratio in  $\eta$  than that in  $V_{OC}$  is due to the increase in  $J_{SC}$  with increasing concentration ratio. That is, the nitride-based solar cells operate effectively even at 200 suns. The conversion efficiency of 3.4% is the highest ever reported value for nitride solar cells.

**5 Summary** In conclusion, we investigated the nitride-based solar cells under concentrator conditions.  $V_{OC}$ ,  $J_{SC}$ , and  $\eta$  monotonically increased from 1 to 200 suns, while FF decreased slightly.  $J_{SC}$ ,  $V_{OC}$ , FF, and  $\eta$  were 510 mA/cm<sup>2</sup>, 1.9 V, 70%, and 3.4%, respectively, at AM 1.5G and 200 suns at RT.

**Acknowledgement** This study was partially supported by a New Energy and Industrial Technology Development Organization (NEDO) Project on the Research and Development of Innovative Solar Cells.

## References

- [1] J. Wu, W. Walukiewicz, K. M. Yu, W. Shan, J. W. Ager, E. E. Haller, H. Lu, W. J. Schaff, W. K. Metzger, and S. Kurtz, *J. Appl. Phys.* **94**, 6477 (2003).
- [2] Y. Kuwahara, T. Fujii, Y. Fujiyama, T. Sugiyama, M. Iwaya, T. Takeuchi, S. Kamiyama, I. Akasaki, and H. Amano, *Appl. Phys. Express* **3**, 111001 (2010).
- [3] Y. Kuwahara, T. Fujii, T. Sugiyama, D. Iida, Y. Isobe, Y. Fujiyama, Y. Morita, M. Iwaya, T. Takeuchi, S. Kamiyama, I. Akasaki, and H. Amano, *Appl. Phys. Express* **4**, 021001 (2011).
- [4] S. Yamamoto, Y. Kuwahara, T. Fujii, D. Iida, Y. Morita, M. Iwaya, T. Takeuchi, S. Kamiyama, I. Akasaki, and H. Amano, to be submitted.
- [5] M. A. Green, K. Emery, D. L. King, Y. Hishikawa, and W. Warta, *Prog. Photovolt.: Res. Appl.* **14**, 45 (2006).
- [6] R. Dahal, J. Li, K. Aryal, J. Y. Lin, and H. X. Jiang, *Appl. Phys. Lett.* **97**, 073115 (2010).
- [7] J. Nelson, *The Physics of Solar Cells* (Imperial College Press, London, 2003).
- [8] R. Sahai and A. G. Milnes, *Solid-State Electron.* **13**, 1289 (1970).

## Relationship between lattice relaxation and electrical properties in polarization doping of graded AlGa<sub>N</sub> with high AlN mole fraction on AlGa<sub>N</sub> template

This content has been downloaded from IOPscience. Please scroll down to see the full text.

2017 Appl. Phys. Express 10 025502

(<http://iopscience.iop.org/1882-0786/10/2/025502>)

View [the table of contents for this issue](#), or go to the [journal homepage](#) for more

Download details:

IP Address: 219.127.71.134

This content was downloaded on 03/03/2017 at 06:37

Please note that [terms and conditions apply](#).

You may also be interested in:

[Investigations of Polarization-Induced Hole Accumulations and Vertical Hole Conductions in GaN/AlGa<sub>N</sub> Heterostructures](#)

Toshiki Yasuda, Kouta Yagi, Tomoyuki Suzuki et al.

[Electron and hole accumulations at GaN/AlInN/GaN interfaces and conductive n-type AlInN/GaN distributed Bragg reflectors](#)

Shotaro Yoshida, Kazuki Ikeyama, Toshiki Yasuda et al.

[Enhanced Hole Generation in Mg-Doped AlGa<sub>N</sub>/GaN Superlattices Due to Piezoelectric Field](#)

Kazuhide Kumakura, Toshiki Makimoto and Naoki Kobayashi

[Polarization Induced High Al Composition AlGa<sub>N</sub> p–n Junction Grown on Silicon Substrates](#)

Zhang Peng, Li Shi-Bin, Yu Hong-Ping et al.

[Hexagonal boron nitride for deep ultraviolet photonic devices](#)

H X Jiang and J Y Lin

[Low-resistance Ohmic contact on polarization-doped AlGa<sub>N</sub>/GaN heterojunction](#)

Li Shi-Bin, Yu Hong-Ping, Zhang Ting et al.

[Improvement of the carrier distribution with GaN/InGa<sub>N</sub>/AlGa<sub>N</sub>/InGa<sub>N</sub>/GaN composition-graded barrier for InGa<sub>N</sub>-based blue light-emitting diode](#)

Min Guo, Zhi-You Guo, Jing Huang et al.

[UV emitters based on an AlGa<sub>N</sub> p–n junction in the form of graded-index separate confinement heterostructure](#)

Haiding Sun and Theodore D. Moustakas



## Relationship between lattice relaxation and electrical properties in polarization doping of graded AlGa<sub>N</sub> with high AlN mole fraction on AlGa<sub>N</sub> template

Toshiki Yasuda<sup>1</sup>, Tetsuya Takeuchi<sup>1\*</sup>, Motoaki Iwaya<sup>1</sup>, Satoshi Kamiyama<sup>1</sup>, Isamu Akasaki<sup>1,2</sup>, and Hiroshi Amano<sup>2,3</sup>

<sup>1</sup>Faculty of Science and Technology, Meijo University, Nagoya 468-8502, Japan

<sup>2</sup>Akasaki Research Center, Nagoya University, Nagoya 464-8062, Japan

<sup>3</sup>Institute of Materials and Systems for Sustainability, Nagoya University, Nagoya 464-8062, Japan

\*E-mail: take@meijo-u.ac.jp

Received November 17, 2016; accepted January 11, 2017; published online January 30, 2017

We investigated polarization doping for hole generation in abrupt and graded GaN/Al<sub>0.7</sub>Ga<sub>0.3</sub>N interfaces on Al<sub>0.99</sub>Ga<sub>0.01</sub>N templates. The abrupt interface exhibited hole generation, whereas the graded interface exhibited electron generation. In the graded Al<sub>x</sub>Ga<sub>1-x</sub>N ( $x = 0.65-0$ ), a graded part with an AlN mole fraction ranging from 0.2 to 0 showed a large relaxation. Theoretical estimation revealed that this part contained positive polarization charges, accumulating electrons. Via Mg doping in the graded AlGa<sub>N</sub> layer, we obtained a high hole concentration of  $3 \times 10^{13} \text{ cm}^{-2}$ . These results indicate that understanding the relaxation conditions in the graded layer is indispensable for polarization doping.

© 2017 The Japan Society of Applied Physics

Nitride semiconductor-based deep-ultraviolet (DUV) light-emitting diodes (LEDs) have been proposed to replace UV lightbulbs. However, the external quantum efficiency of UV LEDs is considerably low, and it is more pronounced in the DUV region.<sup>1-3</sup> Among the reasons for the low efficiency are the poor electrical properties of p-type AlGa<sub>N</sub> with a high AlN mole fraction. Nitride semiconductors can exhibit p-type conductivity after Be, Zn, or Mg doping.<sup>4-7</sup> In general, Mg is mostly used to form p-type AlGa<sub>N</sub>.<sup>8,9</sup> However, it is almost impossible to generate holes in AlGa<sub>N</sub> layers with high AlN mole fractions, because acceptors such as Mg in such AlGa<sub>N</sub> layers have large ionization energies.<sup>10,11</sup> For instance, the resistivity of Mg-doped Al<sub>0.7</sub>Ga<sub>0.3</sub>N exceeds 1,000 Ω·cm. This is why most nitride DUV LEDs contain a relatively thick p-type GaN, providing holes in the active regions and an ohmic contact to the p-electrode.<sup>12-18</sup> However, GaN absorbs UV light with wavelengths shorter than 365 nm; thus, there is a tradeoff between the electrical and optical properties.

Polarization doping has been proposed as an alternative approach for generating carriers in nitride semiconductors.<sup>19</sup> The polarization charge concentration,  $N_{P,2D}$  (cm<sup>-2</sup>), is estimated as  $N_{P,2D} = P/q$ , where  $P$  (C/cm<sup>2</sup>) is the polarization charge density, and  $q$  (C) is the elementary charge. The polarization charge density includes spontaneous and piezoelectric polarization components.<sup>20,21</sup> The polarization charge concentration accumulates the free carrier concentration,  $N_{2D}$ , with opposite signs to satisfy the charge neutrality,  $N_{2D} \cong N_{P,2D}$ . For instance, two-dimensional (2D) electron gas has been accumulated to the polarization positive charges at an AlGa<sub>N</sub>/GaN interface in a heterostructure field-effect transistor. Furthermore, 2D hole gas was observed at the other GaN/AlGa<sub>N</sub> interface. In addition, Simon et al. proposed Mg-doped graded Al<sub>x</sub>Ga<sub>1-x</sub>N ( $x = 0.3-0$ ) structures in which holes are three-dimensionally distributed, so that the polarization doping is also useful in optoelectronic devices that require vertical conduction.<sup>22</sup> For the graded structure, the three-dimensional (3D) polarization charge concentration,  $N_{P,3D}$  (cm<sup>-3</sup>), is estimated as

$$N_{P,3D} = \frac{\partial P}{q \cdot \partial d},$$

where  $d$  (cm) is the thickness of the graded layer.<sup>19</sup> Thus far, we have shown that the hole concentrations in polarization

doping can be tuned by controlling the AlN mole fractions in GaN/AlGa<sub>N</sub> structures up to 0.34 AlN.<sup>23</sup> Polarization dilution involves compensating unnecessary polarization charges (e.g., positive charges in the p-type layer) with a sufficient amount of ionized impurities (e.g., ionized acceptors) for improving the vertical conductivity.<sup>24</sup> These results have been obtained with AlGa<sub>N</sub> on GaN templates.

Recently, polarization doping on AlN templates, which are more suitable than GaN templates for DUV LEDs, has been reported. Zhang et al. demonstrated hole generation in Mg-doped graded Al<sub>x</sub>Ga<sub>1-x</sub>N ( $x = 0.3-0$ ).<sup>25</sup> Li et al. obtained a high hole concentration in Be-doped graded Al<sub>x</sub>Ga<sub>1-x</sub>N ( $x = 1-0.7$ ).<sup>26</sup> However, p-type graded AlGa<sub>N</sub> with a substantially wider AlN mole fraction range, e.g., 0.7 to 0, should be investigated with practical DUV-LEDs to simultaneously obtain a high hole concentration and a low contact resistivity for the p-electrode. In this study, we investigated polarization doping in GaN/Al<sub>0.7</sub>Ga<sub>0.3</sub>N structures on AlN templates. We measured hole accumulations to the polarization charges in abrupt and graded GaN/Al<sub>0.7</sub>Ga<sub>0.3</sub>N interfaces with and without Mg doping with respect to the measurement temperature. We found a lattice relaxation in the graded AlGa<sub>N</sub> layer with AlN mole fractions ranging from 0.2 to 0 and demonstrated that this lattice relaxation affected the conductivity type.

All samples were prepared on AlN templates grown on *c*-plane sapphire substrates by metalorganic vapor phase epitaxy. The AlN templates were grown with the addition of a small amount of trimethylgallium to improve the surface morphology, resulting in a 2-μm Al<sub>0.99</sub>Ga<sub>0.01</sub>N layer on an AlN buffer layer.<sup>27</sup> We then prepared three different Hall samples. The first had an abrupt interface comprising a 100-nm layer of undoped Al<sub>0.74</sub>Ga<sub>0.26</sub>N, a 10-nm layer of undoped GaN, and a 40-nm layer of p-GaN on the Al<sub>0.99</sub>Ga<sub>0.01</sub>N template, as shown in Fig. 1(a). The second Hall sample had a graded interface comprising a 100-nm layer of undoped Al<sub>0.65</sub>Ga<sub>0.35</sub>N, a 100-nm layer of undoped graded Al<sub>x</sub>Ga<sub>1-x</sub>N ( $x = 0.65-0$ ), and a 40-nm layer of p-GaN on the Al<sub>0.99</sub>Ga<sub>0.01</sub>N template, as shown in Fig. 1(b). The third Hall sample was similar to the second one but contained a 100-nm layer of Mg-doped ( $2 \times 10^{19} \text{ cm}^{-3}$ ) graded Al<sub>x</sub>Ga<sub>1-x</sub>N ( $x = 0.65-0$ ) instead of the undoped Al<sub>x</sub>Ga<sub>1-x</sub>N. The 40-nm p-GaN layers were required as p-contact layers to inject the current. For X-ray diffraction

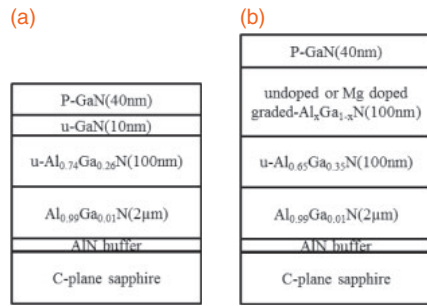


**Fig. 1.** Hall-sample structures containing (a) the abrupt GaN/ $\text{Al}_{0.74}\text{Ga}_{0.26}\text{N}$  heterostructure and (b) the undoped and Mg-doped graded  $\text{Al}_x\text{Ga}_{1-x}\text{N}$  ( $x = 0.65-0$ ) layers.

(XRD) measurements, another sample was prepared on the  $\text{Al}_{0.99}\text{Ga}_{0.01}\text{N}$  template, comprising a 100-nm layer of undoped  $\text{Al}_{0.65}\text{Ga}_{0.35}\text{N}$  and a 100-nm layer of Mg-doped graded  $\text{Al}_x\text{Ga}_{1-x}\text{N}$  ( $x = 0.65-0.3$ ) without a p-GaN contact layer. Hall-effect measurements were performed to determine the carrier concentrations with respect to the temperature. Asymmetric reciprocal space mappings (RSMs) were obtained via XRD. The AlN mole fractions in the graded AlGaN layer were estimated using secondary ion mass spectrometry (SIMS).

Figure 2 shows the carrier concentrations of the three Hall samples with respect to the temperature. As shown in Fig. 2(a), the first Hall sample with the abrupt interface showed p-type conductivity (with red dots) throughout the temperature range. The sheet hole concentration at room temperature was  $1.5 \times 10^{13} \text{ cm}^{-2}$ , showing almost no temperature dependence.<sup>23)</sup> For comparison, the sheet carrier concentrations of a 100-nm Mg-doped p-GaN layer are plotted with black dots in the same figure, showing a significant temperature dependence due to the large ionization energy of Mg. Thus, we conclude that the observed holes were accumulated to the polarization negative charges at the GaN/ $\text{Al}_{0.74}\text{Ga}_{0.26}\text{N}$  interface. On the other hand, as shown in Fig. 2(b), the second Hall sample with the undoped graded AlGaN unexpectedly showed n-type conductivity (with blue dots) with a weak temperature dependence. The sheet electron concentrations were  $\sim 1 \times 10^{13} \text{ cm}^{-2}$  in the measured temperature range. As shown in Fig. 2(c), the third Hall sample with Mg-doped graded AlGaN exhibited p-type conductivity with a sheet hole concentration of  $3 \times 10^{13} \text{ cm}^{-2}$  at room temperature. The  $3 \times 10^{13} \text{ cm}^{-2}$  sheet hole concentration corresponds to a volume hole concentration of  $3 \times 10^{18} \text{ cm}^{-3}$ , considering the graded 100-nm distribution. The conductivity type changed from p-type (with red dots) to n-type (with blue dots) as temperature was reduced below 240 K.

The structural properties of the Hall samples were investigated to investigate the reason for this conductivity-type behavior. First, polarity inversion was suspected; thus, we performed KOH wet etching (80 °C, 1 min) on all the Hall samples. No changes in the surface morphologies of the samples were observed, suggesting that the samples had typical Al polarity and that the polarity inversion was not a cause of the n-type conductivity. Second, the AlN mole fractions in the Mg-doped graded AlGaN layer of the third Hall sample were measured via SIMS. Figure 3 shows that the AlN mole fractions decreased monotonically towards the Al-polar surface side, as designed, indicating that no net positive polarization charges were generated and thus no

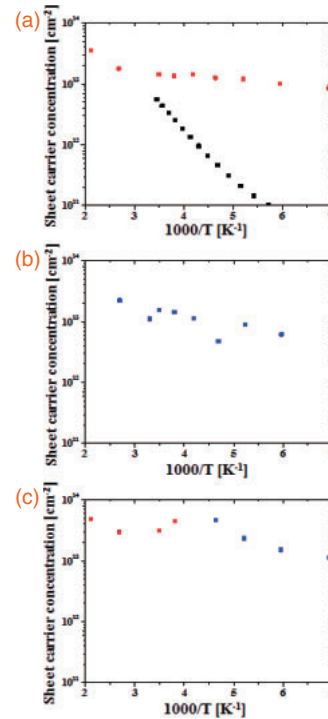


**Fig. 2.** Sheet carrier concentrations with respect to the temperature for (a) the abrupt GaN/AlGaN structure, (b) the undoped graded AlGaN layer, and (c) the Mg-doped graded AlGaN layer. Red and blue dots indicate the hole and electron concentrations, respectively.

electrons could be accumulated. Third, the strain and relaxation conditions of the lattices in the samples were investigated. Figure 4(a) shows the (2024) XRD RSM of the first Hall sample with the abrupt GaN/ $\text{Al}_{0.74}\text{Ga}_{0.26}\text{N}$  interface. The results clearly indicate that the underlying  $\text{Al}_{0.74}\text{Ga}_{0.26}\text{N}$  was 5% relaxed and that the GaN was fully relaxed. The theoretical polarization charge concentrations were calculated to be  $3.7 \times 10^{13}$  and  $1.7 \times 10^{13} \text{ cm}^{-2}$  for the fully strained GaN (to the  $\text{Al}_{0.74}\text{Ga}_{0.26}\text{N}$ ) and fully relaxed GaN, respectively. The measured hole concentration of  $1.5 \times 10^{13} \text{ cm}^{-2}$  shown in Fig. 2(a) is well-explained by the value ( $1.7 \times 10^{13} \text{ cm}^{-2}$ ) for the fully relaxed GaN. Figures 4(b) and 4(c) show the corresponding RSMs for the third Hall sample with the Mg-doped graded  $\text{Al}_x\text{Ga}_{1-x}\text{N}$  ( $x: 0.65-0$ ) layer and the other XRD sample with the Mg-doped graded  $\text{Al}_x\text{Ga}_{1-x}\text{N}$  ( $x = 0.65-0.3$ ) layer. Figure 4(c) indicates that the underlying  $\text{Al}_{0.65}\text{Ga}_{0.35}\text{N}$  was 20% relaxed and that the graded AlGaN with AlN mole fractions ranging from 0.65 to 0.3 was coherently grown on the underlying  $\text{Al}_{0.65}\text{Ga}_{0.35}\text{N}$ . In contrast, Fig. 4(b) suggests that the graded AlGaN with AlN mole fractions ranging from 0.65 to 0 comprised the following parts: 1) the graded AlGaN with an AlN mole fraction ranging from 0.65 to 0.2, which was fully strained to the  $\text{Al}_{0.65}\text{Ga}_{0.35}\text{N}$  layer, and 2) the graded AlGaN with AlN mole fractions ranging from 0.2 to 0, which was gradually and then fully relaxed with increasing proximity to the GaN at the surface.

According to the strain and relaxation conditions observed in the graded AlGaN layer, the theoretical absolute polarization charge concentrations ( $\text{cm}^{-2}$ ) and net polarization charge concentrations ( $\text{cm}^{-3}$ ),  $N_{\text{P,3D}}$ , of the graded AlGaN layer were calculated with respect to the depth (or AlN mole fraction) of the graded AlGaN layer, as indicated by the solid lines in Figs. 5(a) and 5(b), respectively. For comparison, the

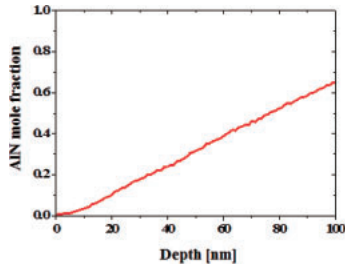


**Fig. 3.** AlN mole-fraction profile for the Mg-doped graded AlGaN layer, measured by SIMS.

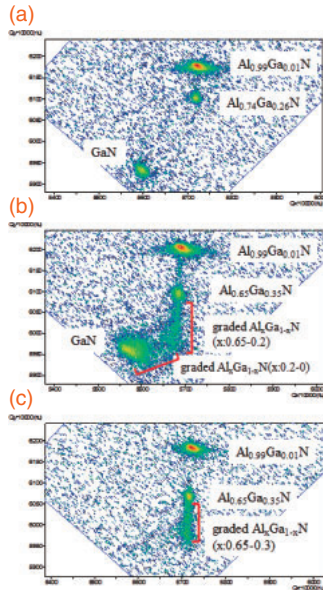


**Fig. 4.** (2024) XRD RSM patterns of (a) the abrupt GaN/AlGaN structure, (b) the Mg-doped graded  $\text{Al}_x\text{Ga}_{1-x}\text{N}$  layer ( $x = 0.65-0$ ), and (c) the Mg-doped graded  $\text{Al}_x\text{Ga}_{1-x}\text{N}$  layer ( $x = 0.65-0.3$ ).

theoretical absolute polarizations in the cases of the AlGaN fully strained to the  $\text{Al}_{0.65}\text{Ga}_{0.35}\text{N}$  layer and the fully relaxed AlGaN are plotted in Fig. 5(a) with dashed and dotted lines, respectively. As shown in Fig. 5(a), because the part with AlN mole fractions ranging from 0.65 to 0.2 was fully strained to the  $\text{Al}_{0.65}\text{Ga}_{0.35}\text{N}$  layer, the values in this part are the same as those in the strained case. In contrast, the part with the AlN mole fraction ranging from 0.2 to 0 is gradually and then fully relaxed so that the absolute polarization charge concentrations in this part gradually change from the value of the strained  $\text{Al}_{0.2}\text{Ga}_{0.8}\text{N}$  to the value of the relaxed GaN, resulting in the opposite sign of the slope compared with the simply strained and simply relaxed cases. The aforementioned 3D polarization charge concentration  $N_{P,3D}$  containing the  $\partial P/\partial d$  component is plotted in Fig. 5(b). This figure reveals that the net polarization charge concentration in the gradually relaxed part (graded AlGaN with AlN mole fractions ranging from 0.2 to 0) has the opposite sign (positive) with a polarization charge concentration of  $\sim 3.4 \times 10^{18} \text{ cm}^{-3}$ . This suggests that electrons — no longer holes — were accumulated on the graded AlGaN with AlN mole fractions ranging from 0.2 to 0. The measurable electron sheet concentration was theoretically estimated to be  $1 \times 10^{13} \text{ cm}^{-2}$  by considering the thickness of the graded AlGaN ( $3.4 \times 10^{18} \text{ cm}^{-3} \times 30 \text{ nm}$ ). This value agrees well with the measured electron value ( $1 \times 10^{13} \text{ cm}^{-2}$ ), as shown in Fig. 2(b).

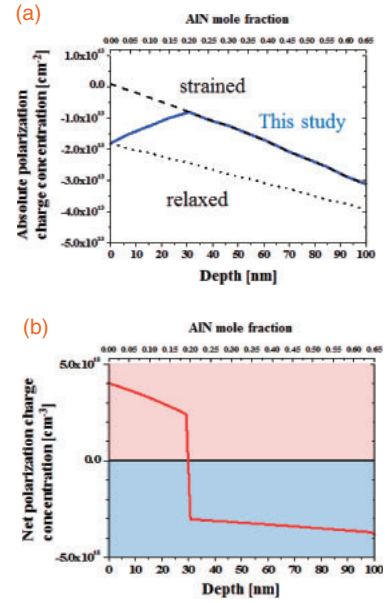


**Fig. 5.** (a) Theoretical absolute polarization charge concentrations ( $\text{cm}^{-2}$ ) and (b) theoretical measurable net polarization charge concentrations ( $\text{cm}^{-3}$ ) for the partially relaxed graded AlGaN layer.

Finally, we theoretically estimated the carrier concentration of the Mg-doped graded AlGaN with an AlN mole fraction ranging from 0.2 to 0, which was gradually relaxed. Because ionized Mg acceptors — rather than electrons — should neutralize the positive polarization charges,<sup>24)</sup> we solved the following charge-neutrality condition using Shockley's graphical method:<sup>28)</sup>

$$n + N_A^- = p + N_D^+ + N_P^+, \quad (1)$$

$$n = N_C \exp\left(-\frac{E_C - E_F}{kT}\right), \quad (2)$$

$$p = N_V \exp\left(-\frac{E_F - E_V}{kT}\right), \quad (3)$$

$$N_D^+ = \frac{N_D}{1 + 2 \exp\left(\frac{E_F - E_D}{kT}\right)}, \quad (4)$$

$$N_A^- = \frac{N_A}{1 + 4 \exp\left(\frac{E_A - E_F}{kT}\right)}. \quad (5)$$

Equation (1) expresses the charge-neutrality condition, including the positive polarization charge. Here,  $n$  and  $p$  are the electron and hole concentrations, respectively;  $N_D$  and  $N_A$  are the donor and acceptor concentrations ( $0$  and  $2 \times 10^{19} \text{ cm}^{-3}$ ), respectively;  $N_D^+$  and  $N_A^-$  are the ionized-donor and ionized-acceptor concentrations, respectively;  $N_P^+$  is the positive polarization charge density ( $3.4 \times 10^{18} \text{ cm}^{-3}$ );  $N_C$  and  $N_V$  are the effective density of states at the conduction and valence bands, respectively;  $E_A$  and  $E_D$  are the acceptor and donor energy levels ( $0.2$  and  $3.58 \text{ eV}$ ), respectively;  $E_V$  and  $E_C$  are the valence- and conduction-band edge energy levels ( $0$  and  $3.6 \text{ eV}$ ), respectively;  $k$  is Boltzmann's constant, and  $T$  is the temperature. For simplicity, we used the average parameters for the Mg-doped graded AlGaN layer, i.e.,  $\text{Al}_{0.1}\text{Ga}_{0.9}\text{N}$ . Figure 6 shows the total negative [left side of Eq. (1): blue line] and positive [right side of Eq. (1): red line] charge densities with respect to the Fermi energy in the Mg-doped graded AlGaN.

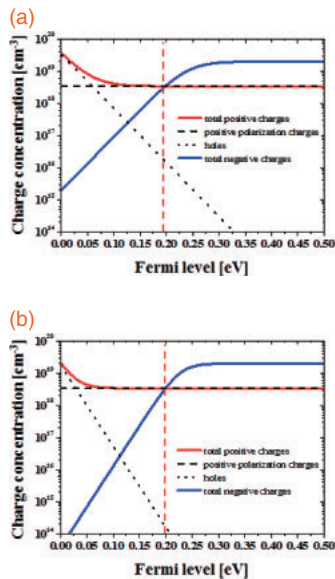


**Fig. 6.** Calculated total negative/positive charges and components of the positive charges in the graded AlGaIn with a mole fraction ranging from 0.2 to 0 with respect to the Fermi energy at (a) 300 K and (b) 200 K. The energy the valence-band edge is 0 eV.

The intersection satisfies the charge-neutrality condition for a given Fermi energy. Figure 6 also shows the two components of the total positive charges, the hole concentrations (dotted black line), and the positive polarization charge concentrations (dashed black line). At room temperature, the Fermi energy of 0.198 eV yielded the charge-neutrality condition, resulting in p-type AlGaIn with a hole concentration of  $1.4 \times 10^{16} \text{ cm}^{-3}$ , as shown in Fig. 6(a). Considering that the hole concentration of the strained graded AlGaIn with an AlN mole fraction ranging from 0.65 to 0.2 was  $3.4 \times 10^{18} \text{ cm}^{-3}$ , we calculated the measurable hole concentration of the third Hall sample to be  $2.4 \times 10^{13} \text{ cm}^{-2}$  ( $3.4 \times 10^{18} \text{ cm}^{-3} \times 70 \text{ nm} + 1.4 \times 10^{16} \text{ cm}^{-3} \times 30 \text{ nm}$ ), which agrees well with the measured value ( $3 \times 10^{13} \text{ cm}^{-2}$ ) shown in Fig. 3(c).

To elucidate the reason for the observed change in the conductivity from p- to n-type around 240 K, Fig. 6(b) describes the charge-neutrality condition for the same case at 200 K. The hole concentration clearly decreased to  $2 \times 10^{14} \text{ cm}^{-3}$ . However, the Fermi energy remained relatively constant, indicating p-type conductivity. Therefore, the observed conductivity switching in the third Hall sample cannot presently be explained. Furthermore, the reason why the observed electron concentration of the third Hall sample at a low temperature was higher than that of the second Hall sample is unknown. Nevertheless, we point out that the strain and relaxation conditions drastically affect not only the magnitude but also the type of conductivity in the graded layers for polarization doping. To properly utilize the polarization doping in the graded layers, we must further investigate the strain and relaxation conditions.

In this study, we investigated polarization doping for hole generation in GaN/Al<sub>0.7</sub>Ga<sub>0.3</sub>N structures on AlN templates. The abrupt GaN/Al<sub>0.7</sub>Ga<sub>0.3</sub>N interface generated holes, whereas the graded GaN/Al<sub>0.7</sub>Ga<sub>0.3</sub>N interface generated electrons. The lattice relaxations drastically affected not only the magnitude but also the type of conductivity in the graded

layers, which explains the observed electron generation in the undoped graded AlGaIn layer with a wide grading range of AlN mole fractions. A combination of Mg doping and polarization doping resulted in a high sheet carrier concentration of  $3 \times 10^{13} \text{ cm}^{-2}$  (or  $3 \times 10^{18} \text{ cm}^{-3}$  in 100 nm), which is useful for sufficient hole injections in DUV LEDs.

**Acknowledgments** This study was partially supported by the MEXT Program for the Strategic Research Foundation at Private Universities (2012–2016), MEXT-Grants-in-Aid for Scientific Research and Specially Promoted Research (No. 25000011), JSPS Grant-in-Aid for Scientific Research A (No. 15H02019), JSPS Grant-in-Aid for Scientific Research B (No. 26286045), JSPS KAKENHI (No. 16H06416), JST CREST (No. 16815710), and the Nippon Sheet Glass Foundation for Materials Science and Engineering.

- 1) Y. Taniyasu and M. Kasu, *Appl. Phys. Lett.* **98**, 131910 (2011).
- 2) H. Hirayama, S. Fujikawa, N. Noguchi, J. Norimatsu, T. Takano, K. Tsubaki, and N. Kamata, *Phys. Status Solidi A* **206**, 1176 (2009).
- 3) J. R. Grandusky, S. R. Gibb, M. C. Mendrick, and L. J. Schowalter, *Appl. Phys. Express* **3**, 072103 (2010).
- 4) H. Amano, M. Kito, K. Hiramatsu, and I. Akasaki, *Jpn. J. Appl. Phys.* **28**, L2112 (1989).
- 5) S. Nakamura, N. Iwasa, M. Senoh, and T. Mukai, *Jpn. J. Appl. Phys.* **31**, 1258 (1992).
- 6) O. Brandt, H. Yang, H. Kostial, and K. H. Ploog, *Appl. Phys. Lett.* **69**, 2707 (1996).
- 7) K. S. Kim, M. S. Han, G. M. Yang, C. J. Youn, H. J. Lee, H. K. Cho, and J. Y. Lee, *Appl. Phys. Lett.* **77**, 1123 (2000).
- 8) M. L. Nakarmi, N. Nipal, J. Y. Lin, and H. X. Jiang, *Appl. Phys. Lett.* **94**, 091903 (2009).
- 9) S.-R. Jeon, Z. Ren, G. Cui, J. Su, M. Gherasimova, J. Han, H.-K. Cho, and L. Zhou, *Appl. Phys. Lett.* **86**, 082107 (2005).
- 10) P. Kozodoy, H. Xing, S. P. DenBaars, U. K. Mishra, A. Saxler, R. Perrin, S. Elhamri, and W. C. Mitchel, *J. Appl. Phys.* **87**, 1832 (2000).
- 11) M. L. Nakarmi, N. Nepal, C. Ugolini, T. M. Altahtamouni, J. Y. Lin, and H. X. Jiang, *Appl. Phys. Lett.* **89**, 152120 (2006).
- 12) K. Tadatomo, H. Okagawa, Y. Ohuchi, T. Tsunekawa, Y. Imada, M. Kato, and T. Taguchi, *Jpn. J. Appl. Phys.* **40**, L583 (2001).
- 13) C. Pernot, S. Fukahori, T. Inazu, T. Fujita, M. Kim, Y. Nagasawa, A. Hirano, M. Ippommatsu, M. Iwaya, S. Kamiyama, I. Akasaki, and H. Amano, *Phys. Status Solidi A* **208**, 1594 (2011).
- 14) H. Hirayama, Y. Tsukada, T. Maeda, and N. Kamata, *Appl. Phys. Express* **3**, 031002 (2010).
- 15) A. Fujioka, T. Misaki, T. Murayama, Y. Narukawa, and T. Mukai, *Appl. Phys. Express* **3**, 041001 (2010).
- 16) J.-S. Jang, I.-S. Chang, H.-K. Kim, T.-Y. Seong, S. Lee, and S.-J. Park, *Appl. Phys. Lett.* **74**, 70 (1999).
- 17) H.-K. Kim, T.-Y. Seong, I. Adesida, C. W. Tang, and K. M. Lau, *Appl. Phys. Lett.* **84**, 1710 (2004).
- 18) H. W. Jang, S. Y. Kim, and J. L. Lee, *J. Appl. Phys.* **94**, 1748 (2003).
- 19) D. Jena, S. Heikman, D. Green, D. Buttari, R. Coffie, H. Xing, S. Keller, S. DenBaars, J. S. Speck, and U. K. Mishra, *Appl. Phys. Lett.* **81**, 4395 (2002).
- 20) F. Bernardini, V. Fiorentini, and D. Vanderbilt, *Phys. Rev. B* **56**, R10024 (1997).
- 21) T. Takeuchi, S. Sota, M. Katsuragawa, M. Komori, H. Takeuchi, H. Amano, and I. Akasaki, *Jpn. J. Appl. Phys.* **36**, L382 (1997).
- 22) J. Simon, V. Protasenko, C. Lian, H. Xing, and D. Jena, *Science* **327**, 60 (2010).
- 23) T. Yasuda, K. Yagi, T. Suzuki, T. Nakashima, M. Watanabe, T. Takeuchi, M. Iwaya, S. Kamiyama, and I. Akasaki, *Jpn. J. Appl. Phys.* **52**, 08JJ05 (2013).
- 24) T. Yasuda, K. Hayashi, S. Katsuno, T. Takeuchi, S. Kamiyama, M. Iwaya, I. Akasaki, and H. Amano, *Phys. Status Solidi A* **212**, 920 (2015).
- 25) L. Zhang, K. Ding, J. C. Yan, J. X. Wang, Y. P. Zeng, T. B. Wei, Y. Y. Li, B. J. Sun, R. F. Duan, and J. M. Li, *Appl. Phys. Lett.* **97**, 062103 (2010).
- 26) S. Li, T. Zhang, J. Wu, Y. Yang, Z. Wang, Z. Wu, Z. Chen, and Y. Jiang, *Appl. Phys. Lett.* **102**, 062108 (2013).
- 27) S. Katsuno, T. Yasuda, K. Hagiwara, N. Koide, M. Iwaya, T. Takeuchi, S. Kamiyama, I. Akasaki, and H. Amano, *Jpn. J. Appl. Phys.* **56**, 015504 (2017).
- 28) W. Shockley, *Electrons and Holes in Semiconductors* (D. Van Nostrand, New York, 1950).

# Polarization dilution in a Ga-polar UV-LED to reduce the influence of polarization charges

Toshiki Yasuda<sup>\*1</sup>, Kento Hayashi<sup>1</sup>, Syouta Katsuno<sup>1</sup>, Tetsuya Takeuchi<sup>1</sup>, Satoshi Kamiyama<sup>1</sup>, Motoaki Iwaya<sup>1</sup>, Isamu Akasaki<sup>\*\*1,2</sup>, and Hiroshi Amano<sup>\*\*2,3</sup>

<sup>1</sup> Faculty of Science and Technology, Meijo University, Nagoya 468-8502, Japan

<sup>2</sup> Akasaki Research Center, Nagoya University, Nagoya 464-8062, Japan

<sup>3</sup> Graduate School of Engineering, Nagoya University, Nagoya 464-8062, Japan

Received 30 September 2014, revised 20 November 2014, accepted 25 November 2014

Published online 15 January 2015

**Keywords** AlGaIn, light-emitting diodes, polarization

\* Corresponding author: e-mail 143441506@c alumni.meijo-u.ac.jp, Phone: +81-52-832-1151

\*\* Isamu Akasaki and Hiroshi Amano are laureates of the Nobel Prize in Physics 2014.

We investigated the influence of polarization charges in nitride-based semiconductors. The influence due to polarization charges was calculated excluding the influences of the band offset. We found that the polarization charges ( $1 \times 10^{13} \text{ cm}^{-2}$ ) resulted in an energy spike of more than 100 meV at the location of the charges, which is a similar value to the band offset. We then proposed the concept of polarization dilution to suppress the energy spike for better hole transport by using a

graded Mg-doped AlGaIn layer in UV-LEDs. Device simulation results indicate lower operating voltage and higher injection efficiency by using the polarization dilution. So far, our actual 350 nm LED with the polarization dilution showed lower operating voltage. These results suggested such polarization-charge management is important in the design of the nitride semiconductors.

© 2015 WILEY-VCH Verlag GmbH & Co. KGaA, Weinheim

**1 Introduction** AlGaIn-based ultraviolet (UV) light-emitting diodes (LEDs) are expected to be highly efficient, reliable, and compact light sources for sterilization, water purification, printing, and so on. Currently, external quantum efficiencies (EQEs) of the UV-LEDs are much lower than those of commercialized visible LEDs. For instance, the reported highest EQEs of UV-A, UV-B, and UV-C are 44% at 365 nm [1], 10.4% at 278 nm [2], 0.2% at 227 nm [3], respectively. One of the reasons for such low EQEs is the inferior p-type characteristic of AlGaIn resulting in poor hole injection into the active region. While the ionization energy of Mg acceptors in GaN is 170 meV [4], that in AlN is 600 meV [5]. Therefore, p-type AlGaIn especially with high AlN mole fraction shows very low hole concentrations [6].

On the other hand, the nitride semiconductors are well known to show large polarization characteristics. Large spontaneous [7] and piezoelectric [8] polarization charges are generated, and remain at heterointerfaces. As these charges are fixed charges, they do not contribute as mobile carriers in principle. The concentrations of the polarization charges in the

nitride semiconductors, however, are comparable to or even higher than those of electrons and holes in impurity-doped layers. Thus, the polarization charges largely influence the mobile carriers as well as energy-band structures in nitride semiconductors. A favorable example to utilize the polarization charges is a two-dimensional electron gas (2DEG) in a heterofield effect transistor (HFET) [9]. The 2DEG is accumulated even without any impurity doping at one of the AlGaIn/GaN interfaces where positive polarization charges are generated. For instance, as the concentration of the polarization charges at the  $\text{Al}_{0.2}\text{Ga}_{0.8}\text{N}/\text{GaN}$  interface is more than  $1 \times 10^{13} \text{ cm}^{-2}$ , almost the same high number of the electrons is built up. Furthermore, the polarization charges with the opposite sign are also generated at the other side of the interface, and now 2D hole gas is accumulated there. In addition, a new concept, “polarization doping” [10] was proposed, in which such a large number of the polarization “sheet” charges are three-dimensionally distributed by forming compositionally graded interfaces, resulting in a three-dimensional (3D) carrier distribution. With the polarization doping, a compositionally

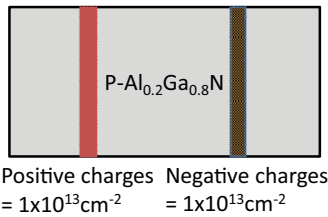


**Figure 1** Assumed structure (putting positive and negative charges in p- $\text{Al}_{0.2}\text{Ga}_{0.8}\text{N}$ ).

graded p-AlGa<sub>0.8</sub>N showed a much higher 3D hole concentration allowing vertical carrier transport [11]. Then, this concept was proved in a light emitting device, an N-polar UV-LED, showing higher hole injection [12].

In our previous study, we attempted to use polarization doping in a more conventional Ga-polar blue LED [13]. Even though we clearly observed high hole accumulation at an AlGa<sub>0.8</sub>N graded layer with a separate Hall measurement, the blue LED with the similar graded layer, which corresponded to an electron blocking layer, showed very low output power. This fact indicates that the polarization doping works in N-polar LEDs but not in Ga-polar LEDs. The difference between N-polar and Ga-polar in terms of the polarization is the sign of the polarization charges. The polarization charges with the opposite sign are generated at the equivalent interfaces in the same device structure.

In this study, we first calculated the influence of the positive and negative polarization charges on energy-band profiles in the impurity-doped layer. Then, we proposed a technique to reduce the influence of the polarization charges, “polarization dilution”. Finally, we performed theoretical and experimental investigations on the effect of the polarization dilution in 350 nm LED.

**2 Influence of polarization** First, we calculated the influence of polarization charges with a commercially available device simulator (SiLENSE) implementing a 1D drift-diffusion model in consideration of the strong piezoelectric/spontaneous polarization charges. Here, we are interested in just the influence of the polarization charges on the energy-band profiles. Thus, we

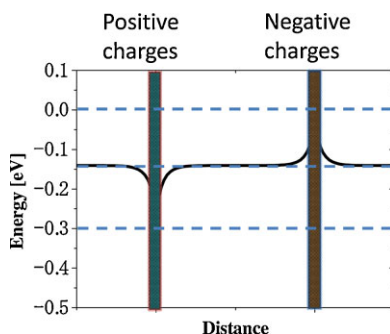


**Figure 2** The calculated valence-band energy profile of the assumed structure (Fig. 1). Energy spike and dip for hole is 160 meV and 140 meV, respectively.

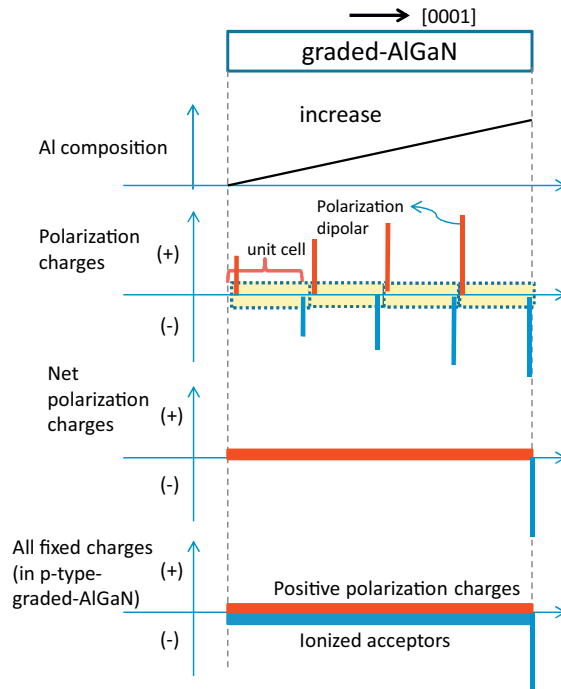


**Figure 3** Mechanism of polarization dilution. Positive polarization charges are distributed in a graded layer by grading with increase of Al composition. Positive polarization charges are compensated by ionized acceptors under charge-neutrality conditions.

assumed a simple uniform p-type material, Mg-doped  $\text{Al}_{0.2}\text{Ga}_{0.8}\text{N}$ , containing positive and negative sheet charges,  $1 \times 10^{13} \text{cm}^{-2}$ , separately located, as shown in Fig. 1. The assumed structure allows us to solely estimate the influence of the charges, excluding that of a band offset that must be formed at the heterostructure interface. The fixed charges,  $1 \times 10^{13} \text{cm}^{-2}$ , correspond to the number of polarization charges at the  $\text{Al}_{0.2}\text{Ga}_{0.8}\text{N}/\text{Al}_{0.4}\text{Ga}_{0.6}\text{N}$  interface.

The calculated valence-band energy profile of the assumed structure is plotted in Fig. 2. An energy spike and an energy dip to the holes in the valence band are observed at the locations of

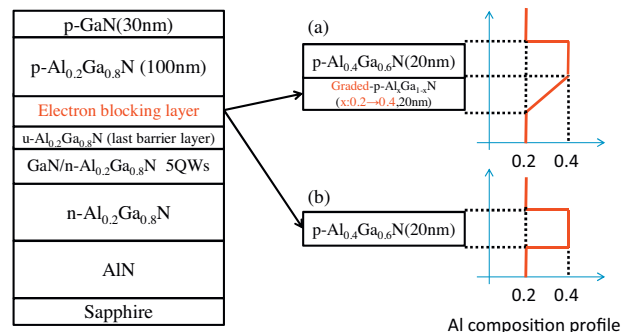


**Figure 4** Sample structures, (a) LED with polarization dilution, (b) LED without polarization dilution (basic structure).

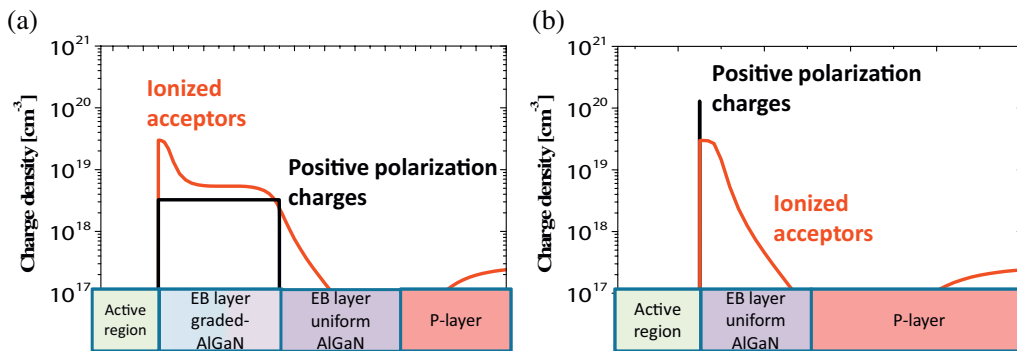


**Figure 5** Distribution of positive polarization charges and ionized acceptors around EB layer, (a) LED with polarization dilution, (b) LED without polarization dilution

positive and negative charges, respectively. The reason for forming the energy spike (dip) simply indicates the result of Coulomb's force between the positive (negative) sheet charges and the holes in the valence band. What we must pay attention to here is the heights of the energy spike and the dip, 160 meV and 140 meV, respectively, similar to that of the heterobarrier at the  $\text{Al}_{0.2}\text{Ga}_{0.8}\text{N}/\text{Al}_{0.4}\text{Ga}_{0.6}\text{N}$  interface. This calculation result clearly indicates that the influence of the polarization charges on the energy band is large enough to affect device performances. We carefully consider the energy spike due to the polarization charges in the device design. For instance, such an energy spike should be useful for carrier confinement but harmful for carrier transport in the same analogy as the heterobarrier. Thus, it is worthwhile to control and reduce the polarization charges for better carrier transport. However, it is difficult to only reduce the polarization charges while keeping the same mole fraction values at the interfaces.

**3 Polarization dilution** We then proposed a useful technique to “dilute” the polarization charges, as shown in Fig. 3. Again, it seems impossible to just reduce the polarization charges, but the charges could be neutralized by other charges with the opposite sign. In the case of the

energy spike in the p-type layer, negative charges are necessary because the energy spike is caused by the positive polarization charges. Unfortunately, the electron cannot be a candidate in this case as the layer is p-type. Thus, another negative charge that can exist in a p-type layer is necessary, and that is an ionized acceptor. If the ionized acceptor concentration is equal to or higher than the positive polarization charge density, the positive polarization charges will be completely neutralized. Note that a  $1 \times 10^{13} \text{ cm}^{-2}$  sheet concentration is equivalent to a  $2 \times 10^{20} \text{ cm}^{-3}$  volume concentration, assuming that the sheet charges are distributed in one unit-cell thickness (0.5 nm). Such a high concentration is achievable as it is already used in p-contact layers and tunnel junctions. However, the high concentration could degrade the adjacent active region in this case. Thus, we borrow the same concept from polarization doping but in order to dilute the polarization charges so that the required ionized acceptor concentration will be reduced as much as possible. Here, the interface with the positive polarization charges is compositionally graded with some thickness. In other words, the interface thickness is expanded from 0 to the graded thickness. For instance, if the interface with  $1 \times 10^{13} \text{ cm}^{-2}$

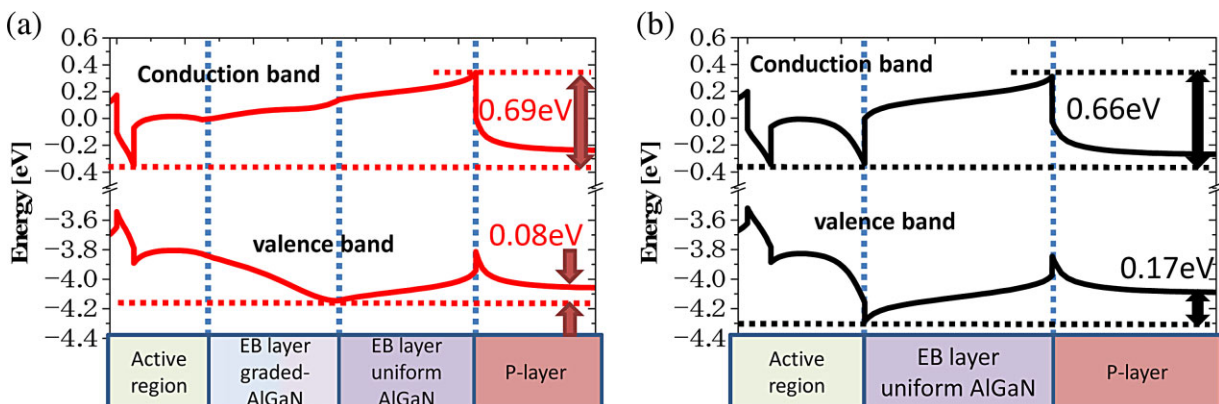


**Figure 6** Comparison of band diagram (injected current density:  $1 \text{ kA/cm}^2$ ), (a) LED with polarization dilution, (b) LED without polarization dilution.

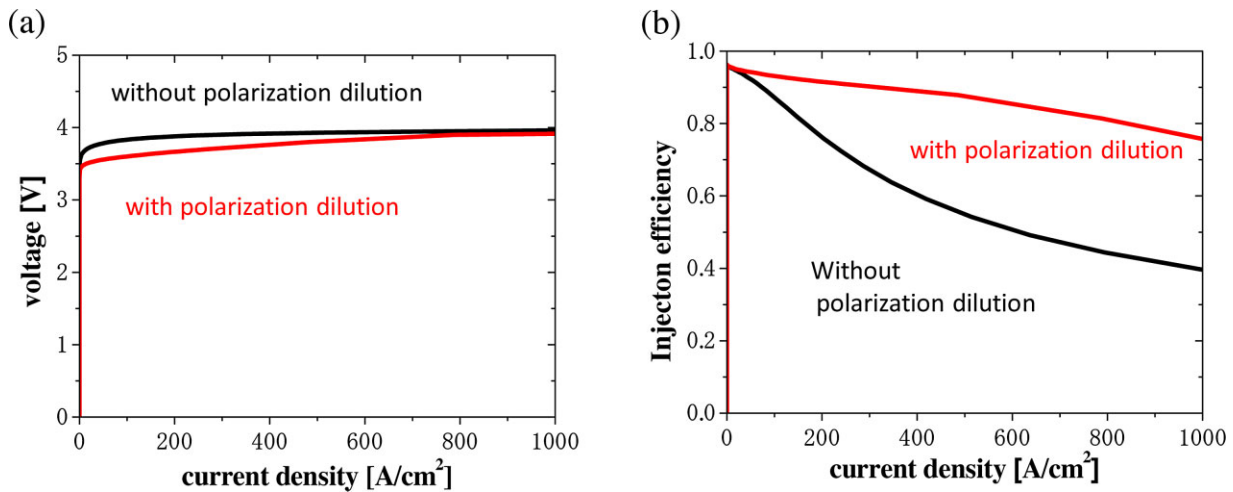


**Figure 7** Calculated LED characteristics. (a)  $J$ - $V$  characteristic, (b) carrier injection efficiency.

is graded with 20 nm, the volume concentration is diluted from  $2 \times 10^{20} \text{ cm}^{-3}$  to  $5 \times 10^{18} \text{ cm}^{-3}$ , which is a required value as a sufficient ionized acceptor concentration and is easily achieved by a conventional growth technique. Thus the polarization dilution should be a very practical technique to suppress the influence of the positive polarization charges. The differences between the polarization doping and the polarization dilution are (1) the sign of the polarization charges and (2) the requirement of impurity doping. In the polarization doping case, the graded layer is formed at the interface generating the charges with the opposite sign to the interested carriers, and the impurity doping is not indispensable. On the contrary, in the polarization dilution case, the graded layer is formed at the interface generating the polarization charges with the same sign as the interested carriers, and the impurity doping is necessary to neutralize the charges.

#### 4 Device simulation and experimental results

Finally, we theoretically and experimentally investigated the impact of the polarization dilution in Ga-polar 350 nm LEDs. Sample structures with and without (conventional) the polarization dilution are shown in Fig. 4a and b, respectively. A structural difference between the two LED samples was (a) with and (b) without a compositional graded p-AlGa<sub>0.8</sub>N layer (Al composition from 0.2 to 0.4) at the interface of the Al<sub>0.2</sub>Ga<sub>0.8</sub>N barrier/p-Al<sub>0.4</sub>Ga<sub>0.6</sub>N electron blocking layer. Other than that, the layer structure consists of a 2  $\mu\text{m}$  AlN, a 1.5  $\mu\text{m}$  n-Al<sub>0.2</sub>Ga<sub>0.8</sub>N, 3 nm GaN/10 nm Al<sub>0.2</sub>Ga<sub>0.8</sub>N five quantum wells, the 10 nm u-AlGa<sub>0.8</sub>N last barrier layer, the 20 nm p-Al<sub>0.4</sub>Ga<sub>0.6</sub>N electron blocking layer, a 100 nm p-Al<sub>0.2</sub>Ga<sub>0.8</sub>N, and a 30 nm p-GaN. Figures 5 and 6 show calculated profiles of the positive polarization charge density and the ionized acceptor concentration, and corresponding band-energy profiles, respectively. In the

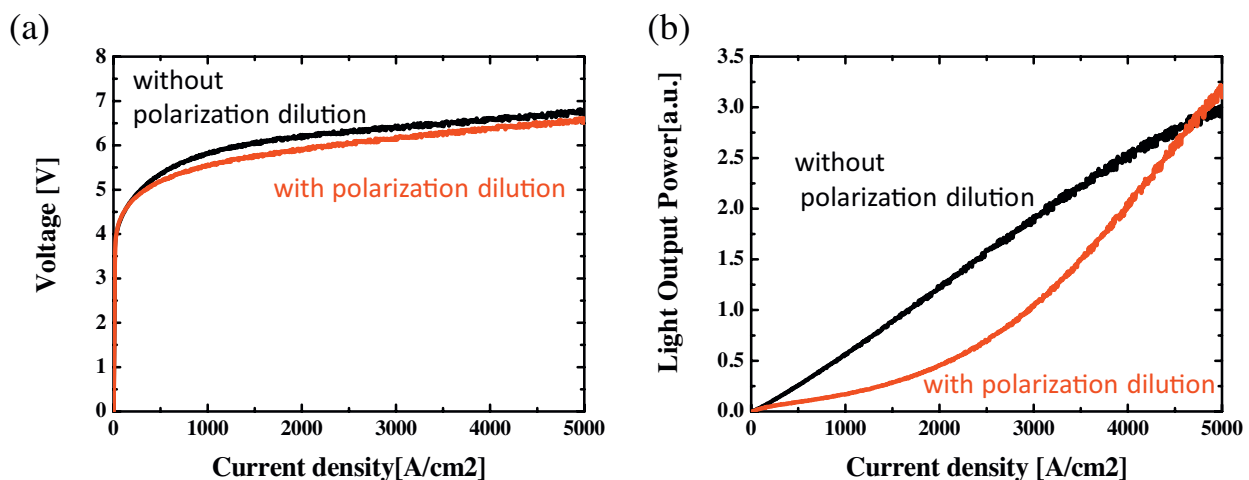


**Figure 8** Measured LED characteristics. (a)  $J$ - $V$  characteristic, (b)  $J$ - $L$  characteristic.

conventional LED case, the large polarization still remained unneutralized at the active region/electron blocking layer interface, as shown in Fig. 5, resulting in a large energy spike, as shown in Fig. 6. On the other hand, in the LED with the polarization dilution case, the positive polarization charges are fully neutralized with the ionized acceptor and no energy spike is observed in the valence band at the interface. In addition, while an  $\sim 100$  meV reduction is obtained at the valence band, no reduction of the potential barrier is obtained at the conduction band. These results should dramatically improve hole injection into the active region. Figure 7 shows calculated  $J$ - $V$  characteristics and injection efficiency characteristics of the two LEDs. Due to the reduction of the energy spike, the operating voltage is decreased and the injection efficiency is increased in the LED with the polarization dilution. These results suggest that such a polarization-charge management is important to obtain superior performance in nitride-based UV-LEDs.

We then fabricated actual LEDs with the layer structures shown in Fig. 4a and b. Figure 8 shows measured  $J$ - $L$ - $V$  characteristics of the two LEDs. We obtained  $J$ - $V$  characteristics consistent with the calculated result. In the meantime, the LED with the polarization dilution showed a smaller light output power at low current injection region, which is inconsistent with the calculated result. On the contrary, in the high current injection region the light output power of the LED with the polarization dilution was equal to or even higher than that of the LED without the polarization dilution. At this time, the reason for the low light output power is unclear. However, the result at high current injection indicates the potential of the polarization dilution and encourages us to investigate the reason in the future.

**5 Conclusions** In summary, the influence of the polarization charges was calculated without the influence of the band offset. The calculation result indicated the polarization charges resulted in an energy spike of more than 100 meV, affecting the carrier transport. Then, we proposed the polarization dilution to suppress the energy spike for better hole transport by using a Mg-doped graded AlGaIn layers in the UV-LEDs. The calculated results suggested that the polarization dilution led to the lower operating voltage and the higher injection efficiency. Our actual 350 nm LED also showed a lower operating voltage, while

lower output power was simultaneously observed for some reason. However the result at high current injection indicates the potential of the polarization dilution. These results suggested such polarization-charge management is important in the nitride semiconductors.

**Acknowledgements** This study was supported by MEXT-Grants-in-Aid for Scientific Research Specially Promoted Research (#25000011), Grant-in-Aid for Scientific Research (B) (#26286045), Nippon Sheet Glass Foundation for Materials Science and Engineering, and The Asahi Glass Foundation.

## References

- [1] D. Morita, M. Yamamoto, K. Akaishi, K. Matoba, K. Yasutomo, Y. Kasai, M. Sano, S. Nagahama, and T. Mukai, *Jpn. J. Appl. Phys.* **43**, 5945 (2004).
- [2] M. Shatalov, W. Sun, A. Lunev, X. Hu, A. Dobrinsky, Y. Bilenko, J. Yang, M. Shur, R. Gaska, C. Moe, G. Garrett, and M. Wraback, *APEX* **5**, 082101 (2011).
- [3] H. Hirayama, S. Fujikawa, N. Noguchi, J. Norimatsu, T. Takano, K. Tsubaki, and N. Kamata, *Phys. Status Solidi A* **206**, 1176 (2009).
- [4] W. Gotz, N. M. Johnson, J. Walker, D. P. Bour, and R. A. Street, *Appl. Phys. Lett.* **68**, 667 (1996).
- [5] Y. Taniyasu, M. Kasu, and T. Makimoto, *Nature* **441**, 325 (2006).
- [6] H. Amano, K. Nagamatsu, K. Takeda, T. Mori, H. Tsuzuki, M. Iwaya, S. Kamiyama, and I. Akasaki, *Proc. SPIE* **7216**, 72161B (2009).
- [7] F. Bernardini, V. Fiorentini, and D. Vanderbilt, *Phys. Rev. B* **56**, R10024 (1997).
- [8] T. Takeuchi, S. Sota, M. Katsuragawa, M. Komori, H. Takeuchi, H. Amano, and I. Akasaki, *Jpn. J. Appl. Phys.* **36**, L382 (1997).
- [9] M. A. Khan, J. M. van Hove, J. N. Kuznia, and D. T. Olsen, *Appl. Phys. Lett.* **58**, 2408 (1991).
- [10] D. Jena, S. Heikman, D. Green, D. Buttari, R. Coffie, H. Xing, S. Keller, S. DenBaars, J. Speck, U. K. Mishra, and I. Smorchkova, *Appl. Phys. Lett.* **81**, 4395 (2002).
- [11] J. Simon, V. Protasenko, C. Lian, H. Xing, and D. Jena, *Science* **327**, 60 (2010).
- [12] J. Verma, J. Simon, V. Protasenko, T. Kosel, H. G. Xing, and D. Jena, *Appl. Phys. Lett.* **99**, 171104 (2011).
- [13] T. Yasuda, K. Yagi, T. Suzuki, T. Nakashima, M. Watanabe, T. Takeuchi, S. Kamiyama, M. Iwaya, and I. Akasaki, *Jpn. J. Appl. Phys.* **52**, 08JJ05 (2013).

## Electron and hole accumulations at GaN/AlInN/GaN interfaces and conductive n-type AlInN/GaN distributed Bragg reflectors

This content has been downloaded from IOPscience. Please scroll down to see the full text.

2016 Jpn. J. Appl. Phys. 55 05FD10

(<http://iopscience.iop.org/1347-4065/55/5S/05FD10>)

View [the table of contents for this issue](#), or go to the [journal homepage](#) for more

Download details:

IP Address: 219.127.71.134

This content was downloaded on 03/03/2017 at 06:40

Please note that [terms and conditions apply](#).

You may also be interested in:

[Room-temperature continuous-wave operation of GaN-based vertical-cavity surface-emitting lasers with n-type conducting AlInN/GaN distributed Bragg reflectors](#)

Kazuki Ikeyama, Yugo Kozuka, Kenjo Matsui et al.

[Relationship between lattice relaxation and electrical properties in polarization doping of graded AlGaIn with high AlN mole fraction on AlGaIn template](#)

Toshiki Yasuda, Tetsuya Takeuchi, Motoaki Iwaya et al.

[The effect of AlN interlayer thicknesses on scattering processes in lattice-matched AlInN/GaN two-dimensional electron gas heterostructures](#)

A Teke, S Gökden, R Tülek et al.

[Current status of AlInN layers lattice-matched to GaN for photonics and electronics](#)

R Butté, J-F Carlin, E Feltin et al.

[Investigations of Polarization-Induced Hole Accumulations and Vertical Hole Conductions in GaN/AlGaIn Heterostructures](#)

Toshiki Yasuda, Kouta Yagi, Tomoyuki Suzuki et al.

[Characterization of electrical properties of AlGaIn/GaN interface using coupled Schrödinger and Poisson equation](#)

S. Das, A. K. Panda and G. N. Dash

[MOVPE of device-oriented wide-band-gap III-N heterostructures](#)

W V Lundin, A V Sakharov, A F Tsatsulnikov et al.

[Mobility limiting scattering mechanisms in nitride-based two-dimensional heterostructures](#)

S Gökden, R Tülek, A Teke et al.



# Electron and hole accumulations at GaN/AlInN/GaN interfaces and conductive n-type AlInN/GaN distributed Bragg reflectors

Shotaro Yoshida<sup>1\*</sup>, Kazuki Ikeyama<sup>1</sup>, Toshiki Yasuda<sup>1</sup>, Takashi Furuta<sup>1</sup>, Tetsuya Takeuchi<sup>1</sup>, Motoaki Iwaya<sup>1</sup>, Satoshi Kamiyama<sup>1</sup>, and Isamu Akasaki<sup>1,2</sup>

<sup>1</sup>Faculty of Science and Technology, Meijo University, Nagoya 468-8502, Japan

<sup>2</sup>Akasaki Research Center, Nagoya University, Nagoya 464-8603, Japan

Received December 31, 2015; accepted February 9, 2016; published online April 21, 2016

We investigated electron and hole accumulations at GaN/AlInN/GaN interfaces by Hall effect measurement. The InN mole fraction and temperature dependences on the sheet carrier densities at the interfaces reveal that electrons and holes were induced by large positive and negative polarization charges to satisfy the charge neutrality conditions, respectively. On the basis of the above results, we then designed and demonstrated a low-resistivity 10-pair Si-doped n-type AlInN/GaN distributed Bragg reflector (DBR) by using high Si doped and graded layers at the GaN/AlInN interfaces. The low-resistivity n-type AlInN/GaN DBR will reduce the resistance and the internal loss in blue vertical-cavity surface emitting lasers. © 2016 The Japan Society of Applied Physics

## 1. Introduction

AlInN is one of the important nitride-based alloys, which can be lattice-matched to GaN, so that a high-quality AlInN/GaN heterostructure can be achieved instead of a conventional AlGaInN/GaN. In optoelectronic devices, a thick AlInN cladding layer<sup>1,2)</sup> and an AlInN/GaN distributed Bragg reflector (DBR)<sup>3-5)</sup> were reported. One of the disadvantages in growing thick AlInN had been the very low growth rate (less than 0.2  $\mu\text{m}/\text{h}$ <sup>6-8)</sup> like GaInN alloys,<sup>9,10)</sup> but recently, a relatively high growth rate,  $\sim 0.5 \mu\text{m}$ , of the AlInN has been obtained by using a combination of high growth temperature and high In/III ratio.<sup>11)</sup> Now, a low-resistivity current injection in the vertical direction of the AlInN/GaN interfaces is required for various optoelectronic device applications. In this case, a large hetero barrier ( $\sim 0.9 \text{ eV}$ ) at the AlInN/GaN interface in the lattice matching<sup>12)</sup> could lead to a high resistance, and a graded layer between AlInN and GaN should be a solution as already proved in the AlGaAs/GaAs system.<sup>13,14)</sup>

On the other hand, it is well known that large polarization charges are induced at nitride-based hetero-interfaces,<sup>15,16)</sup> and the lattice-matched AlInN/GaN is not an exception.<sup>17)</sup> That is why a large electron accumulation to positive polarization charges at the AlInN/GaN interface is leveraged in a heterostructure field-effect transistor structure.<sup>18,19)</sup> Then, a hole accumulation to negative polarization charges was observed at a GaN/AlGaInN interface<sup>20)</sup> in turn, and the AlN mole fraction dependence on the sheet hole density was systematically investigated.<sup>21)</sup> Thus, the hole accumulation and its mole fraction dependence should be observed at the AlInN/GaN interface in the same manner, but such systematic investigations have not been performed yet. The important thing is that not only the large hetero barrier height but also such large negative polarization charges (and hole accumulations) at the AlInN/GaN surely affect the current injection across the AlInN/GaN interface.

In this study, we first investigated not only electron but also hole accumulations to the GaN/AlInN/GaN interface charges. The InN mole fraction and temperature dependences on the sheet carrier densities at the interface were systematically investigated. On the basis of the results, we then

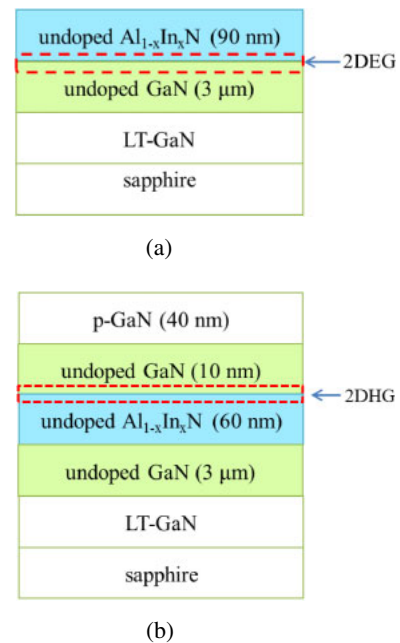


**Fig. 1.** (Color online) Sample structures (a) for the electron accumulation at the bottom AlInN/GaN interface, and (b) for the hole accumulation at the top GaN/AlInN interface.

designed and demonstrated conductive n-type AlInN/GaN DBRs with high Si doped and graded layers.

## 2. Experiment methods

All the samples were grown on *c*-plane sapphire substrates by metalorganic vapor phase epitaxy. In this study, we prepared two series of samples. One is a series of test structures for Hall effect measurement to investigate the electron and hole accumulations at AlInN/GaN in the lattice matching and GaN/AlInN interfaces with various InN mole fractions, respectively. The other is a series of Si-doped 10-pair AlInN/GaN DBRs to investigate vertical current injection through the DBRs.

Figures 1(a) and 1(b) show sample structures for the electron accumulation at the interface of the AlInN/GaN (the bottom interface of the AlInN) and for the hole accumulation at the interface of the GaN/AlInN interface (the top interface

of the AlInN), respectively. The electron accumulation structure, the so-called two-dimensional electron gas (2DEG), consists of a 20 nm low-temperature-deposited GaN buffer layer (LT-GaN), a 3 μm undoped GaN, and a 90 nm undoped AlInN. Six samples with various InN mole fractions from 0.13 to 0.23 in the AlInN were prepared. The hole accumulation structure, the so-called two-dimensional hole gas (2DHG), consists of the LT-GaN, the undoped GaN, a 60 nm undoped AlInN, a 10 nm undoped GaN and, a 40 nm p-GaN contact layer. Four samples with various InN mole fractions from 0.16 to 0.21 in the AlInN were prepared. X-ray diffraction (XRD) patterns of  $2\theta/\omega$  scan around the 0002 peak were measured to determine the InN mole fractions in the AlInN layers. The sheet carrier densities at the interfaces were measured by Hall effect measurement. Electrodes for the 2DEG and 2DHG samples were Cr/Ni/Au and Ni/Au, respectively. In addition, we determined the temperature dependence of sheet carrier density by low-temperature Hall effect measurement.

Regarding the 10-pair Si-doped AlInN/GaN DBRs, four different samples were prepared. After growing a 2 μm Si-doped GaN layer on the sapphire substrate, 10 pairs of about 45 nm AlInN and about 40 nm GaN were grown. The InN mole fraction of the AlInN was adjusted to be 0.18 to be lattice-matched to the GaN. Graded layers and high Si doping at the top interfaces were investigated to see if better vertical current injections through the DBRs were obtained. A standard DBR was uniformly doped with Si ( $3 \times 10^{18} \text{ cm}^{-3}$  in GaN and  $1 \times 10^{19} \text{ cm}^{-3}$  in AlInN), as shown in Fig. 2(a). Note that the Si concentrations were measured by secondary ion mass spectroscopy with reference samples of GaN:Si and AlN:Si for calibration. A graded DBR was formed by using 9 nm graded AlGaInN layers at all the top interfaces of the AlInN in the standard DBR, as shown in Fig. 2(b). The compositional graded AlGaInN layer was grown by changing Al, In, and Ga source flow rates from a condition of AlInN to a condition of GaN. A modulation-doped DBR consisted of 10 pairs of a 35.5 nm standard Si-doped ( $3 \times 10^{18} \text{ cm}^{-3}$ ) GaN, a 4.5 nm highly Si-doped ( $1 \times 10^{19} \text{ cm}^{-3}$ ) GaN, a 4.5 nm highly Si-doped ( $5 \times 10^{19} \text{ cm}^{-3}$ ) AlInN, and a 35.5 nm standard Si-doped ( $1 \times 10^{19} \text{ cm}^{-3}$ ) AlInN, as shown in Fig. 2(c). Finally, a graded/modulation-doped DBR was formed by a combination of the graded DBR and the modulation-doped DBR, as shown in Fig. 2(d). To measure the vertical conductance of the 10-pair DBRs, a 60 μm mesa was formed by etching the entire 10-pair DBRs to expose an underlying n-GaN and depositing the top and bottom n-type electrodes. Then, the current–voltage ( $I$ – $V$ ) characteristics of the mesa DBRs were measured at room temperature.

### 3. Results and discussion

Figures 3(a) and 3(b) show the XRD patterns of (0002)  $2\theta/\omega$  scan from the six AlInN/GaN structures for the investigation of electron accumulations [as shown in Fig. 1(a)] and the four GaN/AlInN/GaN structures for the investigation of hole accumulations [as shown in Fig. 1(b)], respectively. All the samples show not only strong single peaks but also clear Pendellösung fringes, meaning that the crystal and interface qualities of AlInN/GaN layers in the lattice matching were high. The InN mole fractions of the AlInN layers in the structures were then estimated as indicated in the figures.

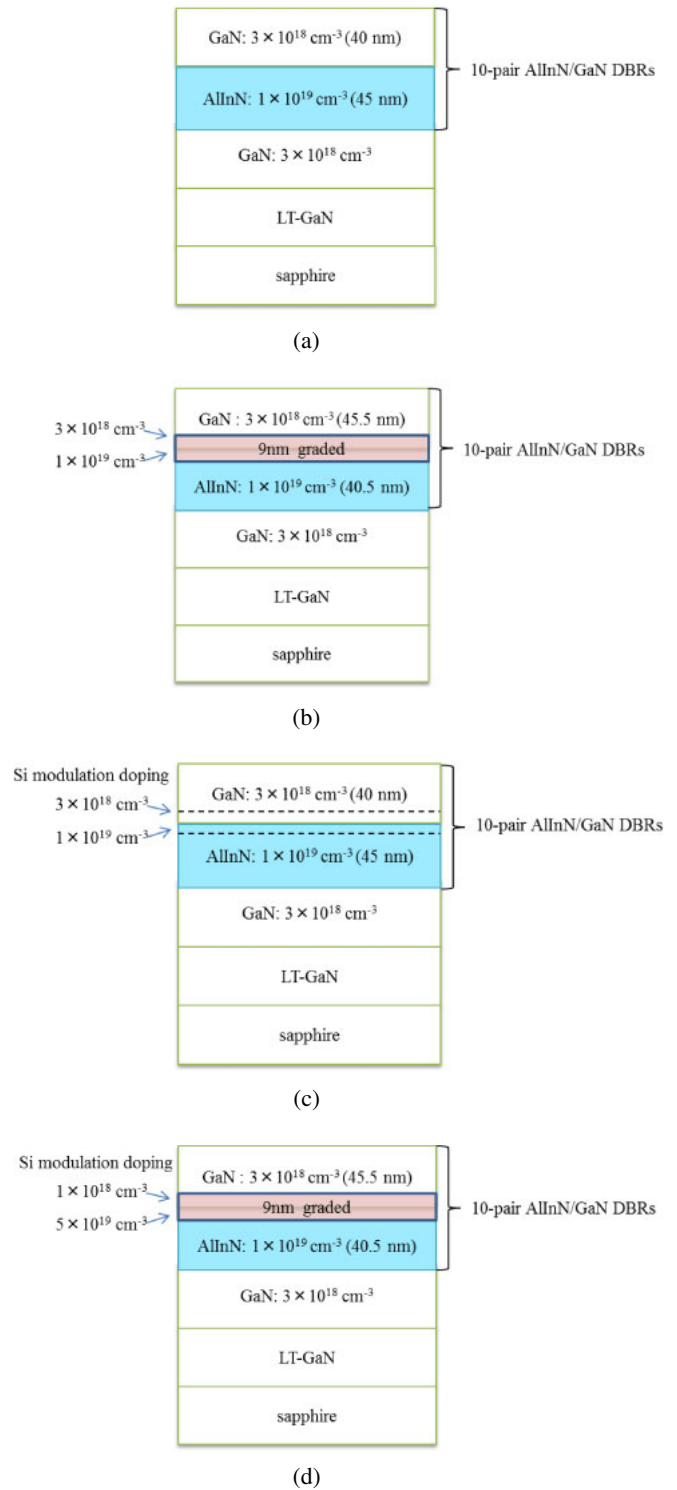


**Fig. 2.** (Color online) One pair of layer structures in the Si-doped AlInN/GaN DBRs. (a) Standard DBR uniformly doped with Si ( $3 \times 10^{18} \text{ cm}^{-3}$  in GaN and  $1 \times 10^{19} \text{ cm}^{-3}$  in AlInN), (b) graded DBR formed with a 9 nm graded AlGaInN layer at the top interface of the AlInN, (c) modulation-doped DBR consisting of a 35.5 nm standard Si-doped GaN, a 4.5 nm highly Si-doped GaN, a 4.5 nm highly Si-doped ( $5 \times 10^{19} \text{ cm}^{-3}$ ) AlInN, and a 35.5 nm standard Si-doped ( $1 \times 10^{19} \text{ cm}^{-3}$ ) AlInN, and (d) graded/modulation-doped DBR formed by a combination of the graded DBR and the modulation-doped DBR.

Next, we investigated the electrical properties of the samples by Hall effect measurement. Clear n-type conductivity was obtained in the samples shown in Fig. 1(a) even without any Si doping. The measured sheet electron concentrations at the bottom interfaces as a function of InN mole

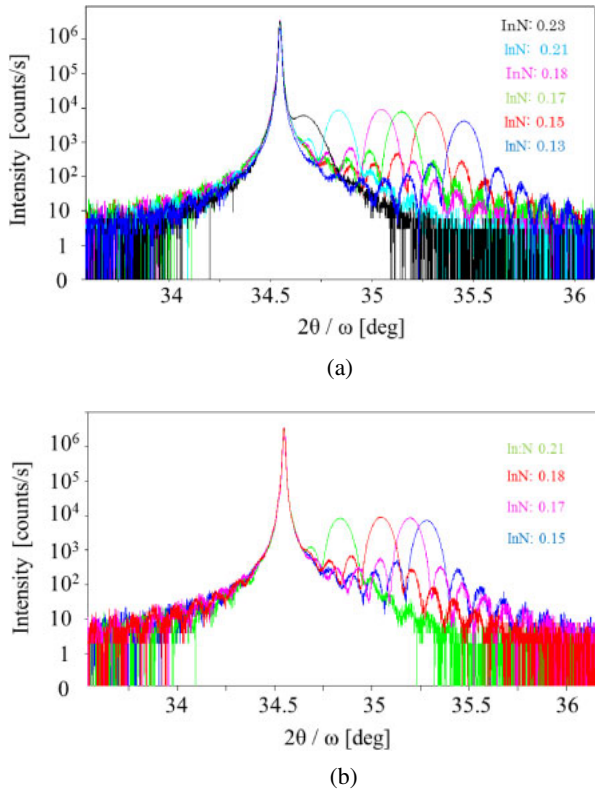


**Fig. 3.** (Color online) XRD patterns of (0002)  $2\theta/\omega$  scan (a) from the six AlInN/GaN structures [as shown in Figs. 1(a) and 1(b)] from the four GaN/AlInN structures [as shown in Fig. 1(b)]. The  $34.5^\circ$  peak is GaN, and the other peak is AlInN.

fraction are plotted with the red squares in Fig. 4(a). In addition, theoretical positive polarization charge concentrations are also plotted in the same figure. The theoretical polarization charge density  $\sigma$  was calculated using the following equation:<sup>22)</sup>

$$\begin{aligned} \sigma &= P_{sp} + P_{pz} \\ &= P_{sp} + 2 \left( e_{31} - \frac{c_{13}}{c_{33}} e_{33} \right) \times \frac{a_s - a_e}{a_e}, \end{aligned} \quad (1)$$

where  $P_{sp}$  and  $P_{pz}$  are the spontaneous and piezoelectric polarization charge densities,  $e_{31}$  and  $e_{33}$  are the piezoelectric constants,  $c_{13}$  and  $c_{33}$  are the elastic constants, and  $a_e$  and  $a_s$  are the lattice constants of the AlInN layers and the underlying GaN layer, respectively. In this calculation, the material parameters listed in Table I were used, and all the AlInN parameters were estimated assuming Vegard's law. We found that the measured sheet electron concentrations as a function of InN mole fractions are in good agreement with the theoretical polarization charge concentrations, meaning that the electrons were accumulated to the positive polarization charges to satisfy the charge neutrality condition. Also, no temperature dependence on the sheet electron concentration was clearly observed, as shown in Fig. 4(b), indicating that electrons were not directly generated from nearby donor impurities.

Accordingly, p-type conductivity was clearly observed in the samples shown in Fig. 1(b) even with Mg doping just for the contact layer. The measured sheet hole concentrations at the top interfaces of AlInN as a function of InN mole fraction were plotted with the blue triangles in Fig. 5(a).

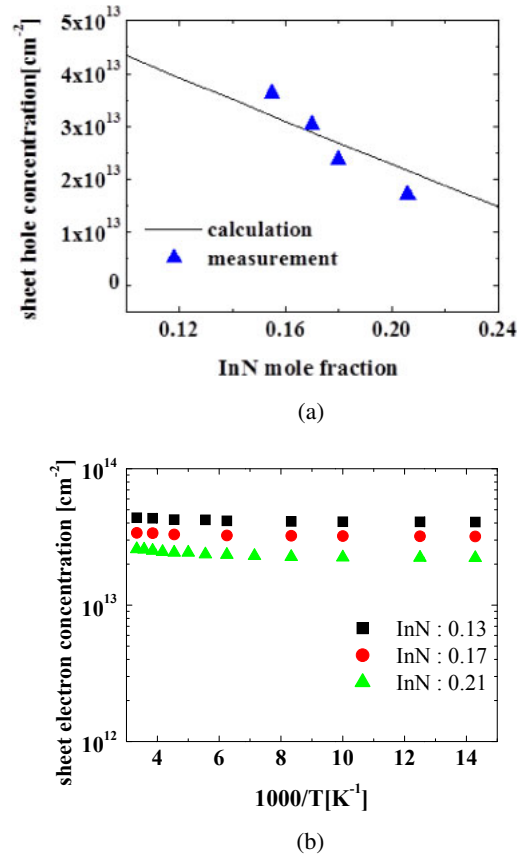


**Fig. 4.** (Color online) (a) Room-temperature sheet electron concentrations as a function of InN mole fractions at the bottom interface of the AlInN/GaN interface. The theoretical positive polarization charge densities are also plotted. (b) Temperature dependences on sheet electron concentrations at the bottom interface of the AlInN/GaN interface.

**Table I.** Material parameters used in the calculations.<sup>16,23)</sup>

	GaN	AlN	InN	AlInN
Lattice constant ( $\text{\AA}$ )				
$a$	3.189	3.112	3.548	$3.112x + 3.548(1-x)$
$c$	5.185	4.982	5.76	$4.982x + 5.760(1-x)$
Spontaneous polarization ( $\text{C/m}^2$ )				
$P_{sp}$	-0.029	-0.081	-0.032	$-0.081x - 0.032(1-x)$
Piezoelectric constant ( $\text{C/m}^2$ )				
$e_{31}$	-0.49	-0.6	-0.57	$-0.6x - 0.57(1-x)$
$e_{33}$	0.73	1.46	0.97	$1.46x + 0.97(1-x)$
Elastic constant (GPa)				
$c_{13}$	100	127	108	$127x + 108(1-x)$
$c_{33}$	392	382	399	$382x + 399(1-x)$

Similarly, theoretical negative polarization charge concentrations were plotted in the same figure. The measured sheet hole concentrations are in good agreement with the theoretical polarization charge concentrations. Also, almost no temperature dependence was observed in the sheet hole concentrations as shown in Fig. 5(b). Thus, we concluded that not just electrons but also holes are accumulated in the polarization charges, resulting in high carrier concentrations without standard impurity doping.

On the basis of the above results, a band diagram of undoped GaN/AlInN/GaN is depicted in Fig. 6. This figure

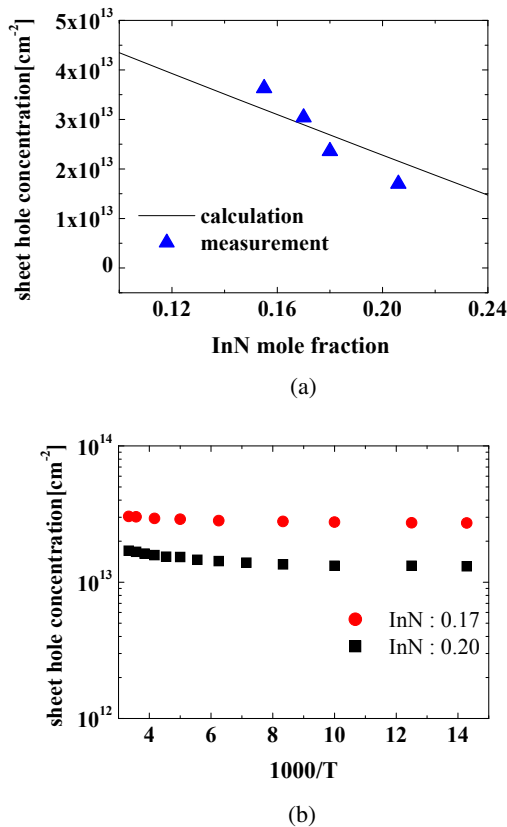


**Fig. 5.** (Color online) (a) Room-temperature sheet hole concentrations as a function of InN mole fractions at the top interface of the GaN/AlInN interface. The theoretical negative polarization charge densities are also plotted. (b) Temperature dependences on sheet hole concentrations at the top interface of the GaN/AlInN interface.

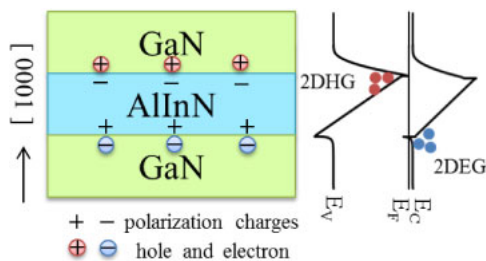


**Fig. 6.** (Color online) Band diagram of undoped GaN/AlInN/GaN.

clearly suggests that almost no Si doping is required at the bottom interfaces of AlInN while heavy Si doping is indispensable at the top interfaces of AlInN to obtain conductive n-type DBRs. This is the reason why we tried to utilize not only graded layers but also heavy Si doping in the AlInN/GaN DBRs. Actually, the large negative polarization charges could be neutralized with the ionized Si atoms,<sup>24</sup> so the amount of Si doping should be close to that of the polarization charge. For instance, the polarization sheet charge density at the Al<sub>0.83</sub>In<sub>0.17</sub>N/GaN is calculated and measured to be about  $3 \times 10^{13} \text{ cm}^{-2}$ , which corresponds to  $3 \times 10^{19} \text{ cm}^{-3}$  volume concentrations in a 10 nm layer. Thus, the 10 nm area around the GaN/AlInN interface should be doped with Si up to such a high concentration.

We then calculated the band profiles of the four AlInN/GaN DBRs described above by using a commercially available device simulator. Figure 7 shows the conduction

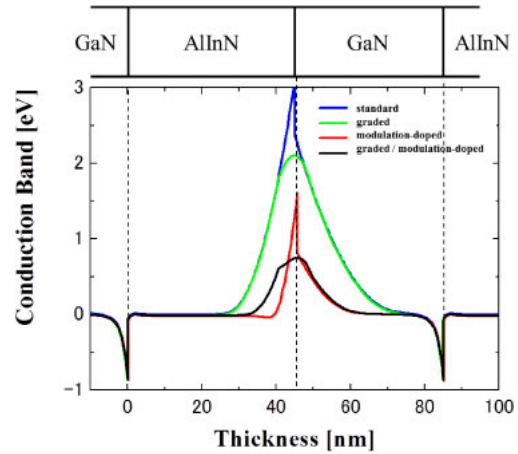


**Fig. 7.** (Color online) Conduction band profiles of one pair in the standard DBR, the graded DBR, the modulation-doped DBR, and the graded/modulation-doped DBR.

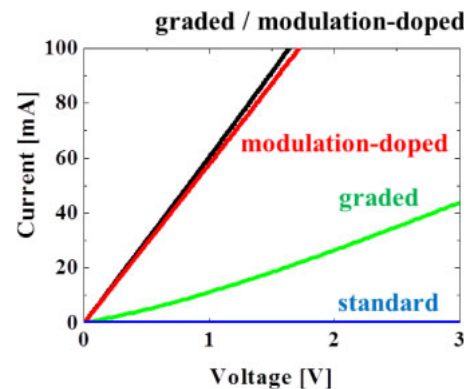


**Fig. 8.** (Color online) *I*-*V* characteristics of the standard DBR, the graded DBR, the modulation-doped DBR, and the graded/modulation-doped DBR.

band profiles of one pair in the four AlInN/GaN DBRs. Note that the Fermi level was set to be zero in Fig. 7. The calculated results clearly show that the graded layer and the Si modulation-doped at the top GaN/AlInN interfaces are very useful for reducing the potential height around the top interfaces.

Figure 8 shows the *I*-*V* characteristics of the four 10-pair Si-doped AlInN/GaN DBRs. The modulation-doped DBR and the graded/modulation-doped DBR showed clear ohmic characteristics with very low resistances. The graded/modulation-doped DBR showed the lowest resistance among the samples as the calculated results suggested. The values resistance is 16 Ω, but includes not only a vertical component of the DBR but also a lateral component of the underlying GaN, so the vertical resistance of the DBR must be smaller than 16 Ω. On the other hand, almost no current passed through the standard DBR within 3 V of the applied voltage range. Interestingly, the graded DBR showed some current flowing but a high resistance. The above results suggest that the layer with high Si doping is more effective than the graded layer to obtain the conductive n-type AlInN/GaN DBRs, meaning that the impact of the polarization charges on the electrical properties is huge in nitride-based materials. So far, laser operations of nitride-based vertical cavity surface emitting lasers (VCSELs) with undoped AlInN/GaN DBRs

were reported,<sup>25–27)</sup> and the undoped DBRs were not conductive at all, so that intracavity contacts must be used, resulting in high resistance and internal loss. As a result, such a conductive nitride-based DBR will lead to high-performance blue VCSELs, like the already commercialized infrared VCSELs with the conductive DBRs.<sup>28)</sup>

#### 4. Conclusions

We demonstrated the low-resistivity 10-pair Si-doped AlInN/GaN DBR by using the graded layer and high Si doping at the top interfaces of the AlInN layers. The reason for the high Si doping is to neutralize the large negative polarization charges at the interface which resulted in the large potential barrier. We also demonstrated electron and hole accumulations induced by the polarization charges at the interfaces by investigating InN mole fractions and temperature dependences on the sheet carrier densities measured by Hall effect measurement.

#### Acknowledgments

This study was supported by the MEXT Program for the Strategic Research Foundation at Private Universities, 2012–2016, Grants-in-Aid for Scientific Research Specially Promoted Research (No. 25000011), and Grant-in-Aid for Scientific Research (B) (No. 26286045).

- 1) A. Castiglia, E. Feltin, J. Dorsaz, G. Cosendey, J.-F. Carlin, R. Butté, and N. Grandjean, *Electron. Lett.* **44**, 521 (2008).
- 2) R. Charash, H. Kim-Chauveau, J.-M. Lamy, M. Akther, P. P. Maaskant, E. Frayssinet, P. de Mierry, A. D. Dräger, J.-Y. Duboz, A. Hangleiter, and B. Corbett, *Appl. Phys. Lett.* **98**, 201112 (2011).
- 3) J.-F. Carlin, J. Dorsaz, E. Feltin, R. Butté, N. Grandjean, M. Ilegems, and M. Lügt, *Appl. Phys. Lett.* **86**, 031107 (2005).
- 4) H. Ishikawa, T. Jimbo, and T. Egawa, *Phys. Status Solidi C* **5**, 2086 (2008).
- 5) A. Krost, C. Berger, J. Bläsing, A. Franke, T. Hempel, A. Dadgar, and J. Christen, *Appl. Phys. Lett.* **97**, 181105 (2010).
- 6) S. Yamaguchi, M. Kariya, S. Nitta, T. Takeuchi, C. Wetzel, H. Amano, and

- I. Akasaki, *Appl. Phys. Lett.* **73**, 830 (1998).
- 7) J.-F. Carlin and M. Ilegems, *Appl. Phys. Lett.* **83**, 668 (2003).
- 8) T. C. Sadler, M. J. Kappers, and R. A. Oliver, *J. Cryst. Growth* **314**, 13 (2011).
- 9) N. Yoshimoto, T. Matsuoka, T. Sasaki, and A. Katsui, *Appl. Phys. Lett.* **59**, 2251 (1991).
- 10) S. Nakamura, T. Mukai, and M. Senoh, *Jpn. J. Appl. Phys.* **32**, L16 (1993).
- 11) Y. Kozuka, K. Ikeyama, T. Yasuda, T. Takeuchi, S. Kamiyama, M. Iwaya, and I. Akasaki, *MRS Proc.* **1736**, mrsf14-1736-t13-08 (2015).
- 12) M. Akazawa, T. Matsuyama, T. Hashizume, M. Hiroki, S. Yamahata, and N. Shigekawa, *Appl. Phys. Lett.* **96**, 132104 (2010).
- 13) R. S. Geels, S. W. Corzine, J. W. Scott, D. B. Young, and L. A. Corliden, *IEEE Photonics Technol. Lett.* **2**, 234 (1990).
- 14) K. Tai, L. Yang, Y. H. Wang, J. D. Wynn, and A. Y. Cho, *Appl. Phys. Lett.* **56**, 2496 (1990).
- 15) T. Takeuchi, S. Sota, M. Katsuragawa, M. Komori, H. Takeuchi, H. Amano, and I. Akasaki, *Jpn. J. Appl. Phys.* **36**, L382 (1997).
- 16) F. Bernardini, V. Fiorentini, and D. Vanderbilt, *Phys. Rev. B* **56**, R10024 (1997).
- 17) R. Butté, J.-F. Carlin, E. Feltin, M. Gonschorek, S. Nicolay, G. Christmann, D. Simeonov, A. Castiglia, J. Dorsaz, H. J. Buehlmann, S. Christopoulos, G. Baldassarri Höger von Högersthal, A. J. D. Grundy, M. Mosca, C. Pinquier, M. A. Py, F. Demangeot, J. Frandon, P. G. Lagoudakis, J. J. Baumberg, and N. Grandjean, *J. Phys. D* **40**, 6328 (2007).
- 18) J. Kuzmík, *Semicond. Sci. Technol.* **17**, 540 (2002).
- 19) A. Dadgar, F. Schulze, J. Bläsing, A. Diez, A. Krost, M. Neuburger, E. Kohn, I. Daumiller, and M. Kunze, *Appl. Phys. Lett.* **85**, 5400 (2004).
- 20) A. Nakajima, Y. Sumida, M. H. Dhyani, H. Kawai, and E. M. S. Narayanan, *Appl. Phys. Express* **3**, 121004 (2010).
- 21) T. Yasuda, K. Yagi, T. Suzuki, T. Nakashima, M. Watanabe, T. Takeuchi, M. Iwaya, S. Kamiyama, and I. Akasaki, *J. Appl. Phys.* **52**, 08JJ05 (2013).
- 22) E. T. Yu and M. O. Manasreh, *III–V Nitride Semiconductors Applications and Devices* (Taylor & Francis, London, 2003) Vol. 16, Chap. 4, p. 161.
- 23) K. Kim, W. R. L. Lambrecht, and B. Segall, *Phys. Rev. B* **53**, 16310 (1996).
- 24) T. Yasuda, K. Hayashi, S. Katsuno, T. Takeuchi, S. Kamiyama, M. Iwaya, I. Akasaki, and H. Amano, *Phys. Status Solidi A* **212**, 920 (2015).
- 25) G. Cosendey, A. Castiglia, G. Roszbach, J.-F. Carlin, and N. Grandjean, *Appl. Phys. Lett.* **101**, 151113 (2012).
- 26) T. Furuta, K. Matsui, K. Horikawa, K. Ikeyama, Y. Kozuka, S. Yoshida, T. Akagi, T. Takeuchi, S. Kamiyama, M. Iwaya, and I. Akasaki, ISGN-6, 2015, We-B8.
- 27) K. Matsui, Y. Kozuka, K. Ikeyama, K. Horikawa, T. Furuta, T. Akagi, S. Iwayama, N. Koide, T. Takeuchi, S. Kamiyama, M. Iwaya, and I. Akasaki, MRS Fall Meet., 2015, RR8.03.
- 28) W. W. Chow, K. D. Choquette, M. H. Crawford, K. L. Lear, and G. R. Hadley, *IEEE J. Quantum Electron.* **33**, 1810 (1997).

## High-photosensitivity AlGa<sub>N</sub>-based UV heterostructure-field-effect-transistor-type photosensors

This content has been downloaded from IOPscience. Please scroll down to see the full text.

2016 Jpn. J. Appl. Phys. 55 05FJ04

(<http://iopscience.iop.org/1347-4065/55/5S/05FJ04>)

View [the table of contents for this issue](#), or go to the [journal homepage](#) for more

Download details:

IP Address: 219.127.71.134

This content was downloaded on 03/03/2017 at 06:41

Please note that [terms and conditions apply](#).

You may also be interested in:

[Realization of high-performance hetero-field-effect-transistor-type ultraviolet photosensors using p-type GaN comprising three-dimensional island crystals](#)

Yuma Yamamoto, Akira Yoshikawa, Toshiki Kusafuka et al.

[Control of the Detection Wavelength in AlGa<sub>N</sub>/GaN-Based Hetero-Field-Effect-Transistor Photosensors](#)

Mami Ishiguro, Kazuya Ikeda, Masataka Mizuno et al.

[All AlGa<sub>N</sub> epitaxial structure solar-blind avalanche photodiodes with high efficiency and high gain](#)

Hualong Wu, Weicong Wu, Hongxian Zhang et al.

[Ultraviolet photodiodes based on AlGa<sub>N</sub> solid solutions](#)

I Lamkin and S Tarasov

[Solar-Blind UV Photodetectors Based on GaN/AlGa<sub>N</sub> p-i-n Photodiodes](#)

Cyril Pernot, Akira Hirano, Motoaki Iwaya et al.

[Comparison of AlGa<sub>N</sub> p-i-n ultraviolet avalanche photodiodes grown on free-standing GaN and sapphire substrates](#)

Jeomoh Kim, Mi-Hee Ji, Theeradetch Detchprohm et al.

[Recent progress and future prospects of AlGa<sub>N</sub>-based high-efficiency deep-ultraviolet light-emitting diodes](#)

Hideki Hirayama, Noritoshi Maeda, Sachie Fujikawa et al.

[Laser diodes with 353 nm wavelength enabled by reduced-dislocation-density AlGa<sub>N</sub> templates](#)

Mary H. Crawford, Andrew A. Allerman, Andrew M. Armstrong et al.



## High-photosensitivity AlGa<sub>N</sub>-based UV heterostructure-field-effect-transistor-type photosensors

Akira Yoshikawa<sup>1,2\*</sup>, Yuma Yamamoto<sup>1</sup>, Takuya Murase<sup>1</sup>, Motoaki Iwaya<sup>1</sup>, Tetsuya Takeuchi<sup>1</sup>, Satoshi Kamiyama<sup>1</sup>, and Isamu Akasaki<sup>1,3</sup>

<sup>1</sup>Faculty of Science and Technology, Meijo University, Nagoya 468-8502, Japan

<sup>2</sup>Asahi Kasei Corporation, Fuji, Shizuoka 416-8501, Japan

<sup>3</sup>Akasaki Research Center, Nagoya University, Nagoya 464-8603, Japan

\*E-mail: yoshikawa.ac@om.asahi-kasei.co.jp

Received November 5, 2015; accepted January 4, 2016; published online April 5, 2016

We report the development of high-performance AlGa<sub>N</sub>/AlN heterostructure-field-effect-transistor-type (HFET) photosensors with a p-type Ga<sub>N</sub> optical gate and detection wavelengths that are restricted to 220–280 nm. These photosensors employ a two-dimensional electron gas induced at the hetero-interface between Al<sub>0.6</sub>Ga<sub>0.4</sub>N and Al<sub>0.5</sub>Ga<sub>0.5</sub>N as a highly conductive channel. In addition, a p-type Ga<sub>N</sub> optical gate is employed to deplete a channel. Consequently, we obtained a high photosensitivity of over  $4 \times 10^3$  A/W and an externally low dark current density of approximately  $5 \times 10^{-10}$  A/mm at a source–drain voltage of 3 V. We also determined that the detection range of light wavelength in these HFET photosensors can be controlled by controlling the AlN molar fraction in the AlGa<sub>N</sub> channel layer. The results are very promising for the development of completely solar-blind high-performance photosensors with high photosensitivity.

© 2016 The Japan Society of Applied Physics

### 1. Introduction

Group-III nitride semiconductors are widely used as light-emitting diodes (LEDs)<sup>1–4</sup> and laser diodes.<sup>5,6</sup> Since the band gap of AlGa<sub>N</sub> ternary alloys covers a broad range from 3.39 to 6.2 eV at room temperature,<sup>7,8</sup> these alloys are suitable as UV emitters and in photosensor applications.<sup>9–13</sup> Recently, high-performance UV LEDs with an external quantum efficiency close to 10% have been developed for sterilization and medical applications.<sup>14–18</sup> To make these UV LEDs practical, photosensors are indispensable.

The photosensors are required to be small, durable, low-cost, solar-blind and highly sensitive, and possess a high rejection ratio. Furthermore, the most important feature is that the detection wavelength must be freely controlled. The detection of specific wavelengths leads to detection of flames or organic matter, which is advantageous. In the case of a flame sensor, the detection of a specific wavelength is very important because almost all wavelengths from a flame are buried under sunlight and only a 250 to 280 nm peak is separated from sunlight.<sup>19</sup>

Until now, photomultiplier tubes (PMTs) or Si-based photodiodes with a visible light cut-off filter have been used as UV sensors.<sup>20,21</sup> However, even with its high photosensitivity, there are issues regarding PMT miniaturization, such as cost, heat resistance, and high operating voltage. Furthermore, the Si-based photodiodes is up to four orders of magnitude lower than that of PMTs. Nitride semiconductors have the potential to solve the above-mentioned problem of PMTs and Si photodiodes. Thus far, we have reported high-sensitivity AlGa<sub>N</sub>/Ga<sub>N</sub> heterostructure-field-effect-transistor-type (HFET) photosensors with a p-type Ga<sub>N</sub> optical gate.<sup>22,23</sup> These photosensors employ a two-dimensional electron gas (2DEG) induced at the hetero-interface between AlGa<sub>N</sub> and Ga<sub>N</sub> as a highly conductive channel. Although these sensors exhibited a high photosensitivity of  $10^5$  A/W, they detected all wavelengths lower than 365 nm.

We assumed that the detection wavelength is in accordance with the band gap of the channel layer. Therefore, we tried to

control the detection wavelength by changing the AlN molar fraction of the AlGa<sub>N</sub> channel layer.

In this study, we employed an Al<sub>0.5</sub>Ga<sub>0.5</sub>N channel layer because a band gap of 4.5 eV was required to detect 280 nm UV light. However, the fabrication of an AlGa<sub>N</sub>/AlGa<sub>N</sub> HFET is a big challenge. One reason for this is the pre-reaction between Al and NH<sub>3</sub>.<sup>24</sup> The higher the Al molar fraction of AlGa<sub>N</sub>, the more drastic the reaction. Therefore, investigating optimum growth condition is important. The other reason is that many cracks are generated because of the tensile stress between AlGa<sub>N</sub> and the Ga<sub>N</sub> substrate.<sup>25</sup> An AlN substrate or an AlN template substrate is efficient at solving this problem because it has a smaller lattice size than Ga<sub>N</sub>. Moreover, there are other problems; only a 1-in. AlN substrate could be obtained and the crystallinity of an AlN template substrate is worse than that of a Ga<sub>N</sub> template substrate.<sup>26,27</sup>

For the above reasons, until Akita et al. reported an Al<sub>0.51</sub>Ga<sub>0.49</sub>N-based HEMT, there were only a few reports of AlGa<sub>N</sub>/AlGa<sub>N</sub>-HEMT and the AlN molar fraction  $x$  of Al <sub>$x$</sub> Ga<sub>1– $x$</sub> N was lower than 0.4.<sup>28</sup>

In this study, we fabricated high-performance AlGa<sub>N</sub>/AlGa<sub>N</sub> HFET photosensors with a p-Ga<sub>N</sub> optical gate on high-quality AlN template substrates for the detection of wavelengths that are restricted to 220–280 nm. We will also show that the AlN molar fraction of the AlGa<sub>N</sub> channel layer is the key to controlling the detection wavelength.

### 2. Experimental Procedure

Figure 1 shows a schematic view of an AlGa<sub>N</sub> HFET-type photosensor with a p-type Ga<sub>N</sub> optical gate. The device was grown using metalorganic vapor phase epitaxy on a sapphire (0001) substrate. The growth condition of the AlN template was based on a previous report.<sup>29</sup> After the growth of a 1.8- $\mu$ m AlN layer, a 320-nm unintentionally doped Al<sub>0.5</sub>Ga<sub>0.5</sub>N layer, a 35-nm unintentionally doped Al<sub>0.6</sub>Ga<sub>0.4</sub>N barrier layer, and a 100-nm Mg-doped p-Ga<sub>N</sub> layer with a Mg concentration of  $2 \times 10^{19}$  cm<sup>-3</sup> was grown. The Al molar fraction  $x$  of Al <sub>$x$</sub> Ga<sub>1– $x$</sub> N was determined using  $2\theta/\omega$  scans and

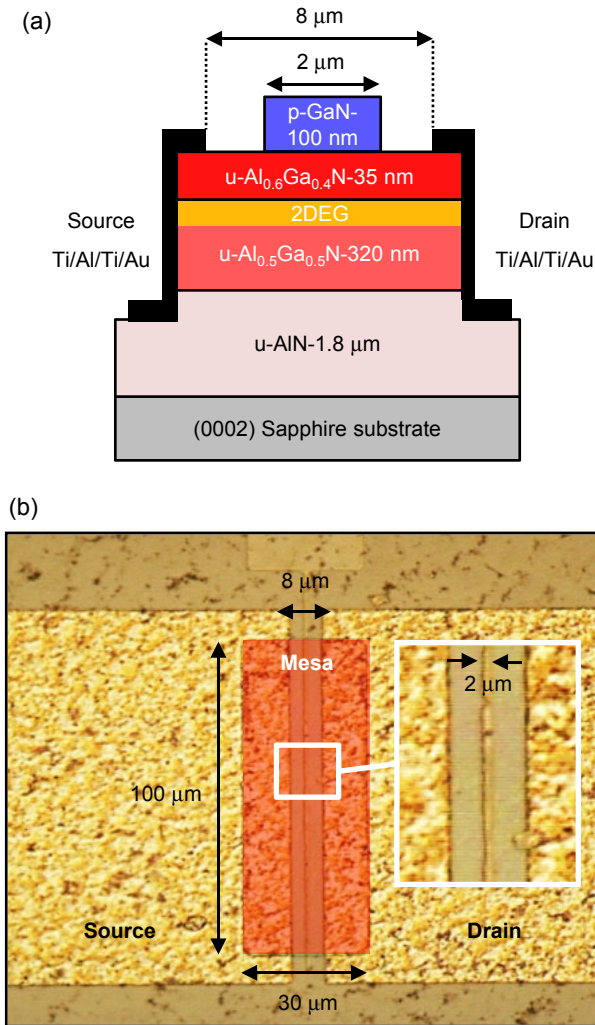


**Fig. 1.** (Color online) Schematic views of the device structure: (a) cross-sectional view and (b) plan view.

reciprocal space mapping measurements with X-ray diffraction. The Mg acceptors were activated by annealing at 850 °C for 5 min in N<sub>2</sub>. Mesa isolation was performed using Cl<sub>2</sub> inductively coupled plasma (ICP) etching. The p-type GaN optical gate was etched using ICP etching, except in the light-detection area. Then, Ti (30 nm)/Al (100 nm)/Ti (20 nm)/Au (150 nm) was deposited as the source and drain electrodes on the u-Al<sub>0.6</sub>Ga<sub>0.4</sub>N barrier layer and annealed at 810 °C in N<sub>2</sub>. The length and width of the p-GaN optical gate were 2 and 100 μm, respectively, and the interval between the source and drain electrodes was 8 μm. No anti-reflection coating was used for any of the devices in this study.

The photocurrent at each light wavelength (220–1100 nm) was measured using a semiconductor parameter analyzer (HP-4155B) and a spectroscope with a Xe lamp (HAL-320) at room temperature (RT). Furthermore, the photocurrent was measured under room lighting conditions and air mass (AM) 1.5G pseudo sunlight (HAL-320), respectively. The photosensitivity was calculated from the photocurrent, light-detection area, and irradiation density of the spectroscope, respectively. In this study, we employed a monochromatic light irradiation density of approximately 45 μW/cm<sup>2</sup> and a light-detection area of 200 μm<sup>2</sup>. For the evaluation of the sensor as a flame sensor, a Bunsen burner was used to produce a flame and was placed 10 cm from the sensor.

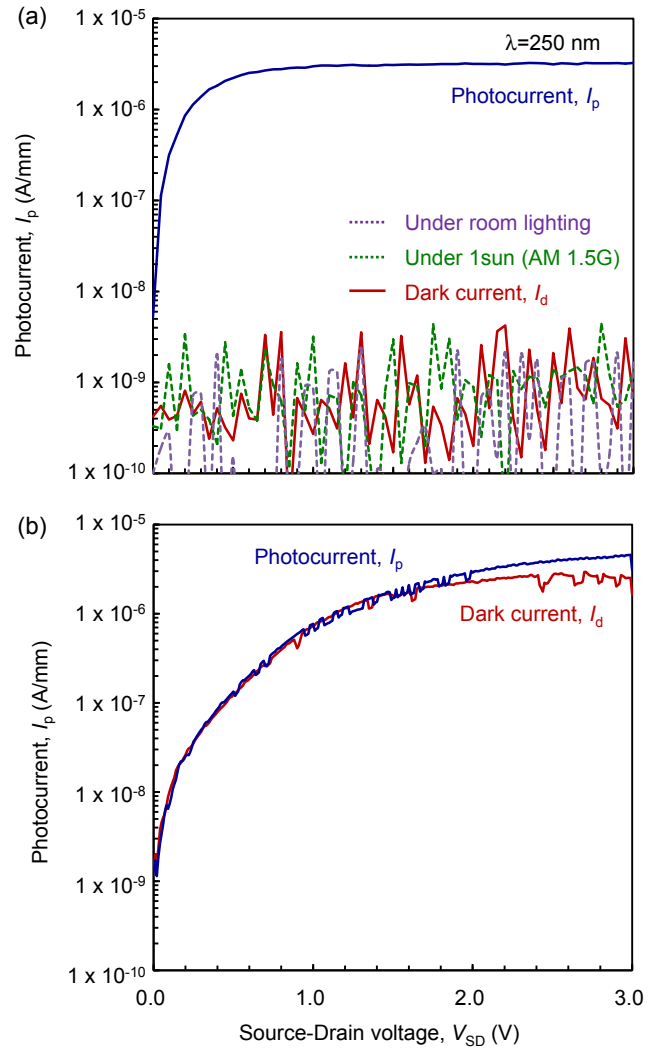


**Fig. 2.** (Color online)  $I_{SD}$ - $V_{SD}$  characteristics of the Al<sub>0.6</sub>Ga<sub>0.4</sub>N/Al<sub>0.5</sub>Ga<sub>0.5</sub>N HFET photosensors at RT in the  $V_{SD}$  range from 0 to 3 V with and without irradiation from a UV lamp ( $\lambda = 250$  nm, irradiation density = 45 μW/cm<sup>2</sup>). (a) With and (b) without an optical p-type GaN gate.

### 3. Results and Discussion

Figure 2 shows the  $I_{SD}$ - $V_{SD}$  characteristics of the HFET photosensors (a) with and (b) without an optical p-type GaN gate. The photocurrent from UV light irradiation at 250 nm (irradiation density: 45 μW/cm<sup>2</sup>) and the dark current at RT were measured. An extremely low dark current of  $5 \times 10^{-10}$  A/mm was obtained using the HFET in the presence of an optical p-GaN gate when  $V_{SD}$  was 3 V, as shown in Fig. 2(a). This dark current was almost the same as the measurement limit of our measurement system. In contrast, a large dark current of approximately  $1 \times 10^{-6}$  A/mm was observed when using HFET photosensors without an optical p-GaN gate when  $V_{SD}$  was 3 V, as shown in Fig. 2(b).

In addition, we compared the photocurrents of photosensors with an optical p-GaN gate under room lighting conditions and an AM 1.5 G solar simulator (HAL-320) at a light intensity of 1 sun. Consequently, we measured a photocurrent of  $5.7 \times 10^{-10}$  A/mm under room lighting conditions and  $1.1 \times 10^{-9}$  A/mm under 1 sun (AM 1.5 G). These values are in an order of magnitude equal to that of the dark current. The results indicate that the photosensors

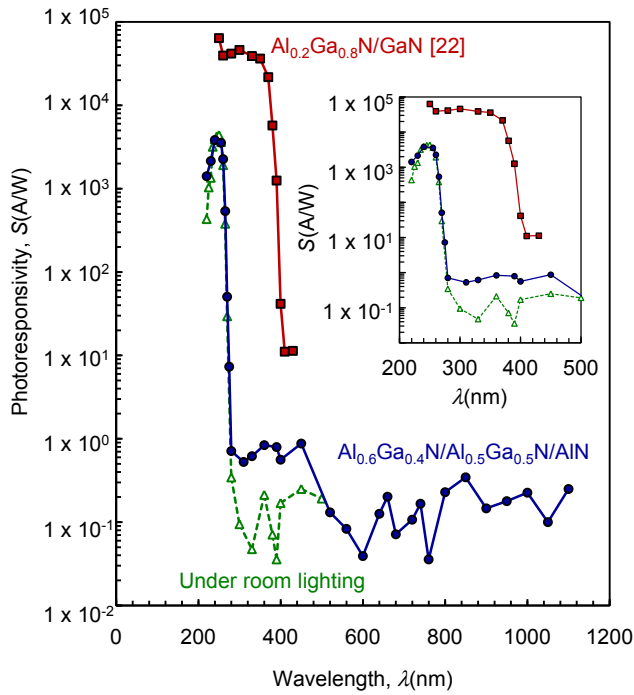


**Fig. 3.** (Color online) Relationship between the photosensitivity with a  $V_{SD}$  of 3 V and the wavelength of irradiating light. The inset is focused between 200 and 500 nm. The circular plots show the photosensitivity of  $Al_{0.6}Ga_{0.4}N/Al_{0.5}Ga_{0.5}N$ -HFET with a  $V_{SD}$  of 3 V. The triangular plots refer to  $Al_{0.6}Ga_{0.4}N/Al_{0.5}Ga_{0.5}N$ -HFET with a  $V_{SD}$  of 3 V under room lighting conditions. The square plots refer to  $Al_{0.2}Ga_{0.8}N/GaN$ -HFET with a  $V_{SD}$  of 5 V.

were almost non-responsive to sunlight. However, they were capable of detecting very weak light with a wavelength of 250 nm. Therefore, this device is a completely solar-blind UV sensor.

Figure 3 shows the monochromatic photosensitivity of HFET-type photosensors from 200 to 1100 nm. The circular plots show the photosensitivity of  $Al_{0.6}Ga_{0.4}N/Al_{0.5}Ga_{0.5}N$ -HFET (with an operating voltage of 3 V between the source and the drain) obtained using a Xe lamp and a spectrometer. The photosensors can achieve a high external photosensitivity exceeding  $10^3$  A/W. The inset in Fig. 3 is focused between 200 and 500 nm. The absorption edge and peak photosensitivity wavelengths of the photosensors were approximately 280 and 250 nm, respectively. The rejection ratio of the photosensors was greater than  $10^4$ .

The triangular plots show the photosensitivity under room lighting conditions. Almost identical absorption edge and peak photosensitivity was obtained. In contrast, for the darkroom measurement, little absorption was observed between 280 and 450 nm, compared with that between 520 and 1100 nm for room lighting measurements. This absorption may be caused by the p-GaN layer.

The square plots show the photosensitivity of  $Al_{0.2}Ga_{0.8}N/GaN$ -HFET obtained at  $V_{SD} = 5$  V.<sup>22)</sup> The absorption edge and peak photosensitivity wavelengths of the photosensors were approximately 410 and 300 nm, respectively. The photocurrent and dark current are higher compared with those of  $Al_{0.6}Ga_{0.4}N/Al_{0.5}Ga_{0.5}N$ -HFET. From simulation results (SiLENSe), we determined the sheet carrier density of  $Al_{0.6}Ga_{0.4}N/Al_{0.5}Ga_{0.5}N$ -HFET to be  $1 \times 10^6$  cm<sup>-2</sup>, while it was  $3 \times 10^{12}$  cm<sup>-2</sup> for  $Al_{0.2}Ga_{0.8}N/GaN$ . Therefore, we

**Table I.** Photosensitivity of a Si UV sensor, a photoelectric tube, a Si photodiode, a GaN UV sensor, a photomultiplier tube, and the photosensor used in this study.

	Peak wavelength (nm)	Photosensitivity (A/W)
This work	250	$3 \times 10^3$
Si UV sensor	254	$3 \times 10^{-2}$
Photoelectric tube	254	$2 \times 10^{-2}$
GaN photodiode	254	$6 \times 10^{-2}$
Photomultiplier tube	400	$2 \times 10^5$

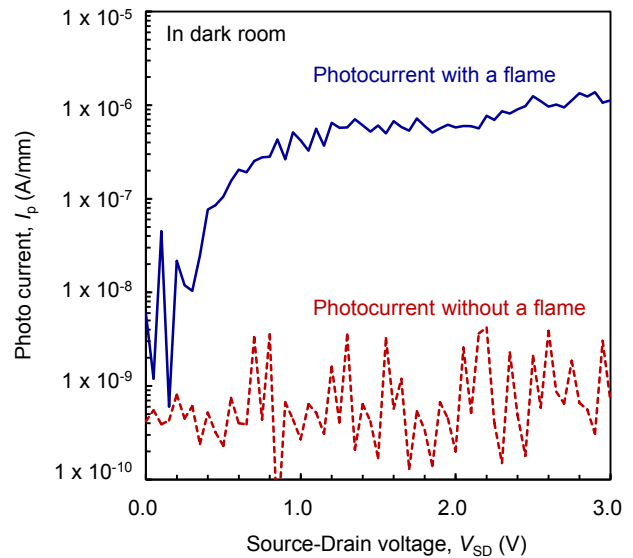


**Fig. 4.** (Color online)  $I_{SD}$ - $V_{SD}$  characteristics of the  $Al_{0.6}Ga_{0.4}N/Al_{0.5}Ga_{0.5}N$ -HFET photosensors at RT under a  $V_{SD}$  that varied from 0 to 3 V with flame irradiation from a Bunsen burner.

speculate that these results were caused by the difference in the carrier concentration of 2DEG.

From the above, these results indicate that the absorption edge and peak photosensitivity wavelengths of the photosensors were controlled by the AlN molar fraction of the AlGaN channel layer. In addition, the photocurrent and dark current is probably adjustable by altering the AlN molar fraction and the thickness of the AlGaN barrier layer.

We also compared the photosensitivity of the photosensors with those of commercially available photosensors. Table I shows the monochromatic photosensitivity of each photosensor. From this table, the photosensors used in this study possessing photosensitivity that is superior to those of a Si UV sensor (KYOSEMI KPDU400F-2), a photoelectric tube (Hamamatsu Photonics R765), a Si photodiode (Hamamatsu Photonics S1087), and a GaN photodiode (KYOSEMI KPDU27HQ1). Moreover, the results imply that the photosensors used in this study have a photosensitivity that is equivalent to that of photomultiplier tubes.

We also investigated the performance of the photosensors as flame sensors. The photocurrent was measured in a darkroom, under room lighting conditions, and at 1 sun (AM 1.5G) using a parameter analyzer both with a flame and without a flame. The result in a dark room is shown in Fig. 4. Table II summarizes the results for the photocurrent with and without a flame, respectively. For all conditions, a sensitivity

**Table II.** Photocurrent of HFET when  $V_{SD}$  was 3 V both with and without a flame.

	Photocurrent (A/mm)	
	with a flame	without a flame
Darkroom	$1.12 \times 10^{-7}$	$9.98 \times 10^{-10}$
Under room lighting	$1.34 \times 10^{-7}$	$5.68 \times 10^{-10}$
Under 1 sun (AM 1.5G)	$1.09 \times 10^{-7}$	$1.06 \times 10^{-9}$

to noise (S/N) of over  $10^2$  was obtained. These results indicate that the photosensors can be used as a flame sensor under practical environmental conditions.

#### 4. Summary and conclusion

We fabricated high-performance  $\text{Al}_{0.6}\text{Ga}_{0.4}\text{N}/\text{Al}_{0.5}\text{Ga}_{0.5}\text{N}$ -HFET-type photosensors on AlN for the detection of 220 to 280 nm wavelengths. It was shown that the AlN molar fraction of the AlGa<sub>x</sub>N channel layer is the key to controlling the detection wavelength. The measured photosensitivity of  $3.4 \times 10^3$  A/W greatly surpasses those of commercially available photosensors and is comparable with those of photomultiplier tubes. These photosensors are completely solar-blind and exhibit high performance as a flame sensor under both room lighting conditions and 1 sun (AM 1.5G).

#### Acknowledgments

This study was partially supported by the Program for the Strategic Research Foundation at Private Universities, 2012–2016, supported by the MEXT, a MEXT Grant-in-Aid for Specially Promoted Research No. 25000011, and the MEXT Grant-in-Aid for Scientific Research A No. 15H02019. The authors would like to thank Ph.D. T. Morishita, T. Okumura, and S. Ushida for discussions and advice.

- 1) Y. Ohki, Y. Toyoda, H. Kobayashi, and I. Akasaki, *Jpn. J. Appl. Phys.* **28**, L2112 (1989).
- 2) S. Nakamura, M. Senoh, and T. Mukai, *Jpn. J. Appl. Phys.* **32**, L8 (1993).
- 3) T. Mukai, H. Narimatsu, and S. Nakamura, *Jpn. J. Appl. Phys.* **37**, L479

- (1998).
- 4) V. Adivarahan, W. H. Sun, A. Chitnis, M. Shatalov, S. Wu, H. P. Maruska, and M. Asif Khan, *Appl. Phys. Lett.* **85**, 2175 (2004).
- 5) I. Akasaki, S. Sota, H. Sakai, T. Tanaka, M. Koike, and H. Amano, *Electron. Lett.* **32**, 1105 (1996).
- 6) S. Nakamura, M. Senoh, S. Nagahama, N. Iwasa, T. Yamada, T. Matsushita, H. Kiyoku, and Y. Sugimoto, *Jpn. J. Appl. Phys.* **35**, L74 (1996).
- 7) B. Monemar, *Phys. Rev. B* **10**, 676 (1974).
- 8) H. Yamashita, K. Fukui, S. Misawa, and S. Yoshida, *J. Appl. Phys.* **50**, 896 (1979).
- 9) D. Walker, X. Zhang, P. Kung, A. Saxler, S. Javadpour, J. Xu, and M. Razeghi, *Appl. Phys. Lett.* **68**, 2100 (1996).
- 10) B. W. Lim, Q. C. Chen, J. Y. Yangand, and M. Asif Khan, *Appl. Phys. Lett.* **68**, 3761 (1996).
- 11) C. Pernot, A. Hirano, M. Iwaya, T. Detchprohm, H. Amano, and I. Akasaki, *Jpn. J. Appl. Phys.* **38**, L487 (1999).
- 12) C. Pernot, A. Hirano, M. Iwaya, T. Detchprohm, H. Amano, and I. Akasaki, *Jpn. J. Appl. Phys.* **39**, L387 (2000).
- 13) H. Jiang, T. Egawa, H. Ishikawa, C. Shao, and T. Jimbo, *Jpn. J. Appl. Phys.* **43**, L683 (2004).
- 14) M. Ippommatsu, *Optronics* **2**, 71 (2014).
- 15) M. Shatalov, W. Sun, A. Lunev, X. Hu, A. Dobrinsky, Y. Bilenko, and J. Yang, *Appl. Phys. Express* **5**, 082101 (2012).
- 16) S. Inoue, N. Tamari, T. Kinoshita, T. Obata, and H. Yanagi, *Appl. Phys. Lett.* **106**, 131104 (2015).
- 17) J. R. Grandusky, J. Chen, S. R. Gibb, M. C. Mendrick, C. G. Moe, L. Rodak, G. A. Garrett, M. Wraback, and L. J. Schowalter, *Appl. Phys. Express* **6**, 032101 (2013).
- 18) H. Hirayama, N. Maeda, S. Fujikawa, S. Toyoda, and N. Kamata, *Jpn. J. Appl. Phys.* **53**, 100209 (2014).
- 19) M. Razeghi and A. Rogalski, *J. Appl. Phys.* **79**, 7433 (1996).
- 20) A. Haapalinna, P. Kärhä, and E. Ikonen, *Appl. Opt.* **37**, 729 (1998).
- 21) Hamamatsu Photonics K.K. [<http://www.hamamatsu.com/>].
- 22) M. Iwaya, S. Miura, T. Fujii, S. Kamiyama, H. Amano, and I. Akasaki, *Phys. Status Solidi C* **6**, S972 (2009).
- 23) M. Ishiguro, K. Ikeda, M. Mizuno, M. Iwaya, T. Takeuchi, S. Kamiyama, and I. Akasaki, *Jpn. J. Appl. Phys.* **52**, 08JF02 (2013).
- 24) J. R. Creighton, *J. Electron. Mater.* **31**, 1337 (2002).
- 25) A. Kumar, G. Iyer, and A. Subramaniam, *Phys. Status Solidi C* **12**, 399 (2015).
- 26) S. G. Mueller, R. T. Bondokov, K. E. Morgan, G. A. Slack, S. B. Schujman, J. Grandusky, J. A. Smart, and L. J. Schowalter, *Phys. Status Solidi A* **206**, 1153 (2009).
- 27) P. Kung, A. Saxler, X. Zhang, D. Walker, T. C. Wang, I. Ferguson, and M. Razeghi, *Appl. Phys. Lett.* **66**, 2958 (1995).
- 28) M. Akita, S. Hashimoto, Y. Yamamoto, H. Tokuda, M. Kuzuhara, M. Iwaya, and H. Amano, *SEI Tech. Rev.* **180**, 83 (2012) [in Japanese].
- 29) M. Imura, K. Nakano, T. Kitano, N. Fujimoto, N. Okada, K. Balakrishnan, M. Iwaya, S. Kamiyama, H. Amano, I. Akasaki, K. Shimono, T. Noro, T. Takagi, and A. Bandoh, *Phys. Status Solidi A* **203**, 1626 (2006).

## Correlation between Device Performance and Defects in GaInN-Based Solar Cells

This content has been downloaded from IOPscience. Please scroll down to see the full text.

2012 Appl. Phys. Express 5 082301

(<http://iopscience.iop.org/1882-0786/5/8/082301>)

View [the table of contents for this issue](#), or go to the [journal homepage](#) for more

Download details:

IP Address: 202.11.1.201

This content was downloaded on 03/03/2017 at 07:02

Please note that [terms and conditions apply](#).

You may also be interested in:

[GaInN-Based Solar Cells Using Strained-Layer GaInN/GaN Superlattice Active Layer on a Freestanding GaN Substrate](#)

Yousuke Kuwahara, Takahiro Fujii, Toru Sugiyama et al.

[Concentrating Properties of Nitride-Based Solar Cells Using Different Electrodes](#)

Mikiko Mori, Shinichiro Kondo, Shota Yamamoto et al.

[Microstructures of GaInN/GaN Superlattices on GaN Substrates](#)

Toru Sugiyama, Yosuke Kuwahara, Yasuhiro Isobe et al.

[Realization of Nitride-Based Solar Cell on Freestanding GaN Substrate](#)

Yosuke Kuwahara, Takahiro Fujii, Yasuharu Fujiyama et al.

[Microstructure Analysis of AlGaIn on AlN Underlying Layers with Different Threading Dislocation Densities](#)

Kimiyasu Ide, Yuko Matsubara, Motoaki Iwaya et al.

[InGaIn/GaN Multiple Quantum Well Solar Cells with Good Open-Circuit Voltage and Concentrator Action](#)

Xue-Fei Li, Xin-He Zheng, Dong-Yan Zhang et al.

[Barrier Thickness Dependence of Photovoltaic Characteristics of InGaIn/GaN Multiple Quantum Well Solar Cells](#)

Noriyuki Watanabe, Haruki Yokoyama, Naoteru Shigekawa et al.

[Progress and Prospect of the Growth of Wide-Band-Gap Group III Nitrides: Development of the Growth Method for Single-Crystal Bulk GaN](#)

Hiroshi Amano

## Correlation between Device Performance and Defects in GaInN-Based Solar Cells

Mikiko Mori<sup>1\*</sup>, Shinichiro Kondo<sup>1</sup>, Shota Yamamoto<sup>1</sup>, Tatsuro Nakao<sup>1</sup>, Takahiro Fujii<sup>1</sup>, Motoaki Iwaya<sup>1</sup>, Tetsuya Takeuchi<sup>1</sup>, Satoshi Kamiyama<sup>1</sup>, Isamu Akasaki<sup>1,3</sup>, and Hiroshi Amano<sup>2,3</sup>

<sup>1</sup>Faculty of Science and Technology, Meijo University, Nagoya 468-8502, Japan

<sup>2</sup>Graduate School of Engineering, Nagoya University, Nagoya 464-8603, Japan

<sup>3</sup>Akasaki Research Center, Nagoya University, Nagoya 464-8603, Japan

Received June 20, 2012; accepted June 26, 2012; published online July 13, 2012

We investigated the correlation between the device performance and defects, such as V-shaped pits and threading dislocations, in GaInN-based solar cells. To realize high-performance GaInN-based solar cells with a high open-circuit voltage and fill factor, it is essential to realize a low pit density of less than  $10^7 \text{ cm}^{-2}$ . In this study, we were unable to observe clear evidence of any effect of the threading dislocation density in the GaN underlying layer. © 2012 The Japan Society of Applied Physics

**N**itride semiconductor material systems including AlN, GaN, InN, and their alloys are widely used as light-emitting diodes (LEDs) and laser diodes. Since the bandgap of GaInN ternary alloys covers a broad range from 0.65 to 3.43 eV, these alloys are suitable for solar cell applications.<sup>1)</sup> Using a combination of GaInN alloys, one may theoretically design a multijunction photovoltaic device with a bandgap spanning the infrared to ultraviolet regions of the solar spectrum. This makes it possible to achieve high-efficiency multijunction solar cells.<sup>2)</sup>

So far, we have succeeded in fabricating GaInN-based solar cells.<sup>3–7)</sup> By improving the crystal quality of GaInN using freestanding *c*-plane GaN substrates<sup>3)</sup> and applying GaInN superlattice (SL) structures,<sup>4)</sup> the conversion efficiency has been improved.

In general, GaN films on sapphire substrates covered with a low-temperature buffer layer<sup>8,9)</sup> have a high density of threading dislocations ranging from  $10^8$  to  $10^{10} \text{ cm}^{-2}$ . In contrast, GaN substrates grown by hydride vapor phase epitaxy<sup>10)</sup> with a low dislocation density of  $10^5$  to  $10^7 \text{ cm}^{-2}$  are commercially available. In addition, GaInN films exceeding the critical thickness on a GaN template have been reported to induce the generation of misfit dislocations and the growth of V-shaped pits.<sup>11)</sup> There have been many reports discussing the correlation between device performance and crystal defects in GaInN-based LEDs, laser diodes, and so forth. For instance, because dislocations act as nonradiative recombination centers, reducing the dislocation density in GaN is very important for the realization of high-efficiency nitride-based LEDs.<sup>12,13)</sup> In addition, it has been reported that dislocations have a strong impact on the device lifetime of violet laser diodes.<sup>14)</sup> The impact of V-shaped pits and misfit dislocations on the performances of LEDs and laser diodes have also been reported.<sup>15,16)</sup>

In contrast, we reported that the leakage current in GaInN-based solar cells increases with increasing density of V-shaped pits in the devices.<sup>3)</sup> However, there have been few reports discussing the correlation between device performance and the density of defects such as dislocations and V-shaped pits in GaInN-based solar cells. Understanding the factors limiting the performance of such devices is essential for realizing high-performance GaInN-based solar cells. In this study, we investigated the correlation between the device performance and defects in GaInN-based solar cells.

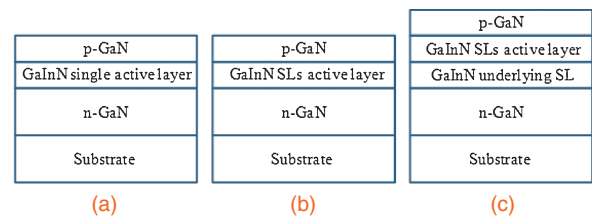


**Fig. 1.** Schematic view of the sample structures of nitride-based solar cells: (a) type I, (b) type II, and (c) type III.

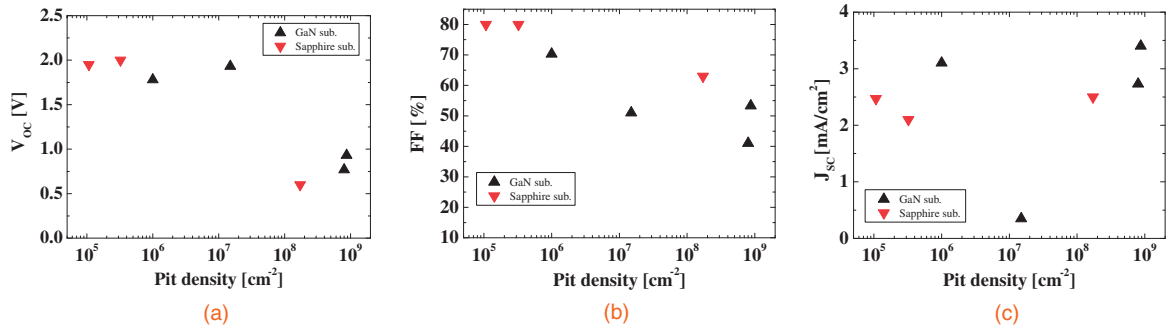
All samples were grown by metalorganic vapor phase epitaxy. *c*-Plane sapphire and freestanding *c*-plane GaN were used as the substrates. In the case of the sapphire substrate, GaN underlying layers were grown using a low-temperature buffer layer. The threading dislocation densities of GaN on sapphire and freestanding GaN substrates are approximately  $3 \times 10^8$  and less than  $10^7 \text{ cm}^{-2}$ , respectively. Trimethylindium, trimethylaluminum, trimethylgallium, triethylgallium, and ammonia were used as the source gases. Figures 1(a)–1(c) show schematic views of the sample structures. We prepared three types of samples on freestanding GaN and sapphire substrates. In the type I samples [Fig. 1(a)], a single GaInN active layer was used as an active layer. In the type II samples [Fig. 1(b)], GaInN-based SLs were used as an active layer. In the type III samples [Fig. 1(c)], to suppress the formation of pits and the threading of misfit dislocations,<sup>17)</sup> we used thick GaInN-based SLs as the active region instead of GaInN SLs (underlying SLs). Table I summarizes the detailed structure of the GaInN active layer and substrate of each sample. Pits with a diameter of more than  $50 \text{ nm}\phi$  were counted when determining the pit density using plan-view scanning electron microscope images. The thickness and InN molar fraction in the GaInN active layer were determined by X-ray diffraction  $2\theta/\omega$  scans of (0002) and (20 $\bar{2}$ 4) diffractions. We also confirmed the thickness of each layer in some samples by cross-sectional transmission electron microscopy. The density of V-shaped pits ranged from  $1.1 \times 10^5$  to  $8.8 \times 10^8 \text{ cm}^{-2}$  as shown in Table I. The threading dislocation density also ranged over two orders of magnitude from  $10^7$  to  $10^9 \text{ cm}^{-2}$ .

Semitransparent Ni (5 nm)/Au (5 nm) ohmic contacts to p-GaN and Ti/Al/Ti/Au ohmic contacts to n-GaN were formed by electron beam evaporation. No antireflection coating was used for all the devices. The solar cell characteristics were analyzed using a solar simulator (air mass 1.5G, irradiation strength  $155 \text{ mW/cm}^2$ ). All measurements were carried out at room temperature (RT).

\*E-mail address: 113434038@ccalumni.meijo-u.ac.jp

**Table I.** Device structure parameters of GaInN-based solar cells on sapphire and GaN substrates. In this table, the pit density of each sample is also given.

Sample No.	Substrate	Underlying SL	Active layer	Pit density (cm <sup>-2</sup> )
1	GaN	None	Ga <sub>0.88</sub> In <sub>0.12</sub> N single layer (200 nm)	8.0 × 10 <sup>8</sup>
2	GaN	None	50 pairs Ga <sub>0.83</sub> In <sub>0.17</sub> N (3 nm) / Ga <sub>0.93</sub> In <sub>0.07</sub> N (0.6 nm) SLs	8.7 × 10 <sup>8</sup>
3	GaN	None	50 pairs Ga <sub>0.83</sub> In <sub>0.17</sub> N (3 nm) / Ga <sub>0.93</sub> In <sub>0.07</sub> N (3 nm) SLs	1.5 × 10 <sup>7</sup>
4	GaN	10 pairs Ga <sub>0.90</sub> In <sub>0.10</sub> N: Si (3 nm) / GaN: Si (3 nm) SLs	50 pairs Ga <sub>0.83</sub> In <sub>0.17</sub> N (3 nm) / Ga <sub>0.93</sub> In <sub>0.07</sub> N (0.6 nm) SLs	1.0 × 10 <sup>6</sup>
5	Sapphire	10 pairs Ga <sub>0.92</sub> In <sub>0.08</sub> N: Si (1.8 nm) / GaN: Si (2.2 nm) SLs	30 pairs Ga <sub>0.90</sub> In <sub>0.10</sub> N (3 nm) / Ga <sub>0.90</sub> In <sub>0.10</sub> N (0.6 nm) SLs	3.2 × 10 <sup>5</sup>
6	Sapphire	10 pairs Ga <sub>0.90</sub> In <sub>0.10</sub> N: Si (2.2 nm) / Ga <sub>0.95</sub> In <sub>0.05</sub> N: Si (2.2 nm) SLs + 10 pairs Ga <sub>0.94</sub> In <sub>0.06</sub> N: Si (1.8 nm) / GaN: Si (2.2 nm) SLs	50 pairs Ga <sub>0.82</sub> In <sub>0.18</sub> N (3 nm) / Ga <sub>0.88</sub> In <sub>0.12</sub> N (0.6 nm) SLs	1.7 × 10 <sup>8</sup>
7	Sapphire	10 pairs Ga <sub>0.94</sub> In <sub>0.06</sub> N: Si (2.2 nm) / GaN: Si (1.8 nm) SLs	30 pairs Ga <sub>0.88</sub> In <sub>0.12</sub> N (3 nm) / Ga <sub>0.93</sub> In <sub>0.07</sub> N (0.6 nm) SLs	1.1 × 10 <sup>5</sup>


**Fig. 2.** (a)  $V_{OC}$  of GaInN-based solar cells as a function of pit density. (b) FF as a function of pit density. (c)  $J_{SC}$  as a function of pit density.

Figures 2(a)–2(c) show the open-circuit voltage ( $V_{OC}$ ), fill factor (FF), and short-circuit current density ( $J_{SC}$ ) of the GaInN-based solar cells on freestanding GaN and sapphire substrates as a function of the pit density at the surface. From these figures,  $J_{SC}$  was found to be independent of the pit density. In contrast, there is a significant dependence of  $V_{OC}$  and FF on the pit density. No significant difference was found between  $J_{SC}$ ,  $V_{OC}$ , and FF for the samples grown on GaN and those grown on sapphire substrates, meaning that these characteristics are not affected by the threading dislocation density in the underlying layer.

Figures 3(a)–3(c) summarize the leakage current density ( $J_{leak}$ ) at a reverse bias voltage of  $-3$  V, the shunt resistance ( $R_{SH}$ ), and the series resistance ( $R_S$ ), respectively, of each sample as a function of pit density. We calculated  $R_S$  and  $R_{SH}$  from the slope of the  $I$ - $V$  curves.<sup>18)</sup> From these results,  $J_{leak}$  and  $R_{SH}$  were found to be strongly dependent on the pit density. In Fig. 3(a), the results for  $J_{leak}$  are fitted to the formula

$$J_{leak} = 4 \times 10^{-8} \sqrt{D_p}, \quad (1)$$

where  $D_p$  and  $4 \times 10^{-8}$  A/cm are the pit density and fitting parameter, respectively, as shown by the blue dotted line in Fig. 3(a). There have been several reports that suggest that the origin of the leakage current in an LED structure is related to V-shaped pits, although the carrier conduction mechanism is still unclear at present.<sup>19,20)</sup> In this experiment,

$J_{leak}$  exhibits sublinear dependence on the pit density and is almost proportional to the square root of  $D_p$ . Because  $R_{SH}$  should be expressed as the reverse bias voltage divided by  $J_{leak}$ , in Fig. 3(b) we inserted the theoretical line (blue dotted line) given by

$$R_{SH} = \frac{V_R}{J_{leak}} = \frac{V_R}{4 \times 10^{-8} \sqrt{D_p}}. \quad (2)$$

In this case,  $V_R$  is the reverse bias voltage of  $-3$  V. In this figure, the fitting curve closely matches the experimental results. From Figs. 2(a), 2(b), and 3(b),  $R_{SH}$  should exceed  $10^4 \Omega \text{cm}^2$  and  $D_p$  should be less than  $10^7 \text{cm}^{-2}$  to obtain suitable values of  $V_{OC}$  and FF.

Next, we compared these results with the solar cell characteristics of other material systems. Table II summarizes  $R_{SH}$ ,  $V_{OC}$ , and the bandgap of each material in refs. 21–23. According to this table, to realize a high  $V_{OC}$  in a GaInN-based solar cell,  $R_{SH}$  should be one to two orders of magnitude higher than that in the other material systems.

Note that  $V_{OC}$  is defined by the formula<sup>24)</sup>

$$V_{OC} = \frac{nk_B T}{q} \ln \left[ \frac{I_{ph} - (V_{OC}/R_{SH})}{I_0} + 1 \right], \quad (3)$$

where  $n$ ,  $k_B$ ,  $T$ ,  $I_{ph}$ , and  $I_0$  are the nonideality factor, Boltzmann constant, absolute temperature, photocurrent, and reverse saturation current, respectively. From this formula,  $V_{OC}$  is significantly dependent on  $R_{SH}$ . In contrast, there was no

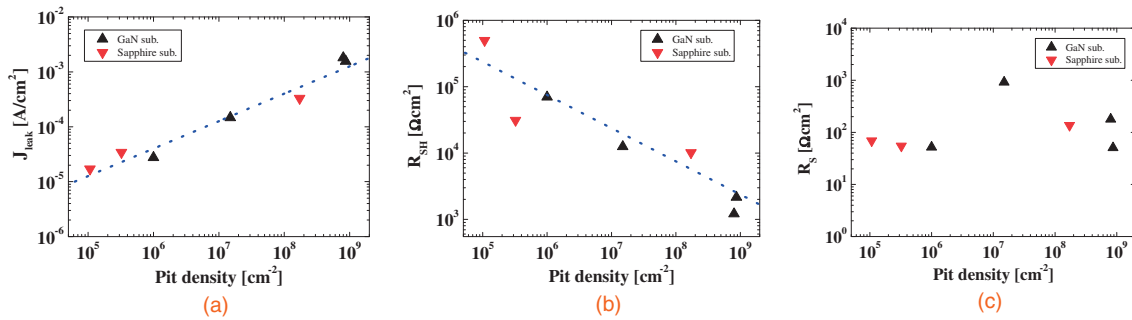


**Fig. 3.** (a)  $J_{\text{leak}}$  of GaInN-based solar cells at a reverse bias voltage of  $-3$  V as a function of pit density. (b)  $R_{\text{SH}}$  as a function of pit density. (c)  $R_{\text{S}}$  as a function of pit density.

**Table II.**  $R_{\text{SH}}$ ,  $V_{\text{OC}}$ , and bandgap of each material in this study and in refs. 21–23.

Material system	Bandgap energy (eV)	$R_{\text{SH}}$ ( $\Omega \text{ cm}^2$ )	$V_{\text{OC}}$ (V)
$\text{Si}^{21)}$	1.12	$6.7 \times 10^2$	0.56
$\text{GaInP}^{22)}$	1.96	$1.1 \times 10^2$	1.33
$\text{CdS/CdTe}^{23)}$	1.4	$1 \times 10^3$	0.84
GaInN	2.8	$7 \times 10^5$	1.95
	2.8	$1 \times 10^4$	1.8
	2.8	$2.15 \times 10^3$	0.93

correlation between  $R_{\text{S}}$  and pit density as shown in Fig. 3(c). In general, considering the equivalent circuit model of a solar cell under illumination, the resistive component is expressed as<sup>22)</sup>

$$I = I_{\text{ph}} - I_0 \left\{ \exp \left[ \frac{q(V + R_{\text{S}}I)}{nk_{\text{B}}T} \right] - 1 \right\} - \frac{V + R_{\text{S}}I}{R_{\text{SH}}}, \quad (4)$$

where  $I_0$  is the reverse saturation current. Equation (4) shows that  $J_{\text{SC}}$  was strongly affected by the value of  $R_{\text{S}}$ . Therefore,  $J_{\text{SC}}$  is independent of the pit density.

In conclusion, we investigated the correlation between the device performance and defects in GaInN-based solar cells. To realize high-performance GaInN-based solar cells with a high  $V_{\text{OC}}$  and FF, it is essential to realize a low  $D_{\text{p}}$  and high  $R_{\text{SH}}$ , which should be lower than  $10^7 \text{ cm}^{-2}$  and exceed  $10^4 \Omega \text{ cm}^2$ , respectively. In contrast, no significant correlation could be confirmed between these device performances and the threading dislocation density in the GaN underlying layer. Therefore, reduction of the pit density is essential for the realization of high-performance GaInN-based solar cells.

**Acknowledgments** This study was partially supported by the New Energy and Industrial Technology Development Organization (NEDO) Project, “Research and Development on Innovative Solar Cells” and the Program for the Strategic Research Foundation at Private Universities, 2012–2016, supported by the Ministry of Education, Culture, Sports, Science and Technology.

1) V. Y. Davydov, A. A. Klochikhin, R. P. Seisyan, V. V. Emtsev, S. V. Ivanov, F. Bechstedt, J. Furthmüller, H. Harima, A. V. Mudryi, J. Aderhold, O. Semchinova, and J. Graul: *Phys. Status Solidi B* **229** (2002) r1.

2) H. Hamzaoui, A. S. Bouazzi, and B. Rezig: *Sol. Energy Mater. Sol. Cells* **87** (2005) 595.  
 3) Y. Kuwahara, T. Fujii, Y. Fujiyama, T. Sugiyama, M. Iwaya, T. Takeuchi, S. Kamiyama, I. Akasaki, and H. Amano: *Appl. Phys. Express* **3** (2010) 111001.  
 4) Y. Kuwahara, T. Fujii, T. Sugiyama, D. Iida, Y. Isobe, Y. Fujiyama, Y. Morita, M. Iwaya, T. Takeuchi, S. Kamiyama, I. Akasaki, and H. Amano: *Appl. Phys. Express* **4** (2011) 021001.  
 5) T. Nakao, T. Fujii, T. Sugiyama, S. Yamamoto, D. Iida, M. Iwaya, T. Takeuchi, S. Kamiyama, I. Akasaki, and H. Amano: *Appl. Phys. Express* **4** (2011) 101001.  
 6) S. Yamamoto, M. Mori, Y. Kuwahara, T. Fujii, T. Nakao, S. Kondo, M. Iwaya, T. Takeuchi, S. Kamiyama, I. Akasaki, and H. Amano: *Phys. Status Solidi: Rapid Res. Lett.* **6** (2012) 145.  
 7) Y. Kuwahara, Y. Fujiyama, M. Iwaya, S. Kamiyama, H. Amano, and I. Akasaki: *Phys. Status Solidi C* **7** (2010) 1807.  
 8) H. Amano, N. Sawaki, I. Akasaki, and Y. Toyoda: *Appl. Phys. Lett.* **48** (1986) 353.  
 9) I. Akasaki and H. Amano: *Jpn. J. Appl. Phys.* **45** (2006) 9001.  
 10) A. Usui, H. Sunakawa, A. Sakai, and A. A. Yamaguchi: *Jpn. J. Appl. Phys.* **36** (1997) L899.  
 11) R. Liu, J. Mei, S. Srinivasan, H. Omiya, F. A. Ponce, D. Cherns, Y. Narukawa, and T. Mukai: *Jpn. J. Appl. Phys.* **45** (2006) L549.  
 12) H. Amano, A. Miyazaki, K. Iida, T. Kawashima, M. Iwaya, S. Kamiyama, I. Akasaki, R. Liu, A. Bell, F. A. Ponce, S. Sahonta, and D. Cherns: *Phys. Status Solidi A* **201** (2004) 2679.  
 13) Q. Dai, M. F. Schubert, M. H. Kim, J. K. Kim, E. F. Schubert, D. D. Koleske, M. H. Crawford, S. R. Lee, A. J. Fischer, G. Thaler, and M. A. Banas: *Appl. Phys. Lett.* **94** (2009) 111109.  
 14) S. Nakamura, M. Senoh, S. Nagahama, N. Iwasa, T. Yamada, T. Matushita, H. Kiyoku, Y. Sugimoto, T. Kozaki, H. Umemoto, M. Sano, and K. Chocho: *Jpn. J. Appl. Phys.* **36** (1997) L1568.  
 15) S. W. Lee, D. C. Oh, H. Goto, J. S. Ha, H. J. Lee, T. Hanada, M. W. Cho, T. Yao, S. K. Hong, H. Y. Lee, S. R. Cho, J. W. Choi, J. H. Choi, J. H. Jang, J. E. Shin, and J. S. Lee: *Appl. Phys. Lett.* **89** (2006) 132117.  
 16) M. Ohta, Y. Ohizumi, Y. Hoshina, T. Tanaka, Y. Yabuki, K. Funato, S. Tomiya, S. Goto, and M. Ikeda: *Phys. Status Solidi A* **204** (2007) 2068.  
 17) T. Sugiyama, Y. Kuwahara, Y. Isobe, T. Fujii, K. Nonaka, M. Iwaya, T. Takeuchi, S. Kamiyama, I. Akasaki, and H. Amano: *Appl. Phys. Express* **4** (2011) 015701.  
 18) R. Sahai and A. G. Milnes: *Solid-State Electron.* **13** (1970) 1289.  
 19) K. Koike, S. Lee, S. R. Cho, J. Park, H. Lee, J. S. Ha, S. K. Hong, H. Y. Lee, M. W. Cho, and T. Yao: *IEEE Photonics Technol. Lett.* **24** (2012) 449.  
 20) K. C. Shen, D. S. Wu, C. C. Shen, S. L. Ou, and R. H. Horng: *J. Electrochem. Soc.* **158** (2011) H988.  
 21) A. Gordijn, J. K. Rath, and R. E. I. Schropp: *Prog. Photovoltaics* **14** (2006) 305.  
 22) Y. Chang, Z. Li, H. Kuo, T. Lu, S. Yang, L. Lai, L. Lai, and S. Wang: *Semicond. Sci. Technol.* **24** (2009) 085007.  
 23) J. Britt and C. Ferekides: *Appl. Phys. Lett.* **62** (1993) 2851.  
 24) J. Nelson: *The Physics of Solar Cells* (Imperial College Press, London, 2003).